Alien hunters make their biggest push yet p. 1288

New books, fresh for fall p. 1292

The great seismic noise quiet period pp. 1299 & 1338

Science

$15
11 SEPTEMBER 2020
sciencemag.org

AAAS

SPECIAL ISSUE

GENETIC VARIATION

Dissection of tissue-specific traits

CONTENTS

11 SEPTEMBER 2020 • VOLUME 369 • ISSUE 6509

1288
A Fresnel lens could capture the flash of an alien laser.

PHOTO: FRANK ROGOZIENSKI

NEWS

IN BRIEF

1278 News at a glance

IN DEPTH

1280 Why obesity worsens COVID-19
Even people in the overweight category face higher risk of serious disease
By M. Wadman

1282 Speaking science to power
A young disease modeling expert has found her voice during the pandemic *By K. Servick*

1283 Narrow path charted for editing genes of human embryos
Panel outlines most justifiable uses if safety is ensured *By J. Cohen*

1284 Indigenous Alaskans demand a voice in research on warming
NSF program struggles to bridge scientists and communities
By R. Stone

1285 Census experts fear rush to finish tally will yield flawed data
Mounting fears of massive U.S. undercount spur push for independent oversight, more time to complete 2020 count *By J. Mervis*

1286 Massive project reveals complexity of gene regulation
Data from tissues around the body boost search for genetic basis of disease *By E. Pennisi*
GENETIC VARIATION SECTION p. 1316

FEATURES

1288 Listen up
Flush with money and a hard-won respectability, alien hunters are deploying new telescopes and tactics *By D. Clery*
PODCAST

INSIGHTS

BOOKS *ET AL.*

1292 A reading list for uncertain times

PERSPECTIVES

1298 Searching for sex differences
Evolved sex differences in gene expression are pervasive, but so too is sampling bias
By M. A. Wilson
GENETIC VARIATION SECTION P. 1316; LETTER P. 1313

1299 Quiet Anthropocene, quiet Earth
Seismic noise levels that correlate with human activities fell when pandemic lockdown measures were imposed
By M. A. Denolle and T. Nissen-Meyer
REPORT p. 1338

1300 A key piece of the ferroelectric hafnia puzzle
Dipolar slices explain the origin of ferroelectricity in a material now used for memory devices
By B. Noheda and J. Íñiguez
REPORT p. 1343

1302 Modulating gut microbes
Fecal microbiota transplant and modulation of microbial species show therapeutic promise
By J. A. Wargo

1304 Laser cooling of larger quantum objects
A nonlinear polyatomic molecule, $CaOCH_3$, has been laser-cooled to below 1 millikelvin *By E. R. Hudson*
REPORT p. 1366

1305 Reactive polymers guide nanoparticle clustering
Tailored polymer shells drive the assembly of a desired class of nanoparticle architectures
By O. Gang
REPORT p. 1369

1306 Coronavirus dons a new crown
A transmembrane pore reveals parallels with other viruses
By N. Unchwaniwala and P. Ahlquist
REPORT p. 1395

Published by AAAS

SPECIAL SECTION

GENETIC VARIATION

INTRODUCTION

1316 The custom transcriptome

RESEARCH

1318 The GTEx Consortium atlas of genetic regulatory effects across human tissues *GTEx Consortium*

1331 The impact of sex on gene expression across human tissues *M. Oliva* et al.

1332 Cell type–specific genetic regulation of gene expression across human tissues *S. Kim-Hellmuth* et al.

1333 Determinants of telomere length across human tissues *K. Demanelis* et al.
PODCAST

1334 Transcriptomic signatures across human tissues identify functional rare genetic variation *N. M. Ferraro* et al.

ON THE COVER

Genetic variation among individuals affects the transcriptome differently. Here, heatmaps of differential gene expression are shown within individual bodies to visualize the results obtained by the Genotype-Tissue Expression (GTEx) Project. This special issue presents research from the final phase of the project. See page 1316. *Illustration: V. Altounian/*Science*, in collaboration with Christian Stolte; (Data) GTEx Consortium*

SEE ALSO: NEWS STORY p. 1286; PERSPECTIVE p. 1298; *SCIENCE ADVANCES* RESEARCH ARTICLE BY M. PIVIDORI *ET AL*. 10.1126/SCIADV.ABA2083; *SCIENCE ADVANCES* RESEARCH ARTICLE BY A. DUFFY *ET AL*. 10.1126/SCIADV.ABB6242; SCIENCEMAG.ORG/COLLECTIONS/GENETIC-VARIATION

1308 Flossie Wong-Staal (1946–2020)
Trailblazing HIV researcher
By G. Franchini

POLICY FORUM

1309 An ethical framework for global vaccine allocation
The Fair Priority Model offers a practical way to fulfill pledges to distribute vaccines fairly and equitably
By E. J. Emanuel et al.

LETTERS

1313 NIH must confront the use of race in science
By M. Yudel
PERSPECTIVE p. 1298

1314 Accumulation of plastic waste during COVID-19
By T. M. Adyel

1315 Microplastic's role in antibiotic resistance
By M. S. Bank et al.

1315 TECHNICAL COMMENT ABSTRACTS

RESEARCH

IN BRIEF

1335 From *Science* and other journals

REPORTS

1338 Seismology
Global quieting of high-frequency seismic noise due to COVID-19 pandemic lockdown measures *T. Lecocq* et al.
PERSPECTIVE p. 1299

1343 Ferroelectrics
Scale-free ferroelectricity induced by flat phonon bands in HfO_2
H.-J. Lee et al.
PERSPECTIVE p. 1300

1347 Cosmology
An excess of small-scale gravitational lenses observed in galaxy clusters
M. Meneghetti et al.

1351 Trophic cascades
Keystone predators govern the pathway and pace of climate impacts in a subarctic marine ecosystem
D. B. Rasher et al.

Structural biology

1355 Structural basis of transcription-translation coupling and collision in bacteria
M. W. Webster et al.

1359 Structural basis of transcription-translation coupling
C. Wang et al.

1366 Ultracold physics
Direct laser cooling of a symmetric top molecule *D. Mitra* et al.
PERSPECTIVE p. 1304

1369 Colloids
Self-limiting directional nanoparticle bonding governed by reaction stoichiometry *C. Yi* et al.
PERSPECTIVE p. 1305

1374 Atmospheric aerosols
Multiphase buffer theory explains contrasts in atmospheric aerosol acidity
G. Zheng et al.

1378 Tropical forest
Long-term forest degradation surpasses deforestation in the Brazilian Amazon
E. A. T. Matricardi et al.

1383 Global climate
An astronomically dated record of Earth's climate and its predictability over the last 66 million years
T. Westerhold et al.

1388 Circadian rhythms
The hepatocyte clock and feeding control chronophysiology of multiple liver cell types *D. Guan* et al.

1395 Coronavirus
A molecular pore spans the double membrane of the coronavirus replication organelle *G. Wolff* et al.
PERSPECTIVE p. 1306

DEPARTMENTS

1277 Editorial
Systemic equity in education
By Gilda A. Barabino

1402 Working Life
Data-driven advice for grad school
By Abigail M. Brown

New Products.....1399
Science Careers.....1400

SCIENCE (ISSN 0036-8075) is published weekly on Friday, except last week in December, by the American Association for the Advancement of Science, 1200 New York Avenue, NW, Washington, DC 20005. Periodicals mail postage (publication No. 484460) paid at Washington, DC, and additional mailing offices. Copyright © 2020 by the American Association for the Advancement of Science. The title SCIENCE is a registered trademark of the AAAS. Domestic individual membership, including subscription (12 months): $165 ($74 allocated to subscription). Domestic institutional subscription (51 issues): $2148; Foreign postage extra: Air assist delivery: $98. First class, airmail, student, and emeritus rates on request. Canadian rates with GST available upon request, GST #125488122. Publications Mail Agreement Number 1069624. **Printed in the U.S.A.**
Change of address: Allow 4 weeks, giving old and new addresses and 8-digit account number. **Postmaster:** Send change of address to AAAS, P.O. Box 96178, Washington, DC 20090–6178. **Single-copy sales:** $15 each plus shipping and handling available from backissues.sciencemag.org; bulk rate on request. **Authorization to reproduce** material for internal or personal use under circumstances not falling within the fair use provisions of the Copyright Act can be obtained through the Copyright Clearance Center (CCC), www.copyright.com. The identification code for *Science* is 0036-8075. *Science* is indexed in the *Reader's Guide to Periodical Literature* and in several specialized indexes.

Published by AAAS

EDITORIAL

Systemic equity in education

Gilda A. Barabino
is the president of Olin College of Engineering, Needham, MA, USA.
gbarabino@olin.edu

Too often in higher education, the legacy of laws, policies, and practices that have systematically denied educational opportunities to Blacks is ignored, thereby perpetuating racial inequities. In the United States, higher education is a key route to career success and upward socioeconomic mobility. Unfortunately, this path is increasingly becoming most accessible to privileged communities. As the new president of Olin College of Engineering in Massachusetts, and as a woman of color, I am in a position to help unburden higher education from systemic racism and promote positive change that extends beyond academic boundaries.

My parents instilled in me the importance of education for personal and familial uplifting as well as a means of helping other Black Americans to achieve success. They reminded me that all people are created equal and have inalienable rights—a right to education among them. At a young age, I realized why they tried to enforce this notion. I vividly recall that as a third grader in 1963, I had to walk past a newly built all-white school to be picked up and bused to a dilapidated all-Black school in another part of Panama City, Florida. I wondered what it was like inside. Surely the pristine brick exterior and the well-appointed playground were indicators that, within those walls, white students had new and current textbooks, unlike the worn and outdated ones in my Black school. I wondered what justification there was for denying Blacks the same educational experiences as those afforded to whites. On the bus, I saw the stark contrast as we traveled from an integrated to a segregated neighborhood. As we turned down the dirt road leading to the Black school, I remember a sense of moving between two very different worlds.

Separate worlds indeed, but not equal. The U.S. Supreme Court ruling on *Plessy v. Ferguson* in 1896 legalized "separate but equal" educational institutions and opportunities for Blacks. Even though the landmark decision of *Brown v. Board of Education* in 1954 declared "separate but equal" to be unconstitutional, many schools remained segregated, including the one in Florida near where my military family lived nearly 10 years later. In higher education, historically Black colleges and universities (HBCUs) were established in the United States in the early 19th century for Blacks to obtain advanced degrees. Until *Brown*, most college-educated Blacks graduated from HBCUs.

I eventually became the first Black student to get a doctorate in chemical engineering from Rice University; the fifth woman in the nation to obtain that degree; and the first Black woman in the country to hold a tenure-track position in chemical engineering. But it is discouraging that the challenges that existed along my journey remain challenges faced today by Black students interested in pursuing careers in science, technology, engineering, and mathematics. There is still a lack of diversity among faculty and students in engineering schools. This environment has negative consequences and feeds a vicious cycle. The dearth of Black faculty role models and mentors contributes to the underrepresentation of Black students. Structural and social barriers such as hostile climates, bias, and tokenism make it difficult to achieve a sense of belonging and limit career choices and opportunities for Black students and faculty, further perpetuating the persistent underrepresentation. Today, 3.9% of students in the United States who graduate with a bachelor's degree in engineering are Black. And only 4.1% of students who graduate with a Ph.D. in engineering in the nation are Black.

> **"It's time to abandon the myth that students and faculty of color can't be found."**

Dismantling systemic racism in higher education will require efforts to think and operate in new ways beyond existing programs that support students of color—those efforts are typically targeted to individuals, and what's needed in addition are efforts that promote institutional change. Engineering colleges are a good place for breaking things down and rebuilding. Olin, for example, is committed to applying a co-creation model of change (where students, faculty, and administration work together) that relies on a combination of leadership, shared responsibility and accountability, courageous and effective discourse, mutual understanding, community engagement, and design approaches that have the potential for meaningful change. The lessons learned in our process of experimentation and discovery hopefully can be shared to help other colleges interested in achieving similar goals.

It's time to abandon the myth that students and faculty of color can't be found. Higher education must challenge the status quo.

–Gilda A. Barabino

PHOTO: LEISE JONES PHOTOGRAPHY/COURTESY OLIN COLLEGE OF ENGINEERING

10.1126/science.abe6517

Published by AAAS

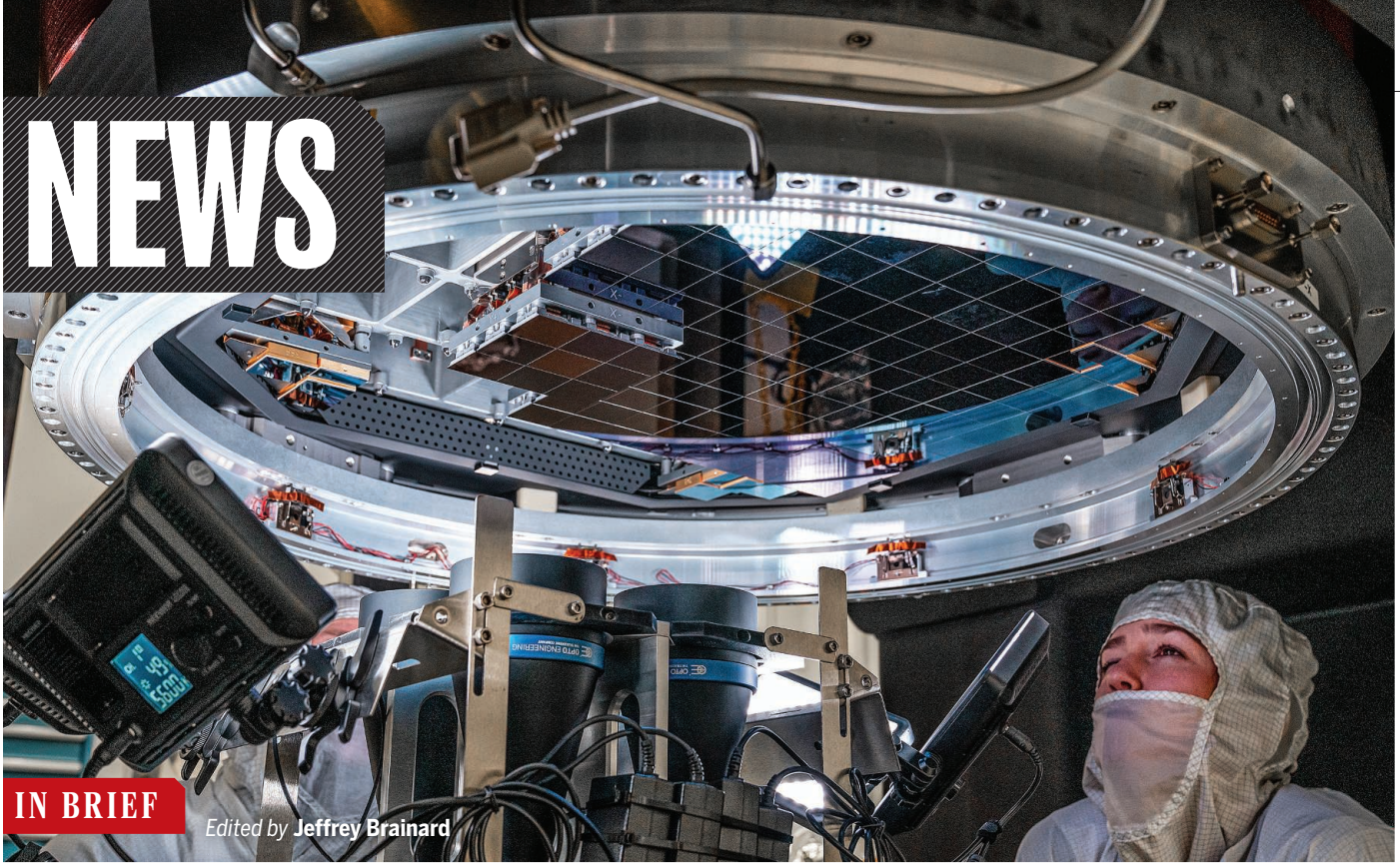

Edited by **Jeffrey Brainard**

ASTRONOMY

Telescope's giant sensor snaps most detailed photo ever

Talk about a sharper image: A recently constructed imaging sensor array (above) that will be used when the Vera C. Rubin Observatory in Chile opens in 2021 has captured a world-record 3200 megapixels in a single shot. It recorded a variety of objects, including a Romanesco broccoli, at that resolution, which is detailed enough to show a golf ball clearly from 24 kilometers away. The sensor array's focal plane is more than 60 centimeters wide, much larger than the 3.5-centimeter sensors on high-end consumer digital cameras, says the SLAC National Accelerator Laboratory, which built the array. When the telescope, funded by the U.S. National Science Foundation, begins operating next year, it will image the entire southern sky every few nights for 10 years, cataloguing billions of galaxies each time. The surveys will shed light on mysterious dark energy and dark matter, which make up most of the universe's mass. With its repeat coverage, the telescope will make the equivalent of an astronomical movie in order to discover objects that suddenly appear, move, or go bang.

WHO endorses COVID-19 drugs

BIOMEDICINE | Corticosteroids given orally or intravenously should be the standard therapy for people with "severe and critical" COVID-19, the World Health Organization (WHO) said in new guidelines issued last week—but they should not be given to patients with mild cases. In June, a large U.K. trial named Recovery first showed that the steroid dexamethasone cut deaths among ventilated COVID-19 patients by 35% after 28 days of treatment. That result was confirmed by a WHO-sponsored meta-analysis published in *JAMA* on 2 September that included Recovery and six other studies testing dexamethasone, as well as two other corticosteroids—hydrocortisone and methylprednisolone. Many countries, including the United States, had already included corticosteroids in their national treatment guidelines. But WHO's recommendations will be important as a signal to low- and middle-income countries, says Martin Landray, one of Recovery's principal investigators.

Virus may move through pipes

PUBLIC HEALTH | COVID-19 virus particles drifting through a Chinese apartment building's plumbing may have infected some residents, a study has found, raising fears of yet another way that the disease could spread. The case echoes a 2003 outbreak of severe acute respiratory syndrome (SARS) that spread through the pipes of a Hong Kong apartment building. Such transmission is difficult to prove. But scientists suspect that aerosolized coronavirus may have spread from the bathroom of a Guangzhou family of five through a floor drain and into the building's wastewater pipes. Two middle-aged couples living in apartments above the family later contracted COVID-19. The study appeared last week in *Annals of Internal Medicine*.

Africa's 'green wall' rises slowly

CONSERVATION | A plan to reforest a cross-continental strip of Africa to hold back expansion of the Sahara Desert and the semi-arid Sahel has made little progress—even though the project is halfway toward its planned completion date in 2030, a report says. Participating countries have planted only 4 million hectares of trees and other vegetation for the Great Green Wall, well short of the 100 million planned to stretch 7000 kilometers from Senegal to Djibouti,

PHOTO: JACQUELINE ORRELL/SLAC NATIONAL ACCELERATOR LABORATORY

Published by AAAS

says the report by the Climatekos consulting firm, presented on 7 September at a meeting of the countries' ministers. Supporters predicted the project would also create jobs and capture carbon dioxide. Scientists have said creating grasslands may be more effective than planting trees to resist desertification, *The Guardian* reported.

Large gift for materials research

PHILANTHROPY | Rice University last week received a $100 million gift for materials science. It is the largest to date in that discipline recorded in a database of gifts for engineering maintained by *The Chronicle of Philanthropy*. The funding will be used to pair materials science with artificial intelligence to advance the design and manufacturing of new materials, for applications that include sustainable water systems, energy, and telecommunications. The donor was the Robert A. Welch Foundation, which supports chemistry research in Texas.

EU bans lead ammo in wetlands

CONSERVATION | Scientists hailed a move last week by the European Union to ban the use of lead ammunition near wetlands and waterways. The European Chemicals Agency has estimated that as many as 1.5 million aquatic birds die annually from lead poisoning because they swallow some of the 5000 tons of lead shot that land in European wetlands each year. Its persistence in the environment is also considered a human health hazard. The EU Registration, Evaluation, Authorisation and Restriction of Chemicals (REACH) committee approved the ban after years of controversy. The German delegation, which had abstained in a July vote on the issue, changed its stance to support the measure after a letter from 75 scientists and petitions signed by more than 50,000 people called for it to do so. The European Commission and the European Parliament are expected to formally approve the ban, allowing it to go into effect in 2022. REACH may debate a complete ban on lead ammunition and fishing weights later this year.

PHOTO: DIETMAR NILL/MINDEN PICTURES

One-third of white-tailed eagles whose deaths were recorded in Germany were poisoned by lead shot, scientists found.

Russian dissident poisoned

CHEMICAL WEAPONS | Alexei Navalny, a Russian opposition politician, was poisoned with a nerve agent "identified unequivocally in tests" as a Novichok, an exotic Soviet-era chemical weapon, German Chancellor Angela Merkel said on 2 September. Navalny fell ill on 20 August after drinking a cup of tea at a Siberian airport. He was flown to Berlin and this week emerged from a coma. German military scientists at the Bundeswehr Institute of Pharmacology and Toxicology in Munich haven't released details of their tests, but they had clear targets to hunt for: Like other nerve agents, Novichoks bind to the enzymes acetylcholinesterase and butyrylcholinesterase, creating a telltale conjugate compound. Novichok agents came to wide public notice in 2018 after one was used in an assassination attempt against former Russian spy Sergei Skripal in the United Kingdom. The attack prompted nations to push for a crackdown on Novichok agents, and last year they were added to the list of toxic chemicals regulated under the Chemical Weapons Convention.

Depression follows lockdowns

COVID-19 | In one of the largest surveys of Americans since COVID-19 lockdowns began, a majority reported having some symptoms of depression, up from one-quarter in a prepandemic survey. The prevalence of symptoms graded as moderate to severe tripled, to 27.8% of respondents. A research team compared results from two surveys used to screen for depression: one administered to more than 5000 people in 2017 and 2018 by the U.S. Centers for Disease Control and Prevention, the other given to 1400 people in early April by NORC at the University of Chicago. Prevalence of depression symptoms rose in all demographic groups and especially among individuals facing financial problems, job loss, or family deaths. The increases in self-reported symptoms are larger than those recorded in previous surveys after large-scale traumatic events in other countries, including outbreaks of the severe acute respiratory syndrome, H1N1, and Ebola, the authors write in the 2 September issue of *JAMA Network Open*.

FEATURED INTERVIEW

A U.S. vaccine leader's vow: Politics stays out

"I would immediately resign if there is undue interference in this process." So said Moncef Slaoui, scientific director of Operation Warp Speed, the U.S. effort to quickly develop a vaccine for COVID-19, in an interview with *Science*.

To date, Warp Speed has invested more than $10 billion in eight vaccine candidates. Three are now in large-scale efficacy trials, and interim reviews of their data by independent safety and monitoring boards could reveal evidence of protection as early as October.

Slaoui, an immunologist who formerly headed vaccine development at GlaxoSmithKline, answered questions from *Science* last week about how Warp Speed operates and addressed concerns that political pressure before the 3 November U.S. presidential election may lead to an emergency use authorization of a COVID-19 vaccine before it is proven safe and effective. (On 8 September, nine companies developing vaccines for the pandemic coronavirus pledged not to seek a premature authorization.)

"It needs to be absolutely shielded from the politics," Slaoui says. "Trust me, there will be no [authorization request] filed if it's not right. ... The science is what is going to guide us. ... And at the end of the day, the facts and the data will be made available to everyone who wants to look at them and will be transparent."

Slaoui defended Warp Speed's decision to not consider vaccines made of whole, inactivated viruses, a time-tested approach. China has three such vaccines in efficacy trials, but he worries they could cause serious side effects in people who receive them. Slaoui also said if it had been his choice, the United States would have participated in COVAX, a mechanism for countries to invest collectively in vaccines and share them; the Trump administration declined to join. The full interview—one of Slaoui's most detailed since taking the job in May—is at http://scim.ag/SlaouiQA.

Published by AAAS

IN DEPTH

Many very sick COVID-19 patients, like some in this Brazilian intensive care unit, have obesity.

COVID-19

Why obesity worsens COVID-19

Even people in the overweight category face higher risk of serious disease

By **Meredith Wadman**

This spring, after days of flulike symptoms and fever, a man arrived at the emergency room at the University of Vermont Medical Center. He was young—in his late 30s—and adored his wife and small children. And he had been healthy, logging endless hours running his own small business, except for one thing: He had severe obesity. Now, he had tested positive for COVID-19 and was increasingly short of breath.

He was admitted directly to the intensive care unit (ICU) and was on a ventilator within hours. Two weeks later, he died.

"He was a young, healthy, hardworking guy," recalls MaryEllen Antkowiak, a pulmonary critical care physician who is medical director of the hospital's ICU. "His major risk factor for getting this sick was obesity."

Since the pandemic began, dozens of studies have reported that many of the sickest COVID-19 patients have been people with obesity. In recent weeks, that link has come into sharper focus as large new population studies have cemented the association and demonstrated that even people who are merely overweight are at higher risk. For example, in the first metaanalysis of its kind, published on 26 August in *Obesity Reviews*, an international team of researchers pooled data from scores of peer-reviewed papers capturing 399,000 patients. They found that people with obesity who contracted SARS-CoV-2 were 113% more likely than people of healthy weight to land in the hospital, 74% more likely to be admitted to an ICU, and 48% more likely to die.

A constellation of physiological and social factors drives those grim numbers. The biology of obesity includes impaired immunity, chronic inflammation, and blood that's prone to clot, all of which can worsen COVID-19. And because obesity is so stigmatized, people with obesity may avoid medical care.

"We didn't understand early on what a major risk factor obesity was. … It's not until more recently that we've realized the devastating impact of obesity, particularly in younger people," says Anne Dixon, a physician-scientist who studies obesity and lung disease at the University of Vermont. That "may be one reason for the devastating impact of COVID-19 in the United States, where 40% of adults are obese."

People with obesity are more likely than normal-weight people to have other diseases that are independent risk factors for severe COVID-19, including heart disease, lung disease, and diabetes. They are also prone to metabolic syndrome, in which blood sugar levels, fat levels, or both are unhealthy and blood pressure may be high. A recent study from Tulane University of 287 hospitalized COVID-19 patients found that metabolic syndrome itself substantially increased the risks of ICU admission, ventilation, and death.

But on its own, "BMI [body mass index] remains a strong independent risk factor" for severe COVID-19, according to several studies that adjusted for age, sex, social class, diabetes, and heart conditions, says Naveed Sattar, an expert in cardiometabolic disease at the University of Glasgow. "And it seems to be a linear line, straight up."

The impact extends to the 32% of people in the United States who are overweight. The largest descriptive study yet of hospitalized U.S. COVID-19 patients, posted as a preprint last month by Genentech researchers, found that 77% of nearly 17,000 patients hospitalized with COVID-19 were overweight (29%) or obese (48%). (The Centers for Disease Control and Prevention defines overweight as having a BMI of 25 to 29.9 kilograms per square meter, and obesity as a BMI of 30 or greater.)

Another study captured the rate of COVID-19 hospitalizations among more than 334,000 people in England. Published last month in the *Proceedings of the National Academy of Sciences*, it found that although the rate peaked in people

Science's COVID-19 reporting is supported by the Pulitzer Center and the Heising-Simons Foundation.

PHOTO: GUSTAVO BASSO/NURPHOTO/GETTY IMAGES

Published by AAAS

with a BMI of 35 or greater, it began to rise as soon as someone tipped into the overweight category (see graphic, below). "Many people don't realize they creep into that overweight category," says first author Mark Hamer, an exercise physiologist at University College London.

The physical pathologies that render people with obesity vulnerable to severe COVID-19 begin with mechanics: Fat in the abdomen pushes up on the diaphragm, causing that large muscle, which lies below the chest cavity, to impinge on the lungs and restrict airflow. This reduced lung volume leads to collapse of airways in the lower lobes of the lungs, where more blood arrives for oxygenation than in the upper lobes. "If you are already starting [with] this mismatch, you are going to get worse faster" from COVID-19, Dixon says.

Other issues compound these mechanical problems. For starters, the blood of people with obesity has an increased tendency to clot—an especially grave risk during an infection that, when severe, independently peppers the small vessels of the lungs with clots (*Science*, 5 June, p. 1039). In healthy people, "the endothelial cells that line the blood vessels are normally saying to the surrounding blood: 'Don't clot,'" says Beverley Hunt, a physician-scientist who's an expert in blood clotting at Guy's and St. Thomas' hospitals in London. But "we think that signaling is being changed by COVID," Hunt says, because the virus injures endothelial cells, which respond to the insult by activating the coagulation system.

Add obesity to the mix, and the clotting risk shoots up. In COVID-19 patients with obesity, Hunt says, "You've got such sticky blood, oh my—the stickiest blood I have ever seen in all my years of practice."

Immunity also weakens in people with obesity, in part because fat cells infiltrate the organs where immune cells are produced and stored, such as the spleen, bone marrow, and thymus, says Catherine Andersen, a nutritional scientist at Fairfield University. "We are losing immune tissue in exchange for adipose tissue, making the immune system less effective in either protecting the body from pathogens or responding to a vaccine," she says.

The problem is not only fewer immune cells, but less effective ones, adds Melinda Beck, a co-author of the *Obesity Reviews* metaanalysis who studies obesity and immunity at the University of North Carolina, Chapel Hill. Beck's studies of how obese mice respond to the influenza virus demonstrated that key immune cells called T cells "don't function as well in the obese state," she says. They make fewer molecules that help destroy virus-infected cells, and the corps of "memory" T-cells left behind after an infection, which is key to neutralizing future attacks by the same virus, is smaller than in healthy weight mice.

Beck's work suggests the same thing happens in people: She found that people with obesity vaccinated against flu had twice the risk of catching it as vaccinated, healthy weight people. That means trials of vaccines for SARS-CoV-2 need to include people with obesity, she says, because "coronavirus vaccines may be less effective in those people."

Beyond an impaired response to infections, people with obesity also suffer from chronic, low-grade inflammation. Fat cells secrete several inflammation-triggering chemical messengers called cytokines, and more come from immune cells called macrophages that sweep in to clean up dead and dying fat cells. Those effects may compound the runaway cytokine activity that characterizes severe COVID-19. "You end up causing a lot of tissue damage, recruiting too many immune cells, destroying healthy bystander cells," says Ilhem Messaoudi, an immunologist who studies host responses to viral infection at the University of California, Irvine. Of the added risk from obesity, she adds: "I would say a lot of it is immune-mediated."

The severity of COVID-19 in people with obesity helps explain the pandemic's disproportionate toll in some groups. In American Indians and Alaska Natives, for example, poverty, lack of access to healthy food, lack of health insurance, and poor exercise opportunities combine to render "rates of obesity … remarkably high," says Spero Manson, a Pembina Chippewa who is a medical anthropologist at the University of Colorado's School of Public Health. And obesity "is connected to all these other [illnesses], such as diabetes and cardiovascular disease, rendering us susceptible" to severe COVID-19, Manson says.

In addition, a large body of literature shows that people with obesity may delay seeking medical care due to fear of being stigmatized, increasing their likelihood of severe disease or death. "Patients that experience weight stigma are less likely to seek care and less likely to seek follow up because they don't feel welcome in the health care environment," says Fatima Cody Stanford, an obesity medicine physician-scientist at Harvard Medical School and Massachusetts General Hospital.

COVID-19–specific research on this question is urgently needed, she adds. "We don't know how many people are dying in the community that are never making it in," Stanford says. "Maybe that was [due] to their weight or to their race, the two most prevalent forms of stigma in the U.S."

For people with obesity, the extra risk adds a psychological burden, says Patty Nece, vice chair of the Obesity Action Coalition. "My anxiety is just totally ramped up," she says, adding that because of stress eating she's recently regained 30 of the 100 pounds she lost before the pandemic. "You have the general anxiety of this pandemic … and then you layer on top of it: 'You in particular, you could get really sick.'"

Data on how to treat COVID-19 patients with obesity are scant. Published evidence supports giving such patients higher doses of anticoagulants, says Scott Kahan, an obesity medicine physician who directs the National Center for Weight and Wellness. But very little is known about whether and how to adjust other treatments such as remdesivir and dexamethasone, partly because patients with obesity "are often excluded from clinical trials," he says. He urges that COVID-19 treatment trials include people with high BMIs wherever possible.

People with obesity should take extra care to avoid getting sick, Messaoudi says. "If you are a person with obesity, be extra, extra cautious," she says. "Wear your mask. Wash your hands. Avoid large gatherings."

In addition, exercising and, separately, losing even a little weight can improve the metabolic health of a person with obesity, and, in doing so, reduce their chances of developing severe COVID-19 if they become infected, says Stephen O'Rahilly, a physician-scientist who directs the MRC Metabolic Diseases Unit at the University of Cambridge. "If you're 300 pounds, even losing a modest amount is likely to have a disproportionate benefit on how well you do with coronavirus infection. You don't have to become a slim Jim to benefit." ■

The danger of extra kilos

Among 334,000 people in England this spring, the chances of being hospitalized with COVID-19 increased steadily with their body mass index (BMI).

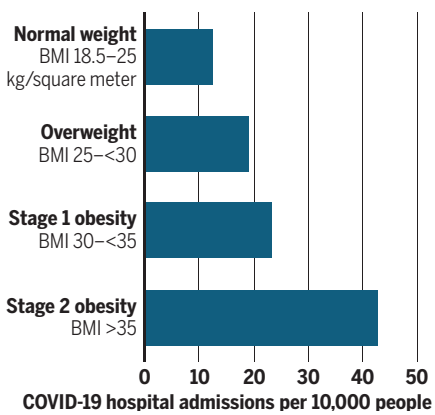

CREDITS: (GRAPHIC) N. DESAI/*SCIENCE* (DATA) HAMER *ET AL*., *PNAS*, 10.1073/PNAS.2011086117

Published by AAAS

VOICES OF THE PANDEMIC

Speaking science to power

A young disease modeling expert has found her voice during the pandemic

By **Kelly Servick**

In May, epidemiologist Caitlin Rivers made a rare outing amid coronavirus stay-at-home orders. She had been called for the first time in her career to testify before Congress—and she was intimidated. "You're looking at the dais and seeing all these eminent people. It's a really powerful experience," she says.

Then, questions about the U.S. response to COVID-19 started to fly, and Rivers was in her element. Five years out of graduate school, she is already well-versed in talking to policymakers about the science of pandemics. She has developed models to predict the spread of Middle East respiratory syndrome and Ebola, briefed the Department of Defense (DOD) on outbreak response, and tracked respiratory disease among Army service members. She's now at the Johns Hopkins Center for Health Security, a think tank that advises U.S. and international leaders on epidemics and disasters.

In formal reports, private conversations with congressional staffers and local officials, and a growing presence on Twitter and in the popular press, Rivers has emerged as a clear-eyed, tactful narrator of the unfolding pandemic. "One of my goals," she says, "is keeping the energy—the intention—around the bigger question, 'Are we headed in the right direction?'"

Rivers got interested in epidemiology as an undergraduate at the University of New Hampshire, inspired in part by Tracy Kidder's book *Mountains Beyond Mountains: The Quest of Dr. Paul Farmer, a Man Who Would Cure the World,* which describes the medical anthropologist's efforts to eradicate disease in developing countries. Rivers admired "the respect that he brought to the populations that he was working with," she says, "and just the vision—he was not about to let anything stop him."

Rivers majored in anthropology, and she brings an "anthropologist's understanding of how what seem to be totally different cultures can communicate with each other—the policy world and the modeling epidemiologists," says Stephen Eubank, an epidemiological modeler at the University of Virginia (UVA) who mentored Rivers during her graduate training in epidemiology and infectious disease at the Virginia Polytechnic Institute and State University (Virginia Tech).

Her Ph.D. coincided with the outbreak of Ebola in West Africa, and in the lab of Virginia Tech epidemiologist Bryan Lewis, she helped prepare weekly updates for experts at DOD. "Caitlin would often be emailing me at like three in the morning: 'I updated this to get this little thing in! You can put this on slide 12!'" Lewis, now also at UVA, recalls.

"We must not become numb. Those numbers represent ... people who were loved."

Caitlin Rivers, Johns Hopkins Center for Health Security

The demands of an epidemic are "well-suited to my personality," Rivers says. "I don't mind working hard, and I like having a purpose."

As she sat before an appropriations subcommittee in the House of Representatives in May, the country had made progress. Stay-at-home orders were starting to bring down new COVID-19 cases. But the nation was on the verge of widespread reopening that would put hard-won gains at risk. "We are in a critical moment of this fight," she told the representatives, warning that a clear national plan for testing, contact tracing, and strengthening health care systems was essential to prevent tens of thousands more deaths.

As early as March, Rivers, former Food and Drug Administration Commissioner Scott Gottlieb, and colleagues at the American Enterprise Institute had laid out criteria for safely reopening businesses, including waiting for a sustained reduction in cases. In her May congressional testimony, she urged the federal government to develop a national plan to eliminate test shortages and anticipate bottlenecks in the supply of reagents and materials.

Things might have gone differently if more people in positions of power had taken Rivers's advice. Four months later, the United States still logs tens of thousands of new cases per day and accounts for about one-fifth of the COVID-19 deaths documented worldwide.

"Things did not unfold as I would have liked them to, certainly," Rivers says of the U.S. reopening. "Politics can get so frustrating because it feels—not necessarily as an adviser, but as a citizen—like, 'Why can't you see it the way that I see it?'" But, she adds, she's sympathetic to the pressures that local decision-makers felt to restore their economies.

Laying blame and stirring controversy isn't productive for someone eager to influence policy, Eubank says, citing National Institute of Allergy and Infectious Diseases Director Anthony Fauci's aversion to publicly discussing his relationship with the Trump administration. Of course, Eubank adds, Fauci has decades of experience threading this needle. But Rivers understands it too, and is holding her own just a few years out of grad school.

"As a junior faculty, we don't have anyone helping. We don't have staff," says Natalie Dean, a biostatistician at the University of Florida who has co-authored editorials with Rivers on how to interpret antibody studies and the need for more detailed, transparent epidemiological data. "I think we're both adjusting to just having so many more people ask things of us."

ILLUSTRATION: KATTY HUERTAS

Published by AAAS

It's not just politicians who are turning to Rivers for clarity on the pandemic. On Twitter, which she previously used mostly to discuss new results with colleagues, she's made an art of giving a big-picture, 280-character view to her followers, who now number more than 140,000.

"Early in an outbreak, we often find only the most severe cases," she tweeted in February. "It seems like people are quite sick, which is scary. It's something of an illusion."

As some regions turned a corner in April, she predicted "growing agitation about whether staying home was necessary. Make no mistake, it is and was."

"We must not become numb," she urged in July as the United States passed 150,000 deaths. "Those numbers represent people, people who were loved."

Readers gravitate to these level-headed summaries even when the news is bad, says Dean, who describes Rivers as her "pandemic pal." Their friendship was born on Twitter, she says, where they connected over the struggle of caring for young children while working from home. (Rivers has 19-month-old twins and a 6-year-old.)

Rivers admits the demands of the pandemic have been "a lot to manage," but she also sees opportunities, including the chance to revive a proposal that would better prepare the country for the next viral threat. While she was in graduate school, Rivers and colleagues proposed creating a National Infectious Disease Forecasting Center, akin to the National Weather Service, that would put a coordinated team of epidemic modeling experts inside the government.

Currently, academic experts largely volunteer their time. "There is no other capability of national strategic importance that we handle like that," she says. "We don't let the military self-organize. We don't let the national hurricane center be academics in various universities who volunteer."

In 2015, the proposal seemed to have a chance. Rivers, with colleagues including biodefense adviser Dylan George, then at the White House Office of Science and Technology Policy, discussed the idea at a White House meeting on epidemic preparedness. But it never advanced to a formal initiative or a line in the federal budget. "We hit the budget cycle at the wrong time," says George, who is now at the national security investment firm In-Q-Tel.

COVID-19 has put new momentum behind the effort. Rivers says she has been meeting with congressional staff about it, and she is hopeful that the past efforts laid the groundwork even though they didn't pay off in time to help with COVID-19. She wishes the initiative had been launched in 2015, she says, "but the second best time is now." ■

BIOMEDICINE

Narrow path charted for editing genes of human embryos

Panel outlines most justifiable uses if safety is ensured

By **Jon Cohen**

When He Jiankui announced the creation of the first gene-edited babies in 2018, the work was widely seen as dangerous, unethical, and premature. Two years later, an international committee has concluded that the dangers remain too great for anyone to follow in He's footsteps. But its report, released last week, also lays out rare circumstances that might justify "heritable human genome editing" (HHGE) and calls for a global scientific body to help countries assess future proposals.

The committee, organized by the U.K.'s Royal Society and two branches of the U.S. National Academies of Sciences, Engineering, and Medicine, reviewed the latest on CRISPR and other ways to modify DNA and consulted scientists, physicians, ethicists, and patient groups. Its report, which Harvard University genome-editing researcher David Liu calls "thoughtful, balanced, and well-bounded," emphasizes that making heritable genome changes remains too risky for now. "There are a lot of gaps in our knowledge and further research is needed," says Kay Davies, a geneticist at the University of Oxford who co-chaired the commission.

> **"It is a ban on editing the genome of the embryo in principle."**
> **Denis Rebrikov**, Pirogov Medical University

But Liu is uneasy with the report's analysis of when and how embryo editing might be implemented. "I continue to struggle to imagine plausible situations in which clinical germline editing provides a path forward to address an unmet medical need."

The report largely steers clear of the complex social and ethical implications of creating gene-edited babies. But it does call for an international panel of scientists to assess proposed uses of HHGE, provide regular updates about related technologies, and review clinical outcomes if an edited embryo implanted into a mother is born.

It also categorizes uses of HHGE into a hierarchy ranging from potentially justifiable to strictly off limits. The most justifiable use, the commission said, would be helping those rare couples who, even with in vitro fertilization (IVF) and screening of embryos before implantation, have little or no chance of having a baby that does not inherit a genetic condition leading to "severe morbidity or premature death." A couple in which one partner is homozygous for the Huntington disease mutation is an example; without intervention, their children will inherit the mutation and develop the fatal disease.

Genetic diseases that have less serious effects and can be corrected or treated in other ways, such as deafness, rank lower. At the bottom—most taboo in the eyes of the panel—is the use of HHGE for genetic enhancement, creating children who are smarter, better at sports, or resistant to HIV, which was the goal of He's experiments.

If HHGE is allowed, the panel said, any embryo edit should only "specifically change one DNA sequence into a specific desired sequence" that is common in "the relevant population." This means the simplest, most frequently used form of CRISPR, which can cripple genes but does not fix them, should never be used in embryos. The panel also noted there may one day be a way to avoid the danger of unintended "off-target" DNA changes. Scientists have proposed editing the stem cells that produce human sperm or eggs before any embryo is created. Those gametes could then be tested for off-target changes before they are used for IVF.

The report's criteria for future use of HHGE are so stringent that "it is a ban on editing the genome of the embryo in principle," says Denis Rebrikov of Pirogov Russian National Research Medical University, who has pursued a project to correct a deafness mutation in embryos of couples who each have the aberrant gene. (Rebrikov has not moved forward because he is not yet satisfied he can safely edit a human embryo.)

Fyodor Urnov, a CRISPR researcher at the University of California, Berkeley, is glad the commission was so restrictive. "The careful guidelines laid out in this report show that the list of problems that could be addressed by such editing is, in fact, quite small," he says. "It is an open secret in the gene-editing community that human reproductive editing is a solution in search of a problem." ■

Published by AAAS

Sea ice loss has sped up the shoreline erosion threatening the Indigenous Alaskan village of Kivalina.

PHOTO: JOE RAEDLE/GETTY IMAGES

CLIMATE CHANGE

Indigenous Alaskans demand a voice in research on warming

NSF program struggles to bridge scientists and communities

By **Richard Stone**

Climate scientist Darcy Peter is Gwich'in Athabascan and hails from the Yukon River village of Beaver, Alaska, population 25. There, she says, "The concept of a grocery store is overwhelming." She laments that climate change threatens the village's subsistence economy. "The Yukon's channels are changing like crazy" as its banks erode, and a major source of sustenance—king salmon—is dwindling.

But Peter, who studies greenhouse gases and permafrost thaw at the Woodwell Climate Research Center in Falmouth, Massachusetts, is just as dismayed that to many colleagues studying Arctic warming, its impact on Indigenous Alaskans is often "out of sight, out of mind"—despite a recently launched U.S. National Science Foundation (NSF) initiative meant to change that.

The Navigating the New Arctic (NNA) initiative handed out its first round of grants totaling $37.5 million in October 2019, doubling the amount NSF spends on Arctic research. It aims to improve understanding of Arctic change, but also encourages scientists to enlist Indigenous communities in the "coproduction of knowledge" by involving them in planning and executing projects.

"I'm glad NSF went in that direction," says Kaare Erickson, North Slope science liaison for Ukpeaġvik Iñupiat Corporation (UIC) in Utqiagvik, formerly Barrow. But NNA's execution, he says, has been flawed. NSF and researchers "expected everyone to drop their guard and begin working together. They didn't foresee the backlash they'd get."

Many NNA projects ignore Indigenous Alaskans or include them as an afterthought, a coalition asserted in a letter sent to NSF this spring. "We continue to lack meaningful access and voice in the vast landscape that is the 'research process,'" wrote Kawerak, Inc., a consortium of 20 tribes in the Bering Strait region, and three other organizations representing dozens of Indigenous communities.

NSF is urging outside scientists to take such concerns to heart—for starters, by grasping the concept of knowledge coproduction. "We made a mistake in assuming that scientists knew what that meant," says anthropologist Colleen Strawhacker, program officer for NSF's Arctic System Science Program. "We definitely have a lot of work to do to make sure that Arctic sciences is diversified and equitable." In an open letter on 3 August, NSF's Arctic Sciences Section, which funds a separate research slate from NNA, called for proposals "that will enrich interactions and improve collaboration between Arctic residents," including Indigenous-led projects.

Few question the need to better understand the impacts of climate change in Alaska. Spawning salmon are dying from heat stress, reducing catches. As winter sea ice grows sparser, Indigenous hunters must often travel farther over open water, at their peril, to reach walruses and seals hauling out. Diminished ice also means higher waves and storm surges that pummel shoreline villages. "Some parts of Alaska have the highest erosion rates on Earth," says Thomas Douglas, a geochemist with the U.S. Army Cold Regions Research and Engineering Laboratory near Fairbanks. The assault forced Newtok, a Yupik village near the Bering Sea, to relocate last fall and is threatening others.

This spring, Douglas came across another warning sign: a young moose that died after stumbling into a sinkhole that formed as permafrost thawed. Permafrost loss renders the ground suddenly permeable, "like unplugging the plug in your bathtub. We hear reports of fishing holes and freshwater sources draining overnight," says Merritt Turetsky, director of the Institute of Arctic and Alpine Research at University of Colorado, Boulder.

As these challenges have unfolded, Indigenous Alaskans have sought to be part of the solution. "For many decades," the coalition wrote to NSF, "we have asked to be active partners with agencies and academics that wish to come onto our lands and waters to conduct research."

That plea is often ignored, says Lauren Divine, director of the Ecosystem Conservation Office for the Aleut Community of St. Paul, a volcanic island in the Bering Sea. St. Paul is a microcosm of the upheaval the region is enduring, with heavy coastal erosion and mass die-offs of puffins and other seabirds. Scientists studying these woes sometimes seem to view Indigenous participation as an exercise in ticking a box, says Divine, who is a marine biologist by training. "We ended up just getting cold-called. Solicitations to hop onto a proposal without any thought for what funding would be directed to the tribe."

In their letter to NSF, Indigenous leaders recommended NNA focus on projects that address the sustainability of Arctic communities—food security and infrastructure, in particular—and set aside 25% of NNA funds for Indigenous-led projects. "We would love to see more proposals coming in on those topics," Strawhacker says. But an agency spokesperson says NSF has no plans to reserve funding for Indigenous-led projects.

Another irritant for Bering Sea communities like Divine's is NSF's focus on Alaska's North Slope, facing the Arctic Ocean. The March letter notes that "the majority of com-

Published by AAAS

munities with the greatest threat to infrastructure from permafrost degradation lie outside this area."

For NSF-funded scientists, a big draw on the North Slope is a research center and environmental observatory near Utqiagvik that UIC runs on an NSF contract. Still, "I don't think lack of research infrastructure is the main impediment" keeping outside researchers from connecting with Indigenous Alaskans, says anthropologist Julie Raymond-Yakoubian, social science program director for Kawerak. It's more that scientists have not historically made bridge-building a priority, she says.

There are success stories. One early example Raymond-Yakoubian points to is a Kawerak workshop in 2014 on ocean currents that brought oceanographers together with Indigenous hunters and fishers. "At the end, a lightbulb went on for everybody," she says. The oceanographers had a handle on deep off-shore currents, while the Indigenous Alaskans had an intimate knowledge of near-shore currents: how animals navigate them, for instance, and where eddies form, trapping choice driftwood for boatmaking. "There's a body of knowledge you develop as a community that cannot be replicated by Western science," Raymond-Yakoubian says.

Pacific walruses also led to a meeting of the minds. For thousands of years, many Indigenous Alaskan communities have hunted walruses for food. But as ice in the Bering and Chukchi seas began to diminish 2 decades ago, biologists worried about the future of the animals, and in 2009, the nonprofit Center for Biological Diversity petitioned the U.S. Fish and Wildlife Service (USFWS) to list the species as threatened or endangered. At the same, the retreat of the ice was making it harder and more dangerous for subsistence hunters to reach walruses, and in 2013, two St. Lawrence Island Yupik communities declared harvest disasters, says Vera Metcalf, director of the Eskimo Walrus Commission.

To gauge the population's health, USFWS and the commission set up workshops to tap Indigenous insights on issues such as where walruses calve. "The best walrus expertise exists out there in the hunting communities," says USFWS marine mammal expert Joel Garlich-Miller, who is based in Alaska. USFWS determined the walrus population appears to be relatively large and healthy, and in 2017 declined to list the species.

The cooperation continues. "Things are much better now," says Metcalf, who is Yupik. It's one case where "Our Indigenous voice is being heard." ■

Richard Stone is senior science editor at the Howard Hughes Medical Institute's Tangled Bank Studios.

SOCIAL SCIENCE

Census experts fear rush to finish tally will yield flawed data

Mounting fears of massive U.S. undercount spur push for independent oversight, more time to complete 2020 count

By **Jeffrey Mervis**

With the 2020 census in its final month, the U.S. statistical community fears rushed deadlines and political interference could lead to a seriously flawed head count. They want Congress to take two steps to avoid that fate: ensure that the Census Bureau has enough time to do the job right, and create an independent oversight body to track the agency's efforts.

The primary purpose of the decennial census is to determine how many seats each state gets in the 435-member House of Representatives. The data are also used to allocate some $1.5 trillion per year in federal spending, and they fuel countless research studies of U.S. demographic trends.

But many social scientists believe several recent actions by the Trump administration have undermined the bureau's ability to meet those obligations without sacrificing its rigorous standards for quality. Last month, the administration cut by nearly half the time the bureau had earlier said it needed for its final push to complete the census. Demographers fear that could result in a major undercount of people who are traditionally hard to reach—including immigrants, the poor, and people of color—and distort the country's demographic profile. And some observers charge that the recent insertion of three political appointees into new, high-level Census positions is part of a broader effort by the White House to produce a 2020 census that will benefit Republican-leaning states by giving them greater representation in Congress.

"Forcing the bureau to meet the current deadlines will sacrifice the accuracy of the census, and waste $16 billion in taxpayer dollars," says Arturo Vargas, head of the National Association of Latino Elected and Appointed Officials (NALEO) Educational Fund, one of several groups that have criticized the Trump administration's approach to the 2020 census. He says the administration's actions, which include a failed last-minute attempt to add a citizenship question to the census, have also tarnished the agency's "well-earned global reputation as a respected statistical agency, independent of political agendas."

The most expensive element of every census is tracking down the one-third of all U.S. residents who do not respond to repeated reminders to answer the 10 questions and submit the form. The bureau begins its nonresponse follow-up (NRFU) campaign roughly 6 weeks after the official 1 April start of the decennial census. But the COVID-19 pandemic delayed the NRFU and also led the bureau to ask Congress for a 4-month extension of its 31 December deadline for submitting the state-by-state numbers used for the apportionment of House seats.

The Trump administration later rescinded that request, however, and on 3 August Census Bureau Director Steven Dillingham announced that the agency would meet its end-of-the-year deadline by halting field operations on 30 September, 4 weeks earlier than planned. (Last week a federal judge blocked the bureau's effort to wrap things up early pending a 17 September hearing.)

Last week, the House committee that oversees the Census Bureau released an internal agency report warning that the compressed period "creates risks for serious errors" and that eliminating some operations "will reduce accuracy." Census officials have also canceled an exercise this month designed to ensure enumerators don't miss so-called group quarters—places that are home to large numbers of residents, including college dormitories, prisons, and nursing homes.

Such last-minute changes will most likely mean greater reliance on a process called imputation to fill in any data gaps. Imputation uses information on file with other government agencies to infer the demographic characteristics of non-respondents. But experts say demographic groups with lower self-response rates are also less likely to be found in existing administrative records, increasing the odds they will be undercounted.

In recent censuses, the nonresponse rate has been less than 1%—it was about 0.4% in 2010—leaving few holes to fill with imputation. But many experts believe the nonresponse rate could reach double digits in 2020. "And you can't impute 15%" without seriously jeopardizing the accuracy of the overall count, warns Kenneth Prewitt, a former Census director.

Published by AAAS

To reduce that number, Prewitt and other census advocates want to give the bureau the 4-month extension it originally requested. In May, the Democrat-controlled House included the extension in a pandemic relief package. But that bill has stalled in the Republican-led Senate.

Prewitt and three other former Census directors also want Congress to establish an independent body to monitor the census in real time. On 29 July, Prewitt told the House panel that the group would "assess if the final 2020 numbers reasonably match what the bureau knows they should be and, if not, what steps the country should take." The panel's chair, Representative Carolyn Maloney (D–NY), supports the idea but hasn't settled on a legislative strategy to make it happen, according to a committee aide. And advocates worry the administration might balk at providing the outside body with the access it will need to do its job.

Last month, the bureau took a small step toward greater transparency by posting daily updates on the percentage of addresses in each state from which it has collected information. But such state-level data don't tell the whole story. Advocates for an outside panel say it could dig deeper by examining response rates and NRFU data from smaller geographic areas, such as several city blocks or a portion of a rural community. Such analyses might result in the panel issuing "a red flag for the possibility of a disproportionate undercount," says Robert Groves, another former Census director who supports outside oversight.

The expert body could also examine how often field workers have used proxies—interviewing a neighbor, for example—to obtain information. Such proxies are less reliable than self-responses in determining whether a particular dwelling is occupied, as well as the race, sex, and age of every resident. Other helpful indicators of census quality might include the share of returned forms that didn't answer one or more questions.

This summer's arrival of three political appointees holding newly created positions at the bureau has also spurred calls for more oversight. Social scientists fear that the appointees—including Benjamin Overholt, an Army veteran with a 2013 Ph.D. in applied statistics and research methods as the deputy director for data—might bring a political agenda to how the bureau completes its work and releases the data.

Census officials declined to make Overholt available for an interview, and the bureau has not spelled out his duties. But Thomas Louis, a former chief scientist at the agency and emeritus professor at Johns Hopkins University, says that "Of all the things the Census Bureau doesn't need at this point, a deputy director for data is at the top of my list. ... Ensuring data quality is the job of everybody involved in the collection, curation, and dissemination of census products."

Social scientists also worry that a 21 July Trump order requiring the Census Bureau to exclude undocumented residents from the state-by-state count will damage the overall quality of the 2020 census (*Science*, 7 August, p. 611). Civil rights groups have sued to block the order, which they say violates a constitutional requirement to count every resident.

Given all these unanswered questions, some observers are already speculating about a possible early do-over. A badly flawed census, says one census expert who requested anonymity, could create "a groundswell for a mid-decade census." ■

Residents in Greenville, Texas, are urged to fill out the 2020 census at a walk-in center.

PHOTO: AP PHOTO/LM OTERO

GENOMICS

Massive project reveals complexity of gene regulation

Data from tissues around the body boost search for genetic basis of disease

By **Elizabeth Pennisi**

When the human genome was sequenced almost 20 years ago, many researchers were confident they'd be able to quickly home in on the genes responsible for complex diseases such as diabetes or schizophrenia. But they stalled fast, stymied in part by their ignorance of the system of switches that govern where and how genes are expressed in the body. Such gene regulation is what makes a heart cell distinct from a brain cell, for example, and distinguishes tumors from healthy tissue. Now, a massive, decadelong effort has begun to fill in the picture by linking the activity levels of the 20,000 protein-coding human genes, as shown by levels of their RNA, to variations in millions of stretches of regulatory DNA.

By looking at up to 54 kinds of tissue in hundreds of recently deceased people, the $150 million Genotype-Tissue Expression (GTEx) project set out to create "one-stop shopping for the genetics of gene regulation," says GTEx team member Emmanouil Dermitzakis, a geneticist at the University of Geneva. In a brace of papers in *Science* (pp. 1318, 1331–34), *Science Advances*, *Cell*, and other journals this week, GTEx researchers roll out the final big analyses of these free, downloadable data, as well as tools for further exploiting the data.

"This resource is invaluable" for anyone interested in particular diseases, or studying tissues or cell types, says Jan Korbel, a human geneticist at European Molecular Biology Laboratory (EMBL), Heidelberg. "It's a public treasure trove," says Jun Li, a geneticist at the University of Michigan, Ann Arbor.

But the complex main analysis (p. 1318) drives home just how convoluted the interconnections between genes and their regulatory DNA can be. The papers "are written in bureaucratese," and the announced re-

Published by AAAS

sults are hard to decipher, says Dan Graur, an evolutionary biologist at the University of Houston and a well-known critic of big science. And like other critics, he notes that the project, with 85% white donors, sorely lacks diversity and thus will miss genetic variation in other groups.

GTEx can't yet pin down sequences responsible for illnesses such as heart disease and kidney failure, or trace how the layers of gene regulation work together. "We shouldn't pack up our bags and say gene expression is solved," says genomicist Ewan Birney, deputy director general of EMBL, who led another big genomics project called ENCODE.

After GTEx was launched in 2010, families of more than 900 deceased subjects who had already pledged their organs or tissues for transplants agreed researchers could also take samples of their loved ones' healthy tissues, for example brain, muscle, fat, pancreas, and heart. Having multiple tissues from the same subject gave researchers confidence that variation in gene expression between, say, muscle and pancreas, was real and meaningful. "For the first time, we have this homogeneous set so we could get at biological differences between tissues," says GTEx member Barbara Stranger, a geneticist at Northwestern University.

Researchers described each sample, then imaged and froze all the tissues for future analysis. They deciphered genomes and quantified RNA to measure gene activity. In addition to comparing tissues within one person, they could also compare the same tissue in different individuals. They were able to link variations in DNA to gene expression levels using statistical analyses to find correlated patterns of change. The heart of the GTEx database is a compilation of the complex relationships between stretches of regulatory DNA called expression quantitative trait loci, or eQTLs, and the genes they regulate.

A pilot phase, completed in 2015, examined nine tissues in depth (*Science* 8 May 2015, p. 618) and demonstrated that samples from corpses were reasonable stand-ins for living tissue, says GTEx co-leader Tuuli Lappalainen, a human geneticist at the New York Genome Center. Now, after analyzing almost 20,000 samples, GTEx "has reached a size where we can gain much clearer, crisper insights," says co-leader Kristin Ardlie, a human geneticist at the Broad Institute. She and her colleagues found that almost every human gene is regulated by at least one eQTL, many of which target multiple genes and presumably affect multiple traits.

Stranger uncovered another key result: Almost every tissue including, for example, skin and heart, showed differences in gene expression between males and females (p. 1331). "The vast majority of biology is shared by males and females," Stranger says, but the expression differences may help explain why men and women have different disease patterns or reactions to drugs. "I consider that a major finding," Korbel says.

Likewise, Broad co-leader François Aguet and colleagues confirmed certain eQTLs extend their reach to distant genes, even those on other chromosomes. GTEx documented 143 such "trans" elements, some of which affect multiple genes across the genome.

Kelly Frazer at the University of California, San Diego, is already using the data to help make sense of so-called genome-wide association studies (GWAS), which pose major mysteries. In a GWAS, massive consortia look at the genomes of thousands of patients with a particular disease or trait and note hundreds of subtle genetic changes, often outside of genes themselves. But researchers often have no clue which of these many suspects triggers the disease or shapes the trait.

For example, GWAS studies had identified more than 500 genetic variations that appeared to affect heart rhythm and electrical conductance. Frazer wanted to know how a heart-specific transcription factor called NKX2-5 influenced those traits. Her team had identified thousands of DNA variations that might affect NKX2-5's activity and so perhaps shift heart rhythm.

Paola Benaglio in Frazer's lab analyzed and compared those DNA variations, GWAS data, and GTEx data in order to identify which DNA variations actually regulate NKX2-5 activity. She was able to first narrow the candidate eQTLs to 55, then to nine and finally, using GWAS data on heart rhythms and other tools, she zeroed in on a single variable base on chromosome 1. Next, she blocked that DNA base using the genome editor CRISPR and confirmed that it alters NKX2-5 binding, Benaglio, Frazer, and their colleagues reported last year in *Nature Genetics*.

"I'm sure there are hundreds of people like me" who appreciate the database, Frazer says. The statistics back her up. Monthly, 16,000 people visit the GTEx portal, and others examine the data on other sites. In 2018, 900 papers cited it.

Birney understands the enthusiasm, but cautions that spurious correlations between eQLTs and genes can arise. Homing in on a disease-causing variant via GTEx "is not a slam dunk."

Graur, for his part, remains skeptical that gene activity in corpses adequately reflects what's going on in the living, despite the team's data on the preservation of gene expression. "It's like studying the mating behavior of roadkill," he says.

As the project winds down, the U.S. National Institutes of Health is planning a developmental GTEx that will enroll people under age 20 to create an atlas of gene expression from birth to adulthood. In such follow-up efforts, a more diverse set of tissue donors "would be very valuable," Korbel says. GTEx initially shot for that goal but faltered because tissue and organ donors are disproportionately white. Researchers need to "communicate more effectively," says Laura Siminoff, a social scientist at Temple University who was funded early on to look at GTEx ethics. "Otherwise we will be doing this science for white people."

The results so far cannot tell the full story of how the genome gives rise to a human being's myriad tissues and diseases. Still, Birney predicts, "GTEx will get used and reused again and again, and there will be some uses I cannot predict." ■

A regulatory universe expands

Genotype-Tissue Expression (GTEx) donors, tissues, and samples have grown with each publication milestone. The project's results, such as the number of genes linked to specific regulatory sequences, have blossomed accordingly.

GTEX PUBLICATIONS	RNA SAMPLES	TISSUES	GENOTYPED DONORS	EUROPEAN ANCESTRY (%)
2015	991	9	175	84.6
2017	7051	44	449	84
2020	15,201	49	838	85.3

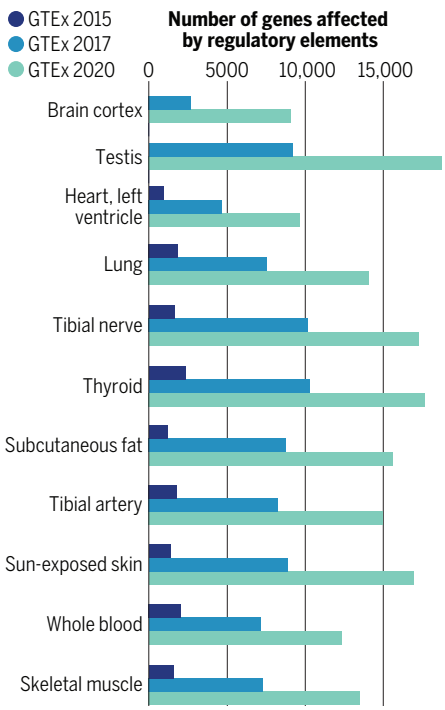

CREDITS: (GRAPHIC) V. ALTOUNIAN/*SCIENCE* (DATA) GTEX CONSORTIUM

Published by AAAS

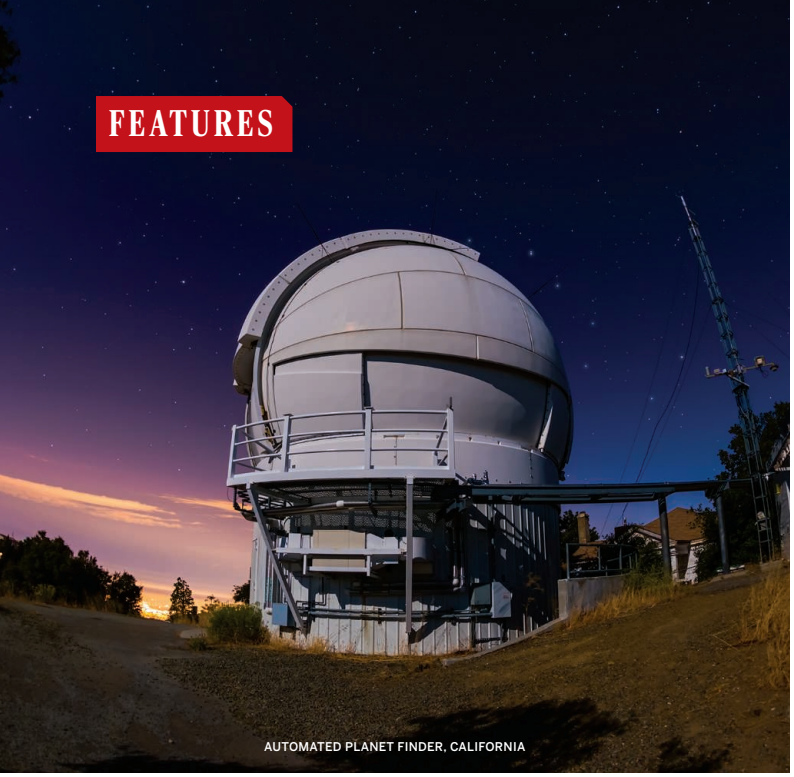

AUTOMATED PLANET FINDER, CALIFORNIA

PARKES RADIO TELESCOPE, AUSTRALIA

PHOTOS (LEFT TO RIGHT): © LAURIE HATCH; AUSCAPE/UNIVERSAL IMAGES GROUP VIA GETTY IMAGES

LISTEN UP

Flush with money and a hard-won respectability, alien hunters are deploying new telescopes and tactics

By **Daniel Clery**

In 2015, Sofia Sheikh was at loose ends. Her adviser at the University of California (UC), Berkeley, with whom she studied hot, giant exoplanets, had left for a new job. Browsing reddit, she saw a post about a lavishly funded new search for extraterrestrial intelligence (SETI) and noticed that its leader was also at UC Berkeley: astrophysicist Andrew Siemion. She asked her former adviser for an introduction and met with Siemion when he was still unpacking boxes in a new office. "Everything's kind of history from there," says Sheikh, who became the team's first undergraduate student.

Sheikh is now a Ph.D. student at Pennsylvania State University (Penn State), University Park, where she led a radio survey of 20 nearby star systems aligned with Earth's orbital plane. If an intelligent civilization inhabited one of these systems and pointed a powerful telescope our way, they would see Earth passing in front of the Sun, and they might detect signs of life in our atmosphere. They might even decide to send us a message. The results, published in February in *The Astrophysical Journal*, were unsurprising. "Spoiler alert: no aliens," Sheikh jokes.

SETI researchers are used to negative results, but they are trying harder than ever to turn that record around. Breakthrough Listen, the $100 million, 10-year, privately funded SETI effort Siemion leads, is lifting a field that has for decades relied on sporadic philanthropic handouts. Prior to Breakthrough Listen, SETI was "creeping along" with a few dozen hours of telescope time a year, Siemion says; now it gets thousands. It's like "sitting in a Formula 1 racing car," he says. The new funds have also been "a huge catalyst" for training scientists in SETI, says Jason Wright, director of the Penn State Extraterrestrial Intelligence Center, which opened this year. "They really are nurturing a community."

Breakthrough Listen is bolstering radio surveys, which are the mainstay of SETI. But the money is also spurring other searches, in case aliens opt for other kinds of messages—laser flashes, for example—or none at all, revealing themselves only through passive "technosignatures." And because the data gathered by Breakthrough Listen are posted in a public archive, astronomers are combing through it for nonliving phenomena: mysterious deep-space pulses called fast radio bursts and proposed dark matter particles called axions. "There are untapped possibilities here," says axion searcher Matthew Lawson of Stockholm University.

Perhaps the most important consequence of Breakthrough Listen is that it has nudged SETI, once considered fringe science, toward the mainstream. "Journals are relaxing and letting good technosignature papers be published," says astrobiologist Jacob Haqq-Misra of the Blue Marble Space Institute of Science. "The giggle factor is reducing." After nearly 3 decades of eschewing SETI, NASA organized a technosignature workshop in 2018. In June, it awarded a grant to model the detectability of possible technosignatures in the atmospheres of exoplanets, its first ever SETI-related grant not involving radio searches.

But some astronomers worry the funding boon is distorting science. Fernando Camilo, chief scientist of the South African Radio

Published by AAAS

MEERKAT ARRAY, SOUTH AFRICA

GREEN BANK TELESCOPE, WEST VIRGINIA

CREDITS: (PHOTOS, LEFT TO RIGHT) SOUTH AFRICAN RADIO ASTRONOMY OBSERVATORY; MICHAEL S. WILLIAMSON/*THE WASHINGTON POST* VIA GETTY IMAGES (GRAPHIC) N. DESAI/*SCIENCE* (DATA) JASON WRIGHT/PENN STATE

The four main telescopes used by Breakthrough Listen are scanning nearby stars and galaxies for any radio or laser messages beamed at Earth.

Astronomy Observatory, says Breakthrough Listen's voracious appetite for time on large telescopes leaves him uncomfortable. "It leaves less time to do astronomy." Others say SETI's high-risk, rush-for-the-prize approach could distract funders from a more rational, stepwise search for extraterrestrial life. "We do have a really thoughtful process on what gets funded and what doesn't," says Harvard University astronomer David Charbonneau. "That doesn't happen with rich individuals."

But SETI proponents don't see themselves as separatists. They are increasingly working hand in hand with those searching for exoplanets and studying astrobiology. "Looking for intelligence is the logical conclusion of this search for life," says astronomer David Kipping of Columbia University.

SETI STARTED SMALL. In 1960, astronomer Frank Drake pointed a 26-meter radio telescope in Green Bank, West Virginia, at two nearby Sun-like stars. He scanned frequencies around 1.42 gigahertz, which correspond to wavelengths of about 21 centimeters—the part of the spectrum where clouds of interstellar hydrogen emit photons. This 21-centimeter glow is ubiquitous, and Drake supposed it might be a universal channel on the cosmic dashboard, a natural place for a clarion "We are here!" But his targets, Tau Ceti and Epsilon Eridani, were expressionless. The survey, called Project Ozma, saw no sign of artifice, such as an intense spike squeezed into a narrow frequency band.

With funding from NASA and the National Science Foundation (NSF), however, searches continued, with bigger telescopes to listen for fainter signals and hardware that could scan thousands and eventually millions of narrow frequency channels at once. Drake devised his now famous, eponymous equation that estimates how many communicative extraterrestrial civilizations may exist in the Milky Way. It depends on seven variables, from the rate of star formation to the average lifetime of a civilization. Even though only one of the seven factors—star-formation rate—was known with any certainty, alien hunters were on the prowl.

In 1992, NASA decided to look harder, only to quickly reverse course. It embarked on the Microwave Observing Project, a 10-year, $100 million SETI search using several large telescopes. But the following year, the project was ridiculed and cut by lawmakers focused on reducing the federal budget deficit. Ever since, NASA has mostly shied away from SETI.

Even as federal funding shriveled, the 1990s gave SETI an unexpected gift. Until then no one had detected an exoplanet, much less a potentially hospitable one, but that decade brought a host of discoveries. Since then, missions such as NASA's Kepler telescope have suggested that planetless stars are rare, and that about one in five Sun-like stars has potentially habitable Earth-size planets—two more factors in the Drake equation that have fueled optimism among SETI advocates. The turn-of-the-century tech boom offered another boost: newly minted billionaires with a taste for space. A high point came in 2007 with the inauguration of the Allen Telescope Array, a SETI observatory in California kickstarted with $11.5 million from Microsoft cofounder Paul Allen.

Then the field took another plunge. The 2008 financial crisis struck and within a few years, with federal and state funding tight, UC Berkeley withdrew from the project. The array was put into hibernation for 8 months. A planned expansion from 42 to 350 dishes never materialized. "SETI was entirely decimated," Siemion says. "I was one of maybe two or three in the whole world working on SETI."

That was when Yuri Milner called.

Bigger haystacks

Searches for extraterrestrial intelligence (SETI) have grown in reach since a first survey in 1960. But if Earth's oceans represent all possible searches, SETI researchers have scanned only a hot tub's worth.

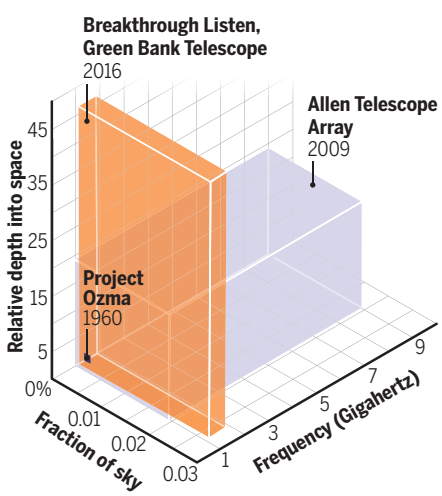

Published by AAAS

BORN AND EDUCATED in Moscow, Milner worked as a particle physicist at the Lebedev Physical Institute. In 1990, as the Soviet Union collapsed, he left to study business at the University of Pennsylvania, and in 1999 he founded an internet investment fund. The fund was an early backer of Facebook and Twitter, and later Spotify and Airbnb. *Forbes* magazine puts Milner's net worth at $3.8 billion. "I made some lucky investments," he tells *Science*.

Milner says he's always felt a connection with space and SETI. He was born in 1961, days after Drake convened the first SETI conference. He is named after Yuri Gagarin, the first cosmonaut. Once he had built up a fortune, "I discovered that now I can give back to science," he says. He knew of SETI's dire financial straits, and he believed his money and knowledge of the tech industry could help speed up the search. Siemion's UC Berkeley center, across the San Francisco Bay from Milner's home in Silicon Valley, became the beneficiary.

> **"Just knowing we are not alone ... is something that can bring us together here on Earth."**
>
> **Yuri Milner**, Breakthrough Listen

Breakthrough Listen set out ambitious goals (*Science*, 24 July 2015, p. 357). It would survey 1 million of the closest stars to Earth and 100 nearby galaxies using two of the world's most sensitive steerable telescopes, the 100-meter Green Bank Telescope in West Virginia and the 64-meter Parkes radio telescope in Australia. Buying up about 20% and 25% of the time on those telescopes, Breakthrough Listen promised to cover 10 times more sky than previous surveys and five times more of the radio spectrum, and gather data 100 times faster.

Achieving these goals required new hardware. The key electronic component is a digital backend, which chops telescope data into ultrathin frequency slices and records it. Siemion says Breakthrough Listen's backends are "orders of magnitude more powerful than anything else on site." The instruments are available for 100 hours every year to other astronomers interested in such fine frequency resolution. That allocation is often oversubscribed at Green Bank, Siemion says, ever since the backend helped characterize the first repeating fast radio burst.

The project is adding a major new telescope to its mix of collaborations: MeerKAT, a South African array of 64 dishes each 13.5 meters across (*Science*, 22 June 2018, p. 1285). Instead of buying time on the array, Breakthrough Listen is tapping into the data stream while the telescope observes its regular targets—a procedure known as commensal observing. "You take what you can get," Camilo says. "When it works, it's fantastic." Commensal observing will also be added to the Karl G. Jansky Very Large Array in New Mexico, the workhorse of U.S. radio astronomy, in a project led by the privately funded SETI Institute.

Gathering data sets is one thing; scouring heaps of them for alien messages is another. SETI researchers have long looked for energy packed into narrow frequency signals—something that is hard for nature to replicate, although astronomers need to exclude humanmade signals. One test is to see whether the signal's frequency drifts over time: An alien transmitter would be on a moving planet, causing a Doppler shift. If the frequency is rock steady, it's likely to be earthly interference. Similarly, if the signal persists when the telescope moves from its target, it's noise from Earth.

But aliens might send something more complex than a single loud note. How do you scan SETI data for something that just seems anomalous or weird? Researchers have been trying to enlist artificial intelligence (AI), but it hasn't been easy. One species of AI, natural language algorithms, can recognize key words in the flow of human speech—think of Amazon's Alexa, or eavesdroppers at the National Security Agency—after being trained on vast speech data sets. But the huge number of narrow frequency channels in SETI data overwhelms these algorithms.

Converting the data stream into 2D diagrams that resemble images works better, at least in tests, in which machine vision algorithms picked out strange pictures from a torrent of similar ones. "We have to guess what an anomaly might look like and train the algorithm to look for this, or look for things that look similar," says Steve Croft of UC Berkeley's SETI Research Center.

THE FOCUS OF SETI searches tends to reflect the technology of the times. Radio was in its heyday when Drake started out. But as lasers have grown in power and sophistication, so have efforts to spot alien laser signals with so-called optical SETI.

Astronomers have carried out optical searches with modest telescopes since the 1990s. Breakthrough Listen is doing its own, with time on the 2.4-meter Automated Planet Finder (APF) telescope at the Lick Observatory in California. APF has been scanning a sample of stars to distances up to 160 light-years but will now work through a new list: stars with potentially habitable planets identified by NASA's Transiting Exoplanet Survey Satellite (*Science*, 30 March 2018, p. 1453).

Others are developing telescopes that wouldn't need to target individual stars. The LaserSETI project, funded by the SETI Institute, is a collection of $30,000 mini-observatories, made up of an off-the-shelf fisheye lens, two cameras, and electronics that would gather light from the entire sky. The first was installed last year on an observatory roof north of San Francisco. Eventually, the institute wants to install 60 instruments around the world for 24/7 coverage.

LaserSETI's small telescopes would only pick up an especially bright flash from a nearby source. Shelley Wright of UC San Diego hopes to see much farther with the Pulsed All-sky Near-infrared Optical SETI (PANOSETI), an all-sky telescope able to detect ultrashort laser pulses across all optical wavelengths.

PANOSETI's design includes lightning-fast photon counters sensitive to pulses less than one-billionth of 1 second long. "It's hard for nature to make that," Shelley Wright says. It relies on a Fresnel lens, a type used in lighthouses to focus light into a narrow beam. Flipped over, a Fresnel can gather light from a 10°-wide patch of sky onto the photon counters. The team is building two observatories, each an array of 80 telescopes with lenses 50 centimeters across, bunched together in a fly's eye arrangement. The plan is to site the pair 1 kilometer apart—to help root out false positives—at the Palomar Observatory in California. Funded by Qualcomm cofounder Franklin Antonio, the project has built five telescopes but has been stalled by the COVID-19 pandemic.

THEN AGAIN, even intelligent aliens might be too busy or too shy to send messages to the stars. So SETI researchers also hope to detect passive signs of technology. People's ideas about what to look for often reflect their time: Consider the 19th century "discovery" of canals on Mars when canals were still a common form of transport on Earth. In 1960, amid rapid economic growth and concerns about energy shortages, physicist Freeman Dyson imagined an advanced society might build a megastructure surrounding a star to capture its energy (*Science*, 3 June 1960, p. 1667). Such "Dyson spheres" continue to fascinate and were suggested as an explanation for the strange dimmings of the star KIC 8462852, known as Tabby's Star. In 2015, Jason Wright led a search for the glow of Dyson spheres in 100,000 nearby galaxies, using data from NASA's Wide-field Infrared Survey Explorer satellite.

Technosignatures could be more subtle. In the not-too-distant future, ultrasensitive radio telescopes might be able to pick up the

Published by AAAS

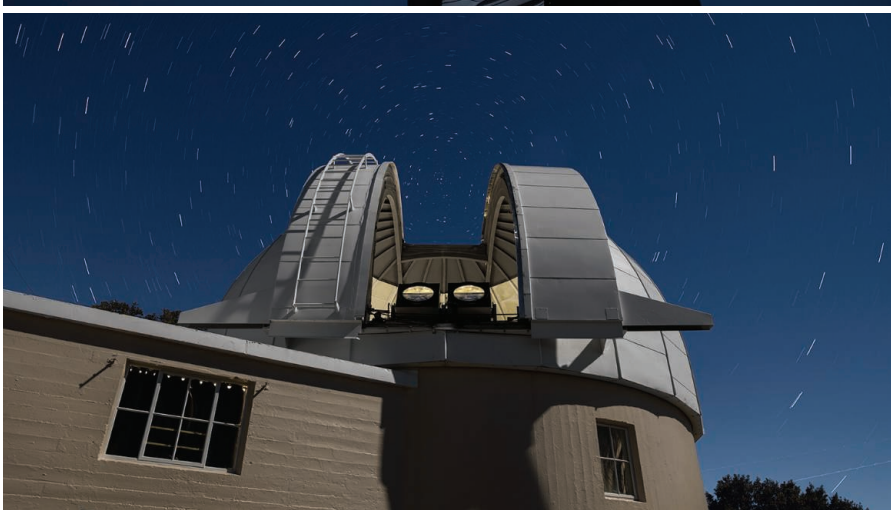

Shelley Wright (top) is using the wide light-gathering power of Fresnel lenses, similar to those used in lighthouses, to search for alien laser signals. Two are being tested at Lick Observatory in California (bottom).

PHOTOS (TOP TO BOTTOM): FRANK ROGOZIENSKI; © LAURIE HATCH

beams of a radar, like the ones used for air traffic control, from a distant exoplanet. Future optical telescopes might reveal the glow of a city's lights or its infrared warmth. Heavy industry or geoengineering might leave fingerprints in a planet's atmosphere.

These efforts chime with searches for biosignatures, detectable marks that organic life might leave on an exoplanet (*Science*, 3 November 2017, p. 578). "The line between technosignatures and biosignatures is blurring," Sheikh says. "It makes sense to observe both." In deciding to fund the 2018 workshop on technosignatures, NASA felt that they could be discussed "on a firmer scientific foundation than before," says Michael New, the agency's deputy associate administrator for research. After the workshop, the wording in NASA funding calls that had for some years excluded SETI-related proposals quietly disappeared.

In June, Jason Wright and his colleagues benefited from the new openness when they were awarded a grant to model exoplanet atmospheres and put together a "library" of potential technosignatures, which astronomers can refer to when observing exoplanets. The team will first model chlorofluorocarbons—a pollutant that isn't produced naturally—and vast solar power arrays, because they would leave an obvious cutoff in the ultraviolet part of the spectrum. "What we should look for is things that can't be avoided, civilization's manifestations in the biosphere," says Adam Frank, lead investigator on the grant at the University of Rochester.

BUT EVEN AFTER the fanfare of Breakthrough Listen, SETI remains far from a central concern for most astronomers. In 2018, panels of researchers convened by the National Academies of Sciences, Engineering, and Medicine (NASEM) drew up strategies for NASA on astrobiology and exoplanets. They made scant mention of technosignatures and didn't advise NASA to spend any money on the topic, or, more generally, SETI.

SETI enthusiasts say they are trying to avoid being shut out of an even bigger NASEM effort: its decadal survey of astrophysics, a once-a-decade priority setting exercise that is influential with funding agencies and legislators. The survey is due to report early next year. "We've made a big push to get the decadal survey … to explicitly say that NASA and the NSF need to nurture this field," Jason Wright says. He and colleagues made nine submissions, known as white papers, to the survey, compared with a single white paper in the previous survey. Sheikh says: "There are signs the winds are starting to shift."

But many astronomers think the more important hunt is for alien life of a more basic kind, not the higher risk search for technological societies. "We have to invest in general questions," says Charbonneau, who co-chaired the NASEM panel that developed the NASA exoplanet hunting strategy. "If we just go for the prize and don't find anything, what have we learned from that?"

Mainstream astrobiologists hope the decadal survey will give a thumbs up to the Large UV/Optical/IR Surveyor, or LUVOIR, a proposed NASA space telescope as much as six times wider than the Hubble Space Telescope (*Science*, 14 December 2018, p. 1230). It would scrutinize habitable planets for biosignatures and estimate the fraction of them that support life—another term in the Drake equation. "The progress we've made as scientists follows the terms of the Drake equation in order," says astrobiologist Shawn Domagal-Goldman of NASA Goddard Space Flight Center. "That progress could lead to a search for technosignatures. I could see LUVOIR being used to do that, even though it wasn't designed for such a search."

Jason Wright, however, thinks the potential payoff of SETI is just too tempting to put off the search. In July, he and his colleagues reported the "discovery space"—all the possible locations, frequencies, sensitivities, bandwidths, timings, polarizations, and modulations—that SETI radio surveys have so far explored. The result: If the entire discovery space is represented by the world's oceans, SETI has so far searched the volume of a hot tub.

Milner seems ready to support at least a few more SETI hot tubs. He says he wants Breakthrough Listen to continue past 2025, when his initial funding runs out. "It's one of the most existential questions in our universe," he says. "Just knowing we are not alone … is something that can bring us together here on Earth." ■

Published by AAAS

FALL BOOKS

A reading list for uncertain times

From an incisive ethnography of predictive policing to a compelling indictment of technology-enabled learning tools, the books on this year's fall reading list offer valuable context to the myriad challenges currently facing humanity. Dive deep into a public health disaster shrouded in secrecy, sit with the uncomfortable questions raised by a fictional foray into the future of intimacy, confront the challenges to sustainable development posed by environmental racism, and learn what a QR-coded chicken in rural China portends about the future of agriculture. When you are through, sit back and marvel at the odds stacked against humanity from the start with an entertaining romp through evolution and then leave your earthly worries behind with an ambitious tour of the Solar System. **—Valerie Thompson**

A Series of Fortunate Events

Reviewed by **Ivor Knight**[1]

Through a series of chance events, the pathogen we now know as severe acute respiratory syndrome coronavirus 2 emerged in 2019 and infected millions of humans within a span of 6 months. But chance has driven more than just the planet's latest pandemic. In his new book, *A Series of Fortunate Events: Chance and the Making of the Planet, Life, and You*, Sean B. Carroll takes readers on an entertaining tour of biological discovery that emphasizes the dominant role played by chance in shaping the conditions for life on Earth. Along the way, he provides insights and humor that make the book a quick, lively read that both educates and entertains.

Carroll begins with one of the most consequential chance events to have occurred in the history of our planet: the Cretaceous-Paleogene asteroid impact on the Yucatán Peninsula that resulted in the extinction of the dinosaurs and expansion of mammals. Given Earth's rotational speed, if the asteroid had hit 30 minutes earlier or later, scientists believe it would have made a much less consequential impact, landing in either the Atlantic or Pacific Ocean. If that had happened, there might still be dinosaurs today, but no humans. As he does throughout the book, Carroll compares the example from science with an example from popular culture, describing the comedian Seth MacFarlane's good fortune to have narrowly missed (by 30 minutes) one of the flights that was hijacked on 11 September 2001.

Fundamental topics such as the roles that mutation and natural selection play in the evolution of diverse life-forms, the genetics of human reproduction, cellular mechanisms of acquired immunity, and the development of cancer are all treated

ILLUSTRATION: KAILEY WHITMAN

Published by AAAS

within a framework where chance dominates. Carroll explains in detail how chance creates the genetic diversity upon which natural selection acts and results in the richness of species on Earth, as well as how random combinations among just 163 gene segments make possible a human immune system that can produce up to 10 billion different antibodies. Readers will likely be particularly interested to learn that their genome is only one of the 70 trillion possibilities that could have been produced by their parents.

Written in a conversational style, the book reads like an updated version of Jacques Monod's 1970 *Chance and Necessity* that speaks directly to the reader, making complex subject matter more accessible. There is also a suggested reading list and an extensive bibliography included for further exploration.

Carroll's central argument, that we are all here by luck, is certainly clear and compelling. What we choose to do with that luck, however, is where things really get interesting. Books such as this remind us to make our unlikely time here count.

A Series of Fortunate Events: Chance and the Making of the Planet, Life, and You, *Sean B. Carroll*, Princeton University Press, 2020. 224 pp.

Unsustainable Inequalities

Reviewed by **Gillian Bowser**[2]

Does a hurricane discriminate between the wealthy and the poor? Do earthquakes target specific victims? How does systemic racism influence development goals? In academic explorations of sustainable development and environmental responsibilities, our assumptions about the relationship between income and energy consumption remain largely rooted in the idea that social inequalities decrease as countries develop, thus reducing environmental inequality. No such relationship appears to actually exist.

In his sobering but essential new book, *Unsustainable Inequalities*, economist Lucas Chancel explores the intersections of social justice and environmental sustainability with a focus on global goals established at the 2012 United Nations Conference on Sustainable Development, which informed the underlying philosophy of the 2015 Paris Agreement of the United Nations Framework Convention on Climate Change (UNFCCC) (*1*). Framing his narrative through the lens of intragenerational economic inequalities, he identifies social inequality as a core driver of environmental unsustainability that leads to a vicious circle wherein the rich consume more and the poor lose access to environmental resources and become increasingly vulnerable to environmental shocks.

In 1987, the World Commission on Environment and Development issued a report called "Our Common Future" that defined sustainable development as "development that meets the need of the present without compromising the ability of future generations to meet their own needs" (*2*). The idea of intergenerational environmental equity became a cornerstone concept, shifting climate policy toward the common but differentiated responsibilities enshrined in the UNFCCC. Yet questions about intergenerational responsibility and the equitable impacts of climate change and environmental degradation remain. Environmental racism, wherein communities of color are disproportionately exposed to environmental risks, is inseparable from social justice, Chancel argues, and the attainment of sustainable development that also protects the environment across generations is "extremely difficult" without first addressing economic inequality within a single generation.

The notion that we may be able to attain sustainable development and achieve equal responsibility for environmental deg-

Published by AAAS

radation feels more unreachable than ever in a world upended by a global pandemic. In prepandemic times, many nations had already failed to implement or participate in local and global environmental justice efforts, and taxation schemes to level responsibilities for environmental pollution have proven wildly unpopular. And while Chancel argues that common indicator frameworks such as the United Nations' Sustainable Development Goals encourage nations to learn from one another, the continued rise of social inequality is a stark reminder of the difficult road ahead.

REFERENCES AND NOTES

1. Paris Agreement to the United Nations Framework Convention on Climate Change, 12 December 2015, TIAS No. 16-1104.
2. World Commission on Environment and Development, *Our Common Future* (Oxford Univ. Press, 1987).

Unsustainable Inequalities: Social Justice and the Environment, *Lucas Chancel*, *Malcolm DeBevoise, translator,* Belknap Press, 2020. 184 pp.

Failure to Disrupt

Reviewed by **Kanwal Singh**[3]

As the pandemic forces so many school systems and learning institutions to move online, the desire to educate students well using online tools and platforms is more pressing than ever. But as Justin Reich illustrates in his new book, *Failure to Disrupt*, there are no easy solutions or one-size-fits-all tools that can aid in this transition, and many recent technologies that were expected to radically change schooling have instead been used in ways that perpetuate existing systems and their attendant inequalities.

The first half of the book discusses the brief histories, limited successes, and challenges of three types of large-scale technology-driven learning environments: instructor-guided, such as lectures taught through massive open online courses (MOOCs); algorithm-guided (e.g., Khan Academy); and peer-guided (e.g., the online coding community known as Scratch). Reich gives a solid accounting of the conditions needed for success with these models, the difficulties and limitations involved in adopting them in K–12 schooling, and the challenges that arise when we attempt to compare different approaches to one another. He argues that although we might think that the availability of a technology is its biggest limiter, the truth is that educational systems are simply not constructed to allow for experimentation and new ways of learning.

Reich describes himself as committed to "methodological pluralism." He supports the use of an array of learning tools and mechanisms, although he confesses to a particular admiration for peer-guided environments. He argues, however, that the incentive structures in formal education do not encourage the more innovative and deeper learning that can blossom in these environments. If we insist on maintaining current methods of assessment and ranking, which center on individual achievement, then peer-guided instruction will remain relegated to the sidelines.

The second part of the book expands on the challenges of implementing educational technologies. Reich's main argument here is that educational systems are inherently conservative and that change will happen, albeit slowly and incrementally, only if technology designers, teachers, and administrators work in partnership to understand the desired learning goals and the parameters that define and constrain the learning environments.

One of the most intractable pieces of the educational technology puzzle is the need to effectively conduct large-scale assessment, especially when the skills being assessed are not things that computers can do. Here, Reich cites a humorous example of an automated grading system giving high marks to an essay that begins with the technically grammatically correct sentence: "Educatee on an assassination will always be a part of mankind."

At the end of the book, Reich offers four questions that he finds especially useful to consider when examining a new large-scale educational technology. Perhaps the most useful question is the first: "What's new?" Despite what "edtech evangelists" might claim, new technologies often have closely related ancestors that can help predict their success, he argues. In the end, however, new technologies alone are unlikely to have a substantial impact on schooling. We must also be open to changing educational goals and expectations according to the possibilities offered by emergent technologies.

Failure to Disrupt: Why Technology Alone Can't Transform Education, *Justin Reich,* Harvard University Press, 2020. 336 pp.

Blockchain Chicken Farm

Reviewed by **Arti Garg**[4]

In *Blockchain Chicken Farm*, Xiaowei Wang reveals the myriad ways that technology is transforming our lives. They unveil, for example, the unexpected connections that exist between industrial oyster farming in rural China, livestream-fueled multilevel marketing schemes in the United States, and the app-enabled gig economy in which Chinese influencers participate. Following the threads of places and people woven together by new technologies, Wang helps readers trace the patterns emerging in the tapestry of our tech-infused world.

Each chapter provides a view into not just how we use technology but why and to what end. Emphasizing the often-hidden human engine that powers our app-driven economy, Wang exposes the flaw in our tendency to conflate societal and cultural aspirations with the promises of technology and challenges us to honestly measure what value technology delivers. In the 21st century, they argue, we demand that technologists solve the problems that our governments and communities have not. In doing so, we inadvertently empower companies to exploit and amplify those same problems.

Our current educational systems, many of which have recently gone virtual, are not built for experimentation.

PHOTO: ASLAM IQBAL/SOPA IMAGES/LIGHTROCKET VIA GETTY IMAGES

Published by AAAS

Farms, like this one in China's Hebei Province, must overcome growing distrust in the food chain. Some have turned to tracking livestock with blockchain technology.

PHOTO: XINHUA NEWS AGENCY/GETTY IMAGES

Most of Wang's vignettes relate to Chinese agriculture. This decision, which roots the narrative in the visceral language of human sustenance, grounds the heady subject matter. The titular example takes readers to the GoGoChicken farm in Sanqiao, a "dreamlike" village that sits in one of the poorest regions in China. Here, Wang introduces the straw-hatted "Farmer Jiang," who has partnered with his village government and a blockchain company to sell free-range chickens via an e-commerce site. Jiang's chickens sell for RMB 300 (~$35) each, an amount equal to 6% of the average annual household income in that part of China. Wang explains that high-profile failures of regulatory oversight have left many Chinese with a deep distrust of the food supply chain and that upper-class Chinese urbanites will pay a premium for reassurance about food safety, which, in this case, takes the form of a vacuum-sealed chicken that comes with a QR code revealing blockchain-logged details of its life on the farm.

Wang suggests that Americans, driven by concerns over animal welfare, may desire similar reassurance about their food's provenance. In both China and America, they observe, technology allows the upper class to buy its way around governmental and societal shortcomings at prices that are out of reach for most people. Technology does not correct the intrinsic problems, and most cannot reap the benefits of the technological "solutions."

Without resorting to an overly romanticized notion of rural wisdom, Wang treats individuals like Jiang, whose future remains uncertain owing to the vagaries of e-commerce supply chains, with respect and empathy. Because of this, they largely succeed in their goal of reframing our understanding of technology as neither the cause of nor the solution to our problems but rather as a force reshaping the human experience in fundamental ways.

Blockchain Chicken Farm: And Other Stories of Tech in China's Countryside, *Xiaowei Wang*, Farrar, Straus and Giroux, 2020. 256 pp.

The Secret Lives of Planets

Reviewed by **Heather Bloemhard**[5]

The Secret Lives of Planets by Paul Murdin includes a plethora of information about our Solar System. Murdin covers planets, asteroids, moons, dwarf planets, and more, approximately one per chapter. Even exoplanets—the planets that orbit a star other than our Sun—are referenced frequently, although not in their own chapter. Using only a few images, Murdin illustrates the historical and physical concepts that surround each of these elements in prose peppered with anecdotes from his own career as an astronomer.

While the book's tone is pleasant and conversational, the discussions are often technical in nature, and I worry that some readers may be frustrated by its many tangents and loose organizational structure. For example, in his discussion of the formation of Mercury, Murdin references the formation of exoplanets, the discovery of 'Oumuamua, and Earth's fossil record. The same chapter also refers to Earth and Venus to help explain orbital eccentricity and precession, but this analogy may fall short for lay readers.

I was also disappointed that Murdin relied almost exclusively on the accomplishments of European men to tell the story of how our understanding of the Solar System emerged over time. He writes, for example, of Nicolaus Copernicus's revelations about the geometry of our solar system but neglects the work of Muslim astronomers who developed models of heliocentric orbits hundreds of years earlier. Murdin is far from alone in this misstep, but it is well worth striving to do better.

Despite these criticisms, every reader will learn something from this ambitious book. Did you know, for example, that some scientists once believed there were oases of vegetation on Mars, or that others believed that martians might try to colonize Earth? From the exchange of planetary material by way of meteorites to the formation of asteroids, Murdin covers a wide range of astronomical topics, including the aurora of Jupiter, the mysteries of Uranus, and the potential of the moons of Jupiter and Saturn to support recognizable life.

I found Murdin's personal recollections to be the most compelling feature of *The Secret Lives of Planets*. He tells the story of how, as a student, he observed the shadows cast by the tops of clouds of different heights on Venus using a telescope similar to the one used by Galileo and uses this anecdote as a starting point to explain what the Italian astronomer discovered about the planet. Recounting the time he observed the launch of Cassini-Huygens,

Published by AAAS

A port official surveys the aftermath of the 1943 air raid on Bari, Italy. Injuries were exacerbated by a secret cache of mustard gas on the *John Harvey* Liberty ship.

a probe sent to Saturn's moon Titan, Murdin explains what scientists had hoped to learn from this mission and what they ended up discovering. He also discusses attending the 2006 International Astronomical Union conference, where a debate was held about the definition of a planet, and reveals what it was like to cast a vote on the final decision.

In the end, there is much to recommend *The Secret Lives of Planets* as an introductory text on our solar system.

The Secret Lives of Planets: Order, Chaos, and Uniqueness in the Solar System, *Paul Murdin,* Pegasus, 2020. 288 pp.

The Great Secret

Reviewed by **Peter Reczek**[6]

Modern cancer therapies are often the result of years of targeted research and development, making it easy to forget that many of the field's early breakthroughs had as much to do with chance as they did with preparation. In *The Great Secret,* Jennet Conant recounts one such breakthrough, which was made in the wake of a deadly disaster.

Conant's engrossing story is set in the Italian port town of Bari, which was used as an important staging area for the distribution of supplies supporting Allied troops as they pushed north through Italy during World War II. On 2 December 1943, a day that would later be referred to as "a little Pearl Harbor," German military aircraft sank more than 20 Allied ships anchored in Bari, leading to the loss of more than 1000 Allied servicemen and Italian civilians.

Lieutenant Colonel Stewart Alexander, a medical officer attached to General Eisenhower's headquarters in North Africa, was sent to coordinate medical relief efforts. In Bari, Alexander found "a nightmarish scene." In the aftermath of the air raid, "The walking wounded staggered in [to the hospital] unaided, suffering from shock, burns, and exposure after having been in the cold water for hours before being rescued. Others had to be supported, as they cradled fractured arms in improvised slings or dragged mangled limbs…Almost all of them were covered in thick, black crude oil," writes Conant. In addition to the acutely injured, Alexander discovered victims whose injuries had emerged days after the attack and could not be attributed to the percussive effects of the bombing.

After analyzing the positions of the ailing seamen, Alexander reported that an American Liberty ship, the *John Harvey*, was the source of the problem, speculating that it likely contained a secret cache of nitrogen mustard (i.e., mustard gas). Both the American and British governments denied any such cache, but Conant reveals that Alexander persisted, and his controversial report—which, crucially, documented a decrease in white blood cell counts in the victims—was accepted by the Allied High Command with a classification of "Secret."

After the war, Colonel C. P. "Dusty" Rhoads, who had been Alexander's superior during the Bari investigation, reasoned that an agent that reduced white blood cells might be useful in treating some forms of leukemia. While serving as the first director of the Sloan Kettering Institute, Rhoads oversaw a clinical trial to test nitrogen mustards as potential therapeutic agents for the treatment of neoplastic disease. The results exceeded expectations. "In their first attempt to treat patients with inoperable lung cancer with nitrogen mustard, the Memorial team reported that of the thirty-five patients, 74 percent showed some clinical improvement" writes Conant. Many similar compounds, collectively known as alkylating agents, are still the foundation of the combination chemotherapy used to treat some forms of leukemia.

Drawing largely from archival research, Conant relies on a loose conversational style to convey a fast-paced medical detective story that demonstrates how careful scientific observation can yield unexpected benefits and serves as a reminder of the difficult choices made by governments to balance public health and secrecy in matters of security.

The Great Secret: The Classified World War II Disaster That Launched the War on Cancer, *Jennet Conant,* Norton, 2020. 400 pp.

[1]Department of Biology, The Behrend College, Pennsylvania State University, Erie, PA 16563, USA. Email: itk2@psu.edu; [2]Department of Ecosystem Science and Sustainability, Colorado State University, Fort Collins, CO 80523, USA. Email: gillian.bowser@colostate.edu; [3]Sarah Lawrence College, Bronxville, NY 10708, USA. Email: ksingh@sarahlawrence.edu; [4]Hewlett Packard Enterprise, San Jose, CA 95112, USA. Email: arti.garg@stanfordalumni.org; [5]Vanderbilt University Office of Federal Relations, Washington, DC 20002, USA. Email: hbloemhard@gmail.com; [6]Standards Coordinating Body for Regenerative Medicine, Gaithersburg, MD 20899, USA. Email: peter.reczek@gmail.com; [7]Office of Science and Technology Cooperation, U.S. Department of State, Washington, DC 20520, USA. Email: esha.mathew@gmail.com; [8]Government Relations Office, American Psychological Association, Washington, DC 20002, USA. Email: joseph.keller1@gmail.com.

PHOTO: (U.S. ARMY SIGNAL CORPS) HENRY UTLEY MILNE COLLECTION/ U.S. ARMY HERITAGE CENTER AND EDUCATION CENTER, CARLISLE, PA

Published by AAAS

Entanglements

Reviewed by **Esha Mathew**[7]

In quantum physics, entanglement is a property wherein two particles are inextricably linked. Put another way, entangled particles are never truly independent of each other, no matter the distance between them. It is fitting then that *Entanglements* is an anthology of short stories about inextricably linked people and the impact of emerging technologies on their relationships. A talented set of authors, with deft editing by Sheila Williams, explore the full spectrum of intimacy and technology to great effect. As an added visual treat, illustrations by Tatiana Plakhova punctuate each story with a blend of science, mathematics, and art that complements the subject matter.

Even with the length limitations of a short story, the world-building in this compilation is frequently full and often insidiously terrifying, particularly in those stories that use the familiar as breadcrumbs to lure the reader in. The very first tale, "Invisible People" by Nancy Kress, begins with a mundane morning routine and carefully layers in a story about two parents reeling from an unsanctioned genetic experiment on their child. In "Don't Mind Me," Suzanne Palmer uses the shuffle between high school classes as a foundation on which to build a story about how one generation uses technology to enshrine its biases and inflict them on the next. The ethical implications in these stories offer fodder enough for plenty of late-night discussions. It is also chilling how entirely possible many of the fictional futures seem.

But looking forward need not always be bleak. This volume balances darker-themed stories with those in which technology and people collide in uplifting and charming ways. In Mary Robinette Kowal's "A Little Wisdom," for example, a museum curator, aided by her robotic therapy dog–cum–medical provider, finds the courage within herself to inspire courage in others and save the day. Meanwhile, in Cadwell Turnbull's "Mediation," a scientist reeling from a terrible loss finally accepts her personal AI's assistance to start the healing process. And in arguably the cheekiest tale in this compilation, "The Monogamy Hormone," Annalee Newitz tells of a woman who ingests synthetic vole hormones to choose between two lovers, delivering a classic tale of relationship woes with a bioengineered twist.

With such a dizzying array of technologies discussed in relation to a range of human emotion and behavior, readers may experience cognitive whiplash as they move from one story to the next. But it is definitely worth the risk. The 10 very different thought experiments presented in this volume make for a fun ride, revealing that human relationships will continue to be as complicated and affirming in the future as they are today. I would recommend the Netflix approach to this highly readable collection: Binge it in one go, preferably with a friend.

Entanglements: Tomorrow's Lovers, Families, and Friends, *Sheila Williams, editor,* MIT Press, 2020. 240 pp.

Therapy robots, like this plush seal, are moving out of the realm of science fiction and into reality.

Predict and Surveil

Reviewed by **Joseph B. Keller**[8]

The U.S. police system is experiencing a reckoning. Protesters across the country (and around the world) have taken to the streets, arguing that police brutality disproportionately harms minority communities, and the current value of policing is being debated by city councils, lawmakers, and members of the news media. Into this tumultuous context enters Sarah Brayne's book, *Predict & Surveil: Data, Discretion, and the Future of Policing*.

A sociologist by training, Brayne synthesizes interview data and field notes from 5 years of observation within the Los Angeles Police Department, employing a firsthand ethnographic approach to reveal how big data are currently used in tech-forward police departments in America. She chronicles both consequential and mundane interactions between officers, civilians, and data. For example, she documents officers uploading license plate numbers, field interview notes, traffic citations, and potential gang affiliations onto a private industry data platform, as well as their active surveillance of hotspots in Los Angeles predicted to be criminogenic. This fly-on-the-wall perspective captures the human aspect of a police force grappling with automated systems and machine-learning decisions in real time, juxtaposing the experiences of individual officers with institutional directives being handed down from administrators and lawmakers.

Many police departments contend that the adoption of predictive analytics can improve objectivity and transparency, reduce bias, and increase accountability. Yet Brayne's book reveals how few of these metrics actually improve with predictive policing and exposes the scant evidence that supports the idea that it reduces crime rates. On the contrary, she insists, predictive policing raises glaring civil rights concerns and reinforces harmful racial biases. We all leave digital traces throughout our daily lives, and innocent people can be caught in the dragnet and cataloged in a digital criminal justice system, where a case can be built from benign data. Police unions, Brayne notes, often vehemently oppose the tracking of their own officers. She records incidents of officers turning off their car locator signals, for example, as well as other tactics used to thwart tech-infused managerial oversight.

Many officers view policing as an art form rather than a scientific system that can be optimized. To some, big data policing threatens their sense of police instincts and identity. "They worry that they will become nothing more than line workers and insist that their years of accumulated experiential knowledge is irreplaceable," observes Brayne.

Brayne's book raises timely issues relevant to mass surveillance and policing amid a growing debate about facial recognition systems, which makes their omission from this work notable. Although banned in several major American cities, these systems remain a common tool for identifying potential offenders, despite abundant evidence of dangerous inconsistencies.

Predictive policing can drive societal inequalities, but Brayne suggests that reducing instances of general police contact may mitigate disparities. In addition to offering immediate recommendations for changing law enforcement in the digital age, she asserts that effective programmatic reforms are typically influenced by external social organizing and guided by communities. (The likelihood of real transformation from within the police system is small, she believes.) For judicial and policing institutions genuinely seeking reform, this book provides powerful observations and analysis that suggest how we can begin. ■

Predict and Surveil: Data, Discretion, and the Future of Policing, *Sarah Brayne,* Oxford University Press, 2020. 224 pp.

10.1126/science.abe2994

PHOTO: FRANTICOO/ISTOCK

Published by AAAS

PERSPECTIVES

HUMAN GENOMICS

Searching for sex differences

Evolved sex differences in gene expression are pervasive, but so too is sampling bias

By **Melissa A. Wilson**

The behemoth effort, started a decade ago, known as the Genotype-Tissue Expression (GTEx) Consortium aims to discover how DNA variation affects gene expression across human tissues (*1*, *2*). As part of this consortium, on page 1331 of this issue, Oliva *et al.* (*3*) find that more than one-third of genes show sex-biased expression in at least one tissue. Four other GTEx studies, on pages 1318, 1334, 1333, and 1332 of this issue, respectively, discuss the effects of gene regulation in human tissues (*4*), identify functional rare genetic variation (*5*), study predictors of telomere length (*6*), and report cell type–specific gene regulation (*7*). What is especially notable about Oliva *et al.* is the careful analysis, which revealed that in addition to reported genetic and hormonal effects (*8*), there are cell type–specific sex differences in tissue composition. Furthermore, their work highlights that rather than being strictly dimorphic, interindividual variation results in overlapping distributions of gene expression between the sexes.

It has been hypothesized that selection shaped sex differences in immune function in response to the evolution of pregnancy and the placenta in mammals, beginning more than 90 million years ago and contributing to the observed sex differences in diseases today, including a female bias in autoimmune disease and male bias in most cancers (*9*). Sex differences in gene expression are broadly shared across mammals, but their role in shaping sex differences in disease etiology has not been thoroughly explored. Oliva *et al.* report that genes that show differences between sexes are enriched for multiple pathways, including in immune responses and cancer. Furthermore, they identify sex differences in a cluster of genes that target histone H3 lysine 27 trimethylation (H3K27me3) sites; these histone marks have also been reported to show sex-differentiated expression in the placenta (*10*). Oliva *et al.* provide a comprehensive baseline for sex differences in gene expression in unaffected tissues that can be used for future comparisons with diseased tissues. These observations may also inform about which pathways are most important in sex differences in disease etiology and aid in the development of targeted therapies.

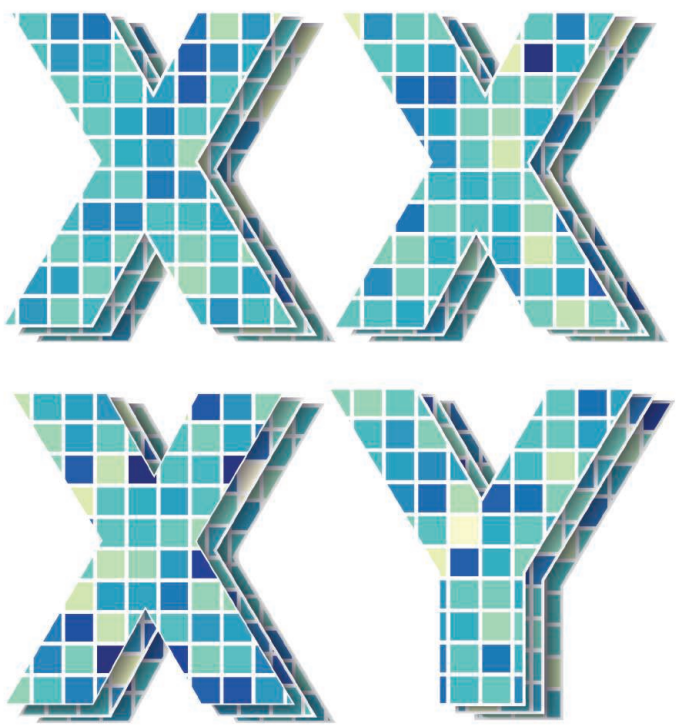

Sex differences in gene expression vary across the genome and between individuals, as represented by these heatmaps.

(GRAPHIC) V. ALTOUNIAN/*SCIENCE* AND M. ATAROD/*SCIENCE*; (DATA) GTEX CONSORTIUM

Oliva *et al.* identified hundreds to thousands of genes (1.3 to 12.9% of the genes expressed per tissue) that show sex differences in gene expression in any given tissue but found that the effect for each individual gene is subtle (the median fold change in expression was just 1.04). This is after accounting for the cellular composition of tissues that came from males versus females. The authors hypothesize that this sex difference in cell type composition—particularly of immune-related cells, such as monocytes and neutrophils [previously reported by (*11*)]—may contribute to the underlying sex-specific dysregulation for some diseases. These sex differences in cell type composition affect estimates of gene expression and, if unaccounted for, can skew results that compare groups with unequal sex ratios. Future studies that include samples from males and females will now need to account for cell type composition in addition to sex chromosome complement and hormonal environment. This is because different sex ratios in cell type in cases versus controls may drive the gene expression signal more than the phenotype of interest.

Although the genes with the highest fold change in expression were found on the X chromosome, the X chromosome contains only 4% of genes with sex-differential expression; the remaining 96% are spread across the genome (*3*). This is important because the X chromosome is often excluded from genome-wide analyses (*12*), but in doing so, studies may be missing genes with the largest effects. Additionally, Oliva *et al.* call attention to the importance of autosomal (non–sex chromosome) gene regulation in contributing to sex differences in humans. Given this, it is also noteworthy that they show that sex-biased autosomal gene expression is not very specific for predicting the sex of the donor from which the sample was taken (84% accurate, with 56% specificity), emphasizing how labile sex-biased gene expression is across people.

The GTEx Consortium has generated an invaluable resource through the generous involvement of patients and their families. However, like many consortia, sampling biases hinder investigation of interindividual variation. Details about the sampling are, with much appreciation, made transparent by the consortium on the GTEx Portal (*13*).

School of Life Sciences, Center for Evolution and Medicine, The Biodesign Institute, Arizona State University, Tempe, AZ, USA. Email: mwilsons@asu.edu

Published by AAAS

Just over two-thirds (67.1%) of the samples are from males. This means that studies are unevenly statistically powered to detect sex differences. It also means that studies that use the GTEx data as a reference set for comparison with disease state, for example, should take into account the relative proportion of samples from males and females (in both sets) because the relative sex effects on gene expression may not be the same in both.

Also, more than half of the samples come from people 50 years and older. This means that the samples are skewed toward understanding gene expression in tissues that have had many different exposures, potentially contributing to the observed interindividual variation, and does not reflect expression of tissues across the life span. Considering variation across the life span is especially critical for understanding how puberty and menopause, for example, affect gene regulation between the sexes.

Last, representation of global human genetic variation is low, with nearly 85% of samples collected from white people of European descent. There is a dearth of information about genetic variation and gene expression outside of a narrow range of recent genetic ancestries (*14*). This is critical for human health because inferences about genetic risk from one group of people with recent shared ancestry often do not generalize to others (*15*).

Given these limitations of the samples, it is even more surprising—and should be motivating to human geneticists—how much interindividual variation is observed in gene expression among the people included in the GTEx Consortium. This should be a call to projects to expand the representation of human variation in future studies. ■

REFERENCES AND NOTES

1. GTEx Consortium, *Nat. Genet.* **45**, 580 (2013).
2. NIH, "NIH launches Genotype-Tissue Expression project," NIH News 7 October 2010; www.genome.gov/27541670/2010-release-nih-launches-genotype-tissue-expression-project (accessed 15 August 2020).
3. M. Oliva *et al.*, *Science* **369**, eaba3066 (2020).
4. GTEx Consortium, *Science* **369**, 1318 (2020).
5. N. M. Ferraro *et al.*, *Science* **369**, eaaz5900 (2020).
6. K. Demanelis *et al.*, *Science* **369**, eaaz6876 (2020).
7. S. Kim-Hellmuth *et al.*, *Science* **369**, eaaz8528 (2020).
8. A. P. Arnold, *J. Neuroendocrinol.* **21**, 377 (2009).
9. H. Natri, A. R. Garcia, K. H. Buetow, B. C. Trumble, M. A. Wilson, *Trends Genet.* **35**, 478 (2019).
10. B. M. Nugent, C. M. O'Donnell, C. N. Epperson, T. L. Bale, *Nat. Commun.* **9**, 2555 (2018).
11. E. Bongen *et al.*, *Cell Rep.* **29**, 1961 (2019).
12. A. L. Wise, L. Gyi, T. A. Manolio, *Am. J. Hum. Genet.* **92**, 643 (2013).
13. GTEx Portal; https://gtexportal.org/home/tissueSummaryPage (accessed August 15, 2020).
14. A. B. Popejoy, S. M. Fullerton, *Nature* **538**, 161 (2016).
15. A. R. Martin *et al.*, *Am. J. Hum. Genet.* **100**, 635 (2017).

ACKNOWLEDGMENTS

The author is supported by the National Institute of General Medical Sciences of NIH (R35GM124827).

10.1126/science.abd8340

SEISMOLOGY

Quiet Anthropocene, quiet Earth

Seismic noise levels that correlate with human activities fell when pandemic lockdown measures were imposed

By **Marine A. Denolle**[1] *and* **Tarje Nissen-Meyer**[2]

Our planet vibrates incessantly, sometimes with notable but more often with imperceptible intensity. Conventional seismology attempts to decipher vibrational sources and path effects by studying seismograms—records of vibrations measured with seismometers. In doing so, scientists seek either to understand the tectonic processes that lead to strong ground motions and earthquake failure (*1*) or to probe otherwise inaccessible planetary interiors (*2*). Progress in these areas of research typically has relied on the rare and geographically irregular occurrence of large earthquakes. However, anthropogenic (human) activities at Earth's surface also generate seismic waves that instruments can detect over great distances. On page 1338 of this issue, Lecocq *et al.* (*3*) report on a quieting of anthropogenic vibrations since the start of the severe acute respiratory syndrome coronavirus 2 (SARS-CoV-2) pandemic.

Seismology has benefited from a surge in seismic data volume, computational power, and corresponding methodological development. These advances have enabled seismologists to branch away from traditional source and subsurface characterization of the energy from earthquakes and human-made blasts. The expansion of seismic networks has allowed the observation of previously unseen natural processes as diverse as wildlife activity (*4*), bed load transport in rivers, glacier sliding (*5*), and surface-mass wasting (*6*). In particular, scientists use continuous, ambient seismic vibrations to probe volcanic activities (*7*) and groundwater resources (*8*), to track storms (*9*), and to decipher ice sheet processes (*10*).

Human cultural noise carries seismic signatures mostly at frequencies above 1 Hz, whether the source is transient (entertainment; individual cars, trains, or planes), harmonic (wind turbines, machinery), or diffuse (railroads, highways) (*11*, *12*) (see the figure). Overall, anthropogenic seismic noise levels have increased over the past few decades, and there is a clear positive correlation between this increase and gross domestic product (*13*). But when the SARS-CoV-2 pandemic began to ravage the planet, humans—and Earth—went quiet.

Through a global analysis of seismic noise levels, Lecocq *et al.* found that most sites experienced a drastic reduction in noise levels in the 4- to 14-Hz frequency band. This reduction was much greater than those observed during the annual noise-level cycles of national or religious holidays. Daily CO_2 emissions fell only 11 to 25% (*14*), whereas anthropogenic vibrations dropped by 75% in most countries that imposed lockdown measures. Among countries with the greatest noise reductions were China, Italy, and France—all densely populated places with strong government responses (that is, with high virus-containment indices) (*15*).

Lecocq *et al.* also detected a correlation between seismic data and new types of time series, such as urban audible sound from acoustics data and cell phone mobility data. The authors observed the greatest correlations between seismic noise levels and two common types of pandemic mitigation: surface transportation and nonessential business activities. Lecocq *et al.* did not detect a strong correlation between lockdown and seismic noise reduction at other frequency bands, which might be explained by certain uninterrupted human activities such as power generation (*14*).

For all its hardships, the lockdown has unlocked a door to scientific inquiry into environmental noise and global collaboration. At a fundamental level, low noise benefits traditional seismology, hence the recent noise decrease might open new windows of opportunity; study areas hindered by urban noise might now be targets for detecting microseismicity or for improved subsurface imaging. The crucial next step, as ever in seismology, is to determine the causative nature of these signals beyond their correlation—thus turning anthropogenic noise into informative signals that allow scientists to address new questions. For example: Is there feedback between anthropogenic vibrations and Earth processes? And will seismic monitoring of anthropogenic and environmental activities become complementary, economically valuable alternatives to conventional techniques? To achieve these advances, seismologists must develop new ways of processing data

[1]Department of Earth and Planetary Sciences, Harvard University, Cambridge, MA 02138, USA. [2]Department of Earth Sciences, University of Oxford, Oxford OX1 3AN, UK. Email: mdenolle@fas.harvard.edu; tarje.nissen-meyer@earth.ox.ac.uk

Published by AAAS

and modeling and interpreting results.

Lecocq *et al.* exemplify seismological progress through best practices in scientific research: public data, open-access software and hardware, global cooperation, and crowdsourcing of citizen-science projects. All of the data are publicly available through open-access data centers at the Incorporated Research Institutions for Seismology (IRIS), which hosts and redistributes real-time seismograms from most of the stations participating in the Federation of Digital Seismograph Networks archive. A large proportion of the data used in the Lecocq *et al.* study was measured on seismic instruments that are powered on open-source Raspberry Pi computers hosted by citizen scientists. The Raspberry Shake network counts more than 3500 stations globally, all installed in homes, schools, and research institutions at 2 to 7% of the cost of conventional research or industrial sensors. The authors performed data analyses with open-source Python software Obspy, demonstrating the prevalence and usefulness of open-source community codes in modern science.

Like the pandemic, the seismological community also is shaking up norms. One important example is the reorganization of research activities. Although physical borders are closed, Lecocq *et al.* demonstrate that, much like the global medical research on SARS-CoV-2, seismological research is and ought to be without borders. The new study represents scientists from 25 countries on five continents, and the authors shared the manuscript on public editing platforms (Google Docs, Slack) that allowed for all members of the community to contribute. Indeed, social seismology, which directly relates human activities and seismic waves, has sparked enthusiasm in the scientific community for urban seismology. The fall meeting of the American Geophysical Union (December 2020) will highlight the imminent wave of SARS-CoV-2–related seismological science in a special session called "Social Seismology." ■

REFERENCES AND NOTES

1. M. A. Denolle, E. M. Dunham, G. A. Prieto, G. C. Beroza, *Science* **343**, 399 (2014).
2. K. Hosseini *et al.*, *Geophys. J. Int.* **220**, 96 (2020).
3. T. Lecocq *et al.*, *Science* **369**, 1338 (2020).
4. B. Mortimer, W. L. Rees, P. Koelemeijer, T. Nissen-Meyer, *Curr. Biol.* **28**, R547 (2018).
5. E. A. Podolskiy, F. Walter, *Rev. Geophys.* **54**, 708 (2016).
6. G. Ekström, C. P. Stark, *Science* **339**, 1416 (2013).
7. G. Olivier, F. Brenguier, R. Carey, P. Okubo, C. Donaldson, *Geophys. Res. Lett.* **46**, 3734 (2019).
8. T. Clements, M. A. Denolle, *Geophys. Res. Lett.* **45**, 6459 (2018).
9. L. Gualtieri, S. J. Camargo, S. Pascale, F. M. E. Pons, G. Ekström, *Earth Planet. Sci. Lett.* **484**, 287 (2018).
10. A. Mordret, T. D. Mikesell, C. Harig, B. P. Lipovsky, G. A. Prieto, *Sci. Adv.* **2**, e1501538 (2016).
11. J. Díaz, M. Ruiz, P. S. Sánchez-Pastor, P. Romero, *Sci. Rep.* **7**, 15296 (2017).
12. S. Schippkus, M. Garden, G. Bokelmann, *Seismol. Res. Lett.* **91**, 2803 (2020).
13. T.-K. Hong, R. Martin-Short, R. M. Allen, *Seismol. Res. Lett.* **91**, 2343 (2020).
14. C. Le Quéré *et al.*, *Nat. Clim. Chang.* **10**, 647 (2020).
15. P. Poli, J. Boaga, I. Molinari, V. Cascone, L. Boschi, *Sci. Rep.* **10**, 9404 (2020).

ACKNOWLEDGMENTS

We thank L. Ermert and B. Liposky for their comments.

10.1126/science.abd8358

Humans and nature excite seismic waves

Seismometers record vibrations from everything, not only earthquakes. Shown are sources that induce seismic waves of different vibration modes (harmonic, diffuse, transient), detectable over large distances.

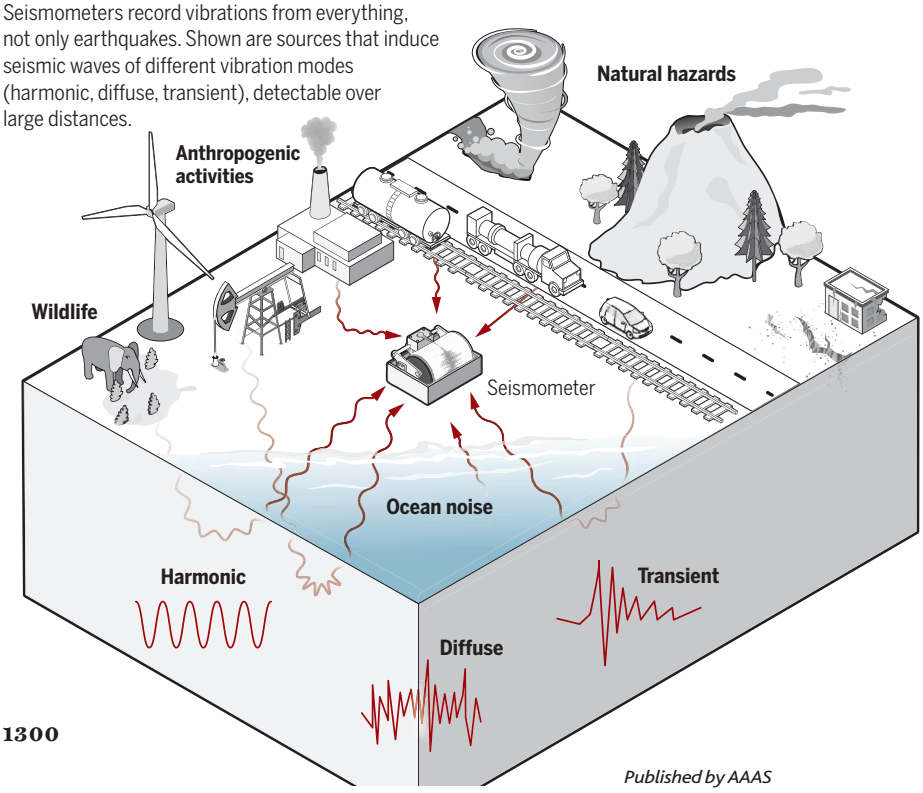

GRAPHIC: N. DESAI/*SCIENCE*

FERROELECTRICS

A key piece of the ferroelectric hafnia puzzle

Dipolar slices explain the origin of ferroelectricity in a material now used for memory devices

By **Beatriz Noheda**[1,2] *and* **Jorge Íñiguez**[3,4]

The ferroelectrics community is witnessing one of those moments in which serendipity changes the course of science. The story of ferroelectric hafnia (HfO_2) resembles that of Cinderella: Not invited to the polar dielectrics ball, nanoscale HfO_2 was dismissed as not being a real ferroelectric, a material that has a switchable spontaneous polarization, despite the experimental evidence for this response. On page 1343 of this issue, Lee *et al.* (*1*) bring us closer to a real-life fairy tale ending with their theoretical calculations, which show that nanoscale HfO_2 becomes a ferroelectric through a different mechanism. Polarization manifests in the form of two-dimensional (2D) slices separated by nonpolar spacers, associated with flat polar phonon bands that allow for homogeneous switching of electric dipoles.

The story starts with research that began in 2006 but was not published until 2011 (*2*). Scientists fabricating silicon transistors with HfO_2-based insulating layers spent several years trying to explain the origin of a strange peak observed in the capacitance-voltage characteristics. The peak looked very much like the ones observed in ferroelectrics when an applied electric field switches the direction of the spontaneous polarization. This feature has made ferroelectrics one of the oldest nonvolatile semiconductor memory types (*3*).

[1]Zernike Institute for Advanced Materials, University of Groningen, Nijenborgh 4, 9747AG Groningen, Netherlands. [2]CogniGron Center, University of Groningen, Nijenborgh 4, 9747AG Groningen, Netherlands. [3]Materials Research and Technology Department, Luxembourg Institute of Science and Technology (LIST), Avenue des Hauts-Fourneaux 5, L-4362 Esch/Alzette, Luxembourg. [4]Department of Physics and Materials Science, University of Luxembourg, Rue du Brill 41, L-4422 Belvaux, Luxembourg. Email: b.noheda@rug.nl

Published by AAAS

However, ferroelectricity was unlikely for two reasons: No polar phases had ever been reported in HfO_2, a refractory material with a long history of research (*4*), and these HfO_2 layers were only a few nanometers thick. Ferroelectricity is not expected at the nanoscale because it is a cooperative phenomenon. The local dipoles in ferroelectric materials, which result from the relative displacement of positive and negative ions, interact electrically with the dipoles of the neighboring cells and have a tendency to align collectively in the same direction, akin to what happens in a ferromagnet with the electron spins. The collective ordering leads to a spontaneous polarization. However, when the dimensions of the ferroelectric sample are small, as needed in microelectronics, a substantial number of dipoles lie on its surface. The stabilization of the ferroelectric phase is hampered by the energy cost of the depolarizing electric field that such dipoles create inside and outside the ferroelectric material, as dictated by Maxwell's equations.

In nature, this electrostatic penalty is reduced by domain formation, in which regions with alternating polarization (up and down) form in the sample. In theory, compensation of the dipolar surface charges can also be achieved by sandwiching the ferroelectric in between two metallic electrodes. The free carriers of the metal should screen the polarization charges and eliminate the depolarizing field, avoiding the need to form domains. In practice, this approach does not work perfectly with real metals, and screening is not complete (*5*). How to work around this issue has been one of the main research focuses of the ferroelectrics community for more than 30 years, driven by the vision of a ferroelectric nonvolatile memories that would be faster, denser, and less power-consuming than their magnetic counterparts (*6*).

Thus, even when the paper reporting on ferroelectric HfO_2 was published (*2*), the ferroelectrics community largely dismissed this result as an artifact, assuming that a material that is not polar in bulk would not become polar at the nanoscale. Moreover, at the nanoscale, it is hard to distinguish ferroelectric switching peaks from the voltammetry characteristics that could arise from electrochemical reactions at interfaces (*7*). However, after many subsequent studies from several groups (*8*), the evidence for robust switching became difficult to ignore. The current consensus is that ferroelectric-like switching in HfO_2-based ferroelectrics does exist, but its origin is still highly debated. Only one or two reports have shown a ferroelectric phase transition in this material (*9*, *10*). In addition, switching requires large applied fields and does not seem to proceed as in other ferroelectrics through movement of domain walls (*11*).

How HfO_2 becomes ferroelectric at the nanoscale and how it screens polarization charges at surfaces are the main questions to resolve. The former has been explained by a combination of effects (surface energy, ordered dopants, and oxygen vacancies) that favor the occurrence of the polar phase (*3*, *7*). The latter could be explained by the much lower dielectric permittivity of HfO_2 compared with other ferroelectrics, but why is it so low?

Theoretical calculations by Lee *et al*. now show that ferroelectricity in HfO_2 is of a different type (see the figure). The polar features of HfO_2 are associated with a nearly flat phonon band (similar frequency of the different modulations along the energy band). Thus, a homogeneous polar order, in which all electric dipoles align parallel as in a regular 3D ferroelectric phase, is as likely as any transversally modulated inhomogeneous order in which an arbitrary sequence of ferroelectric domains are separated by 180° domain walls. Put differently, the domain walls in HfO_2 have essentially zero energy cost and a negligible width.

This situation, which is reminiscent of the effect called pressure-induced amorphization (*12*), has two important consequences: HfO_2 has essentially 2D polar instabilities, meaning that a polar 2D plane (polarization within the plane) can in principle appear by itself, even if the rest of the material remains nonpolar. The polarization of such 2D slices has a very small electrostatic penalty (depolarizing field) associated with it, much smaller than that for 3D polar order, which helps explain why ferroelectricity can occur in HfO_2 at the nanoscale.

Also, the 2D polar slices are all but decoupled from each other, so in HfO_2, the switching of one domain has no effect on its surrounding domains. Lee *et al*. argue that this process must have dramatic effects in how ferroelectric switching proceeds in this material because nucleation of reversed domains is not followed by growth, which should yield very large coercive fields, as is indeed observed. The occurrence of individual switching of 2D polar planes offers the possibility of multilevel polarization switching with ideally as many intermediate states as the number of unit cells. This capability is of much interest for adaptable electronics and brain-inspired computing applications.

Lee *et al*. have found that a flat phonon band gives rise to dipolar localization, a phenomenon reminiscent of localization effects for electrons, photons, and other particles but whose implications in the case of ferroelectrics have not been fully explored. In this way, dipolar order can occur without the need for cooperative 3D behavior, allowing miniaturization and multivalued nonvolatile storage. The next step will be to use this knowledge to engineer lower switching voltages for memory applications in this material that is already compatible with silicon electronics. ■

Figuring out a thin ferroelectric

The theoretical study by Lee *et al*. explains how an ultrathin material, hafnia, can be a ferroelectric by comparing it with a classical three-dimensional (3D) ferroelectric. In both cases, alternating domains of polarization (arrows representing ferroelectric dipoles along the *z* crystal direction) eliminate net surface charges and prevent depolarization.

2D dipolar crystal

In hafnia, the localization of dipoles in layers that are separated by nonpolar atomic sheets, represented by the gray "spacers," allows domains to form with no energy cost.

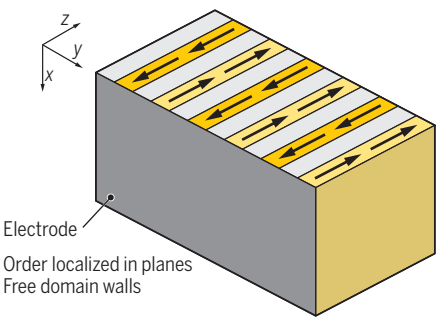

3D dipolar crystal

Domain formation creates an energy penalty caused by the existing interaction between neighboring dipoles in the *y* direction.

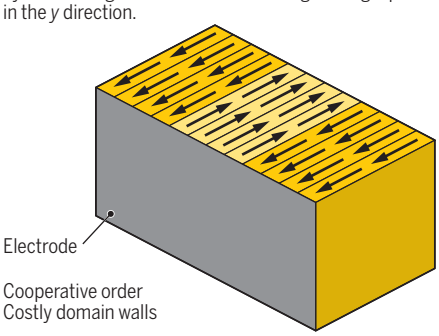

GRAPHIC: JOSHUA BIRD/*SCIENCE*

REFERENCES AND NOTES

1. H.-J. Lee, *Science* **369**, 1343 (2020).
2. T. S. Böscke, J. Müller, D. Bräuhaus, U. Schröder, U. Böttger, *Appl. Phys. Lett.* **99**, 102903 (2011).
3. J. Handy, "FRAM turns 68," The Memory Guy 10 July 2020; https://thememoryguy.com/fram-turns-68.
4. S. V. Ushakov *et al*., *Phys. Status Solidi B* **241**, 2268 (2004).
5. J. Junquera, P. Ghosez, *Nature* **422**, 506 (2003).
6. J. F. Scott, C. A. Paz de Araujo, *Science* **246**, 1400 (1989).
7. S. V. Kalinin, S. Jesse, A. Tselev, A. P. Baddorf, N. Balke, *ACS Nano* **5**, 5683 (2011).
8. U. Schroeder, C. Shong Hwang, H. Funakubo, *Ferroelectricity in Doped Hafnium Oxide: Materials, Properties and Devices* (Woodhead Publishing, 2019)
9. T. Shimizu *et al*., *Sci. Rep.* **6**, 32931 (2016).
10. T. S. Böscke *et al*., *Appl. Phys. Lett.* **99**, 112904 (2011).
11. M. Hoffmann *et al*., *Nature* **565**, 464 (2019).
12. M. H. Cohen, J. Íñiguez, J. B. Neaton, *J. Non-Crystal. Solids* **307-310**, 602 (2002).

10.1126/science.abd1212

Published by AAAS

MEDICINE

Modulating gut microbes

Fecal microbiota transplant and modulation of microbial species show therapeutic promise

By **Jennifer A. Wargo**

There are hundreds of trillions of microbes within the human body, which have a profound impact on modulating host function. Many of these microbes reside in the gastrointestinal tract and have been shown to influence normal physiology across all body systems (*1*). Disruptions in the delicate balance of microbes within the gut and other niches are associated with numerous disease states—including neurologic disorders, cardiovascular disease, gastrointestinal disorders, and even cancer (*2*). Accordingly, there is intense interest in targeting these microbes to promote overall health and to abrogate disease, with considerable advances made recently. Strategies to modulate gut microbes include fecal microbiota transplant (FMT), which involves the transfer of fecal material from one individual to another for a desired physiologic effect. This approach, among other gut microbiota modulation strategies, has shown promise in treating several disease conditions, although opportunities exist to iterate and build on these approaches.

The idea that disruptions in the gastrointestinal tract could contribute to systemic disease was championed centuries ago by Hippocrates, a physician in ancient Greece. Strategies to modulate the composition of the gut have also been around for centuries, with the first reports of the use of FMT dating back to the fourth century BCE in China where fecal preparations were used to treat gastrointestinal disorders (*3*). Parallels have also been observed in the animal kingdom, where coprophagia (ingesting fecal material) is common and may confer an increase in gut microbial diversity and associated enhancements in host function for digestion and other physiologic processes. However, the first successful clinical application of FMT was not published until 1958 with the report of FMT from healthy donors used for patients with pseudomembranous enterocolitis from *Clostridioides difficile* infection (CDI) (*4*). Numerous clinical trials have since been undertaken, using FMT and other gut microbiota modulation strategies to treat diseases of the gut (such as CDI, and inflammatory bowel disease, IBD) as well as other systemic diseases—including metabolic syndrome, autism, multiple sclerosis, Parkinson's disease, and even cancer (*2*).

Strategies to alter gut microbiota

Fecal microbiota transplant (FMT) involves transfer of fecal microbiota from a donor to another individual. Alternatively, microbial consortia (targeted formulations used to augment host microbiota) are being developed. Diet, prebiotics, and postbiotics can also influence the microbial community.

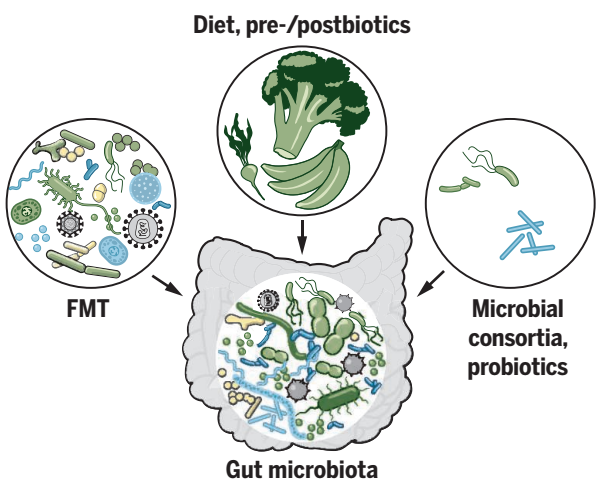

To date, many of the strategies to target gut microbes have involved the two extremes: either transfer of entire microbial communities (by using FMT) or transfer of a single microbial taxon. However, a growing number of approaches are now being developed as more is learned about the functional aspects and physiologic impact of microbes throughout the body. These iterative approaches transcend efforts that focus on taxonomic characterization of microbial niches through next-generation genomic sequencing, incorporating interrogation of functional characteristics of gut microbes (by metabolomic profiling and studies in preclinical models) to mediate the desired physiologic response. This has led to a host of therapeutic strategies from microbial consortia to pre-, pro-, and postbiotic interventions. Nonetheless, much still needs to be learned to implement true "precision" modulation of the gut microbiota.

When considering strategies to modulate the gut microbiota, the indication for intervention in the intended population must be considered. Gut dysbiosis, an imbalance in the composition of commensal microbial communities, has been linked to numerous disease states, substantiating the use of FMT and other gut microbiota modulation strategies (*5*). This link is fortified by data demonstrating that although there has been a decrease in infectious diseases over the past several decades with the widespread use of antibiotics, there has been a concurrent increase in allergy and autoimmune diseases (*6*) presumably at least partially due to disruption of the gut microbiota. Notably, some of the diseases being treated by gut microbiota modulation have a profound dysbiosis (such as CDI), whereas others have a more subtle disruption of gut microbes, which has implications for choosing the appropriate strategy for gut microbiota modulation.

Numerous other factors should be taken into account when contemplating modulation of the gut microbiota. These include the means of gut microbiota modulation, preparative regimen, measurement of engraftment of gut microbes and of the desired physiologic effect, and concurrent dietary intake (*7*). In general, the approach aims to restore a more "healthy" gut microbial community—although the definition of a "healthy" gut microbiota is not clearly established. However, data suggest that a diverse microbial community with a high degree of functional redundancy is associated with better overall health (*2*) and better outcomes in several disease states (*8*, *9*).

The most successful application of FMT thus far is in the treatment of refractory CDI, where treatment with FMT has been shown to be generally safe and highly effective (*2*). Nonetheless, guidelines for proper treatment and screening of donor stool are critical for safety and include screening for infectious diseases and disorders that are associated with perturbations of the gut microbiota, as well as the use of medications that can affect gut microbes such as antibiotics and proton pump inhibitors (*10*). Notably, these guidelines are iterative, as new recommendations are made to expand screening and testing of donors based on insights gained from ongo-

Departments of Surgical Oncology and Genomic Medicine, The University of Texas MD Anderson Cancer Center, Houston, TX 77030, USA. Email: jwargo@mdanderson.org

GRAPHIC: N. CARY/*SCIENCE*

Published by AAAS

ing trials. For example, screening of donors for multidrug-resistant organisms and severe acute respiratory syndrome coronavirus 2 (SARS-CoV-2) is now recommended. This follows reports of several patients with CDI who developed systemic infection with antibiotic-resistant bacterial infections following FMT (*11*), as well as concerns about possible infections with SARS-CoV-2.

The use of FMT is being investigated across numerous other disease conditions, although most of these are associated with a less profound dysbiosis and greater heterogeneity in assessed endpoints and outcomes. However, there is clear evidence of success in some trials across a number of indications, including IBD, after hematopoietic stem cell transplant and in autism spectrum disorders (*5*). Limitations in measuring efficacy in FMT trials may arise from "true negative" results, or from numerous other confounding factors, including features not dependent on gut microbes that contribute to the development and persistence of disease in the recipient, as well as variability in trial design and outcome measures. Additionally, there may be factors inherent to the FMT donor that may affect efficacy (such as composition and functional aspects of the transplanted microbiota); however, such "donor effects" may be less prominent for indications in which a more profound dysbiosis is present, such as in CDI and even IBD (*12*). Optimal dosing and route of delivery for FMT are also incompletely understood and may be context dependent. Additional studies are critically needed to interrogate the success (or failure) of this approach for these indications and to develop optimal strategies for use of FMT.

One attribute of FMT not possessed by other strategies to modulate the gut microbiota is the diversity of microbes that may be administered (including not only bacteria, but also viruses, fungi, and archaea) (see the figure). This provides potential functional redundancy for favorable impact on host physiology. In a profoundly dysbiotic state, this diversity represents a potential advantage over strategies that administer minimal-complexity microbial consortia, which may not engraft and may not be sufficient in reestablishing a "favorable" gut microbiota. However, the same attribute of increased diversity and complexity of FMT is also a limitation that creates issues with reproducibility and scalability.

There are also concerted efforts under way to develop consortia of microbes that can be reliably and consistently manufactured and administered to favorably modulate the gut microbiota to address gastrointestinal and systemic disease, offering improved scalability over FMT. This includes commercially available probiotics, which are live microorganism preparations with presumed health benefits. The impact of administration of many of these formulations across disease indications has been studied in clinical trials with mixed results, and to date none of these commercially available formulations are approved for use by major regulatory bodies such as the U.S. Food and Drug Administration (*13*). However, next-generation live biotherapeutics (live microorganisms developed as therapeutic agents with defined clinical benefit claims) are now being developed based on insights gained from sequencing data in human cohorts and from studies in preclinical models (*13*)—with many now in clinical trials.

The first wave of these next-generation live biotherapeutics focused mainly on taxonomy—incorporating single or several bacterial taxa within a consortia based on insights gained from profiling gut microbial species in human cohort studies and in preclinical models. An example of this is in cancer immunotherapy: Clinical trials are now under way using modulation of the gut microbiota through administration of microbial consortia (*7*). These formulations range from simple (monoclonal microbial formulations) to complex (involving consortia of 50 or more bacterial taxa and strains). However, there is a growing appreciation that focusing on the functional aspects of these microbes may be far more important than simply focusing on taxonomy, and genetically modified organisms are now being developed with a wide range of functional attributes (*13*). Although overall these formulations are generally well-tolerated, safety still needs to be taken into account because there are reports of bacterial translocation of these organisms from the gut into the bloodstream in critically ill patients receiving gut microbiota modulation through administration of commercially available probiotics (*14*).

Another strong consideration in gut microbiota modulation is the role of diet and prebiotics, as these can profoundly influence existing commensal gut microbes and those administered for therapeutic intent. These may ultimately serve as a stand-alone intervention in appropriate individuals with more subtle gut dysbiosis. Short-term studies have shown that large changes in diet can have a marked impact on gut microbes and associated physiology in the short term (*15*). However, this reliably reverts to a pre-intervention state if the instituted change in diet is not sustained. Nonetheless, numerous dietary intervention studies are currently under way (*7*), ranging from a somewhat simple intervention of adding one cup of canned beans per day to existing diets (NCT02843425) to extended (or longer-term) dietary interventions, where meals are prepared for (and shipped to) participants (NCT03950635). Such dietary modifications have potential relevance even if recipients are also treated with other gut microbiota modulation strategies such as FMT or live biotherapeutics, as they may sustain and promote optimal function of the transferred gut microbes, although optimal approaches of dietary intervention in these scenarios has yet to be defined. The use of prebiotic supplementation (such as resistant starches, polyphenols, and polyunsaturated fatty acids) is also being studied, because these compounds may provide optimal substrate to beneficial commensal (or administered) microbes.

It is becoming evident that modulation of gut microbes will be increasingly employed to promote overall health and to help treat disease, although optimal strategies for "precision" gut microbiota modulation remain incompletely understood. It is probable that a personalized approach will be needed, incorporating strategies such as FMT, administration of live biotherapeutics, dietary strategies, and prebiotics—although it is not inconceivable that an ideal "one-size-fits-all" approach could be identified. Through additional research and collaborative efforts, the true definition of dysbiosis in the gut microbiota as it relates to disease states can be better understood, as well as what constitutes an optimal gut microbiota to promote overall health, which could have broad impact for public health. ■

REFERENCES AND NOTES

1. I. Cho, M. J. Blaser, *Nat. Rev. Genet.* **13**, 260 (2012).
2. J. R. Allegretti, B. H. Mullish, C. Kelly, M. Fischer, *Lancet* **394**, 420 (2019).
3. F. Zhang *et al.*, *Am. J. Gastroenterol.* **107**, 1755 (2012).
4. B. Eiseman, W. Silen, G. S. Bascom, A. J. Kauvar, *Surgery* **44**, 854 (1958).
5. S. W. Olesen *et al.*, *Lancet Gastroenterol. Hepatol.* **5**, 241 (2020).
6. J. F. Bach, *N. Engl. J. Med.* **347**, 911 (2002).
7. J. L. McQuade, C. R. Daniel, B. A. Helmink, J. A. Wargo, *Lancet Oncol.* **20**, e77 (2019).
8. J. U. Peled *et al.*, *N. Engl. J. Med.* **382**, 822 (2020).
9. V. Gopalakrishnan *et al.*, *Science* **359**, 97 (2018).
10. G. Cammarota *et al.*, *Gut* **68**, 2111 (2019).
11. Z. DeFilipp *et al.*, *N. Engl. J. Med.* **381**, 2043 (2019).
12. S. W. Olesen, Y. Gerardin, *medRxiv* 19011635 (2019).
13. J. Suez, N. Zmora, E. Segal, E. Elinav, *Nat. Med.* **25**, 716 (2019).
14. I. Yelin *et al.*, *Nat. Med.* **25**, 1728 (2019).
15. L. A. David *et al.*, *Nature* **505**, 559 (2014).

ACKNOWLEDGMENTS

J.A.W. is supported by the National Institutes of Health (1R01CA219896-01A1), the Melanoma Research Alliance (4022024), American Association for Cancer Research Stand Up To Cancer (SU2C-AACR-IRG-19-17), and the MD Anderson Melanoma Moonshot Program. J.A.W. is an inventor on U.S. patent application (PCT/US17/53.717) and receives compensation from and is on the advisory boards for Imedex, Dava Oncology, Omniprex, Illumina, Gilead, PeerView, Physician Education Resource, AstraZeneca, Bristol-Myers Squibb, and Ella Therapeutics.

10.1126/science.abc3965

Published by AAAS

ULTRACOLD PHYSICS

Laser cooling of larger quantum objects

A nonlinear polyatomic molecule, $CaOCH_3$, has been laser-cooled to below 1 millikelvin

By **Eric R. Hudson**

Surfers have a concept they call progression. It is roughly the idea that each successive generation of wave riders is not constrained by the same idea of what is "impossible." Progression often comes in small steps, usually helped by improvements in technology but every so often—like Laird Hamilton's Millennium Wave at Teahupoo, Tahiti (*1*)—it comes in a giant leap when somebody does what everyone else was too scared to try. On page 1366 of this issue, Mitra *et al.* (*2*) have progressed molecular physics in a step that was unthinkable only a few years ago by laser-cooling a nonlinear polyatomic molecule, $CaOCH_3$.

Like stopping a bowling ball by repeatedly hitting it with ping-pong balls (*3*), laser cooling utilizes the repeated scattering of photons from a particle to cool it to ultracold temperatures (<1 mK). The technique, which garnered the 1997 Nobel Prize, has been the workhorse of atomic physics for roughly three decades and underlies virtually all experiments in the field, in areas as diverse as quantum computing and timekeeping. Extending the technique to more complicated objects such as diatomic and polyatomic molecules holds promise for new routes to important quantum science and technology (*4*). For atoms, their simple electronic structure enables their quick relaxation, through spontaneous emission, to only one of a few low-lying electronic states from which they can be re-excited. However, the ro-vibrational degrees of freedom of molecules lead to an increase in the number of low-energy states accessible by spontaneous emission. In general, scattering many photons from molecules requires an unwieldy number of lasers to address all of the possible low-lying ro-vibrational states.

The beginning of a solution to this problem came in two steps. In 2004, Di Rosa (*5*) pointed out that certain diatomic molecules, whose atoms were bound by roughly the same force in their ground and excited electronic states, were unlikely to change their vibrational state when spontaneously emitting a photon (see the figure, top right). In 2008, Stuhl *et al.* (*6*) proposed a method, based on a so-called "type II" magneto-optical trap demonstrated in atoms (*7*) and only recently understood (*8*), to handle the pesky rotational degree of freedom. Less than a year later, Shuman *et al.* (*9*) provided the first experimental demonstration of these ideas on the molecule SrF. Since then, three-dimensional laser cooling and trapping have been demonstrated for a number of diatomics including CaF (*10*, *11*), and laser cooling along one dimension has been observed in linear triatomic molecules such as SrOH (*12*).

The choice of these molecules can be understood by considering their gross electronic structure (*13*). For example, in CaF and SrF, the ns^2 configuration of the alkaline earth atom donates one electron to the halogen. The remaining valence electron remains localized on the metal such that the molecular electronic structure resembles that of the alkaline earth, making a nearly ideal molecule for laser cooling. If, however, O is used instead of F, the resulting electronic structure of CaO is markedly different from that of the parent metal atom and the molecule is a poor choice (see the figure, top left). Interestingly, the OH group in the triatomics behaves essentially like a halogen atom, accepting one electron from the ns^2 configuration of the

Department of Physics and Astronomy and Center for Quantum Science and Engineering, University of California, Los Angeles, CA, USA. Email: eric.hudson@ucla.edu

Choosing molecules for laser cooling

A molecule can be laser-cooled if it absorbs and emits photons upon an electronic transition without changing its vibrational state. Mitra *et al.* have extended laser cooling from linear molecules to $CaOCH_3$, a nonlinear polyatomic molecule.

Criteria for coolness

The Franck-Condon principle roughly dictates that this is possible for molecules that have similar bond lengths in the ground and excited states.

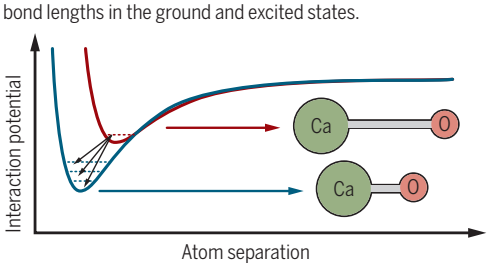

Difficult to cool
In CaO, the excited-state potential is shifted relative to the ground state. As a result, decays from the excited state populate many vibrational levels, making cooling difficult.

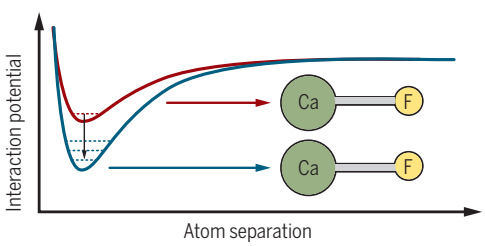

Easier to cool
In CaF, the range and shape of the excited-state potential are similar to those of the ground-state potential. As a result, decays from the excited state typically do not change the vibrational state.

Cooling larger molecules

Recent work has suggested that the ligand on a metal atom need not be a simple atom but can also be a functional group, which has allowed cooling of larger nonlinear symmetric top polyatomics such as $CaOCH_3$. The size and symmetry limits of this design principle are the subject of current research.

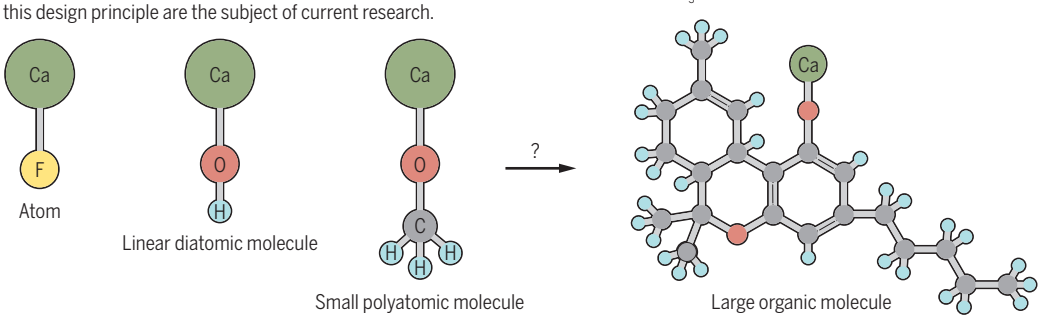

GRAPHIC: MELISSA THOMAS BAUM/*SCIENCE*

Published by AAAS

metal and yielding an atomic-like molecular electronic structure.

Kozyryev *et al.* continued this trend of cooling larger, more complex molecules by showing that the methoxy group should also behave similarly to the halogen, and proposed $CaOCH_3$ as a candidate for laser cooling (see the figure, bottom) (*14*). Although this choice may sound like a straightforward expansion, the extension to a nonlinear polyatomic molecule comes fraught with pitfalls. The spectroscopy of such molecules is much more complicated than the diatomics and triatomics studied previously. Effects normally neglected in smaller molecules can lead to a breakdown of the Born-Oppenheimer approximation and open new loss channels, such as coupling between the 12 vibrational modes of the molecule. Thus, like the Millennium Wave, the experiment had every chance of failure, but Mitra *et al.* demonstrated laser cooling of $CaOCH_3$ along one dimension of a beam down to a temperature of ~700 μK. They also demonstrated separate deterministic cooling of the two nuclear spin isomers.

The immediate impact of this result is that we now know it is possible to laser-cool molecules with non-$C_{\infty v}$ symmetry. This result opens the door to full three-dimensional cooling and trapping of a new class of quantum objects that possess previously inaccessible properties such as chirality. If the history of laser cooling is any guide, this capability should enable major advances in quantum computing and sensing, timekeeping, chemistry, and precision tests of fundamental physics (*15*). ■

REFERENCES AND NOTES

1. *Riding Giants*, directed by Stacy Peralta (Studio Canal, 2004); excerpt at www.youtube.com/watch?v=NcaZarxilJQ.
2. D. Mitra, N. B. Vilas, C. Hallas, L. Anderegg, B. L. Augenbraun, L. Baum, C. Miller, S. Raval, J. M. Doyle, *Science* **369**, 1366 (2020).
3. W. D. Phillips, *Rev. Mod. Phys.* **70**, 721 (1998).
4. M. R. Tarbutt, *Contemp. Phys.* **59**, 356 (2019).
5. M. D. Di Rosa, *Eur. Phys. J. D* **31**, 395 (2004).
6. B. K. Stuhl, B. C. Sawyer, D. Wang, J. Ye, *Phys. Rev. Lett.* **101**, 243002 (2008).
7. E. L. Raab, M. Prentiss, A. Cable, S. Chu, D. E. Pritchard, *Phys. Rev. Lett.* **59**, 2631 (1987).
8. J. A. Devlin, M. R. Tarbutt, *New J. Phys.* **18**, 123017 (2016).
9. E. S. Shuman, J. F. Barry, D. R. Glenn, D. DeMille, *Phys. Rev. Lett.* **103**, 223001 (2009).
10. S. Truppe, H. J. Williams, M. Hambach, L. Caldwell, N. J. Fitch, E. A. Hinds, B. E. Sauer, M. R. Tarbutt, *Nat. Phys.* **13**, 1173 (2017).
11. L. Anderegg, B. L. Augenbraun, E. Chae, B. Hemmerling, N. R. Hutzler, A. Ravi, A. Collopy, J. Ye, W. Ketterle, J. M. Doyle, *Phys. Rev. Lett.* **119**, 103201 (2017).
12. I. Kozyryev, L. Baum, K. Matsuda, B. L. Augenbraun, L. Anderegg, A. P. Sedlack, J. M. Doyle, *Phys. Rev. Lett.* **118**, 173201 (2017).
13. T. A. Isaev, R. Berger, *Phys. Rev. Lett.* **116**, 063006 (2016).
14. I. Kozyryev, L. Baum, K. Matsuda, J. M. Doyle, *ChemPhysChem* **17**, 3641 (2016).
15. I. Kozyryev, N. R. Hutzler, *Phys. Rev. Lett.* **119**, 133002 (2017).

10.1126/science.abd1657

GRAPHIC: A. KITTERMAN/*SCIENCE*

NANOTECHNOLOGY

Reactive polymers guide nanoparticle clustering

Tailored polymer shells drive the assembly of a desired class of nanoparticle architectures

By **Oleg Gang**[1,2,3]

From the early days of nanoparticle synthesis, researchers understood the need for adaptable methods that coordinated particles in clusters with precise nanoarchitecture. The similarity between the building of nanoscale clusters from particles and the formation of molecules from atoms goes beyond a structural analogy. As with molecules, which demonstrate properties not found in atoms, clusters exhibit synergistic functional responses beyond the properties of individual nanoparticles (*1*–*3*). For atomic systems, the formation of molecules is rationalized by orbital hybridization principles. Because this concept is not suitable for nanoparticles, scientists have explored other particle-assembly methods. On page 1369 of this issue, Yi *et al.* (*4*) describe a high-yield method for the assembly of targeted nanoparticle clusters.

Although a variety of methods exist for building nanoparticle clusters, they all follow a similar set of main concepts. In the first approach (called "packing"), possible mutual arrangements of attractive micron-sized particles determine the formation of specific clusters (*5*). Although a similar approach can be applied at the nanoscale, nanoparticles typically exhibit more complex interactions caused by the ligand shell grafted to their surface and the contribution of electrostatic, van der Waals, and other forces. For spherical nanoparticles, the ligand shell might modify the cluster structure expected for hard spheres, but the isotropic nature of interactions typically is preserved. Thus, a similar, albeit modified, "packing" concept still applies, however, the realization is often challenging. For nanoparticles with multiligand shells and complex interparticle interactions, intricate organizations might occur, but control over the resulting structures is limited.

The central idea of this anisotropic binding concept is to mimic atomic valence by establishing specifically located affinity patches on particles, forming so-called "patchy particles." This idea has been intensively investigated theoretically (*6*), and several implementations have been demonstrated for micron-sized particles (*7*, *8*).

Because this fabrication approach is limited to larger particles, a different strategy—molecular patterning—was used to create patchy nanoscale particles (*9*, *10*). This third concept provides the highest degree of control over cluster formation

Polymers guide cluster design

Nanoparticle A is grafted with charged copolymers (red lines) bearing a block of acidic groups; B is grafted with neutral copolymers (blue lines) bearing a block of basic groups.

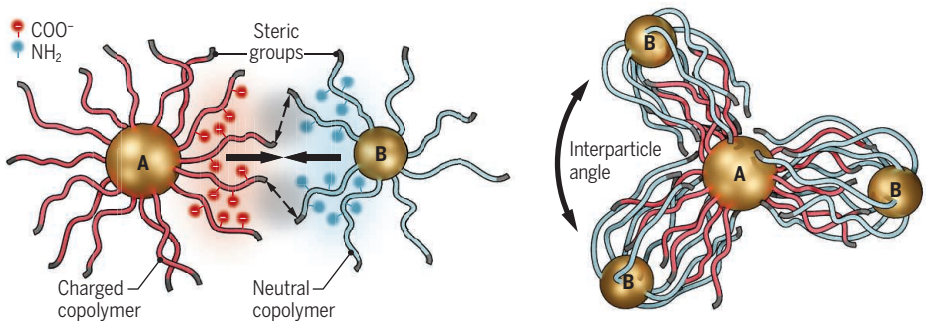

Interplay
A neutralization reaction drives attractive interactions, whereas the steric groups induce repulsion.

Cluster formation
The acid:base ratio per particle governs the cluster's architecture and defines the interparticle angle.

Published by AAAS

by using an underlying molecular (*2*, *3*, *11*) or nano-object (*12*) scaffold that prescribes the position of each nanoparticle and coordinates them in a targeted cluster. Thus, the spectrum of cluster-assembly methods ranges from a packing-based strategy with minimal particle engineering, to more elaborate patchy-particle strategies with designed particle-based directional interactions, to fully prescribed scaffold-based clusters. Among these diverse methods, none mimics a special aspect of interatomic bonds: Valence electrons, although delocalized within each atom, still support formation of well-defined molecules through directional bonds.

The new nanoparticle assembly strategy of Yi *et al*. resembles the "delocalized" feature of atomic systems. It relies on polymer-mediated reactions and interactions to regulate binding between two types of gold spherical nanoparticles (A and B) (see the figure). To form polymeric shells, the authors grafted two kinds of block copolymers containing either acid (a) or base (b) groups to the surfaces of these particles. The copolymer design allowed for control over the number and arrangement of reactive groups and inclusion of a chain portion on the outer part of the shells, so as to tailor steric repulsion between the shells or enable hydrophobic or hydrophilic interactions.

A neutralization reaction between the acid groups of the charged copolymers on one particle and base groups of neutral copolymers on the other particle drove the attractive interparticle interactions. Controlling the number of acid and base groups within grafted chains and the number of chains per particle allowed regulation of the ratio ($Z_{a/b}$) between acid and base groups. In this approach, $Z_{a/b}$ represents an effective valence for AB binding (see the figure). A neutralization reaction should progress until all the acid and base groups are reacted. This might require a specific reaction stoichiometry between particles A and B, which should be satisfied in the formation of an AB_x cluster. Yi *et al*. experimentally observed a direct correspondence between $Z_{a/b}$ and x.

The polymeric properties of the interacting shells proved critical for realization of the "delocalized" concept. The polymeric chains formed a weakly localized "cloud" of acid and base groups within the shell of each particle, which resembled delocalized electrons in atomic orbitals. After neutralization, polymer chains adopted confirmations that permitted acid and base groups to reorganize and react to the fullest extent possible. Thus, the number of B particles that reacted with A particles was fully determined by the $Z_{a/b}$. Moreover, given the steric repulsion between the particles and the Coulombic repulsion between the charged polymers in the bonds, the resulting nanoparticle clusters accommodated a spatial configuration that possessed equal angles between the B particles, thus leading to the demonstrated directional binding. The system also exhibited a self-limiting mechanism for cluster assembly, because the resulting reorganization of the grafted chains depleted the base groups in the outer hemisphere of B particles (see the figure). Electrostatic repulsion by the charged copolymers further reduced clustering beyond the designated stoichiometry.

"...this new methodology offers the ability to assemble with ease a desired class of nanoparticle architectures."

Given the large variety of copolymer structures, this new methodology offers the ability to assemble with ease a desired class of nanoparticle architectures. Further, by making use of copolymer motifs with hydrophobic and hydrophilic shells, the clusters can be hierarchically assembled into more complex organizations, possibly permitting the creation of highly engineered nanoparticle-based materials. ■

REFERENCE AND NOTES

1. J. A. Fan *et al*., *Science* **328**, 1135 (2010).
2. R. Schreiber *et al*., *Nat. Commun.* **4**, 2948 (2013).
3. H. Zhang *et al*., *ACS Nano* **14**, 1369 (2020).
4. C. Yi *et al*., *Science* **369**, 1369 (2020).
5. G. Meng, N. Arkus, M. P. Brenner, V. N. Manoharan, *Science* **327**, 560 (2010).
6. F. Romano, E. Sanz, P. Tartaglia, F. Sciortino, *J. Condens. Matter Phys.* **24**, 064113 (2012).
7. Q. Chen, S. C. Bae, S. Granick, *Nature* **469**, 381 (2011).
8. Z. Gong, T. Hueckel, G.-R. Yi, S. Sacanna, *Nature* **550**, 234 (2017).
9. T. G. W. Edwardson, K. L. Lau, D. Bousmail, C. J. Serpell, H. F. Sleiman, *Nat. Chem.* **8**, 162 (2016).
10. Y. Xiong *et al*., *ACS Nano* **14**, 6823 (2020).
11. S. Sun *et al*., *Nat. Commun.* **11**, 2279 (2020).
12. F. Lu, K. G. Yager, Y. Zhang, H. Xin, O. Gang, *Nat. Commun.* **6**, 6912 (2015).

ACKNOWLEDGMENTS

O.G. is supported by the U.S. Department of Defense (grant W911NF-19-1-0395), U.S. National Science Foundation (grant 1905920), and U.S. Department of Energy (grant DE-SC0008772).

[1]Department of Chemical Engineering, Columbia University, New York, NY 10027, USA. [2]Department of Applied Physics and Applied Mathematics, Columbia University, New York, NY 10027, USA. [3]Center for Functional Nanomaterials, Brookhaven National Laboratory, Upton, NY 11973, USA. Email: og2226@columbia.edu

10.1126/science.abd8183

CORONAVIRUS

Coronavirus dons a new crown

A transmembrane pore reveals parallels with other viruses

By **Nuruddin Unchwaniwala**[1,2] *and* **Paul Ahlquist**[1,2,3]

Severe acute respiratory syndrome coronavirus 2 (SARS-CoV-2), which causes coronavirus disease 2019 (COVID-19), belongs to the positive-strand RNA [(+)RNA] viruses, a large class of viruses that includes Zika, hepatitis C, and chikungunya viruses. (+)RNA viruses package their genomes in infectious virions as messenger-sense RNA and reproduce these genomes solely through RNA intermediates in replication complexes (RCs) formed by rearranging intracellular membranes (*1*). RNA replication is a major target of antiviral drugs, including remdesivir, which shows promise for treating COVID-19 patients. RCs of coronaviruses and some other (+)RNA viruses are ~250- to 300-nm-diameter double-membrane vesicles (DMVs) that contain viral double-stranded RNA (dsRNA) replication intermediates (*2*–*4*). On page 1395 of this issue, Wolff *et al*. (*5*) identify a crown-like double-membrane–spanning molecular pore on SARS-CoV-2 and other coronavirus DMVs that likely solves the longstanding problem of how progeny (+)RNA genomes are released from DMVs.

Like other (+)RNA viruses, most (~70%) of the SARS-CoV-2 genome encodes functions for RNA replication, underscoring the importance of this process for understanding and controlling these viruses. RCs support genome replication by organizing viral RNA replication proteins, viral RNA templates, specific host factors required for RNA replication, and successive reproductive steps. The RC-bounding membranes sequester RNA replication templates and intermediates from translation, virion as-

[1]John and Jeanne Rowe Center for Research in Virology, Morgridge Institute for Research, Madison, WI, USA. [2]University of Wisconsin–Madison, Madison, WI, USA. [3]Howard Hughes Medical Institute, University of Wisconsin–Madison, Madison, WI, USA. Email: unchwaniwala@wisc.edu; ahlquist@wisc.edu

Published by AAAS

sembly, RNA decay, and host defenses such as RNA interference and interferon-stimulated antiviral responses.

Although infection by coronaviruses induces several types of membrane rearrangements, multiple lines of evidence identified the dsRNA-containing DMVs as the viral RNA synthesis sites (*2*, *6*). However, because DMVs lacked known openings, it was unclear how new (+)RNA genomes copied from dsRNA templates in the DMV interior could transit to the cytoplasm to be translated, packaged into virions, and potentially form new RCs.

Wolff *et al.* provide a compelling solution to this conundrum by using advanced cryo–electron tomography (cryo-ET) to identify a cylindrical protein pore complex traversing DMV double membranes in cells infected by SARS-CoV-2 or another coronavirus (see the figure). They also showed that this pore contains six copies of the large viral transmembrane protein nsp3 (nonstructural protein 3), which is essential for RNA replication and induces the formation of DMVs with viral nsp4. Consistent with the interaction of nsp3 with multiple viral replication proteins, the authors imaged frequent, apparently dynamic interaction of the pore's DMV luminal and cytoplasmic sides with other macromolecules. Thus, the pore may interact with the viral RNA polymerase and other luminal RNA replication factors to guide newly synthesized RNAs to the cytoplasm, where the interaction of nsp3 with the viral nucleocapsid protein may facilitate RNA packaging into new virions.

The DMV pore is also an attractive solution for coronaviral RNA release because of similarities with a product RNA-release channel first identified in nodaviruses, a well-characterized model for (+)RNA virus replication. In addition to DMVs, another prominent class of RCs is necked spherular membrane invaginations (spherules) that are formed by numerous families of (+)RNA viruses including flaviviruses, such as Zika virus (*7*, *8*), alphaviruses, such as chikungunya virus (*9*), and nodaviruses (*10*). Cryo-ET showed that the ~50- to 80-nm-diameter nodavirus spherules (see the figure) contain viral dsRNA replication templates and that the cytoplasmic side of the spherule neck is surmounted by a ring, or crown, of 12 copies of nodavirus RNA replication protein A (*11*, *12*). These crowns are frequently origins for cytoplasmic filaments that appear to represent new (+)RNA genomes being released. Crown-forming protein A contains all viral activities for RNA synthesis and shares distant sequence similarities to alphavirus RNA replication proteins (*11*–*13*).

Despite some differences in the membrane organization of DMV and spherule

Replication complex crowns

RNA replication complexes (RCs) are distinct types of membrane compartments containing double-stranded RNA (dsRNA). A crown-like pore complex on coronavirus RCs (*5*) parallels a similar crown of viral proteins on nodavirus RCs (*12*), providing a channel to release RNA progeny to the cytoplasm.

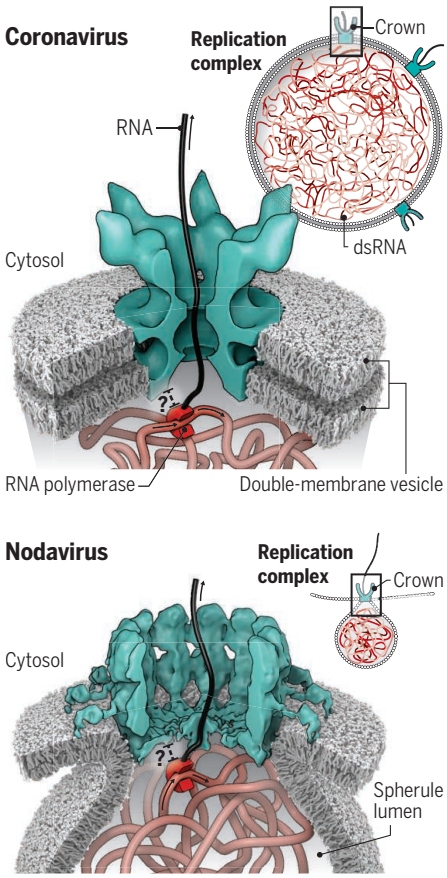

RCs, the DMV pores of coronaviruses show multiple parallels with nodavirus spherule crowns. These include their ringed multimeric structure, their apparent role as channels to release progeny RNA replication products, and potential involvement or interaction with active RNA synthesis. Consistent with these similarities, Wolff *et al.* also refer to the cytosolic portion of the coronaviral pore as a crown. However, it is important to note that this intracellular DMV RC crown is unrelated to the crown-like halo of virion envelope spike proteins that gave coronaviruses their name (*14*).

The recognition that RCs of coronaviruses and nodaviruses share fundamentally similar crown-like channels is notable given the considerable evolutionary separation of these viruses. Additional studies will further define the similarities and differences between these crowns, with functional and potentially evolutionary implications. Although the cytosolic portion of the coronavirus crown has sixfold symmetry, some membrane-interacting regions of the pore show rings of 12 similar electron-dense elements. Because the volume of the coronaviral pore complex shows that it must contain additional proteins beyond nsp3, the stoichiometry and symmetry of these regions remains uncertain. Even if only sixfold symmetric, do these 12-member rings bear any structural similarities to the 12-fold symmetric nodavirus crown?

Detailed interactions of these crowns with membrane lipids will also be of interest and might be more similar than seeming differences in DMV and spherule architectures suggest. The nodavirus spherule membrane folds at the neck into two sections that independently approach the crown, mirroring the connection of double membranes at nuclear pores. Similarly, hydrophobic surfaces on the coronaviral pore might induce lipids in the two DMV membranes to converge or interact, again approximating nuclear pores. Higher-resolution imaging of the nodavirus crown (*12*) bodes well for addressing such questions.

Additional questions include what other coronaviral and perhaps host proteins comprise the crown-like DMV channel. Viral nsp4 is one attractive candidate because it functions with nsp3 to form DMVs. Equally enticing is the identity of the dynamic RNA and protein interactions at both ends of the DMV channel and how these may promote RNA synthesis, transport, and virion assembly. Perhaps most important, recognizing conserved processes such as crown-mediated release of new genomic RNAs should provide a foundation for potentially broader-spectrum control, through pharmacologic or genetic means, of ubiquitous (+)RNA virus pathogens. ■

REFERENCES AND NOTES

1. J. A. den Boon, A. Diaz, P. Ahlquist, *Cell Host Microbe* **8**, 77 (2010).
2. E. J. Snijder *et al.*, *PLOS Biol.* **18**, e3000715 (2020).
3. G. A. Belov *et al.*, *J. Virol.* **86**, 302 (2012).
4. I. Romero-Brey *et al.*, *PLOS Pathog.* **8**, e1003056 (2012).
5. G. Wolff *et al.*, *Science* **369**, 1395 (2020).
6. K. Knoops *et al.*, *PLOS Biol.* **6**, e226 (2008).
7. S. Welsch *et al.*, *Cell Host Microbe* **5**, 365 (2009).
8. L. K. Gillespie, A. Hoenen, G. Morgan, J. M. Mackenzie, *J. Virol.* **84**, 10438 (2010).
9. K. Kallio *et al.*, *J. Virol.* **87**, 9125 (2013).
10. B. G. Kopek, G. Perkins, D. J. Miller, M. H. Ellisman, P. Ahlquist, *PLOS Biol.* **5**, 2022 (2007).
11. K. J. Ertel *et al.*, *eLife* **6**, e25940 (2017).
12. N. Unchwaniwala *et al.*, *Proc. Natl. Acad. Sci. U.S.A.* **117**, 18680 (2020).
13. T. Ahola, D. G. Karlin, *Biol. Direct* **10**, 16 (2015).
14. D. Tyrrell, P. Sparrow, A. S. Beare, *Nature* **220**, 819 (1968).

ACKNOWLEDGMENTS

We thank the Rowe Center for Research in Virology, Howard Hughes Medical Institute, and National Institutes of Health for funding, and H. Adam Steinberg for creative graphics assistance.

10.1126/science.abe0322

GRAPHIC: H. ADAM STEINBERG ADAPTED BY V. ALTOUNIAN/*SCIENCE*; (ELECTRON MICROSCOPY DATA) WOLFF *ET AL.* (*5*) AND UNCHWANIWALA *ET AL.* (*12*)

Published by AAAS

RETROSPECTIVE

Flossie Wong-Staal (1946–2020)

Trailblazing HIV researcher

By **Genoveffa Franchini**

Flossie Wong-Staal, a leader in HIV research at the onset of the AIDS epidemic, died on 8 July at the age of 73. A pioneer in the genetic structure and regulatory mechanisms of HIV, Wong-Staal played a key role in showing that HIV causes AIDS. She was also a trailblazer for female scientists.

Born in Guangzhou, China, on 27 August 1946 as Yee Ching Wong, Wong-Staal moved to Hong Kong with her family when she was 7 years old. At the age of 18, she westernized her name (taking the name "Flossie" from a typhoon that had recently hit southern China) and emigrated to the United States. The first woman in her family to obtain a higher education, she graduated with a bachelor's degree in bacteriology in 1968 and a Ph.D. in molecular biology in 1972, both from the University of California, Los Angeles. In 1973, Wong-Staal began a postdoctoral position at the Laboratory of Tumor Cell Biology, led by biomedical researcher Robert C. Gallo, in the National Cancer Institute of the National Institutes of Health (NIH) in Bethesda, Maryland. She was promoted to section chief within a few years, and in the next decade she coauthored more than 100 journal articles.

In 1990, Wong-Staal left the NIH to accept an appointment as the Florence Seeley Riford Chair in AIDS Research at the University of California, San Diego (UCSD). She was named director of the newly created UCSD Center for AIDS Research in 1994 and began pioneering the investigation of gene therapy approaches for HIV/AIDS. After her retirement from UCSD in 2002, she became vice president of Immusol, a biopharmaceutical company she cofounded, now known as iTherX Pharmaceuticals, where she pursued treatments for hepatitis C. Throughout her career, Wong-Staal trained a large number of postdoctoral fellows, many of whom went on to be leaders in their fields.

When Gallo's team cultured the first human retrovirus in the late seventies, Wong-Staal was focused on retroviruses that caused leukemia in animals. She quickly pivoted to follow up on Gallo's work, and her section became the leading group working on the molecular biology of human retroviruses. In these early years of research on human retroviruses, the skepticism regarding their existence was widespread. Gallo later framed a letter from a reviewer who, citing the "fact" that there were no human retroviruses, rejected the initial human T cell leukemia virus (HTLV) paper. But Wong-Staal was among those who thought there was a connection between retroviruses and human diseases, and she was proved right.

The molecular virology skills Wong-Staal brought to her laboratory were critical to her ability to apply state-of-the-art molecular biology techniques to quickly unravel the HIV genome organization and its replication strategies. In the early 1980s, Wong-Staal discovered molecular evidence of variations in HIV within and among infected individuals, which led to a fundamental realization: HIV is constantly mutating in response to immune pressures, so every isolation of the virus results in different virus clones. This understanding shaped the development of effective antiviral therapies to manage AIDS. Wong-Staal also provided the molecular biology necessary for the development of the second-generation blood test for HIV, one based on detection of the viral genome rather than antibodies to the virus. Her groundbreaking work on the molecular biology of HIV inspired scientists worldwide to join the field of human retrovirology, an entirely uncharted but increasingly exciting area of research in the 1980s and early 1990s.

PHOTO: BILL BRANSON/NATIONAL CANCER INSTITUTE

Wong-Staal's contributions were not limited to HIV. She had a keen interest in the molecular virology of HTLV-1, the retroviral causative agent of human adult T cell leukemia. Her work on nonstructural viral factors such as the HTLV-1 and HIV-1 transcriptional activators Tax and Tat and the posttranslational regulators Rex and Rev also had far-reaching implications in areas of basic biology, including transcription regulation and RNA transport.

I joined Wong-Staal's lab in 1979 as a postdoctoral fellow. She was a very talented scientist who had an exceptional ability to sharply analyze data, focus, and move quickly to address the most essential research questions. She was willing to take risks and propose daring hypotheses, always expanding her knowledge and moving research forward. This mindset extended beyond her lab work. Decades ago, for a presentation at an AIDS meeting, she told the audience that instead of using the standard slides, she was going to give her presentation using a program called PowerPoint that she had learned about from her daughter. By the next meeting, there was not a slide presentation in sight; everyone was using PowerPoint.

A stylish, elegant, and confident woman with a great sense of humor, Wong-Staal was competitive and tenacious. When she submitted her first grant application from UCSD after leaving the NIH, the reviewers did not give her a fundable score because they thought that, as a molecular biologist, she did not have the immunology experience required to carry out the proposed studies. In response, she conducted the study anyway, published the data, and sent the publication with her next grant application. In this way, Wong-Staal taught me persistence and resilience, skills that I have found to be invaluable in my career.

Flossie Wong-Staal held her own and gained respect in a male-dominated scientific world through her strength, intelligence, kindness, and grace. She was a member of the National Academy of Medicine. In 2002, *Discover* magazine named her one of the 50 most important women in science. In 2019, she was inducted into the National Women's Hall of Fame, along with Angela Davis, Jane Fonda, and Sonia Sotomayor. It was a well-deserved honor for an influential researcher, who served as a role model to mentees and colleagues and will continue to inspire future generations of scientists. ■

Center for Cancer Research, National Cancer Institute, National Institutes of Health, Bethesda, MD, USA.
Email: franchig@mail.nih.gov

10.1126/science.abe4095

Published by AAAS

POLICY FORUM

ETHICS: COVID-19

An ethical framework for global vaccine allocation

The Fair Priority Model offers a practical way to fulfill pledges to distribute vaccines fairly and equitably

By **Ezekiel J. Emanuel[1], Govind Persad[2], Adam Kern[3], Allen Buchanan[4], Cécile Fabre[5], Daniel Halliday[6], Joseph Heath[7], Lisa Herzog[8], R. J. Leland[9], Ephrem T. Lemango[10], Florencia Luna[11], Matthew S. McCoy[1], Ole F. Norheim[12], Trygve Ottersen[13] , G. Owen Schaefer[14], Kok-Chor Tan[15], Christopher Heath Wellman[16], Jonathan Wolff[17], Henry S. Richardson[18]**

Once effective coronavirus disease 2019 (COVID-19) vaccines are developed, they will be scarce. This presents the question of how to distribute them fairly across countries. Vaccine allocation among countries raises complex and controversial issues involving public opinion, diplomacy, economics, public health, and other considerations. Nevertheless, many national leaders, international organizations, and vaccine producers recognize that one central factor in this decision-making is ethics (*1*, *2*). Yet little progress has been made toward delineating what constitutes fair international distribution of vaccine. Many have endorsed "equitable distribution of COVID-19…vaccine" without describing a framework or recommendations (*3*, *4*). Two substantive proposals for the international allocation of a COVID-19 vaccine have been advanced, but are seriously flawed. We offer a more ethically defensible and practical proposal for the fair distribution of COVID-19 vaccine: the Fair Priority Model.

The Fair Priority Model is primarily addressed to three groups. One is the COVAX facility—led by Gavi, the World Health Organization (WHO), and the Coalition for Epidemic Preparedness Innovations (CEPI)—which intends to purchase vaccines for fair distribution across countries (*5*). A second group is vaccine producers. Thankfully, many producers have publicly committed to a "broad and equitable" international distribution of vaccine (*2*). The last group is national governments, some of whom have also publicly committed to a fair distribution (*1*).

These groups need a clear framework for reconciling competing values, one that they and others will rightly accept as ethical and not just as an assertion of power. The Fair Priority Model specifies what a fair distribution of vaccines entails, giving content to their commitments. Moreover, acceptance of this common ethical framework will reduce duplication and waste, easing efforts at a fair distribution. That, in turn, will enhance producers' confidence that vaccines will be fairly allocated to benefit people, thereby motivating an increase in vaccine supply for international distribution.

VACCINE NATIONALISM

Those who think countries will inevitably engage in "vaccine nationalism" (*4*) may deem an ethical framework for vaccine distribution among countries irrelevant. Public sentiment in some countries for retaining vaccine developed within their borders is strong, and many governments will also try to obtain vaccines produced elsewhere. But an ethical framework has broad relevance even in the face of nationalist attitudes. Rather than simply asserting that might makes right, governments typically appeal to national partiality: a country's right and duty to prioritize its own citizens.

Some defend national partiality as ethical (*6*–*8*). Fellow citizens share "associative ties," common governmental, civic, and other institutions, and a sense of shared identity (*6*, *7*). Also, the legitimate authority of representative government officials inheres in their representing and promoting the interests of their citizens. Plausibly, these relations support allowing countries to prioritize citizens over foreigners for vaccines (*6*). Others view national partiality as unethical: People's entitlement to lifesaving resources should not depend on nationality (*9*).

Regardless of whether some national partiality is ethical, unlimited national partiality is not (*6*–*8*). Associative ties only justify a government's giving some priority to its own citizens, not absolute priority (*6*). Moreover, associative ties extend across national borders, and citizens of different countries share common institutions (*7*). Finally, national governments have cross-border responsibilities to help satisfy fundamental needs like basic health care, particularly in a global health emergency (*7*).

Reasonable defenders of national partiality will differ on how much priority countries should give their citizens for vaccines. To establish the need for an equitable international distribution, it is unnecessary to determine an optimal level of priority. It is sufficient to identify a clear upper bound: Reasonable national partiality does not permit retaining more vaccine than the amount needed to keep the rate of transmission (Rt) below 1, when that vaccine could instead mitigate substantial COVID-19–related harms in other countries that have been unable to keep Rt below 1 through ongoing public-health efforts. The marginal benefit of additional doses of vaccine in a country able to keep Rt below 1 generally will pale in comparison to the potential benefits to countries whose Rt remains above 1—at least until booster vaccination is needed to maintain immunity. Hence, with Rt below 1, there will not be sufficient vaccine-preventable harm to justify retaining vaccine. When a government reaches the limit of national partiality, it should release vaccines for other countries. This makes an account of fair allocation among countries relevant to reasonable national governments.

THREE FUNDAMENTAL VALUES

Fairly distributing a COVID-19 vaccine among countries is a problem of distributive justice. Although governments will be the initial recipients of vaccine, fair distribution across countries must reflect a moral concern for the ultimate recipients: individuals. Three values are particularly relevant: benefiting people and limiting

[1]Department of Medical Ethics and Health Policy, Perelman School of Medicine, University of Pennsylvania, Philadelphia, PA, USA. [2]Sturm College of Law, University of Denver, Denver, CO, USA. [3]Department of Politics, Princeton University, Princeton, NJ, USA. [4]Departments of Philosophy, Political Economy and Moral Science, and Freedom Center, University of Arizona, Tucson, AZ, USA. [5]All Souls College, University of Oxford, Oxford, UK. [6]School of Historical and Philosophical Studies, University of Melbourne, Melbourne, Australia. [7]Munk School of Global Affairs and Public Policy, University of Toronto, Toronto, Canada. [8]Faculty of Philosophy, University of Groningen, Groningen, Netherlands. [9]Department of Philosophy, University of Manitoba, Winnipeg, Canada. [10]Jobs Creation Commission, Ethiopia. [11]Bioethics Program, Facultad Latinoamerica de Ciencias Sociales (FLACSO–CONICET), Buenos Aires, Argentina. [12]Bergen Centre for Ethics and Priority Setting, Department of Global Public Health and Primary Care, University of Bergen, Bergen, Norway. [13]Division for Health Services, Norwegian Institute of Public Health, Oslo, Norway. [14]Centre for Biomedical Ethics, Yong Loo Lin School of Medicine, National University of Singapore, Singapore. [15]Department of Philosophy, University of Pennsylvania, Philadelphia, PA, USA. [16]Department of Philosophy, Washington University, St. Louis, MO, USA. [17]Blavatnik School of Government, University of Oxford, Oxford, UK. [18]Department of Philosophy and Kennedy Institute of Ethics, Georgetown University, Washington, DC, USA. Email: MEHPchair@upenn.edu

Published by AAAS

harm, prioritizing the disadvantaged, and equal moral concern.

Benefiting people and limiting harm is widely recognized as important across ethical theories. Realizing this value requires defining relevant benefits, measuring them, and assessing the relative urgency—the importance and time sensitivity—of countries' needs. A successful vaccine produces direct benefits by protecting people against death and morbidity caused by infection. It also produces indirect benefits by reducing death and morbidity arising from health systems overstressed by the pandemic, and by reducing poverty and social hardship such as closed schools.

A family member prays at a relative's grave in Comas, in the outskirts of Lima. Peru has one of the highest COVID-19 death tolls among countries in Latin America and the Caribbean region.

Prioritizing the disadvantaged is a fundamental value in ethics and global health (*10*, *11*). Realizing this value requires that vaccine distribution reflect special concern for people who are disadvantaged. Fairly distributing a COVID-19 vaccine internationally therefore requires assessing different types of disadvantage. Are the worst-off countries those experiencing the greatest poverty? Those where people have the lowest life expectancies?

Equal moral concern requires treating similar individuals similarly and not discriminating on the basis of morally irrelevant differences, such as sex, race, and religion. Distributing different quantities of vaccine to different countries is not discriminatory if it effectively benefits people while prioritizing the disadvantaged.

THE FAIR PRIORITY MODEL

To guide fair distribution of vaccine across countries, we propose the Fair Priority Model. Fair allocation must seek to mitigate future adverse effects of COVID-19. We focus on three types of harms directly or indirectly caused by COVID-19. First, COVID-19 kills people and causes permanent organ damage. Second, the pandemic indirectly harms health even for the uninfected by straining health care systems, raising mortality rates for common conditions, causing stress that harms mental health, and accelerating the spread of disease by hindering immunizations. Third, the pandemic has devastated the global economy, causing unemployment, economic decline, poverty, and starvation. Economics and health interact: Worsening economic conditions harm health, and a worsening pandemic harms the economy.

The pandemic forces allocators to decide where a vaccine's harm-reducing powers are most urgently needed. Three dimensions of harm are important. Are the harms irreversible? How devastating are they? And can they be compensated?

On these three dimensions, preventing death—especially premature death—is particularly urgent. Death is uniquely devastating, and those who die for want of vaccine cannot be compensated later on. Surveys further suggest popular agreement that a premature death that prevents someone's exercising their skills or realizing their goals later in life is worse than a death later in life (*11*, *12*). Ethicists have similarly argued that preventing early deaths—deaths that are more prevalent in poorer countries—is both prudent and ethical (*10*, *13*).

Death, however, is not the only irreversible and devastating harm. COVID-19 causes strokes and organ damage with long-term consequences. It also diminishes education and causes unemployment and poverty that impose long-term devastation.

The Fair Priority Model proceeds in three phases, preventing more urgent harms earlier (see the Table). Phase 1 aims at reducing premature deaths and other irreversible direct and indirect health impacts. Phase 2 continues to address enduring health harms but additionally aims at reducing serious economic and social deprivations such as the closure of nonessential businesses and schools. Restoring these activities will lower unemployment, reduce poverty, and improve health. Finally, phase 3 aims at reducing community transmission, which in turn reduces spread among countries and permits the restoration of prepandemic freedoms and economic and social activities.

Implementing each phase of the model requires determining the number of vaccine doses each country should receive and the order of receipt. The countries will then allocate vaccine internally to individuals. We expect that they will initially focus on areas where premature mortality can be reduced. Determining how many vaccine doses are allocated to each country depends on the marginal improvement in ethically relevant metrics that each dose achieves. There are likely to be multiple distributions of vaccine as supply becomes available over time.

Five factors guide the choice of metrics for each phase: (i) fidelity to the underlying ethical values; (ii) simplicity; (iii) previous use in global health and development; (iv) ease of obtaining rapid but reasonable estimates as the pandemic evolves; and (v) sensitivity to relevant harms that are difficult to measure directly.

In phase 1, we propose using Standard Expected Years of Life Lost (SEYLL) averted per dose of vaccine as the metric for premature death (*14*). SEYLL calculates life years lost compared to a standardized reference life table—that is, a person's life expectancy at each age as estimated on the basis of the lowest observed age-specific mortality rates anywhere in the world.

SEYLL has three major advantages. First, it regards all deaths as important but earlier deaths as particularly important. Thus, it integrates the aims of limiting harm and of prioritizing the least advantaged, particularly because early deaths are more frequent in low-income countries and are a proxy for being disadvantaged overall (*10*). Second, SEYLL incorporates equal moral concern by valuing a life saved at a given age identically across countries, regardless of preexisting conditions or differences in national life expectancy. Finally, SEYLL is a standard metric used in global burden-of-disease calculations (*14*).

PHOTO: RAUL SIFUENTES/GETTY IMAGES

Published by AAAS

Three phases of Fair Vaccine Distribution

DISTRIBUTION PHASE	PRIMARY AIM	METRIC TO DISTRIBUTE VACCINE DOSES	HOW THE METRIC FULFILLS VALUES	PRIORITIZATION
Reducing premature deaths	Reducing foreseeable premature deaths directly or indirectly caused by COVID-19.	Standard expected years of life lost (SEYLL) averted by administering vaccine.	Prevents substantial harms and gives priority to the worst-off by giving weight to premature deaths. Recognizes equal moral concern by valuing a life saved at a given age identically across countries.	Priority to countries that would reduce more SEYLL per dose of vaccine.
Reducing serious economic and social deprivations	Reducing serious economic, social, and fatal and nonfatal health harms caused by COVID-19.	SEYLL averted. Reduction in absolute poverty measured by poverty gap. Declines in gross national income (GNI) averted by administering vaccine.	Prevents harm by recognizing a wide range of economic, social, and health deficits. Gives priority to the worst-off by prioritizing people in poverty.	Priority to countries that would reduce more poverty, avert more loss of GNI, and avert more SEYLL per dose of vaccine.
Returning to full functioning	Ending community spread of COVID-19.	Ranking of different countries' transmission rates.	Prevents harm and gives priority to the worst-off by prioritizing countries with higher transmission rates.	Priority to countries with higher transmission rates.

Phase 2 retains SEYLL as the health metric, treating it as a mortality measure and a proxy for morbidity. The novelty and uncertain long-term effects of COVID-19 preclude using more typical measures of morbidity, such as Years Lived with Disability.

No single socioeconomic metric integrates benefiting people and prioritizing the disadvantaged. Accordingly, we propose two metrics for phase 2 that capture overall economic improvement and the extent to which people would be spared from poverty. Because poverty is an extreme form of deprivation, people's moral claim to avoid poverty is especially urgent. The Fair Priority Model measures poverty by the projected reduction in the absolute size of the poverty gap per dose of vaccine, with the poverty line set at a uniform absolute level to be selected by the implementers. The poverty gap is the ratio by which the mean income of the poor falls below the poverty line; it accounts for both the prevalence and depth of poverty. Overall economic impact is measured by the projected absolute improvement in gross national income (GNI) per vaccine dose. Considering absolute improvement in GNI per dose is preferable to considering improvement in per capita GNI or percentage improvement in GNI, which would favor countries with smaller populations or economies and permit unnecessary harm without prioritizing the disadvantaged. Moreover, increased GNI in one country will also lead to cross-border gains through trade, employment, and transfers. These simple economic metrics combine to ensure that vaccines prevent substantial harms and prioritize the disadvantaged.

In phase 3, countries with higher transmission rates are initially prioritized, but all countries should eventually receive sufficient vaccine to halt transmission, which is projected to require that 60 to 70% of the population be immune.

FLEXIBILITY OF THE MODEL

Specifying how vaccines should be allocated will require integration of the model with data and empirical forecasts. For instance, in phase 1, minimizing SEYLL might mean immunizing those at high risk of death, those most likely to transmit infection, or those most at risk of initial infection. The vaccination strategy that best averts SEYLL depends on each country's demography, prevalent comorbidities, and health system capacity, as well as open scientific questions: Will vaccines reduce severity but not transmission, be less effective in the elderly, or require periodic boosters? The WHO's Strategic Advisory Group of Experts is currently evaluating how much harm each strategy prevents. Similarly, the World Bank is evaluating the impact of COVID-19 on countries' economic activity and world poverty. These or similar organizations can provide the analytic forecasts to guide actual distribution of the vaccines over time by the COVAX facility or vaccine producers. By specifying metrics that should guide allocation and monitoring the vaccine's effect on outcomes, the Fair Priority Model naturally accommodates changes in our knowledge of COVID-19.

How much vaccine should be distributed in each phase? Empirical uncertainty makes it impractical to fully specify the transition between phases now. However, distributors might set the first transition at the point where a vaccine successfully reduces the burden of COVID-19 from an emergency to the level of established health challenges. For example, phase 2 might commence once a vaccine reduces worldwide SEYLL due to COVID-19 to a level analogous to the burden of influenza. Similarly, the transition to phase 3 might begin once additional vaccines either successfully narrow the poverty gap to prepandemic levels or encounter substantially diminishing returns in that effort. Because the distribution of vaccine doses among countries is linked to the impact of the vaccine on common worldwide metrics, all countries should progress to the next phase approximately simultaneously. This is approximate; some countries may struggle to control their outbreaks even with vaccine, but that should not preclude the rest of the world progressing to the next phase. Although we have delineated the ethical framework and metrics, epidemiological and economic assessments using the best available data will be needed to help determine when a phase should be considered complete.

COMPARISON WITH OTHER PROPOSALS

Two schemes for the international distribution of COVID-19 vaccine have been proposed. First, the WHO suggests that countries receive doses proportional to population in phase I (*15*). Phase I begins with 3% of each country's population receiving vaccines, and population-proportional allocation continues until every country has vaccinated 20% of its population. The COVAX facility currently accepts this proposal, which is undergoing revision (*5*).

A population-based distribution appears to express equal moral concern and may appear to be politically tenable. However, it mistakenly assumes that equality requires treating differently situated countries identically rather than equitably responding to their different needs. Equally populous countries can face markedly different levels of premature death and economic devastation from COVID-19. Aid to countries typically is provided in approximate response to the severity of problems. Providing aid merely in proportion to population is unjustified and almost never used. For instance, it would be unethical to allocate antiretrovirals for HIV on the basis of population, rather than on HIV burden. Likewise, a fair distribution of COVID-19 vaccines should respond to the pandemic's differential severity in different countries.

The second proposal distributes vaccine to countries according to the number of frontline health care workers, the proportion of population over 65, and the number of people with comorbidities in the country (*15*). This proposal seems to prioritize protecting those judged most likely to die and preventing health system collapse due to health care

Published by AAAS

workers' illness. But it is an empirical question whether this prioritization optimally reduces death, let alone premature death or serious economic harms. Preferentially immunizing health care workers may not substantially reduce harm in higher-income countries where personal protective equipment effectively protects health workers. Instead, vaccinating those whose housing or occupation or age puts them at greatest risk of spreading infection, or people at highest risk of becoming infected, might best prevent harm. Only data can determine which approach best fulfills the ethical value of reducing premature deaths.

Further, because the second proposal does not use SEYLL to correct for disadvantages due to differential national life expectancy, it compounds disadvantage compared to the Fair Priority Model. Since low- and middle-income countries have fewer older residents and health care workers per capita than high-income countries, this scheme allocates less vaccine to countries already disadvantaged by weaker health systems and shorter average life spans.

OBJECTIONS CONSIDERED

We consider three potential objections to the Fair Priority Model. First, some might argue that countries should receive vaccine only if they can provide assurance that they will distribute it to minimize premature deaths and mitigate economic harms, and have the infrastructure to effectively do so.

Allocating vaccine doses to countries lacking the infrastructure to administer them would unjustifiably waste a lifesaving resource. Consequently, fair allocation may be conditional on infrastructural capacity and might also require efforts to help poorer countries develop such infrastructure.

Conditioning vaccine on fair distribution within countries is more problematic. A fair distribution of emergency supplies ultimately aims at helping individuals: They are the ones who live or die, prosper or are impoverished. Some authoritarian countries may do an excellent job of distributing vaccine to minimize health, economic, and other harms. As long as individuals benefit, fair global distribution among countries should neither require that intranational distribution of a vaccine be perfectly just nor seek to punish unrelated injustices. However, some countries may grossly mismanage their domestic vaccine allocations, by, for instance, hoarding doses for a ruling elite. Addressing such hoarding may require making actual vaccine distribution among countries in subsequent phases or subsequent tranches within a phase conditional on a country's having distributed the vaccine reasonably fairly to its members. But outside of extreme cases, withholding vaccines to enforce conditionality inflicts disproportionate burdens, making conditionality rarely appropriate.

Second, some might suggest that the Fair Priority Model unfairly disadvantages countries that have effectively suppressed viral transmission without a vaccine and rewards those who have responded ineffectively.

A fair distribution of vaccine among countries must mitigate future health, economic, and other harms spawned by COVID-19. It should not be backward looking, punishing or rewarding countries for their COVID-19 response or aiming to redress past injustices. The individuals whose lives and livelihoods are at risk often had little say in their governments' response to COVID-19. Further, medicine espouses treating people regardless of responsibility for their illness. Smokers who develop lung cancer and malaria patients who did not use bed nets are not denied care.

Moreover, though the Fair Priority Model recommends allocating vaccine on the basis of expected benefits, it does not exclude countries that have effectively suppressed COVID-19 transmission by making economic sacrifices. If these sacrifices translate into ongoing economic harms that vaccines can alleviate—an empirical question—they are addressed in phase 2. Waiting until phase 2 to address these economic harms is appropriate because premature deaths are more urgent and less compensable. Furthermore, development aid might address the effects of economic sacrifices more effectively than COVID-19 vaccines.

Third, some might worry that the metrics are too uncertain and demanding to calculate, or could perversely incentivize countries to exaggerate the spread and harm of COVID-19 to secure more vaccine earlier.

In a novel, rapidly evolving pandemic, any approach sufficiently sophisticated to meaningfully operationalize ethical values will require approximations as well as judgments about the relative weight to assign different metrics, such as SEYLL and the poverty gap. Simple metrics like population size avoid approximations and trade-offs but fail to measure what morally matters. Moreover, the proposed metrics are routinely used in global health, and basing vaccine distribution on these metrics will encourage collection and reporting of accurate data on changes in mortality and poverty related to COVID-19.

Regarding perverse incentives, countries are unlikely to exaggerate the spread and harm of COVID-19 to secure more vaccine. Any temptation to exaggerate suffering from the pandemic will be tempered by a country's need to reassure its public, visitors, investors, and others about control of COVID-19 to stimulate economic activity and allow travel. Also, as Taiwan and New Zealand show, there are notable soft power advantages associated with an effective pandemic response.

CONCLUSION

The Fair Priority Model is the best embodiment of the ethical values of limiting harms, benefiting the disadvantaged, and recognizing equal concern. The responsibility for implementing the model rests with countries, international organizations, and vaccine producers. They need to use the cooperative mechanisms that have been created to deal with the pandemic, such as the COVAX facility. Organizations also have indispensable roles in empirically assessing how vaccine distribution in fact affects countries with respect to metrics like SEYLL, poverty, and GNI. Ultimately, the model offers governments, international organizations, and vaccine producers a practical way to fulfill their pledges to distribute vaccine fairly and equitably, and make their words a reality. ■

REFERENCES AND NOTES

1. J. Trudeau *et al.*, "The international community must guarantee equal global access to a covid-19 vaccine," *The Washington Post*, 15 July 2020; https://wapo.st/32xNEp0.
2. AstraZeneca, "AstraZeneca takes next steps towards broad and equitable access to Oxford University's potential COVID-19 vaccine," press release, 4 June 2020; https://bit.ly/31vqeRP.
3. Nuffield Council on Bioethics, "Policy briefing: Key challenges for ensuring fair and equitable access to COVID-19 vaccines and treatments," press release, 29 May 2020; https://bit.ly/3b6r62D.
4. T. J. Bollyky, C. P. Bown, *The Tragedy of Vaccine Nationalism. Foreign Affairs* (27 July 2020); https://fam.ag/32sqwZ7.
5. The World Health Organization, "More than 150 countries engaged in COVID-19 vaccine global access facility," press release, 15 July 2020; https://bit.ly/34AE2MZ.
6. D. Miller, *Ethical Theory Moral Pract*. **8**, 63 (2005).
7. A. Sangiovanni, *Philos. Public Aff*. **35**, 3 (2007).
8. K.-C. Tan, Justice Without Borders: Cosmopolitanism, Nationalism, and Patriotism (Cambridge Univ. Press, 2004).
9. S. Caney, *Justice Beyond Borders: A Global Political Theory* (Oxford Univ. Press, 2005).
10. D. Sharp, J. Millum, *J. Appl. Philos*. **35**, 112 (2018).
11. T. Ottersen, D. Mbilinyi, O. Maestad, O. F. Norheim, *Health Policy* **85**, 218 (2008).
12. A. Tsuchiya, P. Dolan, R. Shaw, *Soc. Sci. Med*. **57**, 687 (2003).
13. N. Daniels, Am I My Parents' Keeper? An Essay on Justice Between the Young and the Old (Oxford Univ. Press, 1988).
14. R. J. Marshall, *Aust. N. Z. J. Public Health* **28**, 452 (2004).
15. World Health Organization, A Global Framework to Ensure Equitable and Fair Allocation of COVID-19 Products and Potential implications for COVID-19 Vaccines, 18 June 2020; https://bit.ly/32rhHPb.

ACKNOWLEDGMENTS

This project is supported by the generosity of Eric and Wendy Schmidt by recommendation of the Schmidt Futures program, and the Colton Foundation. We are grateful to C. Saenz for considerable intellectual contributions. Thanks to S. Ahmad, G. Alleyne, K. Chalkidou, A. Deaton, A. Gutmann, B. Keohane, J. Nye, T. Pippo, M. Roses, J.-A. Rottingen, H. Schofield, S. A. Schroeder, S. Subramanian, L. Summers, L. Temkin, and D. Thompson for helpful comments on the manuscript. We also thank A. Glickman and A. Diana for research and other assistance. The views expressed here, and any errors, are solely those of the authors and should not be attributed to any of their employers.

Published online 3 September 2020
10.1126/science.abe2803

Published by AAAS

PHOTO: AP PHOTO/MATT ROURKE

LETTERS

Edited by **Jennifer Sills**

NIH must confront the use of race in science

Recent protests across the United States and the world have called attention to anti-Black racism in policing, employment, housing, and education. Science and medicine also have long histories of racism (*1*, *2*). This unfortunate yet persistent aspect of science and medicine includes the use of obsolete concepts of race to measure human biological difference and the false belief, by some, that differences in disease outcomes stem primarily from pathophysiological differences between racial groups (*3*, *4*).

We are particularly concerned that explanations for the disproportionate rates of coronavirus disease 2019 (COVID-19) in Black, Latino, Indigenous, and other communities of color will mistakenly point to innate racial differences instead of long-standing institutionalized racism and other underlying social, structural, and environmental determinants. Although genetic risk factors may contribute to severity of COVID-19 (*5*, *6*), race is a poor proxy to understand the population distribution of such risk factors (*7*). Compelling evidence shows that racism, not race, is the most relevant risk factor (*8*, *9*). We are hopeful that scientists will not turn to racial science—a reflection of long-standing beliefs about superiority and inferiority that have no place in scientific and clinical practice (*1*, *10*)—to explain COVID-19 disparities and justify policy responses to it. However, racial categories have been misused in the past.

In 2016, we called for the elimination of the use of race as a means to classify biological diversity in both laboratory and clinical research. Since that time, little has changed (*11*). The National Institutes of Health (NIH) made progress by releasing a request for applications in support of research leading to the creation of best practices for the study of race and other population identifiers (*12*). However, R01 awards could take years to address these issues, and NIH still offers no guidance about the use of racial and ethnic identifiers in research beyond recruitment. There is an urgent need for NIH to provide scientists with information about what utility racial data have beyond fostering diversity in research, how such information should or should not be used in data analysis, and what identifiers of human populations might be better suited for use in biomedical research.

To begin to address the misuse of racial measures in scientific and clinical practice, we urge the director of NIH to lead education efforts directed at both scientists and the public about the nature of human genetic diversity and the ongoing need and obligation to confront racism in science. In these troubled times, a clear statement regarding use and misuse of population identifiers in the pursuit of characterizing human difference could help alleviate ongoing and widespread confusion on such matters.

A member of the Black Doctors COVID-19 Consortium, formed to help address health disparities in the African American community, tests a patient. Racial disparities in COVID-19 cases are better explained by structural racism than by genetic differences.

NIH should then support the National Academy of Sciences to bring together a diverse group of scientists and scholars to develop a consensus statement on best practices in genetic, clinical, and social scientific studies for characterizing human genetic diversity, including guidance for using racial categories to study racism's impact on human health. Guidelines for federally funded science should also include best practices for the integration of biological, social, structural, and environmental health determinants into the study of human health and disease.

NIH should continue and expand its work to hire more career scientists and clinicians from underrepresented minority groups. It should also substantially increase the extramural funding that supports scientists from underrepresented groups at every level of training and throughout career development. We have the tools to remedy this challenge. The time to act is now.

Michael Yudell[1]*, Dorothy Roberts[2], Rob DeSalle[3], Sarah Tishkoff[4], and 70 signatories
[1]Department of Community Health and Prevention, Drexel University School of Public Health,

Published by AAAS

Philadelphia, PA 19104, USA. [2]Law School and Departments of Africana Studies and Sociology, University of Pennsylvania, Philadelphia, PA 19104, USA. [3]American Museum of Natural History, New York, NY 10024, USA. [4]Departments of Genetics and Biology, University of Pennsylvania, Philadelphia, PA 19104, USA.
*Corresponding author. Email: myudell@drexel.edu

REFERENCES AND NOTES

1. D. Roberts, *Fatal Invention: How Science, Politics, and Big Business Re-Create Race in the Twenty-First Century* (The New Press, New York, 2012).
2. E. M. Hammonds, R. M. Herzig, *The Nature of Difference: Sciences of Race in the United States from Jefferson to Genomics* (MIT Press, 2008).
3. J. L. Graves Jr., *The Emperor's New Clothes: Biological Theories of Race at the Millennium* (Rutgers University Press, New Brunswick, NJ, 2001).
4. D. A. Vyas, L. G. Eisenstein, D. S. Jones, *N. Engl. J. Med*. 10.1056/NEJMms2004740 (2020).
5. D. Ellinghaus *et al*., *N. Engl. J. Med*. 10.1056/NEJMoa2020283 (2020).
6. M. W. Hooper, A. M. Nápoles, E. J. Pérez-Stable, *JAMA* **323**, 24 (2020).
7. C. W. Yancy, *JAMA* **323**, 19 (2020).
8. A. van Dorn, R. E. Cooney, M. L. Sabin, *Lancet* **395**, 10232 (2020).
9. C. Wallis, "Why racism, not race, is a risk factor for dying of COVID-19," *Scientific American* (2020).
10. T. Duster, *Science* **307**, 1050 (2005).
11. M. Yudell, D. Roberts, R. DeSalle, S. Tishkoff, *Science* **351**, 564 (2016).
12. Ethical, Legal and Social Implications (ELSI) Research (R01 Clinical Trial Optional) (Department of Health and Human Services, 2020); https://grants.nih.gov/grants/guide/pa-files/PAR-20-254.html.

SUPPLEMENTARY MATERIALS

List of signatories
www.sciencemag.org/content/369/6509/1313/suppl/DC1

10.1126/science.abd4842

Accumulation of plastic waste during COVID-19

Medical waste generated by COVID-19 protocols has overwhelmed waste treatment facilities in Wuhan, China.

PHOTO: CHINE NOUVELLE/SIPA/NEWSCOM

As lockdowns took effect to slow the spread of coronavirus disease 2019 (COVID-19), the global demand for petroleum collapsed. As a result, oil prices plummeted, making the manufacture of virgin plastics from fossil fuels less expensive than recycling (*1*). This cost incentive, along with lifestyle changes that increase plastic use, has complicated the challenge of overcoming plastic pollution.

During the pandemic, personal protective equipment (PPE) has driven increased plastic pollution. In response to high PPE demand among the general public, health care workers, and service workers, single-use face mask production in China soared to 116 million per day in February, about 12 times the usual quantity (*2*). The World Health Organization has requested a 40% escalation of disposable PPE production (*3*). If the global population adheres to a standard of one disposable face mask per day after lockdowns end, the pandemic could result in a monthly global consumption and waste of 129 billion face masks and 65 billion gloves (*4*). Hospitals in Wuhan, the center of the COVID-19 outbreak, produced more than 240 tons of single-use plastic-based medical waste (such as disposable face masks, gloves, and gowns) per day at the peak of the pandemic, 6 times more than the daily average before the pandemic occurred (*5*). If the increases observed in Wuhan hold true elsewhere, the United States could generate an entire year's worth of medical waste in 2 months (*6*).

Individual choices during lockdowns are also increasing plastic demand. Packaged take-out meals and home-delivered groceries contributed an additional 1400 tons of plastic waste during Singapore's 8-week lockdown (*7*). The global plastic packaging market size is projected to grow from USD 909.2 billion in 2019 to 1012.6 billion by 2021, at a compound annual growth rate of 5.5%, mainly due to pandemic response (*8*).

This global health crisis puts extra pressure on regular waste management practices, leading to inappropriate management strategies, including mobile incineration, direct landfills, and local burnings (*9*). Improper disposal of just 1% of face masks translates to more than 10 million items, weighing 30,000 to 40,000 kg (*10*). Waterlogged COVID-19–related plastic has been observed on beaches and in water (*11*), potentially aggravating the challenge of curtailing microplastics.

At the regional and national levels, prioritization of human health over environmental health has led to the delay or reversal of policies aiming to reduce single-use plastic (*9*). As a result, demand for recycled plastic material has dropped, the profit margins of recycling have decreased, and the environmental footprint of plastics has increased (*9*). We need urgent and coordinated commitment to circular economy approaches, including recycling practices and strict policies against plastic pollution. Companies should continue efforts to curtail virgin plastic use and increase plastic recycling to live up to their corporate social and environmental responsibilities. Without a concerted effort to protect the environment during and after the pandemic, we are unlikely to meet the United Nations' Sustainable Development Goals (*12*).

Tanveer M. Adyel
Department of Civil Engineering, Monash University, Clayton, Melbourne, VIC 3800, Australia. Email: tanveer.adyel@monash.edu

REFERENCES AND NOTES

1. A. Kimini, "How the COVID-19 plastic boom could save the oil industry," OilPrice.com (2020).
2. F. Bermingham, S.-L. Tan, "Coronavirus: China's mask-making juggernaut cranks into gear, sparking fears of over-reliance on world's workshop," *South China Morning Post* (2020); www.scmp.com/economy/global-economy/article/3074821/coronavirus-chinas-mask-making-juggernaut-cranks-gear.
3. "Shortage of personal protective equipment endangering health workers worldwide" (WHO, 2020).
4. J. C. Prata, A. L. Patrício Silva, T. R. Walker, A. C. Duarte, T. Rocha Santos, *Environ. Sci. Tech.* **54**, 7760 (2020).
5. M. Zuo, "Coronavirus leaves China with mountains of medical waste," *South China Morning Post* (2020).
6. S. Cutler, "Mounting medical waste from COVID-19 emphasizes the need for a sustainable waste management strategy" (Frost & Sullivan, 2020).

Published by AAAS

7. S. Bengali, "The COVID-19 pandemic is unleashing a tidal wave of plastic waste," *The Los Angeles Times* (2020).
8. "COVID-19 impact on packaging market by material type, application and region—global forecast to 2021," *Business Insider* (2020).
9. A. L. P. Silva *et al.*, *Sci. Total Environ.* **742**, 140565 (2020).
10. "In the disposal of masks and gloves, responsibility is required" (World Wildlife Fund, 2020); www.wwf.it/scuole/?53500%2FNello-smaltimento-di-mascherine-e-guanti-serve-responsabilita [in Italian].
11. G. Stokes, "No shortage of surgical masks at the beach" (Oceans Asia, 2020).
12. United Nations, "Sustainable development goals" (2015); www.un.org/sustainabledevelopment/sustainable-development-goals/.

10.1126/science.abd9925

Microplastic's role in antibiotic resistance

Plastic pollution is universal and now viewed as an emerging environmental and human health crisis (*1*, *2*). Successful management of plastic waste (*3*) is vital to meeting United Nations Sustainable Development Goal 14, which aims to protect marine ecosystems from pollution and other threats (*4*). Plastic pollution is projected to escalate over the upcoming decades (*5*, *6*), but critical knowledge gaps and uncertainties remain about its effects. Evidence that microplastic surfaces in aquatic environments host microorganisms that are resistant to antibiotics (*7*, *8*) suggests that plastic pollution could have ramifications on disease transmission and treatment in addition to environmental consequences and human exposure to contaminated air, water, and food.

Bacterial biofilms found on microplastics in aquatic ecosystems have been shown to include bacteria with antibiotic-resistant genes (*7*, *8*). These resistant bacteria likely originate in human and animal populations treated with antibiotics and then travel downstream through wastewater into riverine and marine ecosystems (*9*). The increasing surface area provided by waste plastics, such as polyethylene, may enable higher rates of biofilm growth, including those containing antibiotic-resistant genes (*7*). The possibility that plastic pollution can facilitate resistance to antibiotics has critical implications for the spread of disease and the management and regulation of antibiotic resistance in the environment (*10*).

Although scientists have made important strides in understanding the direct effects of microplastics on animal and plant life (*11*), the indirect effects of plastic pollution, including the sources and transport dynamics of antibiotic resistance, remain unclear. Scientists and policy-makers should prioritize the evaluation of both direct and indirect effects of plastic pollution to fully assess the environmental and public health risks.

Michael S. Bank[1,2]*, Yong Sik Ok[3,4], Peter W. Swarzenski[5]
[1]Institute of Marine Research, Bergen, Norway. [2]University of Massachusetts, Amherst, MA 01003, USA. [3]Korea University, Seoul, Korea. [4]Association of Pacific Rim Universities Sustainable Waste Management Program, Korea University, Seoul, Korea. [5]International Atomic Energy Agency, Principality of Monaco, 98000, Monaco.
*Corresponding author: Email: michael.bank@hi.no

REFERENCES AND NOTES

1. M. S. Bank, S. V. Hansson, *Environ. Sci. Technol.* **53**, 7177 (2019).
2. I. A. Kane *et al.*, *Science* **368**, 1140 (2020).
3. S. You *et al.*, *Science* **368**, 1438 (2020).
4. United Nations Development Programme, Sustainable Development Goals, Goal 14: Life Below Water (www.undp.org/content/undp/en/home/sustainable-development-goals/goal-14-life-below-water.html).
5. J. R. Jambeck *et al.*, *Science* **347**, 768 (2015).
6. W. W. Y. Lau *et al.*, *Science*, 10.1126/science.aba9475 (2020).
7. X.-p. Guo *et al.*, *Sci. Tot. Environ.* **745**, 140916 (2020).
8. Y. Yang *et al.*, *Appl. Microbiol. Biotechnol.* **104**, 6501 (2020).
9. S. Berkner *et al.*, *EMBO Rep.* **15**, 740 (2014).
10. Y.-G. Zhu, M. Gillings, J. Penuelas, *One Earth* **3**, 23 (2020).
11. S. Anbumani, P. Kakkar, *Environ. Sci. Pollut. Res.* **25**, 14373 (2018).

10.1126/science.abd9937

TECHNICAL COMMENT ABSTRACTS

Comment on "No consistent ENSO response to volcanic forcing over the last millennium"

Alan Robock

Dee *et al.* (Reports, 27 March 2020, p. 1477) claimed that large volcanic eruptions do not produce a detectable El Niño response. However, they come to the wrong conclusion because they have ignored the fundamental climate response to large volcanic eruptions: Volcanic eruptions cool the surface, thus masking the relative El Niño warming.

Full text: dx.doi.org/10.1126/science.abc0502

Response to Comment on "No consistent ENSO response to volcanic forcing over the last millennium"

Sylvia G. Dee, Kim M. Cobb, Julien Emile-Geay, Toby R. Ault, R. Lawrence Edwards, Hai Cheng, Christopher D. Charles

Robock claims that our analysis fails to acknowledge that pan-tropical surface cooling caused by large volcanic eruptions may mask El Niño warming at our central Pacific site, potentially obscuring a volcano–El Niño connection suggested in previous studies. Although observational support for a dynamical response linking volcanic cooling to El Niño remains ambiguous, Robock raises some important questions about our study that we address here.

Full text: dx.doi.org/10.1126/science.abc1733

Where Science Gets Social.

AAAS.ORG/COMMUNITY

AAAS' Member Community is a one-stop destination for scientists and STEM enthusiasts alike. It's "Where Science Gets Social": a community where facts matter, ideas are big and there's always a reason to come hang out, share, discuss and explore.

Member COMMUNITY AAAS

Cite as: A. Robock, *Science* 10.1126/science.abc0502 (2020).

Response to Comment on "No consistent ENSO response to volcanic forcing over the last millennium"

Alan Robock

Department of Environmental Sciences, Rutgers University, New Brunswick, NJ 08901, USA.

Email: robock@envsci.rutgers.edu

Dee *et al.* (Reports, 27 March 2020, p. 1477) claimed that large volcanic eruptions do not produce a detectable El Niño response. However, they come to the wrong conclusion because they have ignored the fundamental climate response to large volcanic eruptions: Volcanic eruptions cool the surface, thus masking the relative El Niño warming.

The recent report by Dee *et al.* (*1*) claims that large volcanic eruptions do not produce a detectable El Niño response. However, they come to the wrong conclusion because the coral temperature reconstructions they use measure actual sea surface temperature (SST) and not the temperature relative to the rest of the tropics. Volcanic eruptions cool the surface, thus masking the relative El Niño warming, if expressed in absolute temperature changes. El Niño is a dynamical ocean response, which warms the eastern and central tropical Pacific with respect to the surrounding water. When the entire tropics cools in response to stratospheric aerosols from volcanic eruptions, the absolute temperature in the El Niño region will cool, too, and the impact will only be clear with respect to the surrounding region. This is called the relative SST (RSST), as shown by Khodri *et al.* (*2*).

Dee *et al.* have produced a valuable climate record by using oxygen isotope records from Palmyra corals to give a record of SST near the center of the region in the central Pacific Ocean that warms during an El Niño relative to the regions around it. But this SST is affected both by large-scale climate change and by local El Niños. Whereas Dee *et al.* used RSST in their analysis of climate model simulations in their figure S8, the basic results in figure 4 consider only raw SST, without accounting for the cooling effects of the volcanic eruptions. This is because they do not have a reliable way to calculate the tropical average temperature from proxies, so it is important to interpret the actual SST record they have produced. In this comment I am only addressing the interpretations from the Palmyra $\delta^{18}O$ temperature reconstructions, and not the climate model results, because climate models still imperfectly simulate the El Niño response to volcanic eruptions, as can be seen by the large differences in the climate model simulations shown in figure 4.

The smaller eruptions, shown in figure 4, A and B, would not be expected to show a strong El Niño signal because of the small radiative forcing. Figure 4D shows the signal from the largest eruption in their study, the 1257 CE Samalas eruption. Rather than showing the expected large cooling in year 1 after the eruption, they found basically no signal, which I interpret as an El Niño, counteracted by the volcanic cooling. In fact, if there had not been an El Niño, we would expect to see significant cooling. The dynamical response of the climate system that triggers El Niños does not in general produce larger El Niños for larger eruptions, so the El Niño after this largest eruption would be expected to show a weaker absolute SST warming signal than that from smaller eruptions, because the volcanic cooling would be larger.

Timmreck *et al.* (*3*) have suggested that larger aerosol particles from larger SO_2 stratospheric injections from larger eruptions would make the radiative forcing less than linear as a function of SO_2 input. Still, the radiative forcing as shown in figure 1 of Dee *et al.* for Samalas is approximately twice that of the average of the next three largest eruptions, and therefore we should expect twice as much cooling from that eruption. Guillet *et al.* (*4*) examined Northern Hemisphere responses to the Samalas eruption and found "that 1258 and 1259 experienced some of the coldest Northern Hemisphere summers of the past millennium." They also found that "in North America, volcanic radiative forcing was modulated by a positive phase of the El Niño–Southern Oscillation," evidence indeed that the Samalas eruption produced an El Niño.

Figure 4C of Dee *et al.* shows the SST signal averaged

for the four largest eruptions, including Samalas. Even with the 0.0‰ signal from Samalas at lag 1 year, figure 4C shows a strong El Niño signal, significant at close to the 95% significance level. If the 0.0‰ value from Samalas had not been included in this average, the signal would have been higher by one-third of the signal and would have been 0.13‰, not the current 0.10‰ at lag 1 year, and would certainly have been significant at a 95% level.

If we take into account the expected cooling from volcanic eruptions, the results from Dee *et al.* show a clear El Niño signal from the largest eruptions they considered. The El Niño SST signal for the largest eruption is obscured by the cooling effect of the eruption. The El Niño SST signal from the next three largest eruptions is clear even when looking at the absolute SST signal.

REFERENCES

1. S. G. Dee, K. M. Cobb, J. Emile-Geay, T. R. Ault, R. L. Edwards, H. Cheng, C. D. Charles, No consistent ENSO response to volcanic forcing over the last millennium. *Science* **367**, 1477–1481 (2020). doi:10.1126/science.aax2000 Medline
2. M. Khodri, T. Izumo, J. Vialard, S. Janicot, C. Cassou, M. Lengaigne, J. Mignot, G. Gastineau, E. Guilyardi, N. Lebas, A. Robock, M. J. McPhaden, Tropical explosive volcanic eruptions can trigger El Niño by cooling tropical Africa. *Nat. Commun.* **8**, 778 (2017). doi:10.1038/s41467-017-00755-6 Medline
3. C. Timmreck, S. J. Lorenz, T. J. Crowley, S. Kinne, T. J. Raddatz, M. A. Thomas, J. H. Jungclaus, Limited temperature response to the very large AD 1258 volcanic eruption. *Geophys. Res. Lett.* **36**, L21708 (2009). doi:10.1029/2009GL040083
4. S. Guillet, C. Corona, M. Stoffel, M. Khodri, F. Lavigne, P. Ortega, N. Eckert, P. D. Sielenou, V. Daux, O. V. Churakova (Sidorova), N. Davi, J.-L. Edouard, Y. Zhang, B. H. Luckman, V. S. Myglan, J. Guiot, M. Beniston, V. Masson-Delmotte, C. Oppenheimer, Climate response to the Samalas volcanic eruption in 1257 revealed by proxy records. *Nat. Geosci.* **10**, 123–128 (2017). doi:10.1038/ngeo2875

ACKNOWLEDGMENTS

Supported by the USDA National Institute of Food and Agriculture Hatch project 1006616 through the New Jersey Agricultural Experiment Station, Hatch project NJ07175.

3 April 2020; accepted 28 August 2020
Published online 11 September 2020
10.1126/science.abc0502

Cite as: S. G. Dee *et al.*, *Science* 10.1126/science.abc1733 (2020).

Response to Comment on "No consistent ENSO response to volcanic forcing over the last millennium"

Sylvia G. Dee[1]*, Kim M. Cobb[2], Julien Emile-Geay[3], Toby R. Ault[4], R. Lawrence Edwards[5], Hai Cheng[5,6], Christopher D. Charles[7]

[1]Department of Earth, Environmental, and Planetary Sciences, Rice University, Houston, TX, USA. [2]School of Earth and Atmospheric Sciences, Georgia Institute of Technology, Atlanta, GA, USA. [3]Department of Earth Sciences, University of Southern California, Los Angeles, CA 90089, USA. [4]Department of Earth and Atmospheric Sciences, Cornell University, Ithaca, NY, USA. [5]Minnesota Isotope Laboratory, Department of Earth Sciences, University of Minnesota, Minneapolis, MN 55455, USA. [6]Institute of Global Environmental Change, Xi'an Jiaotong University, Xi'an 710054, China. [7]Scripps Institution of Oceanography, San Diego, CA, USA.

*Corresponding author. Email: sylvia.dee@rice.edu

Robock claims that our analysis fails to acknowledge that pan-tropical surface cooling caused by large volcanic eruptions may mask El Niño warming at our central Pacific site, potentially obscuring a volcano–El Niño connection suggested in previous studies. Although observational support for a dynamical response linking volcanic cooling to El Niño remains ambiguous, Robock raises some important questions about our study that we address here.

Modeling studies suggest that the El Niño–Southern Oscillation (ENSO) is sensitive to sulfate aerosol forcing associated with explosive volcanism, yet observational support for a dynamical chain of events linking large volcanic cooling to El Niño occurrences remains inconclusive. In Dee *et al.* (*1*), we used absolutely dated fossil corals from the central tropical Pacific to test ENSO's response to large volcanic eruptions. Superposed epoch analysis reveals a weak tendency for an El Niño–like response in the year after an eruption, but this response is not statistically significant, nor does it appear after the outsized 1257 Samalas eruption. Dee *et al.* suggested that models showing a strong ENSO response to volcanic forcing may overestimate the size of the forced response relative to natural ENSO variability. In a recent comment (*2*), Robock raises relevant questions about the conclusions of Dee *et al.*, addressed below.

First, Robock advocates the use of relative sea surface temperature (RSST) to separate the ENSO signal from tropics-wide volcanic cooling. RSST focuses on spatial gradients and/or anomalies with respect to a large-scale (i.e., global or basin-scale) average, facilitating isolation of dynamical responses in the midst of tropics-wide warming or cooling. Although we agree that RSST is a powerful diagnostic tool for the study of volcano-ENSO dynamics, individual paleoclimate records such as those presented in our study reflect local changes in absolute SST. Our constraints come from monthly-resolved coral $\delta^{18}O$ anomalies at a single site (Palmyra atoll, northern Line Islands), which offer the advantage of a consistent interpretation with well-characterized uncertainties, but, absent other monthly-resolved constraints on tropical Pacific SST during this time, preclude the computation of RSST. That said, we undertook an investigation of RSST in climate model output, as we show in figure S8 of (*1*). Yet another approach would use paleoclimate data assimilation products [e.g., (*3*)] spanning the last millennium. The latter dataset represents a more integrated approach, yet suffers from additional uncertainties with respect to the calculation of RSST (e.g., uneven proxy coverage, imperfect climate model "priors"). As such, even though our reliance on a single well-dated, well-characterized paleoclimate reconstruction is far from ideal, our study does add a new physically based constraint to ongoing research on this key question.

The second part of Robock's argument concerns the lack of apparent cooling in the Palmyra coral $\delta^{18}O$, given "the expected large cooling" that follows sufficiently large volcanic eruptions. This expectation is based on decades of studies on instrumental climate data and models [see (*1*, *4*–*11*)] but is not quantitatively supported by observations. Indeed, the lack of evidence for large cooling after the eruption of the Samalas complex in 1257 CE (*4*), the strongest eruption of the last millennium, has long puzzled researchers (*5*). As Robock points out, the radiative scaling to aerosol loading is sublinear, so one would expect a response that is somewhat less than twice as large. Recently, Guillet *et al.* (*6*) used both tree-ring mixed latewood density data (a sensitive proxy for summer surface air temperature) and highly calibrated documentary data to constrain this response, finding a relative-

ly weak local temperature response in comparison to the inferred Samalas forcing. Although PMIP3 model simulations do simulate a large cooling in response to Samalas, recent studies suggest that the relatively simplistic representation of stratospheric aerosols in these models leads to exaggerated radiative forcing (*7*, *8*), particularly for Samalas (*9*). The inferred amplitude of the forcing used to drive climate models is derived from ice-core sulfate time series, yet the application of this forcing in models yields a large spread in simulated post-eruption climatic responses for CMIP5 experiments (*10*). As we point out in the text, the variable responses could be a result of uncertain forcing and/or structural uncertainties in model physics. Indeed, several volcanic forcing intermodel comparison projects are ongoing to identify the source of this spread [e.g., (*10*, *11*)]. Potentially important details include the eruption month [often unknown, yet critical for ENSO modulation (*12*)], the stratospheric injection height, and the relative forcing by extratropical (versus tropical) eruptions (*13*). None of these details were resolved in the volcanic forcing applied to PMIP3- and CMIP5-era model experiments, casting doubt on the expectations derived from them.

Third, Robock, citing (*6*), argues "that 1258 and 1259 experienced some of the coldest Northern Hemisphere summers of the past millennium." Recent reconstructions [see (*3*) and (*14*), figure S2b] support the notion that these were indeed cold years, but not exceptionally so in the context of the past millennium. Some compensation may occur, but the fact that Palmyra $\delta^{18}O$ anomalies in that year are neutral suggests that if there was an El Niño, it compensated for a minor global cooling, which does not advocate for a strong volcanic effect on ENSO. Guillet *et al.* (*6*)'s suggestion of a possible El Niño phase in 1259 is actually based on work by one of the authors (*15*), and its conclusions stem from a small number of proxy records located far from the core ENSO region. Our new record from the heart of the ENSO region (*1*) provides a more direct constraint on the tropical Pacific's response to this eruption.

Finally, Robock questions the arbitrariness of the 95% confidence level in ruling out a "significant" influence of volcanic forcing on ENSO. Although the choice of a 5% test level (false positive rate) is indeed arbitrary, it follows best statistical practice because it was chosen before the calculation was made, and we applied it consistently throughout the analysis. Adjusting this threshold a posteriori to support a particular hypothesis would constitute a form of confirmation bias.

In summary, as the text makes clear, our study does not rule out a possible volcanic influence on ENSO state; rather, it asserts that the currently available data do not uniformly support such an effect. Absence of evidence is not evidence of absence, and the effect expected by Robock may be revealed at some point in more comprehensive SST reconstructions based on more abundant monthly-resolved coral observations spanning the global tropics. Until then, the lack of evidence for such a response in our analysis is consistent with the null hypothesis—that the internal variability in ENSO is as large as, if not larger than, any volcanically forced signal in ENSO characteristics.

REFERENCES

1. S. G. Dee, K. M. Cobb, J. Emile-Geay, T. R. Ault, R. L. Edwards, H. Cheng, C. D. Charles, No consistent ENSO response to volcanic forcing over the last millennium. *Science* **367**, 1477–1481 (2020). doi:10.1126/science.aax2000 Medline
2. A. Robock, Comment on "No consistent ENSO response to volcanic forcing over the last millennium". *Science* **369**, eabc0502 (2020).
3. R. Tardif, G. J. Hakim, W. A. Perkins, K. A. Horlick, M. P. Erb, J. Emile-Geay, D. M. Anderson, E. J. Steig, D. Noone, Last Millennium Reanalysis with an expanded proxy database and seasonal proxy modeling. *Clim. Past* **15**, 1251–1273 (2019). doi:10.5194/cp-15-1251-2019
4. F. Lavigne, J.-P. Degeai, J.-C. Komorowski, S. Guillet, V. Robert, P. Lahitte, C. Oppenheimer, M. Stoffel, C. M. Vidal, I. Surono, I. Pratomo, P. Wassmer, I. Hajdas, D. S. Hadmoko, E. de Belizal, Source of the great A.D. 1257 mystery eruption unveiled, Samalas volcano, Rinjani Volcanic Complex, Indonesia. *Proc. Natl. Acad. Sci. U.S.A.* **110**, 16742–16747 (2013). doi:10.1073/pnas.1307520110 Medline
5. C. Timmreck, S. J. Lorenz, T. J. Crowley, S. Kinne, T. J. Raddatz, M. A. Thomas, J. H. Jungclaus, Limited temperature response to the very large AD 1258 volcanic eruption. *Geophys. Res. Lett.* **36**, L21708 (2009). doi:10.1029/2009GL040083
6. S. Guillet, C. Corona, M. Stoffel, M. Khodri, F. Lavigne, P. Ortega, N. Eckert, P. D. Sielenou, V. Daux, O. V. Churakova (Sidorova), N. Davi, J.-L. Edouard, Y. Zhang, B. H. Luckman, V. S. Myglan, J. Guiot, M. Beniston, V. Masson-Delmotte, C. Oppenheimer, Climate response to the Samalas volcanic eruption in 1257 revealed by proxy records. *Nat. Geosci.* **10**, 123–128 (2017). doi:10.1038/ngeo2875
7. M. Stoffel, M. Khodri, C. Corona, S. Guillet, V. Poulain, S. Bekki, J. Guiot, B. H. Luckman, C. Oppenheimer, N. Lebas, M. Beniston, V. Masson-Delmotte, Estimates of volcanic-induced cooling in the Northern Hemisphere over the past 1,500 years. *Nat. Geosci.* **8**, 784–788 (2015). doi:10.1038/ngeo2526
8. N. LeGrande, K. Tsigaridis, S. E. Bauer, Role of atmospheric chemistry in the climate impacts of stratospheric volcanic injections. *Nat. Geosci.* **9**, 652–655 (2016). doi:10.1038/ngeo2771
9. A. Burke, K. A. Moore, M. Sigl, D. C. Nita, J. R. McConnell, J. F. Adkins, Stratospheric eruptions from tropical and extra-tropical volcanoes constrained using high-resolution sulfur isotopes in ice cores. *Earth Planet. Sci. Lett.* **521**, 113–119 (2019). doi:10.1016/j.epsl.2019.06.006
10. C. Timmreck, G. W. Mann, V. Aquila, R. Hommel, L. A. Lee, A. Schmidt, C. Brühl, S. Carn, M. Chin, S. S. Dhomse, T. Diehl, J. M. English, M. J. Mills, R. Neely, J. Sheng, M. Toohey, D. Weisenstein, The Interactive Stratospheric Aerosol Model Intercomparison Project (ISA-MIP): Motivation and experimental design. *Geosci. Model Dev.* **11**, 2581–2608 (2018). doi:10.5194/gmd-11-2581-2018
11. D. Zanchettin, M. Khodri, C. Timmreck, M. Toohey, A. Schmidt, E. P. Gerber, G. Hegerl, A. Robock, F. S. Pausata, W. T. Ball, S. E. Bauer, S. Bekki, S. S. Dhomse, A. N. LeGrande, G. W. Mann, L. Marshall, M. Mills, M. Marchand, U. Niemeier, V. Poulain, E. Rozanov, A. Rubino, A. Stenke, K. Tsigaridis, F. Tummon, The Model Intercomparison Project on the climatic response to Volcanic forcing (VolMIP): Experimental design and forcing input data for CMIP6. *Geosci. Model Dev.* **9**, 2701–2719 (2016). doi:10.5194/gmd-9-2701-2016
12. S. Stevenson, J. T. Fasullo, B. L. Otto-Bliesner, R. A. Tomas, C. Gao, Role of eruption season in reconciling model and proxy responses to tropical volcanism.

Proc. Natl. Acad. Sci. U.S.A. **114**, 1822–1826 (2017). doi:10.1073/pnas.1612505114 Medline

13. M. Toohey, K. Krüger, H. Schmidt, C. Timmreck, M. Sigl, M. Stoffel, R. Wilson, Disproportionately strong climate forcing from extratropical explosive volcanic eruptions. *Nat. Geosci.* **12**, 100–107 (2019). doi:10.1038/s41561-018-0286-2
14. F. Zhu, J. Emile-Geay, G. J. Hakim, J. King, K. J. Anchukaitis, Resolving the differences in the simulated and reconstructed temperature response to volcanism. *Geophys. Res. Lett.* **47**, (2020). doi:10.1029/2019GL086908
15. J. Emile-Geay, R. Seager, M. Cane, E. Cook, G. H. Haug, Volcanoes and ENSO over the Past Millennium. *J. Clim.* **21**, 3134–3148 (2008). doi:10.1175/2007JCLI1884.1

ACKNOWLEDGMENTS

Funding: Supported by a Peter Voss Postdoctoral Fellowship in the Institute at Brown for Environment and Society, Brown University, and a postdoctoral fellowship from the Institute for Geophysics, University of Texas at Austin (S.G.D.); NSF Marine Geology and Geophysics awards 0752091, 1502832, and 1836645 (K.M.C.); NSF OCE award 0752585 (C.D.C. and K.M.C.); and NOAA grant NA18OAR4310426 (J.E.-G.). **Author contributions:** S.G.D., K.M.C., J.E.-G., and T.R.A. formulated research questions; K.M.C. and C.D.C. collected, sampled, and analyzed oxygen isotopes in the coral data with assistance from R.L.E. and H.C.; S.G.D. performed analysis on coral data, generated figures, and extracted model output with guidance from K.M.C., J.E.-G., and T.R.A.; all authors contributed to the writing of the manuscript. **Competing interests:** The authors declare no competing interests. **Data and materials availability:** All data and code are available in the supplementary materials of (*1*) and are publicly available on the National Climatic Data Center website at www.ncdc.noaa.gov/paleo/study/27490.

23 April 2020; accepted 28 August 2020
Published online 11 September 2020
10.1126/science.abc1733

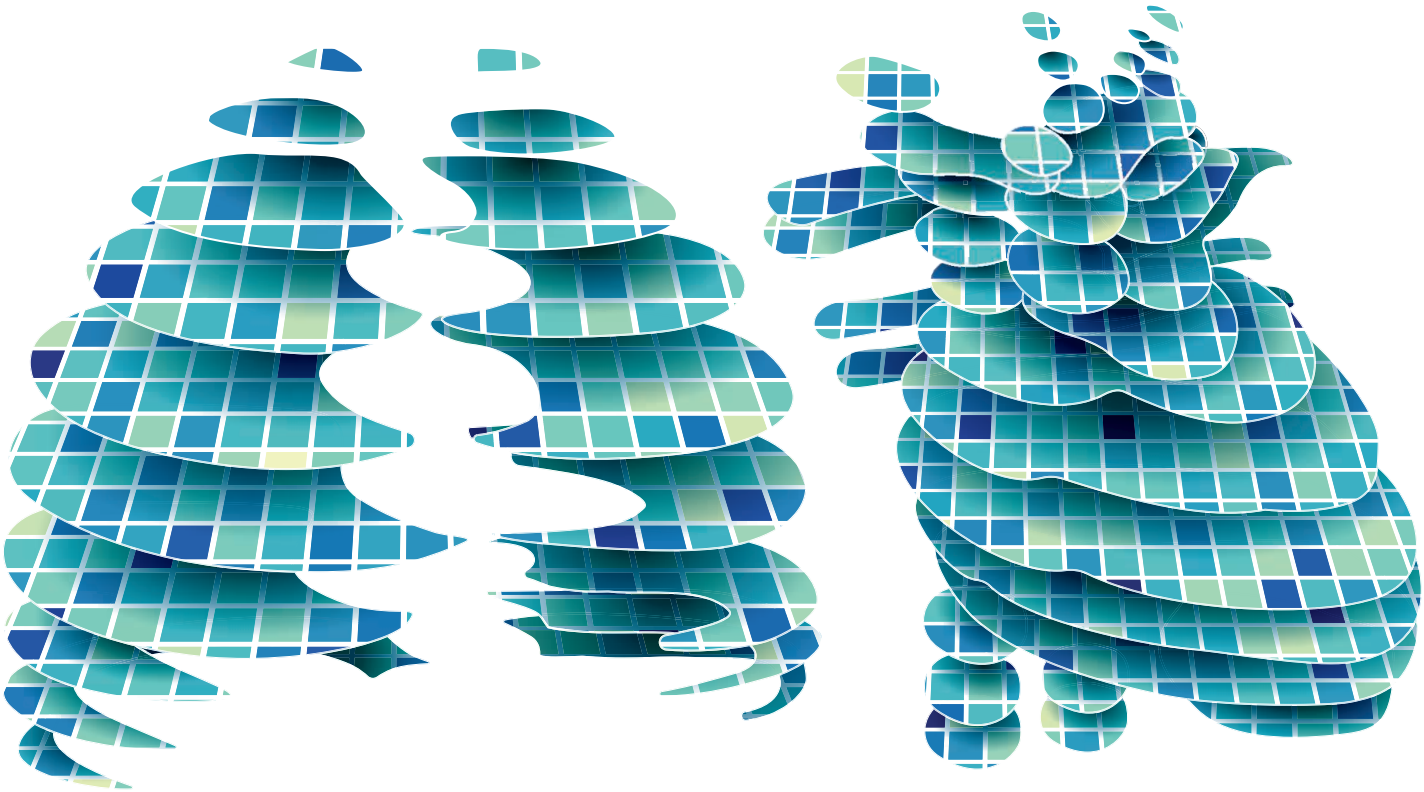

THE CUSTOM TRANSCRIPTOME

Unraveling tissue-specific genomics

RESEARCH ARTICLES

The GTEx Consortium atlas of genetic regulatory effects across human tissues p. 1318
The impact of sex on gene expression across human tissues p. 1331
Cell type–specific genetic regulation of gene expression across human tissues p. 1332
Determinants of telomere length across human tissues p. 1333
Transcriptomic signatures across human tissues identify functional rare genetic variation p. 1334

RELATED ITEMS

NEWS STORY p. 1286 PERSPECTIVE p. 1298 PODCAST
SCIENCE ADVANCES RESEARCH ARTICLE BY M. PIVIDORI *ET AL*. 10.1126/SCIADV.ABA2083
SCIENCE ADVANCES RESEARCH ARTICLE BY A. DUFFY *ET AL*. 10.1126/SCIADV.ABB6242
SCIENCEMAG.ORG/COLLECTIONS/GENETIC-VARIATION

ILLUSTRATION: V. ALTOUNIAN/*SCIENCE*. IN COLLABORATION WITH CHRISTIAN STOLTE. (DATA) GTEX CONSORTIUM

Published by AAAS

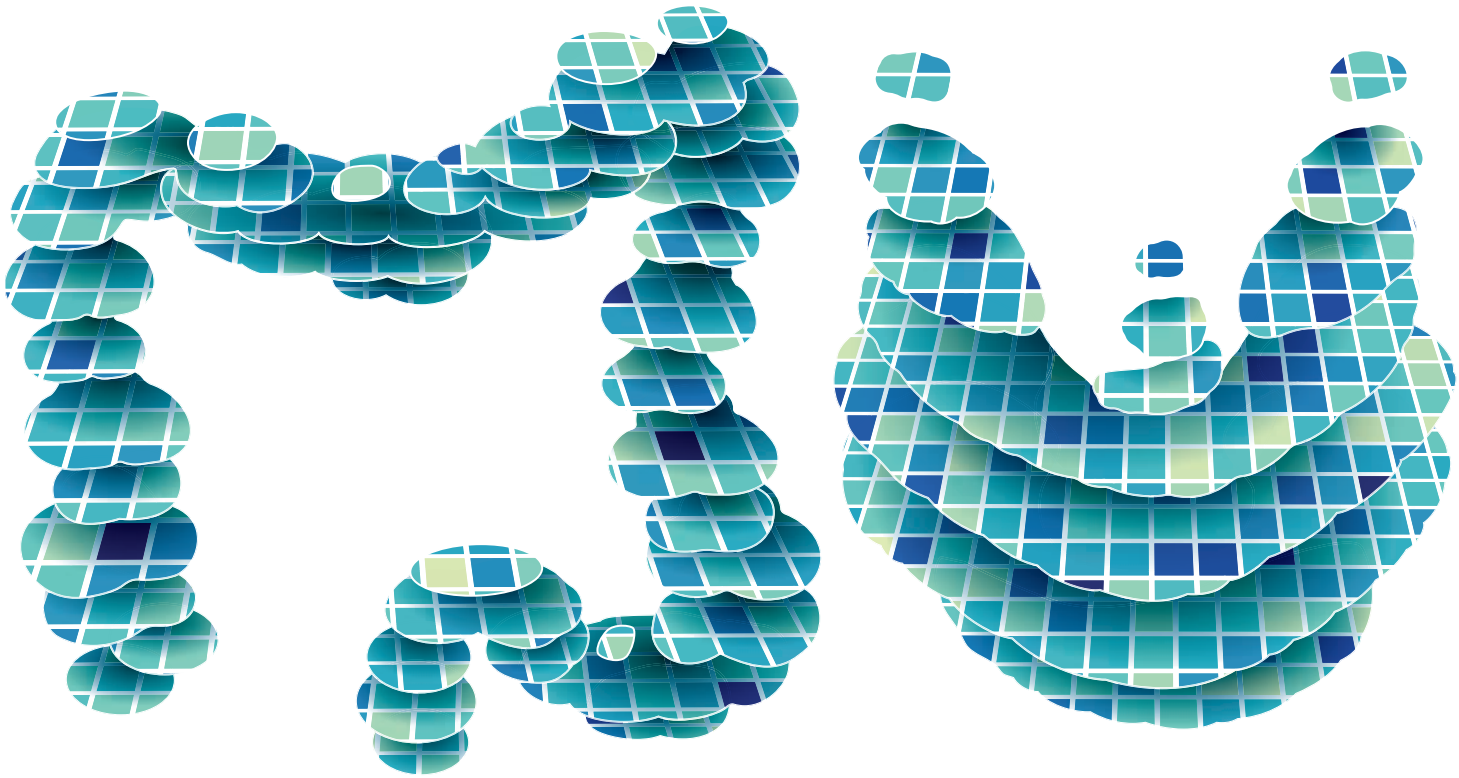

By **Laura M. Zahn**

The panorama of human phenotypes arises from a mix of common and rare genetic variants, some of which affect how genes are expressed and spliced throughout the body. More than a decade ago, scientists aiming to better understand the effects of genetic diversity in healthy individuals launched the Genotype-Tissue Expression (GTEx) Consortium. Here, *Science* unveils the third and final phase of the project, presenting the results from the analysis of the version 8 (v8) GTEx release.

The v8 data release includes an increased number of tissues and individuals, which allows for more accurate mapping of putatively causal variants and identifies cell type–specific differences in gene expression. The increased size of the study also provides the power to link genetic variation to gene expression, both proximally and distally in the genome, so that cis and trans effects as well as population- and sex-specific differences in gene expression can be detected.

The efforts of the GTEx Consortium have led to the development of numerous tools, including Watershed, and have provided a comprehensive resource for the scientific community. The GTEx project has established a foundation to elucidate how genetic variants affect gene regulation and quantitative traits in humans. Such studies of genetic variation and tissue specificity inform on properties of the genome—including noncoding elements and the telomeres found at chromosome ends—and help us understand how gene variants influence aging and disease. This work sets the stage for future exploration into the effects of the common and rare variants that underlie the gamut of humanity.

Heatmaps of differential gene expression among individuals from the Genotype-Tissue Expression Project. From left to right, illustrations represent data obtained for the lungs, heart, intestines, and thyroid.

Published by AAAS

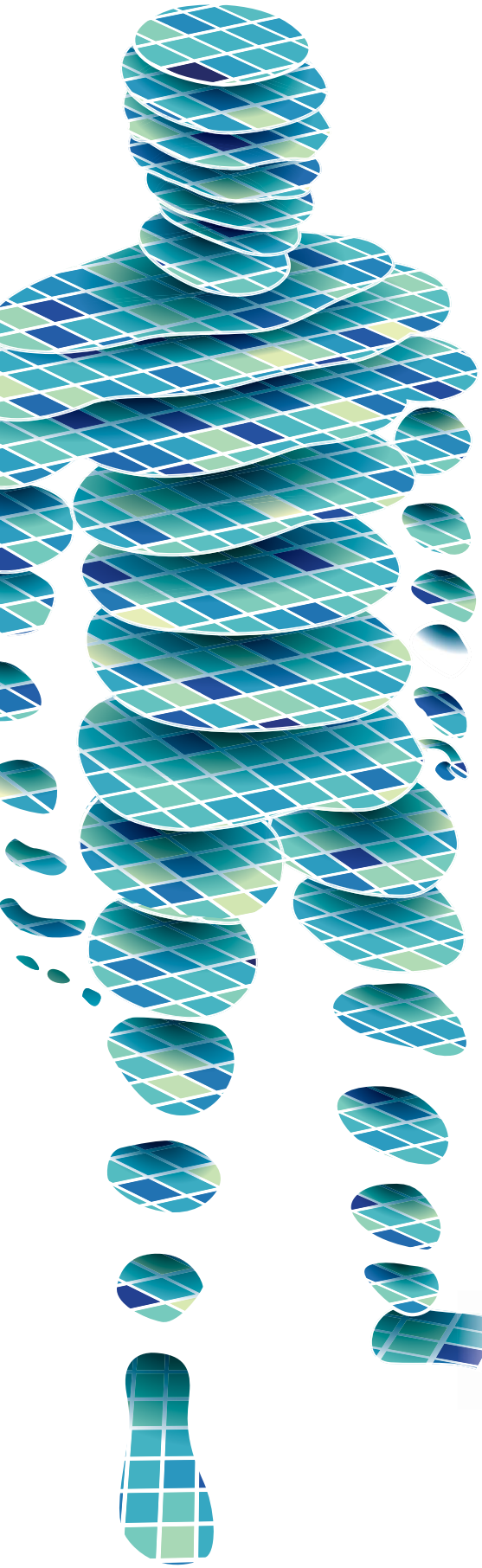

RESEARCH ARTICLE

HUMAN GENOMICS

The GTEx Consortium atlas of genetic regulatory effects across human tissues

The GTEx Consortium*

The Genotype-Tissue Expression (GTEx) project was established to characterize genetic effects on the transcriptome across human tissues and to link these regulatory mechanisms to trait and disease associations. Here, we present analyses of the version 8 data, examining 15,201 RNA-sequencing samples from 49 tissues of 838 postmortem donors. We comprehensively characterize genetic associations for gene expression and splicing in cis and trans, showing that regulatory associations are found for almost all genes, and describe the underlying molecular mechanisms and their contribution to allelic heterogeneity and pleiotropy of complex traits. Leveraging the large diversity of tissues, we provide insights into the tissue specificity of genetic effects and show that cell type composition is a key factor in understanding gene regulatory mechanisms in human tissues.

The characterization and interpretation of the function of the millions of genetic variants across the human genome remain a pressing need in human genetics. Understanding the effects of genetic variation is essential for identifying the molecular mechanisms of genetic risk for complex traits and diseases, which are mainly driven by noncoding loci with largely uncharacterized regulatory functions. To address this challenge, several projects have built comprehensive annotations of genome function across tissues and cell types (*1*, *2*) and mapped the effects of regulatory variation across large numbers of individuals, primarily from whole blood and blood cell types (*3*–*5*). The Genotype-Tissue Expression (GTEx) project provides an essential intersection where variant function can be studied across a wide range of both tissues and individuals.

The GTEx project was launched in 2010 with the aim of building a catalog of genetic effects on gene expression across a large number of human tissues to elucidate the molecular mechanisms of genetic associations with complex diseases and traits and to improve our understanding of regulatory genetic variation (*6*). The project set out to collect biospecimens from ~50 tissues from up to ~1000 postmortem donors and to create standards and protocols for optimizing postmortem tissue collection and donor recruitment (*7*, *8*), biospecimen processing (*7*), and data sharing (www.gtexportal.org).

Following the GTEx pilot (*9*) and midstage results (*10*), we present a final analysis of the version 8 (v8) data release from the GTEx Consortium. We provide a catalog of genetic regulatory variants affecting gene expression and splicing in cis and trans across 49 tissues and describe patterns and mechanisms of tissue and cell type specificity of genetic regulatory effects. Through integration of GTEx data with genome-wide association studies (GWASs), we characterize mechanisms of how genetic effects on the transcriptome mediate complex trait associations.

Quantitative trait locus (QTL) discovery

The GTEx v8 dataset, after quality control (*11*), consists of 838 donors and 17,382 samples from 52 tissues and two cell lines. In the analysis of this study, we used 49 tissues or cell lines that had at least 70 individuals for which both RNA sequencing (RNA-seq) and genotype data from whole-genome sequencing (WGS) were available, for a total of 15,201 samples from 838 donors (Fig. 1A and figs. S1 and S2). Of the 838 donors, 715 (85.3%) were European American, 103 (12.3%) African American, and 12 (1.4%) Asian American, with 16 (1.9%) reporting Hispanic or Latino ethnicity; 557 (66.4%) donors were male and 281 (33.5%) female (fig. S1). WGS was performed for each donor to a median depth of 32×, resulting in the detection of 43,066,422 single-nucleotide variants after quality control and phasing [10,008,325 with minor allele frequency (MAF) ≥ 0.01] and 3,459,870 small indels (762,535 with MAF ≥ 0.01) (fig. S3 and table S1) (*11*). The mRNA of each of the tissue samples was sequenced to a median depth of 82.6 million reads, and alignment, quantification, and quality control were performed as described in (*11*) (figs. S4 to S6).

The resulting data provide a broad survey of individual- and tissue-specific gene expression, enabling a comprehensive view of the

*A full list of the GTEx authors and their affiliations is available at the end of this article.
Corresponding authors: François Aguet (francois@broadinstitute.org); Kristin G. Ardlie (kardlie@broadinstitute.org); Tuuli Lappalainen (tlappalainen@nygenome.org)

V. ALTOUNIAN/*SCIENCE*; IN COLLABORATION WITH CHRISTIAN STOLTE (DATA) GTEX CONSORTIUM

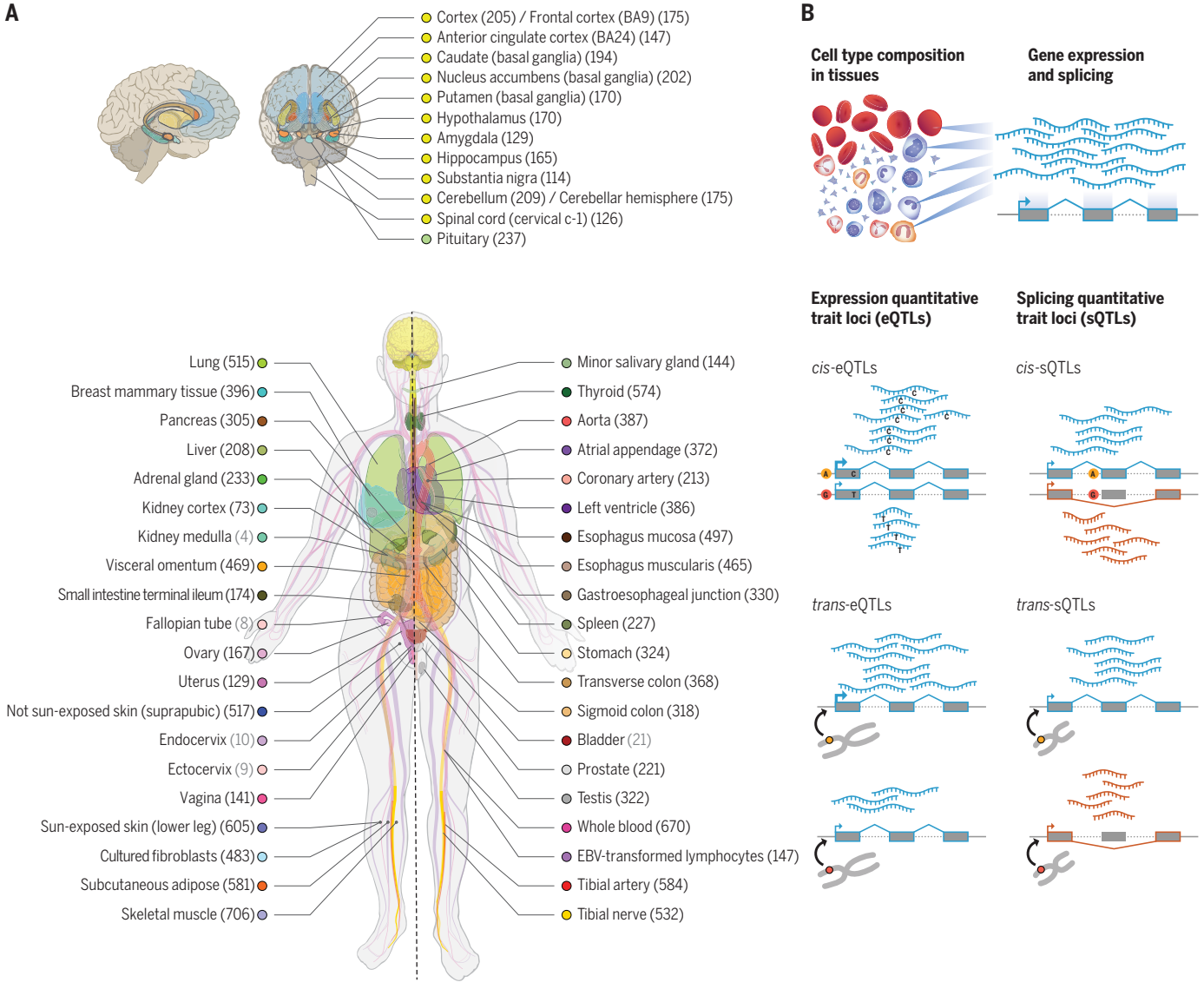

Fig. 1. Sample and data types in the GTEx v8 study. (**A**) Illustration of the 54 tissue types examined (including 11 distinct brain regions and two cell lines), with sample numbers from genotyped donors in parentheses and color coding indicated in the adjacent circles. Tissues with 70 or more samples were included in QTL analyses. (**B**) Illustration of the core data types used throughout the study. Gene expression and splicing were quantified from bulk RNA-seq of heterogeneous tissue samples, and local and distal genetic effects (cis-QTLs and trans-QTLs, respectively) were quantified across individuals for each tissue.

impact of genetic variation on gene regulation (Fig. 1B). We mapped genetic loci that affect the expression (eQTL) or splicing (sQTL) of protein-coding and long intergenic noncoding RNA (lincRNA) genes, both in cis and trans. Genes with an eQTL or sQTL are called eGenes and sGenes, respectively, and the corresponding significant variants are called eVariants and sVariants, respectively.

Across all tissues, we discovered cis-eQTLs [5% false discovery rate (FDR) per tissue (*11*), with 1% FDR results shown in fig. S7] for 18,262 protein-coding and 5006 lincRNA genes [23,268 genes with a cis-eQTL (i.e., cis-eGenes) corresponding to 94.7% of all protein-coding and 67.3% of all lincRNA genes detected in at least one tissue], with a total of 4,278,636 genetic variants (43% of all variants with MAF ≥ 0.01) that were significant in at least one tissue (cis-eVariants) (Fig. 2A, figs. S7 and S8, and table S2). The discovered eQTLs had a high replication rate in external datasets (figs. S12 and S13). Cis-eQTLs for all long noncoding RNAs (lncRNAs), which include lincRNAs and other types, are characterized in (*12*). The genes lacking a cis-eQTL were enriched for those lacking expression in the tissues analyzed by GTEx, including genes involved in early development (fig. S9). While most of the discovered cis-eQTLs had small effect sizes measured as allelic fold change (aFC), across tissues an average of 22% of cis-eQTLs had a greater than twofold effect on gene expression (fig. S14). We mapped sQTLs in cis with intron excision ratios from LeafCutter (*11*, *13*) and discovered 12,828 (66.5%) protein-coding and 1600 (21.5%) lincRNA genes (14,424 total) with a cis-sQTL (5% FDR per tissue) in at least one tissue (cis-sVariants) (Fig. 2A and table S2; with 1% FDR results shown in fig. S7). As expected (*10*), cis-QTL discovery was highly correlated with the sample size for each tissue [Spearman's rank correlation coefficient (ρ) = 0.95 for cis-eQTLs and 0.92 for cis-sQTLs]. The increased cis-eQTL discovery in larger tissues is primarily driven by additional power to discover small effects, with discovery of cis-eGenes with a greater than twofold effect saturating

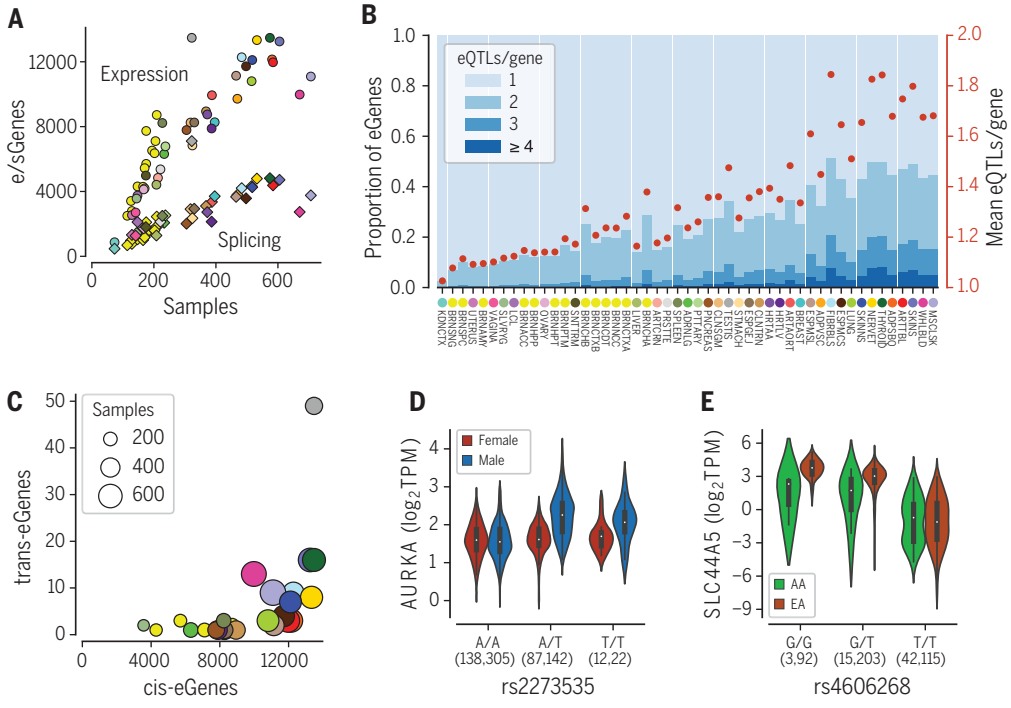

Fig. 2. QTL discovery. (**A**) The number of genes with a cis-eQTL (eGenes) or cis-sQTL (sGenes) per tissue, as a function of sample size. See Fig. 1A for the legend of tissue colors. (**B**) Allelic heterogeneity of cis-eQTLs depicted as proportion of eGenes with one or more independent cis-eQTLs (blue stacked bars; left *y* axis) and as a mean number of cis-eQTLs per gene (red dots; right *y* axis). The tissues are ordered by sample size. (**C**) The number of genes with a trans-eQTL as a function of the number of cis-eGenes. (**D**) Sex-biased cis-eQTL for *AURKA* in skeletal muscle, where rs2273535-T is associated with increased *AURKA* expression in males ($P = 9.02 \times 10^{-27}$) but not in females ($P = 0.75$). (**E**) Population-biased cis-eQTL for *SLC44A5* in esophagus mucosa [aFC = −2.85 and −4.82 and in African Americans (AA) and European Americans (EA), respectively; permutation *P* value = 1.2×10^{-3}]. TPM, transcripts per million.

at ~1500 genes in tissues with >200 samples (fig. S14).

Previous studies have shown widespread allelic heterogeneity of gene expression in cis, that is, multiple independent causal eQTLs per gene (*4*, *14*, *15*). We mapped independent cis-eQTLs and cis-sQTLs using stepwise regression, where the 5% FDR threshold for significance was defined by the single cis-QTL mapping (*10*). We observed widespread allelic heterogeneity, with up to 50% of eGenes having more than one independent cis-eQTL in the tissues with the largest sample sizes (Fig. 2B and fig. S10). Our analysis captured a lower rate of allelic heterogeneity for cis-sQTLs, which could be a result of both underlying biology and lower power in cis-sQTL mapping (fig. S10). These results highlight gains in cis-eQTL mapping with increasing sample sizes, even when the discovery of new eGenes in specific tissues starts to saturate.

Interchromosomal trans-eQTL mapping yielded 143 trans-eGenes (121 protein-coding and 22 lincRNA at 5% FDR assessed at the gene level, separately for each gene type), after controlling for false positives due to read misalignment (*11*, *16*) (table S13). The number of trans-eGenes discovered per tissue is correlated with sample size (Spearman's ρ = 0.68) and to the number of cis-eQTLs (Spearman's ρ = 0.77), with outlier tissues such as testis contributing disproportionately to both cis and trans (Fig. 2C). We identified a total of 49 trans-eGenes in testis, 47 of which were found in no other tissue even at FDR 50%. Greater than twofold effect sizes on trans-eGene expression were observed for 19% of trans-eQTLs (fig. S14). Trans-sQTL mapping yielded 29 trans-sGenes (5% FDR per tissue), including a replication of a previously described trans-sQTL (*3*) and visual support of the association pattern in several loci (*11*) (fig. S11 and table S14). These results suggest that while trans-sQTL mapping is challenging, we can discover robust genetic effects on splicing in trans.

We produced allelic expression (AE) data using two complementary approaches (*11*). In addition to the conventional AE data for each heterozygous genotype, we produced AE data by haplotype, integrating data from multiple heterozygous sites in the same gene, yielding 153 million gene-level measurements (≥8 reads) across all samples (*17*). Allelic expression reflects differential regulation of the two haplotypes in individuals that are heterozygous for a regulatory variant in cis; indeed, cis-eQTL effect size is strongly correlated with allelic expression (median Spearman's ρ = 0.82) (*10*). We hypothesized that cis-sQTLs could also partially contribute to allelic imbalance, even if only for parts of transcripts. However, there is drastically less signal of increased allelic imbalance among individuals heterozygous for cis-sQTLs (median Spearman's ρ = −0.05) (fig. S15), which indicates that AE data primarily capture cis-eQTL effects and that genetic splicing variation in cis is not strongly reflected in gene-level AE data.

Genetic regulatory effects across populations and sexes

Variability in human traits and diseases between sexes and population groups likely partially results from differences in genetic effects (*18*–*20*). To study whether genetic regulatory variants manifest such variability, we analyzed variable cis-eQTL effects between males and females, as well as between individuals of European ancestry and those of African ancestry. Because external replication datasets are sparse, we developed an AE approach for validation with an orthogonal data type from the same samples (*17*): Allelic imbalance in individuals heterozygous for the cis-eQTL allows individual-level quantification of the cis-eQTL effect size (*21*) and can be correlated with the interaction terms used in cis-eQTL analysis

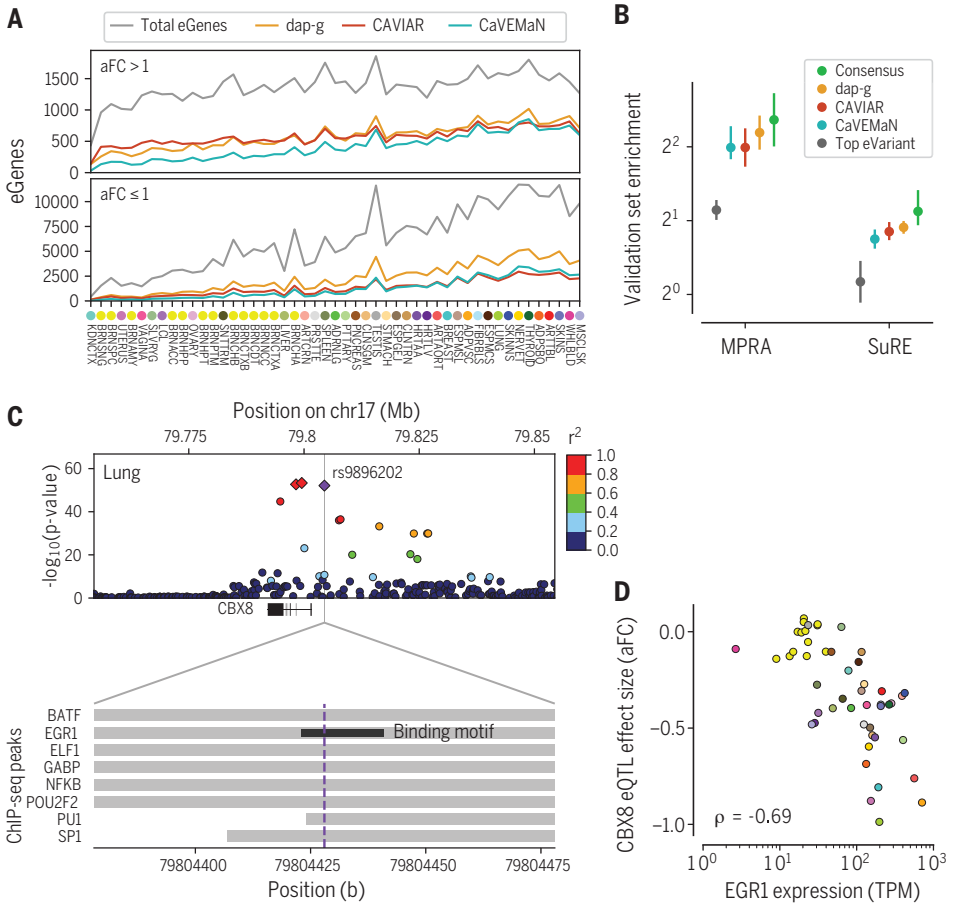

Fig. 3. Fine-mapping of cis-eQTLs. (**A**) Number of eGenes per tissue with variants fine-mapped with >0.5 posterior probability of causality, using three methods. The overall number of eGenes with at least one fine-mapped eVariant increases with sample size for all methods. However, this increase is in part driven by better statistical power to detect small effect size cis-eQTLs (aFC ≤ 1 in $\log_2$ scale; see also fig. S14) with larger sample sizes, and the proportion of well fine-mapped eGenes with small effect sizes increases more modestly with sample size (bottom versus top panels), indicating that such cis-eQTLs are generally more difficult to fine-map. (**B**) Enrichment of variants among experimentally validated regulatory variants, shown for the cis-eVariant with the best *P* value (top eVariant), and those with posterior probability of causality >0.8 according to each of the three methods individually or all of them (consensus). Error bars: 95% confidence interval (CI). (**C**) The cis-eQTL signal for *CBX8* is fine-mapped to a credible set of three variants (red and purple diamonds), of which rs9896202 (purple diamond) overlaps a large number of transcription factor binding sites in ENCODE chromatin immunoprecipitation sequencing (ChIP-seq) data and disrupts the binding motif of *EGR1*. (**D**) The potential role of EGR1 binding driving this cis-eQTL is further supported by correlation between *EGR1* expression and the *CBX8* cis-eQTL effect size across tissues.

to validate modifier effects of the cis-eQTL association (fig. S16).

To characterize sex-differentiated genetic effects on gene expression in GTEx tissues, we mapped sex-biased cis-eQTLs (sb-eQTLs). Analyzing the set of all conditionally independent cis-eQTLs, we identified eQTLs with significantly different effects between sexes by fitting a linear regression model and testing for a significant genotype-by-sex (G×S) interaction (*11*). Across the 44 GTEx tissues shared between sexes, we identified 369 sb-eQTLs (FDR ≤ 25%), characterized further in (*22*). Sex-biased eQTL discovery had a modest correlation with tissue sample size (Spearman's ρ = 0.39, *P* = 0.03), with most sb-eQTLs discovered in breast but others also discovered in muscle, skin, and adipose tissues.

In some cases, the cis-eQTL signal—identified with males and females combined—seems to be driven exclusively by one sex. For example, the cis-eQTL association of rs2273535 with the gene *AURKA* in skeletal muscle (cis-eQTL $P = 6.92 \times 10^{-24}$) is correlated with sex ($P_{G\times S} = 9.28 \times 10^{-12}$, Storey $q_{G\times S} = 1.07 \times 10^{-7}$, AE validation $P = 1.15 \times 10^{-11}$) and present only in males (Fig. 2D and fig. S17). *AURKA* is a member of the serine and threonine kinase family involved in mitotic chromosomal segregation that has been widely studied as a risk factor in several cancers (*23*–*26*) and has recently been shown to be involved in muscle differentiation (*27*).

We also characterized population-biased cis-eQTLs (pb-eQTLs), where a variant's molecular effect on gene expression differs between individuals of European and African ancestry, controlling for differences in allele frequency, linkage disequilibrium (LD), and covariates (*11*). Analyzing 31 tissues with sample sizes >20 in both populations, we mapped genes with a different eQTL effect size measured by aFC. After applying stringent filters to remove differences potentially explained by LD or other artifacts (fig. S18A), we identified 178 pb-eQTLs for 141 eGenes (FDR ≤ 25%) that show a moderate degree of validation in allele-specific expression data (fig. S18, C and D, and table S10).

While some of the pb-eQTL effects are tissue specific, there are also effects that are shared across most tissues (fig. S18E). Figure 2E shows an example of a pb-eQTL for the *SLC44A5* gene involved in transport of sugars and amino acids, which is expressed at different levels in the epidermis of lighter skin and darker skin (reconstructed in vitro) (*28*, *29*). In Europeans, the derived allele of rs4606268 decreases expression of the gene in esophagus mucosa (aFC = −4.82), but this effect is significantly lower in African Americans (aFC = −2.85, permutation *P* value = 1.2×10^{-3}, AE validation *P* = 0.002) (fig. S18C).

Altogether, despite the relaxed FDR, we discovered only a few hundred sex- or population-biased cis-eQTLs out of tens of thousands of cis-eQTLs in GTEx, which indicates that there are few regulatory variants with major modifier effects and that these associations continue to be challenging to identify without a much larger sample size. However, the discovered effects can provide insights into sex- or population-specific regulatory effects on gene expression. Importantly, factors correlated with sex or population—for example, cell type composition or environmental exposures—may contribute to sex- or population-biased cis-eQTLs. These effects are described in detail in (*22*).

Fine-mapping

A major challenge of all genetic association studies is to distinguish the causal variants from their LD proxies. We applied three different

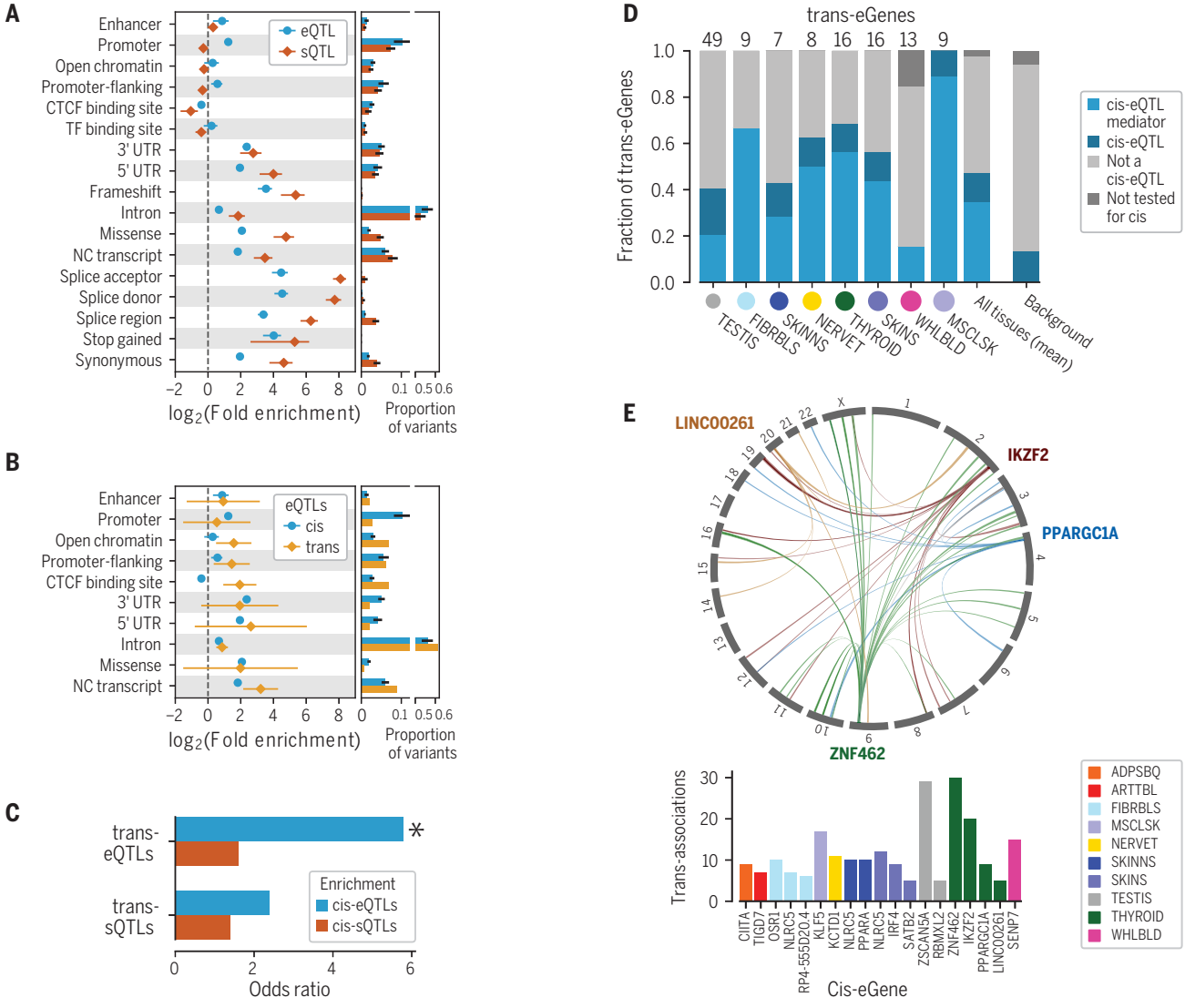

Fig. 4. Functional mechanisms of genetic regulatory effects. QTL enrichment in functional annotations for (**A**) cis-eQTLs and cis-sQTLs and for (**B**) trans-eQTLs. cis-QTL enrichment is shown as mean ± SD across tissues; trans-eQTL enrichment as 95% CI. UTR, untranslated region. (**C**) Enrichment of lead trans-eVariants or trans-sVariants that have been tested for cis-QTL effects also being significant cis-eVariants or cis-sVariants in the same tissue, respectively. Asterisk denotes significant enrichment, $P < 10^{-21}$. (**D**) Proportion of trans-eQTLs that are significant cis-eQTLs or mediated by cis-eQTLs. (**E**) Trans associations of cis-mediating genes identified through colocalization (PP4 > 0.8 and nominal association with discovery trans-eVariant $P < 10^{-5}$). (Top) Associations for four thyroid cis-eQTLs (indicated by gene names); (bottom) cis-mediating genes with five or more colocalizing trans-eQTLs.

statistical fine-mapping methods—CaVEMaN (*30*), CAVIAR (*31*), and dap-g (*32*)—to infer likely causal variants of cis-eQTLs in each tissue (Fig. 3A) (*11*). For many cis-eQTLs, the causal variant can be mapped with a high probability to a handful of candidates. The 90% credible set for each cis-eQTL consists of variants that include the causal variant with 90% probability; using dap-g, we identified a median of six variants in the 90% credible set for each cis-eQTL (fig. S19). Furthermore, 9.3% of the cis-eQTLs have a variant with a posterior probability >0.8 according to dap-g, indicating a single likely causal variant for those cis-eQTLs. We defined a consensus set of 24,740 cis-eQTLs across all tissues (7709 unique variants), for which the posterior probability was >0.8 across all three methods (fig. S20). Fine-mapped variants were significantly more enriched among experimentally validated causal variants from MPRA (*33*) and SuRE (*34*) compared with the lead eVariant across all eGenes (Fig. 3B). The highest enrichment was observed for the consensus set, although with overlapping confidence intervals (Fig. 3B). This demonstrates how careful fine-mapping facilitates the identification of likely causal regulatory variants.

Knowing the likely causal variant enables greater insights into the molecular mechanisms of individual eQTLs, including the mechanisms of their tissue-specific effects. Figure 3C shows an example of an eQTL for the gene *CBX8* that colocalizes with breast cancer risk and birth weight (posterior probability = 0.68 for both in lung). One of the three variants in the confident set overlaps the binding site and disrupts the motif of the transcription factor *EGR1* (*1*) (fig. S21). The role of *EGR1* as an upstream driver of this eQTL is further supported by a cross-tissue correlation of the effect size of the eQTL and the expression level of *EGR1* (Spearman's ρ = −0.69) (Fig. 3D).

Functional mechanisms of QTL associations

Quantitative trait data from multiple molecular phenotypes, integrated with the regulatory annotation of the genome (table S3), offer a

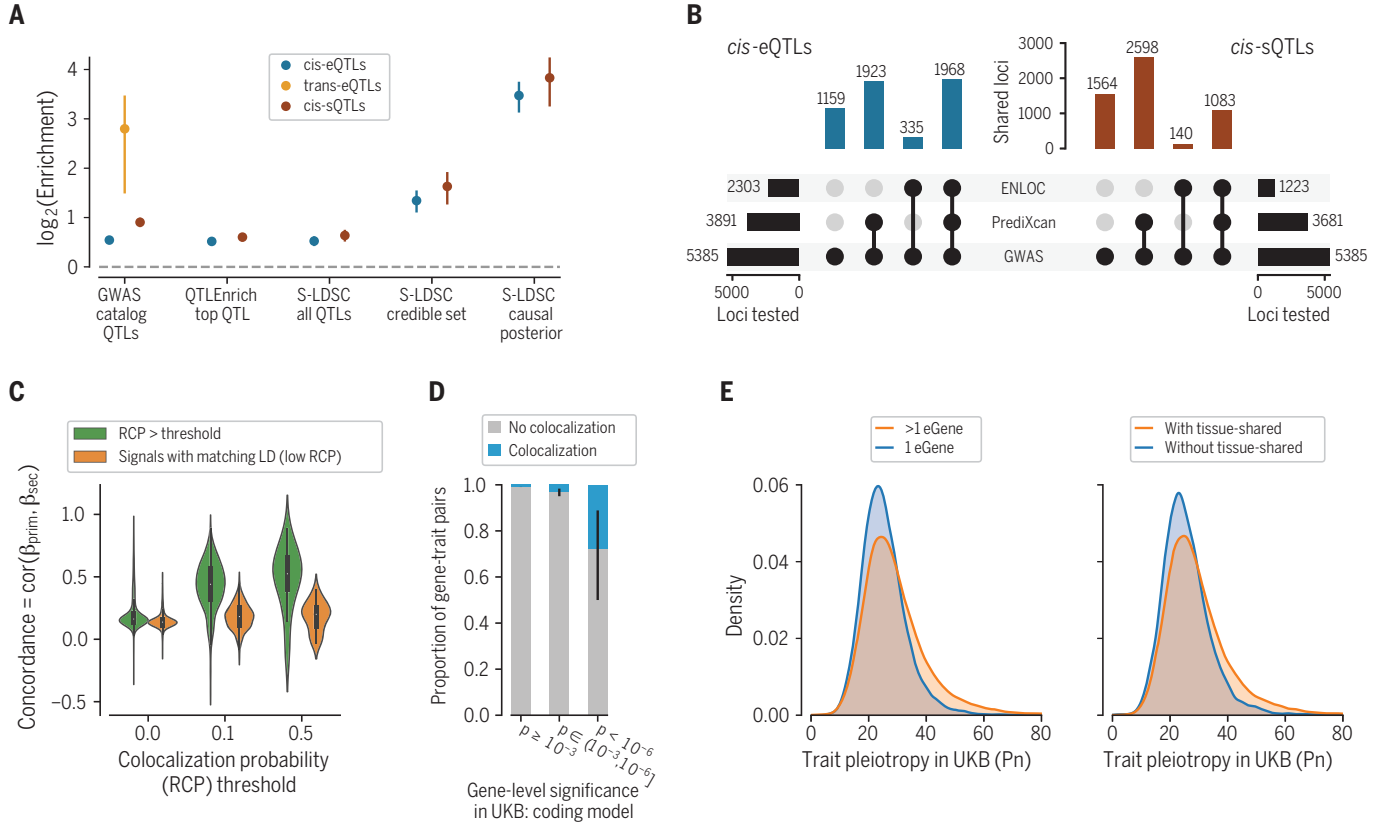

Fig. 5. Regulatory mechanisms of GWAS loci. (**A**) GWAS enrichment of cis-eQTLs, cis-sQTLs, and trans-eQTLs measured with different approaches: enrichment calculated from GWAS summary statistics of the most significant cis-QTL per eGene or sGene with QTLEnrich and LD score regression with all significant cis-QTLs (S-LDSC all QTLs), simple QTL overlap enrichment with all GWAS catalog variants, and LD score regression with fine-mapped cis-QTLs in the 95% credible set (S-LDSC credible set) and using posterior probability of causality as a continuous annotation (S-LDSC causal posterior). Enrichment is shown as mean and 95% CI. (**B**) Number of GWAS loci linked to eGenes or sGenes through colocalization (ENLOC) and association (PrediXcan), aggregated across tissues. (**C**) Concordance of mediated effects among independent cis-eQTLs for the same gene, shown for different levels of regional colocalization probability (RCP) (*32*), which is used as a proxy for the gene's causality. As the null, we show the concordance for LD matched genes without colocalization. (**D**) Proportion of colocalized cis-eQTLs with a matching phenotype for genes with different levels of rare variant trait association in the UK Biobank (UKB). (**E**) Horizontal GWAS trait pleiotropy score distribution for cis-eQTLs that regulate multiple versus a single gene (left) and for cis-eQTLs that are tissue-shared versus specific.

powerful way to understand the molecular mechanisms and phenotypic consequences of genetic regulatory effects. As expected, cis-eQTLs and cis-sQTLs are enriched in functional elements of the genome (Fig. 4A). Although the strongest enrichments are driven by variant classes that lead to splicing changes or nonsense-mediated decay, these account for relatively few variants. Cis-sQTLs are enriched almost entirely in transcribed regions, whereas cis-eQTLs are enriched in both transcribed regions and transcriptional regulatory elements. Previous studies (*4*, *35*) have indicated that cis-eQTL and cis-sQTL effects on the same gene are typically driven by different genetic variants. This observation is corroborated by the GTEx v8 data, where the overlap of cis-eQTL credible sets of likely causal variants, from CAVIAR analysis, have only a 12% overlap with cis-sQTL credible sets (fig. S22). Functional enrichment of overlapping and nonoverlapping cis-eQTLs and cis-sQTLs, using stringent LD filtering, showed that the patterns characteristic for each type—such as enrichment of cis-eQTLs in enhancers and cis-sQTLs in splice sites—are even stronger for distinct loci (fig. S22).

We hypothesized that eVariants and their target eGenes in cis are more likely to be in the same topologically associated domains (TADs) that allow chromatin interactions between more distant regulatory regions and target gene promoters (*36*). To test this supposition, we analyzed TAD data from ENCODE (*1*) and cis-eQTLs from matching GTEx tissues (table S3). Compared to matching random variant-gene pairs and controlling for distance from the transcription start site, cis-eVariant and cis-eGene pairs were significantly enriched for being in the same TAD [median odds ratio (OR) 4.55; all $P < 10^{-12}$] (fig. S23).

Trans-eQTLs are enriched in regulatory annotations that suggest both pre- and post-transcriptional mechanisms (Fig. 4B). Unlike cis-eQTLs, trans-eQTLs are enriched in CTCF binding sites, suggesting that disruption of CTCF binding may underlie distal genetic regulatory effects, potentially via its effect on interchromosomal chromatin interactions (*36*). Trans-eQTLs are also partially driven by cis-eQTLs (*37*, *38*), with a significant enrichment of lead trans-eVariants among cis-eVariants in the same tissue (5.9×; two-sided Fisher's exact test, $P = 5.03 \times 10^{-22}$) (Fig. 4C). A lack of analogous enrichment suggests that cis-sQTLs are less important contributors to trans-eQTLs ($P = 0.064$), and trans-sVariants had no significant enrichment of either cis-eQTLs ($P = 0.051$) or cis-sQTLs ($P = 0.53$). A further demonstration of the important contribution of cis-eQTLs to trans-eQTLs is that, on the basis of mediation analysis, 77% of lead trans-eVariants that are also cis-eVariants (corresponding to 31.6% of all lead trans-eVariants) appear to act through

the cis-eQTL (Fig. 4D and fig. S24). Colocalization of cis-eQTLs and trans-eQTLs was widespread and often tissue specific, with Fig. 4E showing cis-eQTLs with at least 10 nominally significant colocalized trans-eQTLs each [posterior probability of colocalization (PP4) > 0.8 and trans-eQTL $P < 10^{-5}$], pinpointing how local effects on gene expression can potentially lead to downstream regulatory effects across the genome (fig. S25 and table S16). The many remaining trans-eQTLs that do not coincide with a cis-eQTL may arise owing to mechanisms including undetected cis effects in specific cell types or conditions, protein coding changes, effects on cell type heterogeneity, or more complex causality such as a variant that influences a trait with downstream consequences on gene expression.

Genetic regulatory effects mediate complex trait associations

To analyze the role of regulatory variants in genetic associations for human traits, we first asked whether variants in the GWAS catalog were enriched for significant QTLs compared with all variants tested for QTLs (*11*). We observed a 1.46-fold enrichment for cis-eQTLs (63% versus 43%) and 1.86-fold enrichment for cis-sQTLs (37% versus 20%). The enrichment was even stronger for trans-eQTLs [6.97-fold (0.029% versus 0.0042%)], consistent with other analyses (*39*) (Fig. 5A, fig. S26, tables S5 and S6). Cell type proportion may influence detection of trans-eQTLs in heterogeneous tissues and may also be reflected in GWAS associations for blood cell count phenotypes and other complex traits. To minimize the possible impact of cell type heterogeneity on these enrichment statistics, we excluded blood cellularity traits and repeated these analyses. The resulting enrichments were 5.21-fold for trans-eQTLs, 1.43-fold for cis-eQTLs, and 1.81-fold for cis-sQTLs, largely preserving the patterns observed using the full set of GWAS traits.

This approach does not leverage the full power of GWAS and QTL association statistics, nor does it account for LD contamination, a situation wherein the causal variants for QTL and GWAS signals are distinct but LD between the two causal variants can suggest a false functional link (*40*). Therefore, for subsequent analyses (below) we selected 87 GWASs representing a broad array of binary and continuous complex traits that have summary results available in the public domain (*11*, *41*). To match the ancestry of the GWASs, analyses were performed using cis-QTL statistics calculated from the European subset of GTEx donors (fig. S29). The analyses were performed for all pairwise combinations of 87 phenotypes and 49 tissues and are summarized using an approach that accounts for similarity between tissues and variable standard errors of the QTL effect estimates, driven mainly by tissue sample size (fig. S27 and tables S4 and S11) (*11*).

To analyze the mediating role of cis-regulation of gene expression on complex traits (*35*, *42*), we used two complementary approaches, QTLEnrich (*43*) and stratified LD score regression (S-LDSC) (*11*, *44*). To rule out the possibility that enrichment is driven by specific features of cis-QTLs such as allele frequency, distance to the transcription start site, or local level of LD [number of LD proxy variants; coefficient of determination (R^2) ≥ 0.5], we used QTLEnrich. We found a 1.46-fold (SE = 0.006) and 1.56-fold (SE = 0.007) enrichment of trait associations among best cis-eQTLs and cis-sQTLs, respectively, adjusting for enrichment among matched null variants (Fig. 5A and table S7). The fact that these enrichment estimates differ little from those derived from the GWAS catalog overlap (above), even after accounting for the potential confounders, indicates how relatively robust these estimates are. Next, we used S-LDSC, adjusting for functional annotations (*44*), to confirm the robustness of these results and to analyze how GWAS enrichment is affected by the causal eVariant or sVariant being typically unknown (*11*). We computed the heritability enrichment of all cis-QTLs, fine-mapped cis-QTLs (in 95% credible set and posterior probability > 0.01 from dap-g), and fine-mapped cis-QTLs with maximum posterior inclusion probability as continuous annotation (*45*) (Fig. 5A). The largest increase in GWAS enrichment was for likely causal cis-QTL variants [11.1-fold (SE = 1.2) for cis-eQTLs and 14.2-fold (SE = 2.4) for cis-sQTLs, for the continuous annotation], which is strong evidence of shared causal effects of cis-QTLs and GWAS, and for the importance of fine-mapping.

Joint enrichment analysis of cis-eQTLs and cis-sQTLs shows an independent contribution to complex trait variation from both (fig. S28) (*11*), consistent with their limited overlap (fig. S22). The relative GWAS enrichments of cis-sQTLs and cis-eQTLs were similar (Fig. 5A; not significant for the robust QTLEnrich and LDSC analyses), but the larger number of cis-eQTLs discovered (Fig. 2) suggests a greater aggregated contribution of cis-eQTLs.

While these enrichment methods are powerful for genome-wide estimation of the QTL contribution to GWAS signals, they are not informative of regulatory mechanisms in individual loci. Thus, to provide functional interpretation of the 5385 significant GWAS associations in 1167 loci from approximately independent LD blocks (*46*) across the 87 complex traits, we performed colocalization with ENLOC (*32*) to quantify the probability that the cis-QTL and GWAS signals share the same causal variant. We also assessed the association between the genetically regulated component of expression or splicing and complex traits with PrediXcan (*11*, *41*, *47*). Both methods take multiple independent cis-QTLs into account, which is critical in large cis-eQTL studies with widespread allelic heterogeneity, such as GTEx. Of the 5385 GWAS loci, 43 and 23% were colocalized with a cis-eQTL and cis-sQTL, respectively (Fig. 5B). A large proportion of colocalized genes coincide with significant PrediXcan trait associations with predicted expression or splicing (median of 86 and 88% across phenotypes, respectively) (figs. S30 to S33 and tables S8 and S15), with the full resource available in (*41*). While colocalization does not prove a causal role of a QTL in any given locus nor a genome-wide proportion of GWAS loci driven by eQTLs, these results do suggest target genes and their potential molecular changes for thousands of GWAS loci, sometimes including both cis and trans targets (fig. S34).

Having multiple independent cis-eQTLs for a large number of genes allowed us to test whether mediated effects of primary and secondary cis-eQTLs on phenotypes—the ratio of GWAS and cis-eQTL effect sizes—are concordant. To ensure that concordance is not driven by residual LD between primary and secondary signals, we used LD-matched cis-eGenes with low colocalization probability as controls (*11*, *41*) and observed a significant increase in primary and secondary cis-eQTL concordance for colocalized genes (correlated t test $P < 10^{-30}$) (Fig. 5C). Additionally, colocalization of a cis-eQTL increased the colocalization of an independent cis-sQTL in the same locus (OR = 4.27, Fisher's exact test $P < 10^{-16}$) and, correspondingly, colocalization of a cis-sQTL increased cis-eQTL colocalization (OR = 4.54, Fisher's exact test $P < 10^{-16}$) (figs. S35 and S36). These observations indicate that multiple regulatory effects for the same gene often mediate the same complex trait associations. Furthermore, genes with suggestive rare variant trait associations in the UK Biobank (*48*) have a substantially increased proportion of colocalized eQTLs for the same trait (Fig. 5D and fig. S37), showing concordant trait effects from rare coding and common regulatory variants (*49*). These genes, as well as those with multiple colocalizing cis-QTLs, represent bona fide disease genes with multiple independent lines of evidence.

The growing number of genome and phenome studies has revealed extensive pleiotropy, where the same variant or locus associates with multiple organismal phenotypes (*50*). We sought to analyze how this phenomenon can be driven by gene regulatory effects. First, we calculated the number of cis-eGenes of each fine-mapped and LD-pruned cis-eVariant per tissue at local false sign rate (LFSR) < 5%, with cross-tissue smoothing of effect sizes with *mashr* (*11*, *51*). We observed that a median of 57% of variants were associated with more than one gene per tissue, typically co-occurring across tissues, indicating widespread regulatory pleiotropy. Using a binary classification of cis-eVariants with regulatory pleiotropy defined

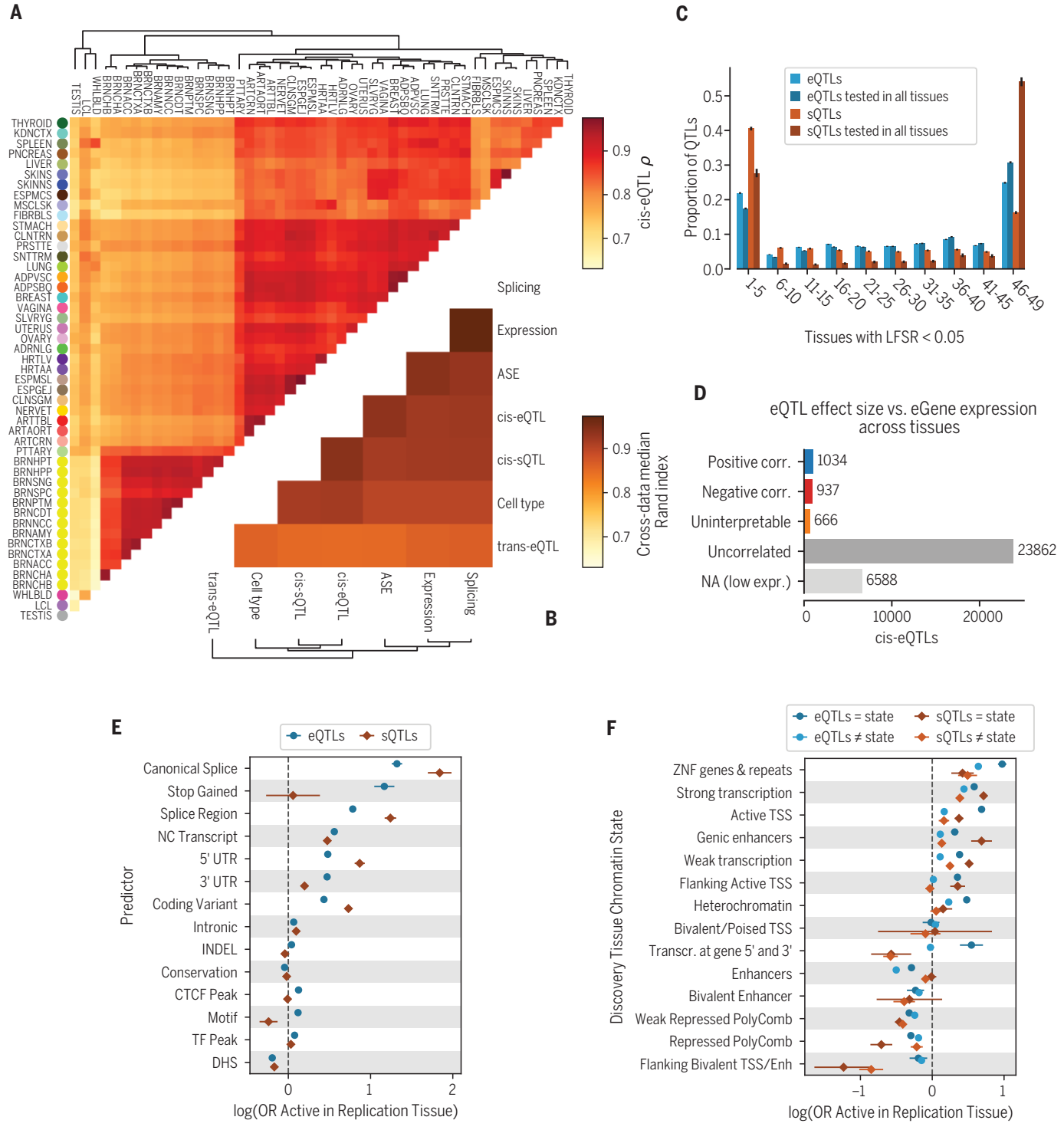

Fig. 6. Tissue specificity of cis-QTLs. (**A**) Tissue clustering with pairwise Spearman correlation of cis-eQTL effect sizes. (**B**) Similarity of tissue clustering across core data types quantified using median pairwise Rand index calculated across tissues. (**C**) Tissue activity of cis expression and splicing QTLs, where an eQTL was considered active in a tissue if it had a *mashr* local false sign rate (LFSR, equivalent to FDR) of <5%. This is shown for all cis-QTLs and only those that could be tested in all 49 tissues (red and blue). (**D**) Spearman correlation (corr.) between cis-eQTL effect size and eGene expression level across tissues. cis-eQTL counts are shown for those not tested owing to low expression (low expr.) level; tested but without significant (FDR < 5%) correlation (uncorrelated); a significant correlation, but effect sizes crossed zero, which made the correlation direction unclear (uninterpretable); positively correlated; and negatively correlated. (**E** and **F**) The effect of genomic function on cis-QTL tissue sharing modeled using logistic regression with functional annotations (E) and chromatin state (F). CTCF peak, motif, TF peak, and DHS (DNase I hypersensitive site) indicate whether the cis-QTL lies in a region annotated as having one of these features in any of the Ensembl Regulatory Build tissues. For chromatin states, model coefficients are shown for the discovery and replication tissues that have the same or different chromatin states. INDEL, insertion or deletion; ZNF, zinc finger; TSS, transcription start site; Transcr., transcription; Enh, enhancers.

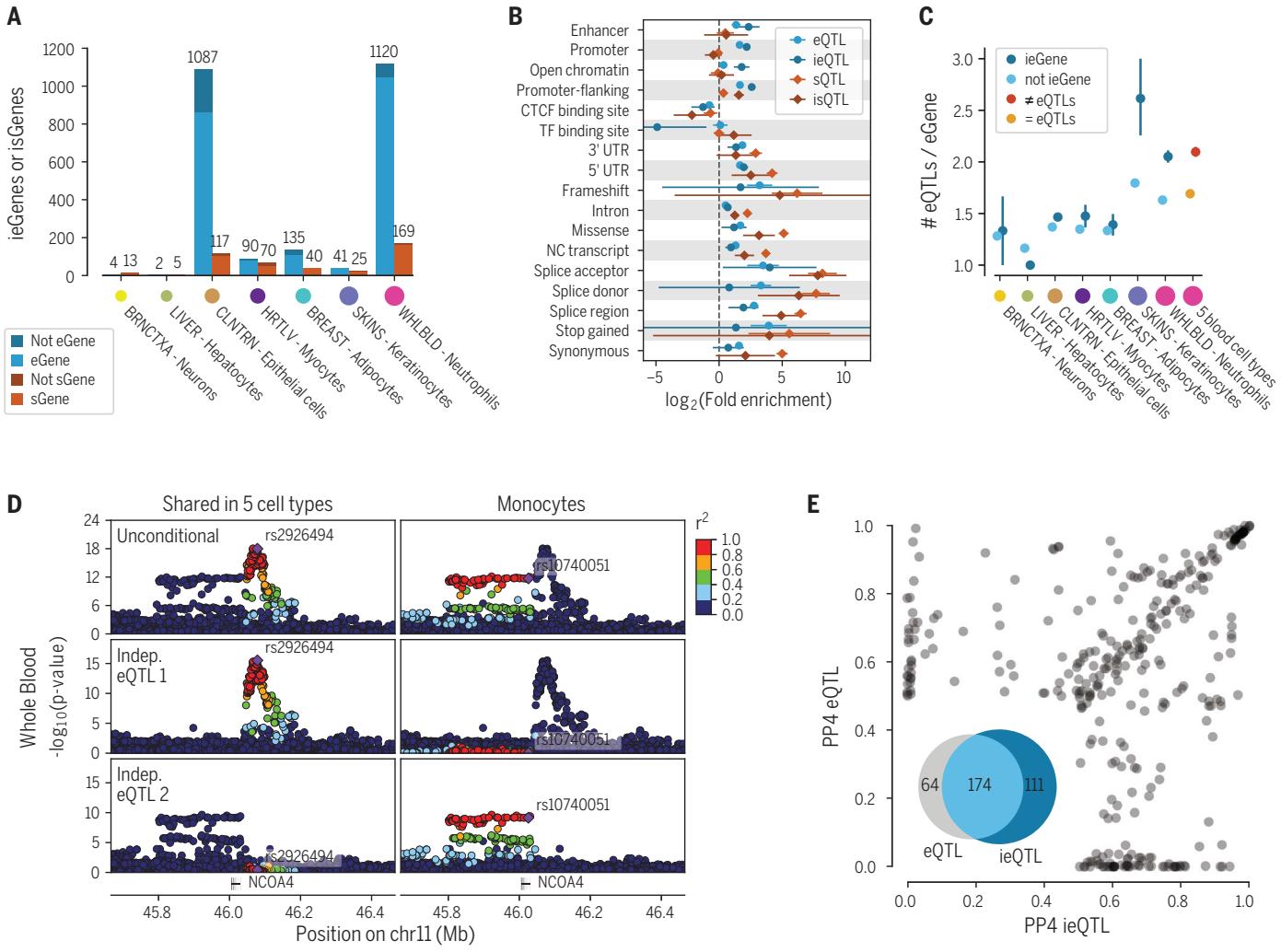

Fig. 7. Cell type interaction cis-eQTLs and cis-sQTLs. (**A**) Number of cell type interaction cis-eQTLs and cis-sQTLs (ieQTLs and isQTLs, respectively) discovered in seven tissue–cell type pairs, with shading indicating whether the ieGene or isGene was discovered by cis-eQTL or cis-sQTL analysis in bulk tissue. Colored dots are proportional to sample size. (**B**) Functional enrichment of neutrophil ieQTLs and isQTLs compared with cis-eQTLs and cis-sQTLs from whole blood. (**C**) Proportion of conditionally independent cis-eQTLs per eGene, for eGenes that do or do not have ieQTLs in GTEx, and for eGenes that have shared (=eQTLs) or nonshared (≠eQTLs) cis-eQTLs across five sorted blood cell types. (**D**) Whole blood cis-eQTL *P* value landscape for *NCOA4*, for the standard analysis (unconditional; top row) and for two independent cis-eQTLs (bottom rows). In a dataset of five sorted cell types (*56*), analyses of all cell types yielded a lead eVariant, rs2926494 (left), which is in high LD with the first independent cis-eQTL but not the second. The lead variant in monocyte cis-eQTL analysis, rs10740051, is in high LD with the second conditional cis-eQTL, indicating that this cis-eQTL is active specifically in monocytes. Thus, the full GTEx whole blood cis-eQTL pattern and allelic heterogeneity is composed of cis-eQTLs that are active in different cell types. (**E**) COLOC posterior probability (PP4) of GWAS colocalization with whole blood ieQTLs and eQTLs of the same eGene. Three hundred forty-nine gene-trait combinations across 132 genes and 36 GWAS traits showed evidence of colocalization (PP4 > 0.5) with an ieQTL and/or eQTL.

as those associated with more than one gene, we observed that they are more significantly associated with complex traits compared with matched cis-eVariants (fig. S38). This could be due to the fact that if a variant regulates multiple genes, there is a higher probability that at least one of them affects a GWAS phenotype.

However, cis-eVariants with regulatory pleiotropy also have higher GWAS complex trait pleiotropy (*50*) than cis-eVariants with effects on a single gene (Fig. 5E). This observation suggests a mechanism for complex trait pleiotropy of genetic effects where the expression of multiple genes in cis, rather than a single eGene effect, translates into diverse downstream physiological effects. Furthermore, GWAS pleiotropy is higher for tissue-shared (*41*) than tissue-specific cis-eQTLs, indicating that regulatory effects affecting multiple tissues are more likely to translate to diverse physiological traits (Fig. 5E).

Tissue specificity of genetic regulatory effects

The GTEx data provide an opportunity to study patterns and mechanisms of tissue specificity of the transcriptome and its genetic regulation. Pairwise similarity of GTEx tissues was quantified from gene expression and splicing, as well as allelic expression, eQTLs in cis and trans, and cis-sQTLs (Fig. 6A and fig. S41) (*11*). These estimates show consistent patterns of tissue relatedness, indicating that the biological processes that drive transcriptome similarity also control tissue sharing of genetic effects (Fig. 6B). As seen in earlier versions of the GTEx data (*9*, *10*), the brain regions form a separate cluster, and testis, lymphoblastoid cell lines, whole blood, and sometimes liver tend to be

outliers, while most other organs have a notably high degree of similarity to each other. This indicates that blood is not an ideal proxy for most tissues and that some other relatively accessible tissues, such as skin, may better capture molecular effects in other tissues.

The overall tissue specificity of QTLs (*11*) follows a U-shaped curve, recapitulating previous GTEx analyses (*9*, *10*), where genetic regulatory effects tend to be either highly tissue specific or highly shared (Fig. 6C), with trans-eQTLs being more tissue specific than cis-eQTLs (fig. S40). Cis-sQTLs appear to be significantly more tissue specific than cis-eQTLs when considering all mapped cis-QTLs, but this pattern is reversed when considering only those cis-QTLs where the gene or splicing event is quantified in all tissues (Fig. 6C and fig. S39). These observations indicate that splicing measures are more tissue specific than gene expression, but genetic effects on splicing tend to be more highly shared, which is consistent with pairwise tissue-sharing patterns (fig. S41). These opposite patterns are important for understanding effects that disease-causing splicing variants may have across tissues and for validation of splicing effects in cell lines that rarely are an exact match to cells in vivo.

Next, we analyzed the sharing of AE across multiple tissues of an individual, which is a metric of sharing of any heterozygous regulatory variant effects in that individual. Variation in AE has been useful for analysis of rare, potentially disease-causing variants (*52*). Using a clustering approach (*11*), we found that in 97.4% of the cases, AE across all tissues forms a single cluster. This suggests that in AE analysis, different tissues are often relatively good proxies for one another, provided that the gene of interest is expressed in the probed tissue (fig. S42).

We next computed the cross-tissue correlation of eQTL effect size and eGene expression level—often a proxy for gene functionality—and discovered that 1971 cis-eQTLs (7.4%; FDR 5%) had a significant and robust correlation between eGene expression and cis-eQTL effect size across tissues (Fig. 6D and fig. S43). These correlated cis-eQTLs are split nearly evenly between negative (937) and positive (1034) correlations. Thus, the tissues with the highest cis-eQTL effect sizes are equally likely to be among tissues with higher or lower expression levels for the gene. Trans-eQTLs show a different pattern, typically being observed in tissues with high expression of the trans-eGene relative to other tissues (fig. S43).

These observations raise the question of how to prioritize the relevant tissues for eQTLs in a disease context. To address this, we chose a subset of GWAS traits with a strong prior indication for the likely relevant tissue(s) (table S12). Analyzing colocalized cis-eQTLs for 1778 GWAS loci (*11*), we discovered that the relevant tissues were significantly enriched in having high expression and effect sizes (paired Wilcoxon sign test $P < 1.5 \times 10^{-4}$), but the relatively weak signal indicates that pinpointing the likely relevant tissue for GWAS loci is challenging (figs. S44 and S45 and table S9). These results indicate that both effect sizes and gene expression levels are important for interpreting the tissue context where an eQTL may have downstream phenotypic effects.

The diverse patterns of QTL tissue specificity raise the question of what molecular mechanisms underlie the ubiquitous regulatory effects of some genetic variants and the highly tissue-specific effects of others. To gain insight into this question, we modeled cis-eQTL and cis-sQTL tissue specificity using logistic regression as a function of the lead eVariant's genomic and epigenomic context (*11*). Cis-QTLs where the top eVariant was in a transcribed region had overall higher sharing than those in classical transcriptional regulatory elements, indicating that genetic variants with post- or cotranscriptional expression or splicing effects have more ubiquitous effects (Fig. 6E). Canonical splice and stop-gained variant effects had the highest probability of being shared across tissues, which may benefit disease-focused studies relying on likely gene-disrupting variants.

We also considered whether varying regulatory activity between tissues contributed to tissue specificity of genetic effects, and we found that shared chromatin states between the discovery and query tissues were associated with increased probability of cis-eQTL sharing and vice versa (Fig. 6F). cis-eQTLs and cis-sQTLs followed similar patterns. Because cis-sQTLs are more enriched in transcribed regions and likely arise via posttranscriptional mechanisms (Fig. 4A), this is likely to contribute to their higher overall degree of tissue sharing (Fig. 6C). In comparison to cis-eQTLs, cis-sQTLs are more often located in regions where regulatory effects are shared.

These data indicate a possible means by which we can predict whether a cis-eQTL observed in a GTEx tissue is active in another tissue of interest, using the variant's annotation and properties in the discovery tissue (*11*). After incorporating additional features including cis-QTL effect size, distance to transcription start site, and eGene and sGene expression levels, we obtain reasonably good predictions of whether a cis-QTL is active in a query tissue (median area under the curve = 0.779 and 0.807, minimum = 0.703 and 0.721, maximum = 0.807 and 0.875 for cis-eQTLs and cis-sQTLs, respectively) (fig. S46). These results suggest that it is possible to extrapolate the GTEx cis-eQTL catalog to additional tissues and potentially developmental stages, where population-scale data for QTL analysis are particularly difficult to collect.

From tissues to cell types

The GTEx tissue samples consist of heterogeneous mixtures of multiple cell types. Hence, the RNA extracted and QTLs mapped from these samples reflect a composite of genetic effects that may vary across cell types and may mask cell type–specific mechanisms. To characterize the effect of cell type heterogeneity on analyses from bulk tissue, we used the xCell method (*53*) to estimate the enrichment of 64 reference cell types from the bulk expression profile of each sample (*11*). Although these results need to be interpreted with caution given the scarcity of validation data (*54*), the resulting enrichment scores were generally biologically meaningful with, for example, myocytes enriched in heart left ventricle and skeletal muscle; hepatocytes enriched in liver; and various blood cell types enriched in whole blood, spleen, and lung, which harbors a large leukocyte population (fig. S47). Interestingly, the pairwise relatedness of GTEx tissues derived from their cell type composition is highly correlated with tissue sharing of regulatory variants (cis-eQTL versus cell type composition Rand index = 0.92) (Fig. 6B and figs. S48 and S41), suggesting that similarity of regulatory variant activity between tissue pairs may often be due to the presence of similar cell types and not necessarily shared regulatory networks within cells. This observation highlights the key role that characterizing cell type diversity will have for understanding not only tissue biology but genetic regulatory effects as well.

Enrichment of many cell types shows inter-individual variation within a given tissue, partially owing to tissue sampling variation between individuals. This variation can be leveraged to identify cis-eQTLs and cis-sQTLs with cell type specificity by including an interaction between genotype and cell type enrichment in the QTL model (*11*, *55*). We applied this approach to seven tissue–cell type pairs with robustly quantified cell types in the tissue where each cell type was most enriched (Fig. 7A) [an additional 36 pairs are described in (*54*)]. The largest numbers of cell type interaction cis-eQTLs and cis-sQTLs (ieQTLs and isQTLs, respectively) were 1120 neutrophil ieQTLs and 169 isQTLs in whole blood and 1087 epithelial cell ieQTLs and 117 isQTLs in transverse colon (Fig. 7A). Of these ieQTLs, 76 and 229, respectively, corresponded to an eGene for which no QTL was detected in bulk tissue.

We validated these effects using published eQTLs from purified blood cell types (*56*), where neutrophil eQTLs had higher neutrophil ieQTL effect sizes than eQTLs from other blood cell types (fig. S49). For other cell types, external replication data was not available. Thus, we verified the robustness of the ieQTLs by the allelic expression validation approach that was used for sex- and population-biased

cis-eQTL analyses: For ieQTL heterozygotes, we calculated the Spearman correlation between cell type enrichment and ieQTL effect size from AE data and observed a high validation rate (*54*). Note that ieQTLs and isQTLs should not be considered cell type–specific QTLs, because the enrichment of any cell type may be (anti)correlated with other cell types (fig. S50). While full deconvolution of cis-eQTL effects driven by specific cell types remains a challenge for the future, ieQTLs and isQTLs can be interpreted as being enriched for cell type–specific effects.

In most subsequent analyses to characterize the properties of ieQTLs and isQTLs, we focused on neutrophil ieQTLs, which are numerous and supported by external replication data. Functional enrichment analyses of these QTLs show that they largely follow the enrichment patterns observed for bulk tissue cis-QTLs (Fig. 7B). However, ieQTLs are more strongly enriched in promoter-flanking regions and enhancers, which are known to be major drivers of cell type–specific regulatory effects (*2*). Epithelial cell ieQTLs yielded similar patterns (fig. S51).

We hypothesized that the widespread allelic heterogeneity observed in the bulk tissue cis-eQTL data could be partially driven by an aggregate signal from cis-eQTLs that are each active in a different cell type present in the tissue. Indeed, the number of cis-eQTLs per gene is higher for ieGenes than for standard eGenes, especially in skin and blood (Fig. 7C). While differences in power could contribute to this pattern, it is corroborated by eGenes that have independent cis-eQTLs ($R^2 < 0.05$) in five purified blood cell types (*56*) also showing an increased amount of allelic heterogeneity in GTEx whole blood (Fig. 7, C and D). Thus, quantifying cell type specificity can provide mechanistic insights into the genetic architecture of gene expression and may be leveraged to improve the resolution of complex patterns of allelic heterogeneity wherein we can distinguish effects manifesting in different cell types.

Next, we analyzed how cell type interaction cis-QTLs contribute to the interpretation of regulatory variants underlying complex disease risk. GWAS colocalization analysis of neutrophil ieQTLs (*11*) revealed multiple loci (111, ~32%) that colocalize only with ieQTLs and not with whole blood cis-eQTLs (Fig. 7E), although 75% (42 of 56) of the corresponding eGenes have both cis-eQTLs and ieQTLs. Improved resolution into allelic heterogeneity appears to contribute to colocalization exclusively with eQTLs. For example, the absence of colocalization between a platelet count GWAS signal and bulk tissue cis-eQTL for *SPAG7* appears to be due to the whole blood signal being an aggregate of multiple independent signals (fig. S52). The neutrophil ieQTL analysis uncovers a specific signal that mirrors the GWAS association, suggesting that platelet counts are affected by *SPAG7* expression only in one or several specific cell types. Thus, in addition to previously undetected colocalizations pinpointing potential causal genes, ieQTL analysis has the potential to provide insights into cell type–specific mechanisms of complex traits.

Outlook

The GTEx v8 data release represents a deep survey of both intra- and interindividual transcriptome variation across a large number of tissues. With 838 donors and 15,201 samples—approximately twice the size of the v6 release used in the previous set of GTEx Consortium papers—we have created a comprehensive resource of genetic variants that influence gene expression and splicing in cis. This substantially expands and updates the GTEx catalog of sQTLs, doubles the number of eGenes per tissue, and saturates the discovery of eQTLs with greater than twofold effect sizes in ~40 tissues. The fine-mapping data of GTEx cis-eQTLs provide a set of thousands of likely causal functional variants. While trans-QTL discovery and the characterization of sex- and population-specific genetic effects are still limited by sample size, analyses of the v8 data provide important insights into each.

Cell type interaction cis-eQTLs and cis-sQTLs, mapped with computational estimates of cell type enrichment, constitute an important extension of the GTEx resource to effects of cell types within tissues. The highly similar tissue-sharing patterns across these data types suggest shared biology from cell type composition to transcriptome variation and genetic regulatory effects. Our results indicate that shared cell types between tissues may be a key factor behind tissue sharing of genetic regulatory effects, which will constitute a key challenge to tackle in the future. Finally, GWAS colocalization with cis-eQTLs and cis-sQTLs provides rich opportunities for further functional follow-up and characterization of regulatory mechanisms of GWAS associations.

Given the very large number of cis-eQTLs, the extensive allelic heterogeneity—multiple independent regulatory variants affecting the same gene—is unsurprising. With well-powered cis-QTL mapping, it becomes possible and important to describe and disentangle these effects; the assumption of a single causal variant in a cis-eQTL locus no longer holds true for datasets of this scale. Similarly, we highlight cis-eQTL and cis-sQTL effects on the same gene, typically driven by distinct causal variants (*4*, *35*). The joint complex trait contribution of independent cis-eQTLs and cis-sQTLs and that of cis-eQTLs and rare coding variants for the same gene highlights how different genetic variants and functional perturbations can converge at the gene level to similar physiological effect. This orthogonal evidence pinpoints highly likely causal disease genes, and these associations could be leveraged to build allelic series, a powerful tool for estimating dosage-risk relationship for the purposes of drug development (*57*).

Finally, we provide mechanistic insights into the cellular causes of allelic heterogeneity, showing the separate contributions from cis-eQTLs active in different cell types to the combined signal seen in a bulk tissue sample. With evidence that this increased cellular resolution improves colocalization in some loci, cell type–specific analyses appear particularly promising for finer dissection of genetic association data.

Integration of GTEx QTL data and functional annotation of the genome provides powerful insights into the molecular mechanisms of transcriptional and posttranscriptional regulation that affect gene expression levels and splicing. A large proportion of cis-eQTL effects are driven by genetic perturbations in classical regulatory elements of promoters and enhancers. However, the magnitude of these enrichments is perhaps unexpectedly modest, which likely reflects the fact that only a small fraction of variants in these large regions have true regulatory effects, leading to a lower resolution of annotating functional variants compared with the nucleotide-level annotation of, for example, nonsense or canonical splice site variants. Context-specific genetic effects of tissue-specific and cell type interaction cis-eQTLs are enriched in enhancers and related elements and their variable activity across tissues and cell types.

While cis-eQTLs are enriched for a wide range of functional regions, the vast majority of cis-sQTL are located in transcribed regions, with likely cotranscriptional and/or posttranscriptional regulatory effects. Interestingly, these appear to be less tissue specific, which likely contributes to the higher tissue sharing of cis-sQTLs than cis-eQTLs. The higher tissue sharing of all cotranscriptional or posttranscriptional regulatory effects may facilitate interpretation of potentially disease-related functional effects of (rare) coding variants triggering nonsense-mediated decay or splicing changes, even when the disease-relevant tissues are not available.

About a third of the observed trans-eQTLs are mediated by cis-eQTLs, demonstrating how local genetic regulatory effects can translate to effects at the level of cellular pathways. All types of QTLs that were studied are strong mediators of genetic associations to complex traits, with a higher relative enrichment for cis-sQTLs than cis-eQTLs and with trans-eQTLs having the highest enrichment of all (*35*). With large genome- and phenome-wide studies having uncovered extensive pleiotropy of complex trait associations, the GTEx data provide important

insights into the molecular underpinnings of this observed pleiotropy: Variants that affect the expression of multiple genes and multiple tissues have a higher degree of complex trait pleiotropy, indicating that some of the pleiotropy arises at the proximal regulatory level. Dissecting this complexity and pinpointing truly causal molecular effects that mediate specific phenotype associations will be a considerable challenge for the future.

This study of the GTEx v8 data has provided insights into genetic regulatory architecture and functional mechanisms. The catalog of QTLs and associated datasets of annotations, cell type enrichments, and GWAS summary statistics requires careful interpretation but provides insights into the biology of gene regulation and functional mechanisms of complex traits. We demonstrate how QTL data can be used to inform on multiple aspects of GWAS interpretation: potential causal variants from fine-mapping, proximal regulatory mechanisms, target genes in cis, and pathway effects in trans, in the context of multiple tissues and cell types. However, our understanding of genetic effects on cellular phenotypes is far from complete. We envision that further investigation into genetic regulatory effects in specific cell types, study of additional tissues and developmental time points not covered by GTEx, incorporation of a diverse set of molecular phenotypes, and continued investment in increasing sample sizes from diverse populations will continue to provide transformative scientific discoveries.

REFERENCES AND NOTES

1. ENCODE Project Consortium, *Nature* **489**, 57–74 (2012).
2. A. Kundaje *et al*., *Nature* **518**, 317–330 (2015).
3. A. Battle *et al*., *Genome Res.* **24**, 14–24 (2014).
4. T. Lappalainen *et al*., *Nature* **501**, 506–511 (2013).
5. M. J. Bonder *et al*., *Nat. Genet.* **49**, 131–138 (2017).
6. J. Lonsdale *et al*., *Nat. Genet.* **45**, 580–585 (2013).
7. L. J. Carithers *et al*., *Biopreserv. Biobank.* **13**, 311–319 (2015).
8. L. A. Siminoff, M. Wilson-Genderson, H. M. Gardiner, M. Mosavel, K. L. Barker, *Biopreserv. Biobank.* **16**, 200–206 (2018).
9. GTEx Consortium, *Science* **348**, 648–660 (2015).
10. GTEx Consortium, *Nature* **550**, 204–213 (2017).
11. See supplementary materials.
12. O. M. de Goede *et al.*, bioRxiv 793091 [Preprint]. 4 October 2019. https://doi.org/10.1101/793091.
13. Y. I. Li *et al*., *Nat. Genet.* **50**, 151–158 (2018).
14. R. Jansen *et al*., *Hum. Mol. Genet.* **26**, 1444–1451 (2017).
15. F. Hormozdiari *et al*., *Am. J. Hum. Genet.* **100**, 789–802 (2017).
16. A. Saha, A. Battle, *F1000Res.* **7**, 1860 (2018).
17. S. E. Castel *et al*., *Genome Biol.* 10.1186/s13059-020-02122-z (2020).
18. E. A. Khramtsova, L. K. Davis, B. E. Stranger, *Nat. Rev. Genet.* **20**, 173–190 (2019).
19. B. E. Stranger *et al*., *PLOS Genet.* **8**, e1002639 (2012).
20. T. Raj *et al*., *Science* **344**, 519–523 (2014).
21. P. Mohammadi, S. E. Castel, A. A. Brown, T. Lappalainen, *Genome Res.* **27**, 1872–1884 (2017).
22. M. Oliva *et al*., *Science* **369**, eaba3066 (2020).
23. T. Sun *et al*., *Carcinogenesis* **25**, 2225–2230 (2004).
24. A. Ewart-Toland *et al*., *Carcinogenesis* **26**, 1368–1373 (2005).
25. Y. Ruan *et al*., *J. Pathol.* **225**, 535–543 (2011).
26. H. M. Koh *et al*., *J. Pathol. Transl. Med.* **51**, 32–39 (2017).
27. K. Dhanasekaran *et al*., *FASEB J.* **33**, 219–230 (2019).
28. S. Girardeau-Hubert *et al*., *Sci. Rep.* **9**, 7456 (2019).
29. L. Yin *et al*., *Exp. Dermatol.* **23**, 731–735 (2014).
30. A. A. Brown *et al*., *Nat. Genet.* **49**, 1747–1751 (2017).
31. F. Hormozdiari, E. Kostem, E. Y. Kang, B. Pasaniuc, E. Eskin, *Genetics* **198**, 497–508 (2014).
32. X. Wen, R. Pique-Regi, F. Luca, *PLOS Genet.* **13**, e1006646 (2017).
33. R. Tewhey *et al*., *Cell* **165**, 1519–1529 (2016).
34. J. van Arensbergen *et al*., *Nat. Genet.* **51**, 1160–1169 (2019).
35. Y. I. Li *et al*., *Science* **352**, 600–604 (2016).
36. O. Delaneau *et al*., *Science* **364**, eaat8266 (2019).
37. K. S. Small *et al*., *Nat. Genet.* **43**, 561–564 (2011).
38. F. Yang, J. Wang, B. L. Pierce, L. S. Chen; GTEx Consortium, *Genome Res.* **27**, 1859–1871 (2017).
39. H.-J. Westra *et al*., *Nat. Genet.* **45**, 1238–1243 (2013).
40. B. Liu, M. J. Gloudemans, A. S. Rao, E. Ingelsson, S. B. Montgomery, *Nat. Genet.* **51**, 768–769 (2019).
41. A. N. Barbeira *et al.*, bioRxiv 814350 [Preprint]. 23 May 2020. https://doi.org/10.1101/814350.
42. D. L. Nicolae *et al*., *PLOS Genet.* **6**, e1000888 (2010).20369019
43. E. R. Gamazon *et al*., *Nat. Genet.* **50**, 956–967 (2018).
44. H. K. Finucane *et al*., *Nat. Genet.* **47**, 1228–1235 (2015).
45. F. Hormozdiari *et al*., *Nat. Genet.* **50**, 1041–1047 (2018).
46. T. Berisa, J. K. Pickrell, *Bioinformatics* **32**, 283–285 (2016).
47. E. R. Gamazon *et al*., *Nat. Genet.* **47**, 1091–1098 (2015).
48. E. T. Cirulli *et al*., *Nat. Commun.* **11**, 542 (2020).
49. N. M. Ferraro *et al*., *Science* **369**, eaaz5900 (2020).
50. D. M. Jordan, M. Verbanck, R. Do, *Genome Biol.* **20**, 222–18 (2019).
51. S. M. Urbut, G. Wang, P. Carbonetto, M. Stephens, *Nat. Genet.* **51**, 187–195 (2019).
52. P. Mohammadi *et al*., *Science* **366**, 351–356 (2019).
53. D. Aran, Z. Hu, A. J. Butte, *Genome Biol.* **18**, 220 (2017).
54. S. Kim-Hellmuth *et al*., *Science* **369**, eaaz8528 (2020).
55. D. V. Zhernakova *et al*., *Nat. Genet.* **49**, 139–145 (2017).
56. J. E. Peters *et al*., *PLOS Genet.* **12**, e1005908 (2016).
57. R. M. Plenge, E. M. Scolnick, D. Altshuler, *Nat. Rev. Drug Discov.* **12**, 581–594 (2013).
58. F. Aguet, broadinstitute/gtex-pipeline: GTEx v8, Zenodo (2020); http://doi.org/10.5281/zenodo.3727189.
59. F. Aguet, broadinstitute/gtex-v8: main_figures, Zenodo (2020); http://doi.org/10.5281/zenodo.3930961.

ACKNOWLEDGMENTS

We thank the donors and their families for their generous gifts of organ donation for transplantation and tissue donations for the GTEx research project; the Genomics Platform at the Broad Institute for data generation; J. Struewing for support and leadership of the GTEx project; M. Khan and C. Stolte for the illustrations in Fig. 1; and R. Do, D. Jordan, and M. Verbanck for providing GWAS pleiotropy scores. **Funding:** This work was supported by the Common Fund of the Office of the Director, U.S. National Institutes of Health, and by NCI, NHGRI, NHLBI, NIDA, NIMH, NIA, NIAID, and NINDS through NIH contracts HHSN261200800001E (Leidos Prime contract with NCI: A.M.S., D.E.T., N.V.R., J.A.M., L.S., M.E.B., L.Q., T.K., D.B., K.R., and A.U.), 10XS170 (NDRI: W.F.L., J.A.T., G.K., A.M., S.S., R.H., G.Wa., M.J., M.Wa., L.E.B., C.J., J.W., B.R., M.Hu., K.M., L.A.S., H.M.G., M.Mo., and L.K.B.), 10XS171 (Roswell Park Cancer Institute: B.A.F., M.T.M., E.K., B.M.G., K.D.R., and J.B.), 10X172 (Science Care Inc.), 12ST1039 (IDOX), 10ST1035 (Van Andel Institute: S.D.J., D.C.R., and D.R.V.), HHSN268201000029C (Broad Institute: F.A., G.G., K.G.A., A.V.S., X.Li., E.T., S.G., A.G., S.A., K.H.H., D.T.N., K.H., S.R.M., and J.L.N.), 5U41HG009494 (F.A., G.G., and K.G.A.), and through NIH grants R01 DA006227-17 (University of Miami Brain Bank: D.C.M. and D.A.D.), Supplement to University of Miami grant DA006227 (D.C.M. and D.A.D.), R01 MH090941 (University of Geneva), R01 MH090951 and R01 MH090937 (University of Chicago), R01 MH090936 (University of North Carolina–Chapel Hill), R01MH101814 (M.M.-A., V.W., S.B.M., R.G., E.T.D., D.G.-M., and A.V.), U01HG007593 (S.B.M.), R01MH101822 (C.D.B.), U01HG007598 (M.O. and B.E.S.), U01MH104393 (A.P.F.), extension H002371 to 5U41HG002371 (W.J.K.), as well as other funding sources: R01MH106842 (T.L., P.M., E.F., and P.J.H.), R01HL142028 (T.L., Si.Ka., and P.J.H.), R01GM122924 (T.L. and S.E.C.), R01MH107666 (H.K.I.), P30DK020595 (H.K.I.), UM1HG008901 (T.L.), R01GM124486 (T.L.), R01HG010067 (Y.Pa.), R01HG002585 (G.Wa. and M.St.), Gordon and Betty Moore Foundation GBMF 4559 (G.Wa. and M.St.), 1K99HG009916-01 (S.E.C.), R01HG006855 (Se.Ka. and R.E.H.), BIO2015-70777-P, Ministerio de Economia y Competitividad and FEDER funds (M.M.-A., V.W., R.G., and D.G.-M.), la Caixa Foundation ID 100010434 under agreement LCF/BQ/SO15/52260001 (D.G.-M.), NIH CTSA grant UL1TR002550-01 (P.M.), Marie-Skłodowska Curie fellowship H2020 Grant 706636 (S.K.-H.), R35HG010718 (E.R.G.), FPU15/03635, Ministerio de Educación, Cultura y Deporte (M.M.-A.), R01MH109905, 1R01HG010480 (A.Ba.), Searle Scholar Program (A.Ba.), R01HG008150 (S.B.M.), 5T32HG000044-22, NHGRI Institutional Training Grant in Genome Science (N.R.G.), EU IMI program (UE7-DIRECT-115317-1) (E.T.D. and A.V.), FNS funded project RNA1 (31003A_149984) (E.T.D. and A.V.), DK110919 (F.H.), F32HG009987 (F.H.), Massachusetts Lions Eye Research Fund Grant (A.R.H.), Wellcome grant WT108749/Z/15/Z (P.F.), and European Molecular Biology Laboratory (P.F. and D.Z.). **Author contributions:** See section 17 of the supplementary materials. **Competing interests:** F.A. is an inventor on a patent application related to TensorQTL. S.E.C. is a cofounder, chief technology officer, and stock owner at Variant Bio. E.R.G. is on the editorial board of Circulation Research and does consulting for the City of Hope/Beckman Research Institute. E.T.D. is chairman and member of the board of Hybridstat Ltd. B.E.E. is on the scientific advisory boards of Celsius Therapeutics and Freenome. G.G. receives research funds from IBM and Pharmacyclics and is an inventor on patent applications related to MuTect, ABSOLUTE, MutSig, MSMuTect, MSMutSig, POLYSOLVER, and TensorQTL. G.G. is a founder of consultant to, and holds privately held equity in Scorpion Therapeutics. S.B.M. is on the scientific advisory board of MyOme. D.G.M. is a cofounder with equity in Goldfinch Bio and has received research support from AbbVie, Astellas, Biogen, BioMarin, Eisai, Merck, Pfizer, and Sanofi-Genzyme. H.K.I. has received speaker honoraria from GSK and AbbVie. T.L. is a scientific advisory board member of Variant Bio with equity and Goldfinch Bio. P.F. is member of the scientific advisory boards of Fabric Genomics, Inc., and Eagle Genomes, Ltd. P.G.F. is a partner of Bioinf2Bio. **Data and materials availability:** All GTEx protected data are available through the database of Genotypes and Phenotypes (dbGaP) (accession no. phs000424.v8). Access to the raw sequence data is now provided through the AnVIL platform (https://gtexportal.org/home/protectedDataAccess). Public-access data, including QTL summary statistics and expression levels, are available on the GTEx Portal as downloadable files and through multiple data visualizations and browsable tables (www.gtexportal.org), as well as in the UCSC and Ensembl browsers. All components of the single-tissue cis-QTL pipeline are available at https://github.com/broadinstitute/gtex-pipeline and Zenodo (*58*), and analysis scripts are available at https://github.com/broadinstitute/gtex-v8 and Zenodo (*59*). Residual GTEx biospecimens have been banked and are available as a resource for further studies (access can be requested on the GTEx Portal at www.gtexportal.org/home/samplesPage).

Authors

Lead Analysts†: François Aguet[1]‡, Alvaro N. Barbeira[2], Rodrigo Bonazzola[2], Andrew Brown[3,4], Stephane E. Castel[5,6], Brian Jo[7,8], Silva Kasela[5,6], Sarah Kim-Hellmuth[5,6,9], Yanyu Liang[2], Meritxell Oliva[2,10], Princy Parsana[11]

Analysts†: Elise D. Flynn[5,6], Laure Fresard[12], Eric R. Gamazon[13,14,15,16], Andrew R. Hamel[17,1], Yuan He[18], Farhad Hormozdiari[19,1], Pejman Mohammadi[5,6,20,21], Manuel Muñoz-Aguirre[22,23], YoSon Park[24,25], Ashis Saha[11], Ayellet V. Segrè[1,17], Benjamin J. Strober[18], Xiaoquan Wen[26], Valentin Wucher[22]

Manuscript Working Group†: François Aguet[1], Kristin G. Ardlie[1], Alvaro N. Barbeira[2], Alexis Battle[18,11], Rodrigo Bonazzola[2], Andrew Brown[3,4], Christopher D. Brown[24], Stephane E. Castel[5,6], Nancy Cox[16], Sayantan Das[26], Emmanouil T. Dermitzakis[3,27,28], Barbara E. Engelhardt[7,8], Elise D. Flynn[5,6], Laure Fresard[12], Eric R. Gamazon[13,14,15,16], Diego Garrido-Martín[22], Nicole R. Gay[29], Gad A. Getz[1,30,31], Roderic Guigó[22,32], Andrew R. Hamel[17,1], Robert E. Handsaker[33,33,35], Yuan He[18], Paul J. Hoffman[5], Farhad Hormozdiari[19,1], Hae Kyung Im[2], Brian Jo[7,8], Silva Kasela[5,6], Seva Kashin[33,34,35], Sarah Kim-Hellmuth[5,6,9], Alan Kwong[26], Tuuli Lappalainen[5,6], Xiao Li[1], Yanyu Liang[2], Daniel G. MacArthur[34,36], Pejman Mohammadi[5,6,20,21], Stephen B. Montgomery[12,29], Manuel Muñoz-Aguirre[22,23], Meritxell Oliva[2,10], YoSon Park[24,25], Princy Parsana[11], John M. Rouhana[17,1], Ashis Saha[11], Ayellet V. Segrè[1,17], Matthew Stephens[37], Barbara E. Stranger[2,38], Benjamin J. Strober[18], Ellen Todres[1], Ana Viñuela[39,3,27,28], Gao Wang[37], Xiaoquan Wen[26], Valentin Wucher[22], Yuxin Zou[40]

Analysis Team Leaders†: François Aguet[1], Alexis Battle[18,11], Andrew Brown[3,4], Stephane E. Castel[5,6], Barbara E. Engelhardt[7,8], Farhad Hormozdiari[19,1], Hae Kyung Im[2], Sarah Kim-Hellmuth[5,6,9], Meritxell Oliva[2,10], Barbara E. Stranger[2,38], Xiaoquan Wen[26]

Senior Leadership†: Kristin G. Ardlie[1], Alexis Battle[18,11], Christopher D. Brown[24], Nancy Cox[16], Emmanouil T. Dermitzakis[3,27,28], Barbara E. Engelhardt[7,8], Gad A. Getz[1,30,31], Roderic Guigó[22,33], Hae Kyung Im[2], Tuuli Lappalainen[5,6], Stephen B. Montgomery[12,29], Barbara E. Stranger[2,38]
Manuscript Writing Group: François Aguet[1], Hae Kyung Im[2], Alexis Battle[18,11], Kristin G. Ardlie[1], Tuuli Lappalainen[5,6]

GTEx Consortium†
Laboratory and Data Analysis Coordinating Center (LDACC): François Aguet[1], Shankara Anand[1], Kristin G. Ardlie[1], Stacey Gabriel[1], Gad Getz[1,30,31], Aaron Graubert[1], Kane Hadley[1], Robert E. Handsaker[33,34,35], Katherine H. Huang[1], Seva Kashin[33,34,35], Xiao Li[1], Daniel G. MacArthur[34,36], Samuel R. Meier[1], Jared L. Nedzel[1], Duyen T. Nguyen[1], Ayellet V. Segrè[1,17], Ellen Todres[1]
Analysis Working Group Funded by GTEx Project Grants: François Aguet[1], Shankara Anand[1], Kristin G. Ardlie[1], Brunilda Balliu[41], Alvaro N. Barbeira[2], Alexis Battle[18,11], Rodrigo Bonazzola[2], Andrew Brown[3,4], Christopher D. Brown[24], Stephane E. Castel[5,6], Donald F. Conrad[42,43], Daniel J. Cotter[29], Nancy Cox[16], Sayantan Das[26], Olivia M. deGoede[29], Emmanouil T. Dermitzakis[3,27,28], Jonah Einson[44,5], Barbara E. Engelhardt[7,8], Eleazar Eskin[45], Tiffany Y. Eulalio[46], Nicole M. Ferraro[46], Elise D. Flynn[5,6], Laure Fresard[12], Eric R. Gamazon[13,14,15,16], Diego Garrido-Martín[22], Nicole R. Gay[29], Gad A. Getz[1,30,31], Michael J. Gloudemans[46], Aaron Graubert[1], Roderic Guigó[22,32], Kane Hadley[1], Andrew R. Hamel[17,1], Robert E. Handsaker[33,34,35], Yuan He[18], Paul J. Hoffman[5], Farhad Hormozdiari[19,1], Lei Hou[47,1], Katherine H. Huang[1], Hae Kyung Im[2], Brian Jo[7,8], Silva Kasela[5,6], Seva Kashin[33,34,35], Manolis Kellis[47,1], Sarah Kim-Hellmuth[5,6,9], Alan Kwong[26], Tuuli Lappalainen[5,6], Xiao Li[1], Xin Li[12], Yanyu Liang[2], Daniel G. MacArthur[34,36], Serghei Mangul[45,48], Samuel R. Meier[1], Pejman Mohammadi[5,6,20,21], Stephen B. Montgomery[12,29], Manuel Muñoz-Aguirre[22,23], Daniel C. Nachun[12], Jared L. Nedzel[1], Duyen T. Nguyen[1], Andrew B. Nobel[49], Meritxell Oliva[2,10], YoSon Park[24,25], Yongjin Park[47,1], Princy Parsana[11], Abhiram S. Rao[50], Ferran Reverter[51], John M. Rouhana[17,1], Chiara Sabatti[52], Ashis Saha[11], Ayellet V. Segrè[1,17], Andrew D. Skol[2,53], Matthew Stephens[37], Barbara E. Stranger[2,38], Benjamin J. Strober[18], Nicole A. Teran[12], Ellen Todres[1], Ana Viñuela[39,3,27,28], Gao Wang[37], Xiaoquan Wen[26], Fred Wright[54], Valentin Wucher[22], Yuxin Zou[40]
Analysis Working Group Not Funded by GTEx Project Grants: Pedro G. Ferreira[55,56,57,58], Gen Li[59], Marta Melé[60], Esti Yeger-Lotem[61,62]
Leidos Biomedical Project Management: Mary E. Barcus[63], Debra Bradbury[63], Tanya Krubit[63], Jeffrey A. McLean[63], Liqun Qi[63], Karna Robinson[63], Nancy V. Roche[63], Anna M. Smith[63], Leslie Sobin[63], David E. Tabor[63], Anita Undale[63]
Biospecimen Collection Source Sites: Jason Bridge[64], Lori E. Brigham[65], Barbara A. Foster[66], Bryan M. Gillard[66], Richard Hasz[67], Marcus Hunter[68], Christopher Johns[69], Mark Johnson[70], Ellen Karasik[66], Gene Kopen[71], William F. Leinweber[71], Alisa McDonald[71], Michael T. Moser[66], Kevin Myer[68], Kimberley D. Ramsey[66], Brian Roe[68], Saboor Shad[71], Jeffrey A. Thomas[71,70], Gary Walters[70], Michael Washington[70], Joseph Wheeler[69]
Biospecimen Core Resource: Scott D. Jewell[72], Daniel C. Rohrer[72], Dana R. Valley[72]
Brain Bank Repository: David A. Davis[73], Deborah C. Mash[73]
Pathology: Mary E. Barcus[63], Philip A. Branton[74], Leslie Sobin[63]
ELSI Study: Laura K. Barker[75], Heather M. Gardiner[75], Maghboeba Mosavel[76], Laura A. Siminoff[75]
Genome Browser Data Integration and Visualization: Paul Flicek[77], Maximilian Haeussler[78], Thomas Juettemann[77], W. James Kent[78], Christopher M. Lee[78], Conner C. Powell[78], Kate R. Rosenbloom[78], Magali Ruffier[77], Dan Sheppard[77], Kieron Taylor[77], Stephen J. Trevanion[77], Daniel R. Zerbino[77]
eGTEx Groups: Nathan S. Abell[29], Joshua Akey[79], Lin Chen[10], Kathryn Demanelis[10], Jennifer A. Doherty[80], Andrew P. Feinberg[81], Kasper D. Hansen[82], Peter F. Hickey[83], Lei Hou[47,1], Farzana Jasmine[10], Lihua Jiang[29], Rajinder Kaul[84,85], Manolis Kellis[47,1], Muhammad G. Kibriya[10], Jin Billy Li[29], Qin Li[29], Shin Lin[86], Sandra E. Linder[29], Stephen B. Montgomery[12,29], Meritxell Oliva[2,10], Yongjin Park[47,1], Brandon L. Pierce[10], Lindsay F. Rizzardi[87], Andrew D. Skol[2,53], Kevin S. Smith[12], Michael Snyder[29], John Stamatoyannopoulos[84,88], Barbara E. Stranger[2,38], Hua Tang[29], Meng Wang[29]
NIH Program Management: Philip A. Branton[74], Latarsha J. Carithers[74,89], Ping Guan[74], Susan E. Koester[90], A. Roger Little[91], Helen M. Moore[74], Concepcion R. Nierras[92], Abhi K. Rao[74], Jimmie B. Vaught[74], Simona Volpi[93]

[1]The Broad Institute of MIT and Harvard, Cambridge, MA, USA. [2]Section of Genetic Medicine, Department of Medicine, University of Chicago, Chicago, IL, USA. [3]Department of Genetic Medicine and Development, University of Geneva Medical School, Geneva, Switzerland. [4]Population Health and Genomics, University of Dundee, Dundee, Scotland, UK. [5]New York Genome Center, New York, NY, USA. [6]Department of Systems Biology, Columbia University, New York, NY, USA. [7]Department of Computer Science, Princeton University, Princeton, NJ, USA. [8]Center for Statistics and Machine Learning, Princeton University, Princeton, NJ, USA. [9]Statistical Genetics, Max Planck Institute of Psychiatry, Munich, Germany. [10]Department of Public Health Sciences, University of Chicago, Chicago, IL, USA. [11]Department of Computer Science, Johns Hopkins University, Baltimore, MD, USA. [12]Department of Pathology, Stanford University, Stanford, CA, USA. [13]Data Science Institute, Vanderbilt University, Nashville, TN, USA. [14]Clare Hall, University of Cambridge, Cambridge, UK. [15]MRC Epidemiology Unit, University of Cambridge, Cambridge, UK. [16]Division of Genetic Medicine, Department of Medicine, Vanderbilt University Medical Center, Nashville, TN, USA. [17]Ocular Genomics Institute, Massachusetts Eye and Ear, Harvard Medical School, Boston, MA, USA. [18]Department of Biomedical Engineering, Johns Hopkins University, Baltimore, MD, USA. [19]Department of Epidemiology, Harvard T.H. Chan School of Public Health, Boston, MA, USA. [20]Scripps Research Translational Institute, La Jolla, CA, USA. [21]Department of Integrative Structural and Computational Biology, The Scripps Research Institute, La Jolla, CA, USA. [22]Centre for Genomic Regulation (CRG), The Barcelona Institute for Science and Technology, Barcelona, Catalonia, Spain. [23]Department of Statistics and Operations Research, Universitat Politècnica de Catalunya (UPC), Barcelona, Catalonia, Spain. [24]Department of Genetics, University of Pennsylvania, Perelman School of Medicine, Philadelphia, PA, USA. [25]Department of Systems Pharmacology and Translational Therapeutics, University of Pennsylvania, Perelman School of Medicine, Philadelphia, PA, USA. [26]Department of Biostatistics, University of Michigan, Ann Arbor, MI, USA. [27]Institute for Genetics and Genomics in Geneva (iGE3), University of Geneva, Geneva, Switzerland. [28]Swiss Institute of Bioinformatics, Geneva, Switzerland. [29]Department of Genetics, Stanford University, Stanford, CA, USA. [30]Cancer Center and Department of Pathology, Massachusetts General Hospital, Boston, MA, USA. [31]Harvard Medical School, Boston, MA, USA. [32]Universitat Pompeu Fabra (UPF), Barcelona, Catalonia, Spain. [33]Department of Genetics, Harvard Medical School, Boston, MA, USA. [34]Program in Medical and Population Genetics, The Broad Institute of Massachusetts Institute of Technology and Harvard University, Cambridge, MA, USA. [35]Stanley Center for Psychiatric Research, Broad Institute, Cambridge, MA, USA. [36]Analytic and Translational Genetics Unit, Massachusetts General Hospital, Boston, MA, USA. [37]Department of Human Genetics, University of Chicago, Chicago, IL, USA. [38]Center for Genetic Medicine, Department of Pharmacology, Northwestern University, Feinberg School of Medicine, Chicago, IL, USA. [39]Department of Twin Research and Genetic Epidemiology, King's College London, London, UK. [40]Department of Statistics, University of Chicago, Chicago, IL, USA. [41]Department of Biomathematics, University of California, Los Angeles, Los Angeles, CA, USA. [42]Department of Genetics, Washington University School of Medicine, St. Louis, MO, USA. [43]Division of Genetics, Oregon National Primate Research Center, Oregon Health & Science University, Portland, OR, USA. [44]Department of Biomedical Informatics, Columbia University, New York, NY, USA. [45]Department of Computer Science, University of California, Los Angeles, Los Angeles, CA, USA. [46]Program in Biomedical Informatics, Stanford University School of Medicine, Stanford, CA, USA. [47]Computer Science and Artificial Intelligence Laboratory, Massachusetts Institute of Technology, Cambridge, MA, USA. [48]Department of Clinical Pharmacy, School of Pharmacy, University of Southern California, Los Angeles, CA, USA. [49]Department of Statistics and Operations Research and Department of Biostatistics, University of North Carolina, Chapel Hill, NC, USA. [50]Department of Bioengineering, Stanford University, Stanford, CA, USA. [51]Department of Genetics, Microbiology and Statistics, University of Barcelona, Barcelona, Spain. [52]Departments of Biomedical Data Science and Statistics, Stanford University, Stanford, CA, USA. [53]Department of Pathology and Laboratory Medicine, Ann & Robert H. Lurie Children's Hospital of Chicago, Chicago, IL, USA. [54]Bioinformatics Research Center and Departments of Statistics and Biological Sciences, North Carolina State University, Raleigh, NC, USA. [55]Department of Computer Sciences, Faculty of Sciences, University of Porto, Porto, Portugal. [56]Instituto de Investigação e Inovação em Saúde, University of Porto, Porto, Portugal. [57]Institute of Molecular Pathology and Immunology, University of Porto, Porto, Portugal. [58]Laboratory of Artificial Intelligence and Decision Support, Institute for Systems and Computer Engineering, Technology and Science, Porto, Portugal. [59]Columbia University Mailman School of Public Health, New York, NY, USA. [60]Life Sciences Department, Barcelona Supercomputing Center, Barcelona, Spain. [61]Department of Clinical Biochemistry and Pharmacology, Ben-Gurion University of the Negev, Beer-Sheva, Israel. [62]National Institute for Biotechnology in the Negev, Beer-Sheva, Israel. [63]Leidos Biomedical, Rockville, MD, USA. [64]UNYTS, Buffalo, NY, USA. [65]Washington Regional Transplant Community, Annandale, VA, USA. [66]Therapeutics, Roswell Park Comprehensive Cancer Center, Buffalo, NY, USA. [67]Gift of Life Donor Program, Philadelphia, PA, USA. [68]Life Gift, Houston, TX, USA. [69]Center for Organ Recovery and Education, Pittsburgh, PA, USA. [70]LifeNet Health, Virginia Beach, VA, USA. [71]National Disease Research Interchange, Philadelphia, PA, USA. [72]Van Andel Research Institute, Grand Rapids, MI, USA. [73]Department of Neurology, University of Miami Miller School of Medicine, Miami, FL, USA. [74]Biorepositories and Biospecimen Research Branch, Division of Cancer Treatment and Diagnosis, National Cancer Institute, Bethesda, MD, USA. [75]College of Public Health, Temple University, Philadelphia, PA, USA. [76]Virginia Commonwealth University, Richmond, VA, USA. [77]European Molecular Biology Laboratory, European Bioinformatics Institute, Hinxton, UK. [78]Genomics Institute, University of California Santa Cruz, Santa Cruz, CA, USA. [79]Carl Icahn Laboratory, Princeton University, Princeton, NJ, USA. [80]Department of Population Health Sciences, The University of Utah, Salt Lake City, UT, USA. [81]Departments of Medicine, Biomedical Engineering, and Mental Health, Johns Hopkins University, Baltimore, MD, USA. [82]Department of Biostatistics, Bloomberg School of Public Health, Johns Hopkins University, Baltimore, MD, USA. [83]Department of Medical Biology, The Walter and Eliza Hall Institute of Medical Research, Parkville, Victoria, Australia. [84]Altius Institute for Biomedical Sciences, Seattle, WA, USA. [85]Division of Genetics, University of Washington, Seattle, WA, USA. [86]Department of Cardiology, University of Washington, Seattle, WA, USA. [87]Hudson Alpha Institute for Biotechnology, Huntsville, AL, USA. [88]Genome Sciences, University of Washington, Seattle, WA, USA. [89]National Institute of Dental and Craniofacial Research, Bethesda, MD, USA. [90]Division of Neuroscience and Basic Behavioral Science, National Institute of Mental Health, National Institutes of Health, Bethesda, MD, USA. [91]National Institute on Drug Abuse, Bethesda, MD, USA. [92]Office of Strategic Coordination, Division of Program Coordination, Planning and Strategic Initiatives, Office of the Director, National Institutes of Health, Rockville, MD, USA. [93]Division of Genomic Medicine, National Human Genome Research Institute, Bethesda, MD, USA.

†Alphabetical order
‡First author

SUPPLEMENTARY MATERIALS

science.sciencemag.org/content/369/6509/1318/suppl/DC1
Supplementary Text
Figs. S1 to S52
Tables S1 to S16
References (*60*–*129*)
MDAR Reproducibility Checklist

View/request a protocol for this paper from *Bio-protocol*.

30 September 2019; accepted 30 July 2020
10.1126/science.aaz1776

RESEARCH ARTICLE SUMMARY

HUMAN GENOMICS

The impact of sex on gene expression across human tissues

Meritxell Oliva*†, Manuel Muñoz-Aguirre†, Sarah Kim-Hellmuth†, Valentin Wucher, Ariel D. H. Gewirtz, Daniel J. Cotter, Princy Parsana, Silva Kasela, Brunilda Balliu, Ana Viñuela, Stephane E. Castel, Pejman Mohammadi, François Aguet, Yuxin Zou, Ekaterina A. Khramtsova, Andrew D. Skol, Diego Garrido-Martín, Ferran Reverter, Andrew Brown, Patrick Evans, Eric R. Gamazon, Anthony Payne, Rodrigo Bonazzola, Alvaro N. Barbeira, Andrew R. Hamel, Angel Martinez-Perez, José Manuel Soria, GTEx Consortium, Brandon L. Pierce, Matthew Stephens, Eleazar Eskin, Emmanouil T. Dermitzakis, Ayellet V. Segrè, Hae Kyung Im, Barbara E. Engelhardt, Kristin G. Ardlie, Stephen B. Montgomery, Alexis J. Battle, Tuuli Lappalainen, Roderic Guigó, Barbara E. Stranger*

INTRODUCTION: Many complex human phenotypes, including diseases, exhibit sex-differentiated characteristics. These sex differences have been variously attributed to hormones, sex chromosomes, genotype × sex effects, differences in behavior, and differences in environmental exposures; however, their mechanisms and underlying biology remain largely unknown. The Genotype-Tissue Expression (GTEx) project provides an opportunity to investigate the prevalence and genetic mechanisms of sex differences in the human transcriptome by surveying many tissues that have not previously been characterized in this manner.

RATIONALE: To characterize sex differences in the human transcriptome and its regulation, and to discover how sex and genetics interact to influence complex traits and disease, we generated a catalog of sex differences in gene expression and its genetic regulation across 44 human tissue sources surveyed by the GTEx project (v8 data release), analyzing 16,245 RNA-sequencing samples and genotypes of 838 adult individuals. We report sex differences in gene expression levels, tissue cell type composition, and cis expression quantitative trait loci (cis-eQTLs). To assess their impact, we integrated these results with gene function, transcription factor binding annotation, and genome-wide association study (GWAS) summary statistics of 87 GWASs.

RESULTS: Sex effects on gene expression are ubiquitous (13,294 sex-biased genes across all tissues). However, these effects are small and largely tissue-specific. Genes with sex-differentiated expression are not primarily driven by tissue-specific gene expression and are involved in a diverse set of biological functions, such as drug and hormone response, embryonic development and tissue morphogenesis, fertilization, sexual reproduction and spermatogenesis, fat metabolism, cancer, and immune response. Whereas X-linked genes with higher expression in females suggest candidates for escape from X-chromosome inactivation, sex-biased expression of autosomal genes suggests hormone-related transcription factor regulation and a role for additional transcription factors, as well as sex-differentiated distribution of epigenetic marks, particularly histone H3 Lys^{27} trimethylation (H3K27me3).

Sex differences in the genetic regulation of gene expression are much less common (369 sex-biased eQTLs across all tissues) and are highly tissue-specific. We identified 58 gene-trait associations driven by genetic regulation of gene expression in a single sex. These include loci where sex-differentiated cell type abundances mediate genotype-phenotype associations, as well as loci where sex may play a more direct role in the underlying molecular mechanism of the association. For example, we identified a female-specific eQTL in liver for the hexokinase HKDC1 that influences glucose metabolism in pregnant females, which is subsequently reflected in the birth weight of the offspring.

CONCLUSION: By integrating sex-aware analyses of GTEx data with gene function and transcription factor binding annotations, we describe tissue-specific and tissue-shared drivers and mechanisms contributing to sex differences in the human transcriptome and eQTLs. We discovered multiple sex-differentiated genetic effects on gene expression that colocalize with complex trait genetic associations, thereby facilitating the mechanistic interpretation of GWAS signals. Because the causative tissue is unknown for many phenotypes, analysis of the diverse GTEx tissue collection can serve as a powerful resource for investigations into the basis of sex-biased traits. This work provides an extensive characterization of sex differences in the human transcriptome and its genetic regulation. ■

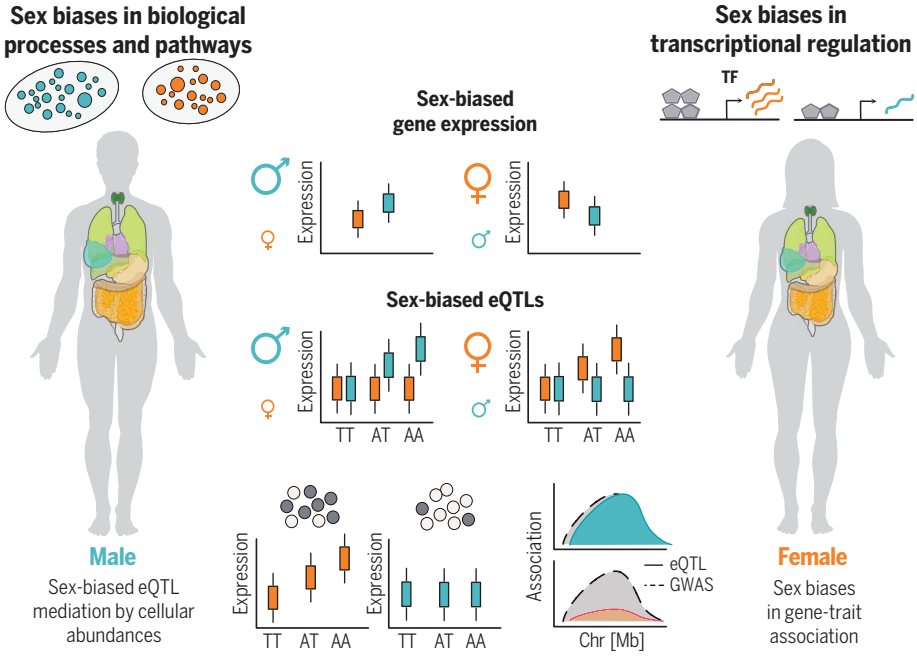

Sex affects gene expression and its genetic regulation across tissues. Sex effects on gene expression were measured in 44 GTEx human tissue sources and integrated with genotypes of 838 subjects. Sex-biased expression is present in numerous biological pathways and is associated to sex-differentiated transcriptional regulation. Sex-biased expression quantitative trait loci in cis (sex-biased eQTLs) are partially mediated by cellular abundances and reveal gene-trait associations. TT, AT, and AA are genotypes for a single-nucleotide polymorphism; TF, transcription factor.

The list of author affiliations and a full list of the GTEx authors and their affiliations are available in the full article online.
†These authors contributed equally to this work.
***Corresponding author. Email: meritxellop@uchicago.edu (M.O.); barbara.stranger@northwestern.edu (B.E.S.)**
Cite this article as M. Oliva *et al.*, *Science* 369, eaba3066 (2020). DOI: 10.1126/science.aba3066

READ THE FULL ARTICLE AT
https://doi.org/10.1126/science.aba3066

RESEARCH ARTICLE

HUMAN GENOMICS

The impact of sex on gene expression across human tissues

Meritxell Oliva[1,2,3]*†, Manuel Muñoz-Aguirre[4,5]†, Sarah Kim-Hellmuth[6,7,8]†‡, Valentin Wucher[4], Ariel D. H. Gewirtz[9], Daniel J. Cotter[10], Princy Parsana[11], Silva Kasela[7,8], Brunilda Balliu[12], Ana Viñuela[13], Stephane E. Castel[7,8], Pejman Mohammadi[14], François Aguet[15], Yuxin Zou[16], Ekaterina A. Khramtsova[1,17], Andrew D. Skol[1,2,18,19], Diego Garrido-Martín[4], Ferran Reverter[20], Andrew Brown[21], Patrick Evans[22], Eric R. Gamazon[22,23], Anthony Payne[24], Rodrigo Bonazzola[1], Alvaro N. Barbeira[1], Andrew R. Hamel[15,25], Angel Martinez-Perez[26], José Manuel Soria[26], GTEx Consortium§, Brandon L. Pierce[3], Matthew Stephens[16,27], Eleazar Eskin[28], Emmanouil T. Dermitzakis[13], Ayellet V. Segrè[15,25], Hae Kyung Im[1], Barbara E. Engelhardt[29,30], Kristin G. Ardlie[15], Stephen B. Montgomery[10,31], Alexis J. Battle[11,32], Tuuli Lappalainen[7,8], Roderic Guigó[4,33], Barbara E. Stranger[1,2,18,34]*

Many complex human phenotypes exhibit sex-differentiated characteristics. However, the molecular mechanisms underlying these differences remain largely unknown. We generated a catalog of sex differences in gene expression and in the genetic regulation of gene expression across 44 human tissue sources surveyed by the Genotype-Tissue Expression project (GTEx, v8 release). We demonstrate that sex influences gene expression levels and cellular composition of tissue samples across the human body. A total of 37% of all genes exhibit sex-biased expression in at least one tissue. We identify cis expression quantitative trait loci (eQTLs) with sex-differentiated effects and characterize their cellular origin. By integrating sex-biased eQTLs with genome-wide association study data, we identify 58 gene-trait associations that are driven by genetic regulation of gene expression in a single sex. These findings provide an extensive characterization of sex differences in the human transcriptome and its genetic regulation.

Many complex human phenotypes, such as anthropometric traits (e.g., waist-to-hip ratio), exhibit sex-differentiated distributions; disease features such as prevalence, progression, age of onset, and response to treatment often differ by sex (*1*–*5*). These sex differences have been variously attributed to hormones, sex chromosomes, genotype × sex effects, differences in behavior, and differences in environmental exposures (*6*), but the mechanisms and underlying biology of the sex differences remain largely unknown. The Genotype-Tissue Expression (GTEx) project (*7*) provides an opportunity to investigate the prevalence and genetic mechanisms of sex differences in transcriptomes and to identify how sex and genetics interact to influence complex traits and disease. The analyses presented here characterize sex differences in a relatively large population sample, including many tissues that generally lack characterization. Because the causative tissue is unknown for many diseases and disorders, analysis of this diverse tissue set can serve as a powerful resource for investigations into the basis of sex-differentiated phenotypes.

We present an extensive characterization of sex differences in the human transcriptome across 44 tissue sources of the GTEx project [v8 data release (*8*)] from 838 individuals (557 males, 281 females), constituting a large collection of multi-tissue bulk gene expression and genotype data (Fig. 1) (*9*). We quantify and characterize sex differences in gene expression levels (sex-biased gene expression) and cis sex-biased expression quantitative trait loci (sb-eQTLs). By incorporating the results of these sex-aware analyses of GTEx data with gene features and transcription factor binding annotation, we describe tissue-specific and tissue-nonspecific drivers and mechanisms contributing to sex differences in the human transcriptome and eQTLs. By integrating data from genome-wide association studies (GWASs), we report multiple sex-differentiated genetic effects on the transcriptome that colocalize with complex trait associations, highlighting the power of characterizing sex bias in GTEx samples for the mechanistic interpretation of GWAS signals.

Sex effects on gene expression are ubiquitous but small

Using GTEx v8 data (table S1), we quantified sex-biased gene expression in each of the 44 tissue sources for all genes expressed in at least one tissue. We considered a total of 35,431 X-linked and autosomal genes, including protein coding, long intergenic noncoding RNA (lincRNA), and other less-characterized gene types such as transcribed pseudogenes (*9*). For each tissue, we first fit a linear model that accounts for known sample and donor characteristics, as well as surrogate variables that capture hidden technical or biological factors of expression variability, including tissue cell type composition (fig. S1, A to C). Consequently, we are able to identify sex-biased gene expression that does not derive from sex differences in cell type abundances. We next modeled sex bias effects across tissues. We discovered a total of 13,294 differentially expressed genes [sex-biased genes; local false sign rate (LFSR) ≤ 0.05], with 473 to 4558 genes discovered per tissue, representing 1.3% to 12.9% of all tested genes, respectively (Fig. 2A, fig. S1, D to F, and table S2). Previous studies have reported widespread sex-biased gene expression (*10*–*12*) and described breast as the most sex-differentiated tissue (*10*, *11*, *13*). However, we did not observe this in the present study after controlling for sex differences in tissue cell type composition

[1]Section of Genetic Medicine, Department of Medicine, University of Chicago, Chicago, IL, USA. [2]Institute for Genomics and Systems Biology, University of Chicago, Chicago, IL, USA. [3]Department of Public Health Sciences, University of Chicago, Chicago, IL, USA. [4]Centre for Genomic Regulation, Barcelona Institute for Science and Technology, Barcelona, Catalonia, Spain. [5]Department of Statistics and Operations Research, Universitat Politècnica de Catalunya, Barcelona, Catalonia, Spain. [6]Statistical Genetics, Max Planck Institute of Psychiatry, Munich, Germany. [7]New York Genome Center, New York, NY, USA. [8]Department of Systems Biology, Columbia University, New York, NY, USA. [9]Lewis-Sigler Institute for Integrative Genomics, Princeton University, Princeton, NJ, USA. [10]Department of Genetics, Stanford University, Stanford, CA, USA. [11]Department of Computer Science, Johns Hopkins University, Baltimore, MD, USA. [12]Department of Computational Medicine, University of California, Los Angeles, CA, USA. [13]Department of Genetic Medicine and Development, University of Geneva Medical School, Geneva, Switzerland. [14]Department of Integrative Structural and Computational Biology, The Scripps Research Institute, Scripps Research Translational Institute, La Jolla, CA, USA. [15]Broad Institute of MIT and Harvard, Cambridge, MA, USA. [16]Department of Statistics, University of Chicago, Chicago, IL, USA. [17]Computational Sciences, Janssen Pharmaceuticals, Spring House, PA, USA. [18]Center for Translational Data Science, University of Chicago, Chicago, IL, USA. [19]Department of Pathology and Laboratory Medicine, Ann and Robert H. Lurie Children's Hospital of Chicago, Chicago, IL, USA. [20]Department of Genetics, Microbiology and Statistics, Faculty of Biology, University of Barcelona, Barcelona, Spain. [21]University of Dundee, Dundee, Scotland, UK. [22]Division of Genetic Medicine, Vanderbilt University Medical Center, Nashville, TN, USA. [23]Clare Hall, University of Cambridge, Cambridge, UK. [24]Wellcome Centre for Human Genetics, Nuffield Department of Medicine, University of Oxford, Oxford, UK. [25]Massachusetts Eye and Ear, Harvard Medical School, Boston, MA, USA. [26]Genomics of Complex Diseases Group, Research Institute Hospital de la Sant Creu i Sant Pau, IIB Sant Pau, Barcelona, Spain. [27]Department of Human Genetics, University of Chicago, Chicago, IL, USA. [28]Departments of Computational Medicine, Computer Science, and Human Genetics, University of California, Los Angeles, CA, USA. [29]Department of Computer Science, Center for Statistics and Machine Learning, Princeton University, Princeton, NJ, USA. [30]Genomics plc, Oxford, UK. [31]Department of Pathology, Stanford University, Stanford, CA, USA. [32]Department of Biomedical Engineering, Johns Hopkins University, Baltimore, MD, USA. [33]Universitat Pompeu Fabra, Barcelona, Catalonia, Spain. [34]Center for Genetic Medicine, Department of Pharmacology, Northwestern University, Chicago, IL, USA.
*Corresponding author. Email: meritxellop@uchicago.edu (M.O.); barbara.stranger@northwestern.edu (B.E.S.)
†These authors contributed equally to this work. ‡Present address: Department of Pediatrics, Dr. von Hauner Children's Hospital, University Hospital LMU Munich, Munich, Germany.
§A full list of the GTEx authors and their affiliations is available at the end of this article.

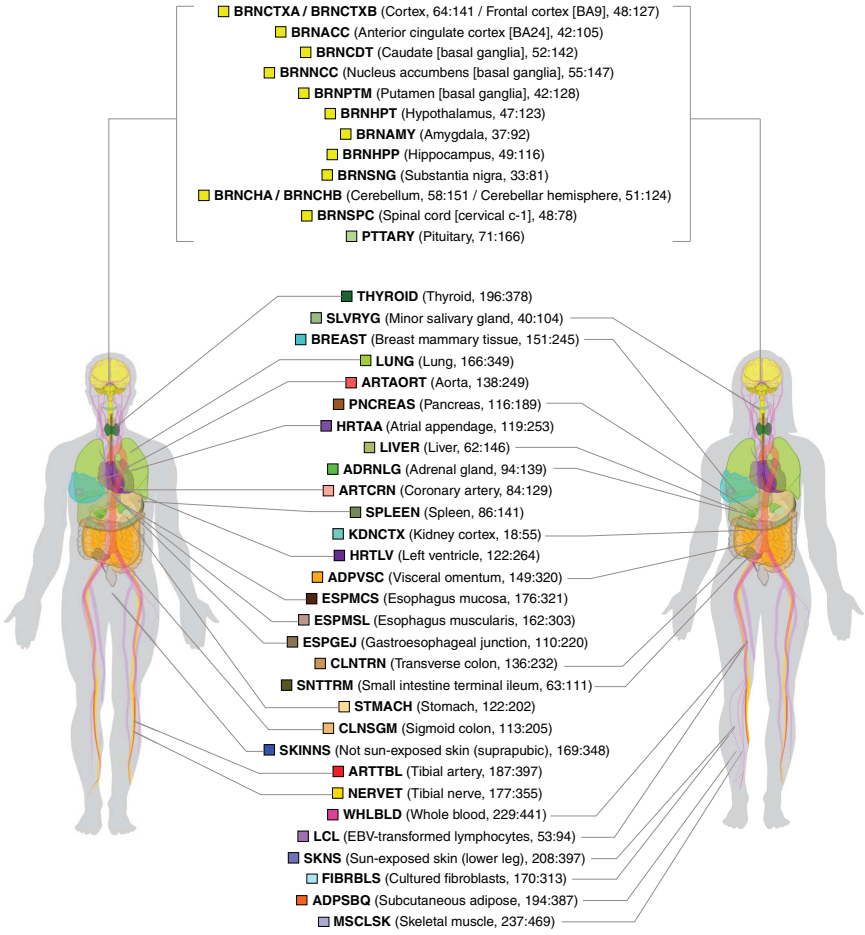

Fig. 1. Sample, data types, and discovery sets in the study of sex differences in GTEx v8. Tissue types (including 11 distinct brain regions and two cell lines) are illustrated, with sample numbers from GTEx v8 genotyped donors (females:males, in parentheses) and color coding indicated for each. This study included $N = 44$ tissue sources present in both sexes with ≥70 samples. Tissue sources comprised two cell lines, 40 tissues, and two additional replicates for brain cerebellum and cortex tissues. Tissue name abbreviations are shown in bold. See (*9*) for specific numbers of donors used in each analysis.

(fig. S1A). We next assessed replication of sex-biased genes in independent gene expression datasets for four tissues (brain cerebellum, brain cortex, heart left ventricle, and lymphocytes; table S2). We observed moderate to strong replication (average $\pi_1 = 0.62$, average effect size Spearman's $\rho = 0.78$). In total, 37.5% (13,294/35,431) of the human transcriptome was differentially expressed in at least one tissue. Of these, 531 genes (4%) were X-linked and 12,763 genes (96%) were autosomal, representing 47% and 37% of all tested X-linked and autosomal genes, respectively. Although abundant, sex effects were mostly small (fig. S2A), particularly for autosomal genes (*9*) (fig. S2B). X-linked genes with higher expression in females (female-biased genes) exhibited larger sex effects [median fold change (FC) = 1.13] than either X-linked genes with higher expression in males (male-biased genes; median FC = 1.08) or autosomal sex-biased genes (median FC_M and $FC_F = 1.04$; fig. S2B), potentially as a result of escape from X-chromosome inactivation (XCI) (*14*). The number of sex-biased genes and the effect sizes were not dominated by either sex (fig. S2C).

Sex-biased gene expression is largely tissue-specific

Sex-biased genes exhibited a skewed pattern of tissue sharing; they were likely to be differentially expressed in only a small subset of tissues (Fig. 2B), as previously reported (*10*–*13*). Of 13,294 total sex-biased genes, 2416 (18.2%) were differentially expressed in only a single tissue (Fig. 2B), suggesting tissue-dependent regulation. Only 30 genes (0.23%), 22 of which are known constitutive XCI escapees (table S3), exhibited consistent sex bias across all 44 tissue sources (Fig. 2B). This tissue specificity did not simply reflect patterns of gene expression across tissues; sex-biased genes tended to be ubiquitously expressed across tissues, whereas sex-biased expression was limited to one or a few tissues (*9*) (Fig. 2C and fig. S2D). The majority (8241/10,878 genes, 76%) of genes with sex bias in two or more tissues exhibited consistent effect direction across tissues, especially for X-linked genes (fig. S2E). Notably, whole blood and cell lines, the most widely studied biospecimen types, were not representative of sex-biased expression across tissues; sex-biased genes in whole blood constituted only 12.9% (1710/13,294) of all sex-biased genes. Although hierarchical clustering of tissues based on gene expression and on sex-biased expression is highly concordant (cophenetic correlation coefficient = 0.75) (*9*) (Fig. 2C and fig. S3, A to C), the intersection between the cluster-defining gene sets (table S4) is less than expected by chance ($P < 2.2 \times 10^{-16}$, hypergeometric test). For example, both gene expression and sex-biased expression supported a cluster of brain subregions that is clearly differentiated from other tissues (Fig. 2C and fig. S3, B and D). However, the cluster based on sex-biased expression was driven by 194 genes, whereas the transcriptome-based brain cluster was driven by 982 genes, from which only six were common with those defining the sex-based brain cluster. Among drivers of the sex-based liver cluster, we identified CYP450 genes—*CYP1A2*, *CYP3A7*, *CYP3A4*—as previously reported (*15*), but we also found genes less well characterized for sex bias, such as *PZP*, *H19*, and *VWCE*, which were previously shown to be sex-differentially expressed as a result of liver-specific sex differences in DNA methylation (*16*). These results suggest that the tissue specificity of sex-biased expression is not driven primarily by tissue-specific gene expression.

X-linked female-biased genes accurately predict sex and suggest tissue-specific candidates for escape from X-chromosome inactivation

We accurately predicted sex from gene expression, as previously explored (*17*), using X-linked genes (*9*) (fig. S4, A to D) with gradient boosted trees. Although the most predictive X-linked genes (fig. S4E) are those known to escape XCI, we identified 40 X-linked female-biased genes predictive of sex (within the top tertile with respect to their Shapley values) not previously described as XCI escapees (table S3). These results suggest further evaluation of these genes as potential XCI escapees; we did not directly test escape from XCI, and female-biased expression of X-linked genes may originate from other mechanisms. Sex prediction from autosomal genes was less accurate (mean accuracy = 84%), less specific (mean specificity = 56%, sensitivity = 96%; fig. S4D), and required more genes (fig. S4F) than prediction based on X-linked genes. However, in two tissues—breast and muscle—autosomal genes predicted sex with specificity ≥ 90% and sensitivity ≥ 98% (fig. S4G).

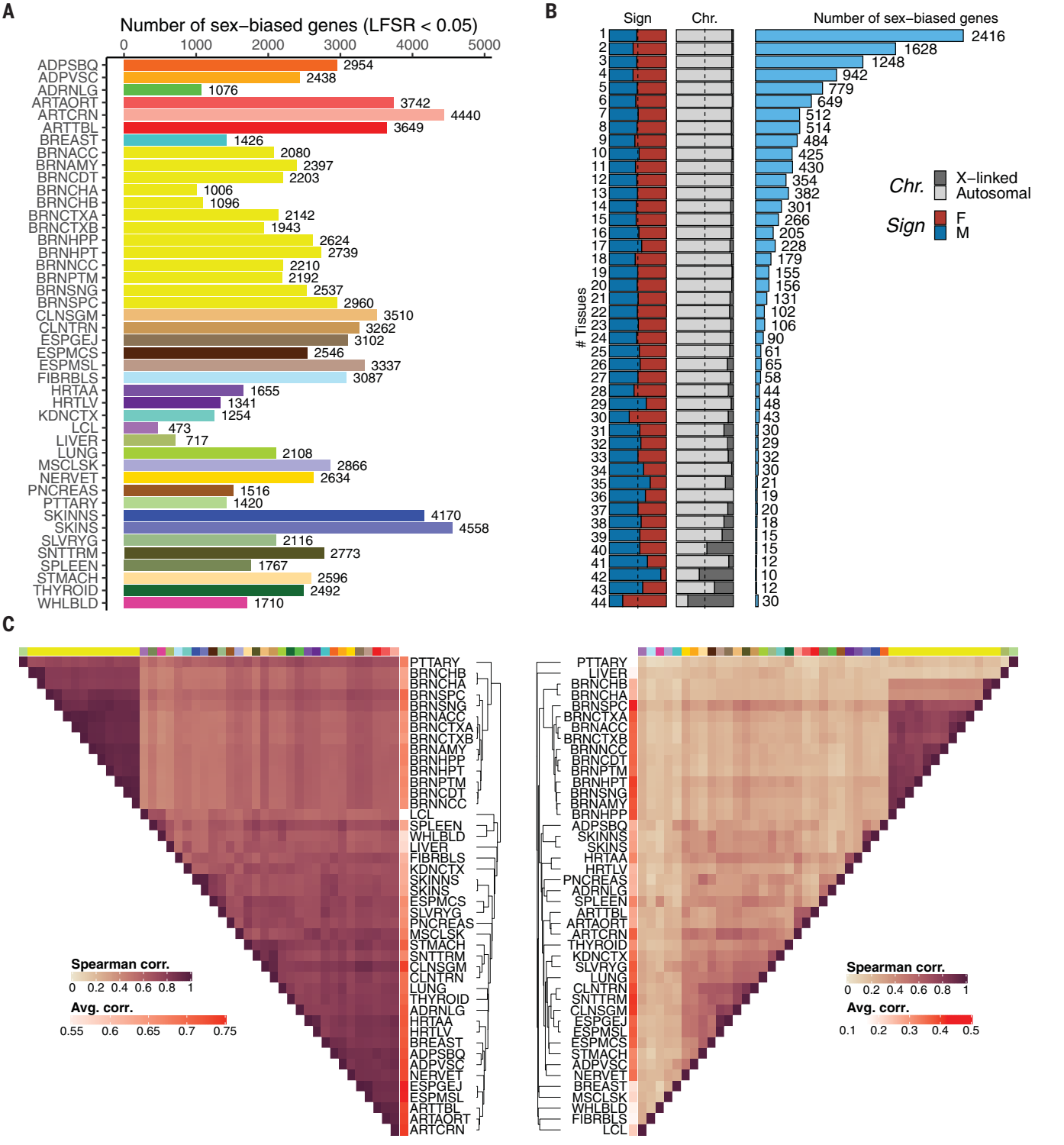

Fig. 2. Sex-differential gene expression. (**A**) Number of sex-differentially expressed genes (sex-biased genes) per tissue. Tissue colors are as in Fig. 1. (**B**) Sex-biased gene discovery (histogram, number of sex-biased genes) and characteristics of sex-biased genes (stacked bar plots) as a function of tissue sharing. Proportions of X-linked and autosomal sex-biased genes (Chr.) and of female- and male-biased genes (Sign) are indicated. (**C**) Hierarchical clustering of tissues based on gene expression (left) and the effect size of sex-biased genes (right). See (*9*) for further details.

Sex-biased genes exhibit nonrandom and tissue-specific genomic distribution

Except for the enrichment of female-biased genes on the X chromosome, little is known about the genome-wide distribution of sex-biased genes. We applied a positional gene enrichment analysis method (*18*) separately for male- and female-biased genes (LFSR ≤ 0.05) from each tissue (*9*) (fig. S5A). We discovered clustering of a total of 1559 sex-biased genes in 134 autosomal and five X-linked regions ($P \leq 0.001$, hypergeometric test) (Fig. 3A and table S5). On the X chromosome, pseudoautosomal region PAR1 and the remainder of the X-chromosome short arm *p* were enriched

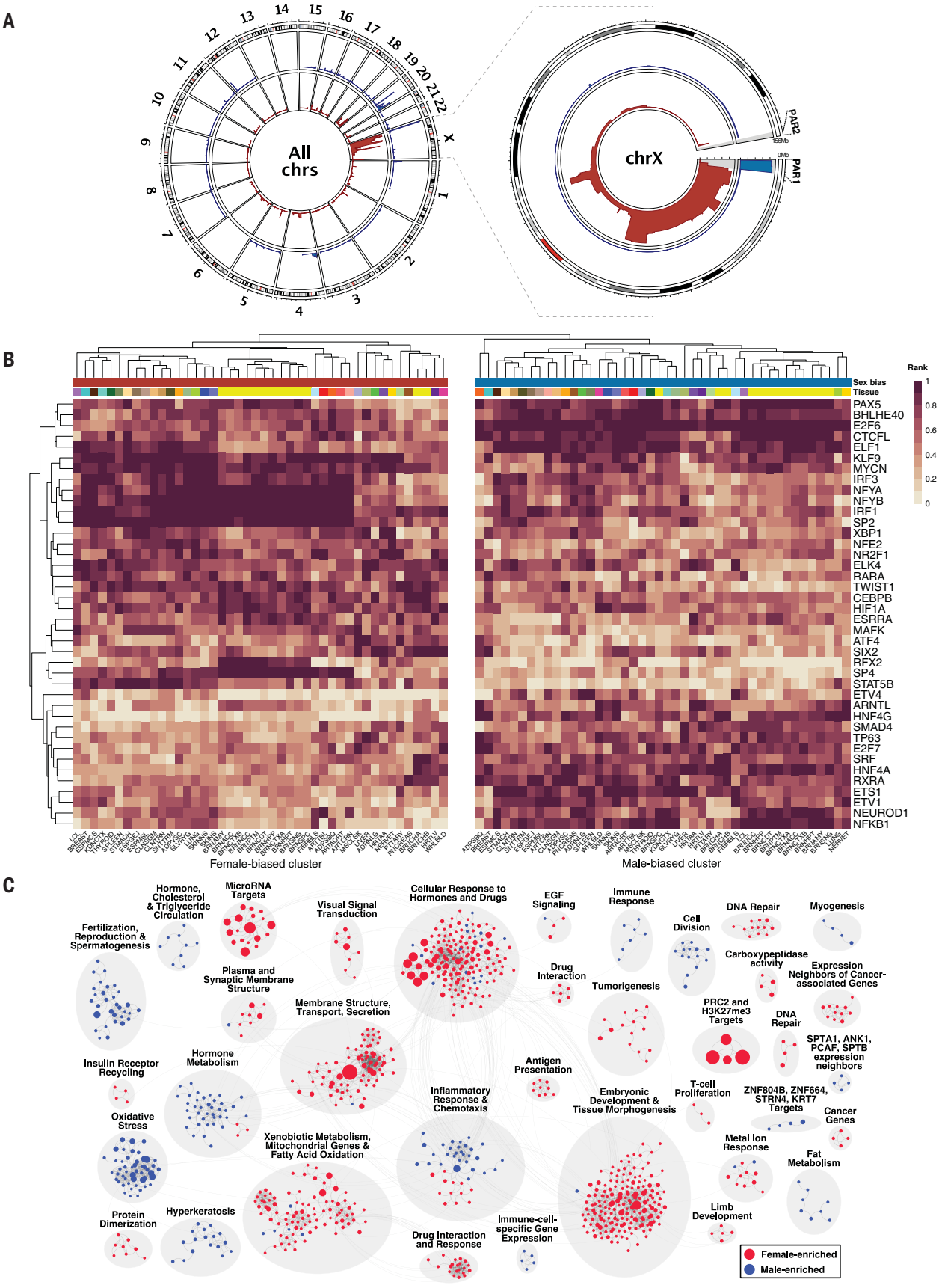
A
All chrs
chrX
PAR2
PAR1
B
Sex bias
Tissue
Rank
PAX5
BHLHE40
E2F6
CTCFL
ELF1
KLF9
MYCN
IRF3
NFYA
NFYB
IRF1
SP2
XBP1
NFE2
NR2F1
ELK4
RARA
TWIST1
CEBPB
HIF1A
ESRRA
MAFK
ATF4
SIX2
RFX2
SP4
STAT5B
ETV4
ARNTL
HNF4G
SMAD4
TP63
E2F7
SRF
HNF4A
RXRA
ETS1
ETV1
NEUROD1
NFKB1
Female-biased cluster
Male-biased cluster
C
Hormone, Cholesterol & Triglyceride Circulation
MicroRNA Targets
Visual Signal Transduction
Cellular Response to Hormones and Drugs
EGF Signaling
Immune Response
DNA Repair
Myogenesis
Fertilization, Reproduction & Spermatogenesis
Cell Division
Carboxypeptidase activity
Expression Neighbors of Cancer-associated Genes
Plasma and Synaptic Membrane Structure
Drug Interaction
Tumorigenesis
Membrane Structure, Transport, Secretion
PRC2 and H3K27me3 Targets
DNA Repair
SPTA1, ANK1, PCAF, SPTB expression neighbors
Insulin Receptor Recycling
Hormone Metabolism
Antigen Presentation
T-cell Proliferation
ZNF804B, ZNF664, STRN4, KRT7 Targets
Inflammatory Response & Chemotaxis
Embryonic Development & Tissue Morphogenesis
Cancer Genes
Oxidative Stress
Xenobiotic Metabolism, Mitochondrial Genes & Fatty Acid Oxidation
Metal Ion Response
Fat Metabolism
Protein Dimerization
Hyperkeratosis
Drug Interaction and Response
Immune-cell-specific Gene Expression
Limb Development
Female-enriched
Male-enriched

Fig. 3. Regulatory mechanisms and biological functions of sex-biased genes. (**A**) Genomic position enrichment of sex-biased genes, as indicated by male-biased (blue) and female-biased (red) genes across all chromosomes (left) and chromosome X (right). The height of each rim represents the tissue sharing of the significant genomic enrichment signal and ranges from 1 to 44 (number of tissue sources). See (*9*) for further details. (**B**) Transcription factor binding site (TFBS) enrichment in promoter regions of sex-biased genes. Of 92 enriched TFBS profiles, the top 40 with the largest difference across all tissues in the enrichment profile derived from male-biased and female-biased genes are displayed. Values represent the TFBS enrichment ranking transformed to [0, 1] per tissue and per sex; a value of 1 corresponds to the highest enrichment. See (*9*) for further details. (**C**) Clusters (gray circles) of gene sets enriched for genes highly expressed (blue and red balloons) in females (red) or males (blue) across tissues. Balloon size corresponds to the *P* value for the across-tissue meta-analysis of GSEA. Faint lines connecting balloons correspond to shared leading-edge genes between gene sets. See (*9*) for further details.

for male-biased and female-biased genes, respectively (Fig. 3A, right), as previously reported (*14*). Female-biased gene enrichment was stronger (Spearman's $\rho = 0.51$, $P = 1.63 \times 10^{-15}$) in the younger strata of arm *p* (fig. S5B), likely driven by escape from XCI (*14*, *19*). Although enriched X-chromosome regions spanned ~126 Mb, only 25% of subregions were enriched in at least two-thirds of the tissues. Among autosomal sex-biased genes, we observed a cluster of male-biased genes on chromosome 20 that was identified in 70% (30/44) of tissues (fig. S5C), but the majority of the 134 autosomal enriched regions were tissue-specific, identified on average in ~7% (3/44) of tissues (fig. S5D and table S5). These results are compatible with tissue-variable escape from XCI (*14*, *20*) and with tissue-specific topologically associating domains, possibly mediated by hormones (*21*). Further investigation is warranted to corroborate these and other hypotheses, as observed patterns may originate from a variety of mechanisms.

Promoters of sex-biased genes are enriched for hormone-related and other transcription factor binding sites

We hypothesized that transcription factor (TF) activity might drive observed patterns of differential expression, because sex-biased gene regulation by TFs has recently been reported (*13*) and TFs contribute to evolutionary changes in sex bias (*12*). We tested for enrichment of TF binding sites (TFBSs) of 231 TFs previously identified through chromatin immunoprecipitation sequencing (*22*) in promoter regions (i.e., 2 kb upstream of the transcription start site) of male- and female-biased genes (*9*) (fig. S5E). We discovered enrichment for TFBSs of a total of 92 TFs (fig. S5F), two of which were X-linked (*AR*, *ELK1*). TFBSs for 54 TFs were enriched among female-biased genes and 60 TFs among male-biased genes, with 22 TFs enriched among both sets of genes (table S6). The 92 TFs include (i) known hormone-related TFs estrogen (*ESR1*), androgen (*AR*), and glucocorticoid (*NR3C1*) receptors, (ii) 10 TFs that colocalize with steroid receptors, and (iii) TFs with a nonreported or less-characterized hormone association, including *SP1*, *E2F6*, *NRF1*, *KLF9*, and *SP2*, the top five TFs with consistent TFBS enrichment across tissues (*9*).

The strongest difference between male- and female-biased enrichment profiles was observed for TFBSs of *SP2*, *SP4*, *NFYB*, *TWIST1*, and *STAT5B* (female-biased) and of *HNF4G*, *NFKB1*, *E2F6*, *HNF4A*, and *ETS1* (male-biased), respectively, which were detected across most tissues (Fig. 3B and table S6). In contrast, we observed tissue specificity for enrichment of TFBSs of several TFs, such as *RFX2* and *ETV4* for brain and breast tissues, respectively (Fig. 3B and fig. S5F). Although *STAT5B* and *HNF4A* play known roles in sex differences in body growth rates and liver gene expression (*15*), less is known about their roles and sex biases across all tissues. The effect of sex on most of the remaining TFs is uncharacterized. Together, these results suggest that hormone-related TFs regulate sex-biased expression as expected, but they also indicate that additional TFs play a role in sex-biased gene expression, in some cases in a tissue-specific manner (table S6). Notably, TFBS enrichment is not driven by sex-biased expression of the TFs themselves (*9*), consistent with the observation that sex-biased TF targeting of genes is independent of sex-biased gene expression (*13*). However, this scenario cannot be discarded if such differences occur at an earlier developmental time point and translate into a more constitutive sex-biased TF binding profile (*23*). Alternatively, other mechanisms involving TFs could be causal drivers [e.g., posttranslational modifications as reported in mice (*24*)].

Sex-biased genes are involved in a highly diverse set of biological functions and suggest sex-specific deposition of epigenetic marks

To gain insight into cellular functions affected by sex-biased genes, we performed gene set enrichment analysis (GSEA) in each tissue, considering the direction of the sex effect (*9*) (fig. S6A and tables S7 and S8). To identify gene sets that are enriched across multiple tissues, we performed a meta-analysis using Fisher's combined probability test and identified 2134 enriched gene sets [false discovery rate (FDR) ≤ 0.05; table S9]. We applied a community detection approach to identify common features across enriched gene sets and defined 36 clusters (table S9). Among the top-scoring clusters (*9*), we identified enrichment of genes in pathways involved in drug and hormone response, epigenetic marks, embryonic development and tissue morphogenesis, fertilization, sexual reproduction and spermatogenesis, fat metabolism, cancer, immune response, and other functions (Fig. 3C and table S9). The top-scoring cluster corresponds to targets of polycomb repressive complex 2 (PRC2) and trimethylation of histone H3 at Lys^{27} (H3K27me3), which is predominantly driven by female-biased genes—a pattern also reported for other epigenetic modifications (*13*). This complex induces gene silencing and is involved in XCI (*25*). Sex-specific deposition of H3K27me3 marks has been previously reported, resulting in sex-biased gene expression in mammalian placenta (*26*) and adult liver (*27*). These differences have been hypothesized to be regulated by sex differences in the secretion of placental glycosyltransferase OGT and pituitary growth hormone. The observed association of H3K27me3 with sex-biased expression in the tissues of this study (table S9) has not been previously reported. We also identified clusters related to drug metabolism that include CYP450 genes. Sex-biased expression of CYP450 has been reported in liver (*15*) and linked to sex-differentiated growth hormone profiles; we observed sex-biased expression in additional tissues (fig. S6B). Sex-biased expression was also identified for clusters related to gonad tissue functions (e.g., meiotic synapsis), which comprise genes expressed largely in testis (fig. S6B). It is possible that some of the cross-tissue sex-biased expression patterns observed in adult tissues are derived from gamete formation and embryogenesis (*28*). Together, these results indicate that sex-biased genes are involved in a wide range of biological functions and pathways, many of which have not been previously associated with sex differences.

Sex and disease influence tissue cellular composition

The GTEx tissue samples are mixtures of heterogeneous cell types, with variation among individuals and tissues (*29*). In whole blood, cell type composition differs between sexes (*30*, *31*), but little is known about sex differences in composition of other tissues. Using a *t* test, we examined each GTEx tissue for sex differences in cellular composition on the basis of estimated abundances of seven cell types (*9*, *29*). We discovered significant (FDR ≤ 0.05) differences for four cell types—keratinocytes, neutrophils, adipocytes, and epithelial cells—in three tissues (fig. S7A and table S10). We hypothesize that additional cell types uncharacterized in this study may influence the cell type composition of GTEx tissues, particularly

of immune cells, because marked sex differences in immune cell abundances have been reported (*30*, *32*). To investigate cellular abundances in disease, we used histological annotations from pathology review of GTEx tissue samples (*9*). We discovered six pathological phenotypes with altered cell type composition (fig. S7, B to E, and table S10). Together, these results suggest that sex is correlated with tissue cellular composition, and that disease may alter cellular abundances in a sex-differentiated manner or in sex-specific pathologies.

Sex differences in the genetic regulation of gene expression are highly tissue-specific and less common than sex effects on gene expression

Sex-differentiated human phenotypes and disease characteristics may derive in part from sex-differentiated genetic effects (*6*, *33*–*36*), some of which may have an impact on gene expression. For each of 491,694 conditionally independent cis-eQTLs identified in the sex-combined cis-eQTL analysis of the GTEx v8 project (*8*), we performed sex-biased cis-eQTL (sb-eQTL) analysis in each of 44 tissues present in both sexes (Fig. 1). We used a linear regression model including genotype, sex, and covariates, and tested for significance of a genotype × sex (G×Sex) interaction on expression (*9*). Notably, this approach captures G×Sex interactions that derive both from sex and from sex-correlated factors, including cell type abundances or environmental factors. Although the contribution of cell type heterogeneity to sb-eQTLs is currently unknown, we observed sex differences in tissue cell type composition (fig. S7A), which may affect sb-eQTL discovery. Hence, we characterized the impact of cell type–specific eQTLs on sb-eQTLs (see below). We discovered a total of 369 sb-eQTLs, corresponding to 366 genes (sb-eGenes) (FDR ≤ 0.25; table S11). The majority of sb-eQTLs were identified in breast tissue (261 sb-eQTLs), but also in muscle (36 sb-eQTLs), skin (18 sb-eQTLs), and adipose tissues (14 sb-eQTLs) (Fig. 4A and fig. S8, A and B). Overall, sb-eQTLs showed strong evidence for tissue specificity (*9*); only one sb-eQTL was significant in two tissues (table S11), and only 21% displayed patterns suggestive of tissue-sharing even at a lenient significance threshold ($P_{G\times Sex} \leq 0.01$). Only 36 sb-eGenes (14%) exhibited sex-biased expression in the discovery tissue [multivariate adaptive shrinkage (MASH) LFSR ≤ 0.05; table S12], similar to recent observations (*37*). This is compatible with small sb-eQTL effects not translating into significant sex-biased gene expression, or with different functional mechanisms contributing to each sex bias type.

To provide additional support for the sb-eQTLs, we used two approaches to assess differential allele-specific expression (ASE) between sexes: allelic fold change (ASE aFC) (*38*) and environment ASE through generalized linear modeling (EAGLE) (*9*, *39*). Allele-specific expression can result from cis-regulatory genetic effects in heterozygous individuals. Differential ASE therefore indicates condition-specific cis effects (*39*), including sex specificity. We observed that both approaches, despite limited power when restricted to heterozygous individuals and differences in methodology, indicate that a portion of the detected sb-eQTLs correspond to sex differences in ASE (fig. S8C): sb-eQTLs were enriched for sex-biased ASE aFC (all tissues, $\pi_1 = 0.36$; breast, $\pi_1 = 0.41$; fig. S8, D and E) and for EAGLE associations ($\pi_1 = 0.13$, empirical test, $P \leq 0.001$). Of the 243 and 163 sb-eQTLs tested by ASE aFC and EAGLE methods, respectively, 65 (26.7%) were supported by ASE aFC (Wilcoxon $P \leq 0.05$) (fig. S7, F and G), 29 (17.8%) were supported by significant EAGLE associations, and 16 sb-eQTLs (10.4% of the 154 sb-eQTLs tested by both methods) were supported by both methods (table S11).

We were limited in our ability to replicate sb-eQTLs because the majority of sb-eQTLs were discovered in breast tissue, and matching well-powered datasets do not exist. We performed internal validation, splitting GTEx breast samples into discovery and validation cohorts, and observed moderate replication (mean $\pi_1 = 0.28$) (*9*) (fig. S8H). We next assessed sb-eQTL replication (considering sb-eQTLs from breast, whole blood, and all tissues) in independent larger (~900 subjects) whole-blood eQTL datasets, including DGN (*40*) and GAIT2 (*41*) cohorts (*9*) (table S13). We observed weak replication ($\pi_1 = 0$ to 0.12, depending on sb-eQTL set and replication cohort). Poor replication of sb-eQTLs has been reported (*40*, *42*, *43*) and has been, in part, attributed to low power (*44*) but also to methodological and study design differences.

For each sb-eGene, we also performed sex-stratified cis-eQTL analysis for each tissue, downsampling males to match the female sample size (*9*). We observed strong correlation (Spearman's rank correlation $\rho = 0.78$, $P \leq 2.2 \times 10^{-16}$) between male and female cis-eQTL effect sizes. For 58% of sb-eQTLs, sex-stratified cis-eQTL analysis revealed associations in both sexes with concordant allelic effect but different effect sizes. For example, rs117380715-*ADRA1A* in adipose subcutaneous tissue showed a stronger effect in females than in males ($\beta_F = -0.78$, $P_F = 4.64 \times 10^{-18}$, $\beta_M = -0.47$, $P_M = 3.98 \times 10^{-10}$) (Fig. 4B and fig. S8I). For the remainder of the sb-eQTLs, a cis-eQTL was detected exclusively in either females (70, 19%) or males (84, 23%). For example, we identified a female-specific cis-eQTL for rs8942-*C4BPB* in breast ($\beta_F = 0.40$, $P_F = 2.68 \times 10^{-7}$, $\beta_M = -0.02$, $P_M = 0.89$) (Fig. 4B and fig. S8I). *C4BPB* encodes the beta unit of the C4b-binding protein and controls activation of the complement cascade (*45*). We also identified a male-specific cis-eQTL for rs2273535-*AURKA* in skeletal muscle ($\beta_M = 0.47$, $\beta_F = 0.01$), described in (*8*). *AURKA*, encoding Aurora kinase A, is a member of the serine/threonine kinase family involved in mitotic chromosomal segregation and muscle differentiation (*46*) and is a known risk factor for several cancers (*47*). These results demonstrate that sex-biased genetic effects on gene expression exist for a small proportion of previously identified cis-eQTLs, and that some sb-eQTLs affect genes implicated in human phenotypes.

Sex differences in genetic regulation of gene expression are partially mediated by cell type–specific eQTLs

Given that the G×Sex interaction term of our eQTL model captures interactions that derive from sex as well as interactions with sex-correlated factors, we next characterized the fraction of sex-biased eQTLs that are driven by cell type–specific eQTLs (fig. S9A). We focused on breast, the tissue with the most sb-eQTLs and the largest sex differences in cellular composition (figs. S7A and S8B). We tested 261 breast sb-eQTLs for enrichment of cell type interacting cis-eQTLs (ieQTLs) (*9*, *29*). These ieQTLs correspond to cis-eQTLs where the effect varies depending on estimated cell type abundances (*29*). Breast sb-eQTLs were strongly enriched ($\pi_1 = 0.66$ and 0.89) for ieQTL signal corresponding to adipocytes and epithelial cells (fig. S9B). After including an interaction term for genotype × epithelial cell abundance estimates in the sb-eQTL model, 58% of breast sb-eQTLs (152/261) remained significant, whereas for 42% of sb-eQTLs (109/261), the genotype × sex effect was strongly attenuated (fig. S9C and table S14). For example, the strongest breast sb-eQTL, rs2289149-*LINC00920* ($P = 4.83 \times 10^{-11}$), was not significant after incorporating the genotype × epithelial cell abundance estimates in the model ($\beta_{G\times Sex} = 0.187$, 95% confidence interval = [−0.004, 0.378]; fig. S9C and table S14).

To formally test the impact of cell type composition on sb-eQTL detection, we performed a mediation analysis, using genotype interactions with estimated epithelial cell abundance as a potential mediator (*9*) (fig. S9D). We discovered that 60 sb-eQTLs (23%) were mediated by cell type abundances (average causal mediation effects $P \leq 0.001$) (Fig. 4C and table S14). Mediation by other cell types cannot be excluded, particularly by immune cells: We observed that breast sb-eGenes are enriched for immunoglobulin variable chain genes (Fisher's exact test, odds ratio = 12, $P = 9.2 \times 10^{-8}$). In all cases, the eQTL effect size is larger in females (table S11). Because immunoglobulin genes are mainly expressed in B cells and are among the most sex-discriminative genes in breast (fig. S7D), we hypothesize that immunoglobulin sb-eQTLs may be driven

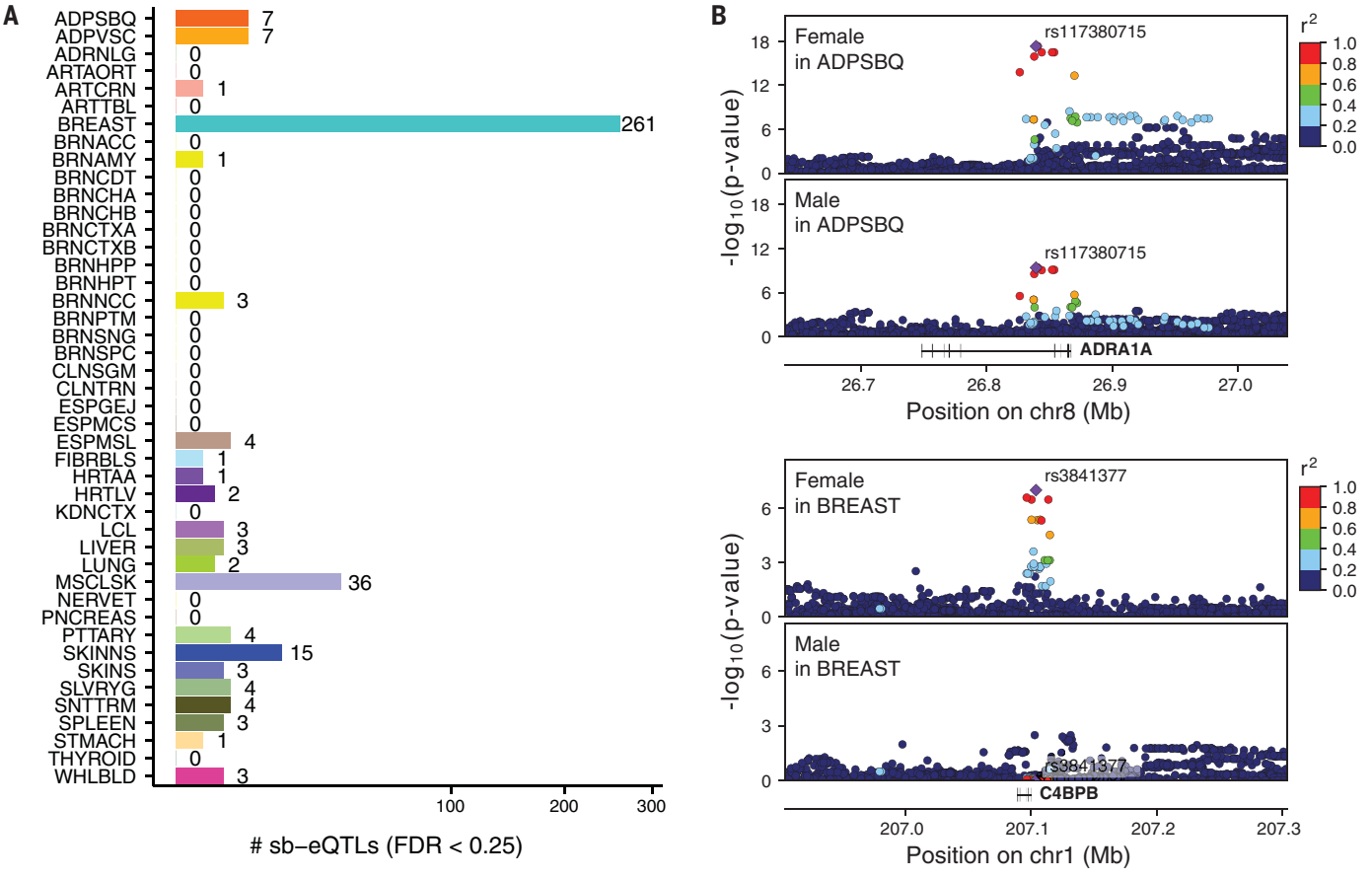

Fig. 4. Sex-biased eQTLs (sb-eQTLs). (**A**) Number of sb-eQTLs discovered per tissue. Square-root transformation was applied to the *x* axis. See Fig. 1 for tissue abbreviations. (**B**) Association *P* values of the female-stratified (top) and male-stratified (bottom) cis-eQTLs in the *ADRA1A* locus in adipose subcutaneous tissue (upper panels; $\beta_F = -0.78$, $P_F = 4.64 \times 10^{-18}$, $\beta_M = -0.47$, $P_M = 3.98 \times 10^{-10}$, $P_{G\times Sex} = 1.05 \times 10^{-5}$) and *C4BPB* locus in breast mammary tissue (lower panels; $\beta_F = 0.40$, $P_F = 2.68 \times 10^{-7}$, $\beta_M = -0.02$, $P_M = 0.89$, $P_{G\times Sex} = 7.22 \times 10^{-5}$). Linkage disequilibrium between loci is quantified by squared Pearson coefficient of correlation (r^2). Diamond-shaped point represents the top significant eQTL variant across sex-stratified *P* values. (**C**) sb-eQTL mediation analysis of 261 breast sb-eQTLs. Point coordinates represent the effect size of G×Sex (*x* axis) and G×Epithelial cells (*y* axis) derived from a linear regression model with both interaction terms. Gray lines represent confidence intervals of the effect sizes of G×Sex (horizontal lines) and G×Epithelial cells (vertical lines). Point size represents sb-eQTL significance; color corresponds to mediation significance. See (9) for further details.

by greater abundances of this cell type in female breasts. Collectively, these results indicate that a large proportion of sb-eQTLs in breast are driven by cell type–specific genetic effects on gene expression that become apparent when cell types differ between sexes, although our analysis cannot distinguish whether the tested cell types or others correlated with them (fig. S9E) are the true mediators of the signal.

Sex-aware eQTL-GWAS colocalization provides insights into the genetic basis of complex traits

To assess whether sb-eQTLs are useful as a means of dissecting the molecular basis of

complex trait associations, we performed colocalization (*48*) between sex-stratified cis-eQTLs and 87 GWASs, representing 74 distinct complex traits, for 1089 sb-eGenes at a more relaxed FDR (≤0.50) (*9*). We identified 74 colocalized gene-trait pairs [posterior probability of sharing the same causal variant (PP4) > 0.5; Fig. 5, A to C]. Of these, 58 were colocalized (PP4 > 0.5) in one sex but not in the other—36 for females and 22 for males—corresponding to 36 unique genetic loci and 27 distinct traits (Fig. 5, A to C, and table S15). For 24/36 (67%) female-stratified and 10/22 (45%) male-stratified cis-eQTL–trait pairs, evidence for colocalization was also found using the male and female combined GTEx v8 cis-eQTLs (fig. S10A). For these 34 loci that colocalized in the sex-combined approach, we found evidence that the colocalization signal is driven by regulatory effects in a single sex. The remaining 12/36 (33%) female and 12/22 (55%) male gene-trait colocalizations were not discovered with the sex-combined approach.

The strongest colocalizations between a trait and a female-stratified cis-eQTL were identified for *CCDC88C* and breast cancer, and for *HKDC1* and birth weight (Fig. 5, C and D). Conversely, the strongest colocalizations between a trait and a male-stratified cis-eQTL were identified for *DPYSL4* and percentage of body fat, and for *CLDN7* and birth weight (Fig. 5, C and E). *CCDC88C* is a negative regulator of the Wnt signaling pathway, a key mechanism in cancer progression (*49*), and the *CCDC88C* female cis-eQTL signal in breast colocalizes with risk of breast cancer (Fig. 5D, left), a trait with highly sex-differentiated incidence and presentation (*50*). For breast cancer, we identified two additional female-driven ($PP4_F$ > $PP4_M$) colocalized sb-eGenes, *NTN4* and *CRLF3* (table S15), previously reported as breast cancer–relevant genes (*51*, *52*).

We also discovered a preferential colocalization of blood and immune traits with female-stratified relative to male-stratified cis-eQTLs (odds ratio = 2.22; $P = 0.047$, Fisher's exact test). This includes inflammatory bowel diseases, which show a higher prevalence in females with increasing age (*53*), and immune cell abundances in blood, which also exhibit sex differences (*30*, *31*). Together, these results suggest that sex-biased genetic regulation of gene expression may contribute to the etiology of diseases with marked sex differences.

Moreover, we identified colocalization signal for eQTLs and GWAS of sex-specific traits as well as signal possibly derived from sex-specific conditions, such as pregnancy in females and balding patterns in males. The *C9orf66* male-stratified cis-eQTL signal in breast colocalized with balding patterns in males, and the *HKDC1* female-stratified cis-eQTL signal in liver colocalized with birth weight, which is strongly influenced by maternal factors (Fig. 5D, right) (*54*). The sb-eQTL for this locus in liver was replicated in an independent dataset (*55*) (rs35696875-*HKDC1* $P_F = 2.73 \times 10^{-8}$, $P_M = 1.60 \times 10^{-4}$, z-test $P = 0.004$; fig. S10B). *HKDC1* encodes a member of the hexokinase protein family and is involved in glucose metabolism. Multiple variants in perfect or high linkage disequilibrium with rs35696875 that cause reduced expression of *HKDC1* have been associated with gestational diabetes mellitus risk (*56*) and glycemic traits during pregnancy (*54*). Here, we confirmed that the *HKDC1* female eQTL signal in the liver colocalizes with maternal glucose levels in plasma during pregnancy (PP4 = 0.92; fig. S10C). Recently, regulatory variants spanning multiple enhancers were found to have a coordinated allelic effect on *HKDC1* expression in hepatocyte-derived cells (*57*). Estimates of hepatocyte abundance in GTEx liver samples did not differ by sex ($P = 0.30$), and the rs35696875-*HKDC1* sb-eQTL showed no evidence of being a hepatocyte ieQTL ($P_{G\times Hepatocytes} = 0.11$) (*29*). Thus, unlike many sb-eQTLs in breast, the *HKDC1* sb-eQTL in liver did not seem to be driven by sex-differentiated cell type abundances. The *HKDC1* sb-eQTL alternative allele is associated with lower *HKDC1* expression, higher maternal glucose levels, and increased birth weight. These results suggest that the *HKDC1* female cis-eQTL influences glucose metabolism in the pregnant female, which is reflected in the birth weight of the offspring. Further investigation is needed, however, to prove causality.

Additionally, the *DPYSL4* male-stratified cis-eQTL signal in skeletal muscle colocalized with genetic signal associated with percentage of body fat (Fig. 5E, right). *DPYSL4* is linked to the pathophysiology of obesity and cancer: p53-inducible *DPYSL4* associates with mitochondrial supercomplexes and regulates energy metabolism in adipocytes and cancer cells. Low *DPYSL4* expression is associated with poor survival of breast cancer patients (*58*). Of note, although the colocalizing signal was detected with the male-stratified cis-eQTL signal, the low probability of colocalization appears to be due to the presence of an additional cis-eQTL in females that is absent in males. These results suggest that characterizing sex differences in the genetic associations of complex traits and molecular phenotypes can prove useful to dissect allelic heterogeneity.

Five colocalized sb-eGenes (*CLDN7*, *CCDC125*, *FAM53B*, *PLEC*, and *SOWAHC*), corresponding to cell type interaction cis-eQTL (cell type ieQTL) signals, also colocalized with reported GWAS signals (birth weight, blood cell counts, height, platelet counts, and schizophrenia, respectively) (*29*). For instance, the male-biased cis-eQTL rs34958987-*CLDN7* in breast (Fig. 5E, left, and fig. S10D) was identified as an epithelial cell ieQTL in breast (*29*). Both the sb-eQTL and cell type ieQTL signals colocalized with the birth weight GWAS signal (fig. S10E). This suggests that the origin of these sex differences in gene-trait associations may be in sex-differentiated cell type abundances.

Finally, to assess whether sex-biased eQTL signals are reflected in sex-biased GWAS effects, we obtained sex-stratified GWAS data for 36 of the 58 colocalized gene-trait pairs (*9*) (table S15). We identified two of 36 loci with sex differences in GWAS effect size (FDR ≤ 0.05, Bonferroni correction). These two signals correspond to *RNASET2* and *CELSR2* genes, which are more strongly associated to hyperthyroidism in females and to heart attack in males, respectively. However, with the current GWAS sample sizes, we observed that, in general, sex-biased effects at the eQTL level do not readily translate into sex-biased effects at the GWAS level, in line with recent power calculations where millions of GWAS samples were estimated to be needed to address this question (*37*).

Overall, our colocalization results identified loci where sex-differentiated cell type abundances mediate genotype-phenotype associations, and also loci where sex may play a more direct role in the underlying molecular mechanism of the association, as in the *HKDC1* locus. For future studies, accounting for context or environment (sex in the present study) in colocalization approaches is a promising approach to the discovery of gene-trait associations and their underlying origins.

Discussion

We identified widespread sex-biased gene expression in all tissues, with 37% of genes exhibiting sex bias in at least one tissue, but with overall small (median FC = 1.04) sex effects. These results derive from overlapping male and female distributions of interindividual expression variation, indicative of differential expression as opposed to completely dimorphic expression. These genes represent diverse molecular and biological functions, and they include genes relevant to disease and clinical phenotypes. As expected, the strongest sex bias was observed for X-chromosome genes, whereas the vast majority of sex-biased genes were autosomal, which suggests the influence of sex on genome-wide regulatory programs. As reported in (*59*) but not well characterized to date, we discovered that a portion of these genes were nonrandomly distributed across the genome, suggesting sex differences in regional regulation. Integration of these results with sex-aware analysis of epigenetic and chromosome conformation capture Hi-C data may provide mechanistic insights into these patterns.

Although we identified a set of X-linked genes with sex-biased expression across many tissues, the overall sharing of sex-biased expression among tissues was strongly skewed

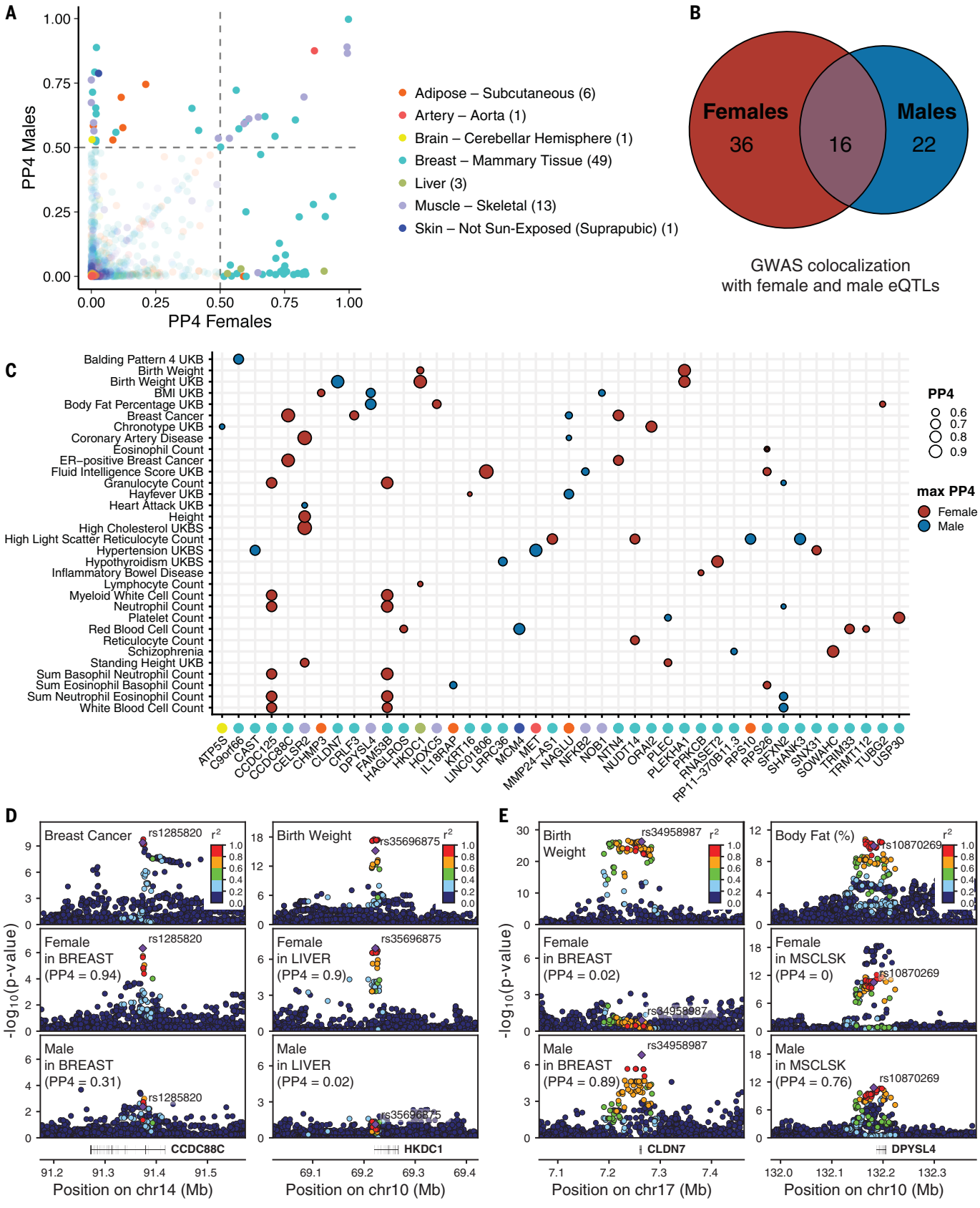
A
PP4 Males
PP4 Females
1.00
0.75
0.50
0.25
0.00
Adipose – Subcutaneous (6)
Artery – Aorta (1)
Brain – Cerebellar Hemisphere (1)
Breast – Mammary Tissue (49)
Liver (3)
Muscle – Skeletal (13)
Skin – Not Sun-Exposed (Suprapubic) (1)
B
Females
36
16
Males
22
GWAS colocalization
with female and male eQTLs
C
Balding Pattern 4 UKB
Birth Weight
Birth Weight UKB
BMI UKB
Body Fat Percentage UKB
Breast Cancer
Chronotype UKB
Coronary Artery Disease
Eosinophil Count
ER−positive Breast Cancer
Fluid Intelligence Score UKB
Granulocyte Count
Hayfever UKB
Heart Attack UKB
Height
High Cholesterol UKBS
High Light Scatter Reticulocyte Count
Hypertension UKBS
Hypothyroidism UKBS
Inflammatory Bowel Disease
Lymphocyte Count
Myeloid White Cell Count
Neutrophil Count
Platelet Count
Red Blood Cell Count
Reticulocyte Count
Schizophrenia
Standing Height UKB
Sum Basophil Neutrophil Count
Sum Eosinophil Basophil Count
Sum Neutrophil Eosinophil Count
White Blood Cell Count
ATP5S
C9orf66
CAST
CCDC125
CCDC88C
CELSR2
CHMP3
CLDN7
CRLF3
DPYSL4
FAM53B
HAGLROS
HKDC1
HOXC5
IL18RAP
KRT16
LINC01806
LRRC36
MCM4
MET
MMP24−AS1
NAGLU
NFKB2
NOB1
NTN4
NUDT14
ORAI2
PLEC
PLEKHA1
PRKCB
RNASET2
RP11−370B11.3
RPS10
RPS26
SFXN2
SHANK3
SNX31
SOWAHC
TRIM33
TRMT112
TUBG2
USP30
PP4
0.6
0.7
0.8
0.9
max PP4
Female
Male
D
Breast Cancer
rs1285820
Female
in BREAST
(PP4 = 0.94)
Male
in BREAST
(PP4 = 0.31)
Birth Weight
rs35696875
Female
in LIVER
(PP4 = 0.9)
Male
in LIVER
(PP4 = 0.02)
-log10(p-value)
CCDC88C
HKDC1
Position on chr14 (Mb)
Position on chr10 (Mb)
E
Birth
Weight
rs34958987
Female
in BREAST
(PP4 = 0.02)
Male
in BREAST
(PP4 = 0.89)
Body Fat (%)
rs10870269
Female
in MSCLSK
(PP4 = 0)
Male
in MSCLSK
(PP4 = 0.76)
-log10(p-value)
CLDN7
DPYSL4
Position on chr17 (Mb)
Position on chr10 (Mb)

Fig. 5. Colocalization of sb-eQTLs with GWAS traits. (**A**) Posterior probability (PP4) of 74 colocalized gene-trait pairs where a GWAS shows evidence of colocalization with the female-stratified and/or male-stratified cis-eQTL signal (PP4 > 0.5). Numbers of colocalizing loci per tissue are shown in parentheses. (**B**) Numbers of colocalizing loci for female and male cis-eQTLs. (**C**) GWAS-eQTL colocalizing genes (PP4 > 0.5) color-labeled by eQTL tissue of origin according to labels in (A) (*x* axis) are categorized by the sex where the colocalization signal is maximized with the corresponding GWAS trait (*y* axis). Comparing the colocalization PP4 values for male and female cis-eQTL signals, the estimates can be maximum in females (red) or males (blue). (**D**) Genotype-phenotype association *P* values of the *CCDC88C* (left) and *HKDC1* (right) loci. For the *CCDC88C* locus, panels illustrate GWAS signal for breast cancer (top) and *CCDC88C* cis-eQTL signal for females (middle) and males (bottom) in breast mammary tissue. For the *HKDC1* locus, panels illustrate GWAS signal for birth weight (top) and *HKDC1* cis-eQTL signal for females (middle) and males (bottom) in liver. (**E**) Genotype-phenotype association *P* values of the *CLDN7* (left) and *DPYSL4* (right) loci. For the *CLDN7* locus, panels illustrate GWAS signal for birth weight (top) and *CLDN7* cis-eQTL signal for females (middle) and males (bottom) in breast mammary tissue. For the *DPYSL4* locus, panels illustrate GWAS signal for body fat (top) and *DPYSL4* cis-eQTL signal for females (middle) and males (bottom) in muscle skeletal tissue. In (D) and (E), linkage disequilibrium between loci is quantified by squared Pearson coefficient of correlation (r^2). Diamond-shaped point represents the top significant cis-eQTL variant across sex-stratified *P* values.

toward tissue specificity, with 18.2% of sex-biased genes discovered in only a single tissue. The high tissue specificity of sex-biased gene expression and the enrichment of TFBSs in sex-biased gene promoters implicate specific TFs in mediating sex-biased expression. Functional experiments to assess sex-differentiated TF binding are needed to evaluate the role of TF function in observed patterns.

In contrast to the large impact of sex on gene expression levels, the overall extent of sex effects on genetic regulation in cis is much less (369 sb-eQTLs). This observation is consistent with an overall weaker role of sex in genetic regulation but is also affected by differences in power of the two analyses (*60*). For sb-eQTLs, the combination of small genotype × sex interaction effect sizes, high interindividual expression heterogeneity, and the sex imbalance in the GTEx collection affects the power of the interaction test. This implies that much larger cohorts are needed to fully characterize this phenomenon, particularly to assess sex effects for all cis variants and genes. The relatively modest number of G×Sex interactions for a factor as impactful as sex suggests that other, more subtle genotype-interacting environmental factors are likely to be challenging to identify [as noted in (*39*)]. The sb-eQTL analysis is also affected by cell type heterogeneity within tissues. We demonstrated that a portion of sb-eQTLs are mediated by cell type composition, which suggests that a portion of the sb-eQTL signal may derive from the combination of cell type–specific eQTLs and sex differences in the tissue's cell type composition. The remaining loci for which we had no evidence of cell type mediation may represent true sex differences in genetic regulation of these genes, but might also derive from unknown factors confounded with sex, including cell types that were not part of our analysis. Thus, the full impact of cell type differences across tissues remains to be determined.

The identification of sb-eQTLs that are unequivocally not derived from sex differences in cell type abundances cannot be assessed with analysis of sb-eQTLs in bulk tissue. We anticipate that single-cell sb-eQTL analysis will help to disentangle sex effects on the genetics of gene expression that derive from sex differences in tissue composition versus those that derive from sex chromosome status. However, this approach also has limitations due to the removal of cells from the in situ tissue environment—including, for example, the presence of other cell types and diverse hormonal environments.

In efforts to understand the molecular basis of sex differences in disease and other phenotypes, it is important to note that the connection between the molecular changes observed here and complex phenotypes is likely to be complicated by many compensatory and buffering effects (*61*). Despite extensive sex differences at the transcriptome level, the majority of biology at all phenotype levels is shared between males and females. Furthermore, the sex differences observed here are based on a snapshot of mostly older individuals. Sex differences that occur during different developmental stages, in specific environments, or in specific disease states are not well represented in our analysis. For example, sex biases are observed in many cancers (*1*). Our results provide a resource of sex effects in "nondiseased" tissues to compare with those of disease cohorts. We note that sex is highly correlated with many features of behavior and external environments [e.g., smoking (*62*)], and disentangling sex differences driven by inherent biology versus gendered environments is an important further challenge.

Beyond gene expression, sex-biased genetic regulation may also contribute to higher-order phenotypes such as complex traits and diseases; colocalization analysis of sex-stratified cis-eQTLs and sex-combined GWAS summary statistics yielded variant-gene-trait associations that were not detected in combined-sex cis-eQTL colocalization analysis. In general, context-aware colocalization analyses may help to elucidate the origin of gene-trait associations, as hypothesized here for *HKDC1*'s impact on birth weight through alteration of glucose metabolism in a pregnant female's liver. We show that sex-biased gene-trait associations are likely attributable to either allelic heterogeneity in the combined-sex cohort or genetic effects on gene expression that are (predominantly) driven by a single sex; colocalized sb-eGenes cannot be considered as proxies of loci harboring sex differences in the genetic architecture of the linked trait. Because sex-aware colocalizations can provide insights into the sex-differentiated genetic architecture of disease, we expect future work in this area combining sex-stratified cis-eQTLs with summary statistics from sex-stratified GWASs to enable us to fully comprehend the impact of sex on human health and disease. The extension of analytical approaches to facilitate widespread genetic analysis of sex chromosomes is an important step toward these new research directions.

Methods summary

Sex-differential expression was performed with voom-limma (*63*) and MASH (*64*) (fig. S1A). Sex-differential effect sizes and gene expression levels were investigated for tissue specificity with the Tau index (*65*), clustered with pvclust (*66*), and compared with dendextend (*67*) (fig. S3A). Sex predictivity of sex-biased genes per tissue was quantified through gradient-boosted tree classifier models (*68*) (fig. S4A). Positional gene enrichment analysis of sex-biased genes was performed with PGE (*18*) (fig. S5A). Transcription factor binding site enrichment in promoter regions of sex-biased genes was performed with Unibind (*22*) and runLOLA (*69*) (fig. S5E). Gene set enrichment analysis was performed with fgsea (*70*) (fig. S6A) and results characterized with Cytoscape (*71*). Sex differences in cell type abundances and their effect on histopathological phenotypes were explored using linear regression. sb-eQTL mapping was implemented using an adaptation of FastQTL (*72*) (fig. S8A); sb-eQTLs were validated using haplotype-level allelic expression data generated with phASER and allele-specific expression modeling using EAGLE. Characterization of sex-specific cis-eQTL effects was performed with linear regression. Mediation of G×Sex by G×Epithelial interactions was tested with the mediation R package. Colocalization of GWAS and eQTLs was performed with coloc (*48*). Further details for each analysis are provided in (*9*).

REFERENCES AND NOTES

1. D. Zheng *et al*., Sexual dimorphism in the incidence of human cancers. *BMC Cancer* **19**, 684 (2019). doi: 10.1186/s12885-019-5902-z; pmid: 31299933
2. G. D. Anderson, Sex and racial differences in pharmacological response: Where is the evidence? Pharmacogenetics, pharmacokinetics, and pharmacodynamics. *J. Womens Health* **14**, 19–29 (2005). doi: 10.1089/jwh.2005.14.19; pmid: 15692274
3. V. Kuan *et al*., A chronological map of 308 physical and mental health conditions from 4 million individuals in the English National Health Service. *Lancet Digit. Health* **1**, e63–e77 (2019). doi: 10.1016/S2589-7500(19)30012-3; pmid: 31650125
4. S. T. Ngo, F. J. Steyn, P. A. McCombe, Gender differences in autoimmune disease. *Front. Neuroendocrinol.* **35**, 347–369 (2014). doi: 10.1016/j.yfrne.2014.04.004; pmid: 24793874
5. D. Westergaard, P. Moseley, F. K. H. Sørup, P. Baldi, S. Brunak, Population-wide analysis of differences in disease progression patterns in men and women. *Nat. Commun.* **10**, 666 (2019). doi: 10.1038/s41467-019-08475-9; pmid: 30737381
6. E. A. Khramtsova, L. K. Davis, B. E. Stranger, The role of sex in the genomics of human complex traits. *Nat. Rev. Genet.* **20**, 173–190 (2019). doi: 10.1038/s41576-018-0083-1; pmid: 30581192
7. J. Lonsdale *et al*., The Genotype-Tissue Expression (GTEx) project. *Nat. Genet.* **45**, 580–585 (2013). doi: 10.1038/ng.2653; pmid: 23715323
8. The GTEx Consortium, The GTEx Consortium atlas of genetic regulatory effects across human tissues. *Science* **369**, 1318 (2020). doi: 10.1126/science.aaz1776; pmid: 25954002
9. See supplementary materials.
10. M. Melé *et al*., The human transcriptome across tissues and individuals. *Science* **348**, 660–665 (2015). doi: 10.1126/science.aaa0355; pmid: 25954002
11. M. Gershoni, S. Pietrokovski, The landscape of sex-differential transcriptome and its consequent selection in human adults. *BMC Biol.* **15**, 7 (2017). doi: 10.1186/s12915-017-0352-z; pmid: 28173793
12. S. Naqvi *et al*., Conservation, acquisition, and functional impact of sex-biased gene expression in mammals. *Science* **365**, eaaw7317 (2019). doi: 10.1126/science.aaw7317; pmid: 31320509
13. C. M. Lopes-Ramos *et al*., Sex Differences in Gene Expression and Regulatory Networks across 29 Human Tissues. *Cell Rep.* **31**, 107795 (2020). doi: 10.1016/j.celrep.2020.107795; pmid: 32579922
14. L. Carrel, H. F. Willard, X-inactivation profile reveals extensive variability in X-linked gene expression in females. *Nature* **434**, 400–404 (2005). doi: 10.1038/nature03479; pmid: 15772666
15. J. L. Rinn, M. Snyder, Sexual dimorphism in mammalian gene expression. *Trends Genet.* **21**, 298–305 (2005). doi: 10.1016/j.tig.2005.03.005; pmid: 15851067
16. S. García-Calzón, A. Perfilyev, V. D. de Mello, J. Pihlajamäki, C. Ling, Sex Differences in the Methylome and Transcriptome of the Human Liver and Circulating HDL-Cholesterol Levels. *J. Clin. Endocrinol. Metab.* **103**, 4395–4408 (2018). doi: 10.1210/jc.2018-00423; pmid: 29846646
17. S. E. Ellis, L. Collado-Torres, A. Jaffe, J. T. Leek, Improving the value of public RNA-seq expression data by phenotype prediction. *Nucleic Acids Res.* **46**, e54 (2018). doi: 10.1093/nar/gky102; pmid: 29514223
18. K. De Preter, R. Barriot, F. Speleman, J. Vandesompele, Y. Moreau, Positional gene enrichment analysis of gene sets for high-resolution identification of overrepresented chromosomal regions. *Nucleic Acids Res.* **36**, e43 (2008). doi: 10.1093/nar/gkn114; pmid: 18346969
19. A. Kelkar, V. Thakur, R. Ramaswamy, D. Deobagkar, Characterisation of inactivation domains and evolutionary strata in human X chromosome through Markov segmentation. *PLOS ONE* **4**, e7885 (2009). doi: 10.1371/journal.pone.0007885; pmid: 19946363
20. T. Tukiainen *et al*., Landscape of X chromosome inactivation across human tissues. *Nature* **550**, 244–248 (2017). doi: 10.1038/nature24265; pmid: 29022598
21. F. Le Dily *et al*., Distinct structural transitions of chromatin topological domains correlate with coordinated hormone-induced gene regulation. *Genes Dev.* **28**, 2151–2162 (2014). doi: 10.1101/gad.241422.114; pmid: 25274727
22. M. Gheorghe *et al*., A map of direct TF-DNA interactions in the human genome. *Nucleic Acids Res.* **47**, e21 (2019). doi: 10.1093/nar/gky1210; pmid: 30517703
23. F. Spitz, E. E. M. Furlong, Transcription factors: From enhancer binding to developmental control. *Nat. Rev. Genet.* **13**, 613–626 (2012). doi: 10.1038/nrg3207; pmid: 22868264
24. N. Leuenberger, S. Pradervand, W. Wahli, Sumoylated PPARα mediates sex-specific gene repression and protects the liver from estrogen-induced toxicity in mice. *J. Clin. Invest.* **119**, 3138–3148 (2009). doi: 10.1172/JCI39019; pmid: 19729835
25. N. Brockdorff, Polycomb complexes in X chromosome inactivation. *Philos. Trans. R. Soc. London Ser. B* **372**, 20170021 (2017). doi: 10.1038/nrg3207; pmid: 22868264
26. B. M. Nugent, C. M. O'Donnell, C. N. Epperson, T. L. Bale, Placental H3K27me3 establishes female resilience to prenatal insults. *Nat. Commun.* **9**, 2555 (2018). doi: 10.1038/s41467-018-04992-1; pmid: 29967448
27. D. Lau-Corona, W. K. Bae, L. Hennighausen, D. J. Waxman, Sex-biased genetic programs in liver metabolism and liver fibrosis are controlled by EZH1 and EZH2. bioRxiv [Preprint]. 14 March 2019. pmid: 577056
28. D. F. Deegan, N. Engel, Sexual Dimorphism in the Age of Genomics: How, When, Where. *Front. Cell Dev. Biol.* **7**, 186 (2019). doi: 10.3389/fcell.2019.00186; pmid: 31552249
29. S. Kim-Hellmuth *et al*., Cell type specific genetic regulation of gene expression across human tissues. *Science* **369**, eaaz8528 (2020).
30. Y. Chen *et al*., Difference in Leukocyte Composition between Women before and after Menopausal Age, and Distinct Sexual Dimorphism. *PLOS ONE* **11**, e0162953 (2016). doi: 10.1371/journal.pone.0162953; pmid: 27657912
31. E. Bongen *et al*., Sex Differences in the Blood Transcriptome Identify Robust Changes in Immune Cell Proportions with Aging and Influenza Infection. *Cell Rep.* **29**, 1961–1973.e4 (2019). doi: 10.1016/j.celrep.2019.10.019; pmid: 31722210
32. W. J. Astle *et al*., The Allelic Landscape of Human Blood Cell Trait Variation and Links to Common Complex Disease. *Cell* **167**, 1415–1429.e19 (2016). doi: 10.1016/j.cell.2016.10.042; pmid: 27863252
33. K. Rawlik, O. Canela-Xandri, A. Tenesa, Evidence for sex-specific genetic architectures across a spectrum of human complex traits. *Genome Biol.* **17**, 166 (2016). doi: 10.1186/s13059-016-1025-x; pmid: 27473438
34. D. Shungin *et al*., New genetic loci link adipose and insulin biology to body fat distribution. *Nature* **518**, 187–196 (2015). doi: 10.1038/nature14132; pmid: 25673412
35. S. L. Pulit *et al*., Meta-analysis of genome-wide association studies for body fat distribution in 694 649 individuals of European ancestry. *Hum. Mol. Genet.* **28**, 166–174 (2019). doi: 10.1093/hmg/ddy327; pmid: 30239722
36. J. Martin *et al*, Examining sex-differentiated genetic effects across neuropsychiatric and behavioral traits. bioRxiv [Preprint]. 5 May 2020. pmid: 076042
37. E. Porcu *et al*, The role of gene expression on human sexual dimorphism: Too early to call. bioRxiv [Preprint]. 17 April 2020. pmid: 042986
38. S. E. Castel *et al*, A vast resource of allelic expression data spanning human tissues. bioRxiv [Preprint]. 3 October 2019. pmid: 792911
39. D. A. Knowles *et al*., Allele-specific expression reveals interactions between genetic variation and environment. *Nat. Methods* **14**, 699–702 (2017). doi: 10.1038/nmeth.4298; pmid: 28530654
40. K. R. Kukurba *et al*., Impact of the X Chromosome and sex on regulatory variation. *Genome Res.* gr.197897.115 (2016). doi: 10.3389/fgene.2019.00313; pmid: 31024623
41. The GAIT2 Project; http://ugcd.github.io/pages/projects/gait2/.
42. J. J. Shen, Y.-F. Wang, W. Yang, Sex-Interacting mRNA- and miRNA-eQTLs and Their Implications in Gene Expression Regulation and Disease. *Front. Genet.* **10**, 313 (2019). doi: 10.3389/fgene.2019.00313; pmid: 31024623
43. C. Yao *et al*., Sex- and age-interacting eQTLs in human complex diseases. *Hum. Mol. Genet.* **23**, 1947–1956 (2014). doi: 10.1093/hmg/ddt582; pmid: 24242183
44. A. C. Leon, M. Heo, Sample Sizes Required to Detect Interactions between Two Binary Fixed-Effects in a Mixed-Effects Linear Regression Model. *Comput. Stat. Data Anal.* **53**, 603–608 (2009). doi: 10.1016/j.csda.2008.06.010; pmid: 20084090
45. K. Iida, V. Nussenzweig, Complement receptor is an inhibitor of the complement cascade. *J. Exp. Med.* **153**, 1138–1150 (1981). doi: 10.1084/jem.153.5.1138; pmid: 6910481
46. K. Dhanasekaran *et al*., Unraveling the role of aurora A beyond centrosomes and spindle assembly: Implications in muscle differentiation. *FASEB J.* **33**, 219–230 (2019). doi: 10.1096/fj.201800997; pmid: 29995440
47. A. Tang *et al*., Aurora kinases: Novel therapy targets in cancers. *Oncotarget* **8**, 23937–23954 (2017). doi: 10.18632/oncotarget.14893; pmid: 28147341
48. C. Giambartolomei *et al*., Bayesian test for colocalisation between pairs of genetic association studies using summary statistics. *PLOS Genet.* **10**, e1004383 (2014). doi: 10.1371/journal.pgen.1004383; pmid: 24830394
49. T. Zhan, N. Rindtorff, M. Boutros, Wnt signaling in cancer. *Oncogene* **36**, 1461–1473 (2017). doi: 10.1038/onc.2016.304; pmid: 27617575
50. D. Ly, D. Forman, J. Ferlay, L. A. Brinton, M. B. Cook, An international comparison of male and female breast cancer incidence rates. *Int. J. Cancer* **132**, 1918–1926 (2013). doi: 10.1002/ijc.27841; pmid: 22987302
51. X. Xu, Q. Yan, Y. Wang, X. Dong, NTN4 is associated with breast cancer metastasis via regulation of EMT-related biomarkers. *Oncol. Rep.* **37**, 449–457 (2017). doi: 10.3892/or.2016.5239; pmid: 27840993
52. M. M. Marjaneh *et al*, High-throughput allelic expression imbalance analyses identify candidate breast cancer risk genes. bioRxiv [Preprint]. 16 January 2019. pmid: 521013
53. J. D. Betteridge, S. P. Armbruster, C. Maydonovitch, G. R. Veerappan, Inflammatory bowel disease prevalence by age, gender, race, and geographic location in the U.S. military health care population. *Inflamm. Bowel Dis.* **19**, 1421–1427 (2013). doi: 10.1097/MIB.0b013e318281334d; pmid: 23518811
54. M. G. Hayes *et al*., Identification of HKDC1 and BACE2 as genes influencing glycemic traits during pregnancy through genome-wide association studies. *Diabetes* **62**, 3282–3291 (2013). doi: 10.2337/db12-1692; pmid: 23903356
55. T. Strunz *et al*., A mega-analysis of expression quantitative trait loci (eQTL) provides insight into the regulatory architecture of gene expression variation in liver. *Sci. Rep.* **8**, 5865 (2018). doi: 10.1007/s11892-015-0709-z; pmid: 26803651
56. W. L. Lowe Jr., D. M. Scholtens, V. Sandler, M. G. Hayes, Genetics of Gestational Diabetes Mellitus and Maternal Metabolism. *Curr. Diab. Rep.* **16**, 15 (2016). doi: 10.1007/s11892-015-0709-z; pmid: 26803651
57. C. Guo *et al*., Coordinated regulatory variation associated with gestational hyperglycaemia regulates expression of the novel hexokinase HKDC1. *Nat. Commun.* **6**, 6069 (2015). doi: 10.1038/ncomms7069; pmid: 25648650
58. H. Nagano *et al*., p53-inducible DPYSL4 associates with mitochondrial supercomplexes and regulates energy metabolism in adipocytes and cancer cells. *Proc. Natl. Acad. Sci. U.S.A.* **115**, 8370–8375 (2018). doi: 10.1073/pnas.1804243115; pmid: 30061407
59. B. J. Matthews, D. J. Waxman, CTCF and Cohesin link sex-biased distal regulatory elements to sex-biased gene expression in mouse liver. bioRxiv [Preprint]. 14 March 2019. pmid: 577577
60. G. Shieh, Effect size, statistical power, and sample size for assessing interactions between categorical and continuous variables. *Br. J. Math. Stat. Psychol.* **72**, 136–154 (2019). doi: 10.1111/bmsp.12147; pmid: 30468259
61. Y. Liu, A. Beyer, R. Aebersold, On the Dependency of Cellular Protein Levels on mRNA Abundance. *Cell* **165**, 535–550 (2016). doi: 10.1016/j.cell.2016.03.014; pmid: 27104977
62. A. M. Allen, T. S. Scheuermann, N. Nollen, D. Hatsukami, J. S. Ahluwalia, Gender Differences in Smoking Behavior and Dependence Motives Among Daily and Nondaily Smokers. *Nicotine Tob. Res.* **18**, 1408–1413 (2016). doi: 10.1093/ntr/ntv138; pmid: 26136526
63. C. W. Law, Y. Chen, W. Shi, G. K. Smyth, voom: Precision weights unlock linear model analysis tools for RNA-seq read counts. *Genome Biol.* **15**, R29 (2014). doi: 10.1186/gb-2014-15-2-r29; pmid: 24485249
64. S. M. Urbut, G. Wang, P. Carbonetto, M. Stephens, Flexible statistical methods for estimating and testing effects in genomic studies with multiple conditions. *Nat. Genet.* **51**, 187–195 (2019). doi: 10.1038/s41588-018-0268-8; pmid: 30478440
65. N. Kryuchkova-Mostacci, M. Robinson-Rechavi, A benchmark of gene expression tissue-specificity metrics. *Brief. Bioinform.* **18**, 205–214 (2017). pmid: 26891983
66. R. Suzuki, H. Shimodaira, pvclust: Hierarchical Clustering with P-Values via Multiscale Bootstrap Resampling (2015).
67. T. Galili, dendextend: An R package for visualizing, adjusting and comparing trees of hierarchical clustering. *Bioinformatics*

31, 3718–3720 (2015). doi: 10.1093/bioinformatics/btv428; pmid: 26209431
68. T. Chen, C. Guestrin, in *Proceedings of the 22nd ACM SIGKDD International Conference on Knowledge Discovery and Data Mining* (2016), pp. 785–794.
69. N. C. Sheffield, C. Bock, LOLA: Enrichment analysis for genomic region sets and regulatory elements in R and Bioconductor. *Bioinformatics* (2016); http://code.databio.org/LOLA.
70. A. A. Sergushichev, An algorithm for fast preranked gene set enrichment analysis using cumulative statistic calculation. bioRxiv [Preprint]. 20 June 2016. pmid: 060012
71. P. Shannon *et al.*, Cytoscape: A software environment for integrated models of biomolecular interaction networks. *Genome Res.* **13**, 2498–2504 (2003). doi: 10.1101/gr.1239303; pmid: 14597658
72. H. Ongen, A. Buil, A. A. Brown, E. T. Dermitzakis, O. Delaneau, Fast and efficient QTL mapper for thousands of molecular phenotypes. *Bioinformatics* **32**, 1479–1485 (2016). doi: 10.1093/bioinformatics/btv722; pmid: 26708335

ACKNOWLEDGMENTS

We thank the donors and their families for their generous gifts of biospecimens to the GTEx research project; the Genomics Platform at the Broad Institute for data generation; J. Struewing for his support and leadership of the GTEx project; B. H. F. Weber and T. Strunz for assistance with replicating the sb-eQTL for *HKDC1* in liver; D. Nicolae and L. Chen for advice on mediation analysis; J. Witkos for comments on an earlier version of the manuscript; M. Gloudemans for making the sex-stratified eQTL data available on LocusCompare (http://locuscompare.com/); D. Muehlschlegel for assistance with replicating sex-biased genes; E. Flynn for assistance in the interpretation of sex-biased gene expression patterns, and G. Hayes for providing GWAS summary statistics for maternal glycemic traits. The summary figure and Fig. 1 were partially generated using www.biorender.com, and M. Khan and C. Stolte contributed to the design. This work was completed in part with computational resources provided by the Center for Research Informatics at the University of Chicago and the Centre for Genomic Regulation. **Funding:** Supported by the Common Fund of the Office of the Director, U.S. National Institutes of Health, and by NCI, NHGRI, NHLBI, NIDA, NIMH, NIA, NIAID, and NINDS through NIH contracts HHSN261200800001E (Leidos Prime contract with NCI: A.M.S., D.E.T., N.V.R., J.A.M., L.S., M.E.B., L.Q., T.K., D.B., K.R., A.U.), 10XS170 (NDRI: W.F.L., J.A.T., G.K., A.M., S.S., R.H., G.Wal., M.J., M.Wa., L.E.B., C.J., J.W., B.R., M.Hu., K.M., L.A.S., H.M.G., M.Mo., L.K.B.), 10XS171 (Roswell Park Cancer Institute: B.A.F., M.T.M., E.K., B.M.G., K.D.R., J.B.), 10X172 (Science Care Inc.), 12ST1039 (IDOX), 10ST1035 (Van Andel Institute: S.D.J., D.C.R., D.R.V.), HHSN268201000029C (Broad Institute: F.A., G.G., K.G.A., A.V.S., Xiao. L., E.T., S.G., A.G., S.A., K.H.H., D.T.N., K.H., S.R.M., J.L.N.), 5U41HG009494 (F.A., G.G., K.G.A.), and through NIH grants R01 DA006227-17 (Univ. of Miami Brain Bank: D.C.M., D.A.D.), Supplement to University of Miami grant DA006227 (D.C.M., D.A.D.), R01 MH090941 (Univ. of Geneva), R01 MH090951 and R01 MH090937 (Univ. of Chicago), R01 MH090936 (Univ. of North Carolina–Chapel Hill), R01MH101814 (M.M-A., V.W., S.B.M., R.G., E.T.D., D.G-M., A.V.), U01HG007593 (S.B.M.), R01MH101822 (C.D.B.), U01HG007598 (M.O., B.E.S.), U01MH104393 (A.P.F.), extension H002371 to 5U41HG002371 (W.J.K.) as well as other funding sources: R01MH106842 (T.L., P.M., E.F., P.J.H.), R01HL142028 (T.L., Si.Ka., P.J.H.), R01GM122924 (T.L., S.E.C.), R01MH107666 (H.K.I.), P30DK020595 (H.K.I.), UM1HG008901 (T.L.), R01GM124486 (T.L.), R01HG010067 (Y.Pa.), R01HG002585 (G.Wan., M.St.), Gordon and Betty Moore Foundation GBMF 4559 (G.Wa., M.St.), 1K99HG009916-01 (S.E.C.), R01HG006855 (Se.Ka., R.E.H.), BIO2015-70777-P, Ministerio de Economía y Competitividad and FEDER funds (M.M-A., V.W., R.G., D.G-M.), la Caixa Foundation ID 100010434 under agreement LCF/BQ/SO15/52260001 (D.G-M.), NIH CTSA grant UL1TR002550-01 (P.M.), Marie-Skłodowska Curie fellowship H2020 Grant 706636 (S.K-H.), R35HG010718 (E.R.G.), FPU15/03635, Ministerio de Educación, Cultura y Deporte (M.M-A.), R01MH109905, 1R01HG010480 (A.Ba.), Searle Scholar Program (A.Ba.), R01HG008150 (S.B.M.), 5T32HG000044-22, NHGRI Institutional Training Grant in Genome Science (N.R.G.), EU IMI program (UE7-DIRECT-115317-1) (E.T.D., A.V.), FNS funded project RNA1 (31003A_149984) (E.T.D., A.V.), DK110919 (F.H.), F32HG009987 (F.H.), Massachusetts Lions Eye Research Fund Grant (A.R.H.), 2R01GM108711 (L.C.), R01MH101820 (B.E.S.), Supplement to R01MH101820 (E.A.K., P.E., B.E.S.), Consolidate Research Group. Generalitat de Catalunya SGR 1736 and CERCA program (A.M.-P., J.M.S.); Rhodes Trust and Natural Sciences and Engineering Research Council of Canada (A.J.P.). All CRG authors acknowledge the support of the Spanish Ministry of Science, Innovation and Universities to the EMBL partnership, the Centro de Excelencia Severo Ochoa and the CERCA Programme / Generalitat de Catalunya. The University of Chicago Center for Research Informatics is funded by the Biological Sciences Division at the University of Chicago with additional funding from NIH award UL1TR000430. **Author contributions:** B.E.S. conceived the study; M.O. and B.E.S. led the writing and editing of the manuscript and supplement; M.O. and B.E.S. coordinated analyses of all contributing authors; M.O., M.M.-A. and V.W. performed differential gene expression analysis; B.B., D.J.C., M.M.-A., M.O., and V.W. characterized effect sizes of sex-biased genes; M.M.-A and M.O., performed sex-biased genes replication in independent datasets, M.M.-A., M.O., and V.W. performed analysis of transcription factor binding sites; M.M.-A., M.O., and V.W. performed tissue clustering based on gene expression levels and sex bias; M.M.-A. built the expression-based sex classifier; Y.Z. performed *MASH* analyses; M.S. and S.K.-H. provided advice on MASH analysis; M.O. generated sb-eQTL pipelines and performed sb-eQTL mapping; F.A., B.B., A.J.B., B.E.E., E.E., P.E., E.R.G., S.K.-H., S.K., E.A.K., S.B.M., P.P., A.D.S., and B.E.S. contributed to sb-eQTL analysis approach; D.J.C., S.K.-H., E.A.K., M.O., and V.W. characterized sb-eGenes; F.A., B.B., and A.V. performed sb-eQTL replication analysis in external datasets; S.K.-H., A.M.-P., and J.-M.S. contributed to sb-eQTL replication analysis; S.K. performed ASE aFC validation of sb-eQTLs; S.E.C., S.K.-H., and P.M. contributed to ASE aFC validation of sb-eQTLs; P.P. performed EAGLE ASE validation of sb-eQTLs; A.J.B. and S.K.-H. provided advice on EAGLE ASE validation; S.K.-H. performed coloc analysis; M.O. performed mediation analysis; S.K.-H. and B.L.P. provided advice on mediation analysis; F.A., D.G., S.K.-H., D.J.C., M.O., M.M.-A., and V.W. generated figures; F.A., K.G.A., and A.V.S. generated and oversaw GTEx v8 data generation, LDACC, and pipelines; A.N.B., R.B., and H.K.I. generated GWAS data; F.A., S.K.-H., and M.O. generated cell type abundances and ieQTL data; S.K.-H., M.M.-A., and M.O. characterized sex differences in cell type abundances; M.M.-A. and V.W. characterized phenotype relationships with cell type abundances; A.B., A.D.H.G., A.R.H., E.A.K., A.J.P., B.E.E., D.G., E.R.G., S.K.-H., A.M.-P., F.R., and A.D.S. performed analysis or provided feedback that significantly shaped this work but was not included in this final version; M.M.-A. and V.W. managed data and code in the GitHub repository; A.J.B., B.E.E., E.T.D., R.G., H.K.I., T.L., S.B.M., B.L.P., M.S., A.V.S., and B.E.S. supervised the work of trainees in their labs; D.J.C., S.K., S.K.-H., M.M.-A., M.O., P.P., V.W., Y.Z., and B.E.S. wrote manuscript text; and B.B., A.J.B., B.E.E., A.D.H.G., R.G., S.K.-H., H.K.I., E.A.K., T.L., M.M.-A., M.O., S.B.M., L.C., S.K., P.P., B.L.P., A.D.S., B.E.S., A.V., and V.W. edited the manuscript. All authors read and approved the final manuscript. **Competing interests:** F.A. is an inventor on a patent application related to TensorQTL; S.E.C. is a co-founder, chief technology officer, and stock owner at Variant Bio; D.G.M. is co-founder with equity in Goldfinch Bio, and has received research support from AbbVie, Astellas, Biogen, BioMarin, Eisai, Merck, Pfizer, and Sanofi-Genzyme; E.A.K. is an employee of Janssen Pharmaceuticals; H.I. has received speaker honoraria from GSK and AbbVie; E.T.D. is chairman and member of the board of Hybridstat LTD; T.L. is a scientific advisory board member of Variant Bio with equity, and Goldfinch Bio. Other GTEx members: E.R.G. is on the Editorial Board of Circulation Research, and does consulting for the City of Hope / Beckman Research Institute; E.T.D. is chairman and member of the board of Hybridstat Ltd.; B.E.E. is on the scientific advisory boards of Celsius Therapeutics and Freenome; G.G. receives research funds from IBM and Pharmacyclics, and is an inventor on patent applications related to MuTect, ABSOLUTE, MutSig, MSMuTect, MSMutSig, POLYSOLVER, and TensorQTL. G.G. is a founder, consultant and holds privately held equity in Scorpion Therapeutics; S.B.M. is on the scientific advisory board of MyOme; P.F. is member of the scientific advisory boards of Fabric Genomics Inc., and Eagle Genomes Ltd. P.G.F. is a partner of Bioinf2Bio. **Data and materials availability:** All GTEx open-access data, including summary statistics of sex-biased genes and sex-biased eQTLs, are available on the GTEx Portal (https://gtexportal.org/home/datasets). Histological images and their annotations are also available on the portal (https://gtexportal.org/home/histologyPage). GTEx v8 sex-stratified eQTL data are available on LocusCompare (http://locuscompare.com/). All GTEx protected data are available via dbGaP (accession phs000424.v8). Access to the raw sequence data are now provided through the AnVIL platform (https://gtexportal.org/home/protectedDataAccess). Code for the sex-biased gene expression analysis is deposited at https://zenodo.org/record/3939042 (doi: 10.5281/zenodo.3939042).

SUPPLEMENTARY MATERIALS

science.sciencemag.org/content/369/6509/eaba3066/suppl/DC1
Materials and Methods
Figs. S1 to S10
Tables S1 to S15
References (*73*–*102*)

View/request a protocol for this paper from *Bio-protocol*.

GTEx Consortium Laboratory and Data Analysis Coordinating Center (LDACC): François Aguet[1], Shankara Anand[1], Kristin G. Ardlie[1], Stacey Gabriel[1], Gad A. Getz[1,2,3], Aaron Graubert[1], Kane Hadley[1], Robert E. Handsaker[4,5,6], Katherine H. Huang[1], Seva Kashin[4,5,6], Xiao Li[1], Daniel G. MacArthur[5,7], Samuel R. Meier[1], Jared L. Nedzel[1], Duyen T. Nguyen[1], Ayellet V. Segrè[1,8], Ellen Todres[1]
Analysis Working Group Funded by GTEx Project Grants: François Aguet[1], Shankara Anand[1], Kristin G. Ardlie[1], Brunilda Balliu[9], Alvaro N. Barbeira[10], Alexis Battle[11,12], Rodrigo Bonazzola[10], Andrew Brown[13,14], Christopher D. Brown[15], Stephane E. Castel[16,17], Donald F. Conrad[18,19], Daniel J. Cotter[20], Nancy Cox[21], Sayantan Das[22], Olivia M. de Goede[20], Emmanouil T. Dermitzakis[13,23,24], Jonah Einson[16,25], Barbara E. Engelhardt[26,27], Eleazar Eskin[28], Tiffany Y. Eulalio[29], Nicole M. Ferraro[29], Elise D. Flynn[16,17], Laure Fresard[30], Eric R. Gamazon[21,31,32,33], Diego Garrido-Martín[34], Nicole R. Gay[20], Gad A. Getz[1,2,3], Michael J. Gloudemans[29], Aaron Graubert[1], Roderic Guigó[34,35], Kane Hadley[1], Andrew R. Hame[8,1], Robert E. Handsaker[4,5,6], Yuan He[11], Paul J. Hoffman[16], Farhad Hormozdiari[1,36], Lei Hou[1,37], Katherine H. Huang[1], Hae Kyung Im[10], Brian Jo[26,27], Silva Kasela[16,17], Seva Kashin[4,5,6], Manolis Kellis[1,37], Sarah Kim-Hellmuth[16,17,38], Alan Kwong[22], Tuuli Lappalainen[16,17], Xiao Li[1], Xin Li[30], Yanyu Liang[10], Daniel G. MacArthur[5,7], Serghei Mangul[28,39], Samuel R. Meier[1], Pejman Mohammadi[16,17,40,41], Stephen B. Montgomery[20,30], Manuel Muñoz-Aguirre[34,42], Daniel C. Nachun[30], Jared L. Nedzel[1], Duyen T. Nguyen[1], Andrew B. Nobel[43], Meritxell Oliva[10,44], YoSon Park[15,45], Yongjin Park[1,37], Princy Parsana[12], Abhiram S. Rao[46], Ferran Reverter[47], John M. Rouhana[1,8], Chiara Sabatti[48], Ashis Saha[12], Ayellet V. Segrè[1,8], Andrew D. Skol[10,49], Matthew Stephens[50], Barbara E. Stranger[10,51], Benjamin J. Strober[11], Nicole A. Teran[30], Ellen Todres[1], Ana Viñuela[13,23,24,52], Gao Wang[50], Xiaoquan Wen[22], Fred Wright[53], Valentin Wucher[34], Yuxin Zou[54]
Analysis Working Group Not Funded by GTEx Project Grants: Pedro G. Ferreira[55,56,57,58], Gen Li[59], Marta Melé[60], Esti Yeger-Lotem[61,62]
Leidos Biomedical Project Management: Mary E. Barcus[63], Debra Bradbury[63], Tanya Krubit[63], Jeffrey A. McLean[63], Liqun Qi[63], Karna Robinson[63], Nancy V. Roche[63], Anna M. Smith[63], Leslie Sobin[63], David E. Tabor[63], Anita Undale[63]
Biospecimen Collection Source Sites: Jason Bridge[64], Lori E. Brigham[65], Barbara A. Foster[66], Bryan M. Gillard[66], Richard Hasz[67], Marcus Hunter[68], Christopher Johns[69], Mark Johnson[70], Ellen Karasik[66], Gene Kopen[71], William F. Leinweber[71], Alisa McDonald[71], Michael T. Moser[66], Kevin Myer[68], Kimberley D. Ramsey[66], Brian Roe[68], Saboor Shad[71], Jeffrey A. Thomas[71,70], Gary Walters[70], Michael Washington[70], Joseph Wheeler[69]
Biospecimen Core Resource: Scott D. Jewell[72], Daniel C. Rohrer[72], Dana R. Valley[72]
Brain Bank Repository: David A. Davis[73], Deborah C. Mash[73]
Pathology: Mary E. Barcus[63], Philip A. Branton[74], Leslie Sobin[63]
ELSI Study: Laura K. Barker[75], Heather M. Gardiner[75], Maghboeba Mosavel[76], Laura A. Siminoff[75]
Genome Browser Data Integration and Visualization: Paul Flicek[77], Maximilian Haeussler[78], Thomas Juettemann[77], W. James Kent[78], Christopher M. Lee[78], Conner C. Powell[78], Kate R. Rosenbloom[78], Magali Ruffier[77], Dan Sheppard[77], Kieron Taylor[77], Stephen J. Trevanion[77], Daniel R. Zerbino[77]
eGTEx Group: Nathan S. Abell[20], Joshua Akey[79], Lin Chen[44], Kathryn Demanelis[44], Jennifer A. Doherty[80], Andrew P. Feinberg[81], Kasper D. Hansen[82], Peter F. Hickey[83], Lei Hou[1,37], Farzana Jasmine[44], Lihua Jiang[20], Rajinder Kaul[84,85], Manolis Kellis[1,37], Muhammad G. Kibriya[44], Jin Billy Li[20], Qin Li[20], Shin Lin[86], Sandra E. Linder[20], Stephen B. Montgomery[20,30], Meritxell Oliva[10,44], Yongjin Park[1,37], Brandon L. Pierce[44], Lindsay F. Rizzardi[87], Andrew D. Skol[10,49], Kevin S. Smith[30], Michael Snyder[20], John Stamatoyannopoulos[84,88], Barbara E. Stranger[10,51], Hua Tang[20], Meng Wang[20]

NIH Program Management: Philip A. Branton[74], Latarsha J. Carithers[74,89], Ping Guan[74], Susan E. Koester[90], A. Roger Little[91], Helen M. Moore[74], Concepcion R. Nierras[92], Abhi K. Rao[74], Jimmie B. Vaught[74], Simona Volpi[93]

Affiliations
[1]Broad Institute of MIT and Harvard, Cambridge, MA, USA. [2]Cancer Center and Department of Pathology, Massachusetts General Hospital, Boston, MA, USA. [3]Harvard Medical School, Boston, MA, USA. [4]Department of Genetics, Harvard Medical School, Boston, MA, USA. [5]Program in Medical and Population Genetics, Broad Institute of MIT and Harvard, Cambridge, MA, USA. [6]Stanley Center for Psychiatric Research, Broad Institute of MIT and Harvard, Cambridge, MA, USA. [7]Analytic and Translational Genetics Unit, Massachusetts General Hospital, Boston, MA, USA. [8]Ocular Genomics Institute, Massachusetts Eye and Ear, Harvard Medical School, Boston, MA, USA. [9]Department of Biomathematics, University of California, Los Angeles, CA, USA. [10]Section of Genetic Medicine, Department of Medicine, The University of Chicago, Chicago, IL, USA. [11]Department of Biomedical Engineering, Johns Hopkins University, Baltimore, MD, USA. [12]Department of Computer Science, Johns Hopkins University, Baltimore, MD, USA. [13]Department of Genetic Medicine and Development, University of Geneva Medical School, Geneva, Switzerland. [14]Population Health and Genomics, University of Dundee, Dundee, Scotland, UK. [15]Department of Genetics, University of Pennsylvania, Perelman School of Medicine, Philadelphia, PA, USA. [16]New York Genome Center, New York, NY, USA. [17]Department of Systems Biology, Columbia University, New York, NY, USA. [18]Department of Genetics, Washington University School of Medicine, St. Louis, MO, USA. [19]Division of Genetics, Oregon National Primate Research Center, Oregon Health & Science University, Portland, OR, USA. [20]Department of Genetics, Stanford University, Stanford, CA, USA. [21]Division of Genetic Medicine, Department of Medicine, Vanderbilt University Medical Center, Nashville, TN, USA. [22]Department of Biostatistics, University of Michigan, Ann Arbor, MI, USA. [23]Institute for Genetics and Genomics in Geneva (iGE3), University of Geneva, Geneva, Switzerland. [24]Swiss Institute of Bioinformatics, Geneva, Switzerland. [25]Department of Biomedical Informatics, Columbia University, New York, NY, USA. [26]Department of Computer Science, Princeton University, Princeton, NJ, USA. [27]Center for Statistics and Machine Learning, Princeton University, Princeton, NJ, USA. [28]Department of Computer Science, University of California, Los Angeles, CA, USA. [29]Program in Biomedical Informatics, Stanford University School of Medicine, Stanford, CA, USA. [30]Department of Pathology, Stanford University, Stanford, CA, USA. [31]Data Science Institute, Vanderbilt University, Nashville, TN, USA. [32]Clare Hall, University of Cambridge, Cambridge, UK. [33]MRC Epidemiology Unit, University of Cambridge, Cambridge, UK. [34]Centre for Genomic Regulation (CRG), The Barcelona Institute for Science and Technology, Barcelona, Catalonia, Spain. [35]Universitat Pompeu Fabra (UPF), Barcelona, Catalonia, Spain. [36]Department of Epidemiology, Harvard T.H. Chan School of Public Health, Boston, MA, USA. [37]Computer Science and Artificial Intelligence Laboratory, Massachusetts Institute of Technology, Cambridge, MA, USA. [38]Statistical Genetics, Max Planck Institute of Psychiatry, Munich, Germany [39]Department of Clinical Pharmacy, School of Pharmacy, University of Southern California, Los Angeles, CA, USA. [40]Scripps Research Translational Institute, La Jolla, CA, USA. [41]Department of Integrative Structural and Computational Biology, The Scripps Research Institute, La Jolla, CA, USA. [42]Department of Statistics and Operations Research, Universitat Politècnica de Catalunya (UPC), Barcelona, Catalonia, Spain. [43]Department of Statistics and Operations Research and Department of Biostatistics, University of North Carolina, Chapel Hill, NC, USA. [44]Department of Public Health Sciences, The University of Chicago, Chicago, IL, USA. [45]Department of Systems Pharmacology and Translational Therapeutics, Perelman School of Medicine, University of Pennsylvania, Philadelphia, PA, USA. [46]Department of Bioengineering, Stanford University, Stanford, CA, USA. [47]Department of Genetics, Microbiology and Statistics, University of Barcelona, Barcelona, Spain. [48]Departments of Biomedical Data Science and Statistics, Stanford University, Stanford, CA, USA. [49]Department of Pathology and Laboratory Medicine, Ann & Robert H. Lurie Children's Hospital of Chicago, Chicago, IL, USA. [50]Department of Human Genetics, University of Chicago, Chicago, IL, USA. [51]Center for Genetic Medicine, Department of Pharmacology, Northwestern University, Feinberg School of Medicine, Chicago, IL, USA. [52]Department of Twin Research and Genetic Epidemiology, King's College London, London, UK. [53]Bioinformatics Research Center and Departments of Statistics and Biological Sciences, North Carolina State University, Raleigh, NC, USA. [54]Department of Statistics, University of Chicago, Chicago, IL, USA. [55]Department of Computer Sciences, Faculty of Sciences, University of Porto, Porto, Portugal. [56]Instituto de Investigação e Inovação em Saúde, University of Porto, Porto, Portugal. [57]Institute of Molecular Pathology and Immunology, University of Porto, Porto, Portugal. [58]Laboratory of Artificial Intelligence and Decision Support, Institute for Systems and Computer Engineering, Technology and Science, Porto, Portugal. [59]Mailman School of Public Health, Columbia University, New York, NY, USA. [60]Life Sciences Department, Barcelona Supercomputing Center, Barcelona, Spain. [61]Department of Clinical Biochemistry and Pharmacology, Ben-Gurion University of the Negev, Beer-Sheva, Israel. [62]National Institute for Biotechnology in the Negev, Beer-Sheva, Israel. [63]Leidos Biomedical, Rockville, MD, USA. [64]Upstate New York Transplant Services, Buffalo, NY, USA. [65]Washington Regional Transplant Community, Annandale, VA, USA. [66]Therapeutics, Roswell Park Comprehensive Cancer Center, Buffalo, NY, USA. [67]Gift of Life Donor Program, Philadelphia, PA, USA. [68]LifeGift, Houston, TX, USA. [69]Center for Organ Recovery and Education, Pittsburgh, PA, USA. [70]LifeNet Health, Virginia Beach, VA. USA. [71]National Disease Research Interchange, Philadelphia, PA, USA. [72]Van Andel Research Institute, Grand Rapids, MI, USA. [73]Department of Neurology, University of Miami Miller School of Medicine, Miami, FL, USA. [74]Biorepositories and Biospecimen Research Branch, Division of Cancer Treatment and Diagnosis, National Cancer Institute, National Institutes of Health, Bethesda, MD, USA. [75]College of Public Health, Temple University, Philadelphia, PA, USA. [76]Virginia Commonwealth University, Richmond, VA, USA. [77]European Molecular Biology Laboratory, European Bioinformatics Institute, Hinxton, UK. [78]Genomics Institute, University of California, Santa Cruz, CA, USA. [79]Carl Icahn Laboratory, Princeton University, Princeton, NJ, USA. [80]Department of Population Health Sciences, The University of Utah, Salt Lake City, UT, USA. [81]Departments of Medicine, Biomedical Engineering, and Mental Health, Johns Hopkins University, Baltimore, MD, USA. [82]Department of Biostatistics, Bloomberg School of Public Health, Johns Hopkins University, Baltimore, MD, USA. [83]Department of Medical Biology, The Walter and Eliza Hall Institute of Medical Research, Parkville, Victoria, Australia. [84]Altius Institute for Biomedical Sciences, Seattle, WA, USA. [85]Division of Genetics, University of Washington, Seattle, WA, USA. [86]Department of Cardiology, University of Washington, Seattle, WA, USA. [87]HudsonAlpha Institute for Biotechnology, Huntsville, AL, USA. [88]Genome Sciences, University of Washington, Seattle, WA, USA. [89]National Institute of Dental and Craniofacial Research, National Institutes of Health, Bethesda, MD, USA. [90]Division of Neuroscience and Basic Behavioral Science, National Institute of Mental Health, National Institutes of Health, Bethesda, MD, USA. [91]National Institute on Drug Abuse, Bethesda, MD, USA. [92]Office of Strategic Coordination, Division of Program Coordination, Planning and Strategic Initiatives, Office of the Director, National Institutes of Health, Rockville, MD, USA. [93]Division of Genomic Medicine, National Human Genome Research Institute, Bethesda, MD, USA.

25 November 2019; accepted 3 August 2020
10.1126/science.aba3066

RESEARCH ARTICLE SUMMARY

HUMAN GENOMICS

Cell type–specific genetic regulation of gene expression across human tissues

Sarah Kim-Hellmuth*, François Aguet, Meritxell Oliva, Manuel Muñoz-Aguirre, Silva Kasela, Valentin Wucher, Stephane E. Castel, Andrew R. Hamel, Ana Viñuela, Amy L. Roberts, Serghei Mangul, Xiaoquan Wen, Gao Wang, Alvaro N. Barbeira, Diego Garrido-Martín, Brian B. Nadel, Yuxin Zou, Rodrigo Bonazzola, Jie Quan, Andrew Brown, Angel Martinez-Perez, José Manuel Soria, GTEx Consortium, Gad Getz, Emmanouil T. Dermitzakis, Kerrin S. Small, Matthew Stephens, Hualin S. Xi, Hae Kyung Im, Roderic Guigó, Ayellet V. Segrè, Barbara E. Stranger, Kristin G. Ardlie, Tuuli Lappalainen*

INTRODUCTION: Efforts to map quantitative trait loci (QTLs) across human tissues by the GTEx Consortium and others have identified expression and splicing QTLs (eQTLs and sQTLs, respectively) for a majority of genes. However, these studies were largely performed with gene expression measurements from bulk tissue samples, thus obscuring the cellular specificity of genetic regulatory effects and in turn limiting their functional interpretation. Identifying the cell type (or types) in which a QTL is active will be key to uncovering the molecular mechanisms that underlie complex trait variation. Recent studies demonstrated the feasibility of identifying cell type–specific QTLs from bulk tissue RNA-sequencing data by using computational estimates of cell type proportions. To date, such approaches have only been applied to a limited number of cell types and tissues. By applying this methodology to GTEx tissues for a diverse set of cell types, we aim to characterize the cellular specificity of genetic effects across human tissues and to describe the contribution of these effects to complex traits.

RATIONALE: A growing number of in silico cell type deconvolution methods and associated reference panels with cell type–specific marker genes enable the robust estimation of the enrichment of specific cell types from bulk tissue gene expression data. We benchmarked and used enrichment estimates for seven cell types (adipocytes, epithelial cells, hepatocytes, keratinocytes, myocytes, neurons, and neutrophils) across 35 tissues from the GTEx project to map QTLs that are specific to at least one cell type. We mapped such cell type–interaction QTLs for expression and splicing (ieQTLs and isQTLs, respectively) by testing for interactions between genotype and cell type enrichment.

RESULTS: Using 43 pairs of tissues and cell types, we found 3347 protein-coding and long intergenic noncoding RNA (lincRNA) genes with an ieQTL and 987 genes with an isQTL (at 5% false discovery rate in each pair). To validate these findings, we tested the QTLs for replication in available external datasets and applied an independent validation using allele-specific expression from eQTL heterozygotes. We analyzed the cell type–interaction QTLs for patterns of tissue sharing and found that ieQTLs are enriched for genes with tissue-specific eQTLs and are generally not shared across unrelated tissues, suggesting that tissue-specific eQTLs originate in tissue-specific cell types. Last, we tested the ieQTLs and isQTLs for colocalization with genetic associations for 87 complex traits. We show that cell type–interaction QTLs are enriched for complex trait associations and identify colocalizations for hundreds of loci that were undetected in bulk tissue, corresponding to an increase of >50% over colocalizations with standard QTLs. Our results also reveal the cellular specificity and potential origin for a similar number of colocalized standard QTLs.

CONCLUSION: The ieQTLs and isQTLs identified for seven cell types across GTEx tissues suggest that the large majority of cell type–specific QTLs remains to be discovered. Our colocalization results indicate that comprehensive mapping of cell type–specific QTLs will be highly valuable for gaining a mechanistic understanding of complex trait associations. We anticipate that the approaches presented here will complement studies mapping QTLs in single cells. ■

The list of author affiliations and a full list of the GTEx authors and their affiliations are available in the full article online.
*Corresponding author. Email: skimhellmuth@gmail.com (S.K.-H.); tlappalainen@nygenome.org (T.L.)
Cite this article as S. Kim-Hellmuth *et al.*, *Science* **369**, eaaz8528 (2020). DOI: 10.1126/science.aaz8528

READ THE FULL ARTICLE AT
https://doi.org/10.1126/science.aaz8528

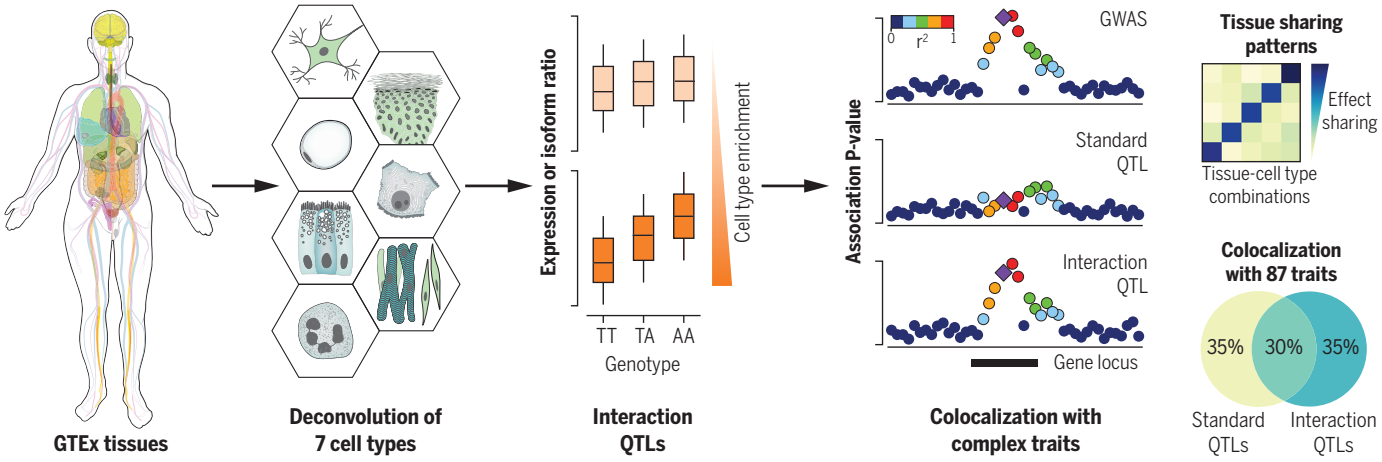

Detection of cell type–specific effects on gene expression. The enrichment of seven cell types is calculated across GTEx tissues, enabling mapping of cell type–interaction QTLs for expression and splicing by testing for significant interactions between genotypes and cell type enrichments. Linking these QTLs to complex trait associations enables discovery of >50% more colocalizations compared with standard QTLs and reveals the cellular specificity of traits.

RESEARCH ARTICLE

HUMAN GENOMICS

Cell type–specific genetic regulation of gene expression across human tissues

Sarah Kim-Hellmuth[1,2,3]*†‡, François Aguet[4]†, Meritxell Oliva[5,6], Manuel Muñoz-Aguirre[7,8], Silva Kasela[2,3], Valentin Wucher[7], Stephane E. Castel[2,3], Andrew R. Hamel[4,9], Ana Viñuela[10,11,12,13], Amy L. Roberts[10], Serghei Mangul[14,15], Xiaoquan Wen[16], Gao Wang[17], Alvaro N. Barbeira[5], Diego Garrido-Martín[7], Brian B. Nadel[18], Yuxin Zou[19], Rodrigo Bonazzola[5], Jie Quan[20], Andrew Brown[11,21], Angel Martinez-Perez[22], José Manuel Soria[22], GTEx Consortium§, Gad Getz[4,23,24], Emmanouil T. Dermitzakis[11,12,13], Kerrin S. Small[10], Matthew Stephens[17], Hualin S. Xi[25], Hae Kyung Im[5], Roderic Guigó[7,26], Ayellet V. Segrè[4,9], Barbara E. Stranger[5,27], Kristin G. Ardlie[4], Tuuli Lappalainen[2,3]*

The Genotype-Tissue Expression (GTEx) project has identified expression and splicing quantitative trait loci in cis (QTLs) for the majority of genes across a wide range of human tissues. However, the functional characterization of these QTLs has been limited by the heterogeneous cellular composition of GTEx tissue samples. We mapped interactions between computational estimates of cell type abundance and genotype to identify cell type–interaction QTLs for seven cell types and show that cell type–interaction expression QTLs (eQTLs) provide finer resolution to tissue specificity than bulk tissue cis-eQTLs. Analyses of genetic associations with 87 complex traits show a contribution from cell type–interaction QTLs and enables the discovery of hundreds of previously unidentified colocalized loci that are masked in bulk tissue.

The Genotype-Tissue Expression (GTEx) project (*1*) and other studies (*2*–*5*) have shown that genetic regulation of the transcriptome is widespread. The GTEx Consortium in particular has built an extensive catalog of expression and splicing quantitative trait loci in cis (cis-eQTLs and cis-sQTLs, respectively) across a large range of tissues, showing that these cis-eQTLs and cis-sQTLs (collectively referred to here as QTLs) are generally either highly tissue specific or widely shared, even across dissimilar tissues and organs (*1*, *6*). However, the majority of these studies have been performed by using heterogeneous bulk tissue samples comprising diverse cell types. This limits the power, interpretation, and downstream applications of QTL studies. Genetic effects that are active only in rare cell types within a sampled tissue may be undetected, a mechanistic interpretation of QTL sharing across tissues and other contexts is complicated without understanding differences in cell type composition, and inference of downstream molecular effects of regulatory variants without the specific cell type context is challenging. Efforts to map eQTLs in individual cell types have been largely restricted to blood, using purified cell types (*7*–*11*) or single-cell sequencing (*12*).

Although there are many ongoing efforts to optimize single-cell and single-nucleus sequencing of human tissues (*13*, *14*), including as part of the Human Cell Atlas (*15*), these methods are not yet scalable to sample sizes and coverage sufficient to achieve power comparable with that of bulk eQTL studies (*16*–*18*). However, cell type–specific eQTLs can be computationally inferred from bulk tissue measurements by using estimated proportions or enrichments of relevant cell types to test for interactions with genotype. To date, such approaches have only been applied to a limited range of cell types, such as blood cells (*19*, *20*) and adipocytes (*21*). These studies identified thousands of cell type interactions in eQTLs discovered in whole-blood samples from large cohorts [5683 samples, (*19*); 2116 samples, (*20*)], indicating that large numbers of interactions are likely to be identified by expanding this type of analysis to other tissues and cell types.

Identifying cell types in silico in bulk tissue

We used computational estimates of cell type enrichment to characterize the cell type specificity of cis-eQTLs and cis-sQTLs for 43 cell type–tissue combinations, using seven cell types across 35 tissues (Fig. 1A). Estimating the cell type composition of a tissue biospecimen from RNA-sequencing (RNA-seq) remains a challenging problem (*22*), and multiple approaches for inferring cell type proportions have been proposed (*23*). We performed extensive benchmarking for multiple cell types across several expression datasets (figs. S1 and S2). The xCell method (*24*), which estimates the enrichment of 64 cell types using reference profiles, was most suitable on the combined basis of correlation with cell counts in blood (fig. S1A), in silico simulations (fig. S1B), correlation with expression of marker genes for each cell type (fig. S1, C and D), and diversity of reference cell types. Concordance between methods was generally high (fig. S1, A and E). Furthermore, the inferred abundances reflected differences in histology (fig. S1C) and tissue pathologies (fig. S2). For each cell type, we selected tissues where the cell type was highly enriched (fig. S3). The xCell scores for these tissue–cell type pairs were highly correlated with the probabilistic estimation of expression residuals (PEER) factors used to correct for unobserved confounders in the expression data for QTL mapping (fig. S4A) (*1*) but were generally weakly correlated with known technical confounders (fig. S4B), suggesting that cell type composition accounts for a large fraction of intersample variation in gene expression.

Mapping cell type–interaction eQTLs and sQTLs

To identify cis-eQTLs and cis-sQTLs whose effect varies depending on the enrichment of the cell type, we leveraged the variability in cell type composition across GTEx samples

[1]Statistical Genetics, Max Planck Institute of Psychiatry, Munich, Germany. [2]New York Genome Center, New York, NY, USA. [3]Department of Systems Biology, Columbia University, New York, NY, USA. [4]The Broad Institute of MIT and Harvard, Cambridge, MA, USA. [5]Section of Genetic Medicine, Department of Medicine, University of Chicago, Chicago, IL, USA. [6]Department of Public Health Sciences, University of Chicago, Chicago, IL, USA. [7]Centre for Genomic Regulation (CRG), The Barcelona Institute for Science and Technology, Barcelona, Catalonia, Spain. [8]Department of Statistics and Operations Research, Universitat Politècnica de Catalunya (UPC), Barcelona, Catalonia, Spain. [9]Ocular Genomics Institute, Massachusetts Eye and Ear, Harvard Medical School, Boston, MA, USA. [10]Department of Twin Research and Genetic Epidemiology, King's College London, London, UK. [11]Department of Genetic Medicine and Development, University of Geneva Medical School, Geneva, Switzerland. [12]Institute for Genetics and Genomics in Geneva (iGE3), University of Geneva, Geneva, Switzerland. [13]Swiss Institute of Bioinformatics, Geneva, Switzerland. [14]Department of Computer Science, University of California, Los Angeles, Los Angeles, CA, USA. [15]Department of Clinical Pharmacy, School of Pharmacy, University of Southern California, Los Angeles, Los Angeles, CA, USA. [16]Department of Biostatistics, University of Michigan, Ann Arbor, MI, USA. [17]Department of Human Genetics, University of Chicago, Chicago, IL, USA. [18]Department of Molecular, Cellular, and Developmental Biology, University of California, Los Angeles, Los Angeles, CA, USA. [19]Department of Statistics, University of Chicago, Chicago, IL, USA. [20]Inflammation & Immunology, Pfizer, Cambridge, MA, USA. [21]Population Health and Genomics, University of Dundee, Dundee, Scotland, UK. [22]Unit of Genomic of Complex Diseases, Institut d'Investigació Biomèdica Sant Pau (IIB-Sant Pau), Barcelona. Spain. [23]Cancer Center and Department of Pathology, Massachusetts General Hospital, Boston, MA, USA. [24]Harvard Medical School, Boston, MA, USA. [25]Foundational Neuroscience Center, AbbVie, Cambridge, MA, USA. [26]Universitat Pompeu Fabra (UPF), Barcelona, Catalonia, Spain. [27]Center for Genetic Medicine, Department of Pharmacology, Northwestern University, Feinberg School of Medicine, Chicago, IL, USA.

***Corresponding author. Email: skimhellmuth@gmail.com (S.K.-H.); tlappalainen@nygenome.org (T.L.)** †These authors contributed equally to this work. ‡Present address: Department of Pediatrics, Dr. von Hauner Children's Hospital, University Hospital LMU Munich, Munich, Germany. §A full list of the GTEx authors and their affiliations is available at the end of this article.

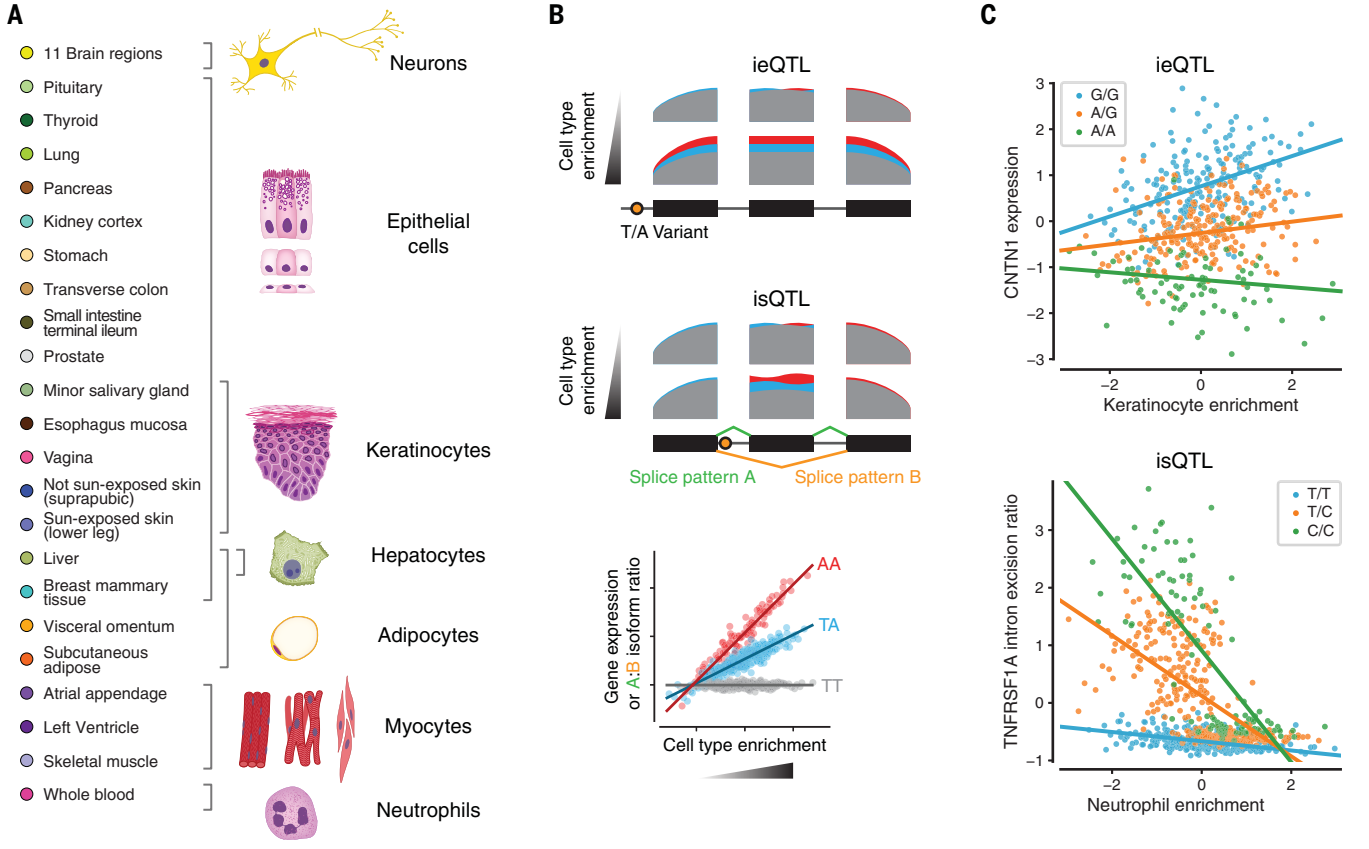

Fig. 1. Study design of mapping cell type ieQTLs and isQTLs in this study. (**A**) Illustration of 43 cell type–tissue pairs included in the GTEx v8 project. The full list of tissues included in the GTEx v8 project is provided in (*1*); two brain regions (frontal cortex and cerebellum) were sampled in replicates. Cell types with median xCell enrichment score >0.1 within a tissue were used (fig. S2). (**B**) Schematic representation of a cell type–interaction eQTL and sQTL. RNA-seq coverage is depicted in gray, blue, and red, representing different genotypes. Differences in coverage between genotypes, corresponding to a QTL effect, are only observed with high cell type enrichment. The scatter plot illustrates the regression model used to identify iQTLs, where the dots indicate individual samples. (**C**) Example cell type ieQTL and isQTL. (Top) The *CNTN1* eQTL effect in skin unexposed to the Sun is associated with keratinocyte abundance ($P = 4.1 \times 10^{-19}$;). (Bottom) The *TNFRSF1A* sQTL effect in whole blood is associated with neutrophil abundance but is only detected in samples with lower neutrophil abundances ($P = 6.7 \times 10^{-78}$). Each data point represents an individual and is colored by genotype. Cell type enrichment scores and gene expression were inverse normal transformed, and intron excision ratios were standardized. The regression lines from the interaction model illustrate how the QTL effect is modulated by cell type enrichment.

to test for an interaction between cell type and genotype using a linear regression model for either gene expression or splicing (Fig. 1, B and C, and fig. S5, A and B) (*25*). Because QTLs identified this way are not necessarily specific to the estimated cell type but may reflect another correlated (or anticorrelated) cell type, we refer to these eQTLs and sQTLs as cell type–interaction eQTLs (ieQTLs) and cell type–interaction sQTLs (isQTLs), respectively (or iQTLs in aggregate).

Across cell types and tissues, we detected 3347 protein coding and long intergenic noncoding RNA (lincRNA) genes with an ieQTL [ieGenes (*26*)] and 987 genes with an isQTL (isGenes) at 5% false discovery rate (FDR) per cell type–tissue combination (Fig. 2A, figs. S5C and S6, and table S1). In the following analyses, we used ieQTLs and isQTLs identified with 5% FDR unless indicated otherwise. Whereas 85% of ieQTLs corresponded to genes with at least one standard cis-eQTL [eGenes; we refer to cis-eQTLs mapped in bulk tissue as standard eQTLs for simplicity (*26*)], 21% of these ieQTLs were not in linkage disequilibrium (LD) [coefficient of determination (R^2) < 0.2] with any of the corresponding eGene's conditionally independent eQTLs (fig. S7, A and B) (*1*). For comparison, the proportion of genes with at least one standard eQTL varies as a function of sample size (*1*), with a median of 42% across tissues (48% in transverse colon and 63% in whole blood). This indicates that ieQTL analysis frequently reveals genetic regulatory effects that are not detected with standard eQTL analysis of heterogeneous tissue samples. Unlike standard cis-QTL discovery, iQTL discovery was only modestly correlated with sample size (Spearman's ρ = 0.53 and 0.35, for ieQTLs and isQTLs, respectively) (fig. S7, C and D). The tissues with most iQTLs included blood, as well as transverse colon and breast, which both stratified into at least two distinct groups on the basis of histology (*27*): epithelial versus adipose tissue (breast) and mucosal versus muscular tissue (colon) (fig. S1C). This suggests that interindividual variance (which partially reflects variation in biospecimen collection) in cell type enrichment driven by tissue heterogeneity is a major determinant in discovery power and benefits iQTL mapping despite being a potential confounding factor for other types of gene expression analyses. Down-sampling analyses in whole blood and transverse colon revealed linear relationships between sample size and ieQTL discovery in these tissues, suggesting that considerably larger numbers of ieQTLs may be discovered with larger sample sizes (fig. S7E). ieQTL discovery was largely robust to the choice of deconvolution method, with ~77% of neutrophil ieQTLs detected with xCell also detected with CIBERSORT, and close to complete replication

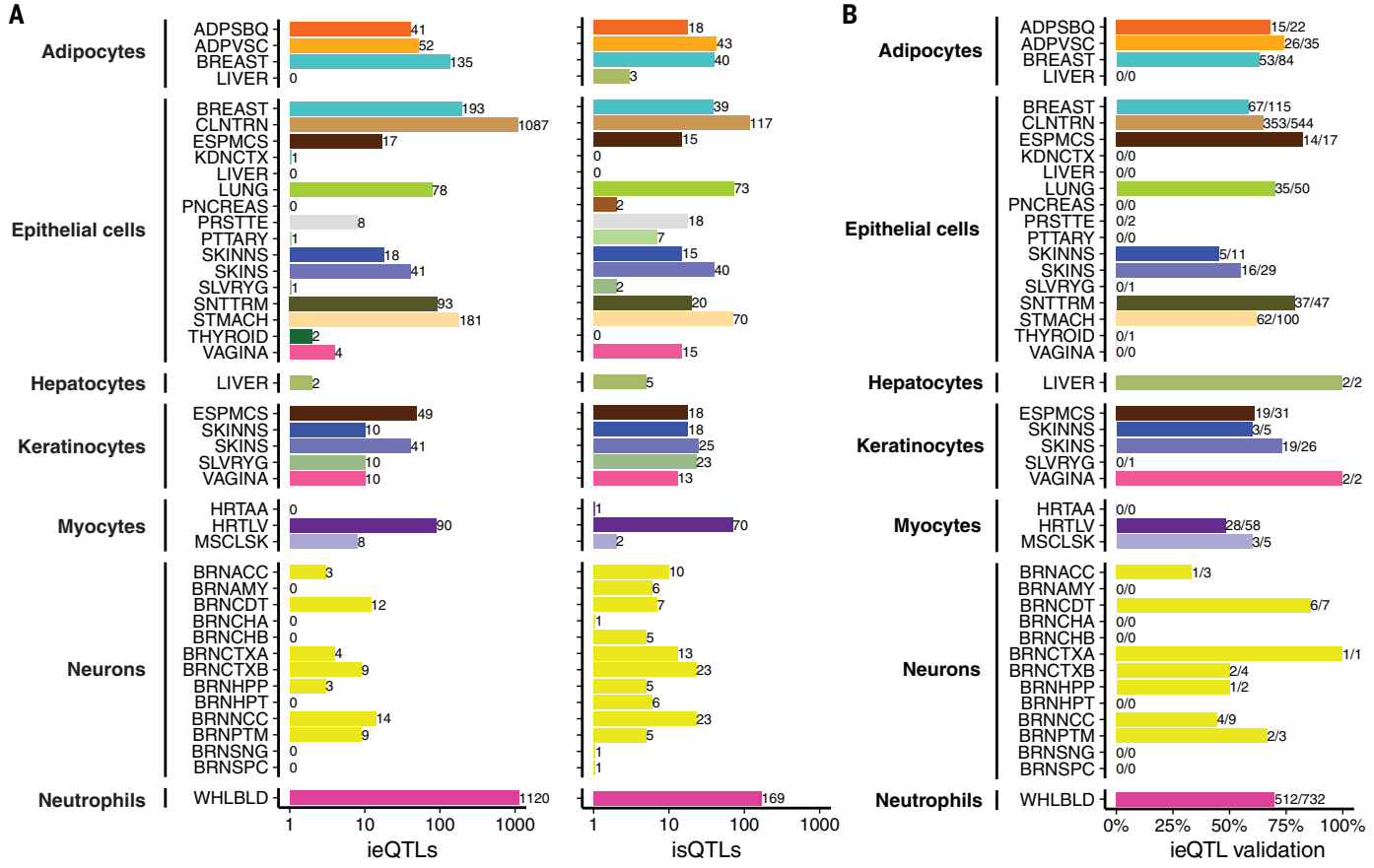

Fig. 2. Cell type ieQTL and isQTL discovery. (**A**) Number of cell type ieQTLs (left) and isQTLs (right) discovered in each cell type–tissue combination at FDR < 5%. Bar labels show the number of ieQTLs and isQTLs, respectively. The color key for the tissues is the same as that of Fig. 1A. (**B**) Proportion of cell type ieQTLs that validated in ASE data. Validation was defined as ieQTLs for which the Pearson correlation between aFC estimates from ASE and cell type estimates was nominally significant (P < 0.05). Tissue abbreviations are provided in table S2. Bar labels indicate the number of ieQTLs with validation per number of ieQTLs tested.

[π_1 > 0.99, where π_1 is the proportion of true positives (*28*)] (fig. S7F).

The QTL effect of ieQTLs and isQTLs can increase or decrease as a function of cell type enrichment (Fig. 1C and fig. S8A). This correlation is usually positive (56%; median across cell type–tissue combinations). As an example, a keratinocyte ieQTL for contactin 1 (*CNTN1*) in skin had a stronger effect in samples with high enrichment of keratinocytes. However, for some ieQTLs the effect was negatively correlated (19%), suggesting that the interaction we identified likely captures an eQTL that is only active in at least one other cell type (fig. S8B). For 24% of ieQTLs, the correlation was ambiguous. At a more stringent FDR cutoff (FDR < 0.01), the median proportion of ieQTLs with ambiguous cell type correlation decreased to 11% (fig. S8B, right), whereas the proportion of ieQTLs with positive correlation increased to 77%. Moreover, the ieQTLs with ambiguous direction tended to have lower minor allele frequency (MAF) (fig. S8C), suggesting that at less stringent FDR, this category might be enriched for false positives.

Altogether, we identified numerous cell type ieQTLs and isQTLs across 43 cell type–tissue combinations, including iQTLs that are not detected with standard eQTLs analysis in bulk tissue. These cell type iQTLs pinpoint the cellular specificity of QTLs that might not necessarily be specific to the tested cell type but may also capture eQTL effects of correlated (or anticorrelated) cell types.

Validation and replication of cell type iQTLs

Because few external replication datasets exist, we used allele-specific expression (ASE) data of eQTL heterozygotes (*29*, *30*) to correlate individual-level quantifications of the eQTL effect size [measured as allelic fold-change (aFC)] with individual-level cell type enrichments. If the eQTL is active in the cell type of interest, we expect to see low aFC in individuals with low cell type abundance and higher aFC in individuals with high cell type abundance (fig. S9). The correlation between cell type abundance and aFC across heterozygous individuals can thus be used as a measure of validation for a specific ieQTL.

Using this approach, the median proportion of ieQTLs with a significant (P < 0.05) aFC–cell type Pearson correlation was 0.62 (Fig. 2B). For 13 cell type–tissue combinations with >20 significant ieQTLs, the corresponding π_1 statistic (*28*) confirmed the high validation rate (mean π_1 = 0.75) (fig. S10). Although this approach does not constitute formal replication in an independent cohort, it is applicable to all tested cell type–tissue combinations and corroborates that ieQTLs are not statistical artifacts of the interaction model.

Next, we performed replication analyses in external cohorts, including whole blood from the GAIT2 study (*31*), purified neutrophils (*9*), adipose and skin tissues from the TwinsUK study for ieQTLs (*5*), and temporal cortex from the Mayo RNA sequencing study for both ieQTLs and isQTLs (*32*). Replication rates ranged from π_1 = 0.32 to 0.67, with the highest rate observed in purified neutrophils for whole blood (fig. S11). The differences in replication rate likely reflect a combination of lower power to detect cell type ieQTLs/isQTLs compared with standard eQTLs/sQTLs, as well as differences in tissue heterogeneity across studies. Taken together, these results show that ieQTLs and isQTLs can be detected with

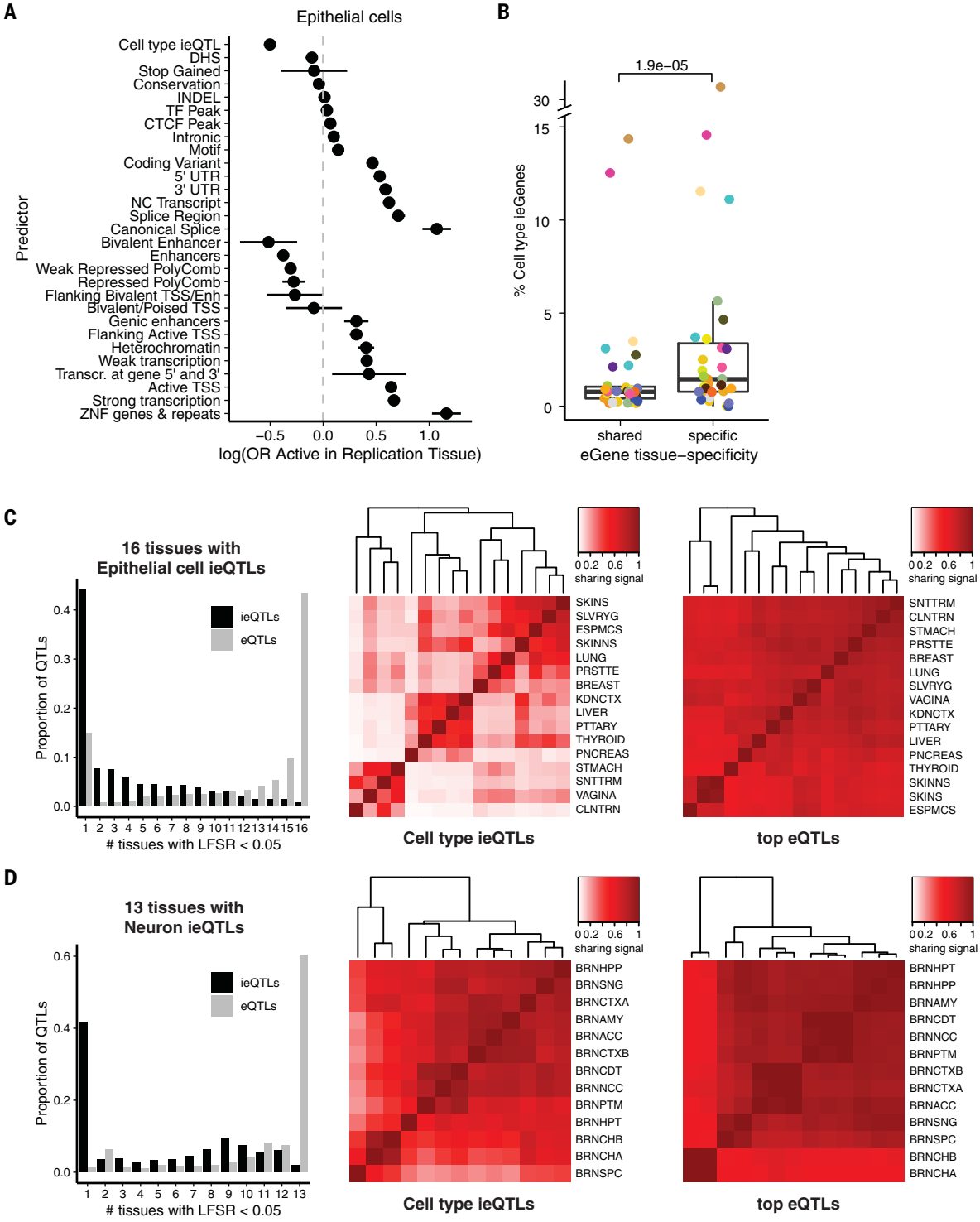

Fig. 3. Cell type ieQTLs contribute to cis-eQTL tissue specificity. (**A**) Coefficients from logistic regression models of cis-eQTL tissue sharing, where epithelial cell ieQTL status is one of the predictors: All significant top cis-eQTLs per tissue were annotated according to whether they were also a significant ieQTL for a given cell type. The coefficients represent the log(odds ratio) that an eQTL is active in a replication tissue given a predictor. Chromatin states were defined by using matched Epigenomics Roadmap tissues and the 15-state ChromHMM (*37*). Genomic annotations, conservation, and overlaps with Ensembl regulatory build transcription factor (TF), CCCTC-binding factor (CTCF), and deoxyribonuclease hypersensitivity site (DHS) peaks are also included. Bars represent the 95% confidence interval. (**B**) Proportion of cell type ieQTL genes (ieGenes) among tissue-specific and tissue-shared eGenes. An eGene is considered tissue specific if its eQTL had a MASH LFSR (equivalent to FDR) < 0.05 only in the cell type ieQTL tissue (or tissue type), otherwise it is considered tissue-shared. Results of all 43 cell type–tissue combinations are shown. The color key for the tissues is the same as that of Fig. 1A. (**C** and **D**) (Left) Tissue activity of cell type ieQTLs and eQTLs, where a cell type ieQTL and eQTL was considered active in a tissue if it had an LFSR < 0.05. (Middle and right) Pairwise tissue-sharing of (middle) ieQTLs or (right) lead standard cis-eQTLs. The color-coded sharing signal is the proportion of significant QTLs (LFSR < 0.05) that are shared in magnitude (within a factor of 2) and sign between two tissues.

reasonable robustness for diverse cell types and tissues.

Cell type ieQTLs contribute to tissue specificity

Next, we sought to determine to what extent cell type ieQTLs contribute to the tissue specificity of cis-eQTLs. First, we analyzed ieQTL sharing across cell types, observing that ieQTLs for one cell type were generally not ieQTLs for other cell types (for example, myocyte ieQTLs in muscle tissues were not hepatocyte ieQTLs in liver) (fig. S12A). To determine whether a significant cell type interaction effect is associated with the tissue specificity of an eQTL, we tested whether cell type ieQTLs are predictors of tissue sharing. We annotated the top cis-eQTLs per gene across tissues with their cell type ieQTL status for the five cell types with at least 20 ieQTLs (adipocytes, epithelial cells, keratinocytes, myocytes, and neutrophils). This annotation was included as a predictor in a logistic regression model of eQTL tissue sharing on the basis of eQTL properties, including effect size, minor allele frequency, eGene expression correlation, genomic annotations, and chromatin state (*1*). In all five cell types, ieQTL status was a strong negative predictor of tissue sharing, with the magnitude of the effect similar to that of enhancers, indicating that ieQTLs are an important mechanism for tissue-specific regulation of gene expression (Fig. 3A and fig. S12B). Testing whether cell type isQTLs are predictors of tissue sharing for four cell types with at least 20 isQTLs (adipocytes, epithelial cells, myocytes, and neutrophils) revealed only neutrophil isQTL status as a significant negative predictor (fig. S13). This is likely due to a combination of lower power to detect isQTLs and higher likelihood of splicing-affecting variants having shared effects if a gene is expressed in a tissue or cell type (*1*).

We corroborated the finding for ieQTLs using multitissue eQTL mapping with MASH (*1*), testing whether eGenes that are tissue specific [eQTLs discovered at local false sign rate (LFSR) < 0.05 only in the tissue type of interest] have a higher proportion of cell type ieQTLs compared with eGenes that are shared across tissues (LFSR < 0.05 in multiple tissues). The proportion of cell type ieQTLs across all 43 cell type–tissue combinations was significantly higher in tissue-specific eGenes as compared with tissue-shared eGenes ($P = 1.9 \times 10^{-05}$, one-sided Wilcoxon rank sum test) (Fig. 3B), further highlighting the contribution of cell type–specific genetic gene regulation to tissue specificity of eQTLs. For tissues with notably high intersample heterogeneity (such as breast, transverse colon, and stomach), the above-average enrichment is likely at least partially driven by higher power to detect ieQTLs.

To examine the sharing patterns of cell type ieQTLs across tissues, we used two cell types with ieQTLs mapped in >10 tissues (16 tissues for epithelial cells and 13 for neurons). We observed that although standard eQTLs were highly shared across the subsets of 16 and 13 tissues, cell type ieQTLs tended to be highly tissue specific, reflected by an average of four and five tissues with shared ieQTL effects compared with 11 and 12 for eQTLs in epithelial and brain tissues, respectively (Fig. 3, C and D, left). These findings were robust to power differences in detecting eQTLs versus ieQTLs, with eQTLs remaining predominantly shared even when limited to 20% of samples (fig. S14). Of neuron ieQTLs, 25.3% were shared between nine brain tissues, highlighting that tissues of the cerebrum (such as the cortex, basal ganglia, and limbic system) show particularly high levels of sharing

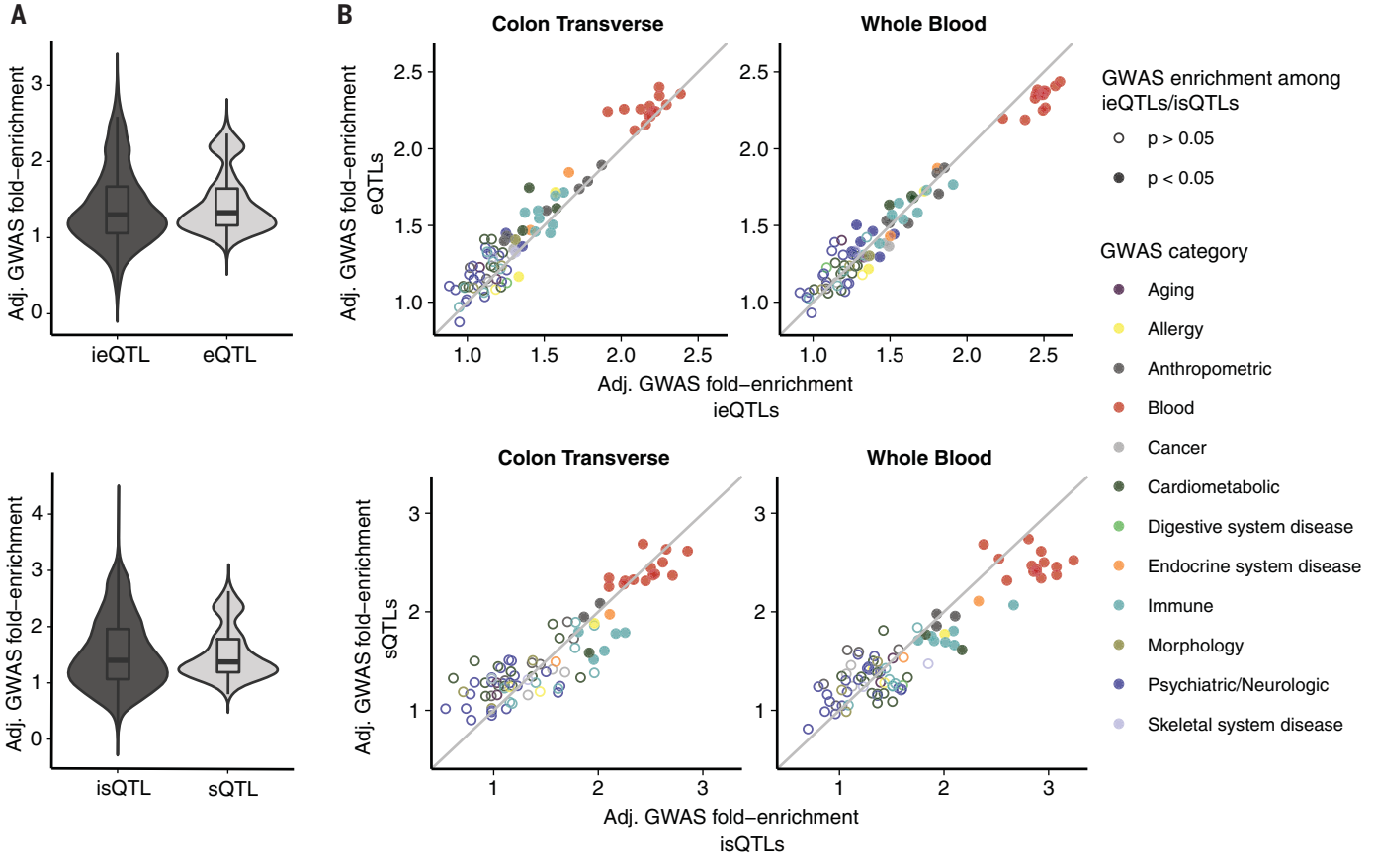

Fig. 4. Cell type iQTLs are enriched for GWAS signals. (**A**) Distribution of adjusted GWAS fold-enrichment of (top) 23×87 and (bottom) 7×87 tissue-trait combinations using the most significant iQTL or standard QTL per eGene or sGene. (**B**) Adjusted GWAS fold-enrichments of 87 GWAS traits among iQTLs on the *x* axis and standard QTLs on the *y* axis. Solid circles indicate significant GWAS enrichment among iQTLs at $P < 0.05$ (Bonferroni-corrected). Colors represent GWAS categories of the 87 GWAS traits (table S3).

compared with that of cerebellar tissues, the hypothalamus, and the spinal cord (Fig. 3D, left). This pattern was absent when analyzing standard eQTLs. Pairwise tissue sharing comparisons further confirmed that cell type ieQTLs showed greater tissue specificity and more diverse tissue sharing patterns than those of standard eQTLs, which were broadly shared across all tissues (Fig. 3, C and D, middle and right). These results show that incorporating cell type composition is essential for characterizing the sharing of genetic regulatory effects across tissues.

GWAS and tissue-specific eQTLs and sQTLs

To study the contribution of cell type–interaction QTLs to genome-wide association study (GWAS) results for 87 complex traits, we first examined the enrichment of iQTLs of each cell type–tissue combination for trait associations (GWAS,

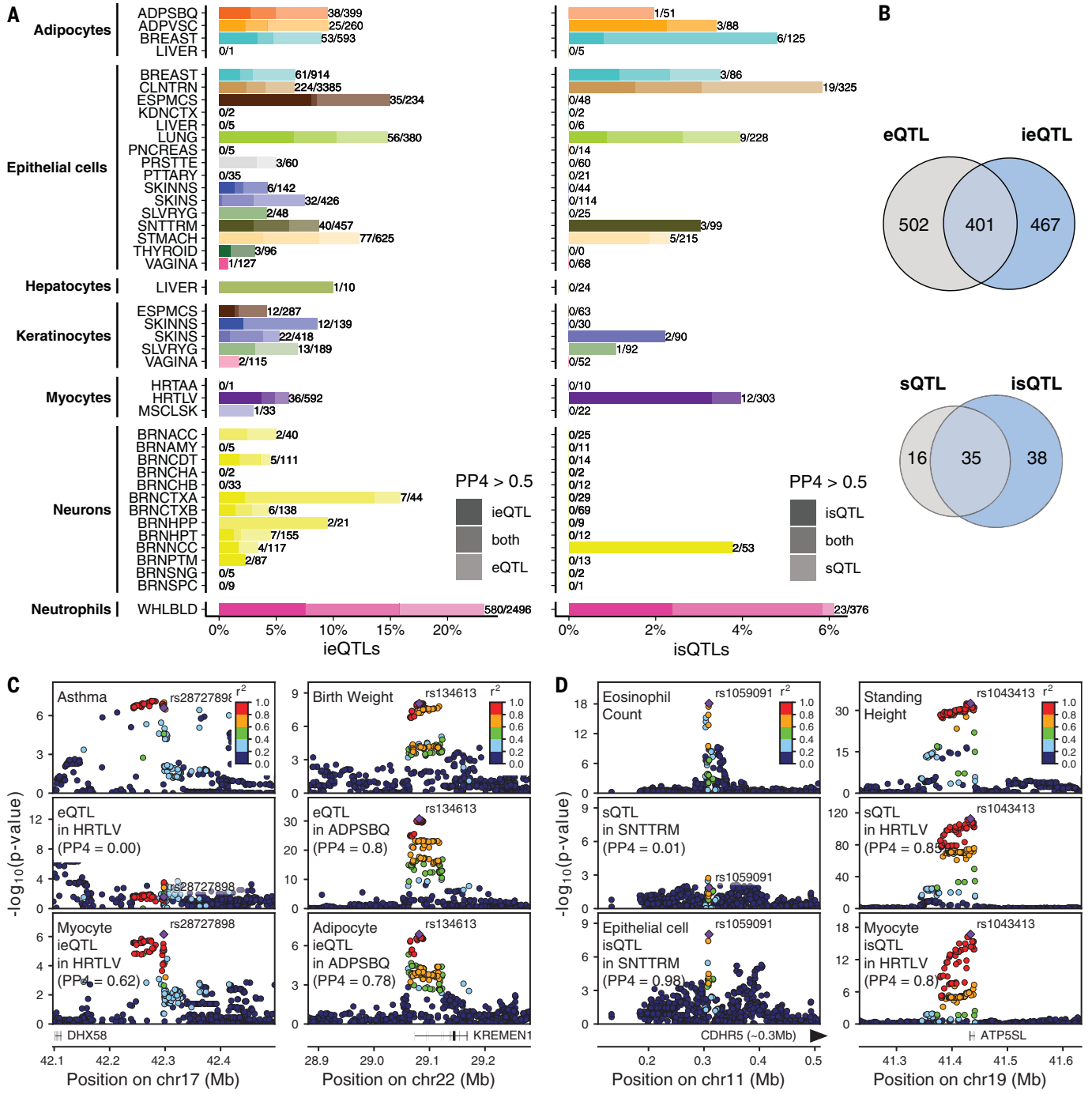

Fig. 5. Cell type iQTLs improve GWAS-QTL matching. (**A**) Proportion of cell type (left) ieQTLs or (right) isQTLs with evidence of colocalization by using COLOC posterior probabilities (PP4 > 0.5) for ieQTLs and isQTL at FDR < 0.4. Color saturation indicates whether a trait colocalized with the cell type iQTL only (dark), the cis-QTL only (light), or both QTLs (medium). Bar labels indicate the number of cell type iQTLs with evidence of colocalization (either as iQTL or cis-QTL) per number of iQTLs tested. (**B**) Summary of all QTL-trait colocalizations from (A). (**C**) Association *P* values in the *DHX58* locus for (top) an asthma GWAS, (middle) standard heart left ventricle cis-eQTL, and (bottom) myocyte ieQTL, and in the *KREMEN1* locus for a (top) birth weight GWAS, (middle) standard subcutaneous adipose cis-eQTL, and (bottom) adipocyte ieQTL. (**D**) Association *P* values in the *CDHR5* locus for (top) an eosinophil count GWAS, (middle) standard small intestine terminal ileum cis-sQTL, and (bottom) epithelial cell isQTL, and in the *ATP5SL* locus for a (top) standing height GWAS, (middle) standard heart left ventricle cis-sQTL, and (bottom) myocyte isQTL.

$P \leq 0.05$) using QTLEnrich (*33*). We used 23 and 7 cell type–tissue pairs (19 and 7 distinct tissues, respectively) with >100 ieQTLs or isQTLs, respectively, at a relaxed FDR of 40% to generate robust enrichment estimates of 87 GWAS traits. Across all tested cell type–tissue trait pairs, the GWAS signal was clearly enriched among ieQTLs and isQTLs (1.3 and 1.4 median fold enrichments, respectively), similarly to standard eQTLs and sQTLs (Fig. 4A and table S4). The GWAS enrichments were robust to the iQTL FDR cutoffs (fig. S15, A and B).

We next analyzed the enrichments of the individual traits for iQTLs of two cell types that we estimated had the largest number of ieQTLs: neutrophil iQTLs in blood and epithelial cell iQTLs in transverse colon. We compared them with the corresponding standard QTLs (Fig. 4B and fig. S15, C and D), focusing on traits that had a significant enrichment for either QTL type (Bonferroni-adjusted $P < 0.05$). In blood, we observed a significant shift toward higher enrichment for ieQTLs (one-sided, paired Wilcoxon rank sum test; $P = 0.0026$) and especially isQTLs ($P = 2.8 \times 10^{-05}$), which appears to be driven by GWAS for blood cell traits, and also immune traits having a higher enrichment for iQTLs. The higher iQTL signal is absent in colon (ieQTL, $P = 1$; isQTL, $P = 0.13$), even though the standard QTL enrichment for blood cell traits appears to be similar for blood and colon. This pattern suggests that cell type–interaction QTLs may have better resolution for indicating relevant tissues and cell types for complex traits as compared with tissue QTLs, but further studies are needed to fully test this hypothesis.

Next, we asked whether cell type iQTLs can be linked to loci discovered in GWASs and used to pinpoint their cellular specificity. To this end, we tested 13,702 ieGenes and 2938 isGenes (40% FDR) for colocalization with 87 GWAS traits (*1*), using both the cell type ieQTL/isQTL and corresponding standard QTL; 1370 (10.3%) cell type ieQTLs and 89 (3.7%) isQTLs colocalized with at least one GWAS trait (Fig. 5, A and B, and tables S5 and S6). The larger number of colocalizations identified for neutrophil ieQTLs and isQTLs in whole blood relative to other cell type–tissue pairs likely reflects a combination of the larger number of ieQTLs and isQTLs and the abundance of significant GWAS loci for blood-related traits in our set of 87 GWASs (Fig. 5B).

Our analysis revealed a substantial proportion of loci for which only the ieQTL/isQTL colocalizes with the trait (467 of 1370, 34%) (Fig. 5B), or where the joint colocalization of the ieQTL/isQTL and corresponding standard eQTL indicates the cellular specificity of the trait as well as its potential cellular origin (401 of 1370, 29%) (Fig. 5B). For example, a colocalization between the DExH-box helicase 58 (*DHX58*) gene in the left ventricle of the heart and an asthma GWAS was only identified through the corresponding myocyte ieQTL [posterior probability of colocalization (PP4) = 0.64] but not the standard eQTL (PP4 = 0.00) (Fig. 5C). Cardiac cells such as cardiomyocytes are not primarily viewed to have a causal role in asthma, but their presence along pulmonary veins and their potential contribution to allergic airway disease have been described (*34*).

An example in which both the standard eQTL and the cell type ieQTL colocalize with the trait is given in Fig. 5C for *KREMEN1* in adipocytes in subcutaneous adipose tissue and a birth weight GWAS (PP4 ~ 0.8); *KREMEN1* has been linked to adipogenesis in mice (*35*). We highlight two analogous examples for isQTLs: The epithelial cell isQTL for *CDHR5* in small intestine colocalized with eosinophil counts, whereas the standard sQTL did not (Fig. 5D), and conversely, both the standard sQTL and myocyte isQTL for *ATP5SL* in the left ventricle of the heart colocalized with standing height (Fig. 5D). Additional examples of ieQTLs and isQTLs colocalizing with trait associations are provided in figs. S16 and S17. Although the iQTLs do not necessarily pinpoint the specific cell type where the regulatory effect is active, they indicate that cell type specificity plays a role in the GWAS locus. Together, our colocalization results indicate that cell type–interaction QTLs yield new potential target genes for GWAS loci that are missed by standard QTLs and provide hypotheses for the cellular specificity of regulatory effects underlying complex traits.

Discussion

By mapping interaction effects between cell type enrichment and genotype on the transcriptome across GTEx tissues, we provide an atlas of thousands of eQTLs and sQTLs that are likely to be cell type–specific. The ieQTLs and isQTLs we report here include several immune and stromal cell types in tissues where cell type–specific QTLs have not been characterized in prior studies. Cell type ieQTLs are strongly enriched for tissue and cellular specificity and provide a finer resolution to tissue specificity than that of bulk cis-QTLs that are highly shared between tissues. Given the enrichment of GWAS signal in cell type iQTLs for cell types potentially relevant to the traits, and the large fraction of colocalizations with GWAS traits that are only found with cell type iQTLs, exhaustive characterization of cell type–specific QTLs is a highly promising approach toward a mechanistic understanding of these loci, complementing experimental assays of variant function. However, the substantial allelic heterogeneity observed in standard QTLs (*1*) and limited power to deconvolve QTLs that are specific to rare cell types or with weak or opposing effects indicate that many more cell type–specific QTLs exist beyond those that can be currently computationally inferred from bulk tissue data. We therefore anticipate that upcoming population-scale single-cell QTL studies will be essential to complement the approaches presented here. However, because those data are still difficult to obtain for many tissues, our demonstration of the insights gained from cell type iQTLs indicates that improving deconvolution approaches and increasing sample sizes will be valuable in this effort and enable discoveries for cell types and tissues not considered in this study.

Methods summary

The GTEx version 8 (v8) data (*1*) was used for all analyses. Cell type enrichments were computed with xCell (*24*). Interaction QTL mapping was performed with tensorQTL (*36*). Full methods are available in (*26*).

REFERENCES AND NOTES

1. GTEx Consortium, The GTEx Consortium atlas of genetic regulatory effects across human tissues. *Science* **369**, 1318 (2020).
2. U. Võsa *et al.*, Unraveling the polygenic architecture of complex traits using blood eQTL meta-analysis. *bioRxiv* 447367 [Preprint] 19 October 2018. doi: 10.1101/447367
3. R. Joehanes *et al.*, Integrated genome-wide analysis of expression quantitative trait loci aids interpretation of genomic association studies. *Genome Biol.* **18**, 16 (2017). doi: 10.1186/s13059-016-1142-6; pmid: 28122634
4. H. Kirsten *et al.*, Dissecting the genetics of the human transcriptome identifies novel trait-related trans-eQTLs and corroborates the regulatory relevance of non-protein coding loci†. *Hum. Mol. Genet.* **24**, 4746–4763 (2015). doi: 10.1093/hmg/ddv194; pmid: 26019233
5. A. Buil *et al.*, Gene-gene and gene-environment interactions detected by transcriptome sequence analysis in twins. *Nat. Genet.* **47**, 88–91 (2015). doi: 10.1038/ng.3162; pmid: 25436857
6. GTEx Consortium, The Genotype-Tissue Expression (GTEx) pilot analysis: Multitissue gene regulation in humans. *Science* **348**, 648–660 (2015). doi: 10.1126/science.1262110; pmid: 25954001
7. B. P. Fairfax *et al.*, Genetics of gene expression in primary immune cells identifies cell type-specific master regulators and roles of HLA alleles. *Nat. Genet.* **44**, 502–510 (2012). doi: 10.1038/ng.2205; pmid: 22446964
8. T. Raj *et al.*, Polarization of the effects of autoimmune and neurodegenerative risk alleles in leukocytes. *Science* **344**, 519–523 (2014). doi: 10.1126/science.1249547; pmid: 24786080
9. V. Naranbhai *et al.*, Genomic modulators of gene expression in human neutrophils. *Nat. Commun.* **6**, 7545 (2015). doi: 10.1038/ncomms8545; pmid: 26151758
10. S. Kim-Hellmuth *et al.*, Genetic regulatory effects modified by immune activation contribute to autoimmune disease associations. *Nat. Commun.* **8**, 266 (2017). doi: 10.1038/s41467-017-00366-1; pmid: 28814792
11. S. Kasela *et al.*, Pathogenic implications for autoimmune mechanisms derived by comparative eQTL analysis of $CD4^+$ versus $CD8^+$ T cells. *PLOS Genet.* **13**, e1006643–e21 (2017). doi: 10.1371/journal.pgen.1006643; pmid: 28248954
12. M. G. P. van der Wijst *et al.*, Single-cell RNA sequencing identifies celltype-specific cis-eQTLs and co-expression QTLs. *Nat. Genet.* **50**, 493–497 (2018). doi: 10.1038/s41588-018-0089-9; pmid: 29610479
13. N. Habib *et al.*, Massively parallel single-nucleus RNA-seq with DroNc-seq. *Nat. Methods* **14**, 955–958 (2017). doi: 10.1038/nmeth.4407; pmid: 28846088
14. M. Slyper *et al.*, A single-cell and single-nucleus RNA-seq toolbox for fresh and frozen human tumors. *Nat. Med.* **26**, 792–802 (2020). doi: 10.1038/s41591-020-0844-1; pmid: 32405060
15. HCA Consortium, The Human Cell Atlas. arXiv:1810.05192 [q-bio.TO] (2018).
16. A. K. Sarkar *et al.*, Discovery and characterization of variance QTLs in human induced pluripotent stem cells. *PLOS Genet.* **15**, e1008045–e16 (2019). doi: 10.1371/journal.pgen.1008045; pmid: 31002671

17. I. Mandric *et al.*, Optimal design of single-cell RNA sequencing experiments for cell-type-specific eQTL analysis. bioRxiv 766972 [Preprint] 12 September 2019. doi: 10.1101/766972
18. M. G. P. van der Wijst *et al.*, Science Forum: The single-cell eQTLGen consortium. *eLife* **9**, e52155 (2020).
19. H.-J. Westra *et al.*, Cell Specific eQTL Analysis without Sorting Cells. *PLOS Genet.* **11**, e1005223–e17 (2015). doi: 10.1371/journal.pgen.1005223; pmid: 25955312
20. D. V. Zhernakova *et al.*, Identification of context-dependent expression quantitative trait loci in whole blood. *Nat. Genet.* **49**, 139–145 (2017). doi: 10.1038/ng.3737; pmid: 27918533
21. C. A. Glastonbury, A. Couto Alves, J. S. El-Sayed Moustafa, K. S. Small, Cell-Type Heterogeneity in Adipose Tissue Is Associated with Complex Traits and Reveals Disease-Relevant Cell-Specific eQTLs. *Am. J. Hum. Genet.* **104**, 1013–1024 (2019). doi: 10.1016/j.ajhg.2019.03.025; pmid: 31130283
22. F. Avila Cobos, J. Vandesompele, P. Mestdagh, K. De Preter, Computational deconvolution of transcriptomics data from mixed cell populations. *Bioinformatics* **34**, 1969–1979 (2018). doi: 10.1093/bioinformatics/bty019; pmid: 29351586
23. G. Sturm *et al.*, Comprehensive evaluation of transcriptome-based cell-type quantification methods for immuno-oncology. *Bioinformatics* **35**, i436–i445 (2019). doi: 10.1093/bioinformatics/btz363; pmid: 31510660
24. D. Aran, Z. Hu, A. J. Butte, xCell: Digitally portraying the tissue cellular heterogeneity landscape. *Genome Biol.* **18**, 220 (2017). doi: 10.1186/s13059-017-1349-1; pmid: 29141660
25. Y. I. Li *et al.*, Annotation-free quantification of RNA splicing using LeafCutter. *Nat. Genet.* **50**, 151–158 (2018). doi: 10.1038/s41588-017-0004-9; pmid: 29229983
26. See supplementary materials.
27. A. Breschi *et al.*, A limited set of transcriptional programs define major cell types. *Genome Res.* **30**, 1047–1059 (2020).
28. J. D. Storey, R. Tibshirani, Statistical significance for genomewide studies. *Proc. Natl. Acad. Sci. U.S.A.* **100**, 9440–9445 (2003). doi: 10.1073/pnas.1530509100; pmid: 12883005
29. S. E. Castel *et al.*, A vast resource of allelic expression data spanning human tissues. *Genome Res.* 10.1186/s13059-020-02122-z (2020).
30. P. Mohammadi, S. E. Castel, A. A. Brown, T. Lappalainen, Quantifying the regulatory effect size of cis-acting genetic variation using allelic fold change. *Genome Res.* **27**, 1872–1884 (2017). doi: 10.1101/gr.216747.116; pmid: 29021289
31. L. Vila *et al.*, Heritability of thromboxane A2 and prostaglandin E2 biosynthetic machinery in a Spanish population. *Arterioscler. Thromb. Vasc. Biol.* **30**, 128–134 (2010). doi: 10.1161/ATVBAHA.109.193219; pmid: 19850905
32. M. Allen *et al.*, Human whole genome genotype and transcriptome data for Alzheimer's and other neurodegenerative diseases. *Sci. Data* **3**, 160089 (2016). doi: 10.1038/sdata.2016.89; pmid: 27727239
33. E. R. Gamazon *et al.*, Using an atlas of gene regulation across 44 human tissues to inform complex disease- and trait-associated variation. *Nat. Genet.* **50**, 956–967 (2018). doi: 10.1038/s41588-018-0154-4; pmid: 29955180
34. S. S. Folmsbee, C. J. Gottardi, Cardiomyocytes of the heart and pulmonary veins: Novel contributors to asthma? *Am. J. Respir. Cell Mol. Biol.* **57**, 512–518 (2017). doi: 10.1165/rcmb.2016-0261TR; pmid: 28481622
35. C. Christodoulides *et al.*, The Wnt antagonist Dickkopf-1 and its receptors are coordinately regulated during early human adipogenesis. *J. Cell Sci.* **119**, 2613–2620 (2006). doi: 10.1242/jcs.02975; pmid: 16763196
36. A. Taylor-Weiner *et al.*, Scaling computational genomics to millions of individuals with GPUs. *Genome Biol.* **20**, 228 (2019). doi: 10.1186/s13059-019-1836-7; pmid: 31675989
37. J. Ernst, M. Kellis, Chromatin-state discovery and genome annotation with ChromHMM. *Nat. Protoc.* **12**, 2478–2492 (2017). doi: 10.1038/nprot.2017.124; pmid: 29120462

ACKNOWLEDGMENTS

We thank the donors and their families for their generous gifts of organ donation for transplantation, and tissue donations for the GTEx research project; we thank M. Khan for the illustrations in Fig. 1A. **Funding:** This work was funded by following funding sources: Marie-Skłodowska Curie fellowship H2020 grant 706636 (S.K.-H.); NIH grant 1K99HG009916-01 (S.E.C.); NIH grant R01HG002585 (G.W. and M.S.); BIO2015-70777-P, Ministerio de Economia y Competitividad and FEDER funds (M.M.-A., V.W., R.G., and D.G.-M.); FPU15/03635, Ministerio de Educación, Cultura y Deporte (M.M-A.); "la Caixa" Foundation (ID 100010434) agreement LCF/BQ/SO15/52260001 (D.G.-M.); EU IMI program (UE7-DIRECT-115317-1) (A.V. and E.T.D.); FNS-funded project RNA1 (31003A_149984) (A.V. and E.T.D.); Massachusetts Lions Eye Research Fund Grant (A.R.H.); MRC grants MR/R023131/1 and MR/M004422/1 (K.S.S.); and Biomedical Big Data Training Grant 5T32LM012424-03 (B.N.). The TwinsUK study was funded by the Wellcome Trust and European Community's Seventh Framework Programme (FP7/2007-2013). The TwinsUK study also receives support from the National Institute for Health Research (NIHR)–funded BioResource, Clinical Research Facility and Biomedical Research Centre based at Guy's and St Thomas' NHS Foundation Trust in partnership with King's College London. This work was further supported by the Common Fund of the Office of the Director, U.S. National Institutes of Health (NIH), and by NCI, NHGRI, NHLBI, NIDA, NIMH, NIA, NIAID, and NINDS through NIH contracts HHSN261200800001E (Leidos Prime contract with NCI: A.M.S., D.E.T., N.V.R., J.A.M., L.S., M.E.B., L.Q., T.K., D.B., K.R., and A.U.), 10XS170 (NDRI: W.F.L., J.A.T., G.K., A.M., S.S., R.H., G.Wa., M.J., M.Wa., L.E.B., C.J., J.W., B.R., M.Hu., K.M., L.A.S., H.M.G., M.Mo., and L.K.B.), 10XS171 (Roswell Park Cancer Institute: B.A.F., M.T.M., E.K., B.M.G., K.D.R., and J.B.), 10X172 (Science Care), 12ST1039 (IDOX), 10ST1035 (Van Andel Institute: S.D.J., D.C.R., and D.R.V.), HHSN268201000029C (Broad Institute: F.A., G.G., K.G.A., A.V.S., X.Li., E.T., S.G., A.G., S.A., K.H.H., D.T.N., K.H., S.R.M., and J.L.N.), 5U41HG009494 (F.A., G.G., and K.G.A.), and through NIH grants R01 DA006227-17 (University of Miami Brain Bank: D.C.M. and D.A.D.), Supplement to University of Miami grant DA006227 (D.C.M. and D.A.D.), R01 MH090941 (University of Geneva), R01 MH090951 and R01 MH090937 (University of Chicago), R01 MH090936 (University of North Carolina–Chapel Hill), R01MH101814 (M.M-A., V.W., S.B.M., R.G., E.T.D., D.G-M., and A.V.), U01HG007593 (S.B.M.), R01MH101822 (C.D.B.), U01HG007598 (M.O. and B.E.S.), U01MH104393 (A.P.F.). Extension H002371 to 5U41HG002371 (W.J.K) as well as other funding sources: R01MH106842 (T.L., P.M., E.F., and P.J.H.), R01HL142028 (T.L., Si.Ka., and P.J.H.), R01GM122924 (T.L. and S.E.C.), R01MH107666 (H.K.I.), P30DK020595 (H.K.I.), UM1HG008901 (T.L.), R01GM124486 (T.L.), R01HG010067 (Y.Pa.), R01HG002585 (G.Wa. and M.St.), Gordon and Betty Moore Foundation GBMF 4559 (G.Wa. and M.St.), R01HG006855 (Se.Ka., R.E.H.), NIH CTSA grant UL1TR002550-01 (P.M.), R35HG010718 (E.R.G.), R01MH109905, 1R01HG010480 (A.Ba.), Searle Scholar Program (A.Ba.), R01HG008150 (S.B.M.), 5T32HG000044-22, NHGRI Institutional Training Grant in Genome Science (N.R.G.), and F32HG009987 (F.H.). **Author contributions:** S.K.-H., F.A., and T.L. conceived the study. S.K.-H. and F.A. led the writing, figure generation, and editing of the manuscript and supplementary materials. S.K.-H. coordinated analyses of all contributing authors; S.K.-H. and F.A. generated pipelines and performed iQTL mapping; S.K.-H., F.A., M.O., M.M.-A., V.W., D.G.-M., S.M., B.N., and J.Q. performed cell type benchmarking analyses; S.K. performed ieQTL validation with ASE data using the validation pipeline and ASE data generated by S.E.C.; F.A., A.V., and A.L.R. performed replication analyses; S.E.C. performed QTL tissue activity prediction analysis; S.K.-H. and S.E.C. generated tissue sharing (MASH) data; S.K.-H. performed tissue specificity, multi-tissue analysis, and colocalization analysis; A.R.H. performed QTLEnrich analysis; G.W. and Y.Z. provided software support for multi-tissue eQTL analysis; X.W. and H.K.I. provided advice on colocalization analysis; A.B., A.M.-P., and J.M.-S. contributed to replication analysis; F.A. and K.G.A. generated and oversaw GTEx v8 data generation, LDACC, pipelines; A.N.B. and R.B. generated GWAS data; K.S.S., M.S., H.S.X., G.G., E.T.D., H.K.I., R.G., A.V.S., B.E.S., K.G.A., and T.L. supervised the work of trainees in their laboratories; and M.O. and T.L. contributed to editing of the manuscript. All authors read and approved the final manuscript. **Competing interests:** F.A. is an inventor on a patent application related to TensorQTL; S.E.C. is a cofounder, chief technology officer, and stock owner at Variant Bio; J.Q. is an employee of Pfizer; H.S.X. is an employee of AbbVie; H.K.I. has received speaker honoraria from GSK and AbbVie; E.T.D. is chairman and member of the board of Hybridstat; G.G. receives research funds from IBM and Pharmacyclics and is an inventor on patent applications related to MuTect, ABSOLUTE, MutSig, MSMuTect, MSMutSig, POLYSOLVER, and TensorQTL. G.G. is a founder, consultant, and holds privately held equity in Scorpion Therapeutics; T.L. is a scientific advisory board member of Variant Bio with equity and Goldfinch Bio. GTEx consortium members: P.F. is member of the scientific advisory boards of Fabric Genomics and Eagle Genomes. P.G.F. is a partner of Bioinf2Bio. E.R.G. is on the Editorial Board of Circulation Research and does consulting for the City of Hope/Beckman Research Institute; B.E.E. is on the scientific advisory boards of Celsius Therapeutics and Freenome; S.B.M. is on the scientific advisory board of Prime Genomics; D.G.M. is a cofounder with equity in Goldfinch Bio and has received research support from AbbVie, Astellas, Biogen, BioMarin, Eisai, Merck, Pfizer, and Sanofi-Genzym. **Data and materials availability:** All GTEx open-access data, including summary statistics and visualizations of cell type iQTLs, are available on the GTEx Portal (https://gtexportal.org/home/datasets). All GTEx protected data are available via dbGaP (accession phs000424.v8). Access to the raw sequence data are now provided through the AnVIL platform (https://gtexportal.org/home/protectedDataAccess). Eighty-seven harmonized and imputed GWAS summary stats described in table S3 are available and linked at https://github.com/hakyimlab/gtex-gwas-analysis and https://zenodo.org/record/3629742#.XxYGoy1h0Ux. Original GWAS studies are cited in (*1*). The QTL mapping pipeline is available at https://github.com/broadinstitute/gtex-pipeline and https://doi.org/10.5281/zenodo.3727189, and tensorQTL is available at https://github.com/broadinstitute/tensorqtl and https://doi.org/10.5281/zenodo.3726360. Residual GTEx biospecimens have been banked and remain available as a resource for further studies (access can be requested on the GTEx Portal, at www.gtexportal.org/home/samplesPage).

SUPPLEMENTARY MATERIALS

science.sciencemag.org/content/369/6509/eaaz8528/suppl/DC1
Materials and Methods
Figs. S1 to S17
References (*38*–*62*)
Tables S1 to S6

View/request a protocol for this paper from *Bio-protocol*.

GTEx Consortium
Laboratory and Data Analysis Coordinating Center (LDACC): François Aguet[1], Shankara Anand[1], Kristin G. Ardlie[1], Stacey Gabriel[1], Gad A. Getz[1,2,3], Aaron Graubert[1], Kane Hadley[1], Robert E. Handsaker[4,5,6], Katherine H. Huang[1], Seva Kashin[4,5,6], Xiao Li[1], Daniel G. MacArthur[5,7], Samuel R. Meier[1], Jared L. Nedzel[1], Duyen T. Nguyen[1], Ayellet V. Segrè[1,8], Ellen Todres[1]
Analysis Working Group (funded by GTEx project grants): François Aguet[1], Shankara Anand[1], Kristin G. Ardlie[1], Brunilda Balliu[9], Alvaro N. Barbeira[10], Alexis Battle[11,12], Rodrigo Bonazzola[10], Andrew Brown[13,14], Christopher D. Brown[15], Stephane E. Castel[16,17], Donald F. Conrad[18,19], Daniel J. Cotter[20], Nancy Cox[21], Sayantan Das[22], Olivia M. de Goede[20], Emmanouil T. Dermitzakis[13,23,24], Jonah Einson[16,25], Barbara E. Engelhardt[26,27], Eleazar Eskin[28], Tiffany Y. Eulalio[29], Nicole M. Ferraro[29], Elise D. Flynn[16,17], Laure Fresard[30], Eric R. Gamazon[21,31,32,33], Diego Garrido-Martín[34], Nicole R. Gay[20], Gad A. Getz[1,2,3], Michael J. Gloudemans[29], Aaron Graubert[1], Roderic Guigó[34,35], Kane Hadley[1], Andrew R. Hame[18,1], Robert E. Handsaker[4,5,6], Yuan He[11], Paul J. Hoffman[16], Farhad Hormozdiari[1,36], Lei Hou[1,37], Katherine H. Huang[1], Hae Kyung Im[10], Brian Jo[26,27], Silva Kasela[16,17], Seva Kashin[4,5,6], Manolis Kellis[1,37], Sarah Kim-Hellmuth[16,17,38], Alan Kwong[22], Tuuli Lappalainen[16,17], Xiao Li[1], Xin Li[30], Yanyu Liang[10], Daniel G. MacArthur[5,7], Serghei Mangul[28,39], Samuel R. Meier[1], Pejman Mohammadi[16,17,40,41], Stephen B. Montgomery[20,30], Manuel Muñoz-Aguirre[34,42], Daniel C. Nachun[30], Jared L. Nedzel[1], Duyen T. Nguyen[1], Andrew B. Nobel[43], Meritxell Oliva[10,44], YoSon Park[15,45], Yongjin Park[1,37], Princy Parsana[12], Abhiram S. Rao[46], Ferran Reverter[47], John M. Rouhana[1,8], Chiara Sabatti[48], Ashis Saha[12], Ayellet V. Segrè[1,8], Andrew D. Skol[10,49], Matthew Stephens[50], Barbara E. Stranger[10,51], Benjamin J. Strober[11], Nicole A. Teran[30], Ellen Todres[1], Ana Viñuela[13,23,24,52], Gao Wang[50], Xiaoquan Wen[22], Fred Wright[53], Valentin Wucher[34], Yuxin Zou[54]
Analysis Working Group (not funded by GTEx project grants): Pedro G. Ferreira[55,56,57,58], Gen Li[59], Marta Melé[60], Esti Yeger-Lotem[61,62]
Leidos Biomedical—project management: Mary E. Barcus[63], Debra Bradbury[63], Tanya Krubit[63], Jeffrey A. McLean[63], Liqun Qi[63], Karna Robinson[63], Nancy V. Roche[63], Anna M. Smith[63], Leslie Sobin[63], David E. Tabor[63], Anita Undale[63]
Biospecimen collection source sites: Jason Bridge[64], Lori E. Brigham[65], Barbara A. Foster[66], Bryan M. Gillard[66], Richard Hasz[67], Marcus Hunter[68], Christopher Johns[69], Mark Johnson[70], Ellen Karasik[66], Gene Kopen[71], William F. Leinweber[71], Alisa McDonald[71], Michael T. Moser[66], Kevin Myer[68], Kimberley D. Ramsey[66], Brian Roe[68], Saboor Shad[71], Jeffrey A. Thomas[71,70], Gary Walters[70], Michael Washington[70], Joseph Wheeler[69]
Biospecimen core resource: Scott D. Jewell[72], Daniel C. Rohrer[72], Dana R. Valley[72]
Brain bank repository: David A. Davis[73], Deborah C. Mash[73]
Pathology: Mary E. Barcus[63], Philip A. Branton[74], Leslie Sobin[63]
ELSI Study: Laura K. Barker[75], Heather M. Gardiner[75], Maghboeba Mosavel[76], Laura A. Siminoff[75]
Genome browser data integration and visualization: Paul Flicek[77], Maximilian Haeussler[78], Thomas Juettemann[77], W. James Kent[78], Christopher M. Lee[78], Conner C. Powell[78],

Kate R. Rosenbloom[78], Magali Ruffier[77], Dan Sheppard[77], Kieron Taylor[77], Stephen J. Trevanion[77], Daniel R. Zerbino[77]
eGTEx groups: Nathan S. Abell[20], Joshua Akey[79], Lin Chen[44], Kathryn Demanelis[44], Jennifer A. Doherty[80], Andrew P. Feinberg[81], Kasper D. Hansen[82], Peter F. Hickey[83], Lei Hou[1,37], Farzana Jasmine[44], Lihua Jiang[20], Rajinder Kaul[84,85], Manolis Kellis[1,37], Muhammad G. Kibriya[44], Jin Billy Li[20], Qin Li[20], Shin Lin[86], Sandra E. Linder[20], Stephen B. Montgomery[20,30], Meritxell Oliva[10,44], Yongjin Park[1,37], Brandon L. Pierce[44], Lindsay F. Rizzardi[87], Andrew D. Skol[10,49], Kevin S. Smith[30], Michael Snyder[20], John Stamatoyannopoulos[84,88], Barbara E. Stranger[10,51], Hua Tang[20], Meng Wang[20]
NIH program management: Philip A. Branton[74], Latarsha J. Carithers[74,89], Ping Guan[74], Susan E. Koester[90], A. Roger Little[91], Helen M. Moore[74], Concepcion R. Nierras[92], Abhi K. Rao[74], Jimmie B. Vaught[74], Simona Volpi[93]

[1]Broad Institute of MIT and Harvard, Cambridge, MA, USA. [2]Cancer Center and Department of Pathology, Massachusetts General Hospital, Boston, MA, USA. [3]Harvard Medical School, Boston, MA, USA. [4]Department of Genetics, Harvard Medical School, Boston, MA, USA. [5]Program in Medical and Population Genetics, Broad Institute of MIT and Harvard, Cambridge, MA, USA. [6]Stanley Center for Psychiatric Research, Broad Institute of MIT and Harvard, Cambridge, MA, USA. [7]Analytic and Translational Genetics Unit, Massachusetts General Hospital, Boston, MA, USA. [8]Ocular Genomics Institute, Massachusetts Eye and Ear, Harvard Medical School, Boston, MA, USA. [9]Department of Biomathematics, University of California, Los Angeles, CA, USA. [10]Section of Genetic Medicine, Department of Medicine, The University of Chicago, Chicago, IL, USA. [11]Department of Biomedical Engineering, Johns Hopkins University, Baltimore, MD, USA. [12]Department of Computer Science, Johns Hopkins University, Baltimore, MD, USA. [13]Department of Genetic Medicine and Development, University of Geneva Medical School, Geneva, Switzerland. [14]Population Health and Genomics, University of Dundee, Dundee, Scotland, UK. [15]Department of Genetics, University of Pennsylvania, Perelman School of Medicine, Philadelphia, PA, USA. [16]New York Genome Center, New York, NY, USA. [17]Department of Systems Biology, Columbia University, New York, NY, USA. [18]Department of Genetics, Washington University School of Medicine, St. Louis, MO, USA. [19]Division of Genetics, Oregon National Primate Research Center, Oregon Health & Science University, Portland, OR, USA. [20]Department of Genetics, Stanford University, Stanford, CA, USA. [21]Division of Genetic Medicine, Department of Medicine, Vanderbilt University Medical Center, Nashville, TN, USA. [22]Department of Biostatistics, University of Michigan, Ann Arbor, MI, USA. [23]Institute for Genetics and Genomics in Geneva (iGE3), University of Geneva, Geneva, Switzerland. [24]Swiss Institute of Bioinformatics, Geneva, Switzerland. [25]Department of Biomedical Informatics, Columbia University, New York, NY, USA. [26]Department of Computer Science, Princeton University, Princeton, NJ, USA. [27]Center for Statistics and Machine Learning, Princeton University, Princeton, NJ, USA. [28]Department of Computer Science, University of California, Los Angeles, CA, USA. [29]Program in Biomedical Informatics, Stanford University School of Medicine, Stanford, CA, USA. [30]Department of Pathology, Stanford University, Stanford, CA, USA. [31]Data Science Institute, Vanderbilt University, Nashville, TN, USA. [32]Clare Hall, University of Cambridge, Cambridge, UK. [33]MRC Epidemiology Unit, University of Cambridge, Cambridge, UK. [34]Centre for Genomic Regulation (CRG), The Barcelona Institute for Science and Technology, Barcelona, Catalonia, Spain. [35]Universitat Pompeu Fabra (UPF), Barcelona, Catalonia, Spain. [36]Department of Epidemiology, Harvard T.H. Chan School of Public Health, Boston, MA, USA. [37]Computer Science and Artificial Intelligence Laboratory, Massachusetts Institute of Technology, Cambridge, MA, USA. [38]Statistical Genetics, Max Planck Institute of Psychiatry, Munich, Germany. [39]Department of Clinical Pharmacy, School of Pharmacy, University of Southern California, Los Angeles, CA, USA. [40]Scripps Research Translational Institute, La Jolla, CA, USA. [41]Department of Integrative Structural and Computational Biology, The Scripps Research Institute, La Jolla, CA, USA. [42]Department of Statistics and Operations Research, Universitat Politècnica de Catalunya (UPC), Barcelona, Catalonia, Spain. [43]Department of Statistics and Operations Research and Department of Biostatistics, University of North Carolina, Chapel Hill, NC, USA. [44]Department of Public Health Sciences, The University of Chicago, Chicago, IL, USA. [45]Department of Systems Pharmacology and Translational Therapeutics, Perelman School of Medicine, University of Pennsylvania, Philadelphia, PA, USA. [46]Department of Bioengineering, Stanford University, Stanford, CA, USA. [47]Department of Genetics, Microbiology and Statistics, University of Barcelona, Barcelona, Spain. [48]Departments of Biomedical Data Science and Statistics, Stanford University, Stanford, CA, USA. [49]Department of Pathology and Laboratory Medicine, Ann & Robert H. Lurie Children's Hospital of Chicago, Chicago, IL, USA. [50]Department of Human Genetics, University of Chicago, Chicago, IL, USA. [51]Center for Genetic Medicine, Department of Pharmacology, Northwestern University, Feinberg School of Medicine, Chicago, IL, USA. [52]Department of Twin Research and Genetic Epidemiology, King's College London, London, UK. [53]Bioinformatics Research Center and Departments of Statistics and Biological Sciences, North Carolina State University, Raleigh, NC, USA. [54]Department of Statistics, University of Chicago, Chicago, IL, USA. [55]Department of Computer Sciences, Faculty of Sciences, University of Porto, Porto, Portugal. [56]Instituto de Investigação e Inovação em Saúde, University of Porto, Porto, Portugal. [57]Institute of Molecular Pathology and Immunology, University of Porto, Porto, Portugal. [58]Laboratory of Artificial Intelligence and Decision Support, Institute for Systems and Computer Engineering, Technology and Science, Porto, Portugal. [59]Mailman School of Public Health, Columbia University, New York, NY, USA. [60]Life Sciences Department, Barcelona Supercomputing Center, Barcelona, Spain. [61]Department of Clinical Biochemistry and Pharmacology, Ben-Gurion University of the Negev, Beer-Sheva, Israel. [62]National Institute for Biotechnology in the Negev, Beer-Sheva, Israel. [63]Leidos Biomedical, Rockville, MD, USA. [64]Upstate New York Transplant Services, Buffalo, NY, USA. [65]Washington Regional Transplant Community, Annandale, VA, USA. [66]Therapeutics, Roswell Park Comprehensive Cancer Center, Buffalo, NY, USA. [67]Gift of Life Donor Program, Philadelphia, PA, USA. [68]LifeGift, Houston, TX, USA. [69]Center for Organ Recovery and Education, Pittsburgh, PA, USA. [70]LifeNet Health, Virginia Beach, VA. USA. [71]National Disease Research Interchange, Philadelphia, PA, USA. [72]Van Andel Research Institute, Grand Rapids, MI, USA. [73]Department of Neurology, University of Miami Miller School of Medicine, Miami, FL, USA. [74]Biorepositories and Biospecimen Research Branch, Division of Cancer Treatment and Diagnosis, National Cancer Institute, National Institutes of Health, Bethesda, MD, USA. [75]College of Public Health, Temple University, Philadelphia, PA, USA. [76]Virginia Commonwealth University, Richmond, VA, USA. [77]European Molecular Biology Laboratory, European Bioinformatics Institute, Hinxton, UK. [78]Genomics Institute, University of California, Santa Cruz, CA, USA. [79]Carl Icahn Laboratory, Princeton University, Princeton, NJ, USA. [80]Department of Population Health Sciences, The University of Utah, Salt Lake City, UT, USA. [81]Departments of Medicine, Biomedical Engineering, and Mental Health, Johns Hopkins University, Baltimore, MD, USA. [82]Department of Biostatistics, Bloomberg School of Public Health, Johns Hopkins University, Baltimore, MD, USA. [83]Department of Medical Biology, The Walter and Eliza Hall Institute of Medical Research, Parkville, Victoria, Australia. [84]Altius Institute for Biomedical Sciences, Seattle, WA, USA. [85]Division of Genetics, University of Washington, Seattle, WA, USA. [86]Department of Cardiology, University of Washington, Seattle, WA, USA. [87]HudsonAlpha Institute for Biotechnology, Huntsville, AL, USA. [88]Genome Sciences, University of Washington, Seattle, WA, USA. [89]National Institute of Dental and Craniofacial Research, National Institutes of Health, Bethesda, MD, USA. [90]Division of Neuroscience and Basic Behavioral Science, National Institute of Mental Health, National Institutes of Health, Bethesda, MD, USA. [91]National Institute on Drug Abuse, Bethesda, MD, USA. [92]Office of Strategic Coordination, Division of Program Coordination, Planning and Strategic Initiatives, Office of the Director, National Institutes of Health, Rockville, MD, USA. [93]Division of Genomic Medicine, National Human Genome Research Institute, Bethesda, MD, USA.

14 October 2019; accepted 31 July 2020
10.1126/science.aaz8528

RESEARCH ARTICLE SUMMARY

HUMAN GENOMICS

Determinants of telomere length across human tissues

Kathryn Demanelis, Farzana Jasmine, Lin S. Chen, Meytal Chernoff, Lin Tong, Dayana Delgado, Chenan Zhang, Justin Shinkle, Mekala Sabarinathan, Hannah Lin, Eduardo Ramirez, Meritxell Oliva, Sarah Kim-Hellmuth, Barbara E. Stranger, Tsung-Po Lai, Abraham Aviv, Kristin G. Ardlie, François Aguet, Habibul Ahsan, GTEx Consortium, Jennifer A. Doherty, Muhammad G. Kibriya, Brandon L. Pierce*

INTRODUCTION: Telomeres are DNA-protein complexes located at the end of chromosomes that protect chromosome ends from degradation and fusion. The DNA component of telomeres shortens with each cell division, eventually triggering cellular senescence. Telomere length (TL) in blood cells has been studied extensively as a biomarker of human aging and risk factor for age-related diseases. The extent to which TL in whole blood reflects TL in disease-relevant tissue types is unknown, and the variability in TL across human tissues has not been well characterized. The postmortem tissue samples collected by the Genotype-Tissue Expression (GTEx) project provide an opportunity to study TL in many human tissue types, and accompanying data on inherited genetic variation, gene expression, and donor characteristics enable us to examine demographic, genetic, and biologic determinants and correlates of TL within and across tissue types.

RATIONALE: To better understand variation in and determinants of TL, we measured relative TL (RTL, telomere repeat abundance in a DNA sample relative to a standard sample) in more than 25 tissue types from 952 GTEx donors (deceased, aged 20 to 70 years old). RTL was measured for 6391 unique tissue samples using a Luminex assay, generating the largest publicly available multitissue TL dataset. We integrated our RTL measurements with data on GTEx donor characteristics, inherited genetic variation, and tissue-specific expression and analyzed relationships between RTL and covariates using linear mixed models (across all tissues and within tissues). Through this analysis, we sought to accomplish four goals: (i) characterize sources of variation in TL, (ii) evaluate whole-blood TL as a proxy for TL in other tissue types, (iii) examine the relationship between age and TL across tissue types, and (iv) describe biological determinants and correlates of TL.

RESULTS: Variation in RTL was attributable to tissue type, donor, and age and, to a lesser extent, race or ethnicity, smoking, and inherited variants known to affect leukocyte TL. RTLs were generally positively correlated among tissues, and whole-blood RTL was a proxy for RTL in most tissues. RTL varied across tissue types and was shortest in whole blood and longest in testis. RTL was inversely associated with age in most tissues, and this association was strongest for tissues with shorter average RTL. African ancestry was associated with longer RTL across all tissues and within specific tissue types, suggesting that ancestry-based differences in TL exist in germ cells and are transmitted to the zygote. A polygenic score consisting of inherited variants known to affect leukocyte TL was associated with RTL across all tissues, and several of these TL-associated variants affected expression of nearby genes in multiple tissue types. Carriers of rare, loss-of-function variants in TL-maintenance genes had shorter RTL (based on analysis of multiple tissue types), suggesting that these variants may contribute to shorter TL in individuals from the general population. Components of telomerase, a TL maintenance enzyme, were more highly expressed in testis than in any other tissue. We found evidence that RTL may mediate the effect of age on gene expression in human tissues.

CONCLUSION: We have characterized the variability in TL across many human tissue types and the contributions of aging, ancestry, genetic variation, and other biologic processes to this variability. The correlation observed among TL measures from different tissues highlights the existence of host factors with effects on TL that are shared across tissue types (e.g., TL in the zygote). These results have important implications for the interpretation of epidemiologic studies of leukocyte TL and disease. ■

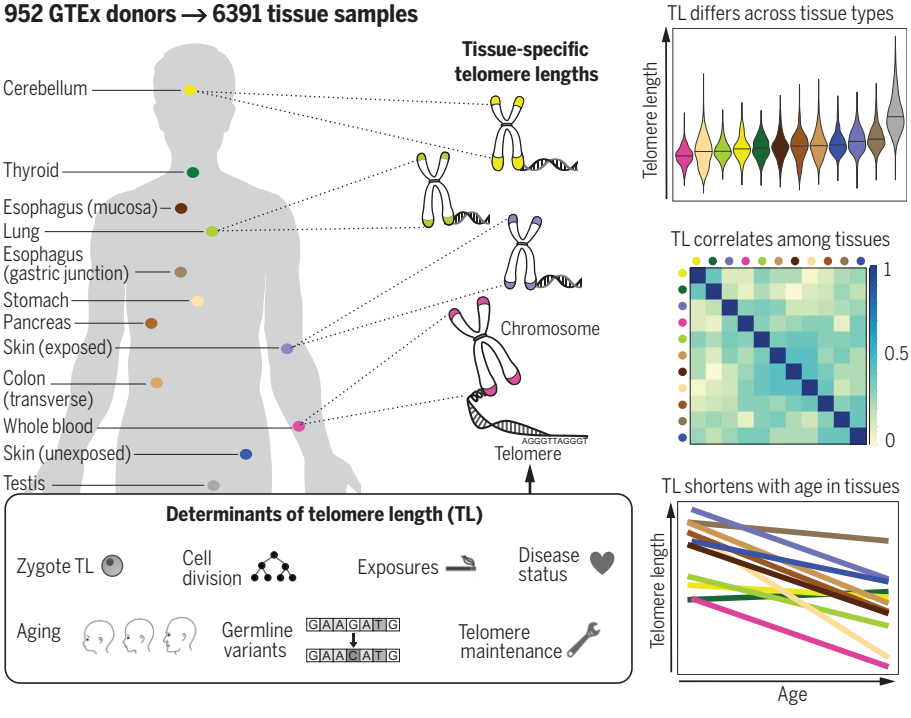

TL in human tissues. Using a Luminex-based assay, TL was measured in DNA samples from >25 different human tissue types from 952 deceased donors in the GTEx project. TL within tissue types is determined by numerous factors, including zygotic TL, age, and exposures. TL differs across tissues and correlates among tissue types. TL in most tissues declines with age.

The list of author affiliations and a full list of the GTEx authors and their affiliations are available in the full article online.
***Corresponding author. Email: brandonpierce@uchicago.edu**
Cite this article as K. Demanelis *et al.*, *Science* 369, eaaz6876 (2020). DOI: 10.1126/science.aaz6876

READ THE FULL ARTICLE AT
https://doi.org/10.1126/science.aaz6876

RESEARCH ARTICLE

HUMAN GENOMICS

Determinants of telomere length across human tissues

Kathryn Demanelis[1], Farzana Jasmine[1], Lin S. Chen[1], Meytal Chernoff[1], Lin Tong[1], Dayana Delgado[1], Chenan Zhang[1], Justin Shinkle[1], Mekala Sabarinathan[1], Hannah Lin[1], Eduardo Ramirez[1], Meritxell Oliva[1,2], Sarah Kim-Hellmuth[3,4,5], Barbara E. Stranger[2,6], Tsung-Po Lai[7], Abraham Aviv[7], Kristin G. Ardlie[8], François Aguet[8], Habibul Ahsan[1,9,10,11], GTEx Consortium*, Jennifer A. Doherty[12], Muhammad G. Kibriya[1], Brandon L. Pierce[1,9,10]†

Telomere shortening is a hallmark of aging. Telomere length (TL) in blood cells has been studied extensively as a biomarker of human aging and disease; however, little is known regarding variability in TL in nonblood, disease-relevant tissue types. Here, we characterize variability in TLs from 6391 tissue samples, representing >20 tissue types and 952 individuals from the Genotype-Tissue Expression (GTEx) project. We describe differences across tissue types, positive correlation among tissue types, and associations with age and ancestry. We show that genetic variation affects TL in multiple tissue types and that TL may mediate the effect of age on gene expression. Our results provide the foundational knowledge regarding TL in healthy tissues that is needed to interpret epidemiological studies of TL and human health.

Telomeres are DNA-protein complexes located at the end of chromosomes that protect chromosome ends from degradation and fusion (*1*). The length of the DNA component of telomeres, a six-nucleotide repeat sequence, shortens as cells divide (*2*), with short telomeres eventually triggering cellular senescence (*3*, *4*). In most human tissues, telomere length (TL) gradually shortens over time, and TL shortening is considered a hallmark (and a potential underlying cause) of human aging (*5*). In human studies, short TL measured in leukocytes is associated with increased risk of aging-related diseases, including cardiovascular disease (*6*) and type 2 diabetes (*7*), as well as overall mortality and human life span (*8*). However, long TL may increase the risks for some types of cancer (*9*–*11*). Leukocyte TL is influenced by inherited genetic variation [single-nucleotide polymorphisms (SNPs)], some of which reside near genes with known roles in telomere maintenance (*12*–*15*). Leukocyte TL is also associated with lifestyle factors (e.g., physical activity), health factors (e.g., obesity, cholesterol), and environmental exposures (e.g., cigarette smoking) (*16*, *17*).

Epidemiologic studies of TL predominantly use blood (occasionally saliva) as a DNA source. Thus, our understanding of variation in TL, its determinants (e.g., demographic, lifestyle, and genetic factors), and its associations with disease phenotypes almost entirely rely on TL measured in leukocytes from whole blood (WB). Few studies have compared TL in leukocytes with TL in other human tissue types; those that have are relatively small (<100 participants; <5 tissue types) but provide evidence that TL differs across tissue types and that TL measurements from different tissue types are correlated (*18*, *19*). Thus, larger studies of many additional tissue types are needed to gain a comprehensive understanding of variation in TL and its determinants within and across a wide range of human tissues and cell types.

To address these gaps in our understanding of TL and its role in disease risk and its relationship with age, we measured TL in >6000 unique tissue samples, representing >20 distinct tissue types and >950 individual donors from the Genotype-Tissue Expression (GTEx) project version 8 (v8) (*20*). In this work, we (i) characterize sources of variation in TL, (ii) evaluate leukocyte TL as a proxy for TL in other tissues, (iii) examine the relationship between age and TL across tissue types, and (iv) describe biological determinants and correlates of TL. This work presents results from tissue-specific and pan-tissue TL analyses that are crucial for improving our understanding of the etiologic role of TL in aging and chronic disease.

We attempted measurement of relative TL (RTL, the telomere repeat abundance relative to a standard reference DNA sample) for 7234 tissue samples from 962 GTEx donors using a Luminex-based assay (*21*). After removing 836 samples with failed RTL measurements and seven RTL measurements that were within-tissue outliers, our analytic dataset included 6391 tissue-specific RTL measurements from 952 donors, with 24 different tissue types having ≥25 RTL measurements (table S1). Each donor provided only one RTL measurement per tissue type, and on average, each donor had RTL measured in seven different tissue types (range: 1 to 26 tissue types) (fig. S1). The median donor age was 55 (range: 20 to 70) years. The majority of donors were male (67%) and of European descent (85%), and there were more postmortem donors (54%) than organ donors (table S1). Extensive validation and characterization of the Luminex-based RTL assay are described in (*21*).

TL varies across (and correlates among) human tissue types

We estimated the contribution of tissue type to the variation in RTL using linear mixed models (LMMs) adjusted for fixed effect covariates [age, sex, body mass index (BMI), race and ethnicity category, donor ischemic time, and technical factors, represented by plate (e.g., batch effects, DNA quality and concentration)] and with random effects representing tissue type and donor (table S2) (*21*). On average, RTL was the shortest in WB and longest in testis, with testis being an outlier tissue type [analysis of variance (ANOVA), $p < 2 \times 10^{-16}$ compared with all other tissues] (Fig. 1A). Tissue type explained 24.3% of the variation in RTL across all tissues but only 11.5% when testis was excluded, indicating that tissue type accounts for substantial variability in human TL.

We examined Pearson pairwise correlations in RTL among tissue types with tissue pairs from same donor, restricting to 20 tissue types with TL data for ≥75 samples (Fig. 1B). Forty-one tissue-pair correlations passed a Bonferroni p value threshold (t tests, $p < 3 \times 10^{-4}$), and all 41 correlations were positive (table S3). Tissue pairs from the same organ were among the strongest correlations observed: sun-exposed and nonexposed skin [Pearson correlation coefficient (r) = 0.24, t test, $p = 9 \times 10^{-3}$, n = 112], transverse and sigmoid colon (Pearson r = 0.40, t test, $p = 8 \times 10^{-7}$, n = 139), and esophagus mucosa (EM) and gastric junction (EGJ) (Pearson r = 0.22, t test, $p = 3 \times 10^{-3}$, n = 188). After applying hierarchical clustering to these pairwise correlations with average linkage, tissue RTLs separated into three clusters (Fig. 1B and fig. S2). Two clusters were characterized

[1]Department of Public Health Sciences, University of Chicago, Chicago, IL, USA. [2]Section of Genetic Medicine, Department of Medicine, Institute for Genomics and Systems Biology, Center for Data Intensive Science, University of Chicago, Chicago, IL, USA. [3]New York Genome Center, New York, NY, USA. [4]Statistical Genetics, Max Planck Institute of Psychiatry, Munich, Germany. [5]Department of Systems Biology, Columbia University, New York, NY, USA. [6]Center for Genetic Medicine, Department of Pharmacology, Northwestern University, Feinberg School of Medicine, Chicago, IL, USA. [7]Center of Human Development and Aging, Rutgers New Jersey Medical School, The State University of New Jersey, Newark, NJ, USA. [8]Broad Institute of MIT and Harvard, Cambridge, MA, USA. [9]Department of Human Genetics, University of Chicago, Chicago, IL, USA. [10]University of Chicago Comprehensive Cancer Center, Chicago, IL, USA. [11]Department of Medicine, University of Chicago, Chicago, IL, USA. [12]Huntsman Cancer Institute, University of Utah, Salt Lake City, UT, USA.
*A full list of the GTEx authors and their affiliations is available at the end of this article.
†Corresponding author. Email: brandonpierce@uchicago.edu

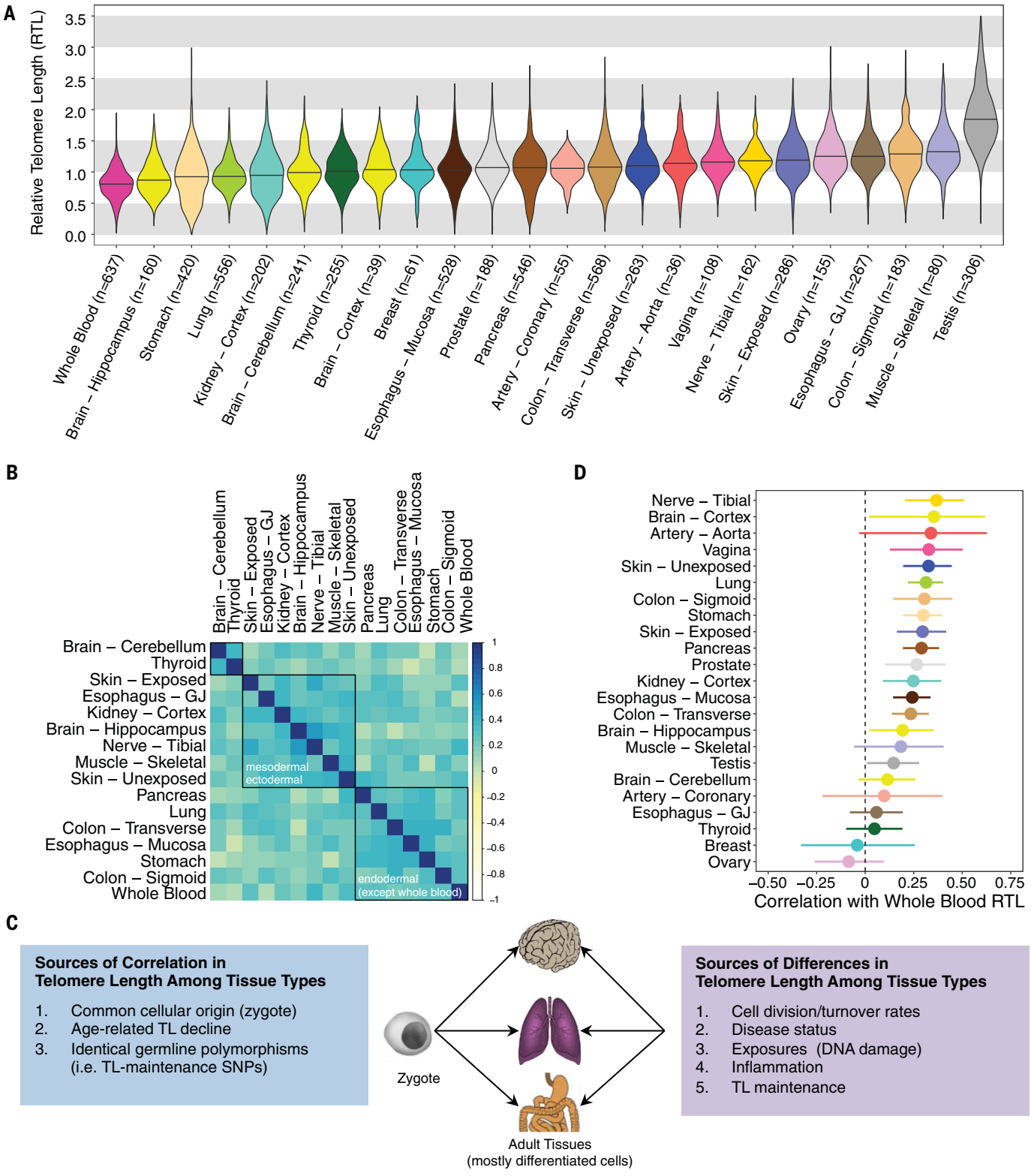

Fig. 1. TLs differ across human tissue types but are correlated among tissues types. (**A**) Distribution of RTL across 24 GTEx tissue types (ordered by median RTL) (see table S1). Nine-hundred fifty-two donors contributed one or more tissue samples to the analysis, and the sample size for each tissue type corresponds to unique donors (i.e., no donors are represented twice for a given tissue type). (**B**) Pearson (*r*) correlations between RTL measures from different tissue types. Tissues included have ≥75 samples and were not sex specific. Red, yellow, and blue correspond to *r* = 1, 0, and −1, respectively. Black boxes are results from hierarchical clustering (three clusters). (Exact correlations are in table S3.) (**C**) Theoretical framework describing determinants of TL across human tissue types. (**D**) Pearson correlations between WB RTL and tissue-specific RTL measurements (with 95% confidence intervals).

by common developmental origin: (i) mesodermal and ectodermal (e.g., muscle and skin) and (ii) endodermal origin tissues (e.g., stomach and lung). Thyroid and brain cerebellum formed the third cluster. Similar clustering patterns among tissue types were observed for females (fig. S3) and males (fig. S4), where testis was also an outlying tissue type and clustered with thyroid. The positive correlations observed among most tissue types are likely due to the fact that the initial TL in the zygote affects TL in all adult tissues through mitotic inheritance. Differences in tissue-type TL and the extent of correlation among tissue-type TLs are likely attributable to variability in both intrinsic (e.g., cell division rate and history, telomere maintenance) and extrinsic (e.g., response to environmental exposures) factors across tissues (Fig. 1C). To assess the possibility that extrinsic factors could modify the correlation between TL in different tissues, we assessed the overall difference in the correlation matrix by smoking history and obesity (as an indicator of disease status and health). In this exploratory analysis, the observed pairwise correlations among tissue types did not substantially differ between obese and normal or overweight donors. However, among individuals with a history of smoking, the correlation among tissue types was somewhat stronger compared with never-smokers (Jennrich's chi-square test, $p = 0.003$), but the underlying reason for this observation is unknown.

WB TL is a proxy for TL in other tissues

WB RTL was positively correlated (Pearson correlation, t test, $p < 0.05$) with tissue-specific RTL measurements from 15 out of 23 tissue types ($n \geq 25$ for each test), with Pearson correlations ranging from 0.15 to 0.37 (Fig. 1D). These results demonstrate that WB TL is a proxy for TL in many tissue types. WB RTL captured between 2% (testis) and 14% (tibial nerve) of the variation in RTL measured in other tissue types. Adjustment for age, sex, BMI, and donor ischemic time did not have a major impact on the associations observed between WB RTL and tissue-type RTL in the 23 tissue types (fig. S5). Notably, tibial nerve RTL had the strongest correlation with WB RTL. The GTEx tibial nerve samples largely contain connective tissue, Schwann cells, and the axons of neuron cells (which do not contain the DNA from neuron cells), and the strong correlation between tibial nerve RTL and WB RTL is likely due to the fact that the tibial nerve tissue and WB have connective tissue origins. Breast and ovary RTL had negative point estimates for their correlations with WB RTL, but the 95% confidence intervals overlapped zero. The relationships between the RTL from these tissue types and WB RTL require further investigation.

RTL measurements have inherent measurement error (*22*), including our Luminex assay (*23*), and this error can attenuate the strength of the correlation observed between RTL measurements taken from two different tissue types. To better understand this error, we conducted extensive validation and characterization of our Luminex-based assay, including comparisons to TL measured by Southern blot of terminal restriction fragments (TRFs) reported previously by Pierce *et al.* (*23*) and conducted within GTEx (*21*). Based on this validation work (*23*), we conclude that that the percentage of variation in our Luminex RTL measures that is due to (nondifferential) measurement error is <50%. The true percentage cannot be estimated because the extent of measurement error in our gold standard TL measure, Southern blot analysis of TRFs, is unknown. Therefore, we used simulated data to estimate the impact of measurement error (ranging from 0 to 50% of the variation in RTL) on the correlations between RTL measurements from different tissues (*21*). Our results show that the correlations observed in this study will be attenuated, and this attenuation will increase with increasing error in the RTL measurements (fig. S6).

In addition to validating our Luminex RTL measurements against TL measured using Southern blot, we have also validated these measurements against RTL measured using quantitative polymerase chain reaction (qPCR) (*24*), both in previous work (*25*) and using GTEx samples (*21*). Within GTEx, RTL measurements from qPCR (*24*) and TL measured from Southern blot (*26*) showed strong correlation with our Luminex RTL measurements and similar differences among tissue types as observed for the Luminex RTL measurements (Fig. 1A) (*21*).

TL varies among individuals and by participant characteristics

TL varied across individuals (donors) (Fig. 2A, top), with 8.7% of the variation in RTL attributable to variability among individuals (estimates obtained from an adjusted LMM) (table S2). This percentage increased to 11.2% when testis was excluded. After adjusting for tissue type and donor (as random effects), age explained 3.3% (among all tissues) and 4.4% (excluding testis) of variation in RTL, whereas BMI, TL-associated SNPs, smoking status, and race and ethnicity category each explained <1% of the variation across all tissues [marginal coefficient of determination (R^2), likelihood-ratio test (LRT), $p < 0.05$] (Fig. 2B, top), demonstrating that these factors contribute to pan-tissue TL dynamics. We observed no clear association between sex and RTL across all tissues (table S2), and sex showed weak evidence of association with RTL in tissue-specific analyses (table S4). Multiple prior studies have reported an association between longer leukocyte TL and female sex (*27*). However, we may be underpowered to detect this association for WB RTL, considering some larger studies have failed to detect it (*28*) and the association may be less evident at younger ages (*29*). The lack of association across all tissue types points to the possibility that this sex difference for leukocyte TL may not be consistent across all tissue types. RTL was shorter among (ever) smokers compared with never-smokers in lung and in WB (LRT, $p < 0.05$) (fig. S7), consistent with prior studies of leukocyte TL (*30*).

We conducted a principal component (PC) analysis of RTL from 11 nonreproductive tissue types (each with $n \geq 200$ samples) from 750 participants (*21*) and generated a composite measure of TL for each donor on the basis of the first PC that explains 51% of the variation in TL among these tissue types (Fig. 2A, bottom). We observed that age, BMI, and smoking status were associated with shorter composite RTL and explained 13.7, 1.3, and 0.6%, respectively, of the variation in this composite TL measure (Fig. 2B, bottom). Race and ethnicity category was associated with longer composite TL in African Americans compared with European Americans and explained 1.6% of the variation in composite TL. This composite TL likely reflects variation in TL present in the zygote (and in tissues during early development) that is mitotically inherited by cells in adult tissues.

TL is longer in genomes of African ancestry

To further explore differences in TL by race and ethnicity category, we first confirmed that PCs derived from genome-wide SNP data (n = 838 donors), representing genetic ancestry, showed clear clustering by reported race and ethnicity category among donors (Fig. 2C, inset). Genetic ancestry (European versus African) explained 0.6% of the variation in RTL across all tissues (marginal R^2, LRT, $p = 1 \times 10^{-5}$) after adjusting for tissue type and donor as random effects and 2.3% of the variation in composite RTL (F test, $p = 7 \times 10^{-5}$). After including adjustments for age, sex, donor ischemic time, technical factors, and random effects of tissue type and donor, RTL was longer among individuals of African ancestry compared with individuals of European ancestry across all tissue types (LRT, $p = 0.007$), demonstrating that the effect of ancestry on TL, reported previously for leukocyte TL (*31*–*34*), extends to TL in other tissue types. The adjusted association between African ancestry and RTL was positive for 16 out of 19 tissues tested, with LRT p values <0.05 for brain cerebellum (p = 0.03), thyroid (p = 0.02), prostate (p = 0.03), lung (p = 0.02), and WB (p = 0.005) (Fig. 2C and table S5). The observation that individuals of African ancestry have longer TL in many tissue types is consistent with the hypothesis that ancestry-based differences in TL are present early in development (*35*) and potentially in

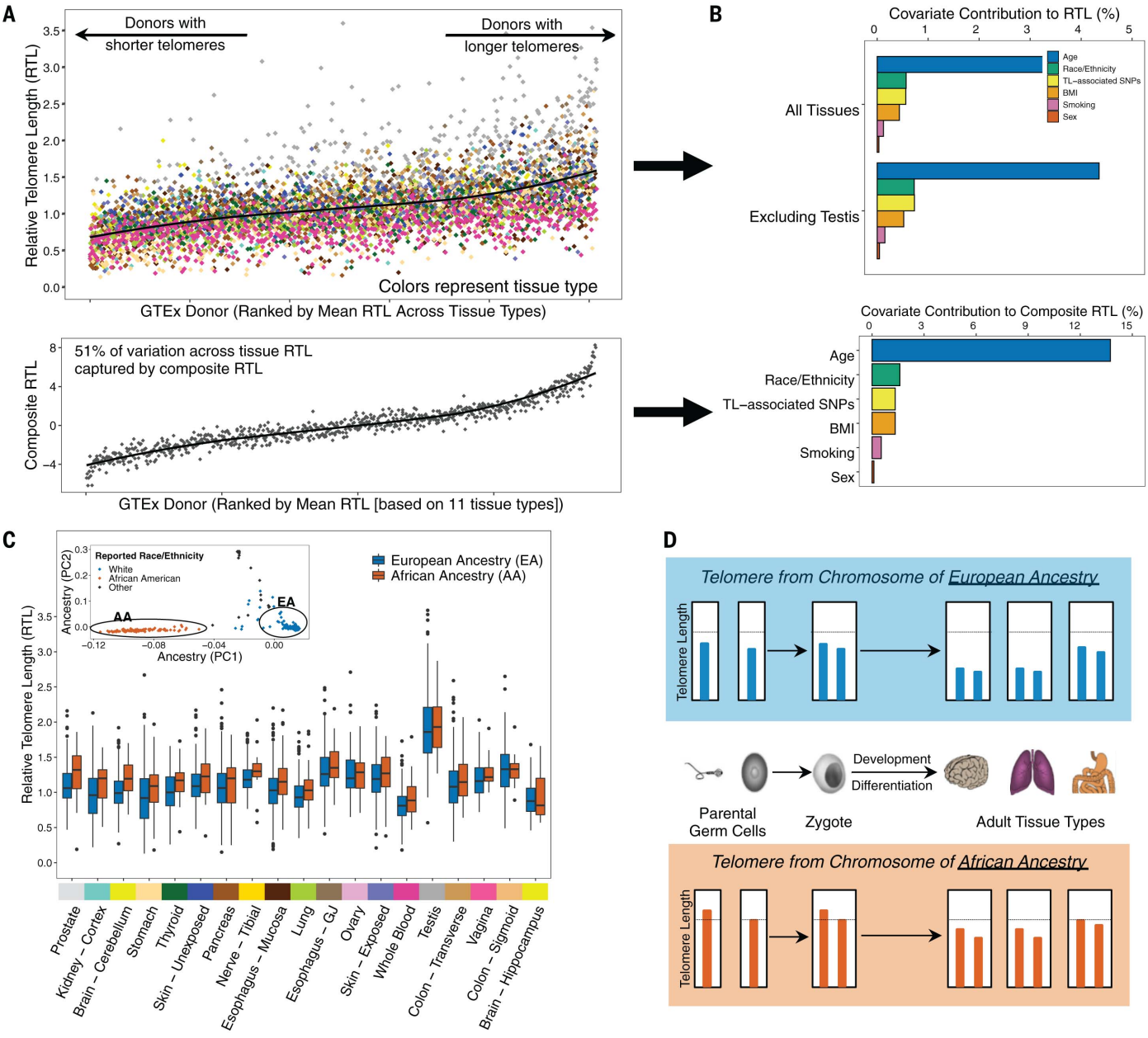

Fig. 2. TL varies among individuals and by ancestry. (**A**) Distribution of RTL across GTEx donors ranked by donors' mean RTL across all measured tissue types (top) and distribution of a "composite RTL" measure (bottom), estimated as the first PC from a PC analysis (PCA) of 11 tissue types (*21*). Colors correspond to GTEx tissue type. (**B**) Contribution of selected covariates to variability in RTL across all tissues (top) and composite RTL (bottom). For the analysis across all tissues, estimates were extracted as marginal R^2 values from LMMs adjusted for tissue type and donor as random effects. (**C**) Distribution of RTL measures for individuals of European ancestry (EA) and African ancestry (AA). Tissue types are ranked by the largest difference between median RTL of the two ancestry groups. The inset shows genotyping PCs, demonstrating consistent clustering of individuals by genetically predicted ancestry. Sample-size information and associations between African ancestry and RTL are reported in table S5. (**D**) Schematic describing the direct inheritance of TL from parental germ cells and expected relationship to TL across adult tissue types for individuals of African and European ancestry. Genetic (and reported race and ethnicity category) ancestry was color coded for African (red) and European (blue) in (C) and (D).

germ cells (preconception). In other words, our results suggest that offspring (zygotes) inherit telomeres from germ cells that vary in TL because of ancestry, and these ancestry-based differences in TL are mitotically transmitted to daughter cells, and eventually to cells in many adult tissue types. This "direct transmission" of TL from parent to offspring (*36*) would result in the observed ancestry-based differences across many tissue types (summarized in Fig. 2D). One likely cause of this ancestry-based difference is natural selection on SNPs know to affect TL (*37*), although selection on TL itself could also contribute.

TL is correlated with age in most tissues

Of 24 tissues with ≥25 samples, RTL was negatively correlated (Pearson $r < 0$) with age in 21 tissue types ($p < 0.05$ in 14 tissue types from t test) (Fig. 3A and fig. S8), providing new evidence to support the hypothesis that age-related TL shortening occurs in most

tissue types. The strongest correlations with age were observed for WB (Pearson $r = -0.35$, t test, $p = 2 \times 10^{-19}$, $n = 637$) and stomach ($r = 0.37$, t test, $p = 7 \times 10^{-15}$, $n = 420$) (table S6). Age explained more of the variation in RTL for tissues with shorter mean RTL [coefficient of determination (r^2) = 0.23, F test, $p = 0.02$] (Fig. 3B). The association between age and RTL differed by sex for hippocampus (t test, $p_{interaction} = 0.04$), transverse colon (t test, $p_{interaction} = 0.01$), and lung (t test, $p_{interaction} = 0.04$), suggesting that TL shortening with age is greater in men compared with women in some tissues. Among tissue types for which RTLs did not have a clear correlation with age (t test, $p > 0.05$), we examined whether RTL differed among 5-year age groups, but we observed no age-related differences in RTL for testis, ovary, cerebellum, vagina, skeletal muscle, thyroid, and EGJ (ANOVA, $p > 0.05$). Although prior studies have observed longer TL in sperm from older men (*38*), we did not observe a clear increasing (or decreasing) trend for testis RTL with increasing age (fig. S9).

Among tissue types for which RTL was correlated with age (t test, $p < 0.05$), the strength of association varied across tissue types (Fig. 3C and table S6). To further explore the hypothesis that TL shortens at different rates in different tissue types, we calculated the difference in RTL (ΔRTL) between all pairs of tissue types available for each donor. We constructed 155 ΔRTL variables, restricting to tissue pairs with complete data for ≥50 donors. The Pearson correlation between ΔRTL and age was estimated for each tissue-type pair to determine if the ΔRTL varies with age (fig. S10). Forty-two of the 155 ΔRTL variables were correlated with age (Pearson correlation, t test, $p < 0.05$), and the absolute values of these correlations ranged from 0.12 to 0.38 (table S7). Four of the ΔRTLs surpassed a Bonferroni p value of 3×10^{-4}: EGJ and stomach ($r = 0.32$, t test, $p = 1 \times 10^{-5}$, $n = 176$), WB and thyroid ($r = 0.30$, t test, $p = 3 \times 10^{-5}$, $n = 182$), EM and stomach ($r = 0.25$, t test, $p = 3 \times 10^{-5}$, and $n = 276$), and WB and ovary ($r = 0.33$, t test, $p = 2 \times 10^{-4}$, $n = 120$). Our results indicate that age explains up to 14% of the variation in the difference in RTL between pairs of tissue types. A prior study of 87 adults reported that the rate of age-related TL shortening was similar for muscle, leukocytes, fat, and skin (i.e., no association between age and ΔRTLs), concluding that age-related TL loss within stem cells is consistent across adult tissue types (*18*). When we examined these tissue types among our ΔRTL pairs ($n \geq 50$), age was correlated with ΔRTL for skeletal muscle and blood ($r = 0.36$, t test, $p = 2 \times 10^{-3}$, $n = 68$) but less for skin (unexposed) and blood ($r = 0.09$, t test, $p = 0.20$, $n = 197$) and skin (exposed) and blood ($r = 0.08$, t test, $p = 0.24$, $n = 200$).

Leukocyte TL–associated genetic variants and TL in other tissues

Prior genome-wide association studies (GWASs) have identified SNPs associated with leukocyte TL (*12*–*15*). We constructed a weighted polygenic SNP score for each donor using nine leukocyte TL–associated SNPs (*21*), with higher score reflecting longer TL (table S8) (*39*).We examined the association between this polygenic SNP score and RTL for tissue types with ≥100 samples. After adjustment for age, sex, genotyping PCs, donor ischemic time, and technical factors as a random effect, an association with the SNP score (LRT, $p < 0.05$) was observed for WB RTL ($p = 0.007$) (fig. S11), cerebellum RTL ($p = 0.03$), pancreas RTL ($p = 0.04$), and transverse colon RTL ($p = 0.02$) (Fig. 4A, fig. S12, and table S9). Among these 18 tissue types, 16 had positive association estimates [binomial test ($p_0 = 0.5$), $p = 0.001$]. In analyses of all tissue types, RTL was positively associated with the SNP score (LRT, $p = 0.01$) after adjustments. These results indicate that at least some of the genetic variants (or regions) that affect leukocyte TL also affect TL in other tissue types.

TL-associated variants influence local gene expression

Among the nine regions known to harbor SNPs associated with leukocyte TL, we examined whether these SNPs also affect local gene expression in GTEx tissue types and cell lines (*21*). Colocalization analysis can be used to determine if a common causal variant affects a trait (e.g., TL) and expression of a nearby gene (*40*). If there is a common causal variant underlying both association signals, then we may infer that SNPs may influence TL via effects on gene expression. We used colocalization analysis to estimate the probability that a common causal variant underlies association signals for leukocyte TL (from GWASs) (*12*–*15*) and cis-eQTL (expression quantitative trait loci) association signals from GTEx (v8) analyses (*20*). Colocalization results indicated that at least

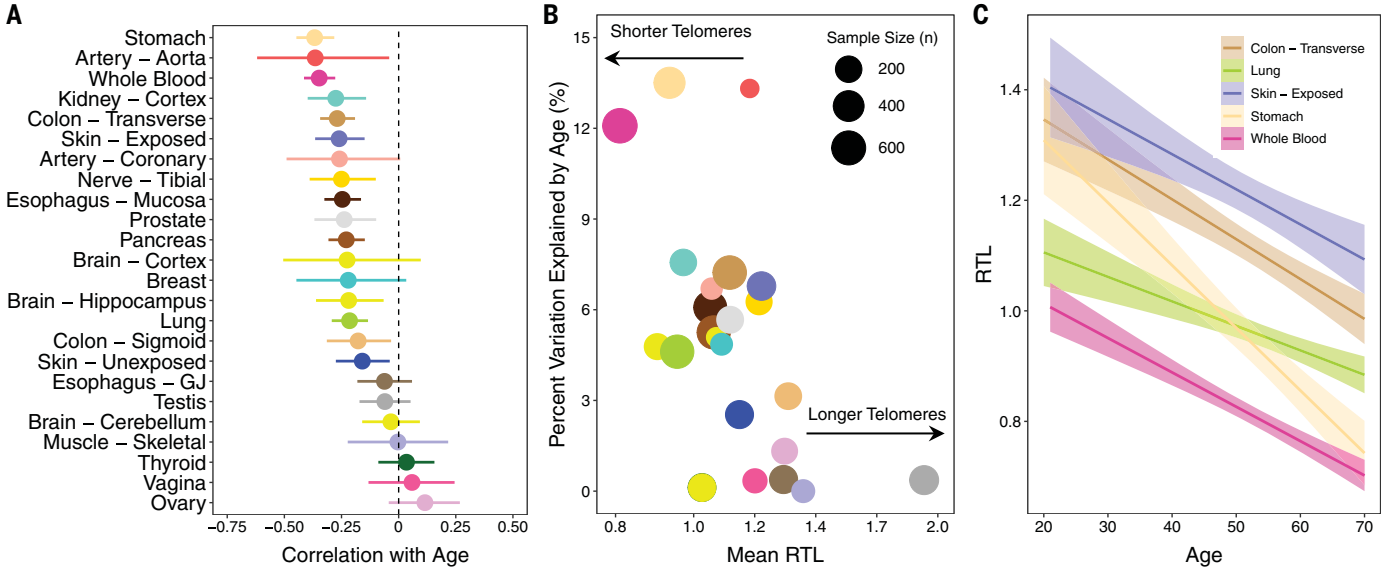

Fig. 3. Age is negatively correlated with TL in most tissues, and correlation is strongest in tissues with shorter telomeres. (**A**) Pearson correlations between age and tissue-specific RTL measures. (**B**) Scatterplot of mean RTL for each tissue versus the percent variation explained by age (r^2) for each tissue. The size of each point is proportional to sample size for that tissue type. (**C**) Relationship between RTL and age for five selected tissue types [WB, lung, stomach, transverse colon, and skin (exposed)]. For all plots, colors correspond to tissue type.

six of the nine TL-associated regions shared a common causal variant with a cis-eQTL in at least one tissue type, on the basis of a posterior probability of colocalization of ≥80% across all three sets of priors tested (Fig. 4, B and C; fig. S13; and table S10).

The association signal for TL on chromosome 19 (represented by rs8105767) showed strong evidence of colocalization with an eQTL affecting expression of gene *ZNF257* in eight tissue types, including skin (sun exposed), transverse colon, and stomach (Fig. 4B). *ZNF257* encodes a zinc-finger protein that may be involved in transcriptional regulation. The association signal for TL on chromosome 10 (represented by rs9420907) colocalized with an eQTL affecting expression of *STN1* in seven tissue types, including skin (sun exposed), transverse colon, and EM (Fig. 4C). Additional TL-associated loci showed colocalization with GTEx eQTLs for *NAF1*, *MYNN*, *RP11-109N23.6*, and *TSPYL6* (fig. S13 and table S10). Although these colocalizations were observed for eQTLs in tissue types with largely differentiated cells, eQTLs observed in induced pluripotent stem cells have been shown to be largely shared with eQTLs in GTEx tissue types (*41*). This finding suggests that the observed evidence of colocalization may be pertinent to TL maintenance within stem and progenitor cells, which have active telomerase activity. Notably, *NAF1* encodes a protein involved in telomere assembly, and loss-of-function (LOF) mutations in this gene are associated with shorter telomere length in pulmonary fibrosis (PF) patients (*42*). These results suggest that TL-associated loci influence TL within human tissues through regulation of the expression of genes known to be involved in telomere maintenance (e.g., *STN1*, *NAF1*) (*12*), as well as genes whose role in telomere maintenance is unclear (e.g., *ZNF257*).

Notably, we observed little evidence of colocalization of the *TERT* or *TERC* TL-associated regions with any cis-eQTLs. TERT and TERC are important components of telomerase. The telomerase enzyme can extend the telomere repeat sequence, typically in stem and/or progenitor cells, to compensate for TL shortening; however, *TERT* and *TERC* have low or undetectable expression in a majority of adult GTEx tissue samples. This suggests that eQTL studies

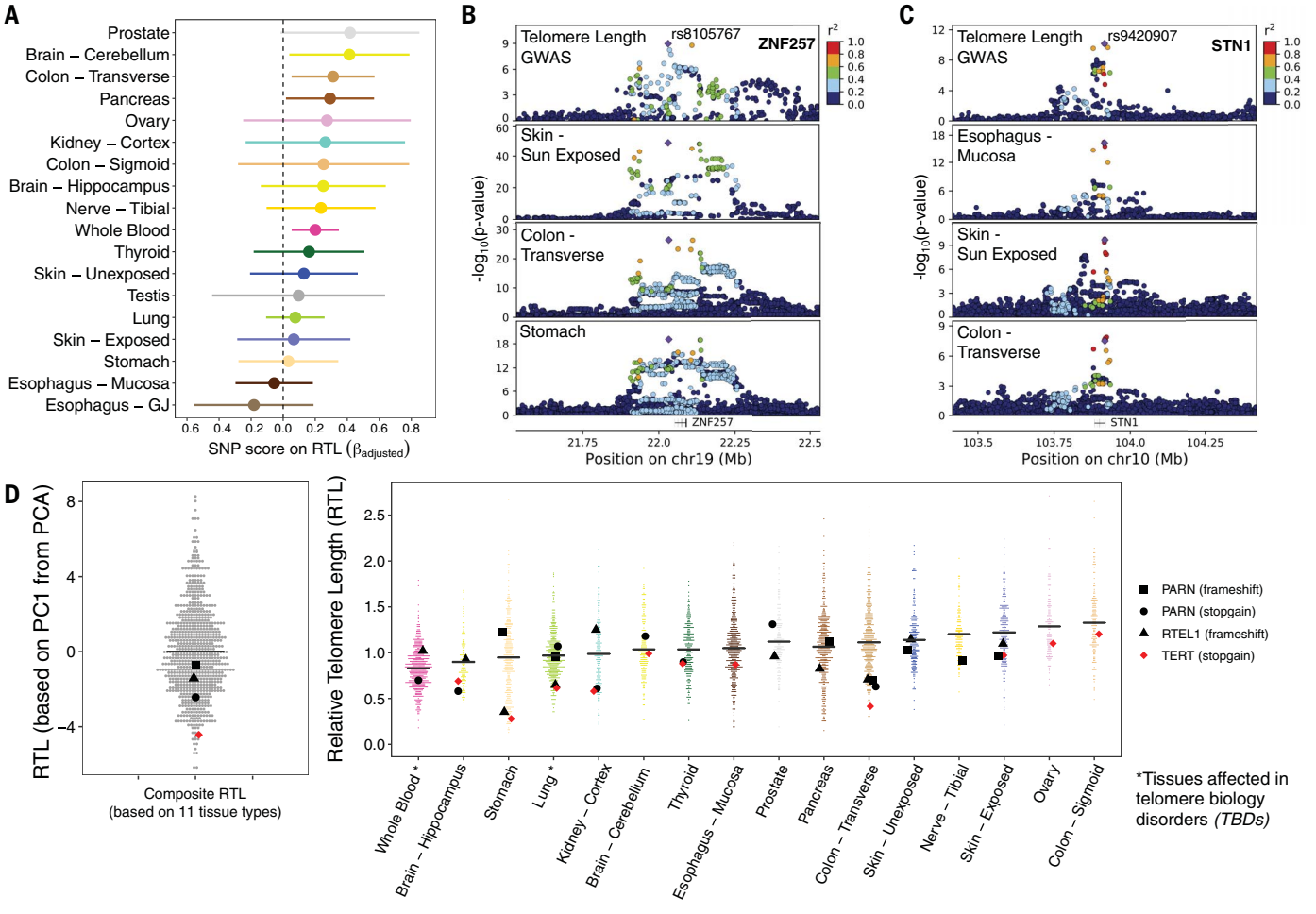

Fig. 4. Inherited genetic variation affects telomere length in multiple tissue types and expression of nearby genes. (**A**) Associations between a polygenic SNP score for leukocyte TL and tissue-specific RTL measures. Colors correspond to tissue type. (**B**) Leukocyte TL association signal from GWASs colocalizes with a cis-eQTL for *ZNF257* (~40 kb upstream of *ZNF208*). The top plot shows results from the ENGAGE Consortium GWAS of leukocyte TL, and the bottom three plots correspond to cis-eQTL results from GTEx tissues: skin–sun exposed, colon–transverse, and stomach. chr19, chromosome 19. (**C**) Leukocyte TL association signal colocalizes with a cis-eQTL for *STN1* (also known as *OBFC1* in human genome reference hg19). The top plot corresponds to results from the ENGAGE Consortium GWAS of leukocyte TL, and the bottom three plots correspond to cis-eQTL results from GTEx tissues: skin–sun exposed, EM, and colon–transverse. (**D**) Distribution of composite RTL (based on PC1 from PCA of 11 tissue types) (left) and tissue type RTL (right), with highlighted dots representing GTEx donors carrying a rare LOF variant in a telomere maintenance gene previously implicated in TBDs. LOF variants are noted in the legend. The black horizontal line corresponds to median composite RTL and tissue type RTL. The tissue types presented contain one or more LOF carriers, and colors correspond to tissue type.

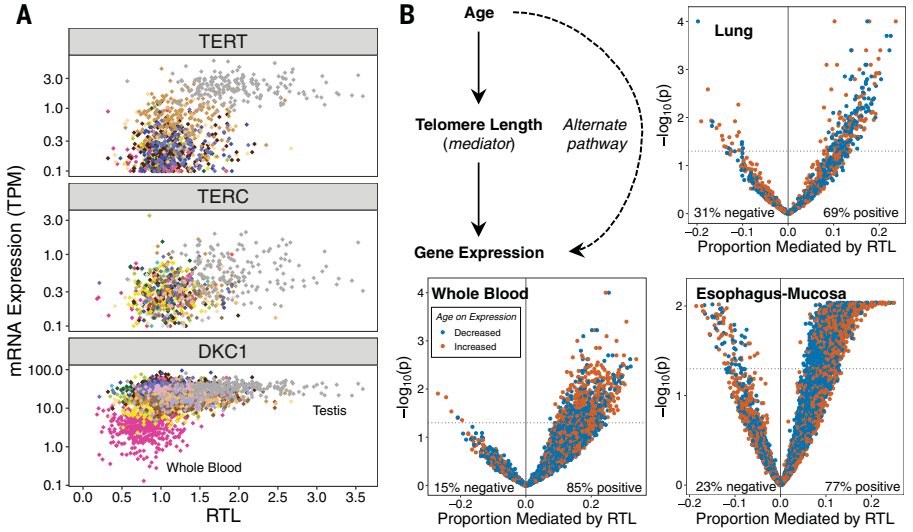

Fig. 5. TL is associated with telomerase subunit gene expression and may mediate the effect of age on gene expression. (**A**) RTL plotted against *TERC*, *TERT*, or *DKC1* expression across tissue types. Colors correspond to GTEx tissue types. (**B**) Analyses addressing the hypothesis that TL mediates the effect of age on expression of specific genes. Scatterplots show estimates of the proportion of the effect of age on gene expression mediated by RTL (for each gene) and the $-\log_{10}(p$ value) corresponding to the average causal mediation effect of RTL (for each gene). Results are presented for all age-associated genes in each of the three selected tissue types (WB, lung, and EM). The mediation p value was obtained using a nonparametric bootstrapping approach (n = 10,000 bootstraps).

of cells from stem and/or developmental tissues may be needed to understand the mechanisms underlying genetic regulation of *TERT* and *TERC* expression.

Carriers of rare LOF variants may have shorter TL

Telomere biology disorders (TBDs, e.g., PF, dyskeratosis congenita, aplastic anemia) are characterized by short TL in affected individuals owing to inherited LOF mutations in telomere maintenance genes (*1*, *43*–*45*). Individuals with TBDs often present with early-onset aging-related phenotypes—such as immune dysfunction, bone failure, liver disease, and lung function decline—and these effects can inform our understanding of how TL contributes to aging in the general population. Using whole-genome sequencing data from GTEx donors, we searched for LOF rare variants in seven genes that have evidence of autosomal dominant (or partial dominant) inheritance in relation to TBDs (e.g., *TERC*, *TERT*, *TINF2*, *RTEL1*, *PARN*, *ACD*, and *NAF1*). We identified four donors carrying a rare exonic variant (minor allele frequency <1%) resulting in a predicted LOF frameshift insertion or deletion or a stop-gain mutation (Fig. 4D). These LOF carriers had shorter TL across all tissues (LRT, p = 0.04) and shorter composite TL (t test, p = 0.03). One donor carried a stop-gain variant in *TERT*, and their composite TL was among the lowest observed (~first percentile), consistent with prior studies of *TERT* mutations among individuals with PF (*46*, *47*).

Our results suggest that rare variants in TL-maintenance genes may contribute to shorter TL in multiple tissues in the general population (i.e., primarily individuals without TBDs). However, the *PARN* and *RTEL1* mutation carriers among the GTEx donors did not have RTL values in the (lower) extreme of the composite TL and tissue-specific RTL distribution(s). Although mutations in TL maintenance genes and very short TL are often found in individuals with TBDs (*43*–*45*), prior studies of individuals with TBDs have shown that TL can vary substantially among carriers (of mutations in *PARN*, *RTEL1*, and *TERT*), and some carriers have TL values similar to noncarriers (*46*, *48*, *49*). Prior studies of PF patients suggest that LOF *TERT* mutations may have a larger impact on TL than LOF mutations in *PARN* or *RTEL1* (*46*, *47*, *49*).

TL is associated with telomerase subunit expression across tissues

The protein products of *TERT*, *TERC*, and *DKC1* comprise the telomerase catalytic subunit. We examined the association between RTL and expression of these genes using 3885 GTEx tissue samples with both RTL and RNA sequencing (RNA-seq) gene expression data (v8). *TERT* and *TERC* expression was detectable [i.e., transcripts per million (TPM) >0.1] in 28% (n = 1089) and 20% (n = 783) of these samples, respectively, but *DKC1* was ubiquitously expressed (n = 3885) in all samples (table S11). Whereas *DKC1* showed correlation with both *TERT* (Pearson r = 0.30, t test, $p < 2 \times 10^{-16}$, n = 1089) and *TERC* (r = 0.23, t test, $p = 3 \times 10^{-11}$, n = 783) across all samples, the correlation between *TERT* and *TERC* expression across samples was stronger (r = 0.49, t test, $p < 2 \times 10^{-16}$, n = 364) (fig. S14). Testis had substantially higher mean expression of *TERT* and *TERC* compared with all other tissues (ANOVA, $p < 2 \times 10^{-16}$) (table S11), but there was no association between testis RTL and *TERT* or *TERC* expression. Across all tissues, RTL was positively correlated with *TERT* (r = 0.58, t test, $p < 2 \times 10^{-16}$, n = 1089), *TERC* (r = 0.33, t test, $p < 2 \times 10^{-16}$, n = 783), and *DKC1* (r = 0.29, t test, $p < 2 \times 10^{-16}$, n = 3885) (Fig. 5A). When testis was removed, the correlation decreased substantially for both *TERT* (r = 0.14, $p = 4 \times 10^{-5}$, n = 890) and *DKC1* (r = 0.23, $p < 2 \times 10^{-16}$, n = 3686) and disappeared for *TERC* (r = 0.02, p = 0.63, n = 617). After adjustment for covariates and random effect of tissue type, RTL showed a positive association with increasing quartiles of *TERT* expression (LRT, p = 0.005 including testis and p = 0.002 excluding testis) and of *DKC1* expression (LRT, p = 0.001 including testis and $p = 3 \times 10^{-4}$ excluding testis) across all tissues. Overall these results support the following: (i) high telomerase activity in testis (i.e., spermatocytes) likely contributes to longer TL observed in that tissue, and (ii) GTEx tissue samples consist primarily of differentiated cells, which typically have little to no telomerase activity, resulting in minimal detectable association between telomerase activity in those cells and the observed TL (*50*, *51*).

TL may mediate the effect of age on gene expression

Aging affects gene expression, so we examined whether TL mediates the association between age and expression of age-associated genes. We analyzed the association between age and RNA-seq–based gene expression levels among tissues with ≥150 samples and selected three tissue types with >1000 age-associated genes [false discovery rate (FDR) of 0.05] (*21*): WB (n = 5239), lung (n = 1366), and EM (n = 6024) (Fig. 5B). Using mediation analysis (*52*), we estimated the proportion of the effect of age on expression that was mediated by TL for each age-associated gene. For each tissue type, we observed substantially more positive than negative estimates of the "proportion mediated" (Fig. 5B), as expected under the hypothesis that TL is a mediator. (An equal number of positive and negative estimates are expected under the hypothesis of no mediation.) If TL is a mediator for a specific gene, then adjustment for TL will attenuate the association between age and gene expression. We observed evidence that RTL mediated the effect of age on expression for 607 genes (12%) in WB, 224 genes (16%) in lung, and 1177 genes (20%) in EM ($p_{\text{mediation}} < 0.05$, and proportion mediated > 0) (tables S12 to S14). In these tissue types, RTL mediated between 4 and 34% of the effect

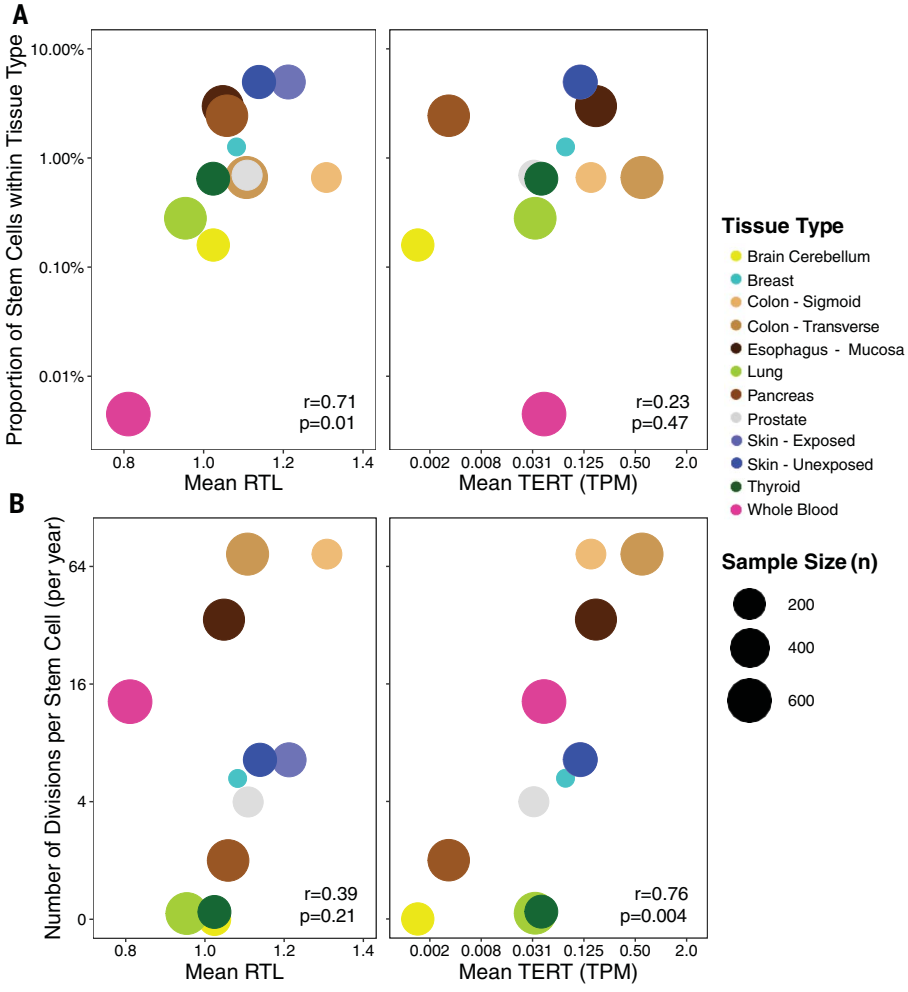

Fig. 6. TL and TERT expression are associated with estimated stem cell features. (**A**) Estimated proportion of stem cells within tissues and its relationship between mean RTL (left) and mean *TERT* expression (right). (**B**) Estimated number of divisions per stem cell (per year) within tissues and its relationship between mean RTL (left) and mean *TERT* expression (right). Colors correspond to GTEx tissue types, and the size of each point reflects the sample size of the tissue type. Pearson correlations and corresponding *p* values are reported. Analysis included nonreproductive tissues only.

of age on expression of individual genes; however, full mediation will be detected as partial mediation in the presence of measurement error (for either the mediator or the outcome) (*53*). We evaluated the enrichment of these RTL-mediated genes in gene ontology (GO) terms among the age-associated genes (Fisher's exact test, FDR < 0.1). Enriched GO terms were identified for lung (5 terms), EM (30 terms), and WB (108 terms) (tables S15 to S17). No GO terms (FDR < 0.1) were common to WB, lung, and EM for any ontology. Among 108 enriched GO terms in WB, several terms related to apoptosis, cell death, and telomere DNA binding were identified. The results from this analysis provide evidence that TL is a potentially relevant biologic factor in the mediation of age on gene expression and may contribute to processes related to biologic aging.

Tissue-level stem cell features are associated with TL and TERT expression

After extracting tissue-specific estimates of the number of divisions per stem cell (per year) and the proportion of stem cells (among all cells) for specific tissue types from Tomasetti and Vogelstein *et al.* (*54*, *55*), we examined their relationship with mean RTL and mean *TERT* expression among nonreproductive GTEx tissue types (n = 12; table S18). No associations were identified between mean *TERC* and *DKC1* expression and these stem cell features. Mean RTL was positively correlated with estimated proportion of stem cells within a tissue type (r = 0.71, t test, p = 0.01) (Fig. 6A), and this association persisted after adjustment for number of divisions per stem cell (t test, p = 0.008) and mean *TERT* expression (t test, p = 0.02). We did not observe a clear association between mean *TERT* expression and the estimated proportion of stem cells within a tissue type. These results suggest that tissue types with a higher proportion of stem cells in their cellular composition may have longer TL measurements in bulk tissues as a consequence.

We observed a positive correlation between mean *TERT* expression and the number of divisions per stem cell (r = 0.76, t test, p = 0.004) (Fig. 6B). This association persisted after adjustment for the proportion of stem cells within a tissue type (t test, p = 0.006) and mean RTL (t test, p = 0.01). Mean RTL showed suggestive evidence of correlation with the number of divisions per stem cell (r = 0.39, t test, p = 0.21), and when we restricted to nonblood tissue types, mean RTL was positively correlated with number of divisions per stem cell (r = 0.65, t test, p = 0.03). This finding suggests that tissue types that undergo more cellular turnover and replacement, such as colon, may have higher telomerase expression to maintain TL in the stem cell compartments.

Cell-type composition is associated with TL within tissues

To determine whether TL varies among the cell types within a given tissue sample, we examined the association between RTL and estimated cell-type enrichment scores (CTES) [generated using RNA-seq data and the xCell software (*56*)]. Seven CTES (for adipocytes, epithelial cells, hepatocytes, keratinocytes, myocytes, neurons, and neutrophils) were benchmarked by the GTEx Consortium (*57*), and we examined the association between these seven CTES and RTL in tissue types with ≥100 samples (n = 16 tissue types). After removing cell types not detected within a tissue type (n = 37 total CTES tested across 16 tissue types) and adjusting for age and sex, we identified eight associations (t test, p < 0.05) between CTES and RTL among 37 associations tested (fig. S15). In exploratory analyses, we examined all 64 CTES provided by xCell that had a detection p value <0.05 for >90% samples within a tissue type. Restricting to tissue types with ≥300 samples that had both CTES and RTL data (WB, lung, and EM), there were 27, 24, and 17 CTES detected in each tissue, respectively (fig. S16). EM and lung had 13 and 14 CTES that were associated with RTL, after adjustment for age and sex (t test, p < 0.05). RTL was positively associated with epithelial cell, smooth muscle cell, keratinocyte, and sebocyte CTES in both lung and EM (p < 0.05). Notably, five CTES were inversely associated with RTL (p < 0.05) in both lung and EM, including fibroblasts and endothelial cells. In WB, lymphoid and myeloid cell CTES accounted for 70% of the CTES detected, and eight CTES were associated with RTL (t test, p < 0.05). Neutrophil CTES were positively associated with RTL. Both $CD8^+$ T cell CTES

were inversely associated with RTL, consistent with prior work examining cell types and TL in blood (*58*). These results provide evidence that TL varies across cell types within a given tissue, and consequently, cell-type composition can affect TL measurement in human tissues.

TL across all tissues is associated with age-related chronic disease status

Using medical history data from GTEx donors, we examined the association between common age-related chronic diseases and RTL within and across tissues. A history of type 2 diabetes (22% of donors) was associated with shorter RTL across all tissues (LRT, $p = 0.02$) as well as shorter pancreas RTL ($p = 0.07$) and coronary artery RTL ($p = 0.01$) (fig. S17). Among all donors, 50% had no history of any chronic disease, and 30, 14, and 6% had a history of one, two, and three (or more) chronic diseases, respectively. Chronic disease burden (sum of chronic diseases from 0 to 5) was associated with shorter RTL across all tissues (LRT, $p = 0.008$) and in testis, coronary artery, kidney cortex, and cerebellum (LRT, $p < 0.05$ for each). When we excluded cancer from the chronic disease burden, these associations persisted across all tissues (LRT, $p = 0.02$) and in all tissues listed above except for kidney cortex (LRT, $p = 0.09$). These observations suggest that TL may capture some aspect of the biologic age-related health decline across tissues.

We did not observe any associations between RTL and history of cancer; however, to test the hypothesis that normal tissues with relatively short (or long) TL are also short (or long) in tumors occurring in that tissue, we compared the mean tissue-to-WB TL ratio for each GTEx tissue with the mean tumor-to-WB TL ratio in corresponding cancer types from The Cancer Genome Atlas (TCGA) (*21*, *59*). The mean cancer TL ratio from TCGA and normal TL ratio from GTEx were positively correlated ($r = 0.44$, t test, $p = 0.04$, $n = 23$) (fig. S18), providing support for this hypothesis.

After reviewing the medical and death report information for diseases and conditions related to TBDs (*21*), we identified six donors with a reported history of PF and/or interstitial lung disease (ILD). Five of these donors had TL measurements ($n = 35$ tissue-type samples). We observed that three of the donors with a history of PF or ILD had composite RTL below the fifth percentile (fig. S19). A history of PF or ILD was associated with shorter TL across all tissues (LRT, $p = 0.02$) and shorter composite RTL (t test, $p = 0.01$). Notably, we observed that within tissues, the median RTL was substantially shorter for WB (Mann-Whitney U test, $p = 0.02$), pancreas ($p = 0.01$), and EM ($p = 0.05$) among donors with a history of PF or ILD.

Discussion

This study provides a view of the substantial variation in human TL that exists across human tissue types and among individuals. We show that TL is generally positively correlated across human tissue types, and that WB TL is a proxy for tissue-specific TL for many tissues, a finding that may support the use of blood TL as a proxy for TL in some tissues in large epidemiological studies. TL was negatively associated with age in the majority of tissues studied, confirming the hypothesis of pervasive age-related telomere shortening in most human tissues. However, our results suggest that the rate of shortening can vary across tissues, and age explained more variation in TL in tissues with shorter mean TL. *TERT* and *TERC* expression were low or undetectable in most tissues and not associated with TL within any tissue, likely because progenitor cells, which express telomerase, are not present in large numbers in adult tissue samples, which consist primarily of differentiated cells. Notably, testicular TL was ~1.5- to 2.5-fold longer than TL in any other tissue type, and *TERT* was expressed in 100% of these samples and at higher levels than in any other tissue, consistent with the predominance of spermatogenic cells in testis (i.e., cells developing from germ cells into spermatozoa), which have high telomerase activity (*51*).

RTL measured in a tissue sample is an average of the TLs among all chromosomes within a heterogeneous population of cell types with different cell division rates and history, stem cell composition, and oxidative and inflammatory environments. To characterize variation in TL within specific cell types, cell type–specific and single-cell TL studies are needed, potentially using interphase quantitative fluorescence in situ hybridization approaches (*60*) and flow cell cytometry to isolate specific cell types, including stem cells.

A large proportion of the variation in RTL was unexplained across all tissue types, potentially attributed to sources such as cell-type composition (e.g., stem and progenitor cells), measurement error, and lifestyle and environmental factors with variable effects across tissues. From our simulation-based analysis of the impact of TL measurement error on our results, we show that random measurement error biases our estimate of the true correlation in TL between two tissues toward zero, suggesting that the correlations presented in this study are attenuated compared with their true associations.

We lack detailed exposure data (e.g., smoking and alcohol use) for GTEx donors; studies that can link human tissue samples to environmental and lifestyle histories are needed to better understand environmental determinants of TL across different tissues and cell types. As of now, all TL-associated SNPs have been identified in GWASs of leukocyte TL (*12*–*15*); our study suggests that some of these effects are also present in other tissue types, but larger studies of tissue-specific TL measurements are needed to characterize how these effects vary across tissues and cell types. Identifying variants that affect TL in all or most cell types (e.g., variants with effects on TL that may be present during development or in stem cells in multiple tissue types) may be ideal for evaluating the causal impact of TL on risk for a wide array of diseases (occurring in diverse tissues or cell types) using Mendelian randomization. TL shortening is an important hallmark of aging in human tissues, but TL should also be studied in conjunction with other hallmarks of aging. Characterizing the relationships among TL and other aging-related processes and biomarkers within and across tissues will improve our understanding of cellular aging and its impact on human health.

Methods summary

We measured RTL in 6391 samples from 952 GTEx donors using a Luminex-based method. These measurements were validated against other TL measurement methods, including TL measured using Southern blot of TRFs (fig. S20) (*26*), relative TL measured using qPCR (fig. S21) (*24*), and TL estimated from whole-genome sequencing data (fig. S22) (*61*). Publicly available GTEx donor covariate, genotyping, and RNA-seq gene expression data (all v8) were integrated into our analyses. We applied LMMs to examine the relationships of RTL with age, genetic ancestry, gene expression of telomerase components, estimates of cell types, and other covariates across and within tissue types. Using GTEx genotyping data, we constructed a weighted polygenic SNP score for each donor using nine leukocyte TL–associated SNPs identified from the ENGAGE GWAS of leukocyte TL (*12*) and examined colocalization of these GWAS association signals with local gene expression using summary statistics from the ENGAGE study and eQTL results from the GTEx Consortium. Mediation analyses were applied to examine the extent to which TL mediates the effect of age on gene expression. Estimates of stem cell division and proportion of stem cells were extracted from prior studies (*54*, *55*) for corresponding GTEx tissues, and their relationship with average RTL and *TERT* expression was examined.

REFERENCES AND NOTES

1. E. H. Blackburn, E. S. Epel, J. Lin, Human telomere biology: A contributory and interactive factor in aging, disease risks, and protection. *Science* **350**, 1193–1198 (2015). doi: 10.1126/science.aab3389; pmid: 26785477
2. C. B. Harley, A. B. Futcher, C. W. Greider, Telomeres shorten during ageing of human fibroblasts. *Nature* **345**, 458–460 (1990). doi: 10.1038/345458a0; pmid: 2342578
3. Y. Zou, A. Sfeir, S. M. Gryaznov, J. W. Shay, W. E. Wright, Does a sentinel or a subset of short telomeres determine

replicative senescence? *Mol. Biol. Cell* **15**, 3709–3718 (2004). doi: 10.1091/mbc.e04-03-0207; pmid: 15181152
4. J. W. Shay, Role of telomeres and telomerase in aging and cancer. *Cancer Discov.* **6**, 584–593 (2016). doi: 10.1158/2159-8290.CD-16-0062; pmid: 27029895
5. C. López-Otín, M. A. Blasco, L. Partridge, M. Serrano, G. Kroemer, The hallmarks of aging. *Cell* **153**, 1194–1217 (2013). doi: 10.1016/j.cell.2013.05.039; pmid: 23746838
6. P. C. Haycock *et al*., Leucocyte telomere length and risk of cardiovascular disease: Systematic review and meta-analysis. *BMJ* **349**, g4227 (2014). doi: 10.1136/bmj.g4227; pmid: 25006006
7. P. Willeit *et al*., Leucocyte telomere length and risk of type 2 diabetes mellitus: New prospective cohort study and literature-based meta-analysis. *PLOS ONE* **9**, e112483 (2014). doi: 10.1371/journal.pone.0112483; pmid: 25390655
8. K. G. Arbeev *et al*., Association of leukocyte telomere length with mortality among adult participants in 3 longitudinal studies. *JAMA Netw. Open* **3**, e200023 (2020). doi: 10.1001/jamanetworkopen.2020.0023; pmid: 32101305
9. L. Rode, B. G. Nordestgaard, S. E. Bojesen, Long telomeres and cancer risk among 95 568 individuals from the general population. *Int. J. Epidemiol.* **45**, 1634–1643 (2016). doi: 10.1093/ije/dyw179; pmid: 27498151
10. P. C. Haycock *et al*., Association between telomere length and risk of cancer and non-neoplastic diseases: A Mendelian randomization study. *JAMA Oncol.* **3**, 636–651 (2017). pmid: 28241208
11. C. Zhang *et al*., Genetic determinants of telomere length and risk of common cancers: A Mendelian randomization study. *Hum. Mol. Genet.* **24**, 5356–5366 (2015). doi: 10.1093/hmg/ddv252; pmid: 26138067
12. V. Codd *et al*., Identification of seven loci affecting mean telomere length and their association with disease. *Nat. Genet.* **45**, 422–427, e1–e2 (2013). doi: 10.1038/ng.2528; pmid: 23535734
13. M. Mangino *et al*., *DCAF4*, a novel gene associated with leucocyte telomere length. *J. Med. Genet.* **52**, 157–162 (2015). doi: 10.1136/jmedgenet-2014-102681; pmid: 25624462
14. M. Mangino *et al*., Genome-wide meta-analysis points to CTC1 and ZNF676 as genes regulating telomere homeostasis in humans. *Hum. Mol. Genet.* **21**, 5385–5394 (2012). doi: 10.1093/hmg/dds382; pmid: 23001564
15. D. A. Delgado *et al*., Genome-wide association study of telomere length among South Asians identifies a second RTEL1 association signal. *J. Med. Genet.* **55**, 64–71 (2018). doi: 10.1136/jmedgenet-2017-104922; pmid: 29151059
16. C. J. Patel, A. K. Manrai, E. Corona, I. S. Kohane, Systematic correlation of environmental exposure and physiological and self-reported behaviour factors with leukocyte telomere length. *Int. J. Epidemiol.* **46**, 44–56 (2017). pmid: 27059547
17. D. H. Rehkopf *et al*., Leukocyte telomere length in relation to 17 biomarkers of cardiovascular disease risk: A cross-sectional study of US adults. *PLOS Med.* **13**, e1002188 (2016). doi: 10.1371/journal.pmed.1002188; pmid: 27898678
18. L. Daniali *et al*., Telomeres shorten at equivalent rates in somatic tissues of adults. *Nat. Commun.* **4**, 1597 (2013). doi: 10.1038/ncomms2602; pmid: 23511462
19. S. Sabharwal *et al*., Telomere length dynamics in early life: The blood-and-muscle model. *FASEB J.* **32**, 529–534 (2018). doi: 10.1096/fj.201700630r; pmid: 28855279
20. GTEx Consortium, The GTEx Consortium atlas of genetic regulatory effects across human tissues. *Science* **369**, 1318 (2020). doi: 10.1126/science.aaz1776
21. Materials and methods are available as supplementary materials.
22. J. H. Barrett, M. M. Iles, A. M. Dunning, K. A. Pooley, Telomere length and common disease: Study design and analytical challenges. *Hum. Genet.* **134**, 679–689 (2015). doi: 10.1007/s00439-015-1563-4; pmid: 25986438
23. B. L. Pierce *et al*., Telomere length measurement by a novel Luminex-based assay: A blinded comparison to Southern blot. *Int. J. Mol. Epidemiol. Genet.* **7**, 18–23 (2016). pmid: 27186324
24. R. M. Cawthon, Telomere measurement by quantitative PCR. *Nucleic Acids Res.* **30**, e47 (2002). doi: 10.1093/nar/30.10.e47; pmid: 12000852
25. M. G. Kibriya, F. Jasmine, S. Roy, H. Ahsan, B. L. Pierce, Novel luminex assay for telomere repeat mass does not show well position effects like qPCR. *PLOS ONE* **11**, e0155548 (2016). doi: 10.1371/journal.pone.0155548; pmid: 27182778
26. M. Kimura *et al*., Measurement of telomere length by the Southern blot analysis of terminal restriction fragment lengths. *Nat. Protoc.* **5**, 1596–1607 (2010). doi: 10.1038/nprot.2010.124; pmid: 21085125
27. M. Gardner *et al*., Gender and telomere length: Systematic review and meta-analysis. *Exp. Gerontol.* **51**, 15–27 (2014). doi: 10.1016/j.exger.2013.12.004; pmid: 24365661
28. S. Y. Gebreab *et al*., Less than ideal cardiovascular health is associated with shorter leukocyte telomere length: The National Health and Nutrition Examination Surveys, 1999–2002. *J. Am. Heart Assoc.* **6**, e004105 (2017). doi: 10.1161/JAHA.116.004105; pmid: 28154163
29. K. Lapham *et al*., Automated assay of telomere length measurement and informatics for 100,000 subjects in the Genetic Epidemiology Research on Adult Health and Aging (GERA) cohort. *Genetics* **200**, 1061–1072 (2015). doi: 10.1534/genetics.115.178624; pmid: 26092717
30. Y. Astuti, A. Wardhana, J. Watkins, W. Wulaningsih; PILAR Research Network, Cigarette smoking and telomere length: A systematic review of 84 studies and meta-analysis. *Environ. Res.* **158**, 480–489 (2017). doi: 10.1016/j.envres.2017.06.038; pmid: 28704792
31. C. L. Carty *et al*., Leukocyte telomere length and risks of incident coronary heart disease and mortality in a racially diverse population of postmenopausal women. *Arterioscler. Thromb. Vasc. Biol.* **35**, 2225–2231 (2015). doi: 10.1161/ATVBAHA.115.305838; pmid: 26249011
32. C. C. Elbers *et al*., Comparison between southern blots and qPCR analysis of leukocyte telomere length in the health ABC study. *J. Gerontol. A Biol. Sci. Med. Sci.* **69**, 527–531 (2014). doi: 10.1093/gerona/glt121; pmid: 23946336
33. S. C. Hunt *et al*., Leukocyte telomeres are longer in African Americans than in whites: The National Heart, Lung, and Blood Institute Family Heart Study and the Bogalusa Heart Study. *Aging Cell* **7**, 451–458 (2008). doi: 10.1111/j.1474-9726.2008.00397.x; pmid: 18462274
34. S. M. Lynch *et al*., Race, ethnicity, psychosocial factors, and telomere length in a multicenter setting. *PLOS ONE* **11**, e0146723 (2016). doi: 10.1371/journal.pone.0146723; pmid: 26752285
35. M. Rewak *et al*., Race-related health disparities and biological aging: Does rate of telomere shortening differ across blacks and whites? *Biol. Psychol.* **99**, 92–99 (2014). doi: 10.1016/j.biopsycho.2014.03.007; pmid: 24686071
36. D. A. Delgado *et al*., The contribution of parent-to-offspring transmission of telomeres to the heritability of telomere length in humans. *Hum. Genet.* **138**, 49–60 (2019). doi: 10.1007/s00439-018-1964-2; pmid: 30536049
37. M. E. Hansen *et al*., Shorter telomere length in Europeans than in Africans due to polygenetic adaptation. *Hum. Mol. Genet.* **25**, 2324–2330 (2016). doi: 10.1093/hmg/ddw070; pmid: 26936823
38. K. I. Aston *et al*., Divergence of sperm and leukocyte age-dependent telomere dynamics: Implications for male-driven evolution of telomere length in humans. *Mol. Hum. Reprod.* **18**, 517–522 (2012). doi: 10.1093/molehr/gas028; pmid: 22782639
39. L. Rode, B. G. Nordestgaard, S. E. Bojesen, Peripheral blood leukocyte telomere length and mortality among 64,637 individuals from the general population. *J. Natl. Cancer Inst.* **107**, djv074 (2015). doi: 10.1093/jnci/djv074; pmid: 25862531
40. C. Giambartolomei *et al*., Bayesian test for colocalisation between pairs of genetic association studies using summary statistics. *PLOS Genet.* **10**, e1004383 (2014). doi: 10.1371/journal.pgen.1004383; pmid: 24830394
41. C. DeBoever *et al*., Large-scale profiling reveals the influence of genetic variation on gene expression in human induced pluripotent stem cells. *Cell Stem Cell* **20**, 533–546.e7 (2017). doi: 10.1016/j.stem.2017.03.009; pmid: 28388430
42. S. E. Stanley *et al*., Loss-of-function mutations in the RNA biogenesis factor NAF1 predispose to pulmonary fibrosis-emphysema. *Sci. Transl. Med.* **8**, 351ra107 (2016). doi: 10.1126/scitranslmed.aaf7837; pmid: 27510903
43. S. A. Savage, Beginning at the ends: Telomeres and human disease. *F1000Res.* **7**, 524 (2018). doi: 10.12688/f1000research.14068.1; pmid: 29770205
44. J. W. Shay, W. E. Wright, Telomeres and telomerase: Three decades of progress. *Nat. Rev. Genet.* **20**, 299–309 (2019). doi: 10.1038/s41576-019-0099-1; pmid: 30760854
45. M. Armanios, E. H. Blackburn, The telomere syndromes. *Nat. Rev. Genet.* **13**, 693–704 (2012). doi: 10.1038/nrg3246; pmid: 22965356
46. B. D. Stuart *et al*., Exome sequencing links mutations in *PARN* and *RTEL1* with familial pulmonary fibrosis and telomere shortening. *Nat. Genet.* **47**, 512–517 (2015). doi: 10.1038/ng.3278; pmid: 25848748
47. A. Dressen *et al*., Analysis of protein-altering variants in telomerase genes and their association with *MUC5B* common variant status in patients with idiopathic pulmonary fibrosis: A candidate gene sequencing study. *Lancet Respir. Med.* **6**, 603–614 (2018). doi: 10.1016/S2213-2600(18)30135-8 pmid: 29891356
48. J. K. Alder *et al*., Diagnostic utility of telomere length testing in a hospital-based setting. *Proc. Natl. Acad. Sci. U.S.A.* **115**, E2358–E2365 (2018). doi: 10.1073/pnas.1720427115; pmid: 29463756
49. C. A. Newton *et al*., Telomere-related lung fibrosis is diagnostically heterogeneous but uniformly progressive. *Eur. Respir. J.* **48**, 1710–1720 (2016). doi: 10.1183/13993003.00308-2016; pmid: 27540018
50. C. Günes, K. L. Rudolph, The role of telomeres in stem cells and cancer. *Cell* **152**, 390–393 (2013). doi: 10.1016/j.cell.2013.01.010; pmid: 23374336
51. S. Ozturk, Telomerase activity and telomere length in male germ cells. *Biol. Reprod.* **92**, 53 (2015). doi: 10.1095/biolreprod.114.124008; pmid: 25568305
52. D. Tingley, T. Yamamoto, K. Hirose, L. Keele, K. Imai, mediation: R package for causal mediation analysis. *J. Stat. Softw.* **59**, 1–38 (2014). doi: 10.18637/jss.v059.i05
53. B. L. Pierce *et al*., Mediation analysis demonstrates that trans-eQTLs are often explained by cis-mediation: A genome-wide analysis among 1,800 South Asians. *PLOS Genet.* **10**, e1004818 (2014). doi: 10.1371/journal.pgen.1004818; pmid: 25474530
54. C. Tomasetti, B. Vogelstein, Variation in cancer risk among tissues can be explained by the number of stem cell divisions. *Science* **347**, 78–81 (2015). doi: 10.1126/science.1260825; pmid: 25554788
55. C. Tomasetti, L. Li, B. Vogelstein, Stem cell divisions, somatic mutations, cancer etiology, and cancer prevention. *Science* **355**, 1330–1334 (2017). doi: 10.1126/science.aaf9011; pmid: 28336671
56. D. Aran, Z. Hu, A. J. Butte, xCell: Digitally portraying the tissue cellular heterogeneity landscape. *Genome Biol.* **18**, 220 (2017). doi: 10.1186/s13059-017-1349-1; pmid: 29141660
57. S. Kim-Hellmuth *et al*., Cell type–specific genetic regulation of gene expression across human tissues. *Science* **369**, eaaz8528 (2020). doi: 10.1126/science.aaz8528
58. J. Lin *et al*., Analyses and comparisons of telomerase activity and telomere length in human T and B cells: Insights for epidemiology of telomere maintenance. *J. Immunol. Methods* **352**, 71–80 (2010). doi: 10.1016/j.jim.2009.09.012; pmid: 19837074
59. F. P. Barthel *et al*., Systematic analysis of telomere length and somatic alterations in 31 cancer types. *Nat. Genet.* **49**, 349–357 (2017). doi: 10.1038/ng.3781; pmid: 28135248
60. M. Sharifi-Sanjani, A. K. Meeker, F. Mourkioti, Evaluation of telomere length in human cardiac tissues using cardiac quantitative FISH. *Nat. Protoc.* **12**, 1855–1870 (2017). doi: 10.1038/nprot.2017.082; pmid: 28817123
61. Z. Ding, M. Mangino, A. Aviv, T. Spector, R. Durbin; UK10K Consortium, Estimating telomere length from whole genome sequence data. *Nucleic Acids Res.* **42**, e75 (2014). doi: 10.1093/nar/gku181; pmid: 24609383
62. K. Demanelis, kdemanelis/gtex_telomerelength v1.1. Zenodo (2020); https://doi.org/10.5281/zenodo.3969532.

ACKNOWLEDGMENTS

We acknowledge the GTEx donors and families for their generous participation in and contribution to the GTEx Consortium. GTEx Consortium members: We thank the donors and their families for their generous gifts of organ donation for transplantation and tissue donations for the GTEx research project; the Genomics Platform at the Broad Institute for data generation; and J. Struewing for his support and leadership of the GTEx project. **Funding:** This work was supported by the National Institute of Aging Specialized Demography and Economics of Aging Training Program (T32AG000243) (K.D. and C.Z.), NIH Research Supplement to Promote Diversity in Health-Related Research (associated with R35ES028379) (K.D. and D.D.), Marie-Skłodowska Curie Fellowship H2020 Grant 706636 (S.K.-H.), Susan G. Komen Fellowship (GTDR16376189) (M.C. and D.D.), Medical Scientist National Research Service Award (T32GM07281) (M.C.), Norwegian Research Council (NFR ES562296) (A.A.), active and past NIH grants (U01HG007601, R35ES028379, and R01ES020506 to B.L.P.; R01CA107431 and P30ES027792 to H.A.; R01GM108711 to L.S.C.; and R01HL134840 and U01AG066529 to A.A.), and the GTEx LDACC (HHSN268201000029C). GTEx Consortium members: This work was supported by the Common Fund of the Office of the Director, NIH, and by NCI, NHGRI, NHLBI, NIDA, NIMH, NIA, NIAID, and NINDS through NIH contracts HHSN261200800001E (Leidos Prime contract with NCI: A.M.S., D.E.T., N.V.R., J.A.M., L.S., M.E.B., L.Q., T.K., D.B., K.R., and A.U.), 10XS170 (NDRI: W.F.L., J.A.T., G.K., A.M., S.S., R.H., G.Wa., M.J., M.Wa., L.E.B., C.J., J.W., B.R., M.Hu., K.M., L.A.S., H.M.G., M.Mo., and L.K.B.), 10XS171 (Roswell Park Cancer Institute: B.A.F., M.T.M.,

E.K., B.M.G., K.D.R., and J.B.), 10X172 (Science Care Inc.), 12ST1039 (IDOX), 10ST1035 (Van Andel Institute: S.D.J., D.C.R., and D.R.V.), HHSN268201000029C (Broad Institute: F.A., G.G., K.G.A., A.V.S., X.Li., E.T., S.G., A.G., S.A., K.H.H., D.T.N., K.H., S.R.M., and J.L.N.), 5U41HG009494 (F.A., G.G., and K.G.A.), and through NIH grants R01 DA006227-17 (University of Miami Brain Bank: D.C.M. and D.A.D.), supplement to University of Miami grant DA006227 (D.C.M. and D.A.D.), R01 MH090941 (University of Geneva), R01 MH090951 and R01 MH090937 (University of Chicago), R01 MH090936 (University of North Carolina–Chapel Hill), R01MH101814 (M.M.-A., V.W., S.B.M., R.G., E.T.D., D.G.-M., and A.V.), U01HG007593 (S.B.M.), R01MH101822 (C.D.B.), U01HG007598 (M.O. and B.E.S.), U01MH104393 (A.P.F.), extension H002371 to 5U41HG002371 (W.J.K) as well as other funding sources: R01MH106842 (T.L., P.M., E.F., and P.J.H.), R01HL142028 (T.L., Si.Ka., and P.J.H.), R01GM122924 (T.L. and S.E.C.), R01MH107666 (H.K.I.), P30DK020595 (H.K.I.), UM1HG008901 (T.L.), R01GM124486 (T.L.), R01HG010067 (Y.Pa.), R01HG002585 (G.Wa. and M.St.), Gordon and Betty Moore Foundation GBMF 4559 (G.Wa. and M.St.), 1K99HG009916-01 (S.E.C.), R01HG006855 (Se.Ka. and R.E.H.), BIO2015-70777-P, Ministerio de Economia y Competitividad and FEDER funds (M.M.-A., V.W., R.G., and D.G.-M.), la Caixa Foundation ID 100010434 under agreement LCF/BQ/SO15/52260001 (D.G.-M.), NIH CTSA grant UL1TR002550-01 (P.M.), Marie-Skłodowska Curie fellowship H2020 Grant 706636 (S.K-H.), R35HG010718 (E.R.G.), FPU15/03635, Ministerio de Educación, Cultura y Deporte (M.M.-A.), R01MH109905, 1R01HG010480 (A.Ba.), Searle Scholar Program (A.Ba.), R01HG008150 (S.B.M.), 5T32HG000044-22, NHGRI Institutional Training Grant in Genome Science (N.R.G.), EU IMI program (UE7-DIRECT-115317-1) (E.T.D. and A.V.), FNS funded project RNA1 (31003A_149984) (E.T.D. and A.V.), DK110919 (F.H.), F32HG009987 (F.H.), and Massachusetts Lions Eye Research Fund Grant (A.R.H.). **Author contributions:** K.D., J.A.D., L.S.C., M.G.K., H.A., and B.L.P. conceived and designed the study. F.J., J.S., M.S., and M.G.K. conducted Luminex assays on all samples. A.A. and T.-P.L. conducted Southern blots of TRFs for the validation study. K.D., L.S.C., M.C., L.T., D.D., C.Z., H.L., E.R., and B.L.P. contributed to the statistical analyses in the study. K.G.A. and F.A. were responsible for the generation of GTEx v8 RNA-seq and genotyping data for the GTEx Consortium. M.O., S.K.-H., and B.E.S. generated the GTEx cell-type estimates for the v8 release. K.D. and B.L.P. wrote the manuscript. All authors contributed to the revision and review of the manuscript. **Competing interests:** J.A.D. is an affiliate investigator at the Fred Hutchinson Cancer Research Center, Seattle, WA, and an adjunct associate professor at The Geisel School of Medicine at Dartmouth, Hanover, NH. F.A. is an inventor on a patent application related to TensorQTL. GTEx Consortium members: S.E.C. is a co-founder, chief technology officer, and stock owner at Variant Bio; E.R.G. is on the Editorial Board of Circulation Research and does consulting for the City of Hope/Beckman Research Institute; E.T.D. is chairman and member of the board of Hybridstat, Ltd.; B.E.E. is on the scientific advisory boards of Celsius Therapeutics and Freenome; G.G. receives research funds from IBM and Pharmacyclics and is an inventor on patent applications related to MuTect, ABSOLUTE, MutSig, MSMuTect, MSMutSig, POLYSOLVER, and TensorQTL. G.G. is a founder of and consultant to and holds privately held equity in Scorpion Therapeutics; S.B.M. is on the scientific advisory board of MyOme; D.G.M. is a co-founder with equity in Goldfinch Bio and has received research support from AbbVie, Astellas, Biogen, BioMarin, Eisai, Merck, Pfizer, and Sanofi-Genzyme; H.K.I. has received speaker honoraria from GSK and AbbVie; T.L. is a scientific advisory board member of Variant Bio with equity and Goldfinch Bio. P.F. is a member of the scientific advisory boards of Fabric Genomics, Inc., and Eagle Genomes, Ltd. P.G.F. is a partner of Bioinf2Bio. **Data and materials availability:** Luminex TL measurement, RNA-seq gene expression, and eQTL summary statistic data are available on the GTEx Portal (www.gtexportal.org) for future research use. All GTEx protected data are available through the database of Genotypes and Phenotypes (dbGaP) (accession no. phs000424.v8). Code has been deposited at Zenodo (*62*).

GTEx Consortium

Laboratory and Data Analysis Coordinating Center (LDACC): François Aguet[1], Shankara Anand[1], Kristin G. Ardlie[1], Stacey Gabriel[1], Gad A. Getz[1,2,3], Aaron Graubert[1], Kane Hadley[1], Robert E. Handsaker[4,5,6], Katherine H. Huang[1], Seva Kashin[4,5,6], Xiao Li[1], Daniel G. MacArthur[5,7], Samuel R. Meier[1], Jared L. Nedzel[1], Duyen T. Nguyen[1], Ayellet V. Segrè[1,8], Ellen Todres[1]

Analysis Working Group Funded by GTEx Project Grants: François Aguet[1], Shankara Anand[1], Kristin G. Ardlie[1], Brunilda Balliu[9], Alvaro N. Barbeira[10], Alexis Battle[11,12], Rodrigo Bonazzola[10], Andrew Brown[13,14], Christopher D. Brown[15], Stephane E. Castel[16,17], Donald F. Conrad[18,19], Daniel J. Cotter[20], Nancy Cox[21], Sayantan Das[22], Olivia M. de Goede[20], Emmanouil T. Dermitzakis[13,23,24], Jonah Einson[16,25], Barbara E. Engelhardt[26,27], Eleazar Eskin[28], Tiffany Y. Eulalio[29], Nicole M. Ferraro[29], Elise D. Flynn[16,17], Laure Fresard[30], Eric R. Gamazon[21,31,32,33], Diego Garrido-Martín[34], Nicole R. Gay[20], Gad A. Getz[1,2,3], Michael J. Gloudemans[29], Aaron Graubert[1], Roderic Guigó[34,35], Kane Hadley[1], Andrew R. Hame[l8,1], Robert E. Handsaker[4,5,6], Yuan He[11], Paul J. Hoffman[16], Farhad Hormozdiari[1,36], Lei Hou[1,37], Katherine H. Huang[1], Hae Kyung Im[10], Brian Jo[26,27], Silva Kasela[16,17], Seva Kashin[4,5,6], Manolis Kellis[1,37], Sarah Kim-Hellmuth[16,17,38], Alan Kwong[22], Tuuli Lappalainen[16,17], Xiao Li[1], Xin Li[30], Yanyu Liang[10], Daniel G. MacArthur[5,7], Serghei Mangul[28,39], Samuel R. Meier[1], Pejman Mohammadi[16,17,40,41], Stephen B. Montgomery[20,30], Manuel Muñoz-Aguirre[34,42], Daniel C. Nachun[30], Jared L. Nedzel[1], Duyen T. Nguyen[1], Andrew B. Nobel[43], Meritxell Oliva[10,44], YoSon Park[15,45], Yongjin Park[1,37], Princy Parsana[12], Abhiram S. Rao[46], Ferran Reverter[47], John M. Rouhana[1,8], Chiara Sabatti[48], Ashis Saha[12], Ayellet V. Segrè[1,8], Andrew D. Skol[10,49], Matthew Stephens[50], Barbara E. Stranger[10,51], Benjamin J. Strober[11], Nicole A. Teran[30], Ellen Todres[1], Ana Viñuela[13,23,24,52], Gao Wang[50], Xiaoquan Wen[22], Fred Wright[53], Valentin Wucher[34], Yuxin Zou[54]

Analysis Working Group Not Funded by GTEx Project Grants: Pedro G. Ferreira[55,56,57,58], Gen Li[59], Marta Melé[60], Esti Yeger-Lotem[61,62]

Leidos Biomedical Project Management: Mary E. Barcus[63], Debra Bradbury[63], Tanya Krubit[63], Jeffrey A. McLean[63], Liqun Qi[63], Karna Robinson[63], Nancy V. Roche[63], Anna M. Smith[63], Leslie Sobin[63], David E. Tabor[63], Anita Undale[63]

Biospecimen Collection Source Sites: Jason Bridge[64], Lori E. Brigham[65], Barbara A. Foster[66], Bryan M. Gillard[66], Richard Hasz[67], Marcus Hunter[68], Christopher Johns[69], Mark Johnson[70], Ellen Karasik[66], Gene Kopen[71], William F. Leinweber[71], Alisa McDonald[71], Michael T. Moser[66], Kevin Myer[68], Kimberley D. Ramsey[66], Brian Roe[68], Saboor Shad[71], Jeffrey A. Thomas[71,70], Gary Walters[70], Michael Washington[70], Joseph Wheeler[69]

Biospecimen Core Resource: Scott D. Jewell[72], Daniel C. Rohrer[72], Dana R. Valley[72]

Brain Bank Repository: David A. Davis[73], Deborah C. Mash[73]

Pathology: Mary E. Barcus[63], Philip A. Branton[74], Leslie Sobin[63]

ELSI Study: Laura K. Barker[75], Heather M. Gardiner[75], Maghboeba Mosavel[76], Laura A. Siminoff[75]

Genome Browser Data Integration and Visualization: Paul Flicek[77], Maximilian Haeussler[78], Thomas Juettemann[77], W. James Kent[78], Christopher M. Lee[78], Conner C. Powell[78], Kate R. Rosenbloom[78], Magali Ruffier[77], Dan Sheppard[77], Kieron Taylor[77], Stephen J. Trevanion[77], Daniel R. Zerbino[77]

eGTEx Group: Nathan S. Abell[20], Joshua Akey[79], Lin Chen[44], Kathryn Demanelis[44], Jennifer A. Doherty[80], Andrew P. Feinberg[81], Kasper D. Hansen[82], Peter F. Hickey[83], Lei Hou[1,37], Farzana Jasmine[44], Lihua Jiang[20], Rajinder Kaul[84,85], Manolis Kellis[1,37], Muhammad G. Kibriya[44], Jin Billy Li[20], Qin Li[20], Shin Lin[86], Sandra E. Linder[20], Stephen B. Montgomery[20,30], Meritxell Oliva[10,44], Yongjin Park[1,37], Brandon L. Pierce[44], Lindsay F. Rizzardi[87], Andrew D. Skol[10,49], Kevin S. Smith[30], Michael Snyder[20], John Stamatoyannopoulos[84,88], Barbara E. Stranger[10,51], Hua Tang[20], Meng Wang[20]

NIH Program Management: Philip A. Branton[74], Latarsha J. Carithers[74,89], Ping Guan[74], Susan E. Koester[90], A. Roger Little[91], Helen M. Moore[74], Concepcion R. Nierras[92], Abhi K. Rao[74], Jimmie B. Vaught[74], Simona Volpi[93]

[1]Broad Institute of MIT and Harvard, Cambridge, MA, USA. [2]Cancer Center and Department of Pathology, Massachusetts General Hospital, Boston, MA, USA. [3]Harvard Medical School, Boston, MA, USA. [4]Department of Genetics, Harvard Medical School, Boston, MA, USA. [5]Program in Medical and Population Genetics, Broad Institute of MIT and Harvard, Cambridge, MA, USA. [6]Stanley Center for Psychiatric Research, Broad Institute of MIT and Harvard, Cambridge, MA, USA. [7]Analytic and Translational Genetics Unit, Massachusetts General Hospital, Boston, MA, USA. [8]Ocular Genomics Institute, Massachusetts Eye and Ear, Harvard Medical School, Boston, MA, USA. [9]Department of Biomathematics, University of California, Los Angeles, CA, USA. [10]Section of Genetic Medicine, Department of Medicine, The University of Chicago, Chicago, IL, USA. [11]Department of Biomedical Engineering, Johns Hopkins University, Baltimore, MD, USA. [12]Department of Computer Science, Johns Hopkins University, Baltimore, MD, USA. [13]Department of Genetic Medicine and Development, University of Geneva Medical School, Geneva, Switzerland. [14]Population Health and Genomics, University of Dundee, Dundee, Scotland, UK. [15]Department of Genetics, University of Pennsylvania, Perelman School of Medicine, Philadelphia, PA, USA. [16]New York Genome Center, New York, NY, USA. [17]Department of Systems Biology, Columbia University, New York, NY, USA. [18]Department of Genetics, Washington University School of Medicine, St. Louis, MO, USA. [19]Division of Genetics, Oregon National Primate Research Center, Oregon Health & Science University, Portland, OR, USA. [20]Department of Genetics, Stanford University, Stanford, CA, USA. [21]Division of Genetic Medicine, Department of Medicine, Vanderbilt University Medical Center, Nashville, TN, USA. [22]Department of Biostatistics, University of Michigan, Ann Arbor, MI, USA. [23]Institute for Genetics and Genomics in Geneva (iGE3), University of Geneva, Geneva, Switzerland. [24]Swiss Institute of Bioinformatics, Geneva, Switzerland. [25]Department of Biomedical Informatics, Columbia University, New York, NY, USA. [26]Department of Computer Science, Princeton University, Princeton, NJ, USA. [27]Center for Statistics and Machine Learning, Princeton University, Princeton, NJ, USA. [28]Department of Computer Science, University of California, Los Angeles, CA, USA. [29]Program in Biomedical Informatics, Stanford University School of Medicine, Stanford, CA, USA. [30]Department of Pathology, Stanford University, Stanford, CA, USA. [31]Data Science Institute, Vanderbilt University, Nashville, TN, USA. [32]Clare Hall, University of Cambridge, Cambridge, UK. [33]MRC Epidemiology Unit, University of Cambridge, Cambridge, UK. [34]Centre for Genomic Regulation (CRG), The Barcelona Institute for Science and Technology, Barcelona, Catalonia, Spain. [35]Universitat Pompeu Fabra (UPF), Barcelona, Catalonia, Spain. [36]Department of Epidemiology, Harvard T.H. Chan School of Public Health, Boston, MA, USA. [37]Computer Science and Artificial Intelligence Laboratory, Massachusetts Institute of Technology, Cambridge, MA, USA. [38]Statistical Genetics, Max Planck Institute of Psychiatry, Munich, Germany [39]Department of Clinical Pharmacy, School of Pharmacy, University of Southern California, Los Angeles, CA, USA. [40]Scripps Research Translational Institute, La Jolla, CA, USA. [41]Department of Integrative Structural and Computational Biology, The Scripps Research Institute, La Jolla, CA, USA. [42]Department of Statistics and Operations Research, Universitat Politècnica de Catalunya (UPC), Barcelona, Catalonia, Spain. [43]Department of Statistics and Operations Research and Department of Biostatistics, University of North Carolina, Chapel Hill, NC, USA. [44]Department of Public Health Sciences, The University of Chicago, Chicago, IL, USA. [45]Department of Systems Pharmacology and Translational Therapeutics, Perelman School of Medicine, University of Pennsylvania, Philadelphia, PA, USA. [46]Department of Bioengineering, Stanford University, Stanford, CA, USA. [47]Department of Genetics, Microbiology and Statistics, University of Barcelona, Barcelona, Spain. [48]Departments of Biomedical Data Science and Statistics, Stanford University, Stanford, CA, USA. [49]Department of Pathology and Laboratory Medicine, Ann & Robert H. Lurie Children's Hospital of Chicago, Chicago, IL, USA. [50]Department of Human Genetics, University of Chicago, Chicago, IL, USA. [51]Center for Genetic Medicine, Department of Pharmacology, Northwestern University, Feinberg School of Medicine, Chicago, IL, USA. [52]Department of Twin Research and Genetic Epidemiology, King's College London, London, UK. [53]Bioinformatics Research Center and Departments of Statistics and Biological Sciences, North Carolina State University, Raleigh, NC, USA. [54]Department of Statistics, University of Chicago, Chicago, IL, USA. [55]Department of Computer Sciences, Faculty of Sciences, University of Porto, Porto, Portugal. [56]Instituto de Investigação e Inovação em Saúde, University of Porto, Porto, Portugal. [57]Institute of Molecular Pathology and Immunology, University of Porto, Porto, Portugal. [58]Laboratory of Artificial Intelligence and Decision Support, Institute for Systems and Computer Engineering, Technology and Science, Porto, Portugal. [59]Mailman School of Public Health, Columbia University, New York, NY, USA. [60]Life Sciences Department, Barcelona Supercomputing Center, Barcelona, Spain. [61]Department of Clinical Biochemistry and Pharmacology, Ben-Gurion University of the Negev, Beer-Sheva, Israel. [62]National Institute for Biotechnology in the Negev, Beer-Sheva, Israel. [63]Leidos Biomedical, Rockville, MD, USA. [64]Upstate New York Transplant Services, Buffalo, NY, USA. [65]Washington Regional Transplant Community, Annandale, VA, USA. [66]Therapeutics, Roswell Park Comprehensive Cancer Center, Buffalo, NY, USA. [67]Gift of Life Donor Program, Philadelphia, PA, USA. [68]LifeGift, Houston, TX, USA. [69]Center for Organ Recovery and Education, Pittsburgh, PA, USA. [70]LifeNet Health, Virginia Beach, VA. USA. [71]National Disease Research Interchange, Philadelphia, PA, USA. [72]Van Andel Research Institute, Grand Rapids, MI, USA. [73]Department of Neurology, University of Miami Miller School of Medicine, Miami, FL, USA. [74]Biorepositories and Biospecimen Research Branch, Division of Cancer Treatment and Diagnosis, National Cancer Institute, National Institutes of Health, Bethesda, MD, USA. [75]Temple University, Philadelphia, PA, USA. [76]Virginia Commonwealth University, Richmond, VA, USA. [77]European Molecular

Biology Laboratory, European Bioinformatics Institute, Hinxton, UK. [78]Genomics Institute, University of California, Santa Cruz, CA, USA. [79]Carl Icahn Laboratory, Princeton University, Princeton, NJ, USA. [80]Department of Population Health Sciences, The University of Utah, Salt Lake City, UT, USA. [81]Departments of Medicine, Biomedical Engineering, and Mental Health, Johns Hopkins University, Baltimore, MD, USA. [82]Department of Biostatistics, Bloomberg School of Public Health, Johns Hopkins University, Baltimore, MD, USA. [83]Department of Medical Biology, The Walter and Eliza Hall Institute of Medical Research, Parkville, Victoria, Australia. [84]Altius Institute for Biomedical Sciences, Seattle, WA, USA. [85]Division of Genetics, University of Washington, Seattle, WA, USA. [86]Department of Cardiology, University of Washington, Seattle, WA, USA. [87]HudsonAlpha Institute for Biotechnology, Huntsville, AL, USA. [88]Genome Sciences, University of Washington, Seattle, WA, USA. [89]National Institute of Dental and Craniofacial Research, National Institutes of Health, Bethesda, MD, USA. [90]Division of Neuroscience and Basic Behavioral Science, National Institute of Mental Health, National Institutes of Health, Bethesda, MD, USA. [91]National Institute on Drug Abuse, Bethesda, MD, USA. [92]Office of Strategic Coordination, Division of Program Coordination, Planning and Strategic Initiatives, Office of the Director, National Institutes of Health, Rockville, MD, USA. [93]Division of Genomic Medicine, National Human Genome Research Institute, Bethesda, MD, USA.

SUPPLEMENTARY MATERIALS

science.sciencemag.org/content/369/6509/eaaz6876/suppl/DC1
Materials and Methods
Figs. S1 to S23
Tables S1 to S18
References (*63*–*71*)
MDAR Reproducibility Checklist

View/request a protocol for this paper from *Bio-protocol*.

3 October 2019; accepted 3 August 2020
10.1126/science.aaz6876

RESEARCH ARTICLE SUMMARY

HUMAN GENOMICS

Transcriptomic signatures across human tissues identify functional rare genetic variation

Nicole M. Ferraro*, Benjamin J. Strober*, Jonah Einson, Nathan S. Abell, Francois Aguet, Alvaro N. Barbeira, Margot Brandt, Maja Bucan, Stephane E. Castel, Joe R. Davis, Emily Greenwald, Gaelen T. Hess, Austin T. Hilliard, Rachel L. Kember, Bence Kotis, YoSon Park, Gina Peloso, Shweta Ramdas, Alexandra J. Scott, Craig Smail, Emily K. Tsang, Seyedeh M. Zekavat, Marcello Ziosi, Aradhana, TOPMed Lipids Working Group, Kristin G. Ardlie, Themistocles L. Assimes, Michael C. Bassik, Christopher D. Brown, Adolfo Correa, Ira Hall, Hae Kyung Im, Xin Li, Pradeep Natarajan, GTEx Consortium, Tuuli Lappalainen, Pejman Mohammadi†‡, Stephen B. Montgomery†‡, Alexis Battle†‡

INTRODUCTION: The human genome contains tens of thousands of rare (minor allele frequency <1%) variants, some of which contribute to disease risk. Using 838 samples with whole-genome and multitissue transcriptome sequencing data in the Genotype-Tissue Expression (GTEx) project version 8, we assessed how rare genetic variants contribute to extreme patterns in gene expression (eOutliers), allelic expression (aseOutliers), and alternative splicing (sOutliers). We integrated these three signals across 49 tissues with genomic annotations to prioritize high-impact rare variants (RVs) that associate with human traits.

RATIONALE: Outlier gene expression aids in identifying functional RVs. Transcriptome sequencing provides diverse measurements beyond gene expression, including allele-specific expression and alternative splicing, which can provide additional insight into RV functional effects.

RESULTS: After identifying multitissue eOutliers, aseOutliers, and sOutliers, we found that outlier individuals of each type were significantly more likely to carry an RV near the corresponding gene. Among eOutliers, we observed strong enrichment of rare structural variants. sOutliers were particularly enriched for RVs that disrupted or created a splicing consensus sequence. aseOutliers provided the strongest enrichment signal when evaluated from just a single tissue.

We developed Watershed, a probabilistic model for personal genome interpretation that improves over standard genomic annotation–based methods for scoring RVs by integrating these three transcriptomic signals from the same individual and replicates in an independent cohort.

To assess whether outlier RVs identified in GTEx associate with traits, we evaluated these variants for association with diverse traits in the UK Biobank, the Million Veterans Program, and the Jackson Heart Study. We found that transcriptome-assisted prioritization identified RVs with larger trait effect sizes and were better predictors of effect size than genomic annotation alone.

CONCLUSION: With >800 genomes matched with transcriptomes across 49 tissues, we were able to study RVs that underlie extreme changes in the transcriptome. To capture the diversity of these extreme changes, we developed and integrated approaches to identify expression, allele-specific expression, and alternative splicing outliers, and characterized the RV landscape underlying each outlier signal. We demonstrate that personal genome interpretation and RV discovery is enhanced by using these signals. This approach provides a new means to integrate a richer set of functional RVs into models of genetic burden, improve disease gene identification, and enable the delivery of precision genomics. ■

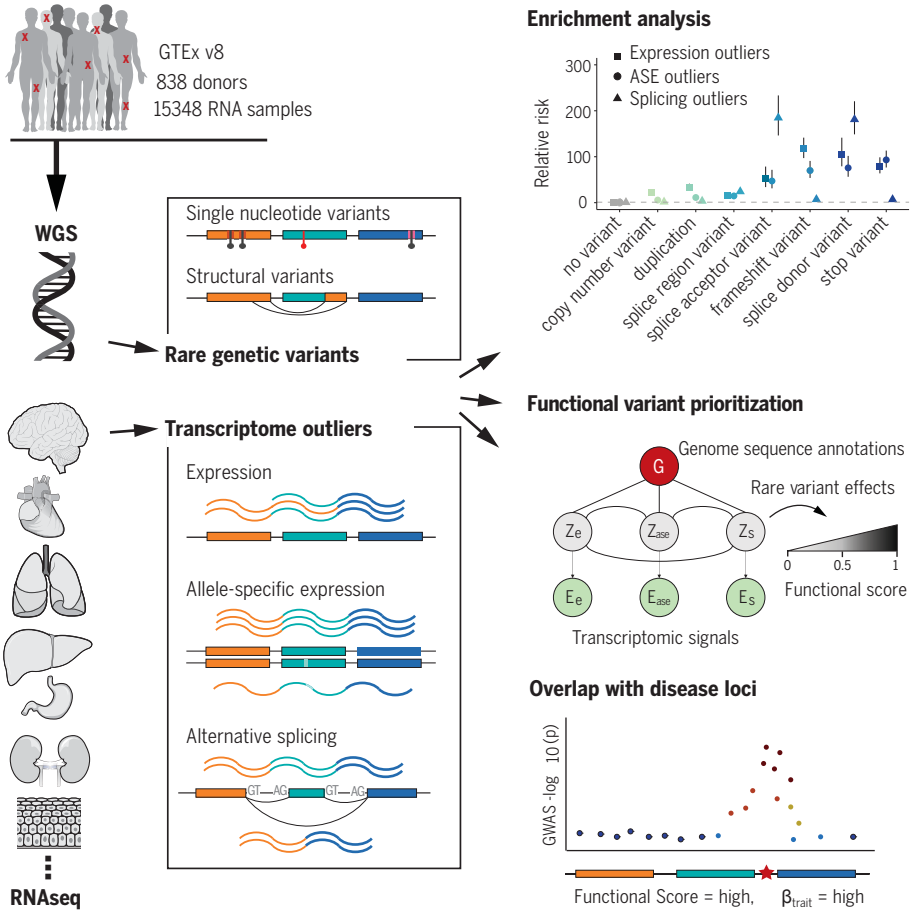

Transcriptomic signatures identify functional rare genetic variation. We identified genes in individuals that show outlier expression, allele-specific expression, or alternative splicing and assessed enrichment of nearby rare variation. We integrated these three outlier signals with genomic annotation data to prioritize functional RVs and to intersect those variants with disease loci to identify potential RV trait associations.

The list of author affiliations and a full list of the GTEx authors and their affiliations are available in the full article online.
*These authors contributed equally to this work.
†These authors contributed equally to this work.
‡Corresponding author. Email: pejman@scripps.edu (P.M.); smontgom@stanford.edu (S.B.M.); ajbattle@jhu.edu (A.B.)
Cite this article as: N. M. Ferraro *et al.*, *Science* **369**, eaaz5900 (2020). DOI: 10.1126/science.aaz5900

READ THE FULL ARTICLE AT
https://doi.org/10.1126/science.aaz5900

RESEARCH ARTICLE

HUMAN GENOMICS

Transcriptomic signatures across human tissues identify functional rare genetic variation

Nicole M. Ferraro[1]*, Benjamin J. Strober[2]*, Jonah Einson[3,4], Nathan S. Abell[5], Francois Aguet[6], Alvaro N. Barbeira[7], Margot Brandt[4,8], Maja Bucan[9], Stephane E. Castel[4,8], Joe R. Davis[10], Emily Greenwald[5], Gaelen T. Hess[5], Austin T. Hilliard[11], Rachel L. Kember[9], Bence Kotis[12], YoSon Park[13], Gina Peloso[14], Shweta Ramdas[9], Alexandra J. Scott[15], Craig Smail[1], Emily K. Tsang[10], Seyedeh M. Zekavat[16], Marcello Ziosi[4], Aradhana[5], TOPMed Lipids Working Group, Kristin G. Ardlie[6], Themistocles L. Assimes[11,17], Michael C. Bassik[5], Christopher D. Brown[9], Adolfo Correa[18], Ira Hall[15], Hae Kyung Im[7], Xin Li[10,19], Pradeep Natarajan[20,21,22], GTEx Consortium, Tuuli Lappalainen[4,8], Pejman Mohammadi[4,12,23]†‡, Stephen B. Montgomery[5,10]†‡, Alexis Battle[2,24]†‡

Rare genetic variants are abundant across the human genome, and identifying their function and phenotypic impact is a major challenge. Measuring aberrant gene expression has aided in identifying functional, large-effect rare variants (RVs). Here, we expanded detection of genetically driven transcriptome abnormalities by analyzing gene expression, allele-specific expression, and alternative splicing from multitissue RNA-sequencing data, and demonstrate that each signal informs unique classes of RVs. We developed Watershed, a probabilistic model that integrates multiple genomic and transcriptomic signals to predict variant function, validated these predictions in additional cohorts and through experimental assays, and used them to assess RVs in the UK Biobank, the Million Veterans Program, and the Jackson Heart Study. Our results link thousands of RVs to diverse molecular effects and provide evidence to associate RVs affecting the transcriptome with human traits.

Background

The human genome contains tens of thousands of rare [minor allele frequency (MAF) <1%] variants (*1*), some of which contribute to rare and common disease risks (*2*, *3*). However, identifying functional rare variants (RVs), especially in the noncoding genome, remains difficult because of their low frequency and the lack of a regulatory genetic code. Outlier gene expression aids in identifying functional, large-effect RVs (*4*–*8*). Furthermore, transcriptome sequencing provides diverse measurements beyond gene expression level, including allele-specific expression (ASE) and alternative splicing, that have yet to be systematically evaluated and integrated into variant effect prediction (*9*–*11*).

Using 838 samples with both whole-genome and transcriptome samples in the Genotype-Tissue Expression (GTEx) project version 8 (v8), we assessed how rare genetic variants contribute to outlier patterns in total expression (hereafter referred to simply as "expression"), allelic expression, and alternative splicing deep into the allele frequency (AF) spectrum. We integrated these three transcriptomic signals across 49 tissues, along with diverse genomic annotations to prioritize high-impact RVs, and assessed their relationship to complex traits in the UK Biobank (UKBB) (*12*), the Million Veterans Program (MVP) (*13*), and the Jackson Heart Study (JHS) (*14*). We further identified dozens of candidate RVs influencing well-studied disease genes, including *APOE*, *FAAH*, and *MAPK3*.

Results

Detection of aberrant gene expression across multiple transcriptomic phenotypes

We quantified three transcriptional phenotypes for each gene to capture a wide range of functional effects caused by regulatory genetic variants. Briefly, to identify expression outliers (eOutliers), we generated *Z* scores from corrected expression data per tissue to determine whether a gene in an individual has extremely high or low expression (fig. S1) (*15*, *16*). To identify genes with excessive allelic imbalance [allele-specific expression (ASE) outliers (aseOutliers)] we used ANEVA-DOT (analysis of expression variation–dosage outlier test; figs. S2 and S3) (*16*, *17*). This method uses estimates of genetic variation in dosage of each gene in a population to identify genes for which an individual has a heterozygous variant with an unusually strong effect on gene regulation (*17*). Splicing outliers (sOutliers) were detected using SPOT (splicing outlier detection), an approach introduced here that fits a Dirichlet-Multinomial distribution directly to counts of reads split across alternatively spliced exon-exon junctions for each gene. SPOT then identifies individuals that deviate significantly from the expectation on the basis of this fitted distribution (figs. S4 to S6) (*16*). Each of the three methods was applied across all GTEx samples. An individual was called a multitissue outlier for a given gene if its median outlier statistic across all measured tissues exceeded a chosen threshold (Fig. 1A) (*16*). Using this multitissue approach for each phenotype, we found that each individual had a median of four eOutlier, four aseOutlier, and five sOutlier genes.

Genes with aberrant expression, ASE, and splicing are enriched for functionally distinct RVs

We observed that multitissue outliers for any of the three transcriptomic phenotypes were significantly more likely to carry a RV (MAF <1%) in the gene body or ±10 kb than individuals without outliers, assessed among 714 individuals with European ancestry. These enrichments were progressively more pronounced for rarer variants and were stronger for structural variants (SVs) than for single-nucleotide variants (SNVs) and indels (Fig. 1B). These trends were not reliant on the specific choice of the threshold used to define outliers (figs. S7 and S8).

We found only 35 cases in which an individual gene was a multitissue outlier for all three transcriptional phenotypes. All but one of these had a nearby RV, and most were annotated as splice variants. Among genes that were outliers for two transcriptional phenotypes

[1]Biomedical Informatics Training Program, Stanford University, Stanford, CA, USA. [2]Department of Biomedical Engineering, Johns Hopkins University, Baltimore, MD, USA. [3]Department of Biomedical Informatics, Columbia University, New York, NY, USA. [4]New York Genome Center, New York, NY, USA. [5]Department of Genetics, Stanford University, Stanford, CA, USA. [6]Broad Institute of MIT and Harvard, Cambridge, MA, USA. [7]Section of Genetic Medicine, Department of Medicine, The University of Chicago, Chicago, IL, USA. [8]Department of Systems Biology, Columbia University, New York, NY, USA. [9]Department of Genetics, University of Pennsylvania, Philadelphia, PA, USA. [10]Department of Pathology, Stanford University, Stanford, CA, USA. [11]Palo Alto Veterans Institute for Research, Palo Alto Epidemiology Research and Information Center for Genomics, VA Palo Alto Health Care System, Palo Alto, CA, USA. [12]Department of Integrative Structural and Computational Biology, The Scripps Research Institute, La Jolla, CA, USA. [13]Department of Systems Pharmacology and Translational Medicine, University of Pennsylvania, Perelman School of Medicine, Philadelphia, PA, USA. [14]Department of Biostatistics, Boston University School of Public Health, Boston, MA, USA. [15]McDonnell Genome Institute, Washington University School of Medicine, St. Louis, MO, USA. [16]Medical & Population Genomics, Yale School of Medicine and Broad Institute of MIT and Harvard, Cambridge, MA, USA. [17]Department of Medicine, Stanford University School of Medicine, Stanford, CA, USA. [18]University of Mississippi Medical Center, Jackson, MS, USA. [19]Shanghai Institutes for Biological Sciences, CAS-MPG Partner Institute for Computational Biology, Chinese Academy of Sciences, Shanghai, China. [20]Cardiovascular Research Center, Massachusetts General Hospital, Boston, MA, USA. [21]Department of Medicine, Harvard Medical School, Boston, MA, USA. [22]Program in Medical and Population Genetics, Broad Institute of Harvard and Massachusetts Institute of Technology, Cambridge, MA, USA. [23]Scripps Translational Science Institute, La Jolla, CA, USA. [24]Department of Computer Science, Johns Hopkins University, Baltimore, MD, USA.
*These authors contributed equally to this work. †These authors contributed equally to this work. ‡Corresponding author. Email: pejman@scripps.edu (P.M.); smontgom@stanford.edu (S.B.M.); ajbattle@jhu.edu (A.B.)
A full list of the GTEx authors and their affiliations is available at the end of this article.

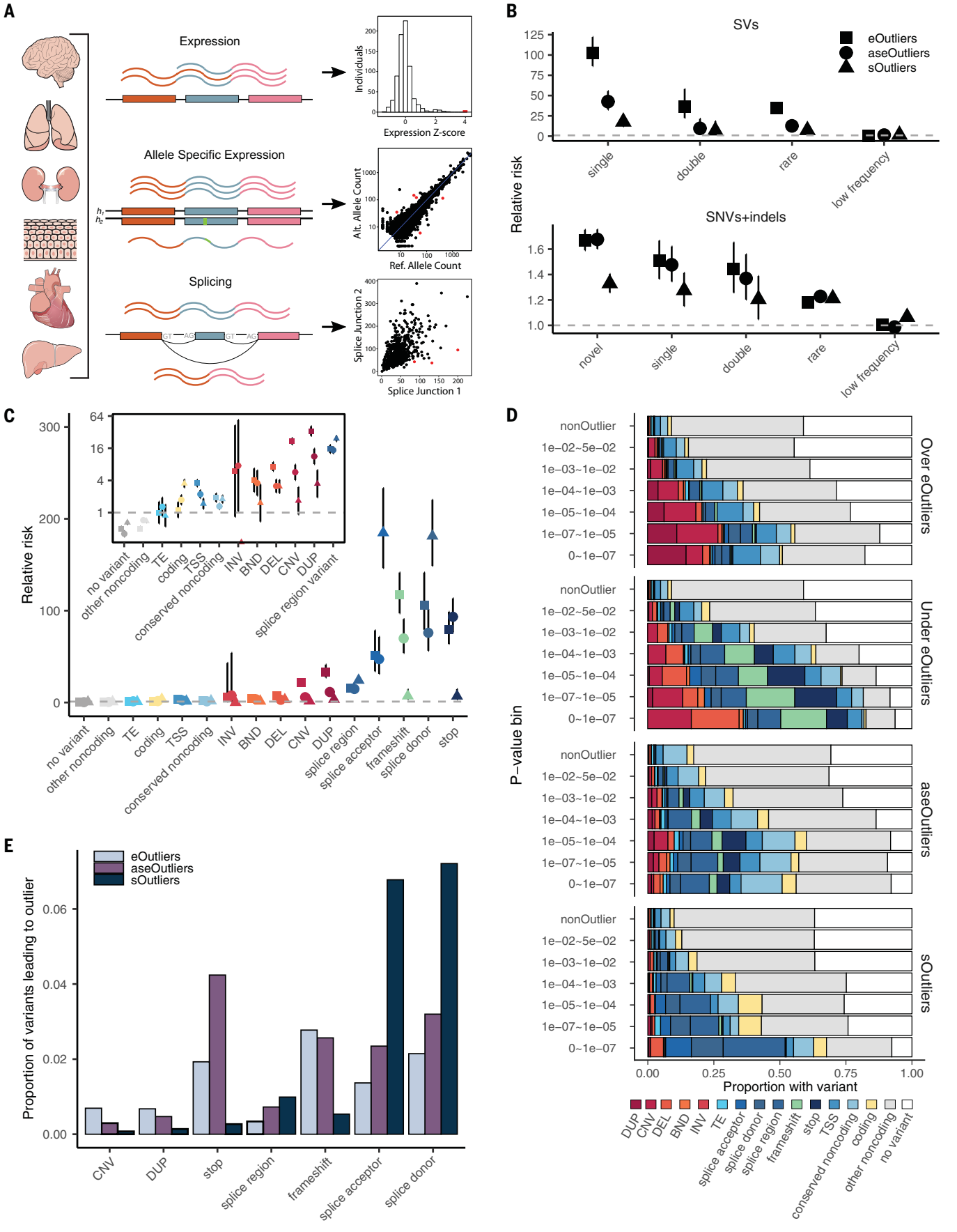
A
Expression
Individuals
Expression Z-score
Allele Specific Expression
Alt. Allele Count
Ref. Allele Count
Splicing
Splice Junction 2
Splice Junction 1
B
SVs
eOutliers
aseOutliers
sOutliers
Relative risk
single
double
rare
low frequency
SNVs+indels
novel
C
Relative risk
no variant
other noncoding
TE
coding
TSS
conserved noncoding
INV
BND
DEL
CNV
DUP
splice region variant
splice region
splice acceptor
frameshift
splice donor
stop
D
nonOutlier
1e−02~5e−02
1e−03~1e−02
1e−04~1e−03
1e−05~1e−04
1e−07~1e−05
0~1e−07
Over eOutliers
Under eOutliers
aseOutliers
sOutliers
P−value bin
Proportion with variant
E
eOutliers
aseOutliers
sOutliers
Proportion of variants leading to outlier

Fig. 1. Enrichment of RVs underlying aberrant expression, splicing, and ASE. (**A**) RNA-seq data in 838 individuals were combined across 49 tissues and used to identify shared tissue expression, ASE, and alternative splicing outliers. (**B**) Relative risk of new (not in gnomAD), singleton, doubleton, rare (MAF <1%), and low-frequency (MAF 1 to 5%) variants in a 10-kb window around the outlier genes across all data types compared with nonoutlier individuals for the same genes. Outliers were defined as those with values >3 SDs from the mean (|median Z| > 3) or, equivalently, a median $P < 0.0027$. Bars represent the 95% confidence interval. (**C**) Assigning each outlier its most consequential nearby RV, the relative risk for different categories of RVs falling within 10 kb of each outlier type. The inset panel shows enrichments for a subset of variant categories on a log(2)-transformed y-axis scale for better visibility. (**D**) Proportion of outliers at a given threshold that have a nearby RV in the given category. eOutlier |median Z scores| were converted to P values using the cumulative probability density function for the normal distribution. TE, transposable element; INV, inversion; BND, break end; DEL, deletion; DUP, duplication. (**E**) Proportion of RVs in a given category that lead to an outlier at a P-value threshold of 0.0027 across types.

in an individual (n = 465), the greatest overlap occurred between aseOutliers and eOutliers (n = 319; fig. S9A). We found that aseOutliers with modest expression changes (1 < |median Z| < 3) showed stronger enrichment for nearby RVs than those without any expression change (fig. S9), highlighting an important benefit of combining these phenotypes to discover diverse RV effects. We found that genes for which no outlier individuals were identified were enriched for Gene Ontology biological process terms relating to sensory perception and detection of chemical stimuli for all outlier types (fig. S10) (*16*), which is consistent with enrichments seen for genes that do not have any cis-expression quantitative trait loci (eQTLs) discovered in GTEx (*18*).

We found that different types of genetic variants contribute to outliers for the three molecular phenotypes, although rare splice donor variants were enriched near all outlier types (Fig. 1C). The largest differences in variant type enrichment among the three outlier types were copy number variations (CNVs) and duplications, which were almost exclusively associated with eOutliers, and splice acceptor variants, which were enriched considerably more within sOutliers (fig. S11).

For all phenotypes, the proportion of outliers with a nearby RV of any category increased with threshold stringency (Fig. 1D). For eOutliers, aseOutliers, and sOutliers, at the strictest threshold of median outlier $P < 1.1 \times 10^{-7}$, most individuals were carrying at least one RV nearby the outlier gene (82 to 94%). When looking further at RVs with functional annotations (from the annotations listed in Fig. 1C), we found that underexpressed eOutliers were the most interpretable, with 88% of outlier-associated RVs having an additional functional annotation, whereas aseOutliers had the lowest proportion at 56% (Fig. 1D). This analysis provides further insight into expectations for causal RV types when an outlier effect of a specific magnitude is observed in an individual.

Conversely, a large proportion of genes with nearby rare genetic variants did not appear as outliers, even for the most predictive classes such as loss-of-function variants. The largest proportion of variants leading to any outlier status were rare splice donor and splice acceptor variants, of which only 7.2 and 6.8%, respectively, led to an sOutlier (Fig. 1E and fig. S11). Overall, whereas some transcriptomic effects may have been missed, the low frequency with which RVs of these classes led to large transcriptome changes reinforces the utility of incorporating functional data in variant interpretation even for specific variant classes already used in clinical interpretation.

Genomic position of RVs predicts the impact on expression

Although we primarily assessed RVs that occur either within an outlier gene or in a 10-kb surrounding window, gene regulation can occur at greater distances (*19*, *20*). Because we observed the strongest enrichments for the lowest-frequency variants, we intersected singleton variants [(SVs); i.e., those appearing only once in GTEx and SNVs and/or indels that do not appear in the Genome Aggregation Database (gnomAD) (*21*)] with 200-kb-length windows exclusive of other windows and upstream from outlier genes and compared their frequency in outlier versus nonoutlier individuals. SNV enrichments dropped off quickly at greater distances from the gene but remained weakly enriched for eOutliers out to 200 kb. The same was true for rare indels, with enrichment at 200 kb only for sOutliers. SVs remained enriched at much longer distances, being enriched 2.33-fold as far as 800 kb to 1 Mb upstream and up to 600 kb downstream of the gene body (Fig. 2A and fig. S12A).

RVs in promoter regions have been previously linked to outlier expression (*5*, *15*). To extend these observations and to assess the types of transcription factor (TF)–binding sites that could lead to outliers, we tested enrichment of rare transcription start site (TSS) proximal variants in specific TF motifs near under- and over-eOutliers. For under-eOutliers, we saw an enrichment of variants in *GABP*, a TF that activates genes that control the cell cycle, differentiation, and other critical functions (*22*). For over-eOutliers, we saw an enrichment of RVs intersecting the *E2F4* motif, a TF that has been reported as a transcriptional repressor (*23*). In both under- and over-eOutliers, we saw RVs in *YY1*, which can act as either an activator or repressor, depending on context (*24*), and has been associated with *GABP* in coregulatory networks (Fig. 2B and fig. S12B) (*25*). Thus, these naturally occurring RV perturbations can provide information about how specific TFs can strongly up- or down-regulate their target genes.

RVs can affect multiple genes and lead to new gene fusion

We observed that RVs can also affect multiple genes in an individual. We found a strong enrichment for multigene effects among eOutliers and, to a lesser degree, aseOutliers (fig. S13). As expected, we did not see enrichment for nearby sOutlier pairs, which are less subject to coregulation (*26*). Within a 100-kb window, neighboring eOutlier genes were 70 times more frequent than would be expected by chance if drawing outlier pairs at random. They were also significantly enriched for rare CNVs, duplications, and TSS variants nearby one or both genes compared with individuals who had outlier expression but for only one of the genes (fig. S13). We also found that rare SV enrichments were present near eOutliers regardless of whether the SV overlapped the gene itself (fig. S14). We observed 27 examples of rare SVs, including deletions, duplications, and break ends, associated with eOutliers in at least two genes in the same individual (fig. S15 and table S1). For one of these, we observed evidence of a fusion transcript resulting from a deletion spanning the end of the gene SPTBN1 and the TSS of EML6. This deletion led to underexpression of SPTBN1 (median Z score = −4.67) and overexpression of EML6 (median Z score = 8.12) compared with all other individuals. Supporting the presence of a new germline fusion transcript, we found evidence of a specific transcript spanning both SPTBN1 and EML6 in multiple tissues for the individual with the deletion (fig. S16). For both of these genes, this individual also showed sOutlier signal (median SPOT P = 0.0005 for EML6 and 0.0035 for SPTBN1). The identification of fusion transcripts has been of particular interest in cancer diagnosis and prognosis (*27*–*30*), and both EML genes and SPTBN1 have been previously implicated in cancer-associated fusions (*31*, *32*).

RVs in splicing consensus sequence drive splicing outliers

Previous studies have shown RVs disrupting splice sites result in outlier alternative splicing patterns (*33*, *34*). We used sOutlier calls made

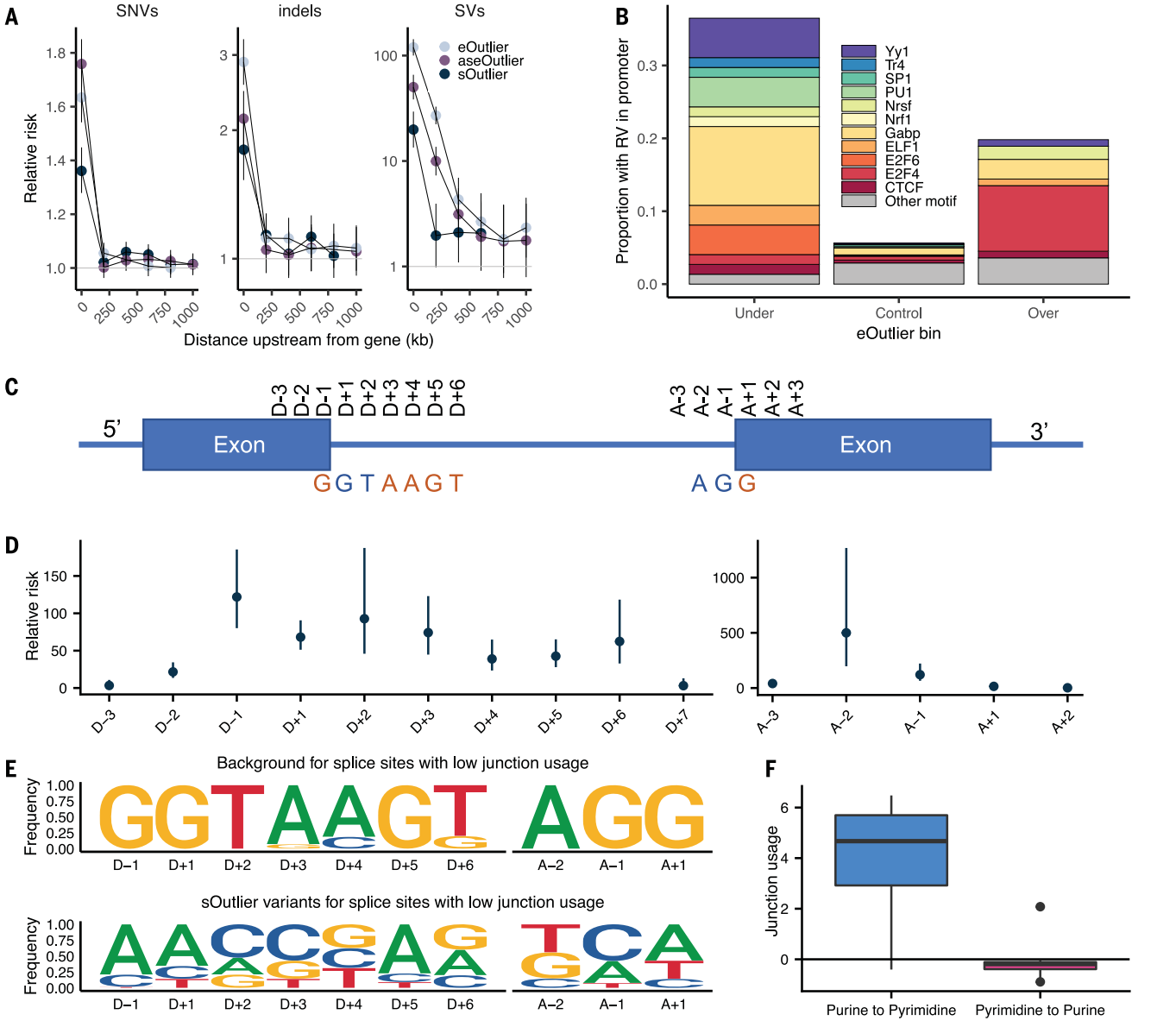

Fig. 2. RV enrichments in specific genomic positions. (**A**) Relative risk of SNVs and indels (not found in gnomAD), and SVs (singleton in GTEx) at varying distances upstream of outlier genes (bins exclusive) across data types. (**B**) Proportion of eOutliers with TSS RVs in promoter motifs within 1000 bp. Under and over bins are defined with a median *Z* score threshold of 3, and controls are all individuals with a median *Z* score <3 for the same set of outlier genes. (**C**) Graphic summarizing positional nomenclature relative to observed donor and acceptor splice sites. (**D**) Relative risk (*y*-axis) of an sOutlier (median LeafCutter cluster $P < 1 \times 10^{-5}$) RV being located at a specific position relative to the splice site (*x*-axis) compared with nonoutlier RVs. Relative risk calculation was done separately for donor and acceptor splice sites. (**E**) Independent position weight matrices showing mutation spectra of sOutlier (median LeafCutter cluster $P < 1 \times 10^{-5}$) RVs at positions relative to splice sites with negative junction usage (i.e., splice sites used less in outlier individuals than in nonoutliers). (**F**) Junction usage of a splice site is the natural log of the fraction of reads in a LeafCutter cluster mapping to the splice site of interest in sOutlier (median LeafCutter cluster $P < 1 \times 10^{-5}$) samples relative to the fraction in nonoutlier samples aggregated across tissues by taking the median (*16*). Junction usage (*y*-axis) of the closest splice sites to RVs that lie within a polypyrimidine tract (A − 5, A − 35) binned by the type of variant (*x*-axis).

for each LeafCutter cluster (*16*, *35*) to assess enrichment of splicing-related variants more precisely. We observed extreme enrichment of RVs near splice sites in sOutliers. An sOutlier was 333 times more likely than a nonoutlier to harbor a RV within a 2-bp window around a splice site (fig. S17A) (*16*), with signal decaying at greater distances but still enriched up to 100 bp away (relative risk = 7.43). To obtain base pair resolution enrichments, we computed the relative risk of sOutlier RVs located at specific positions relative to observed donor and acceptor splice sites (*16*). Ten positions near the splice site showed significant enrichment for RVs in sOutliers compared with controls (Fig. 2, C and D). These positions corresponded precisely to positions that have also been shown to be intolerant to mutations because of their conserved role in splicing (we will refer to these positions as the splicing consensus sequence) (*34*). Among the most enriched positions within the splicing consensus sequence were the four essential splice site positions (D + 1, D + 2, A − 2, A − 1) (*36*), which showed an average relative risk of 195.

sOutliers further captured the transcriptional consequences both for variants that

disrupted a reference splicing consensus sequence and those that created a new splicing consensus sequence. Individuals with sOutlier variants in which the rare allele deviated away from the splicing consensus sequence showed decreased junction usage of the splice site near the variant, whereas individuals with variants in which the rare allele created a splicing consensus sequence showed increased junction usage of the splice site near the variant relative to nonoutliers (Fig. 2E and figs. S17B and S18) (*16*). We saw a related enrichment pattern after separating annotated and new (unannotated) splice sites (fig. S19). sOutliers were also enriched for RVs positioned within the polypyrimidine tract (PPT), a highly conserved, pyrimidine-rich region, ~5 to 35 bp upstream from acceptor splice sites (*37*). A RV was 6.25 times more likely to be located in the PPT near an sOutlier relative to a nonoutlier. sOutliers with a RV that changed a position in the PPT from a pyrimidine to a purine (i.e., disrupting an existing PPT) showed decreased junction usage of the splice site near the variant, whereas the inverse was true for variants that changed a position in the PPT from a purine to pyrimidine (Fig. 2F and fig. S20).

RVs in tissue-specific regulatory regions can lead to tissue-specific outlier expression

Although multitissue outliers offer improved power to detect RV effects, we also evaluated RVs from outliers detected in individual tissues. Single-tissue measurements are subject to greater variation than repeat measurements across tissues but are representative of most experimental designs. First, we performed replication analysis across all individuals with data available for the three methods to evaluate the degree to which outlier status detected in one tissue of an individual was replicated in other tissues (*16*). On average, we found that eOutlier, aseOutlier, and sOutlier status in a discovery tissue was detected in a test tissue 5.1, 10.7, and 8.7% of the time, respectively (Fig. 3A and fig. S21). This is consistent with other findings that measurements of ASE are more consistent across tissues (*18*). Considering clinically accessible tissues, namely whole blood, fibroblasts, and lymphoblastoid cells, if we consider outliers observed for a gene in at least two of these tissues in the same individual, we saw average replication rates across all other tissues of 14.1, 20.9, and 15.0% for eOutliers, aseOutliers, and sOutliers, respectively (fig. S22). Both the higher replication rate for aseOutliers and the increase in outlier replication in nonaccessible tissues when considering more than one accessible measurement are informative for the analysis of functional data from easily accessible tissues to understand disease states most relevant to other tissues.

We next evaluated the ability of single-tissue outliers from each method to prioritize RVs near outlier genes. Single-tissue aseOutliers were most enriched for nearby RVs, followed by sOutliers and then eOutliers, across all outlier cutoff thresholds (Fig. 3B and fig. S21 and S23A). We also observed enrichment of variants likely triggering nonsense-mediated decay among single-tissue eOutliers, aseOutliers, and sOutliers (Fig. 3C and fig. S23B). Additionally, we found that single-tissue sOutliers still showed strong enrichment for RVs in the splicing consensus sequence and the PPT (fig. S24).

Except for rare SVs that notably were enriched at comparable thresholds to multitissue eOutliers, single-tissue eOutliers show far weaker enrichments relative to multitissue outliers for nearby rare SNVs and indels across all thresholds (fig. S25). To improve discovery of tissue-specific outliers, we leveraged the breadth of tissue data available and used observed patterns of correlation across tissues to detect outliers that deviate from the expected covariance of expression in a subset of tissues (*16*). A similar approach has been implemented to identify functional RVs on the basis of the correlation of expression among genes in a single tissue (*5*). We found that outliers identified using this approach were often driven by expression changes in one or a few tissues compared with multitissue eOutliers based on median Z scores (Fig. 3D). The correlation tissue-specific outliers were also enriched for nearby RVs in a 10-kb window around the gene (fig. S26C). However, these outliers were also enriched for RVs in enhancers that were active in the tissue(s) driving the outlier effect (table S2), as determined by single-tissue Z score and within a 500-kb window around the gene (Fig. 3E). Notably, these tissue-specific outliers were depleted for rare variation in enhancers annotated in other, unmatched tissues.

Prioritizing RVs by integrating genomic annotations with diverse personal transcriptomic signals

To incorporate diverse transcriptome signals into a method to prioritize RVs, we developed Watershed, an unsupervised probabilistic graphical model that integrates information from genomic annotations of a personal genome (table S3) with multiple signals from a matched personal transcriptome. Watershed provides scores that can be used for personal genome interpretation or for cataloging potentially impactful rare alleles, quantifying the posterior probability that a variant has a functional effect on each transcriptomic phenotype based on both whole-genome–sequencing (WGS) and RNA-sequencing (RNA-seq) signals (Fig. 4A). The Watershed model can be adapted to any available collection of molecular phenotypes, including different assays, different tissues, or different derived signals. Further, Watershed automatically learns Markov random field (MRF) edge weights reflecting the strength of the relationship between the different tissues or phenotypes included that together allow the model to predict functional effects accurately.

We first applied Watershed to the GTEx v8 data using the three outlier signals examined here, expression, ASE, and splicing (Fig. 4A) (*16*), for which each was first aggregated by taking the median across tissues for the corresponding individual. In agreement with existing evidence of similarity between outlier signals (fig. S9), the learned Watershed edge parameters were strongest between ASE and expression, followed by ASE and splicing, but strictly positive for all pairs of outlier signals (i.e., each outlier signal was informative of all other signals; Fig. 4B). To evaluate our model, we used held-out pairs of individuals that shared the same RV, making Watershed predictions in the first individual and evaluating those predictions using the second individual's outlier status as a label (*15*, *16*). Watershed outperforms methods based on genome sequence alone [our genomic annotation model (GAM) and combined annotation-dependent depletion (CADD); Fig. 4C and fig. S27] (*38*, *39*). We also compared performance of Watershed with RIVER [RNA-informed variant effect on regulation (*15*)], a simplification of the Watershed model in which each outlier signal is treated independently. We found that explicitly modeling the relationship between different molecular phenotypes provided a performance gain for Watershed (Fig. 4D, figs. S28 and S29, and table S4) (*16*). We observed that even the most predictive genomic annotations only resulted in eOutliers, aseOutliers, and sOutliers 2.8, 7.9, and 14.3% of the time, respectively (Figs. 1E and 4C). However, integrating transcriptomic signals with genomic annotations from Watershed (at a posterior threshold of 0.9) detected SNVs that resulted in eOutliers, aseOutliers, and sOutliers with greater frequency 11.1, 33.3, and 71.4% of the time, respectively (Fig. 4C and fig. S30).

We further extended the Watershed framework to prioritize variants on the basis of their predicted tissue-specific impact. We trained three "tissue-Watershed" models (one for each of expression, ASE, and splicing separately), in which each model considers the effects in all tissues jointly, sharing information in the MRF, and ultimately outputs 49 tissue-specific scores for each RV (figs. S29 and S31) (*16*). We observed that the parameters learned for each of the three tissue-Watershed models resembled known patterns of tissue similarity (Fig. 4E and fig. S32) (*18*). Further, using held-out individuals, the tissue-Watershed model outperformed a RIVER model in which each tissue is treated completely independently ($P = 2.00 \times 10^{-5}$, $P = 2.00 \times 10^{-5}$, and $P = 5.90 \times 10^{-3}$ for expression, ASE, and splicing, respectively; one-sided binomial test; Fig. 4F and figs. S33 and S34) and a collapsed RIVER model trained

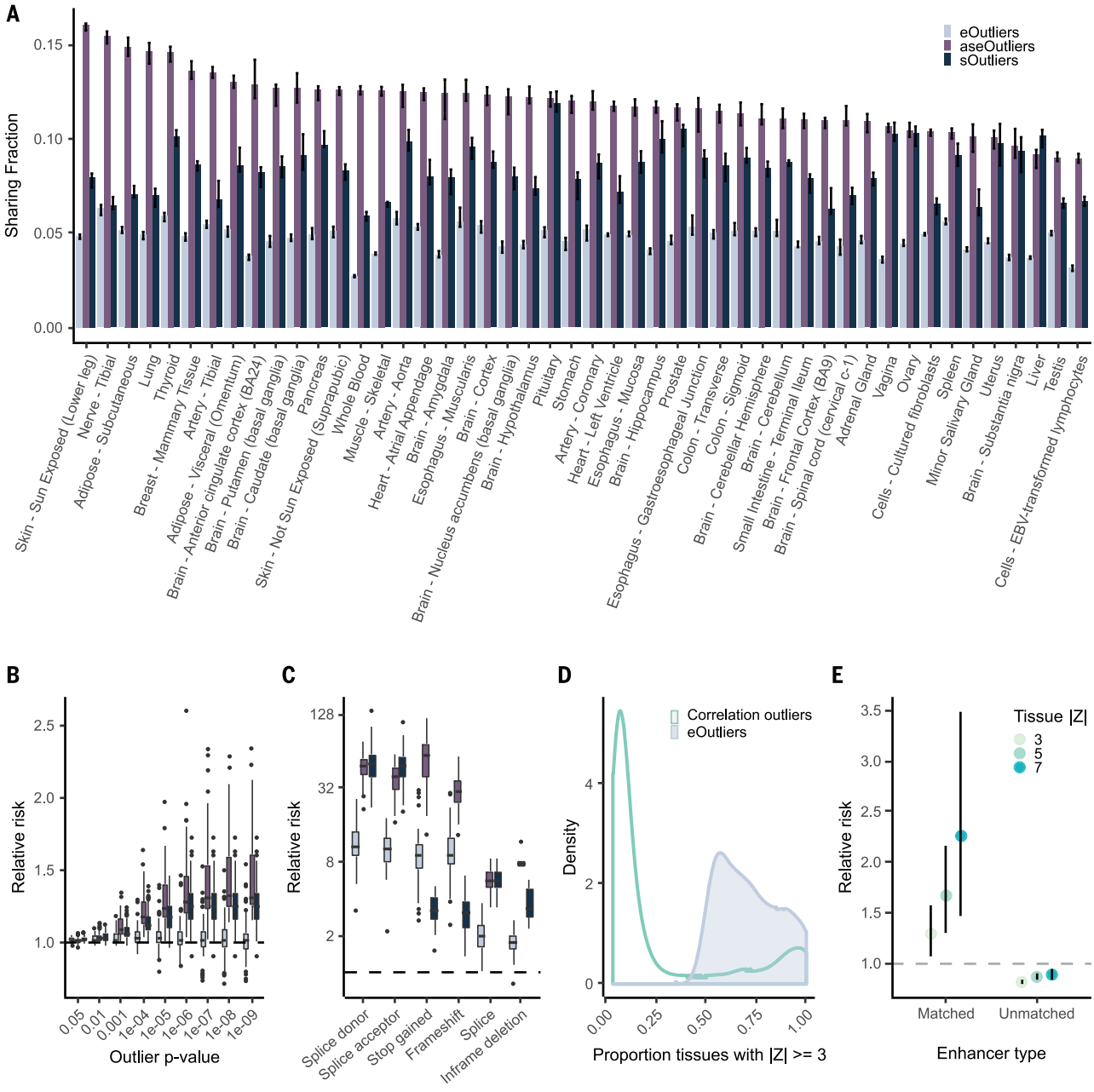

Fig. 3. Single-tissue outlier enrichments and replication. (**A**) Median replication of outliers identified per tissue across every other tissue for each outlier type. (**B**) Relative risk point estimate for nearby rare SNVs for outliers across all tissues individually. (**C**) Relative risk enrichments for likely gene disrupting RVs nearby single-tissue outliers at a threshold of $|Z| > 4$ (equivalently SPOT or ANEVA-DOT $P < 0.000063$), with one point per tissue. (**D**) Distribution of number of tissues with aberrant expression underlying expression outliers defined by median Z score (eOutliers) or Mahalanobis distance P value (correlation). (**E**) Relative risk of correlation outliers driven by a single tissue, defined as significant correlation outliers for which an expression change of the degree indicated by the point color is observed in only a single tissue (*16*) carrying a RV in enhancers annotated to that tissue within a 500-kb window of the outlier gene. Unmatched are defined as all tissue-specific enhancer regions regardless of outlier tissue.

with single median outlier statistics ($P = 0.0577$, $P = 0.251$, and $P = 0.00128$ for expression, ASE, and spicing, respectively; one-sided binomial test; figs. S35 and 36). Critically, integrative models that incorporated transcriptomic signal and genomic annotations from a single tissue still outperformed methods based only on genome sequence annotations (Fig. 4F), supporting the benefit of collecting even a single RNA-seq sample to improve personal genome interpretation.

Replication and experimental validation of predicted RV transcriptome effects

We first assessed the replication of "candidate causal RVs" previously identified by the SardiNIA Project (*6*), using GTEx Watershed prioritization. Of five SardiNIA candidate causal RVs that were also present in a GTEx individual, four had high (>0.7) GTEx Watershed expression posterior probabilities (table S5). Next, we tested replication of GTEx RVs, prioritized by Watershed, in an independent cohort evaluating 97 whole-genome and matched

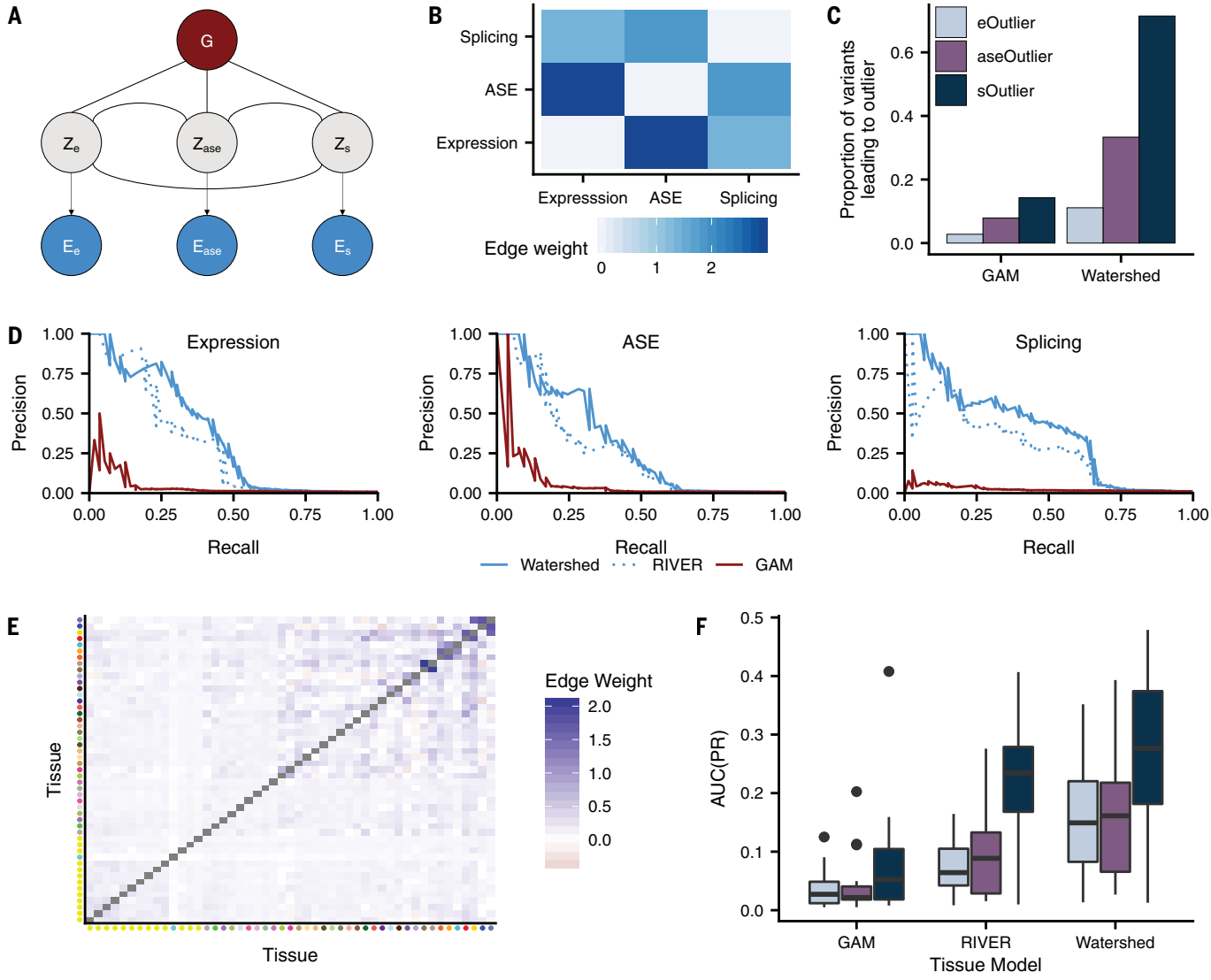

Fig. 4. Prioritizing functional RVs with Watershed. (**A**) Graphic summarizing plate notation for the Watershed model when it is applied to three median outlier signals (expression, ASE, and splicing). (**B**) Symmetric heatmap showing learned Watershed edge parameters (weights) between pairs of outlier signals after training Watershed on three median outlier signals. (**C**) The proportion of RVs with Watershed posterior probability >0.9 (right) and with GAM probability greater than a threshold set to match the number of Watershed variants for each outlier signal (left) that lead to an outlier at a median *P*-value threshold of 0.0027 across three outlier signals (colors). Watershed and GAM models were evaluated on held-out pairs of individuals. (**D**) Precision-recall curves comparing performance of Watershed, RIVER, and GAM (colors) using held-out pairs of individuals for three median outlier signals. (**E**) Symmetric heatmap showing learned tissue-Watershed edge parameters (weights) between pairs of tissue outlier signals after training tissue-Watershed on eOutliers across single tissues. Tissue color to tissue name mapping can be found in fig. S21D. (**F**) Area under precision recall curves [AUC(PR); *y*-axis] in a single tissue between tissue-GAM, tissue-RIVER, and tissue-Watershed (*x*-axis) when applied to outliers across single tissues in all three outlier signals (colors). Precision recall curves in each tissue were generated using held-out pairs of individuals.

transcriptome samples from the Amish Study of Major Affective Disorders (ASMAD) (*40*). We evaluated GTEx RVs also present in this cohort at any frequency, quantifying eOutlier, aseOutlier, and sOutlier signal in each ASMAD individual harboring one of the GTEx variants (*16*). For all three phenotypes, ASMAD individuals with variants having high (>0.8) Watershed posterior probability based on GTEx data had significantly more extreme outlier signals at nearby genes compared with individuals with variants having low (<0.01) GTEx Watershed posterior probability (expression: $P = 2.729 \times 10^{-6}$, ASE: $P = 2.86 \times 10^{-3}$, and splicing: $P = 5.86 \times 10^{-13}$; Wilcoxon rank-sum test; fig. S37). Every variant with a high GTEx Watershed splicing posterior probability (>0.8) resulted in an sOutlier ($P \leq 0.01$) in the ASMAD cohort. Furthermore, ASMAD individuals with variants having high (>0.8) GTEx Watershed posterior probability had significantly larger outlier signals relative to equal size sets of variants prioritized by GAM (expression: $P = 0.00129$, ASE: $P = 0.0287$, and splicing: $P = 0.00058$; Wilcoxon rank-sum test; fig. S37). Overall, RVs prioritized by Watershed using GTEx data displayed evidence of functional effects in ASMAD individuals.

We further applied both a massively parallel reporter assay (MPRA) and a CRISPR-Cas9 assay to assess the impact of Watershed-prioritized RVs. We experimentally tested the regulatory effects of 52 variants with moderate Watershed expression posterior (≥0.5) and 98 variants with low Watershed expression posterior (<0.5) using MPRA (*16*). We observed increased effect sizes for RVs with high Watershed expression posterior relative

to variants with low expression posterior (P = 0.025; one-sided Wilcoxon rank-sum test; fig. S38 and table S6). Next, we assessed the functional effects of 20 variants by editing them into inducible-Cas9 293T cell lines. These included 14 rare stop-gained variants and six non-eQTL common variants as negative controls. Of the 14 rare stop-gained variants, 13 had expression or ASE Watershed posterior >0.8, with the remaining variant [previously tested in (*41*)] having a posterior of 0.22. All control variants had Watershed posteriors <0.03. Of the 13 variants with a Watershed posterior >0.8, 12 showed a significant decrease in expression of the rare allele (P < 0.05, Bonferroni corrected; fig. S39 and table S7) (*16*).

Aberrant expression informs RV trait associations

We found that each individual had a median of three eOutliers, aseOutliers, and sOutliers (median outlier P < 0.0027) with a nearby RV. When filtering by moderate Watershed posterior probability (>0.5) of affecting expression, ASE, or splicing, individuals had a median of 17 genes with RVs predicted to affect expression, 27 predicted to affect ASE, and nine predicted to affect splicing (Fig. 5A). From the set of outlier calls, we found multiple instances of RVs influencing well-known and well-studied genes, including *APOE* and *FAAH* (table S8). In particular, for *APOE*, which has been associated with numerous neurological diseases and psychiatric disorders (*42*), we found two aseOutlier individuals both carrying a rare, missense variant, rs563571689, with ASE Watershed posteriors >0.95, not previously reported. For *FAAH*, which has been linked to pain sensitivity in numerous contexts (*43*, *44*), we found two eOutlier individuals with a rare 5′ untranslated region variant, rs200388505, with ASE and expression Watershed posteriors >0.9.

To assess whether identified rare functional variants from GTEx associate with traits, we intersected this set with variants present in the UKBB (*12*). We focused on a subset of 34 traits for which GWAS association for a UKBB trait had evidence of colocalizations with eQTLs and/or alternative splicing QTLs (sQTLs) in any tissue (table S9) (*16*, *45*). GTEx has demonstrated that genes with RV associations for a trait are strongly enriched for their eQTLs colocalizing with GWAS signals for the same trait (*18*), indicating that QTL evidence can be used to guide RV analysis. Furthermore, RVs near GTEx outliers had larger trait association effect sizes than background RVs near the same set of genes in the UKBB data (P = 3.51×10^{-9}; one-sided Wilcoxon rank-sum test), with a shift in median effect size percentile from 46 to 53%. Notably, outlier variants that fell in or nearby genes with an eQTL or sQTL colocalization had even larger effect sizes (median effect size percentile 88%) than non-outlier variants (P = 1.93×10^{-5}; one-sided Wilcoxon rank-sum test) or outlier variants falling near any gene not matched to a colocalizing trait (P = 4.88×10^{-5}; one-sided Wilcoxon rank-sum test; Fig. 5B).

Although most variants tested in UKBB had low Watershed posterior probabilities of affecting the transcriptome (fig. S40A), we hypothesized that filtering for those variants that do have high posteriors would yield variants in the upper end of the effect size distribution for a given trait. For each variant tested in UKBB, we took the maximum Watershed posterior per variant and compared this with a genomic annotation-defined metric, CADD (*38*, *39*). We found that Watershed posteriors were a better predictor of variant effect size than CADD scores for the same set of RVs in a linear model (Table 1). Across different Watershed posterior thresholds, we found that the proportion of variants falling in the top 25% of RV effect sizes in colocalized regions exceeded the proportion expected by chance (Fig. 5C). Whereas filtering by CADD score did return some high effect size variants, this proportion declined at the highest thresholds (fig. S40D). Furthermore, there was very little overlap between variants with high Watershed posteriors and high CADD variants (fig. S40D), with CADD variants more likely to occur in coding regions and Watershed variants more frequent in noncoding regions (fig. S40D). Thus, the approaches largely identified distinct and complementary sets of variants for these traits.

We identified 33 rare GTEx variant trait combinations in which the variant had a Watershed posterior >0.5 and fell in the top 25% of variants by effect size for the given trait (table S10). We highlight two such examples, for asthma and high cholesterol (Fig. 5, D and E), showing that although RVs usually do not have the frequency to obtain genome-wide significant P values, when they are prioritized by the probability of affecting expression, we could identify those with greater estimated effect sizes on the trait (table S11). In the case of asthma, the RV effect sizes in UKBB were three times greater than the lead colocalized variant. These variants included rs146597587, which is a high-confidence loss-of-function splice acceptor with an overall gnomAD AF of 0.0019, and rs149045797, an intronic variant with a frequency of 0.0019, both of which were associated with the gene *IL33*, the expression of which has been implicated in asthma (*46*, *47*). Previous work has identified the protective association between rs146597587 and asthma (*48*, *49*), and we found that this is potentially mediated by outlier allelic expression of *IL33* leading to moderate decreases in total expression, with median Z scores ranging from −1.08 to −1.77 in individuals with the variant, and median single-tissue Z scores across the six individuals exceeding −2 in 10 tissues. An asthma association had also been reported recently for the other high Watershed asthma-associated variant rs149045797 and was in perfect linkage disequilibrium with rs146597587 (*50*). An additional high Watershed variant, rs564796245, an intronic variant in *TTC38* with a gnomAD AF of 0.0003, had a high effect size for self-reported high cholesterol in the UKBB but was not previously reported. We were able to test this variant against four related blood lipids traits in the MVP (*51*). We found that for these traits, which included high-density lipoprotein (HDL), low-density lipoprotein, total cholesterol, and triglycerides, among rare (gnomAD AF <0.1%) variants within a 250-kb window of rs564796245, this variant was in the top 5% of variants by effect size; for HDL specifically, it was in the top 1% (fig. S41). We also assessed this variant's association with the same four traits in the JHS (*14*), an African American cohort in which four individuals carried the RV. Here, we found that the direction of effect was consistent with MVP and UKBB for all four traits (tables S11 and S12), and the variant fell in the top 28th to 38th percentile of all rare (gnomAD AF <0.1%) variants in this region (fig. S42). Only four of the variants tested in UKBB had Watershed posterior probabilities >0.9 for colocalized genes, but of those, three showed high effect sizes for a relevant trait (table S10).

Discussion

RVs are abundant in human genomes, yet they have remained difficult to study systematically. Using multitissue transcriptome and whole-genome data from GTEx v8, we have been able to identify and assess the properties of RVs, including SVs, that underlie extreme changes in expression, alternative splicing, and ASE.

We observed that each signal informs distinct classes of RVs, demonstrating the benefit of integrating multiple sources of personal molecular data to improve variant interpretation. We expanded characterization of the properties of RVs in multiple contexts, including structural variants affecting multiple genes, rare splice variants that disrupt or create splicing consensus sequences, and RVs occurring in tissue-specific enhancers leading to tissue-specific eOutliers. Together, these provide a map of the properties of large-effect RVs, aiding their identification and evaluation in future studies. We note that although our approach can be used to identify some large-effect RVs underlying disease, it is unlikely to capture the full spectrum of functional RVs contributing to heritability because some effects will not manifest as clear transcriptome aberrations (*8*).

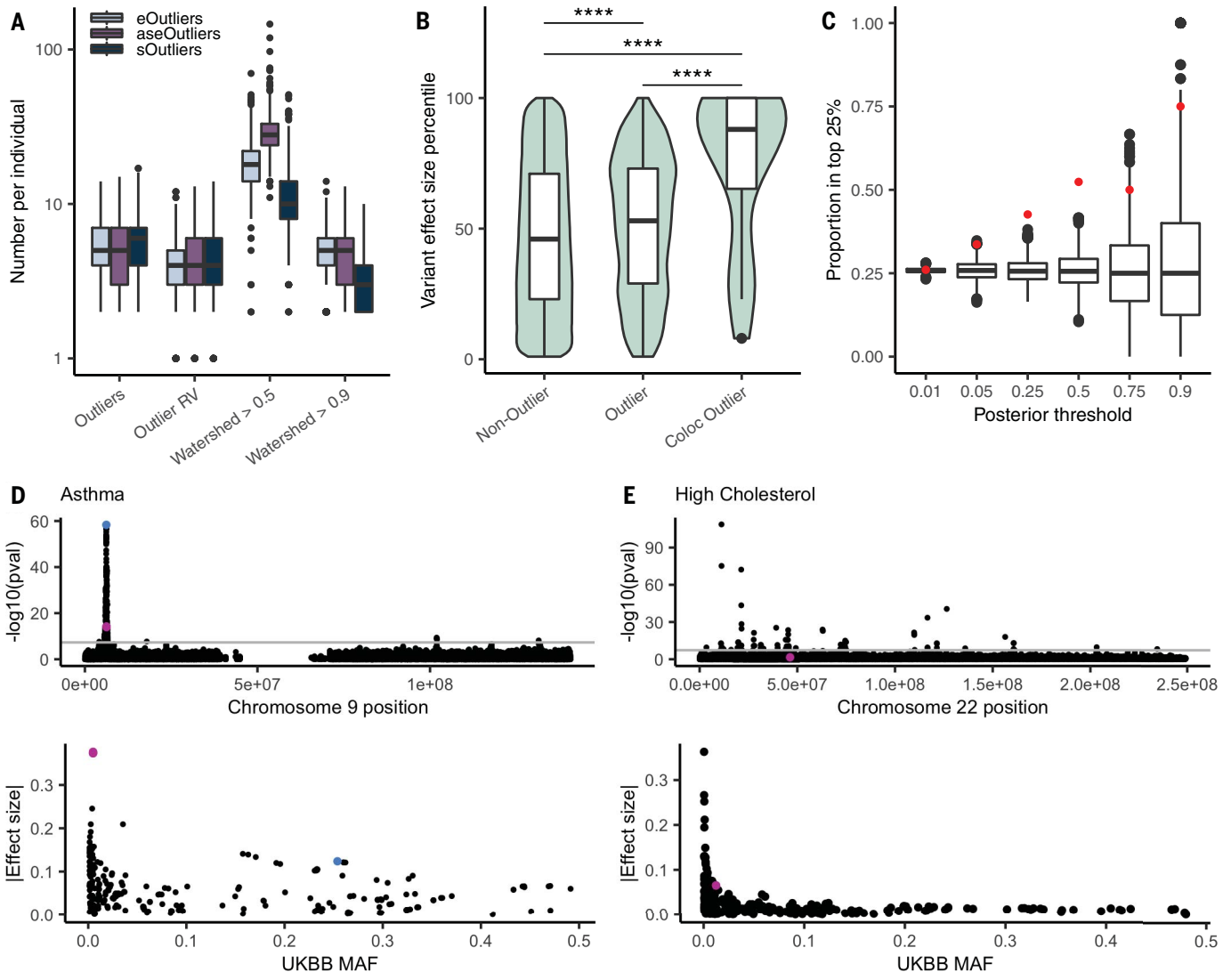

Fig. 5. Trait associations for RVs underlying outlier genes. (**A**) Distribution of the number of outlier genes, outlier genes with a nearby RV, and genes with a high Watershed posterior variant per data type. We added one to all values so that individuals with 0 are included. (**B**) Distribution of effect sizes, transformed to a percentile, for the set of GTEx RVs that appear in UKBB and are not outlier variants, those that are outlier variants, and those outlier variants that fall in colocalizing genes for the matched trait across 34 traits. Percentiles were calculated on the set of rare GTEx variants that overlap UKBB. The set of genes was restricted to those with at least one outlier individual in any data type and a nearby variant included in the test set (4787 variants and 1323 genes). *P* values were calculated from a one-sided Wilcoxon rank-sum test. (**C**) Proportion of variants filtered by Watershed posterior that fell in the top 25% of effect sizes for a colocalized trait (red) and the proportion of randomly selected variants of an equal number that also fall in these regions over 1000 iterations (black). (**D**) Manhattan plot (top) across chromosome 9 for asthma in the UKBB, filtered for non–low-confidence variants, with two high-Watershed variants, rs149045797 and rs146597587, shown in pink and the lead colocalized variant, rs3939286, shown in blue. The variants' effect size ranks were similarly high for both self-reported and diagnosed asthma, but the summary statistics are shown for asthma diagnosis here. The UKBB MAF versus absolute value of the effect size for all variants within 10 kb of the Watershed variant is also shown (bottom). (**E**) Manhattan plot across chromosome 22 for self-reported high cholesterol in the UKBB, filtered to remove low confidence variants, with the high-Watershed variant rs564796245 shown in pink. The UKBB MAF versus absolute value of the effect size for all variants within 10 kb of the Watershed variant is also shown (bottom).

We further developed a probabilistic model for personal genome interpretation, Watershed, which improves standard methods by integrating multiple transcriptomic signals from the same individual. Relevant to ongoing efforts to identify RVs affecting human traits, we found that in RVs within trait-colocalized regions, filtering by Watershed posteriors can identify variants with larger trait effect sizes better than relying on genomic annotations alone. As further demonstrated by our discovery of outlier RVs in well-studied disease genes, application of Watershed and other integrative methods will prove increasingly helpful for cataloging and prioritizing RVs affecting traits, especially those at the lowest ends of the AF spectrum. Our results provide a means to improve the quality and extent of RV prioritization, with potential future impacts enhancing RV association testing and disease gene identification.

Materials and methods summary

Detailed materials and methods are available in the supplementary materials. Briefly, we used RNA-seq and WGS data from the v8 release of the GTEx project, which contains

Table 1. Watershed and CADD as predictors of variant effect size percentile. Shown are the coefficient estimates and 95% confidence intervals from separate linear models with variant effect size percentile as the response and CADD score or Watershed posterior (scaled to have a mean of 0 and an SD of 1 so that values are of comparable range) as the predictor for all tested variants in colocalized regions (n = 5277).

Predictor	Beta	*P* value	95% confidence interval
Watershed posterior	1.61	2.12×10^{-6}	0.95–2.27
CADD score	0.77	2.41×10^{-2}	0.10–1.43

49 biological tissues with at least 70 samples per tissue.

For the set of RVs analyzed, we retained all SNVs and indels that passed quality control in the GTEx v8 variant call format file using the hg38 genome build. Structural variants were called on the subset of individuals available in the GTEx v7 release. We defined RVs as those with <1% MAF within GTEx and, for SNVs and indels, also occurring at <1% frequency in non-Finnish Europeans within gnomAD (*21*). Annotation of protein-coding regions and TF-binding site motifs was generated by running Ensembl VEP (v88).

We next used the RNA-seq data to make outlier calls in each tissue. Briefly, we log2-transformed the expression values [$\log_2$(TPM + 2)], where TPM is the number of transcripts per million mapped reads, restricted to lincRNA and protein-coding genes with at least six reads and TPM >0.1 in at least 20% of individuals. We scaled the expression of each gene to mean of 0 and a standard deviation of 1 to avoid the deflation of outlier values caused by quantile normalization. We corrected for hidden factors using PEER [probabilistic estimation of expression residuals (*52*)] to account for unmeasured technical confounders, as well as the top three genotype principal components, sex, and the genotype of the strongest cis-eQTL per gene in each tissue. We rescaled the residual values per gene and used the resulting corrected Z scores to determine eOutliers.

ASE outlier calls in a single tissue were made using ANEVA-DOT to identify genes in each individual that showed excessive allelic imbalance of ASE relative to the population. Briefly, ANEVA-DOT relies on tissue-specific estimates of genetic variation in gene dosage, V^G, derived by ANEVA on a reference population's ASE data to identify genes in individual test samples that are likely affected by RVs with unusually large regulatory effects.

Splicing outlier calls were made in a single tissue using SPOT to identify genes in each individual that show abnormal splicing patterns. Briefly, For a given LeafCutter cluster in a given tissue, we defined a matrix, X (dim NxJ), where each row corresponds to one of N samples, each column corresponding to one of J exon-exon junctions mapped to the LeafCutter cluster, and each element was the number of raw split read counts corresponding to that row's sample and that column's exon-exon junction. We were able to compute a P value representing how abnormal a given sample's splicing patterns were for the given LeafCutter cluster as follows:

1. Fitted parameters of Dirichlet-Multinomial distribution based on observed data X to capture the distribution of split read counts mapping to this LeafCutter cluster;

2. Used the fitted Dichlet-Multinomial distribution to compute the Mahalanobis distance for each of the N samples; and

3. Computed the Mahalanobis distance for 1,000,000 samples simulated from the fitted Dirichlet-Multinomial distribution and used these 1,000,000 Mahalanobis distances as an empirical distribution to assess the significance of the N real Mahalanobis distances.

To generate multitissue outlier calls for each gene and outlier type, we calculated an individual's median outlier score across all tissues for which data were available, restricting the analysis to individuals with measurements in at least five tissues. To account for situations in which widespread extreme expression might occur in an individual because of nongenetic influences, we excluded individuals in whom the proportion of tested genes that were multitissue outliers, at a P-value threshold of 0.0027, exceeded 1.5 times the interquartile range of the distribution of proportion of outlier genes across all individuals.

For the correlation-aware outlier calls, we determined a subset of individuals and tissues with <75% missingness, leading to 762 individuals and 29 tissues. We imputed missing expression values to improve our estimate of the tissue-by-tissue covariance matrix per gene that would be used in outlier calling. We used K-nearest neighbors in the impute R package (*53*) with k = 200 to impute values for missing tissues per individual on a gene-by-gene basis. From the imputed matrix, we estimated the tissue covariance matrix for each gene. We calculated the Mahalanobis distance for each gene-individual pair and assigned a P value to each gene individual from the chi-squared distribution, with degrees of freedom equal to the number of tissues available for that individual.

Watershed is a hierarchical Bayesian model that predicts the regulatory effects of RVs on a specific outlier signal based on the integration of multiple transcriptomic signals along with genomic annotations describing the RVs. Watershed models instances of gene-individual pairs to predict the regulatory effects of RVs nearby the gene. The Watershed model for a particular gene-individual pair, assuming K outlier signals, consists of three layers (Fig. 4A):

1. A set of variables $\mathbf{G}$, representing the P observed genomic annotations aggregated over all RVs in the individual that are nearby the gene.

2. A set of binary latent variables $\mathbf{Z} = Z_1, \ldots, Z_K$ representing the unobserved functional regulatory status of the RVs on each of the K outlier signals.

3. A set of categorical nodes $\mathbf{E} = E_1, \ldots, E_K$ representing the observed outlier status of the gene for each of the K outlier signals.

A fully connected conditional random field (CRF) is defined over variables Z given G. Variables E_i are each connected only to the corresponding latent variable Z_i. Specifically, the following conditional probability distributions together define the full Watershed model:

- $Z|G \sim \text{CRF}(\alpha, \beta_1, \ldots, \beta_k, \theta)$
- $E_k|Z_k \sim \text{Categorical}(\phi_k) \; \forall \; k \in K$
- $\phi_k \sim \text{Dirichlet}(C, \ldots, C)$
- $\beta_k \sim \text{Normal}\left(0, \frac{1}{\lambda}\right)$

where $\beta_k \in R^P \; \forall \; k \in K$ are the parameters defining the contribution of the genomic annotations to the CRF for each outlier signal (k), $\alpha \in R^K$ are the parameters defining the intercept of the CRF for each outlier signal (k), $\theta \in R^{(Kchoose2)}$ are the parameters defining the edge weights between pairs of outlier signals, $\phi_k \; \forall \; k \in K$ are the parameters defining the categorical distributions of each outlier signal, and C and λ are hyperparameters of the model.

For the CRISPR assay, we selected 14 rare stop-gained variants that were good candidates, eight of which passed quality control through (1) filtering to rare stop-gained variants with expression and ASE watershed posterior >0.9, (2) filtering to multitissue outlier status in both, and (3) keeping four remaining candidates that lie in complex trait genes and the next 10 with the highest individual outlier signal and Watershed posterior. Variants were tested using the polyclonal editing assay described in (*41*). Briefly, inducible-Cas9 293T cells were transfected with a guide RNA and a single-stranded homologous template specific to each variant. After sequencing, the effect size was calculated as $\log_2$[(Alt/Ref in cDNA)/(Alt/Ref in gDNA)] (*54*). These results were combined with six previously tested stop-gained and six non-eQTL control variants for which Watershed posteriors were available.

For the MPRA, we designed a set of synthetic DNA fragments by retrieving the genomic sequence corresponding to a 150-bp window centered at each variant of interest for the set of eOutlier-associated RVs and controls. For each variant, a reference and alternative sequence was designed that corresponded to each allele. GM12878 cells were cultured, electroporated, and collected. MPRA plasmid library construction proceeded as described in (*55*). To assemble oligo-barcode pairings, we merged all paired-end reads using FLASH2 (*56*), requiring a minimum 10-bp overlap to retain each pair. Sequences corresponding to genomic fragments were mapped using STAR (*57*) against a reference assembled using the designed oligo library sequences. To count reads per individual barcode sequence, we took raw single-end reads, extracted the 20-bp region corresponding to the random barcode, and counted the number of reads per individual sequence. Finally, to generate oligo-level read counts, we computed the sum of all barcodes for each oligo within each sample. We used negative binomial regression with an interaction term, implemented using DESeq2 (*58*), to identify significant allele-independent and allele-dependent regulatory effects.

To connect outlier-associated RVs to traits, we assessed genome-wide association study (GWAS0 summary statistics from the UKBB phase 2, made available by the Neale laboratory (www.nealelab.is/uk-biobank/). We subsetted the variants, either genotyped or imputed, in UKBB phase 2 to those that also appeared in any GTEx individuals with a frequency of <1% in GTEx, resulting in 45,415 SNVs. We filtered the set of GTEx RVs in UKBB to those in trait-colocalized regions, defined as being in a colocalized gene or within a 10-kb window. Colocalization calls are detailed in (*45*).

REFERENCES AND NOTES

1. A. Keinan, A. G. Clark, Recent explosive human population growth has resulted in an excess of rare genetic variants. *Science* **336**, 740–743 (2012). doi: 10.1126/science.1217283; pmid: 22582263
2. C. F. Wright, D. R. FitzPatrick, H. V. Firth, Paediatric genomics: Diagnosing rare disease in children. *Nat. Rev. Genet.* **19**, 325 (2018). doi: 10.1038/nrg.2018.12; pmid: 29456250
3. L. Bomba, K. Walter, N. Soranzo, The impact of rare and low-frequency genetic variants in common disease. *Genome Biol.* **18**, 77 (2017). doi: 10.1186/s13059-017-1212-4; pmid: 28449691
4. S. B. Montgomery, T. Lappalainen, M. Gutierrez-Arcelus, E. T. Dermitzakis, Rare and common regulatory variation in population-scale sequenced human genomes. *PLOS Genet.* **7**, e1002144 (2011). doi: 10.1371/journal.pgen.1002144; pmid: 21811411
5. Y. Zeng *et al*., Aberrant gene expression in humans. *PLOS Genet.* **11**, e1004942 (2015). doi: 10.1371/journal.pgen.1004942; pmid: 25617623
6. M. Pala *et al*., Population- and individual-specific regulatory variation in Sardinia. *Nat. Genet.* **49**, 700–707 (2017). doi: 10.1038/ng.3840; pmid: 28394350
7. X. Li *et al*., Transcriptome sequencing of a large human family identifies the impact of rare noncoding variants. *Am. J. Hum. Genet.* **95**, 245–256 (2014). doi: 10.1016/j.ajhg.2014.08.004; pmid: 25192044
8. R. D. Hernandez *et al*., Ultrarare variants drive substantial cis heritability of human gene expression. *Nat. Genet.* **51**, 1349–1355 (2019). doi: 10.1038/s41588-019-0487-7; pmid: 31477931
9. A. Battle *et al*., Genomic variation. Impact of regulatory variation from RNA to protein. *Science* **347**, 664–667 (2015). doi: 10.1126/science.1260793; pmid: 25657249
10. Y. I. Li *et al*., RNA splicing is a primary link between genetic variation and disease. *Science* **352**, 600–604 (2016). doi: 10.1126/science.aad9417; pmid: 27126046
11. L. Frésard *et al*., Identification of rare-disease genes using blood transcriptome sequencing and large control cohorts. *Nat. Med.* **25**, 911–919 (2019). pmid: 31160820
12. C. Bycroft *et al*., The UK Biobank resource with deep phenotyping and genomic data. *Nature* **562**, 203–209 (2018). doi: 10.1038/s41586-018-0579-z; pmid: 30305743
13. J. M. Gaziano *et al*., Million Veteran Program: A mega-biobank to study genetic influences on health and disease. *J. Clin. Epidemiol.* **70**, 214–223 (2016). doi: 10.1016/j.jclinepi.2015.09.016; pmid: 26441289
14. H. A. Taylor Jr. *et al*., Toward resolution of cardiovascular health disparities in African Americans: Design and methods of the Jackson Heart Study. *Ethn. Dis.* **15** (Suppl 6), S6–S4, 17 (2005). pmid: 16320381
15. X. Li *et al*., The impact of rare variation on gene expression across tissues. *Nature* **550**, 239–243 (2017). doi: 10.1038/nature24267; pmid: 29022581
16. Materials and methods are available as supplementary materials.
17. P. Mohammadi *et al*., Genetic regulatory variation in populations informs transcriptome analysis in rare disease. *Science* **366**, 351–356 (2019). doi: 10.1126/science.aay0256; pmid: 31601707
18. F. Aguet *et al*., The GTEx Consortium atlas of genetic regulatory effects across human tissues. bioRxiv 787903 [Preprint]. 3 October 2019. https://doi.org/10.1101/787903. doi: 10.1101/787903
19. F. Spitz, Gene regulation at a distance: From remote enhancers to 3D regulatory ensembles. *Semin. Cell Dev. Biol.* **57**, 57–67 (2016). doi: 10.1016/j.semcdb.2016.06.017; pmid: 27364700
20. P. H. L. Krijger, W. de Laat, Regulation of disease-associated gene expression in the 3D genome. *Nat. Rev. Mol. Cell Biol.* **17**, 771–782 (2016). doi: 10.1038/nrm.2016.138; pmid: 27826147
21. K. J. Karczewski *et al*., The mutational constraint spectrum quantified from variation in 141,456 humans. *Nature* **581**, 434–443 (2020). doi: 10.1038/s41586-020-2308-7; pmid: 32461654
22. Z.-F. Yang, S. Mott, A. G. Rosmarin, The Ets transcription factor GABP is required for cell-cycle progression. *Nat. Cell Biol.* **9**, 339–346 (2007). doi: 10.1038/ncb1548; pmid: 17277770
23. Y. Takahashi, J. B. Rayman, B. D. Dynlacht, Analysis of promoter binding by the E2F and pRB families in vivo: Distinct E2F proteins mediate activation and repression. *Genes Dev.* **14**, 804–816 (2000). pmid: 10766737
24. S. Gordon, G. Akopyan, H. Garban, B. Bonavida, Transcription factor YY1: Structure, function, and therapeutic implications in cancer biology. *Oncogene* **25**, 1125–1142 (2006). doi: 10.1038/sj.onc.1209080; pmid: 16314846
25. T. Han, S. Oh, K. Kang, ETS family protein GABP is a novel co-factor strongly associated with genomic YY1 binding sites in various cell lines. *Genes Genomics* **38**, 119–125 (2016). doi: 10.1007/s13258-015-0358-2
26. A. Saha *et al*., Co-expression networks reveal the tissue-specific regulation of transcription and splicing. *Genome Res.* **27**, 1843–1858 (2017). doi: 10.1101/gr.216721.116; pmid: 29021288
27. V. K. Mittal, J. F. McDonald, De novo assembly and characterization of breast cancer transcriptomes identifies large numbers of novel fusion-gene transcripts of potential functional significance. *BMC Med. Genomics* **10**, 53 (2017). doi: 10.1186/s12920-017-0289-7; pmid: 28851357
28. P. López-Nieva *et al*., Detection of novel fusion-transcripts by RNA-Seq in T-cell lymphoblastic lymphoma. *Sci. Rep.* **9**, 5179 (2019). doi: 10.1038/s41598-019-41675-3; pmid: 30914738
29. C. Neckles, S. Sundara Rajan, N. J. Caplen, Fusion transcripts: Unexploited vulnerabilities in cancer? *Wiley Interdiscip. Rev. RNA* **11**, e1562 (2020). doi: 10.1002/wrna.1562; pmid: 31407506
30. F. Baty, M. Brutsche, Fusion transcripts in lung cancer. *Lung Cancer* (2017).
31. S. Chen, J. Li, P. Zhou, X. Zhi, SPTBN1 and cancer, which links? *J. Cell. Physiol.* **235**, 17–25 (2020). doi: 10.1002/jcp.28975; pmid: 31206681
32. A. M. Fry, L. O'Regan, J. Montgomery, R. Adib, R. Bayliss, EML proteins in microtubule regulation and human disease. *Biochem. Soc. Trans.* **44**, 1281–1288 (2016). doi: 10.1042/BST20160125; pmid: 27911710
33. M. Burset, I. A. Seledtsov, V. V. Solovyev, Analysis of canonical and non-canonical splice sites in mammalian genomes. *Nucleic Acids Res.* **28**, 4364–4375 (2000). doi: 10.1093/nar/28.21.4364; pmid: 11058137
34. S. Zhang *et al*., Base-specific mutational intolerance near splice sites clarifies the role of nonessential splice nucleotides. *Genome Res.* **28**, 968–974 (2018). doi: 10.1101/gr.231902.117; pmid: 29858273
35. Y. I. Li *et al*., Annotation-free quantification of RNA splicing using LeafCutter. *Nat. Genet.* **50**, 151–158 (2018). doi: 10.1038/s41588-017-0004-9; pmid: 29229983
36. M. B. Shapiro, P. Senapathy, RNA splice junctions of different classes of eukaryotes: Sequence statistics and functional implications in gene expression. *Nucleic Acids Res.* **15**, 7155–7174 (1987). doi: 10.1093/nar/15.17.7155; pmid: 3658675
37. C. J. Coolidge, R. J. Seely, J. G. Patton, Functional analysis of the polypyrimidine tract in pre-mRNA splicing. *Nucleic Acids Res.* **25**, 888–896 (1997). doi: 10.1093/nar/25.4.888; pmid: 9016643
38. M. Kircher *et al*., A general framework for estimating the relative pathogenicity of human genetic variants. *Nat. Genet.* **46**, 310–315 (2014). doi: 10.1038/ng.2892; pmid: 24487276
39. P. Rentzsch, D. Witten, G. M. Cooper, J. Shendure, M. Kircher, CADD: Predicting the deleteriousness of variants throughout the human genome. *Nucleic Acids Res.* **47** (D1), D886–D894 (2019). doi: 10.1093/nar/gky1016; pmid: 30371827
40. B. Georgi *et al*., Genomic view of bipolar disorder revealed by whole genome sequencing in a genetic isolate. *PLOS Genet.* **10**, e1004229 (2014). doi: 10.1371/journal.pgen.1004229; pmid: 24625924
41. M. Brandt, A. Gokden, M. Ziosi, T. Lappalainen, A polyclonal allelic expression assay for detecting regulatory effects of transcript variants. bioRxiv 794081 [Preprint]. 7 October 2019. https://doi.org/10.1101/794081.
42. D. A. Forero *et al*., APOE gene and neuropsychiatric disorders and endophenotypes: A comprehensive review. *Am. J. Med. Genet. B. Neuropsychiatr. Genet.* **177**, 126–142 (2018). doi: 10.1002/ajmg.b.32516; pmid: 27943569
43. A. M. Habib *et al*., Microdeletion in a FAAH pseudogene identified in a patient with high anandamide concentrations and pain insensitivity. *Br. J. Anaesth.* **123**, e249–e253 (2019). doi: 10.1016/j.bja.2019.02.019; pmid: 30929760
44. H. Kim, D. P. Mittal, M. J. Iadarola, R. A. Dionne, Genetic predictors for acute experimental cold and heat pain sensitivity in humans. *J. Med. Genet.* **43**, e40 (2006). doi: 10.1136/jmg.2005.036079; pmid: 16882734
45. A. N. Barbeira *et al*., Exploiting the GTEx resources to decipher the mechanisms at GWAS loci. bioRxiv 814350 [Preprint]. 23 May 2020. https://doi.org/10.1101/814350.
46. D. Préfontaine *et al*., Increased IL-33 expression by epithelial cells in bronchial asthma. *J. Allergy Clin. Immunol.* **125**, 752–754 (2010). doi: 10.1016/j.jaci.2009.12.935; pmid: 20153038
47. N. S. Grotenboer, M. E. Ketelaar, G. H. Koppelman, M. C. Nawijn, Decoding asthma: Translating genetic variation in IL33 and IL1RL1 into disease pathophysiology. *J. Allergy Clin. Immunol.* **131**, 856–865 (2013). doi: 10.1016/j.jaci.2012.11.028; pmid: 23380221
48. D. Smith *et al*., A rare IL33 loss-of-function mutation reduces blood eosinophil counts and protects from asthma. *PLOS Genet.* **13**, e1006659 (2017). doi: 10.1371/journal.pgen.1006659; pmid: 28273074
49. A. Mousas *et al*., Rare coding variants pinpoint genes that control human hematological traits. *PLOS Genet.* **13**, e1006925 (2017). doi: 10.1371/journal.pgen.1006925; pmid: 28787443
50. T. A. Olafsdottir *et al*., Eighty-eight variants highlight the role of T cell regulation and airway remodeling in asthma pathogenesis. *Nat. Commun.* **11**, 393 (2020). doi: 10.1038/s41467-019-14144-8; pmid: 31959851
51. D. Klarin *et al*., Genetics of blood lipids among ~300,000 multi-ethnic participants of the Million Veteran Program. *Nat. Genet.* **50**, 1514–1523 (2018). doi: 10.1038/s41588-018-0222-9; pmid: 30275531
52. O. Stegle, L. Parts, M. Piipari, J. Winn, R. Durbin, Using probabilistic estimation of expression residuals (PEER) to obtain increased power and interpretability of gene expression analyses. *Nat. Protoc.* **7**, 500–507 (2012). doi: 10.1038/nprot.2011.457; pmid: 22343431
53. T. Hastie, R. Tibshirani, B. Narasimhan, G. Chu, impute: Imputation for microarray data (2020); http://www.bioconductor.org/packages/release/bioc/manuals/impute/man/impute.pdf.

54. P. Mohammadi, S. E. Castel, A. A. Brown, T. Lappalainen, Quantifying the regulatory effect size of *cis*-acting genetic variation using allelic fold change. *Genome Res.* **27**, 1872–1884 (2017). doi: 10.1101/gr.216747.116; pmid: 29021289
55. R. Tewhey *et al*., Direct identification of hundreds of expression-modulating variants using a multiplexed reporter assay. *Cell* **165**, 1519–1529 (2016). doi: 10.1016/j.cell.2016.04.027; pmid: 27259153
56. T. Magoč, S. L. Salzberg, FLASH: Fast length adjustment of short reads to improve genome assemblies. *Bioinformatics* **27**, 2957–2963 (2011). doi: 10.1093/bioinformatics/btr507; pmid: 21903629
57. A. Dobin *et al*., STAR: Ultrafast universal RNA-seq aligner. *Bioinformatics* **29**, 15–21 (2013). doi: 10.1093/bioinformatics/bts635; pmid: 23104886
58. M. I. Love, W. Huber, S. Anders, Moderated estimation of fold change and dispersion for RNA-seq data with DESeq2. *Genome Biol.* **15**, 550 (2014). doi: 10.1186/s13059-014-0550-8; pmid: 25516281
59. N. M. Ferraro *et al*., Reference variance estimates and blacklisted genes for all GTEx v8 tissues for: Transcriptomic signatures across human tissues identify functional rare genetic variation, Zenodo (2020); https://doi.org/10.5281/zenodo.3899574.
60. N. M. Ferraro *et al*., ANEVA-DOT code for: Transcriptomic signatures across human tissues identify functional rare genetic variation, Zenodo (2020); https://doi.org/10.5281/zenodo.3406690.
61. N. M. Ferraro *et al*., SPOT code for: Transcriptomic signatures across human tissues identify functional rare genetic variation, Zenodo (2020); https://zenodo.org/badge/latestdoi/209325700.
62. N. M. Ferraro *et al*., eOutlier code for: Transcriptomic signatures across human tissues identify functional rare genetic variation, Zenodo (2020); https://zenodo.org/badge/latestdoi/210649448.
63. N. M. Ferraro *et al*., A. Battle, Watershed model for: Transcriptomic signatures across human tissues identify functional rare genetic variation, Zenodo (2020); https://zenodo.org/badge/latestdoi/210165360.
64. N. M. Ferraro *et al*., Code used in all figures for: Transcriptomic signatures across human tissues identify functional rare genetic variation, Zenodo (2020); https://zenodo.org/badge/latestdoi/265935957.

ACKNOWLEDGMENTS

We thank members of the Lappalainen, Mohammadi, Montgomery, and Battle laboratories for helpful discussions and feedback; J. Bonnie for providing comments on the manuscript; K. Tayeb and R. Ungar for reviewing code; the investigators and participants who provided biological samples and data for GTEx, ASMAD, MVP, and JHS Trans-Omics in Precision Medicine (TOPMed); and the staff and participants of the JHS. **Funding:** This work was supported by the Common Fund of the Office of the Director, U.S. National Institutes of Health, and by NCI, NHGRI, NHLBI, NIDA, NIMH, NIA, NIAID, and NINDS through NIH contracts HHSN261200800001E (Leidos Prime contract with NCI: A.M.S., D.E.T., N.V.R., J.A.M., L.S., M.E.B., L.Q., T.K., D.B., K.R., A.U.), 10XS170 (NDRI: W.F.L., J.A.T., G.K., A.M., S.S., R.H., G.Wa., M.J., M.Wa., L.E.B., C.J., J.W., B.R., M.Hu., K.M., L.A.S., H.M.G., M.Mo., L.K.B.), 10XS171 (Roswell Park Cancer Institute: B.A.F., M.T.M., E.K., B.M.G., K.D.R., J.B.), 10X172 (Science Care, Inc.), 12ST1039 (IDOX), 10ST1035 (Van Andel Institute: S.D.J., D.C.R., D.R.V.), HHSN268201000029C (Broad Institute: F.A., G.G., K.G.A., A.V.S., X.Li., E.T., S.G., A.G., S.A., K.H.H., D.T.N., K.H., S.R.M., J.L.N.), 5U41HG009494 (F.A., G.G., K.G.A.) and through NIH grants R01 DA006227-17 (Univ. of Miami Brain Bank: D.C.M., D.A.D.), Supplement to University of Miami grant DA006227 (D.C.M., D.A.D.), R01 MH090941 (Univ. of Geneva), R01 MH090951 and R01 MH090937 (Univ. of Chicago), R01 MH090936 (Univ. of North Carolina–Chapel Hill), R01MH101814 (M.M-A., V.W., S.B.M., R.G., E.T.D., D.G-M., A.V., A.B.), U01HG007593 (S.B.M.), R01MH101822 (C.D.B.), U01HG007598 (M.O., B.E.S.), U01MH104393 (A.P.F.), extension H002371 to 5U41HG002371 (W.J.K.) as well as other funding sources: R01MH106842 (T.L., P.M., E.F., P.J.H.), R01HL142028 (T.L., Si.Ka., P.J.H.), R01GM122924 (T.L., S.E.C.), R01MH107666 (H.K.I.), P30DK020595 (H.K.I.), UM1HG008901 (T.L.), R01GM124486 (T.L.), R01HG010067 (Y.Pa.), R01HG002585 (G.Wa., M.St.), Gordon and Betty Moore Foundation GBMF 4559 (G.Wa., M.St.), 1K99HG009916-01 (S.E.C.), R01HG006855 (Se.Ka., R.E.H.), BIO2015-70777-P, Ministerio de Economia y Competitividad and FEDER funds (M.M-A., V.W., R.G., D.G-M.), la Caixa Foundation ID 100010434 under agreement LCF/BQ/SO15/52260001 (D.G-M.), NIH CTSA grant UL1TR002550-01 (P.M.), Marie-Skłodowska Curie fellowship H2020 Grant 706636 (S.K-H.), R35HG010718 (E.R.G.), FPU15/03635, Ministerio de Educación, Cultura y Deporte (M.M-A.), R01MH109905, 1R01HG010480 (A.B.), Searle Scholar Program (A.B.), R01HG008150 (S.B.M., A.B.), 5T32HG000044-22, NHGRI Institutional Training Grant in Genome Science (N.R.G.), EU IMI program (UE7-DIRECT-115317-1) (E.T.D., A.V.), FNS funded project RNA1 (31003A_149984) (E.T.D., A.V.), DK110919 (F.H.), F32HG009987 (F.H.), Massachusetts Lions Eye Research Fund Grant (A.R.H.), Mr. and Mrs. Spencer T. Olin Fellowship for Women in Graduate Study (A.J.S.), P30DK20595 (H.K.I.), UL1 TR001114 (P.M.), R01AG066490 (S.B.M.), R01HL142015 (S.B.M.), U01HG009431 (S.B.M.), U01HG009080 (S.B.M.), NIMH 1R01MH109905 (A.B.), National Science Foundation Graduate Research Fellowship, grant no. DGE – 1656518 (N.M.F.), graduate fellowship from the Stanford Center for Computational, Evolutionary and Human Genomics (N.M.F.), New York Center for Collaborative Research in Common Disease Genomics grant UM1HG008901 (J.E.), National Science Foundation of China grant 31970554 (X.L.), Shanghai Science and Technology Major Project IHPC 2017SHZDZX01 (X.L.), NIH T32 LM012409 (C.S.), Hewlett-Packard Stanford Graduate Fellowship and a doctoral scholarship from the Natural Science and Engineering Council of Canada (E.K.T.), Lucille P. Markey Stanford Graduate Fellowship (J.R.D.). We used data from the MVP, Office of Research and Development, Veterans Health Administration, supported by award no. MVP000. This publication does not represent the views of the Department of Veterans Affairs, the U.S. Food and Drug Administration, or the U.S. Government. Molecular Data for the TOPMed program was supported by the National Heart, Lung and Blood Institute (NHLBI). Genome sequencing for "NHLBI TOPMed: The Jackson Heart Study" (phs000964.v1.p1) was performed at the Northwest Genomics Center (HHSN268201100037C). Core support including centralized genomic read mapping and genotype calling, along with variant quality metrics and filtering were provided by the TOPMed Informatics Research Center (3R01HL-117626-02S1; contract HHSN268201800002I). Core support including phenotype harmonization, data management, sample-identity QC, and general program coordination were provided by the TOPMed Data Coordinating Center (R01HL-120393; U01HL-120393; contract HHSN268201800001I). This research was also supported by funding from: the Department of Veterans Affairs awards nos. I01-BX03340 and I01-BX003362 (T.L.A.). P.N. and G.M.P. are supported by R01HL142711 from the National Heart, Lung, and Blood Institute (NHLBI). The JHS is supported and conducted in collaboration with Jackson State University (HHSN268201800013I), Tougaloo College (HHSN268201800014I), the Mississippi State Department of Health (HHSN268201800015I) and the University of Mississippi Medical Center (HHSN268201800010I, HHSN268201800011I and HHSN268201800012I) contracts from the National Heart, Lung, and Blood Institute (NHLBI) and the National Institute on Minority Health and Health Disparities (NIMHD). **Author contributions:** N.M.F., B.J.S., J.E., P.M., S.B.M., and A.B. designed the study, performed analyses, and wrote the manuscript. N.M.F., X.L., and S.B.M. conducted eOutlier analysis and N.M.F., E.K.T., J.R.D., and S.B.M. conducted tissue-specific eOutlier analysis. N.M.F. and S.B.M. conducted distance, multigene (with P.M.), and fusion analyses (with N.S.A.). B.J.S. and A.B. developed SPOT and conducted sOutlier analysis. J.E., P.M., B.K., and T.L. conducted aseOutlier analysis. B.J.S. and A.B. developed Watershed. N.M.F., C.S., and S.B.M. conducted trait and known disease gene analyses. F.A. and K.G.A. generated processed expression, splicing, and cis-eQTL data. S.E.C. generated ASE call sets. A.N.B. generated sQTL colocalizations. Y.P. generated eQTL colocalizations. A.T.H. and T.L.A. performed MVP lookups. M.Ze., G.P., and P.N. performed the J.H.S. lookups. A.C. supervised J.H.S. A.J.S. and I.H. generated structural variant data. M.Bu., S.R., R.L.K., and C.D.B. collected and performed data processing on samples in the ASMAD cohort for replication. M.Br. and M.Zi. performed the CRISPR-Cas9 assay for stop-gained variants. N.S.A. and E.G. ran the MPRA experiment and analyzed the data. M.Ba., G.T.H., and Aradhana provided experimental assistance. C.S., E.K.T., J.R.D., and T.L. provided feedback on the manuscript. **Competing interests:** F.A. is an inventor on a patent application related to TensorQTL. S.E.C. is a cofounder, chief technology officer, and stock owner at Variant Bio. E.R.G. is on the editorial board of Circulation Research and does consulting for the City of Hope/Beckman Research Institute. E.T.D. is chairman and member of the board of Hybridstat Ltd. B.E.E. is on the scientific advisory boards of Celsius Therapeutics and Freenome. G.G. receives research funds from IBM and Pharmacyclics and is an inventor on patent applications related to MuTect, ABSOLUTE, MutSig, POLYSOLVER and TensorQTL. S.B.M. is on the scientific advisory board of MyOme. D.G.M. is a cofounder with equity in Goldfinch Bio and has received research support from AbbVie, Astellas, Biogen, BioMarin, Eisai, Merck, Pfizer, and Sanofi-Genzyme. H.K.I. has received speaker honoraria from GSK and AbbVie. T.L. is a scientific advisory board member of Variant Bio with equity and of Goldfinch Bio. P.F. is member of the scientific advisory boards of Fabric Genomics, Inc., and Eagle Genomes, Ltd. P.G.F. is a partner of Bioinf2Bio. G.G. is a founder, consultant, and holds privately held equity in Scorpion Therapeutics. P.N. reports investigator-initiated research grants from Amgen, Apple, and Boston Scientific and is a scientific adviser to Apple and Blackstone Life Sciences. The remaining authors have no competing interests. **Data and materials availability:** The data analyzed for this study are available to authorized users through dbGaP under accession no. phs000424.v8 and on the GTEx portal (https://gtexportal.org/). The complete set of multitissue outlier statistics can be found on the GTEx portal (https://gtexportal.org/). Reference variance estimates and blacklisted genes for all GTEx v8 tissues (*59*), ANEVA-DOT code (*60*), SPOT code (*61*), code for correlation eOutlier (*62*), Watershed (*63*), and the code used to generate all figures in this manuscript (*64*) are available at Zenodo. Data underlying each figure are available to download from https://drive.google.com/open?id=1dCxoYDPjK-E7qTUQhHN5Z-e6hiS5BQCG. J.H.S.'s data were accessed through dbGaP application no. 6213 for the TOPMed Exchange Area and were supported by secondary-use institutional review board approval from the Massachusetts General Hospital. VA MVP data were accessed through dbGaP application no. 2638.

SUPPLEMENTARY MATERIALS

science.sciencemag.org/content/369/6509/eaaz5900/suppl/DC1
Materials and Methods
Figs. S1 to S42
Tables S1 to S12
References (*65*–*91*)
MDAR Reproducibility Checklist

View/request a protocol for this paper from *Bio-protocol*.

GTEx Consortium

Laboratory and Data Analysis Coordinating Center (LDACC): François Aguet[1], Shankara Anand[1], Kristin G. Ardlie[1], Stacey Gabriel[1], Gad A. Getz[1,2,3], Aaron Graubert[1], Kane Hadley[1], Robert E. Handsaker[4,5,6], Katherine H. Huang[1], Seva Kashin[4,5,6], Xiao Li[1], Daniel G. MacArthur[5,7], Samuel R. Meier[1], Jared L. Nedzel[1], Duyen T. Nguyen[1], Ayellet V. Segrè[1,8], Ellen Todres[1]

Analysis Working Group Funded by GTEx Project Grants: François Aguet[1], Shankara Anand[1], Kristin G. Ardlie[1], Brunilda Balliu[9], Alvaro N. Barbeira[10], Alexis Battle[11,12], Rodrigo Bonazzola[10], Andrew Brown[13,14], Christopher D. Brown[15], Stephane E. Castel[16,17], Donald F. Conrad[18,19], Daniel J. Cotter[20], Nancy Cox[21], Sayantan Das[22], Olivia M. de Goede[20], Emmanouil T. Dermitzakis[13,23,24], Jonah Einson[16,25], Barbara E. Engelhardt[26,27], Eleazar Eskin[28], Tiffany Y. Eulalio[29], Nicole M. Ferraro[29], Elise D. Flynn[16,17], Laure Fresard[30], Eric R. Gamazon[21,31,32,33], Diego Garrido-Martín[34], Nicole R. Gay[20], Gad A. Getz[1,2,3], Michael J. Gloudemans[29], Aaron Graubert[1], Roderic Guigó[34,35], Kane Hadley[1], Andrew R. Hame[18,1], Robert E. Handsaker[4,5,6], Yuan He[11], Paul J. Hoffman[16], Farhad Hormozdiari[1,36], Lei Hou[1,37], Katherine H. Huang[1], Hae Kyung Im[10], Brian Jo[26,27], Silva Kasela[16,17], Seva Kashin[4,5,6], Manolis Kellis[1,37], Sarah Kim-Hellmuth[16,17,38], Alan Kwong[22], Tuuli Lappalainen[16,17], Xiao Li[1], Xin Li[30], Yanyu Liang[10], Daniel G. MacArthur[5,7], Serghei Mangul[28,39], Samuel R. Meier[1], Pejman Mohammadi[16,17,40,41], Stephen B. Montgomery[20,30], Manuel Muñoz-Aguirre[34,42], Daniel C. Nachun[30], Jared L. Nedzel[1], Duyen T. Nguyen[1], Andrew B. Nobel[43], Meritxell Oliva[10,44], YoSon Park[15,45], Yongjin Park[1,37], Princy Parsana[12], Abhiram S. Rao[46], Ferran Reverter[47], John M. Rouhana[1,8], Chiara Sabatti[48], Ashis Saha[12], Ayellet V. Segrè[1,8], Andrew D. Skol[10,49], Matthew Stephens[50], Barbara E. Stranger[10,51], Benjamin J. Strober[11], Nicole A. Teran[30], Ellen Todres[1], Ana Viñuela[13,23,24,52], Gao Wang[50], Xiaoquan Wen[22], Fred Wright[53], Valentin Wucher[34], Yuxin Zou[54]

Analysis Working Group Not Funded by GTEx Project Grants: Pedro G. Ferreira[55,56,57,58], Gen Li[59], Marta Melé[60], Esti Yeger-Lotem[61,62]

Leidos Biomedical Project Management: Mary E. Barcus[63], Debra Bradbury[63], Tanya Krubit[63], Jeffrey A. McLean[63], Liqun Qi[63], Karna Robinson[63], Nancy V. Roche[63], Anna M. Smith[63], Leslie Sobin[63], David E. Tabor[63], Anita Undale[63]

Biospecimen Collection Source Sites: Jason Bridge[64], Lori E. Brigham[65], Barbara A. Foster[66], Bryan M. Gillard[66], Richard Hasz[67], Marcus Hunter[68], Christopher Johns[69], Mark Johnson[70], Ellen Karasik[66], Gene Kopen[71], William F. Leinweber[71], Alisa McDonald[71], Michael T. Moser[66], Kevin Myer[68], Kimberley D. Ramsey[66], Brian Roe[68], Saboor Shad[71], Jeffrey A. Thomas[71,70], Gary Walters[70], Michael Washington[70], Joseph Wheeler[69]

Biospecimen Core Resource: Scott D. Jewell[72], Daniel C. Rohrer[72], Dana R. Valley[72]

Brain Bank Repository: David A. Davis[73], Deborah C. Mash[73]
Pathology: Mary E. Barcus[63], Philip A. Branton[74], Leslie Sobin[63]
ELSI Study: Laura K. Barker[75], Heather M. Gardiner[75], Maghboeba Mosavel[76], Laura A. Siminoff[75]
Genome Browser Data Integration and Visualization: Paul Flicek[77], Maximilian Haeussler[78], Thomas Juettemann[77], W. James Kent[78], Christopher M. Lee[78], Conner C. Powell[78], Kate R. Rosenbloom[78], Magali Ruffier[77], Dan Sheppard[77], Kieron Taylor[77], Stephen J. Trevanion[77], Daniel R. Zerbino[77]
eGTEx Group: Nathan S. Abell[20], Joshua Akey[79], Lin Chen[44], Kathryn Demanelis[44], Jennifer A. Doherty[80], Andrew P. Feinberg[81], Kasper D. Hansen[82], Peter F. Hickey[83], Lei Hou[1,37], Farzana Jasmine[44], Lihua Jiang[20], Rajinder Kaul[84,85], Manolis Kellis[1,37], Muhammad G. Kibriya[44], Jin Billy Li[20], Qin Li[20], Shin Lin[86], Sandra E. Linder[20], Stephen B. Montgomery[20,30], Meritxell Oliva[10,44], Yongjin Park[1,37], Brandon L. Pierce[44], Lindsay F. Rizzardi[87], Andrew D. Skol[10,49], Kevin S. Smith[30], Michael Snyder[20], John Stamatoyannopoulos[84,88], Barbara E. Stranger[10,51], Hua Tang[20], Meng Wang[20]
NIH Program Management: Philip A. Branton[74], Latarsha J. Carithers[74,89], Ping Guan[74], Susan E. Koester[90], A. Roger Little[91], Helen M. Moore[74], Concepcion R. Nierras[92], Abhi K. Rao[74], Jimmie B. Vaught[74], Simona Volpi[93]

[1]Broad Institute of MIT and Harvard, Cambridge, MA, USA. [2]Cancer Center and Department of Pathology, Massachusetts General Hospital, Boston, MA, USA. [3]Harvard Medical School, Boston, MA, USA. [4]Department of Genetics, Harvard Medical School, Boston, MA, USA. [5]Program in Medical and Population Genetics, Broad Institute of MIT and Harvard, Cambridge, MA, USA. [6]Stanley Center for Psychiatric Research, Broad Institute of MIT and Harvard, Cambridge, MA, USA. [7]Analytic and Translational Genetics Unit, Massachusetts General Hospital, Boston, MA, USA. [8]Ocular Genomics Institute, Massachusetts Eye and Ear, Harvard Medical School, Boston, MA, USA. [9]Department of Biomathematics, University of California, Los Angeles, CA, USA. [10]Section of Genetic Medicine, Department of Medicine, The University of Chicago, Chicago, IL, USA. [11]Department of Biomedical Engineering, Johns Hopkins University, Baltimore, MD, USA. [12]Department of Computer Science, Johns Hopkins University, Baltimore, MD, USA. [13]Department of Genetic Medicine and Development, University of Geneva Medical School, Geneva, Switzerland. [14]Population Health and Genomics, University of Dundee, Dundee, Scotland, UK. [15]Department of Genetics, University of Pennsylvania, Perelman School of Medicine, Philadelphia, PA, USA. [16]New York Genome Center, New York, NY, USA. [17]Department of Systems Biology, Columbia University, New York, NY, USA. [18]Department of Genetics, Washington University School of Medicine, St. Louis, MO, USA. [19]Division of Genetics, Oregon National Primate Research Center, Oregon Health & Science University, Portland, OR, USA. [20]Department of Genetics, Stanford University, Stanford, CA, USA. [21]Division of Genetic Medicine, Department of Medicine, Vanderbilt University Medical Center, Nashville, TN, USA. [22]Department of Biostatistics, University of Michigan, Ann Arbor, MI, USA. [23]Institute for Genetics and Genomics in Geneva (iGE3), University of Geneva, Geneva, Switzerland. [24]Swiss Institute of Bioinformatics, Geneva, Switzerland. [25]Department of Biomedical Informatics, Columbia University, New York, NY, USA. [26]Department of Computer Science, Princeton University, Princeton, NJ, USA. [27]Center for Statistics and Machine Learning, Princeton University, Princeton, NJ, USA. [28]Department of Computer Science, University of California, Los Angeles, CA, USA. [29]Program in Biomedical Informatics, Stanford University School of Medicine, Stanford, CA, USA. [30]Department of Pathology, Stanford University, Stanford, CA, USA. [31]Data Science Institute, Vanderbilt University, Nashville, TN, USA. [32]Clare Hall, University of Cambridge, Cambridge, UK. [33]MRC Epidemiology Unit, University of Cambridge, Cambridge, UK. [34]Centre for Genomic Regulation (CRG), The Barcelona Institute for Science and Technology, Barcelona, Catalonia, Spain. [35]Universitat Pompeu Fabra (UPF), Barcelona, Catalonia, Spain. [36]Department of Epidemiology, Harvard T.H. Chan School of Public Health, Boston, MA, USA. [37]Computer Science and Artificial Intelligence Laboratory, Massachusetts Institute of Technology, Cambridge, MA, USA. [38]Statistical Genetics, Max Planck Institute of Psychiatry, Munich, Germany [39]Department of Clinical Pharmacy, School of Pharmacy, University of Southern California, Los Angeles, CA, USA. [40]Scripps Research Translational Institute, La Jolla, CA, USA. [41]Department of Integrative Structural and Computational Biology, The Scripps Research Institute, La Jolla, CA, USA. [42]Department of Statistics and Operations Research, Universitat Politècnica de Catalunya (UPC), Barcelona, Catalonia, Spain. [43]Department of Statistics and Operations Research and Department of Biostatistics, University of North Carolina, Chapel Hill, NC, USA. [44]Department of Public Health Sciences, The University of Chicago, Chicago, IL, USA. [45]Department of Systems Pharmacology and Translational Therapeutics, Perelman School of Medicine, University of Pennsylvania, Philadelphia, PA, USA. [46]Department of Bioengineering, Stanford University, Stanford, CA, USA. [47]Department of Genetics, Microbiology and Statistics, University of Barcelona, Barcelona, Spain. [48]Departments of Biomedical Data Science and Statistics, Stanford University, Stanford, CA, USA. [49]Department of Pathology and Laboratory Medicine, Ann & Robert H. Lurie Children's Hospital of Chicago, Chicago, IL, USA. [50]Department of Human Genetics, University of Chicago, Chicago, IL, USA. [51]Center for Genetic Medicine, Department of Pharmacology, Northwestern University, Feinberg School of Medicine, Chicago, IL, USA. [52]Department of Twin Research and Genetic Epidemiology, King's College London, London, UK. [53]Bioinformatics Research Center and Departments of Statistics and Biological Sciences, North Carolina State University, Raleigh, NC, USA. [54]Department of Statistics, University of Chicago, Chicago, IL, USA. [55]Department of Computer Sciences, Faculty of Sciences, University of Porto, Porto, Portugal. [56]Instituto de Investigação e Inovação em Saúde, University of Porto, Porto, Portugal. [57]Institute of Molecular Pathology and Immunology, University of Porto, Porto, Portugal. [58]Laboratory of Artificial Intelligence and Decision Support, Institute for Systems and Computer Engineering, Technology and Science, Porto, Portugal. [59]Mailman School of Public Health, Columbia University, New York, NY, USA. [60]Life Sciences Department, Barcelona Supercomputing Center, Barcelona, Spain. [61]Department of Clinical Biochemistry and Pharmacology, Ben-Gurion University of the Negev, Beer-Sheva, Israel. [62]National Institute for Biotechnology in the Negev, Beer-Sheva, Israel. [63]Leidos Biomedical, Rockville, MD, USA. [64]Upstate New York Transplant Services, Buffalo, NY, USA. [65]Washington Regional Transplant Community, Annandale, VA, USA. [66]Therapeutics, Roswell Park Comprehensive Cancer Center, Buffalo, NY, USA. [67]Gift of Life Donor Program, Philadelphia, PA, USA. [68]LifeGift, Houston, TX, USA. [69]Center for Organ Recovery and Education, Pittsburgh, PA, USA. [70]LifeNet Health, Virginia Beach, VA. USA. [71]National Disease Research Interchange, Philadelphia, PA, USA. [72]Van Andel Research Institute, Grand Rapids, MI, USA. [73]Department of Neurology, University of Miami Miller School of Medicine, Miami, FL, USA. [74]Biorepositories and Biospecimen Research Branch, Division of Cancer Treatment and Diagnosis, National Cancer Institute, National Institutes of Health, Bethesda, MD, USA. [75]Temple University, Philadelphia, PA, USA. [76]Virginia Commonwealth University, Richmond, VA, USA. [77]European Molecular Biology Laboratory, European Bioinformatics Institute, Hinxton, UK. [78]Genomics Institute, University of California, Santa Cruz, CA, USA. [79]Carl Icahn Laboratory, Princeton University, Princeton, NJ, USA. [80]Department of Population Health Sciences, The University of Utah, Salt Lake City, UT, USA. [81]Departments of Medicine, Biomedical Engineering, and Mental Health, Johns Hopkins University, Baltimore, MD, USA. [82]Department of Biostatistics, Bloomberg School of Public Health, Johns Hopkins University, Baltimore, MD, USA. [83]Department of Medical Biology, The Walter and Eliza Hall Institute of Medical Research, Parkville, Victoria, Australia. [84]Altius Institute for Biomedical Sciences, Seattle, WA, USA. [85]Division of Genetics, University of Washington, Seattle, WA, USA. [86]Department of Cardiology, University of Washington, Seattle, WA, USA. [87]HudsonAlpha Institute for Biotechnology, Huntsville, AL, USA. [88]Genome Sciences, University of Washington, Seattle, WA, USA. [89]National Institute of Dental and Craniofacial Research, National Institutes of Health, Bethesda, MD, USA. [90]Division of Neuroscience and Basic Behavioral Science, National Institute of Mental Health, National Institutes of Health, Bethesda, MD, USA. [91]National Institute on Drug Abuse, Bethesda, MD, USA. [92]Office of Strategic Coordination, Division of Program Coordination, Planning and Strategic Initiatives, Office of the Director, National Institutes of Health, Rockville, MD, USA. [93]Division of Genomic Medicine, National Human Genome Research Institute, Bethesda, MD, USA.

30 September 2019; accepted 31 July 2020
10.1126/science.aaz5900

RESEARCH

IN *SCIENCE* JOURNALS

Edited by **Michael Funk**

A Hubble Space Telescope image of galaxy cluster Abell 370, which acts as a lens and bends light from distant stars

IMAGE: NASA, ESA, HUBBLE; PROCESSING & COPYRIGHT: ROGELIO BERNAL ANDREO (DEEPSKYCOLORS.COM)

COSMOLOGY

Gravitational lenses in galaxy clusters

The large mass of a galaxy cluster deflects light from background objects, a phenomenon known as gravitational lensing. The large-scale gravitational lens caused by the whole cluster can be modified by smaller-scale mass concentrations within the cluster, such as individual galaxies. Meneghetti *et al*. examined these small-scale gravitational lenses in observations of 11 galaxy clusters. They found small lenses that were an order of magnitude smaller than would be expected from cosmological simulations. The authors conclude that there is an unidentified problem with either prevailing simulation methods or standard cosmology. —KTS

Science, this issue p. 1347

STRUCTURAL BIOLOGY

Coupling transcription and translation

In bacteria, the rate of transcription of messenger RNA (mRNA) by RNA polymerase (RNAP) is coordinated with the rate of translation by the first ribosome behind RNAP on the mRNA. Two groups now present cryo–electron microscopy structures that show how two transcription elongation factors, NusG and NusA, participate in this coupling. Webster *et al*. found that NusG forms a bridge between RNAP and the ribosome when they are separated by mRNA. With shortened mRNA, NusG no longer links RNAP and the ribosome, but the two are oriented so that newly transcribed mRNA can enter the ribosome. Wang *et al*. provide further insight into the effect of mRNA length on the complex structures. They also include NusA and show that the NusG-bridged structure is stabilized by NusA. —VV

Science, this issue p. 1355, p. 1359

GLOBAL CLIMATE

The states of past climate

Deep-sea benthic foraminifera preserve an essential record of Earth's past climate in their oxygen- and carbon-isotope compositions. However, this record lacks sufficient temporal resolution and/or age control in some places to determine which climate forcing and feedback mechanisms were most important. Westerhold *et al*. present a highly resolved and well-dated record of benthic carbon and oxygen isotopes for the past 66 million years. Their reconstruction and analysis show that Earth's climate can be grouped into discrete states separated by transitions related to changing greenhouse gas levels and the growth of polar ice sheets. Each climate state is paced by orbital cycles but responds to variations in radiative forcing in a state-dependent manner. —HJS

Science, this issue p. 1383

CIRCADIAN RHYTHMS

Keeping rhythm requires communication

In mammals, daily cycles in physiology require the synchronized activity of circadian clocks in peripheral organs such as the liver, a hub of metabolism. Guan *et al*. generated mice with hepatocytes that lack two transcriptional repressors known to be essential for clock function. This experimental manipulation unexpectedly disrupted rhythmic gene expression and metabolism not only in hepatocytes but also in other liver cell types. Feeding behavior also coregulated circadian rhythms in multiple liver cell types. Cell-cell communication thus appears to be important in maintaining the robustness of peripheral circadian clocks. —PAK

Science, this issue p. 1388

TROPHIC CASCADES

A lethal combination

It is well established that predators are essential for the structuring and maintenance of biotic communities. One of the first demonstrations of this importance came from studies of the importance of sea otters to the maintenance of kelp forests. Rasher *et al*. now show that the effects caused by the absence of this predator can be further exacerbated by climate warming. In North Pacific kelp forests, otter absence led to a decline of slow-growing calcareous algae through sea urchin herbivory, and this pattern was amplified by warming

Published by AAAS

temperatures. Keystone predators are thus essential not only for trophic structure but also for mitigating the impacts of climate change. —SNV

Science, this issue p. 1351

PARKINSON'S DISEASE

PARK7 preservation

Mutations in the gene *PARK7* lead to the development of early-onset Parkinson's disease (PD), a neurodegenerative condition for which there are currently no effective treatments. Boussaad *et al*. identified an exonic splicing mutation in *PARK7* linked to PD and studied the effect of this mutation in patient-derived cellular models. The mutation resulted in impaired splicing, reduced production of the protein DJ-1, and consequent mitochondrial dysfunction. Rescuing the aberrant splicing with a chemical rectifier of aberrant splicing rescued neuronal loss in patient-derived brain organoids. These results suggest that precision medicine targeting specific molecular signatures could be an effective strategy for PD and possibly other neurodegenerative diseases. —MM

Sci. Transl. Med. **12**, eaau3960 (2020).

TROPICAL FOREST

Degradation exceeds deforestation

Forest degradation is a ubiquitous form of human disturbance of the forest landscape. Activities such as selective logging and extraction fall short of total deforestation but lead to loss of biomass and/or fragmentation. On the basis of remote sensing data at 30-meter spatial resolution, Matricardi *et al*. analyzed the extent of forest degradation across the entire Brazilian Amazon over a ~22-year period up to 2014. They found that the extent and rate of forest degradation was equal to or greater than deforestation, which has important implications for carbon, biodiversity, and energy balance. —AMS

Science, this issue p. 1378

METABOLISM

Finding calorie restriction mimetics

Calorie restriction extends the health span, and this may be partially mediated by a drop in core body temperature. Guijas *et al*. compared metabolomics data from calorie-restricted mice housed either at thermoneutrality or a cooler temperature. Calorie restriction induced the hypothalamus to produce the gasotransmitter nitric oxide and the opioid peptide leucine enkephalin only in mice housed at the cooler temperature. These and other metabolites differentially altered by ambient temperature may form the basis for treatments that can deliver the beneficial effects of calorie restriction. —WW

Sci. Signal. **13**, eabb2490 (2020).

Roadways in the Brazilian Amazon contribute to damaging forest degradation, even in the absence of outright deforestation.

IN OTHER JOURNALS

Edited by **Caroline Ash** *and* **Jesse Smith**

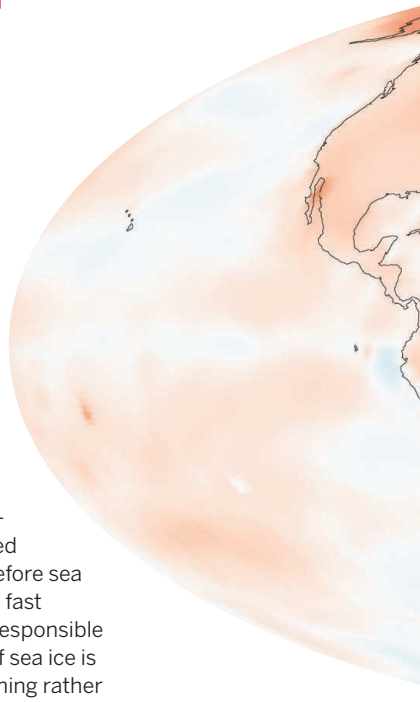

CLIMATE WARMING

Rapid response

As the climate warms, Arctic temperatures are rising faster than temperatures at lower latitudes, a phenomenon called Arctic amplification. Loss of sea ice and snow cover at high northern latitudes have long been understood to contribute to this behavior, but other mechanisms have been suggested as well. Previdi *et al*. analyzed climate model simulations and conclude that this amplified warming response actually begins before sea ice loss becomes important and that fast atmospheric processes are instead responsible for its initiation. Therefore, the loss of sea ice is an amplifier of enhanced Arctic warming rather than a trigger. —HJS

Geophys. Res. Lett. 10.1029/2020GL089933 (2020).

NEUROSCIENCE

Representation of what happened when

Episodic memory depends on the hippocampus and entorhinal cortex. Although the temporal coding properties of hippocampal neurons are well known, the temporal code in the entorhinal cortex, which provides important input to the hippocampus, is less understood. Bright *et al.* examined monkey entorhinal neuron responses in a 5-second period after presentation of an image. Entorhinal neurons were activated shortly after a visual stimulus and then decayed with a variety of rates, enabling reconstruction of when the image was presented. To determine whether the pattern of neuronal activation depended on the identity of the image presented, each image was shown twice during the experiment. These results suggest that entorhinal cortex context cells carry information about what happened in addition to when it happened. —PRS

Proc. Natl. Acad. Sci. U.S.A. **117**, 20274 (2020).

HUMAN GENETICS

Extending genetic predictions

Polygenic risk scores (PRSs) aggregate genomic information to predict an individual's risk of developing diseases with a genetic basis. To determine links between PRSs and health. Wainberg *et al.* profiled the blood plasma of almost 5000 individuals and examined PRSs for 54 diseases. From this, they linked PRSs to 766 detectable traits, including those that affect proteins or metabolites or are clinically relevant. Because many of these relationships were known, this work confirms links between genotype and phenotype and provides a platform for future work. Unexpectedly, some healthy individuals with a PRS indicating high risk for disease had a blood profile similar to those from individuals with disease. This indicates that genetic information can help to separate disease risk factors from the consequences of a pathological condition and

CREDITS (FROM LEFT): ANDRÉ COSTA/ALAMY STOCK PHOTO; NASA IMAGE BY ROBERT SIMMON, BASED ON GISS SURFACE TEMPERATURE ANALYSIS DATA INCLUDING SHIP AND BUOY DATA FROM THE HADLEY CENTRE

Published by AAAS

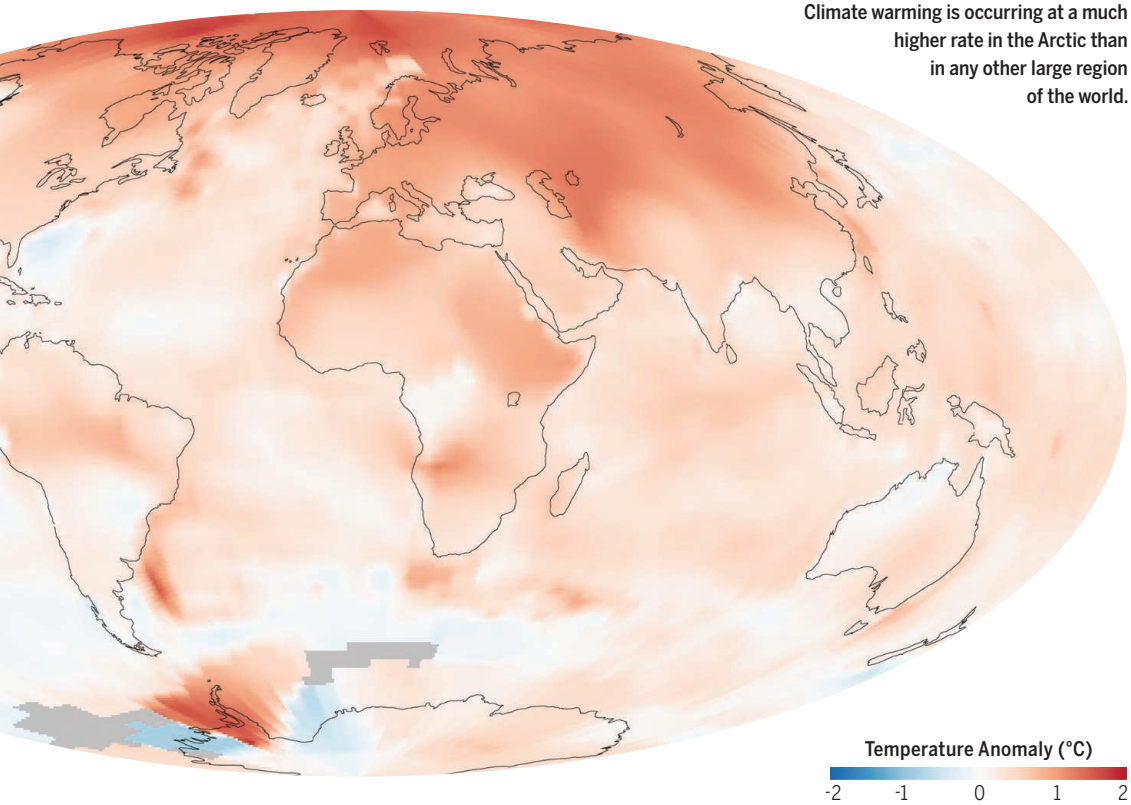

Climate warming is occurring at a much higher rate in the Arctic than in any other large region of the world.

identify potential preventative interventions. —LMZ

Proc. Natl. Acad. Sci. U.S.A. **117**, 21813 (2020).

SIGNAL TRANSDUCTION

Spermatogenesis gets a NOD

NOD-like receptors function as pattern recognition receptors in the innate immune system, but some are only expressed in the mammalian germline. Yin *et al.* describe the function of the NOD-like receptor NLRP14 in mice to promote differentiation of primordial germ cell–like cells and spermatogenesis. In this case, the receptor has a signaling role distinct from that of its immune counterparts. NLRP14 formed a complex with the chaperone cofactor BAG2 and with HSPA2, a member of the HSP70 70-kilodalton heat shock protein family. Such binding prevented ubiquitin-mediated proteasomal degradation of HSPA2, allowing it to translocate to the nucleus, where it helps to package spermatid DNA. —LBR

Proc. Natl. Acad. Sci. U.S.A. 10.1073/pnas.2005533117 (2020).

ULTRAFAST IMAGING

Diffractive imaging in a flash

Ultrashort light pulses on the time scale of attoseconds provide a window into some of the fastest electronic effects occurring in solid-state systems.

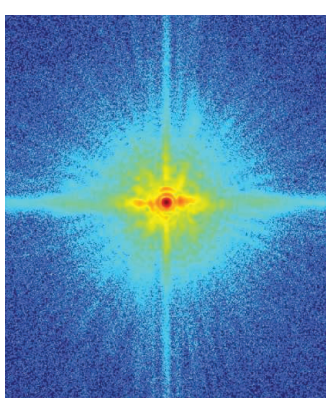

Diffraction pattern generated using simulated attosecond pulses for coherent object imaging

Obtaining structural information through coherent diffractive imaging is usually done with monochromatic x-ray sources. However, ultrashort pulses are inherently broadband, and getting transient structural information on such short time scales is challenging. Rana *et al.* describe a method that works with the broadband nature of ultrashort pulses. They split the pulses into 17 different wavelengths and then used an algorithm to computationally stitch together the diffraction patterns from each wavelength to reveal the structural image optimized across all wavelengths. Demonstrating the technique at optical wavelengths illustrates the feasibility of applying the method to ultrafast x-ray pulses. —ISO

Phys. Rev. Lett. **125**, 086101 (2020).

ELECTROCHEMISTRY

High-performance aqueous Al-ion batteries

Because of its high abundance, low production cost, and three-electron redox properties, aluminum (Al) has received considerable attention in recent years for the development of possible alternatives to conventional lithium-based batteries. Yan *et al.* propose an aqueous Al-ion battery configuration consisting of an Al_xMnO_2 cathode, a zinc substrate–supported Zn-Al alloy anode, and an $Al(OTF)_3$ aqueous electrolyte. This battery demonstrates promising values for key performance indicators such as cycling life, reversible capacity, discharge voltage plateau, and rate capability. The present work is an important step in designing Al-ion–based batteries for practical applications. —YS

J. Am. Chem. Soc. 10.1021/jacs.0c05054 (2020).

CELL BIOLOGY

Getting the size right

Double-membraned autophagosomes enwrap defunct organelles or intracellular aggregates, allowing them to be delivered to lysosomes, where they are degraded. Autophagy also allows cells to survive short periods of starvation by recycling intracellular components for reuse in critical processes. How do cells manufacture autophagosomes of the right size to engulf targets? Yamamoto *et al.* identified a protein, ERdj8, that is localized to the endoplasmic reticulum (a key source of autophagic membranes) and acts as a size regulator of newly formed autophagosomes. When ERdj8 was inactivated through treatment with small interfering RNA, cells produced small autophagosomes that could not engulf large autophagic targets such as damaged mitochondria. Increasing the amount of ERdj8 delayed autophagosome formation and allowed prolonged extension of the phagophore to yield large autophagosomes. Thus, ERdj8 allows targeting of diverse size objects for recycling. —SMH

J. Cell Biol. **219**, e201903127 (2020).

IMAGE: RANA *ET AL.*, *PHYS. REV. LETT.* **125**, 086101 (2020)

Published by AAAS

ALSO IN *SCIENCE* JOURNALS

Edited by **Michael Funk**

HUMAN GENOMICS

A survey of transcription across tissues

Some human genetic variants affect the amount of RNA produced and the splicing of gene transcripts, crucial steps in development and maintaining a healthy individual. However, some of these changes only occur in a small number of tissues within the body. The Genotype-Tissue Expression (GTEx) project has been expanded over time, and, looking at the final data in version 8, Aguet *et al.* present a deep characterization of genetic associations and gene expression and splicing in 838 individuals over 49 tissues (see the Perspective by Wilson). This large study was able to characterize the details underlying many aspects of gene expression and provides a resource with which to better understand the fundamental molecular mechanisms of how genetic variants affect gene regulation and complex traits in humans. —LMZ

Science, this issue p. 1318; see also p. 1298

HUMAN GENOMICS

The role of sex in the human transcriptome

In humans, the inheritance of the XX or XY set of sex chromosomes is responsible for most individuals developing into adults expressing male or female sex-specific traits. However, the degree to which sex-biased gene expression occurs in tissues, especially those that do not contribute to characteristic sexually dimorphic traits. is unknown. Oliva *et al.* examined Genotype-Tissue Expression (GTEx) project data and found that 37% of genes in at least one of the 44 tissues studied exhibit a tissue-specific, sex-biased gene expression. They also identified a sex-specific variation in cellular composition across tissues. Overall, the effects of sex on gene expression were small, but they were genome-wide and mostly mediated through transcription factor binding. With sex-biased gene expression associated with loci identified in genome-wide association studies, this study lays the groundwork for identifying the molecular basis of male- and female-based diseases. —LMZ

Science, this issue p. 1331

HUMAN GENOMICS

Cell type–specific quantitative trait loci

Understanding how human genetic variation affects phenotype requires tissue- or even cell type–specific measurements. Kim-Hellmuth *et al.* used computational methods to identify cell-type proportions within bulk tissues in the Genotype-Tissue Expression (GTEx) project dataset to identify cell-type interaction quantitative trait loci and map these to genetic variants correlated with expression or splicing differences between individuals. By characterizing the cellular context, this study illustrates how genetic variants that operate in a cell type–specific manner affect gene regulation and can be linked to complex traits. This deconvolution and analysis of cell types from bulk tissues allows greater precision in understanding how phenotypes are linked to genetic variation. —LMZ

Science, this issue p. 1332

HUMAN GENOMICS

Telomere length within individuals

Telomeres are DNA-protein complexes that protect chromosome ends. Their length is of great interest because short telomeres are associated with specific diseases and with aging. Demanelis *et al.* measured telomere length from 952 Genotype-Tissue Expression (GTEx) project donors across tissues, of which 24 tissue types have measurements for more than 25 samples. This dataset shows that telomere length is not constant but is correlated across tissues. Most tissue telomeres shorten with age, but some, such as those in the testis and cerebellum, do not. In African Americans, telomeres are longer on average than those from individuals of primarily European descent across many tissue types. This observation is consistent with variability being passed from germ cells to zygote to differentiated cells during development. —LMZ

Science, this issue p. 1333

HUMAN GENOMICS

Functional rare variation in transcriptomes

Every human genome contains tens of thousands of rare genetic variants—which include single nucleotide changes, insertions or deletions, and larger structural variants—and some may have a functional effect. Ferraro *et al.* examined data from individuals in the Genotype-Tissue Expression (GTEx) project for outliers across tissues caused by gene expression, splicing, and allele-specific expression. Single rare variants were observed that affected the expression and allele-specific expression of multiple genes and, in the case of a gene fusion event, splicing. Experimental and computational validation suggest that many individuals carry more than 50 rare variants that affect transcription in some way. Although most variants were predicted to not affect an individual's phenotype, a small percentage showed likely disease-related associations, emphasizing the importance of studying the impact of rare genetic variation on the transcriptome. —LMZ

Science, this issue p. 1334

SEISMOLOGY

The great seismic quiet period

Noise from trains, airplanes, industrial processes, and other sources is recorded on seismometers worldwide. Disentangling this noise is important for extracting out natural signals, but the noise can also roughly track population movements. Lecocq *et al.* compiled seismic observations around the world and found a substantial decrease in noise resulting from lockdown measures imposed in response to the coronavirus disease 2019 pandemic (see the Perspective by Denolle and Nissen-Meyer). These observations tightly correspond to when the measures went into effect and offer a way to track aggregate behavior. This quiet period also offers the chance to extract anthropogenic sources of noise from those of natural processes. —BG

Science, this issue p. 1338; see also p. 1299

MICROBIOLOGY

Microbial therapies

The gut microbiota, diverse microorganisms that inhabit our intestines, have an increasingly recognized number of roles in maintaining human health. These roles include maintaining digestive health and also more systemic roles such as brain health. In a Perspective, Wargo discusses the developments in modulating gut microbiota to treat patients with various diseases, including irritable bowel disease, metabolic syndrome, autism, and cancer. Treatment can be achieved by fecal microbiota transplantation from healthy donors or by using distinct bacterial communities that are associated with overall health. The advances and challenges of this exciting approach to health are discussed. —GKA

Science, this issue p. 1302

Published by AAAS

FERROELECTRICS

Switching to the atomic scale

Ferroelectric materials are attractive because they provide a way to change electrical resistance by using an electric field. Lee *et al.* used simulations to explain the persistence of ferroelectric behavior in very thin films of hafnium oxide (see the Perspective by Noheda and Íñiguez). The authors' calculations show that ferroelectric properties should be found in films below 1 nanometer thick. This makes the material very attractive for the next generation of random access memory. —BG

Science, this issue p. 1343; see also p. 1300

ULTRACOLD PHYSICS

Laser cooling of symmetric top molecule

Experimental progress over the past few decades has led to the mastery of ultracold atomic gases. A major thrust of current research is to extend this success to ultracold molecules, which would open qualitatively new perspectives for quantum information science, precision measurement, quantum chemistry, and other fields. The internal degrees of freedom in molecules preclude immediate implementation of conventional methods. Using a specific combination of rovibronic optical transitions, Mitra *et al.* report direct Sisyphus laser cooling of the symmetric top molecule $CaOCH_3$ to temperatures below 1 millikelvin (see the Perpsective by Hudson). The proposed scheme for cooling is potentially applicable to a wide range of nonlinear polyatomic molecules. —YS

Science, this issue p. 1366; see also p. 1304

COLLOIDS

Self-limiting bonding

Although many routes have been developed to link together colloidal particles into controlled superstructures from dimers all the way up to three-dimensional lattices, they generally depend on coating the nanoparticle surfaces in specific ways to control the way they link up. By contrast, Yi *et al*. developed a ligand chemistry such that, when two particles link together, it changes the electrostatic properties to limit subsequent bonding (see the Perspective by Gang). Particles are coated with complementary polymer strands that undergo an acid-base neutralization reaction. This bonding is controlled by the length of the flexible ligands, whereas the arrangement of the bonded particles is controlled by electrostatic repulsions, thus giving two parameters to tune the shape of the assemblies that form. —MSL

Science, this issue p. 1369; see also p. 1305

ATMOSPHERIC AEROSOLS

A multiphasic effect

Aerosols exert a primary influence on atmospheric chemistry. One of the main controls on their internal chemistry is their acidity, so understanding what determines aerosol pH is fundamental for determining their environmental effects. Zheng *et al*. considered how buffering capacity in a multiphase aerosol system differs from bulk solution and found an important role for water content in determining pH in ammonia-buffered regions. Their conclusions underscore the important influence of ammonia emissions in the Anthropocene. —HJS

Science, this issue p. 1374

CORONAVIRUS

A gateway to the cytosol

Coronaviruses transform host cell membranes into peculiar double-membrane vesicles that have long been thought to accommodate viral genome replication. However, because these compartments appeared to be completely sealed, it has remained unknown how the newly made viral RNA could be exported to the cytosol for translation and packaging into new virions. Wolff *et al*. used cryo–electron microscopy to identify a molecular pore that spans the double membrane (see the Perspective by Unchwaniwala and Ahlquist). Six copies of a large coronavirus transmembrane protein formed the core of this structure, which may constitute a viral RNA export channel and provide a target for future antiviral interventions. —SMH

Science, this issue p. 1395; see also p. 1306

IMMUNE DEVELOPMENT

To each their own

The recombination activating genes *Rag1* and *Rag2* play central roles in assembling functional T and B cell receptors in developing lymphocytes. Expression of *Rag1* and *Rag2* in hematopoiesis is restricted to these two lymphoid lineages, but precisely how this is accomplished has remained a mystery. Miyazaki *et al*. identified three key enhancer elements that recruit the transcription factor E2A to promote the expression of *Rag1* and *Rag2* during lymphocyte development. By generating mouse strains lacking one or more of these enhancer elements, they report that T and B cells use distinct enhancer modules to activate and maintain expression of *Rag1* and *Rag2*. —CNF

Sci. Immunol. **5**, eabb1455 (2020).

HEALTH AND MEDICINE

3D printed composites for cartilage repair

Damage to cartilage of the joints is a common debilitating injury. However, because of its limited capacity for self-repair, regeneration of damaged cartilage has thus far remained beyond reach. Sun *et al.* created a composite that recreates key elements of the native structure of articular cartilage by three-dimensionally printing structural elements and cells together in a gradient manner. When tested in rabbits, the composite showed high levels of cartilage maturation as well as evidence of lubrication at the joint surface, which is essential to maintaining functionality of the joint. Further assessment of these materials in larger animal models is needed, but such gradient composites may provide a basis for future tissue-engineered cartilage replacements. —JST

Sci. Adv. 10.1126/sciadv.aay1422 (2020).

Published by AAAS

REPORT

SEISMOLOGY

Global quieting of high-frequency seismic noise due to COVID-19 pandemic lockdown measures

Thomas Lecocq[1]*, Stephen P. Hicks[2], Koen Van Noten[1], Kasper van Wijk[3], Paula Koelemeijer[4], Raphael S. M. De Plaen[5], Frédérick Massin[6], Gregor Hillers[7], Robert E. Anthony[8], Maria-Theresia Apoloner[9], Mario Arroyo-Solórzano[10], Jelle D. Assink[11], Pinar Büyükakpınar[12,13], Andrea Cannata[14,15], Flavio Cannavo[15], Sebastian Carrasco[16], Corentin Caudron[17], Esteban J. Chaves[18], David G. Cornwell[19], David Craig[20], Olivier F. C. den Ouden[11,21], Jordi Diaz[22], Stefanie Donner[23], Christos P. Evangelidis[24], Läslo Evers[11,21], Benoit Fauville[25], Gonzalo A. Fernandez[26], Dimitrios Giannopoulos[27,28], Steven J. Gibbons[29], Társilo Girona[30], Bogdan Grecu[31], Marc Grunberg[32], György Hetényi[33], Anna Horleston[34], Adolfo Inza[35], Jessica C. E. Irving[34,36], Mohammadreza Jamalreyhani[37,13], Alan Kafka[38], Mathijs R. Koymans[11,21], Celeste R. Labedz[39], Eric Larose[17], Nathaniel J. Lindsey[40], Mika McKinnon[41,42], Tobias Megies[43], Meghan S. Miller[44], William Minarik[45,46], Louis Moresi[44], Víctor H. Márquez-Ramírez[5], Martin Möllhoff[20], Ian M. Nesbitt[47,48], Shankho Niyogi[49], Javier Ojeda[50], Adrien Oth[51], Simon Proud[52], Jay Pulli[53,38], Lise Retailleau[54,55], Annukka E. Rintamäki[7], Claudio Satriano[54], Martha K. Savage[56], Shahar Shani-Kadmiel[21], Reinoud Sleeman[11], Efthimios Sokos[57], Klaus Stammler[23], Alexander E. Stott[58], Shiba Subedi[33], Mathilde B. Sørensen[59], Taka'aki Taira[60], Mar Tapia[61], Fatih Turhan[12], Ben van der Pluijm[62], Mark Vanstone[63], Jerome Vergne[64], Tommi A. T. Vuorinen[7], Tristram Warren[65], Joachim Wassermann[43], Han Xiao[66]

Human activity causes vibrations that propagate into the ground as high-frequency seismic waves. Measures to mitigate the coronavirus disease 2019 (COVID-19) pandemic caused widespread changes in human activity, leading to a months-long reduction in seismic noise of up to 50%. The 2020 seismic noise quiet period is the longest and most prominent global anthropogenic seismic noise reduction on record. Although the reduction is strongest at surface seismometers in populated areas, this seismic quiescence extends for many kilometers radially and hundreds of meters in depth. This quiet period provides an opportunity to detect subtle signals from subsurface seismic sources that would have been concealed in noisier times and to benchmark sources of anthropogenic noise. A strong correlation between seismic noise and independent measurements of human mobility suggests that seismology provides an absolute, real-time estimate of human activities.

Seismometers record signals from more than just earthquakes: Interactions between the solid Earth and fluid bodies, such as ocean swell and atmospheric pressure (*1*, *2*), are now commonly used to image and monitor the subsurface (*3*). Human activity is a third source of seismic signal. Nuclear explosions and fluid injection or extraction result in impulsive signals, but everyday human activity is recorded as a near-continuous signal, especially on seismometers in urban environments. These complicated signals are the superposition of a wide variety of activities happening at different times and places at or near Earth's surface but are typically stronger during the day than at night, weaker on weekends than weekdays, and stronger near population centers than sparsely inhabited areas (*4*–*7*). Seismometers in urban environments are important to maximize the spatial coverage of seismic networks and to warn of local geologic hazards (*8*), even though anthropogenic seismic noise degrades their capability to detect transient signals associated with earthquakes and volcanic eruptions. Therefore, it is vital to understand urban seismic sources, but studies have been limited to confined areas or distinct events, such as road traffic (*9*, *10*), public transport (*7*, *11*), and "football quakes" (*11*, *12*). Broad analysis of the long-term global anthropogenic seismic wavefield has been lacking. The impact of large, coherent changes in human behavior on seismic noise is unknown, as is how far it propagates and whether seismic recordings offer a coarse proxy for monitoring human activity patterns. Answering these questions has proven challenging because datasets are large, monitoring networks are heterogeneous, and the many possible noise sources likely vary spatially and overlap in time (*13*).

The coronavirus disease 2019 (COVID-19) outbreak was declared a global health emergency in January 2020 (*14*) and a pandemic in March 2020 by the World Health Organization. The outbreak resulted in emergency measures to reduce the basic reproduction rate of the virus (*15*), beginning in China and Italy and then followed by most countries. These measures disrupted social and economic behavior (*16*), industrial production (*17*), and tourism (*18*). In this paper, we use the term "lockdown" to

[1]Seismology-Gravimetry, Royal Observatory of Belgium, Brussels, Belgium. [2]Department of Earth Science and Engineering, Imperial College London, London, UK. [3]Department of Physics, University of Auckland, New Zealand. [4]Department of Earth Sciences, Royal Holloway University of London, Egham, UK. [5]Centro de Geociencias, Universidad Nacional Autónoma de México, Campus Juriquilla, Querétaro, Mexico. [6]Swiss Seismological Service, ETH Zurich, Zurich, Switzerland. [7]Institute of Seismology, University of Helsinki, Helsinki, Finland. [8]Albuquerque Seismological Laboratory, U.S. Geological Survey, Albuquerque, NM, USA. [9]Zentralanstalt für Meteorologie und Geodynamik (ZAMG), Vienna, Austria. [10]Escuela Centroamericana de Geología, Universidad de Costa Rica, San José, Costa Rica. [11]R&D Seismology and Acoustics, Royal Netherlands Meteorological Institute (KNMI), De Bilt, Netherlands. [12]Kandilli Observatory and Earthquake Research Institute, Boğaziçi University, Istanbul, Turkey. [13]GFZ German Research Centre for Geosciences, Potsdam, Germany. [14]Dipartimento di Scienze Biologiche, Geologiche e Ambientali, Università Degli Studi di Catania, Catania, Italy. [15]Istituto Nazionale di Geofisica e Vulcanologia, Osservatorio Etneo, Catania, Italy. [16]Bensberg Observatory, University of Cologne, Cologne, Germany. [17]Université. Grenoble Alpes, Université Savoie Mont Blanc, CNRS, IRD, IFSTTAR, ISTerre, Grenoble, France. [18]Volcanological and Seismological Observatory of Costa Rica at Universidad Nacional (OVSICORI-UNA), Heredia, Costa Rica. [19]Department of Geology and Geophysics, School of Geosciences, University of Aberdeen, King's College, Aberdeen, UK. [20]Dublin Institute for Advanced Studies, Geophysics Section, Dublin, Ireland. [21]Department of Geoscience and Engineering, Delft University of Technology, Delft, Netherlands. [22]Geosciences Barcelona, CSIC, Barcelona, Spain. [23]Federal Institute for Geosciences and Natural Resources (BGR), Hannover, Germany. [24]Institute of Geodynamics, National Observatory of Athens, Athens, Greece. [25]Noise Department, Brussels Environment, Brussels-Capital Region, Belgium. [26]Observatorio San Calixto, La Paz, Bolivia. [27]Seismotech S.A., Athens, Greece. [28]Laboratory of Geophysics & Seismology, Department of Environmental & Natural Resources Engineering, Hellenic Mediterranean University, Chania, Greece. [29]Norges Geotekniske Institutt, Oslo, Norway. [30]Geophysical Institute, University of Alaska Fairbanks, Fairbanks, AK, USA. [31]National Institute for Earth Physics, Magurele, Romania. [32]Réseau National de Surveillance Sismique (RENASS), Université de Strasbourg, CNRS, EOST UMS830, Strasbourg, France. [33]Institute of Earth Sciences, Faculty of Geosciences and Environment, University of Lausanne, Lausanne, Switzerland. [34]School of Earth Sciences, University of Bristol, Queen's Road, Bristol, UK. [35]Instituto Geofisico del Peru, Lima, Peru. [36]Department of Geosciences, Princeton University, Princeton, NJ, USA. [37]Institute of Geophysics, University of Tehran, Tehran, Iran. [38]Weston Observatory, Department of Earth and Environmental Sciences, Boston College, Weston, MA, USA. [39]Seismological Laboratory, California Institute of Technology, Pasadena, CA, USA. [40]Geophysics Department, Stanford University, Stanford, CA, USA. [41]SETI Institute, Mountain View, CA, USA. [42]Faculty of Science, Department of Earth, Ocean and Atmospheric Sciences, University of British Columbia, Vancouver, BC, Canada. [43]Ludwig-Maximilians-Universität München, Munich, Germany. [44]Research School of Earth Sciences, Australian National University, Canberra, ACT, Australia. [45]Department of Earth and Planetary Sciences, McGill University, Montréal, QC, Canada. [46]GEOTOP Research Centre, Montréal, QC, Canada. [47]Raspberry Shake, S.A., Boquete, Chiriqui, Panama. [48]Department of Earth and Climate Science, University of Maine, Orono, ME, USA. [49]University of California, Riverside, CA, USA. [50]Departamento de Geofísica, Universidad de Chile, Santiago, Chile. [51]European Center for Geodynamics and Seismology, Walferdange, Grand Duchy of Luxembourg. [52]National Centre for Earth Observation, Department of Physics, University of Oxford, Oxford, UK. [53]Raytheon BBN Technologies, Arlington, VA, USA. [54]Université de Paris, Institut de Physique du Globe de Paris, Paris, France. [55]Observatoire Volcanologique du Piton de la Fournaise, Institut de Physique du Globe de Paris, La Plaine des Cafres, France. [56]School of Geography, Environment and Earth Sciences, Victoria University of Wellington, Wellington, New Zealand. [57]Department of Geology, University of Patras, Patras, Greece. [58]Department of Electrical and Electronic Engineering, Imperial College London, South Kensington Campus, London, UK. [59]Department of Earth Science, University of Bergen, Bergen, Norway. [60]Berkeley Seismological Laboratory, University of California Berkeley, Berkeley, CA, USA. [61]Laboratori d'Estudis Geofísics Eduard Fontserè, Institut d'Estudis Catalans (LEGEF-IEC), Barcelona, Spain. [62]Department of Earth and Environmental Sciences, University of Michigan, Ann Arbor, MI, USA. [63]Geology Department, Truro School, Truro, Cornwall, UK. [64]Institut de Physique du Globe de Strasbourg, UMR 7516, Université de Strasbourg/EOST, CNRS, Strasbourg, France. [65]Department of Physics, University of Oxford, Oxford, UK. [66]Department of Earth Science and Earth Research Institute, University of California, Santa Barbara, CA, USA.
*Corresponding author. Email: thomas.lecocq@seismology.be

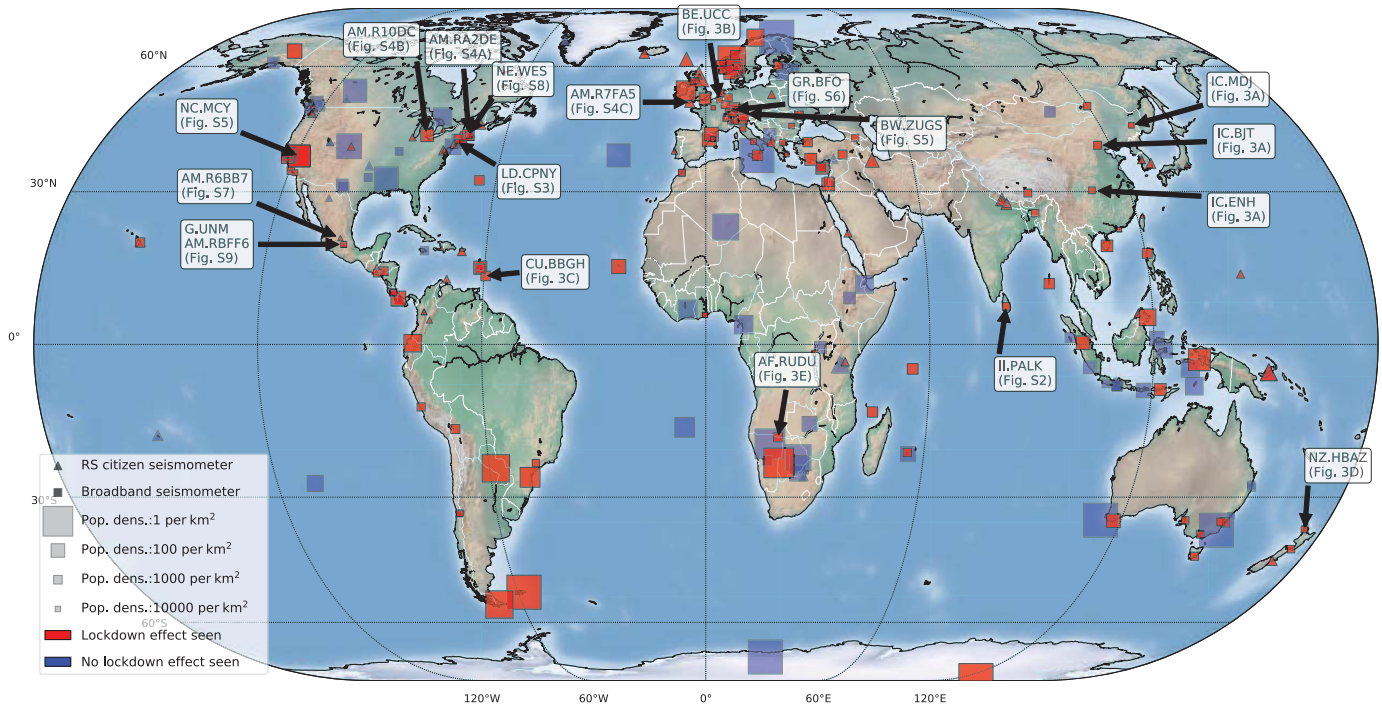

Fig. 1. Locations of analyzed seismic stations throughout the world. The map shows locations of the 268 global seismic stations with usable data (e.g., no long data gaps, working sensors) that we analyzed. Lockdown effects were observed (red) at 185 of 268 stations. Symbol size is scaled by the inverse of population density (*30*) to emphasize stations located in remote areas. The labeled stations are discussed in detail in the text.

broadly encompass many types of emergency measures, such as full quarantine [e.g., in Wuhan, China (*19*–*21*)], enforced physical distancing (e.g., in Italy and the United Kingdom), travel restrictions (*22*), widespread closure of services and industry, and any other emergency measures. These major changes to daily life provide an opportunity to study their environmental impacts, such as reductions in nitrous oxide emissions in the atmosphere (*23*). Recordings of human-generated seismic vibrations that travel through the solid Earth provide insights into the dynamics of pandemic lockdowns.

We assessed the effects of COVID-19 lockdowns on high-frequency (4 to 14 Hz) seismic ambient noise (hiFSAN) (*24*). We compiled a global seismic noise dataset using vertical-component seismic waveform data from 337 broadband and individually operated citizen seismometer stations (*24*), such as Raspberry Shake instruments (RSs), with a self-noise well below the ground motion generated by anthropogenic noise (*25*) and flat responses in the target frequency band (Fig. 1). We obtained usable data (e.g., no large data gaps, working sensors) from 268 stations and detected pronounced reductions in hiFSAN during local lockdown measures at 185 stations (Fig. 2). Periods that are often seismically quiet include weekends, as well as the Christmas and New Year holidays for locations where they are celebrated. Notably, we found a near-global reduction in noise, commencing in China in late January 2020 (*26*), followed by Italy (*26*, *27*), the whole of Europe, and the rest of the world in March to April 2020. This period of reduced noise lasted longer and was often quieter than the Christmas–to–New Year period.

In China (Fig. 3A), the COVID-19 outbreak and subsequent emergency measures occurred during the Chinese New Year (CNY). In Enshi, a city located in Hubei province where the outbreak began (*28*), hiFSAN in 2020 clearly diverged from the normal annual reduction during CNY. The hiFSAN level remained at a minimum, demarcated by the start and end of quarantine in Hubei, for several weeks after CNY. Although the quarantine measures in Beijing were less strict, local hiFSAN reductions were more pronounced and lasted longer than in recent years. As of the end date of our analysis, Beijing has still not reached the average hiFSAN level of previous years, which suggests that the impact of COVID-19 is continuing to restrict anthropogenic noise there. We noticed a later hiFSAN lockdown reduction in April 2020 in Heilongjiang (Fig. 3A), in northeast China, near the Russian border.

Although we observed seismic effects of lockdown in areas with low population density estimates (<1 person per km^2; Fig. 1), the strongest hiFSAN reduction occurred in populated environments. For a permanent seismic station in Sri Lanka, a 50% reduction in hiFSAN occurred after lockdown, which is the strongest we observed in the available data from that station since at least July 2013 (fig. S2). In Central Park, New York, on Sunday nights, hiFSAN was 10% lower during the lockdown than before this period (fig. S3).

Seismic networks in populated areas enable us to correlate hiFSAN with other human activity measurements, such as audible recordings and flight data (*24*). At a surface station in Brussels, Belgium (Fig. 3B), we found a 33% reduction in hiFSAN after lockdown. We compared this noise level with data from a nearby microphone, located close to a major road, that mainly records audible traffic noise. We found a high correlation between prelockdown hiFSAN and audible noise, both showing characteristic diurnal and weekly changes. However, during lockdown, audible noise reductions were more pronounced, which suggests that seismometers are sensitive to a wide distribution of seismic sources, not just nearby traffic. Audible and hiFSAN levels then gradually increased after April 2020. Independent mobility data (*24*) provide insights into what caused these changes. Mobility correlates with hiFSAN at lockdown, with correlation coefficients >0.8 (*24*), except for time spent at places of residence (Google's "residential" category), which is expected given the increased number of people spending more time at home because of government restrictions.

Citizen seismometers provide a different urban ground motion dataset, with denser coverage in some places. Large hiFSAN drops

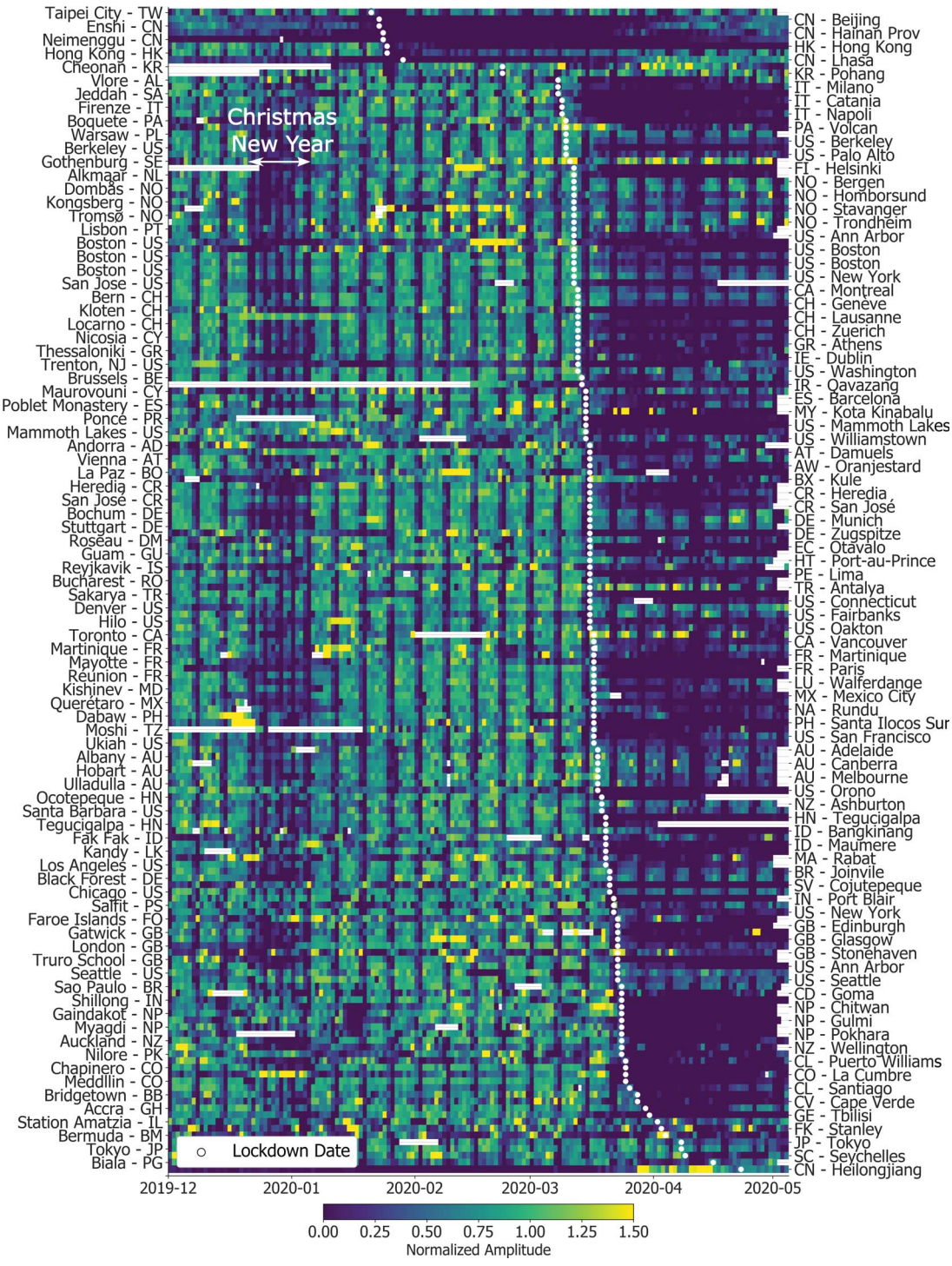

Fig. 2. Global temporal changes in seismic noise. Global daily median hiFSAN is depicted (*24*), normalized to percentage variation of the baseline before lockdown measures and sorted by lockdown date. Each line of the image corresponds to one seismic station. Data gaps are shown in white. Location and country code are indicated for each station; see fig. S1 for network and station codes.

occurred particularly at schools and universities after lockdown-related closures [e.g., in Boston and Michigan (United States) and Cornwall (United Kingdom); fig. S4]. The hiFSAN level was even 20% lower than during school holidays, which indicates sensitivity to the environment outside of the school.

The pandemic has also affected tourism—for example, during the holiday season in the Caribbean. In Barbados (Fig. 3C), hiFSAN decreased by ~45% after lockdown on 28 March 2020 through April 2020 and stayed ~50% below levels observed in previous years for the same period. However, seismic noise levels began to decrease 1 to 2 weeks before a local curfew was implemented. Local flight data (*24*) indicate that travel to Barbados started decreasing after 21 March 2020, and the overall reduction in hiFSAN might have been partly due to tourists repatriating. We also observed noise reductions due to decreased tourist activity at ski resorts in Europe (Zugspitze in Germany) and the United States (Mammoth Mountain in California) (fig. S5).

Although we observed lockdown effects most prominently at surface stations, we also detected them underground. In New Zealand, seismometers installed in boreholes (to minimize the effects of anthropogenic noise) monitor potential hazards associated with the Auckland

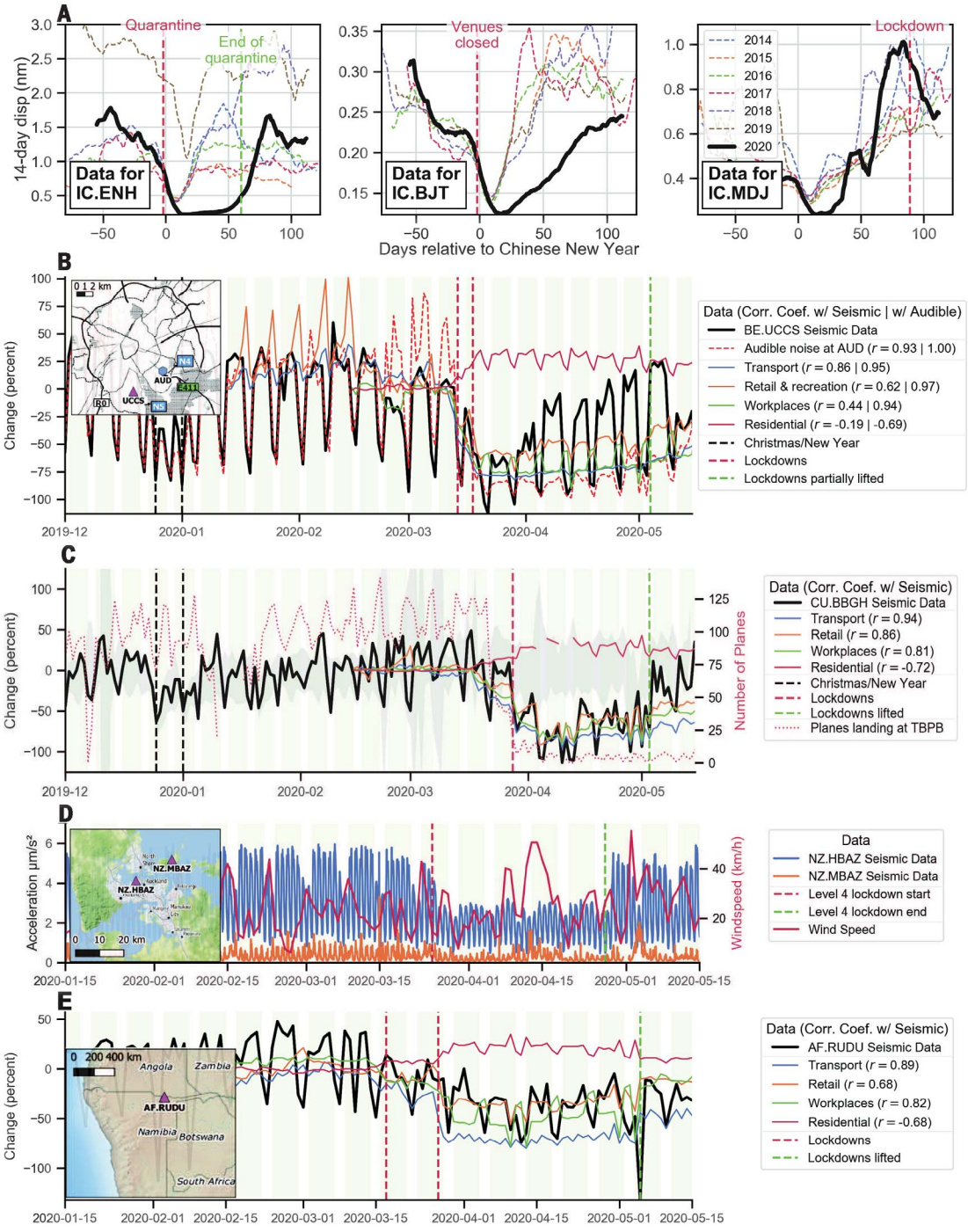

Fig. 3. Regional examples of the 2020 seismic noise quiet period. The examples show different features of the lockdown seismic signal changes in regional settings. We filtered the hiFSAN data between 4 and 14 Hz and present temporal changes as displacement (A), acceleration (D), or percentage change relative to the baseline before lockdown [(B), (C), and (E)], with the panels in (A) also relative to the baseline of corresponding time periods in previous years. Individual seismic stations are identified by codes in "network. station" format (IC.ENH, BE.UCCS, etc.). The keys in (B) to (E) include correlation coefficients (*r*) with mobility data (*24*). (**A**) Lockdown effects at three stations in China compared with the Chinese New Year holiday in previous years. (**B**) Lockdown effects on hiFSAN compared with audible environmental noise and independent mobility data in Brussels, Belgium. (**C**) Lockdown effect in Barbados compared with noise levels of the past decade (gray shading) and correlation with local flight data at the Grantley Adams International Airport (TBPB) (*24*). (**D**) Lockdown noise reduction recorded on borehole seismometers in Auckland, New Zealand. (**E**) Lockdown noise reduction in a region of low population density in Rundu, Namibia.

Volcanic Field (*6*, *8*, *29*). Station HBAZ is 380 m below the city, whereas MBAZ is at 98 m of depth, 14 km from the city center on the uninhabited Motutapu Island (Fig. 3D). The hiFSAN level at both stations varied between weekdays and weekends before the lockdown, which suggests that both are sensitive to anthropogenic activity. Although the island station is quieter overall, the lockdown instigated a reduction in hiFSAN by a factor of 2 for both stations. We attribute the remaining hiFSAN maxima on the island (mid-April 2020 and early May 2020) to strong winds and high waves. On 27 April 2020, New Zealand lifted restrictions, with hiFSAN increasing to the prelockdown levels.

The reduction of hiFSAN was weaker in less populated areas such as Rundu, located along the Namibia-Angola border (Fig. 3E). After COVID-19 was confirmed in Namibia, an emergency was declared on 17 March 2020 to restrict mobility, followed by full lockdown on 27 March 2020. These measures are reflected in the >25% hiFSAN reduction compared with prelockdown levels. Despite Rundu having a population roughly one-eighth and one-fifth as dense as those of Brussels and Auckland, respectively (*30*), we observed a similarly high correlation between seismic and mobility data. The Black Forest Observatory in Germany is an even more remote station, located 150 to 170 m below the surface in crystalline bedrock. Although this station is considered a reference

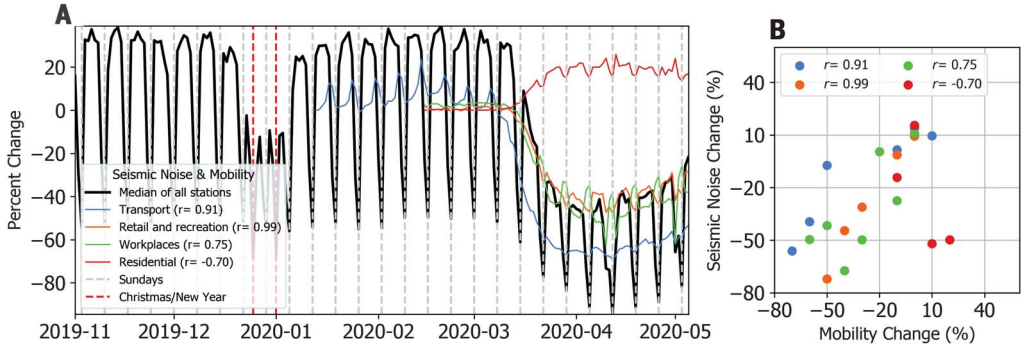

Fig. 4. Global changes in seismic noise compared with population mobility trends. (**A**) Comparison between temporal changes in global daily median hiFSAN based on data from the 185 stations that observed lockdown effects and population mobility changes (*24*). (**B**) Scatter plot to illustrate the correlation between the binned (10% bins) time series of seismic noise changes and all categories of mobility data in (A). Percentage changes are expressed relative to a prelockdown baseline. All categories show a strong positive correlation, apart from time spent in residential premises, which is anticorrelated.

laboratory with low noise overall (*31*), we detected a small hiFSAN reduction during lockdown nights (fig. S6), corresponding to the lowest hiFSAN since at least 25 December 2015.

Here we have provided a global-scale analysis of high-frequency anthropogenic seismic noise. Global median hiFSAN dropped by as much as 50% during March to May 2020 (Fig. 4). The length and quiescence of this period represent the longest and most coherent global seismic noise reduction in recorded history, emphasizing how human activities affect the solid Earth. A globally high correlation exists between changes in hiFSAN and population mobility (*24*), with correlations exceeding 0.9 for many categories.

This distinct low-noise period will help optimize seismic monitoring efforts (*4*). The ability to analyze the full spectrum of seismogenic behavior, including the smallest earthquakes, is essential for monitoring fault dynamics over seismic cycles, as well as for earthquake forecasting and seismic hazard assessment. Small earthquakes should dominate datasets (*32*), but typical operational catalogs using amplitude-based detection do not include many of the smallest earthquakes (*33*). This detection issue is especially problematic in populated areas, where anthropogenic noise energy interferes with earthquake signals. This problem is exemplified by recordings of a moment magnitude 5.0 earthquake at 15 km of depth southwest of Petatlan, Mexico, during lockdown (fig. S7). An earthquake with this magnitude and source mechanism that occurs during the daytime would typically be observed at stations in urban environments only if the signal was filtered. However, the reduction of seismic noise by ~40% during lockdown made this event visible, without any filtering required, at a RS station in Querétaro city, 380 km away. Low noise levels during COVID-19 lockdowns could thus allow detection of signals from previously unrecognized sources in areas with incomplete seismic catalogs. Such newly identified signals could be used as distinct templates (*32*) for finding similar waveforms in noisier data before and after lockdown. This approach also works for tremor signals that are masked by anthropogenic noise yet vital for monitoring potential volcanic unrest (*6*). Although broadband sensors in rural environments are less affected by anthropogenic noise, any densification of and reliance on low-cost sensors in urban areas, such as RSs and low-cost accelerometers (*34*), will require a better understanding of anthropogenic noise sources to suppress false detections. As populations increase globally, more people become exposed to potential natural and induced geohazards (*35*). Urbanization will increase anthropogenic noise in exposed areas, further complicating seismic monitoring efforts. The ability to characterize and minimize anthropogenic noise is becoming increasingly important for accurate detection and imaging of seismic signatures of potentially harmful subsurface hazards.

Anthropogenic seismic noise is thought to be dominated by noise sources <1 km away from detectors (*5*–*7*, *11*, *36*). Because population mobility generates time-varying loads that radiate energy through the shallow subsurface as Rayleigh waves (*11*), local effects such as construction sites and heavy machinery can affect individual stations. However, the 2020 seismic noise quiet period reveals that when considering multiple stations or whole networks over longer time scales, the anthropogenic seismic wavefield affects large areas. With denser networks and more citizen sensors in urban environments, additional features of the seismic noise, rather than just amplitude, will become usable and will help identify different anthropogenic noise sources (*10*, *37*). Characterizing these sources will be useful for imaging the shallow subsurface in three dimensions in urban areas by using high-frequency anthropogenic ambient noise (*38*, *39*). Our finding of a distributed noise field is supported by strong correlations with independent mobility data (Fig. 4). In contrast to mobility data, publicly available data from existing seismometer networks provide an objective absolute baseline of human activity levels. Therefore, hiFSAN can serve as a near–real-time technique for monitoring anthropogenic activity patterns, with fewer potential privacy concerns than those raised by mobility data collection. In addition, although industrial activities may not be captured in mobility data, they may produce a seismic noise signature. The 2020 seismic quiet period is a baseline for using seismic properties (*36*) to identify and isolate the sources contributing to the anthropogenic noise wavefield, especially when combined with data indicative of human behavior. Seismic observations of human activity during COVID-19 lockdowns have enabled us to assess the impact of mitigation policies—particularly the time to establish and recover from lockdowns—on daily life. As such, hiFSAN may provide important constraints for future health and behavioral science studies.

REFERENCES AND NOTES

1. J. N. Brune, J. Oliver, *Bull. Seismol. Soc. Am.* **49**, 349–353 (1959).
2. R. K. Cessaro, *Bull. Seismol. Soc. Am.* **84**, 142–148 (1994).
3. N. M. Shapiro, M. Campillo, *Geophys. Res. Lett.* **31**, L07614 (2004).
4. D. E. McNamara, R. P. Buland, *Bull. Seismol. Soc. Am.* **94**, 1517–1527 (2004).
5. J. C. Groos, J. R. Ritter, *Geophys. J. Int.* **179**, 1213–1231 (2009).
6. C. M. Boese, L. Wotherspoon, M. Alvarez, P. Malin, *Bull. Seismol. Soc. Am.* **105**, 285–299 (2015).
7. D. N. Green, I. D. Bastow, B. Dashwood, S. E. Nippress, *Seismol. Res. Lett.* **88**, 113–124 (2017).
8. C. L. Ashenden *et al.*, *Nat. Hazards* **59**, 507–528 (2011).
9. N. Riahi, P. Gerstoft, *Geophys. Res. Lett.* **42**, 2674–2681 (2015).
10. N. J. Lindsey *et al.*, *Geophys. Res. Lett.* **47**, e2020GL089931 (2020).
11. J. Díaz, M. Ruiz, P. S. Sánchez-Pastor, P. Romero, *Sci. Rep.* **7**, 15296 (2017).
12. P. Denton, S. Fishwick, V. Lane, D. Daly, *Seismol. Res. Lett.* **89**, 1902–1907 (2018).
13. D. Wilson *et al.*, *Bull. Seismol. Soc. Am.* **92**, 3335–3342 (2002).
14. C. Sohrabi *et al.*, *Int. J. Surg.* **76**, 71–76 (2020).
15. R. M. Anderson, H. Heesterbeek, D. Klinkenberg, T. D. Hollingsworth, *Lancet* **395**, 931–934 (2020).
16. M. Nicola *et al.*, *Int. J. Surg.* **77**, 206–216 (2020).
17. T. Laing, *Extr. Ind. Soc.* **7**, 580–582 (2020).
18. A. Hoque, F. A. Shikha, M. W. Hasanat, I. Arif, A. B. A. Hamid, *Asian J. Multidiscip. Stud.* **3**, 52–58 (2020).
19. M. U. G. Kraemer *et al.*, *Science* **368**, 493–497 (2020).
20. H. Tian *et al.*, *Science* **368**, 638–642 (2020).
21. J. Zhang *et al.*, *Science* **368**, 1481–1486 (2020).
22. M. Chinazzi *et al.*, *Science* **368**, 395–400 (2020).
23. M. Bauwens *et al.*, *Geophys. Res. Lett.* **47**, 11 (2020).
24. Materials and methods and network citations are available as supplementary materials.

25. R. E. Anthony, A. T. Ringler, D. C. Wilson, E. Wolin, . *Seismol. Res. Lett.* **90**, 219–228 (2019).
26. H. Xiao, Z. C. Eilon, C. Ji, T. Tanimoto, *Sesimol. Res. Lett.* 10.1785/0220200147 (2020).
27. P. Poli, J. Boaga, I. Molinari, V. Cascone, L. Boschi, *Sci. Rep.* **10**, 9404 (2020).
28. H. Lau *et al*., *J. Travel Med.* **27**, taaa037 (2020).
29. S. Sherburn, B. J. Scott, J. Olsen, C. Miller, *N. Z. J. Geol. Geophys.* **50**, 1–11 (2007).
30. Center for International Earth Science Information Network CIESIN Columbia University, Gridded population of the world, version 4 (GPWv4): Population density. Revision 11, accessed 2 June 2020 (2018); https://doi.org/10.7927/H49C6VHW.
31. W. Zürn *et al*., *Geophys. J. Int.* **171**, 780–796 (2007).
32. B. Gutenberg, C. F. Richter, *Bull. Seismol. Soc. Am.* **34**, 185–188 (1944).
33. Z. E. Ross, D. T. Trugman, E. Hauksson, P. M. Shearer, *Science* **364**, 767–771 (2019).
34. E. S. Cochran, *Nat. Commun.* **9**, 2508 (2018).
35. G. J. H. McCall, *Geol. Soc. London Eng. Geol. Spec. Publ.* **15**, 309–318 (1998).
36. M. Lehujeur, J. Vergne, J. Schmittbuhl, A. Maggi, *Geotherm. Energy* **3**, 3 (2015).
37. G. Hillers, M. Campillo, Y.-Y. Lin, K.-F. Ma, P. Roux, *J. Geophys. Res.* **117**, B06301 (2012).
38. M. Picozzi, S. Parolai, D. Bindi, A. Strollo, *Geophys. J. Int.* **176**, 164–174 (2009).
39. F. Brenguier *et al*., *Geophys. Res. Lett.* **46**, 9529–9536 (2019).
40. T. Lecocq *et al*., ThomasLecocq/2020_Science_GlobalQuieting: First Release - v1.0, Zenodo (2020); https://doi.org/10.5281/zenodo.3944739.

ACKNOWLEDGMENTS

We sincerely thank two anonymous reviewers, T. Nissen-Meyer, and J. Slate for their comments, which have improved the manuscript. We are extremely grateful to all seismic network managers, operators, and technicians who have helped facilitate the raw global seismic dataset (*24*). We also kindly acknowledge all of the passionate community seismologists for running their "home" seismometers and contributing, indirectly, to a better understanding of Earth. Any use of trade, firm, or product names is for descriptive purposes only and does not imply endorsement by the U.S. government. We dedicate this community-led study to all essential workers who have kept our countries going during these difficult times. **Funding:** P.K. was funded by a Royal Society University Research Fellowship (URF\R1\180377). P.B. and M.J. acknowledge support from the International Training Course "Seismology and Seismic Hazard Assessment" funded by the GeoForschungsZentrum Potsdam (GFZ) and the German Federal Foreign Office through the German Humanitarian Assistance program (grant S08-60 321.50 ALL 03/19). P.B. also acknowledges financial support from the Boğaziçi University Research Fund (BAP 15683). O.F.C.d.O acknowledges funding from a Young Investigator Grant from the Human Frontier Science Program (HFSP project RGY0072/2017). C.P.E. and E.S. acknowledge funding from the HELPOS Project "Hellenic Plate Observing System" (MIS 5002697). L.E. and S.S.-K. acknowledge funding from a VIDI project from the Dutch Research Council (NWO project 864.14.005). G.A.F. acknowledges contributions from the Observatorio San Calixto, which is supported by the Air Force Technical Application Center (AFTAC). C.R.L. acknowledges funding from the NSF Graduate Research Fellowship Program (grant DGE-1745301). V.-H.M. and R.D.P. acknowledge support from grant CONACYT-299766. R.D.P. acknowledges support from the UNAM-DGAPA postdoctoral scholarship. J.O. acknowledges support from the Agencia Nacional de Investigación y Desarrollo (Scholarship ANID-PFCHA/Doctorado Nacional/2020-21200903). S.P. acknowledges financial support from the Natural Environment Research Council (NE/R013144/1). A.E.R. acknowledges support from the K.H. Renlund foundation. M.K.S. acknowledges the New Zealand Earthquake Commission (EQC project 20796). H.X. acknowledges support from a Multidisciplinary Research on the Coronavirus and its Impacts (MRCI) grant from UC Santa Barbara. The Australian Seismometers in Schools data used in this research are supported by AuScope, enabled by the Australian Commonwealth NCRIS program. A.O. acknowledges support from the project RESIST, funded by the Belgian Federal Science Policy (contract SR/00/305) and the Luxembourg National Research Fund. **Author contributions:** T.L. designed and led the research. T.L., S.P.H., K.V.N., K.v.W., P.K., and R.S.M.D.P. processed and visualized the data and drafted the manuscript. F.M. contributed to the software development and provided the supplementary movie. G.H. thoroughly edited and reviewed the manuscript. All authors processed seismic data, took part in discussions, and performed a full interactive review of the original and revised manuscripts. **Competing interests:** The authors declare no competing interests. **Data and materials availability:** The raw data used to compute the hiFSAN were obtained from different networks and data providers (*24*). The computed data and codes used to analyze and plot Figs. 1 to 4 are available from the companion repository: https://github.com/ThomasLecocq/2020_Science_GlobalQuieting and (*40*).

SUPPLEMENTARY MATERIALS

science.sciencemag.org/content/369/6509/1338/suppl/DC1
Materials and Methods
Supplementary Text
Figs. S1 to S9
Tables S1 to S3
References (*41*–*56*)
Movie S1

10 June 2020; accepted 14 July 2020
Published online 23 July 2020
10.1126/science.abd2438

FERROELECTRICS

Scale-free ferroelectricity induced by flat phonon bands in HfO_2

Hyun-Jae Lee[1], Minseong Lee[1], Kyoungjun Lee[2], Jinhyeong Jo[1], Hyemi Yang[1], Yungyeom Kim[1], Seung Chul Chae[2], Umesh Waghmare[3], Jun Hee Lee[1]*

Discovery of robust yet reversibly switchable electric dipoles at reduced dimensions is critical to the advancement of nanoelectronics devices. Energy bands flat in momentum space generate robust localized states that are activated independently of each other. We determined that flat bands exist and induce robust yet independently switchable dipoles that exhibit a distinct ferroelectricity in hafnium dioxide (HfO_2). Flat polar phonon bands in HfO_2 cause extreme localization of electric dipoles within its irreducible half-unit cell widths (~3 angstroms). Contrary to conventional ferroelectrics with spread dipoles, those intrinsically localized dipoles are stable against extrinsic effects such as domain walls, surface exposure, and even miniaturization down to the angstrom scale. Moreover, the subnanometer-scale dipoles are individually switchable without creating any domain-wall energy cost. This offers unexpected opportunities for ultimately dense unit cell–by–unit cell ferroelectric switching devices that are directly integrable into silicon technology.

Ferroelectricity arises from the spontaneous ordering of electric dipoles in a crystal that is reversibly switched to opposite directions under an applied electric field. A ferroelectric oxide, hafnium dioxide (HfO_2), recently emerged as an interesting material because of its robust electric dipoles at nanometer thicknesses and ability to directly integrate into silicon devices (*1*–*3*). The switchability of electric dipoles in HfO_2, a fluorite structure, is expected to be different from that in ABO_3 perovskite-structure oxides (*4*), as hinted by its large coercive field (*5*, *6*) and slow domain propagation (*7*). Unfortunately, the underlying reasons for the stable ferroelectricity and distinct switchability of HfO_2 at an atomic level are poorly understood. The relationship between structure and ferroelectric properties of HfO_2 is crucial for their use in advanced nanoelectronic devices such as nonvolatile memories and low-power logic (*2*).

We show that ferroelectric HfO_2 possesses switchability that is robust even down to irreducible, subnanometer-scale dimensions. This behavior is due to the flat phonon bands intrinsic to the material. Whereas flat bands of electrons, photons, and magnons are known to cause exotic phenomena such as electron lattice (*8*), graphene superconductivity (*9*), and photon (*10*) and magnon localization (*11*), flat bands of polar phonons and their consequences in ferroelectrics are not well understood. The emergence of flat phonon bands in HfO_2 provides a missing link to extend those exotic phenomena to ferroelectrics.

We used first-principles calculations to discover flat bands of polar phonons and consequent localized dipoles, which induce a scale-free ferroelectric order in HfO_2. This order contains a lateral array of vertically aligned polar layers separated by nonpolar spacer layers that are each of half–unit cell width (~2.5 Å). The presence of the spacers in HfO_2 laterally localize the vertical dipoles within its half-unit widths in a steplike manner from one polar layer to the next. Contrary to conventional ferroelectrics, whose spread dipoles fade away below critical nano-dimensions (*4*, *12*–*15*), the localized dipoles, which are stable and switchable down to the subnanometer scale, allow storage of bits in angstrom-size lateral domains without costing any domain-wall formation energy. Vanishingly zero interactions between the ferroelectric dipoles, evidenced by flat bands in HfO_2, explain the unusual phenomena of its large coercive field (*5*, *6*) compared with conventional ferroelectrics (*16*–*21*) and its extremely slow domain propagation (*7*). Because HfO_2 is already integrated into silicon technology, fabrication of ultimately dense memories could be accomplished by exploiting its irreducible unit cell–scale switchability.

To determine the origin of unusual structural features of the orthorhombic phase of HfO_2 ($Pca2_1$), we analyzed the sequence of symmetry-lowering steps starting with the cubic $Fm\bar{3}m$ structure of HfO_2, which is known to be stable above 2870 K (*22*). Upon cooling, it transforms into tetragonal $P4_2/nmc$ phase at 2870 K, and then to monoclinic phase at T = 2000 K. By contrast, the ferroelectric orthorhombic phase is stabilized in thin films at

[1]School of Energy and Chemical Engineering, Ulsan National Institute of Science and Technology (UNIST), Ulsan, 44919, Republic of Korea. [2]Department of Physics Education, Seoul National University, Seoul 08826, Republic of Korea. [3]Theoretical Sciences Unit, Jawaharlal Nehru Centre for Advanced Scientific Research, Jakkur, Bangalore 560064, India.
*Corresponding author. Email: junhee@unist.ac.kr

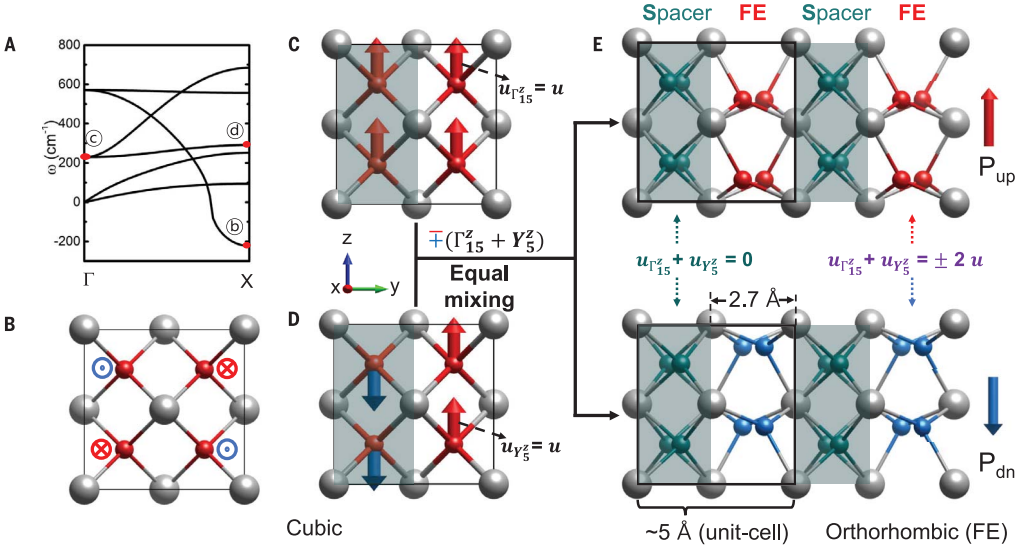

Fig. 1. Structural origin of alternating ferroelectric and nonpolar layers in orthorhombic HfO_2. (**A**) Phonon dispersion of the cubic phase. The red dots labeled b, c, and d denote the primary instability of (**B**) X'_2 mode, (**C**) Γ^z_{15}, and (**D**) Y^z_5, respectively, where arrows denote u, the displacements of oxygen atoms. (**E**) Polar Γ^z_{15} and antipolar Y^z_5 phonons condense in-phase with equal magnitude to generate an orthorhombic structure that consists of alternating spacer layers and ferroelectric layers with up (top), and down (bottom) polarization, respectively. Silver spheres indicate Hf atoms; red and blue spheres indicate oxygen atoms in the ferroelectric layer with up and down polarization, respectively; and green spheres indicate oxygen atoms belonging to the spacer layer.

room temperature (*1*). Phonon spectrum of the high-temperature cubic phase (Fig. 1A) reveals the dominant phonon instability with X'_2 symmetry at $\omega = -i$ 228 cm^{-1}, which involves antiparallel x displacements of neighboring oxygen atoms in the yz plane (Fig. 1B). The cubic structure transforms into a tetragonal structure through the condensation of an X'_2 phonon with zero net polarization. Among the four phonons condensing in the transformation from tetragonal to orthorhombic (fig. S1), we focused on (i) the Γ^z_{15} phonon with all oxygen atoms moving along the z direction (Fig. 1C) generating a uniform polarization and (ii) the cell-doubling antipolar phonon Y^z_5, where oxygen atoms in neighboring xz planes move along the z axis in an antiparallel manner (Fig. 1D), providing A-type ordering with zero net polarization. Similar to strained ZrO_2 (*23*), ferroelectricity of HfO_2 is improperly caused by the nonlinear interaction of stable Γ^z_{15} and X_5 phonons with the primary instability of the X'_2 phonon.

An unusual aspect of the ferroelectric order originates from polar Γ^z_{15} and antipolar Y^z_5 phonons condensing with exactly identical amplitudes, which generate a dipolar partitioning into two types (*24*) of alternating atomically thin layers (Fig. 1E). The first type is the spacer with zero z displacements of oxygen atoms, and the second is the ferroelectric layer with parallel z displacements of its oxygen atoms. Thus, spacers are dead layers that screen the elastic interaction between the ferroelectric active layers. Experimental evidence for these layers can be seen in a study that used transmission electron microscopy and named them as minor and major layers, respectively (*25*). The structural characteristics of the spacer layers is discussed in fig. S2.

Natural dipolar partitioning in orthorhombic HfO_2 has substantial consequences for its polarization domain structure, contrary to that of perovskite ferroelectric $PbTiO_3$. As the local polarization vanishes in the spacer layer even in uniformly polarized HfO_2, it inherently hosts a domain wall of vanishing thickness between oppositely polarized (180°) domains (Fig. 2A). Such a domain wall is essentially strain free (Fig. 2, ε_i, where $i = x, y,$ and z; and fig. S3), with little change in the local structure and supporting unsuppressed bulk polarization in its neighborhood. This should lead us to expect a high energy cost of a sharp domain wall in HfO_2 because of the $g|\vec{\nabla} \times \vec{P}|^2$ term. But $g \sim 0$ is evident in its flat band of polar phonons (Fig. 2B and supplementary text S1) and makes a sharp domain wall feasible. This flatness of the polar bands results in a phonon velocity of nearly zero (Fig. 2D). The origin of the flatness is discussed with a spring model in fig. S4. The Γ point phonon in the flat band of the lowest frequency (Fig. 2B, black line) involves atomic displacements of all the modes condensed during cubic-to-orthorhombic transition, and that of higher frequency (Fig. 2B, red line) involves polar and antipolar modes. Physically, the elastic interaction between ferroelectric domains is screened by the spacer layer. With contribution mostly from dipole-dipole interactions, the domain wall energy of HfO_2 is weakly negative (~–18 mJ/m^2) (supplementary text, section 2). By contrast, a domain wall separating the 180° polar domains in $PbTiO_3$ is diffuse, with a width of a few unit cells, and the polarization is suppressed in its neighborhood (Fig. 2C). This difference is because some of the polar atomic displacements are shared between adjacent domains in $PbTiO_3$. The parameter g is sizable, as evident in its dispersed polar phonons (*26*) and a finite phonon velocity in $PbTiO_3$ (Fig. 2D).

We sought to establish the stability and switchability of a polar domain that is half a unit cell wide, sandwiched between the spacers, by simulating reversal of its local polarization (Fig. 3A and fig. S6). The two-dimensional (2D) layer with flipped polarization has a robust stability, with a large energy barrier of 1.34 eV that prevents it from switching back to the uniformly polarized state (Fig. 3B). The switching of polarization in the adjacent layer (Fig. 3B) results in a domain that consists of two ferroelectric layers sandwiching a spacer, following a path with a comparable energy barrier of 1.38 eV. Low dependence of domain wall energy on the width of polar domains reveals weak inter–domain wall interaction, as expected from the flat bands. By contrast, our simulation of a single–unit cell–wide domain in $PbTiO_3$ (Fig. 3C) has substantially reduced polarization at the diffused domain wall, and its marginal stability is evident in its tendency to expand spontaneously (with a small energy barrier of 0.024 eV) to domains of larger width

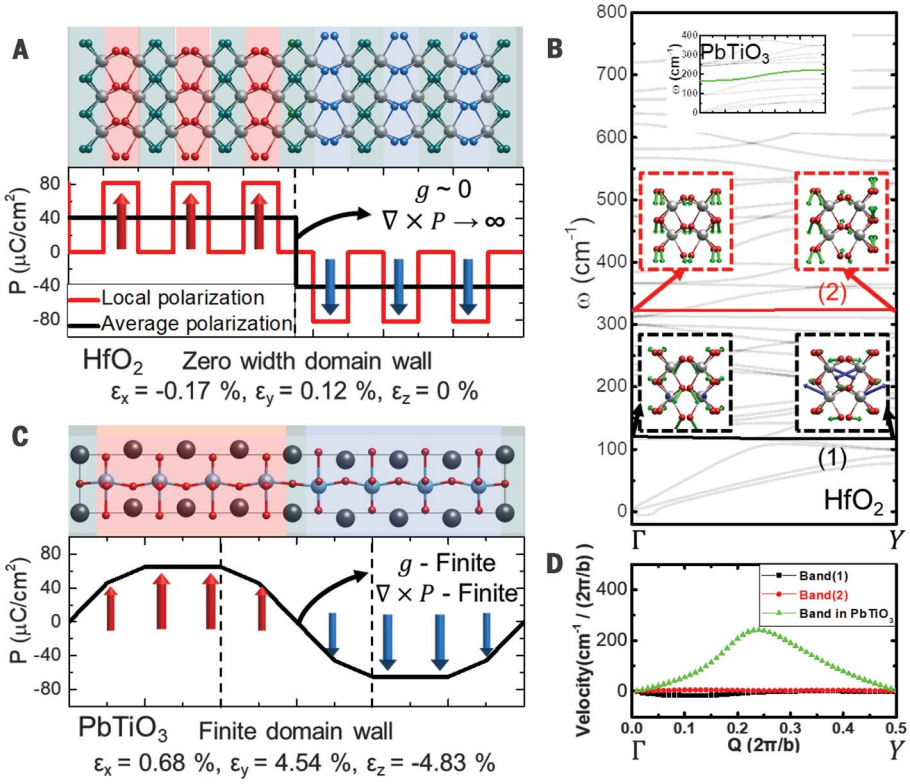

Fig. 2. Flat bands and zero-width domain wall in HfO_2, contrary to the diffused domain wall in $PbTiO_3$. (**A** and **C**) Atomic structure of the domain wall and variation in local polarization along the direction perpendicular to the domain walls in (A) HfO_2 and (C) $PbTiO_3$. Red and black lines correspond to the local polarization averaged over their half– and single–unit cells, respectively. Although ($\vec{\nabla} \times \vec{P} = \frac{\partial P_z}{\partial y}$) is small and spreads over a few unit cells away from the domain wall in $PbTiO_3$, it is singularly large and highly localized at the domain wall in HfO_2. (**B**) This is because of its low energy cost ($g \sim 0$) guaranteed by the flatness of polar phonon bands involving the polar and antipolar modes condensed in orthorhombic HfO_2. Flat polar bands are indicated with black and red lines, and eigenmodes at Γ and Y in the bands are depicted in the insets. This flatness of the bands in HfO_2 is in sharp contrast to a dispersive band in $PbTiO_3$ [(B), top, inset]. (**D**) Phonon velocities of the flat bands in HfO_2 are nearly zero, whereas that of the polar band in $PbTiO_3$ has a finite value. For $PbTiO_3$, black spheres indicate Pb atoms, and light blue and red spheres indicate titanium and oxygen atoms, respectively.

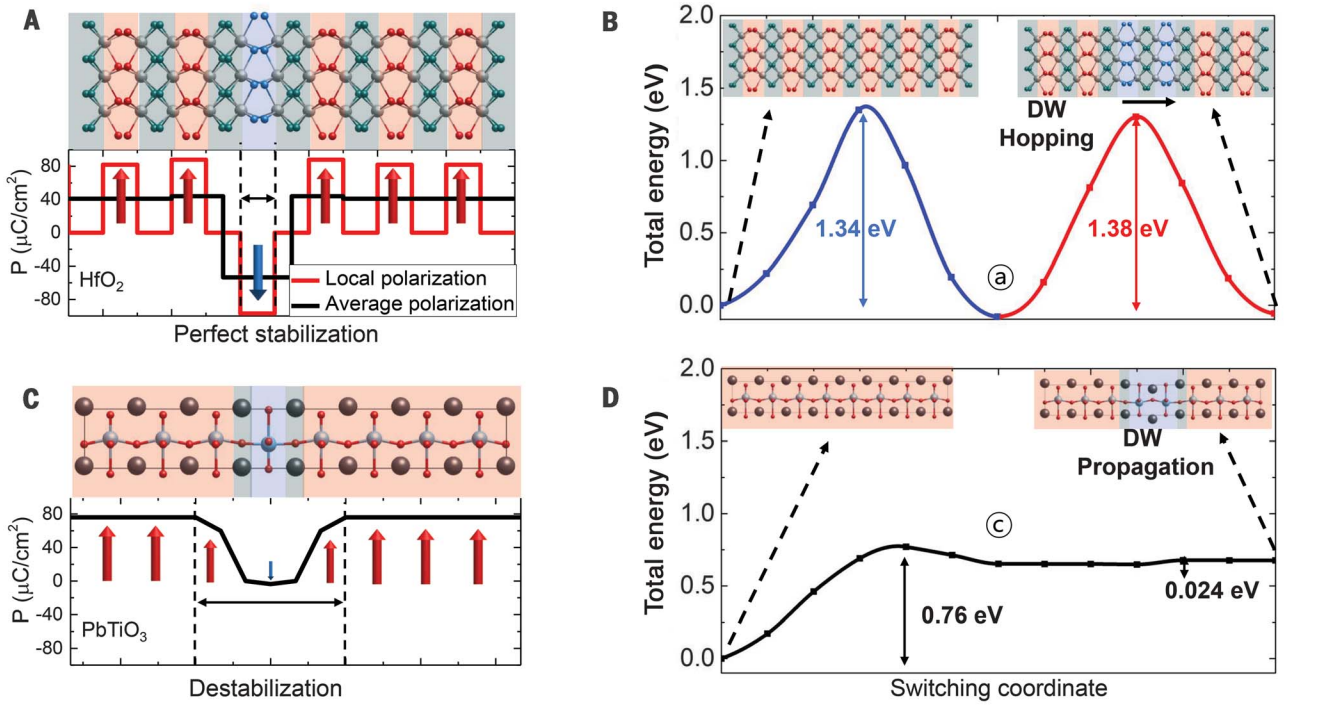

Fig. 3. Robust stability of a half–unit cell–wide ferroelectric domain. (**A**) Atomic structure of the thinnest domain and variation in polarization along the direction perpendicular to the domain walls in HfO_2. (**B**) Energy along the path of polarization switching of HfO_2, starting from the uniformly polarized structure [(B), left inset] to a state with reversed polarization in two layers [(B), right inset] passing through the state in (A). (**C**) In contrast to the domain polarization that is unsuppressed relative to bulk P in HfO_2 (A), it is substantially suppressed inside the switched domain as well as a few unit cells away from the domain wall of $PbTiO_3$. (**D**) The robust stability of a half–unit cell–wide domain of HfO_2 (B) is in complete contrast with the marginal stability of the single–unit cell domain in $PbTiO_3$, which spontaneously expands to wider domains. Successive switching in the next layer [(B), red line] of HfO_2 has an energy barrier comparable with that of the first switching process [(B), blue line] in HfO_2, in contrast to a small energy barrier of successive switching in $PbTiO_3$ (D).

(Fig. 3D). Despite the strongly knit 3D crystal structure of HfO_2, our results establish that it consists of weakly interacting 2D polar layers, allowing stable and switchable ferroelectric domains at the ultimate limit of width (2.7 Å).

We provide a possible explanation of the puzzling observation that the coercive field of polarization switching observed in HfO_2 is unusually large and even comparable with the activation field (E_a). The coercive field (E_c) in conventional ferroelectrics is typically 1/10 of the activation field (Fig. 4A) (*16*) because polarization switching occurs through nucleation and the growth of ferroelectric domains of reversed polarization. Because of such collective behavior, E_c is generally reduced by a factor proportional to the width of the domain wall (*27*). In HfO_2, domain walls are vanishingly thin, and the resulting reduction in E_c (Fig. 4A) is marginal. With weakly interacting domain walls and zero group velocity of the relevant polar modes ($g \sim 0$, by the flat bands of HfO_2), domain walls do not propagate efficiently and can move only by hopping over a large energy barrier (Fig. 3B), suggesting that their sluggish motion observed experimentally could be an intrinsic property (*7*, *28*). By contrast, a domain wall in $PbTiO_3$ encounters a much smaller energy barrier of 0.024 eV (Fig. 3D), and its motion leads to rapid expansion of its polar domain.

We demonstrated the scale-free nature of polarization switching in HfO_2 by comparing reversal of uniform and local polarization (Fig. 4B). Energetics of local and uniform polarization switching in HfO_2 are strikingly similar. Flipping the polarization of a single layer is nearly energetically equivalent (per layer) to flipping the polarization of all layers. By contrast, reversal of local polarization in a single unit cell–wide region is energetically forbidden in $PbTiO_3$. Total energy along the polarization reversal in consecutive 2D polar domains in HfO_2 is a periodic function of the number of unit cell–width domains switched (Fig. 4C). The equal multistability and identical switching barriers show absolutely scale-free behavior that can be labeled by the integer (number of unit cells) and be a basis for a multilevel device whose number of states are similar to the number of lateral unit cells. In contrast to this multistate polar nature in HfO_2, only bistability in $PbTiO_3$ is evident from its uniformly polarized states ($\pm P_0$), which are more stable than the rest of the intermediate polar states (Fig. 4C, bottom).

To establish the intrinsic size limit on ferroelectricity in HfO_2, we simulated Hf-terminated slabs (Fig. 4D) perpendicular to (i) the (010) axis with in-plane polarization and (ii) the (001) axis with out-of-plane polarization. The polarization in a ferroelectric layer of (010) slabs survives in a scale-free manner down to 1.5–unit cell thickness, with spacers acting as natural protective coatings. The polarization retains its bulk value in (001) slabs down to single–unit cell thickness, as expected from the improper nature of fluorite ferroelectricity (*29*). Thus, the intrinsic lateral and perpendicular size limits on ferroelectric order in HfO_2 films are 0.75 and 0.51 nm, respectively (fig. S5). Robust ferroelectric order appears to exist down to 1-nm thickness, as recently reported (*30*), which verifies one of our predictions. Now, the storage size limitation is only from the electrode and the transistor used to interface with it for readout operations.

Because HfO_2 is already compatible in silicon electronics, our discovery of independently switchable polar layers could provide opportunities to realize ultradense and low-cost ferroelectric random-access memory (FeRAM) or a ferroelectric field-effect transistor (FeFET) for memory or logic device applications (figs.

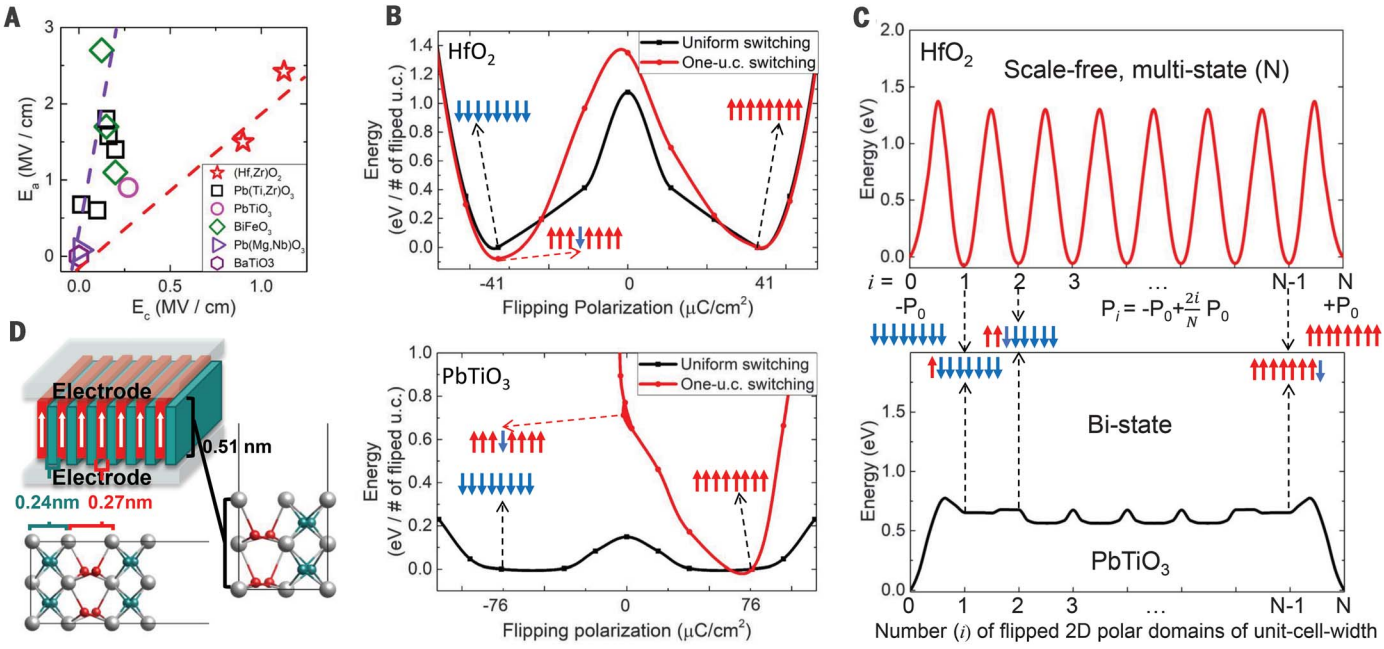

Fig. 4. Experimental activation and coercive fields revealing unusual switching behavior of HfO_2 and simulated energetics demonstrating its fully scale-free 2D domain switching of 0.27-nm width. (**A**) Experimental values of activation (E_a) and coercive (E_c) fields for various ferroelectrics [$BaTiO_3$, (*16*); Pb(Zr,Ti)O_3, (*17*, *18*); $BiFeO_3$, (*19*, *21*); Pb(MgNb)O_3, (*20*); $PbTiO_3$, (*21*); and (Hf,Zr)O_2, (*5*, *6*)]. Although E_c is 10 times smaller than E_a in conventional ferroelectrics, these values are comparable in HZO, implying that collective and individual domain switching occur at the same field. (**B**) Calculated energy curves along paths of switching uniform and local (one unit cell) polarization in HfO_2 (top) and $PbTiO_3$ (bottom). (**C**) Energy of unit cell–by–unit cell width switching. Whereas switching of local polarization in consecutive unit cells in $PbTiO_3$ shows bistable ($\pm P_0$) behavior (bottom), domains of any width in HfO_2 are equally stable with the same energy barrier of switching (top), showing its multistate and scale-free ferroelectric behavior in stability and switchability. (**D**) Schematic of HfO_2-based capacitive memory device with ultrahigh density because the improper ferroelectricity allows no critical thickness, as confirmed with first-principles calculations [(D), right]. There is no critical lateral width of ferroelectricity in HfO_2 [(D), bottom] because of the presence of spacer layers.

S11 and S12). In addition, possibility of unit cell–by–unit cell dipolar control provides different opportunities for deterministic multilevel switching (figs. S6, S7, and S12), ultimately down to the angstrom scale.

REFERENCES AND NOTES

1. T. Böscke, J. Müller, D. Bräuhaus, U. Schröder, U. Böttger, *Appl. Phys. Lett.* **99**, 102903 (2011).
2. T. Mikolajick, S. Slesazeck, M. H. Park, U. Schroeder, *MRS Bull.* **43**, 340–346 (2018).
3. M.-K. Kim, J.-S. Lee, *Nano Lett.* **19**, 2044–2050 (2019).
4. C. H. Ahn, K. M. Rabe, J.-M. Triscone, *Science* **303**, 488–491 (2004).
5. D. Zhou *et al*., *Acta Mater.* **99**, 240–246 (2015).
6. C. Alessandri, P. Pandey, A. Abusleme, A. Seabaugh, *IEEE Electron Device Lett.* **39**, 1780–1783 (2018).
7. P. Buragohain *et al*., *Appl. Phys. Lett.* **112**, 222901 (2018).
8. Z. Li *et al*., *Sci. Adv.* **4**, eaau4511 (2018).
9. Y. Cao *et al*., *Nature* **556**, 43–50 (2018).
10. S. Mukherjee *et al*., *Phys. Rev. Lett.* **114**, 245504 (2015).
11. J. Schulenburg, A. Honecker, J. Schnack, J. Richter, H.-J. Schmidt, *Phys. Rev. Lett.* **88**, 167207 (2002).
12. M.-W. Chu *et al*., *Nat. Mater.* **3**, 87–90 (2004).
13. J. F. Ihlefeld *et al*., *J. Am. Ceram. Soc.* **99**, 2537–2557 (2016).
14. Y. G. Wang, W. L. Zhong, P. L. Zhang, *Phys. Rev. B Condens. Matter* **51**, 17235–17238 (1995).
15. D. D. Fong *et al*., *Science* **304**, 1650–1653 (2004).
16. H. Wieder, *J. Appl. Phys.* **28**, 367–369 (1957).
17. V. Nagarajan *et al*., *J. Appl. Phys.* **86**, 595–602 (1999).
18. J. Son, C. Park, S.-K. Kim, Y.-H. Shin, *J. Appl. Phys.* **104**, 064101 (2008).
19. D. Pantel *et al*., *J. Appl. Phys.* **107**, 084111 (2010).
20. D. Fu, H. Taniguchi, M. Itoh, S. Mori, Pb($Mg_{1/3}Nb_{2/3}$)O_3 (PMN) Relaxor: Dipole glass or nano-domain ferroelectric?, in *Advances in Ferroelectrics*, vol. 3, A. Peláiz-Barranco, Ed. (IntechOpen, 2012).
21. W.-H. Kim, S. M. Yoon, J. Y. Son, *Mater. Lett.* **124**, 47–49 (2014).
22. R. Terki, G. Bertrand, H. Aourag, C. Coddet, *Mater. Lett.* **62**, 1484–1486 (2008).
23. S. E. Reyes-Lillo, K. F. Garrity, K. M. Rabe, *Phys. Rev. B Condens. Matter Mater. Phys.* **90**, 140103 (2014).
24. R. Materlik, C. Künneth, A. Kersch, *J. Appl. Phys.* **117**, 134109 (2015).
25. E. D. Grimley, T. Schenk, T. Mikolajick, U. Schroeder, J. M. LeBeau, *Adv. Mater. Interfaces* **5**, 1701258 (2018).
26. N. Choudhury, E. J. Walter, A. I. Kolesnikov, C.-K. Loong, *Phys. Rev. B Condens. Matter Mater. Phys.* **77**, 134111 (2008).
27. S. Choudhury *et al*., *J. Appl. Phys.* **104**, 084107 (2008).
28. H. Mulaosmanovic *et al*., *ACS Appl. Mater. Interfaces* **9**, 3792–3798 (2017).
29. N. Sai, C. J. Fennie, A. A. Demkov, *Phys. Rev. Lett.* **102**, 107601 (2009).
30. S. S. Cheema *et al*., *Nature* **580**, 478–482 (2020).

ACKNOWLEDGMENTS

We thank N. Spaldin for critical and constructive comments on the manuscript. J.H.L. appreciates Y. Kim, H. Kang, C. H. Kim, and H.-S. Kim for useful discussions. **Funding:** This work is supported by the Creative Materials Discovery (2017M3D1A1040828), the MOTIE (Ministry of Trade, Industry Energy) (10080657), KRSC (Korea Semiconductor Research Consortium) program, and Basic Research Laboratory (NRF2017R1A4A1015323). U.W. thanks UNIST for hospitality and funding from a J. C. Bose National Fellowship of SERB, Government of India, and support from the Department of Science and Technology for the India-Korea Joint Network Center in computational materials science. We appreciate the Supercomputing Center/Korea Institute of Science and Technology Information for supercomputing resources, including technical support (KSC-2020-CRE-0088). **Author contributions:** J.H.L. conceived the idea and supervised the work. H.-J.L., Y.K., U.W., and J.H.L. designed and carried out density functional theory calculations, and M.L., H.Y., and J.J. helped with analysis of the data. K.L. and S.C.C. provided experimental verifications. J.H.L., U.W., and H.-J.L. developed the theory and wrote the manuscript. **Competing interests:** J.H.L. and H.-J.L. are inventors on KR patent application (10-2020-0047206) submitted by the Ulsan National Institute of Science and Technology (UNIST) that covers ultimately high-density ferroelectric memories and deterministic multilevel devices induced by flat phonon bands. **Data and materials availability:** All data are available in the main text or the supplementary materials.

SUPPLEMENTARY MATERIALS

science.sciencemag.org/content/369/6509/1343/suppl/DC1
Materials and Methods
Supplementary Text S1 to S3
Figs. S1 to S15
References (*31*–*70*)

28 October 2019; resubmitted 29 April 2020
Accepted 16 June 2020
Published online 2 July 2020
10.1126/science.aba0067

COSMOLOGY

An excess of small-scale gravitational lenses observed in galaxy clusters

Massimo Meneghetti[1,2,3]*, Guido Davoli[1,4], Pietro Bergamini[1], Piero Rosati[5,1], Priyamvada Natarajan[6], Carlo Giocoli[1,5,7], Gabriel B. Caminha[8], R. Benton Metcalf[7], Elena Rasia[9,10], Stefano Borgani[9,10,11,12], Francesco Calura[1], Claudio Grillo[13,14], Amata Mercurio[15], Eros Vanzella[1]

Cold dark matter (CDM) constitutes most of the matter in the Universe. The interplay between dark and luminous matter in dense cosmic environments, such as galaxy clusters, is studied theoretically using cosmological simulations. Observations of gravitational lensing are used to characterize the properties of substructures—the small-scale distribution of dark matter—in clusters. We derive a metric, the probability of strong lensing events produced by dark-matter substructure, and compute it for 11 galaxy clusters. The observed cluster substructures are more efficient lenses than predicted by CDM simulations, by more than an order of magnitude. We suggest that systematic issues with simulations or incorrect assumptions about the properties of dark matter could explain our results.

In the standard cosmological model, the matter content of the Universe is dominated by cold dark matter (CDM), collisionless particles that interact with ordinary matter (baryons) only through gravity. Gravitationally bound dark-matter halos form hierarchically, with the most massive systems forming through mergers of smaller ones. As structure assembles in this fashion, large dark-matter halos contain smaller-scale substructure in the form of embedded subhalos.

The most massive dark-matter halos at the present time are galaxy clusters, with masses of ~10^{14} to ~10^{15} solar masses ($M_\odot$, one solar mass is ~2×10^{30} kg). Galaxy clusters contain about a thousand member galaxies that are hosted in subhalos. The detailed spatial distribution of dark matter in galaxy clusters can be mapped by observing gravitational lensing of distant background galaxies. When distant background galaxies are in near perfect alignment with the massive foreground cluster, strong gravitational lensing occurs. Strong lensing—nonlinear effects produced by the deflection of light—results in multiple distorted images of individual background galaxies that can be detected in Hubble Space Telescope (HST) imaging.

The probability and strength of these nonlinear strong lensing effects can be predicted theoretically from simulations of structure formation (*1*). We test these predictions using observations of galaxy clusters, combining lensing data from the HST with spectroscopic data from the Very Large Telescope (VLT). Our observed sample of lensing clusters is split into three sets for this analysis: (i) a reference sample comprising three clusters with well-constrained mass distributions (mass models): MACS J1206.2-0847 (MACSJ1206) at redshift $z = 0.439$, MACS J0416.1-2403 (MACSJ0416) at $z = 0.397$, and Abell S1063 (AS1063) at $z = 0.348$ (*2*–*6*); (ii) a sample that includes the publicly available mass models for four Hubble Frontier Fields clusters [HFF, (*7*)], namely Abell 2744 at $z = 0.308$, Abell 370 at $z = 0.375$, MACS J1149.5+2223 (MACSJ1149) at $z = 0.542$, and MACS J0717.5+3745 (MACSJ0717) at $z = 0.545$; and (iii) four clusters from the Cluster Lensing and Supernova Survey with Hubble [CLASH, (*8*)] project, with recent mass reconstructions [(*9*), their "Gold" sample]: RX J2129.7+0005 (RXJ2129) at $z = 0.234$, MACS J1931.8-2635 (MACSJ1931) at $z = 0.352$, MACS J0329.7-0211 (MACSJ0329) at $z = 0.450$, and MACS J2129.4-0741 (MACSJ2129) at $z = 0.587$. A color-composite image of MACSJ1206, one of the clusters in our reference sample (i), is shown in Fig. 1. Images of the other clusters are shown in figs. S1 to S3.

Owing to their large masses, all these galaxy clusters act as strong lenses, producing multiple images of numerous background galaxies. To reconstruct their mass distributions, we combine the images with available spectroscopic data (*3*, *10*). For each cluster, the membership of hundreds of galaxies is confirmed spectroscopically, and their redshifts have been measured. The spectroscopy has also allowed identification of tens of multiply imaged background sources per cluster.

Mass models for the reference cluster sample were constructed by using the publicly available parametric lens inversion code LENSTOOL (*11*) and published previously (*6*). Clusters were modeled as a superposition of large-scale components to account for the large-scale cluster dark-matter halos, and small-scale components that describe the substructure. We associate the spatial positions of cluster member galaxies with the locations of dark-matter substructure. The detailed mass distribution in these cluster galaxies is constrained using stellar kinematics measurements of cluster member galaxies from the VLT spectroscopy.

The mass models for the clusters in the other two samples are built similarly (*12*); however, unlike the reference sample, the mass distribution in the cluster member galaxies is not constrained using data from stellar kinematics. For the HFF sample, a suite of lensing mass models constructed independently by several groups are publicly available from the Mikulski Archive for Space Telescopes (MAST); we used only those built using LENSTOOL for consistency [e.g., (*13*, *14*)]. For the "Gold" sample, we use published models (*9*) that were also built with LENSTOOL.

The multiple images of distant sources lensed by foreground galaxy clusters have angular separations of several tens of arcseconds. The most distorted gravitational arcs occur near lines that enclose the inner regions of the cluster, referred to as critical lines, which delineate the region where strong lensing occurs. The size of the critical lines depends on the redshifts of the background sources. Substructures within each cluster act as smaller-scale gravitational lenses embedded within the larger lens. If these substructures are massive enough and compact enough, they can also produce additional local strong lensing events on much smaller scales with separations of less than a few arcseconds. These small-scale features are expected to appear around the critical lines produced by individual cluster galaxies. We refer to these localized features as Galaxy-Galaxy Strong Lensing (GGSL) events. Sufficiently high-resolution mass reconstructions are necessary to recover these smaller-scale critical lines. For example, Fig. 1 shows the network of critical lines in MACSJ1206 for two possible source redshifts, $z = 1$ and $z = 7$. The cluster produces a large-scale critical line extending to 15 to 30 arc sec and many smaller-scale critical lines around individual substructures, as shown in the insets. The presence of secondary critical lines indicates that the substructures are centrally concentrated and massive enough to act as individual strong lenses.

[1]Osservatorio di Astrofisica e Scienza dello Spazio di Bologna, Istituto Nazionale di Astrofisica Via Gobetti 93/3, I-40129, Bologna, Italy. [2]National Institute for Nuclear Physics, viale Berti Pichat 6/2, I-40127 Bologna, Italy. [3]Division of Physics, Mathematics, and Astronomy, California Institute of Technology, Pasadena, CA 91125, USA. [4]Centro Euro-Mediterraneo sui Cambiamenti Climatici (CMCC), viale Berti Pichat 6/2, I-40127 Bologna, Italy. [5]Dipartimento di Fisica e Scienza della Terra, Università di Ferrara, via Saragat 1, I-44122 Ferrara, Italy. [6]Department of Astronomy, 52 Hillhouse Avenue, Steinbach Hall, Yale University, New Haven, CT 06511, USA. [7]Dipartimento di Fisica e Astronomia, Università di Bologna, via Gobetti 93/2, 40129 Bologna, Italy. [8]Kapteyn Astronomical Institute, University of Groningen, Postbus 800, 9700 AV Groningen, Netherlands. [9]Osservatorio Astronomico di Trieste, Istituto Nazionale di Astrofisica, Via Tiepolo, 11, I-34131 Trieste, Italy. [10]Institute for Fundamental Physics of the Universe, Via Beirut 2, 34014 Trieste, Italy. [11]Department of Physics, University of Trieste, via Tiepolo 11, I-34131 Trieste, Italy. [12]National Institute for Nuclear Physics, Via Valerio 2, I-34127 Trieste, Italy. [13]Dipartimento di Fisica, Università degli Studi di Milano, via Celoria 16, I-20133 Milano, Italy. [14]Niels Bohr Institute, University of Copenhagen, Lyngbyvej 2, 4. sal 2100 Copenhagen, Denmark.
*Corresponding author. Email: massimo.meneghetti@inaf.it

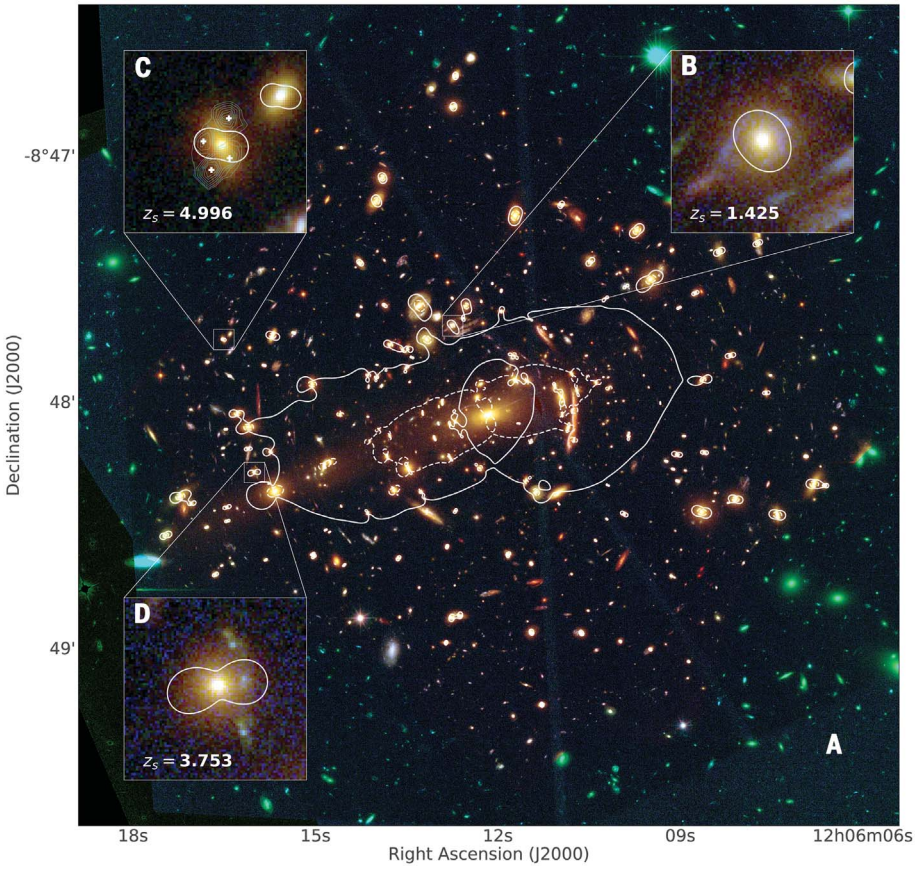

Fig. 1. Color-composite image of the central region of the galaxy cluster MACSJ1206. (**A** to **D**) The image combines HST observations in the filters F105W, F110W, F125W, F140W, F160W (red channel), F606W, F625W, F775W, F814W, F850LP (green channel), and F435W and F475W (blue channel). The dashed and solid lines in (A) show the critical lines of the cluster for source redshifts of 1 and 7, respectively. Panels (B), (C), and (D) zoom into three GGSL events enclosing sources at redshifts 1.425, 4.996, and 3.753, respectively. The white lines in those panels show the critical lines of the lenses for the corresponding source redshifts. In (B) and (D), the background lensed sources are bluer than the foreground lensing galaxies. In (C), the lensed source is not visible in the HST image but is detected in an observation with the Multi-Unit Spectroscopic Explorer (MUSE) spectrograph on the VLT (*12*). The source is detected at a wavelength of ~7289 Å, corresponding to the redshifted Lyman-α spectral line of hydrogen, at locations indicated by the cyan contours. The white crosses indicate the positions of four multiple images of the source. Equivalent images for all the other clusters are shown in figs. S1 to S3.

We identify three GGSL events in the core of the cluster MACSJ1206, shown in Fig. 1, B to D: a ring-shape image (an Einstein ring) originating from a source at $z = 1.42$; a triply imaged galaxy at $z = 3.75$ (*15*); and an Einstein cross with four distinct images of a source at $z = 4.99$. The consistency between the shapes of the GGSL events and the predicted critical lines from the lens modeling, also shown in Fig. 1, B to D, validates our multiscale mass model.

Just as the observed gravitational arcs are lensed images of distant galaxies, the critical lines are the lensed counterparts of the caustic lines (*1*), shown in Fig. 2, B and D. The caustics enclose the regions in which sources have to be located to be strongly lensed by substructures. We quantify the probability of observing GGSL events using the fraction of the area of the sky inside the caustics produced by substructures. Figure 3 shows how the GGSL probability varies as a function of the source redshift for all clusters in our three samples. For MACSJ1206 (upper limit of the reference sample), it is ~10^{-3} at $z > 2$. This probability can in turn be converted into an expected number of GGSL events by assuming the properties of the background source population of galaxies that can be lensed. Using galaxies seen in the Hubble Ultra-Deep Field (HUDF) (*16*) as a representative template for the properties of the background lensed sources, we calculate that $\lesssim$3 GGSL events should occur in MACSJ1206, in agreement with the observations. Equivalent estimates for MACSJ0416 and AS1063 predict ~1 and ~0.9 events, respectively. In these two cases, our calculations underpredict the number of observed GGSL events, as three candidate events have been reported in each of the two clusters (*17*, *18*). This underestimate is likely because the HUDF may not be an appropriate template for background sources in these two clusters (*12*). Nevertheless, we find that GGSL events are detected in multiple clusters. Twenty-four GGSL candidate events have been found in other CLASH clusters, including four events in MACSJ1149 and one event in each of the clusters MACSJ0717, RXJ2129, and MACSJ0329 (*18*).

We next consider whether the observed number of GGSL events are consistent with theoretical predictions within the standard cosmological model. We performed the same analysis and computed the GGSL probability for 25 simulated galaxy clusters, which have masses, redshifts, morphologies, and mass concentrations similar to those in our three observed samples (*12*). The cosmological hydrodynamical simulations from which these simulated clusters are drawn (*19*) incorporate gas cooling, star formation, and energy feedback from supernovae and accreting supermassive black holes (SMBHs).

Figure 2 shows a comparison between the critical lines and the caustics of MACSJ1206 (panels A and B) and those of a simulated cluster of similar mass and concentration (panels C and D). MACSJ1206 has many more secondary critical lines within the observed area. The fractional area of the source plane that is enclosed by substructure caustics is larger in observed clusters than predicted by the simulated sample, as is the probability of GGSL events. Figure 3 shows that the GGSL probability differs by more than an order of magnitude between the observations and simulations.

We performed several tests to investigate potential sources of this discrepancy (*12*). The results remain unchanged even when energy feedback from active galactic nuclei powered by SMBH accretion—which alters the internal structure of halos—is disabled in the simulations. This feedback suppresses star formation in substructures, altering the slope of their inner density profiles, making them less centrally concentrated and, hence, weaker gravitational lenses. Even without feedback, we are unable to completely bridge the gap between simulations and observations. Simulations without feedback are also grossly discrepant from observations for other well-measured quantities, such as the total fraction of baryons in clusters converted into stars. The mass and spatial resolutions of our simulations are sufficiently high to resolve the typical substructures included in the lensing mass models (*12*). We also exclude the possibility that the computed GGSL probability could be enhanced by unassociated halos along the line-of-sight (LOS) to these clusters. Including multiple lens planes in the models generated using cosmological simulations, we find that the substructure

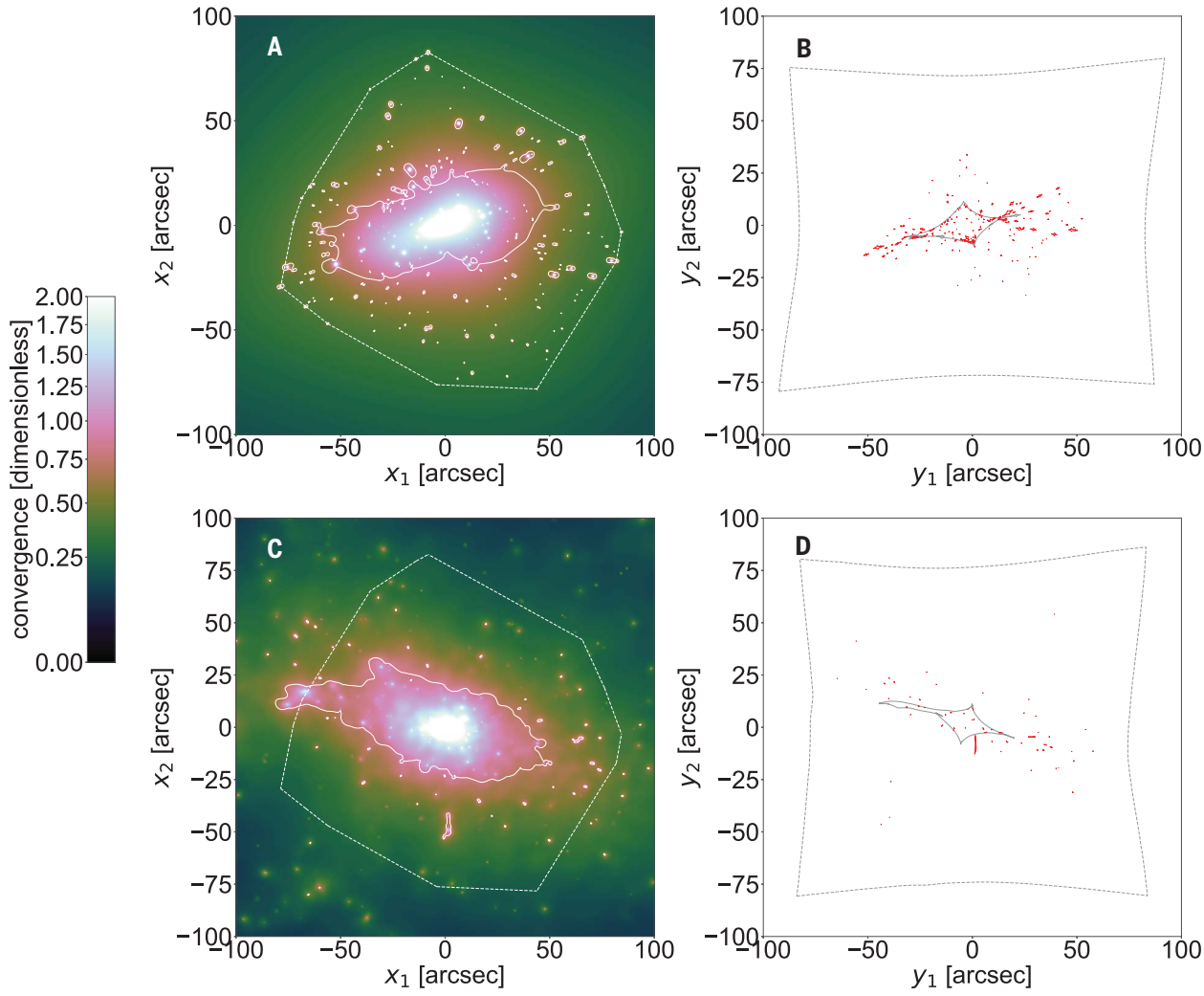

Fig. 2. Comparison between an observed and a simulated gravitational lens. (**A**) The projected mass map (called convergence) of MACSJ1206 (color bar), overlaid with the critical lines for sources at redshift z = 7 (solid white lines). The dashed polygon delimits the region of the HST image within which cluster galaxies were selected and included in the lens model. (**B**) The caustics corresponding to the principal (in gray) and to the secondary critical lines (in red) of MACSJ1206 (12). The dashed gray line shows the limits of the field of view in (A) mapped into the source plane (*12*). The GGSL probability is calculated by dividing the area of the secondary caustics by that enclosed by the dashed gray line. (**C**) The projected mass map and the critical lines for sources at redshift z = 7 of a simulated cluster with a mass similar to that of MACSJ1206 (*12*). The dashed polygon is the same as in (A). (**D**) Caustics of the simulated cluster shown in (C). Although the main critical lines and caustics have similar extents, the secondary critical lines and caustics are larger and more numerous in the lens model of MACSJ1206 than in the simulation.

critical lines and caustics are negligibly affected by halos along the LOS (*12*). The observationally constrained lens models reproduce the shapes and sizes of the observed GGSL events, e.g., the model-predicted image positions match the observations within ~0.5 arc sec.

The discrepancy between observations and simulations may be due to issues with either the CDM paradigm or simulation methods. Gravitational lensing has previously been used to probe detailed properties of dark-matter halos associated with individual cluster galaxies [e.g., (*20*, *21*)]. Simulations show that the mass and radial distributions of subhalos are nearly universal (*22*). Varying results have been reported for the level of agreement between lens model predictions and simulations for other derived quantities; e.g., the mass distribution functions of substructure derived from lensing data agree with simulations, but their radial distributions are more centrally concentrated in observations than in simulations (*5*, *14*, *15*). Strong lensing clusters also contain more high–circular velocity subhalos (i.e., subhalos with maximum circular velocities $V_{\rm circ} > 100\ {\rm km\ s^{-1}}$) compared with simulations (*5*, *15*, *23*). The maximum circular velocity is given by

$$V_{\rm circ} = \max\sqrt{\frac{GM(r)}{r}} \qquad (1)$$

where G is the gravitational constant, $M(r)$ is the galaxy mass profile, and r is the distance from the galaxy center. Figure 4 shows that, in our lens models, observed galaxies have larger circular velocities than their simulated analogs at a fixed mass. This implies that dark-matter subhalos associated with observed galaxies are more compact than theoretically expected. Observed substructures also appear to be in closer proximity to the larger-scale cluster critical lines. Explaining this difference requires the existence of a larger number of compact substructures in the inner regions of simulated clusters. Baryons and dark matter are expected to couple in the dense inner regions of subhalos, leading to alterations in the small-scale density profile of dark matter, so it could be that current understanding of this interplay is incorrect. Alternatively, the difference could arise from incorrect assumptions about the nature of dark matter.

Previous discrepancies between the predictions of the standard cosmological model and data on small scales have arisen from

observations of dwarf galaxies and of satellites of the Milky Way, known as the "missing satellite" (*24*, *25*), "cusp-core" (*26*), and "too-big-to-fail" problems (*27*, *28*), discrepancies with planes of satellite galaxies (*29*). The discrepancy that we report is unrelated to those issues. Previous studies revealed that observed small satellite galaxies were fewer in number and were less compact than expected from simulations; here, we find the opposite results for cluster substructures. The GGSL events that we observe show that subhalos are more centrally concentrated than predicted by simulations; i.e., there is an excess not a deficit. Hypotheses advocated to solve previous controversies on dwarf galaxy scales would only exacerbate the discrepancy in GGSL event numbers that we report.

Our results therefore require alternative explanations. One possibility is numerical effects arising from the resolution limits of simulations (*30*). However, known numerical artefacts are not effective enough at disrupting satellites. We investigated this issue (*12*) and found that it can change the predicted GGSL event rate by at most a factor of 2, which is insufficient to explain the nearly order-of-magnitude discrepancy that we find. Any numerical artefacts would also appear on galactic scales, where they would worsen the missing satellite problem.

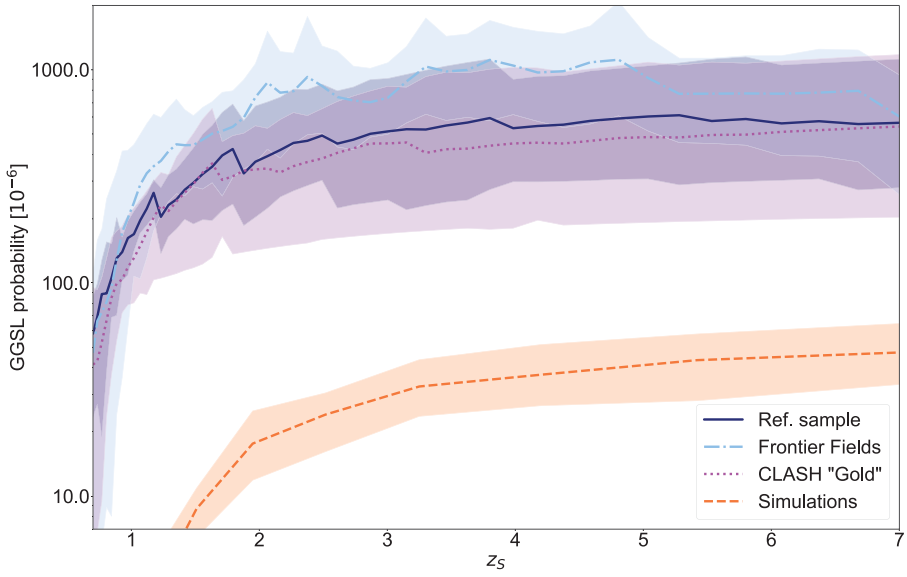

Fig. 3. The GGSL probability as a function of source redshift. The mean GGSL probability for our reference sample is shown with a solid dark blue line. The light blue dot-dashed and violet dotted lines plot the computed GGSL probability for the HFF and CLASH Gold samples. The median GGSL probability measured from simulations is given by the orange dashed line (*12*). The colored bands show the 99.9% confidence intervals for each dataset. The discrepancy between observations and simulations is about an order of magnitude.

REFERENCES AND NOTES

1. M. Meneghetti *et al.*, *Mon. Not. R. Astron. Soc.* **472**, 3177–3216 (2017).
2. G. B. Caminha *et al.*, *Astron. Astrophys.* **607**, A93 (2017).
3. G. B. Caminha *et al.*, *Astron. Astrophys.* **587**, A80 (2016).
4. G. B. Caminha *et al.*, *Astron. Astrophys.* **600**, A90 (2017).
5. M. Bonamigo *et al.*, *Astrophys. J.* **842**, 132 (2017).
6. P. Bergamini *et al.*, *Astron. Astrophys.* **631**, A130 (2019).
7. J. M. Lotz *et al.*, *Astrophys. J.* **837**, 97 (2017).
8. M. Postman *et al.*, *Astrophys. J. Suppl. Ser.* **199**, 25 (2012).
9. G. B. Caminha *et al.*, *Astron. Astrophys.* **632**, A36 (2019).
10. T. Treu *et al.*, *Astrophys. J.* **812**, 114 (2015).
11. E. Jullo *et al.*, *New J. Phys.* **9**, 447 (2007).
12. Materials and methods are available as supplementary materials.
13. T. L. Johnson *et al.*, *Astrophys. J.* **797**, 48 (2014).
14. P. Natarajan *et al.*, *Mon. Not. R. Astron. Soc.* **468**, 1962–1980 (2017).
15. C. Grillo *et al.*, *Astrophys. J.* **800**, 38 (2015).
16. M. Rafelski *et al.*, *Astron. J.* **150**, 31 (2015).
17. E. Vanzella *et al.*, *Astrophys. J.* **842**, 47 (2017).
18. G. Desprez *et al.*, *Mon. Not. R. Astron. Soc.* **479**, 2630–2648 (2018).
19. S. Planelles *et al.*, *Mon. Not. R. Astron. Soc.* **438**, 195–216 (2014).
20. P. Natarajan, J.-P. Kneib, *Mon. Not. R. Astron. Soc.* **287**, 833–847 (1997).
21. P. Natarajan, J.-P. Kneib, I. Smail, R. S. Ellis, *Astrophys. J.* **499**, 600–607 (1998).
22. L. Gao, S. D. M. White, A. Jenkins, F. Stoehr, V. Springel, *Mon. Not. R. Astron. Soc.* **355**, 819–834 (2004).

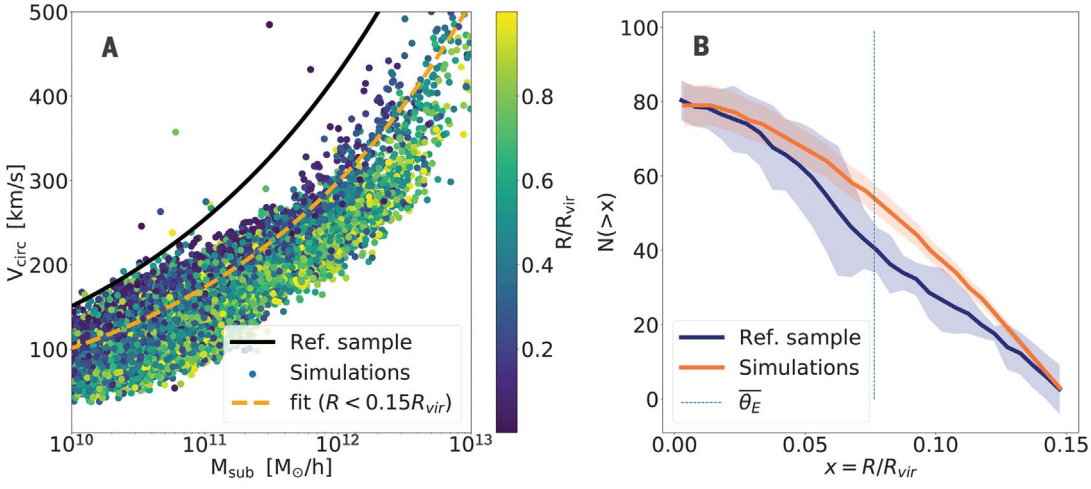

Fig. 4. Circular velocities and positions of substructures in simulated and observed galaxy clusters. (**A**) Substructure circular velocity as a function of substructure mass M_{sub}. The circular velocity is a proxy for the concentration of the substructure mass. The solid black line shows the average relation for the reference sample (*6*). The colored circles show the simulations, color-coded by the substructure distance from the cluster center R in units of the cluster virial radius R_{vir}. The orange dashed curve shows the best-fitting model relation for simulated substructures whose distance is less than 15% of the virial radius. This is roughly the region around the cluster center probed by strong lensing. The observed relation is always above that derived from the simulations, indicating that observed substructures are more compact than the simulated ones. (**B**) Mean cumulative distribution of the substructure distances from the cluster center, $N(>x)$. The distances are scaled by the virial radius of the host cluster, $x = R/R_{vir}$. The blue and orange lines show the distributions for the observed reference sample and the simulations, respectively. The vertical dashed line shows the mean size of the main critical lines of MACSJ1206, MACSJ0416, and AS1063, $\bar{\theta}_E$.

23. E. Munari *et al*., *Astrophys. J.* **827**, L5 (2016).
24. B. Moore *et al*., *Astrophys. J.* **524**, L19–L22 (1999).
25. A. Klypin, A. V. Kravtsov, O. Valenzuela, F. Prada, *Astrophys. J.* **522**, 82–92 (1999).
26. R. Flores, J. Primack, *Astrophys. J.* **427**, L1 (1994).
27. M. Boylan-Kolchin, J. S. Bullock, M. Kaplinghat, *Mon. Not. R. Astron. Soc.* **415**, L40–L44 (2011).
28. M. Boylan-Kolchin, V. Springel, S. D. M. White, A. Jenkins, *Mon. Not. R. Astron. Soc.* **406**, 896 (2010).
29. O. Müller, M. S. Pawlowski, H. Jerjen, F. Lelli, *Science* **359**, 534–537 (2018).
30. F. C. van den Bosch, G. Ogiya, O. Hahn, A. Burkert, *Mon. Not. R. Astron. Soc.* **474**, 3043–3066 (2018).
31. R. B. Metcalf *et al*., GLENCO/GLAMER, version 1.2 (2020); https://doi.org/10.5281/zenodo.3702320.
32. M. Meneghetti, G. Davoli, GGSLcalculator v1.0.0 (2020); https://doi.org/10.5281/zenodo.3935514.

ACKNOWLEDGMENTS

We thank S. White and F. van den Bosch for insightful discussions. We also thank G. Murante for sharing the numerical simulations and A. Benitez-Llambay for making public his code PYSPHVIEWER. **Funding:** This work was performed in part at Aspen Center for Physics, which is supported by National Science Foundation grant PHY-1607611. We acknowledge support from the Italian Ministry of Foreign Affairs and International Cooperation, Directorate General for Country Promotion, from PRIN-MIUR 2015W7KAWC, from PRIN-MIUR 2017WSCC32, from PRIN MIUR 2017-20173ML3WW_001, from ASI through grant ASI-INAF n. 2018-23-HH.0 and ASI-INAF n.2017-14-H.0, from INAF (funding of mainstream projects), and from the INFN INDARK grant. P.N. acknowledges support from the Aspen Center for Physics for the workshop titled "Progress after Impasse: New Frontiers in Dark Matter" in Summer 2019 and the Space Telescope Science Institute grant HST-GO-15117.021. C.G. acknowledges support by VILLUM FONDEN Young Investigator Programme through grant no. 10123. S.B. acknowledges financial support from the EU H2020 Research and Innovation Programme under the ExaNeSt project (grant agreement no. 671553). **Author contributions:** M.M. coordinated the project, performed the lensing analysis of the simulated clusters, measured the lensing cross sections and probabilities of both simulated halos and observed clusters, and contributed to the modeling of the observed clusters. G.D. developed the algorithm to measure the lensing cross sections. P.B., P.R., G.B.C., A.M., and C.G. built the strong lensing models and the spectroscopic catalogs of MACSJ1206, AS1063, and MACSJ0416 and of the "Gold" CLASH sample. C.G. performed the MOKA simulations of MACSJ1206 and analyzed the subhalo catalogs of the simulated clusters. P.N., F.C., and E.V. contributed to the analysis of the simulations and to the interpretation of the results. E.R. and S.B. produced the numerical simulations and the subhalo catalogs. R.B.M. produced the multilens plane simulations used to test effects of matter along the line of sight. M.M., P.N., and F.C. wrote the manuscript, including contributions from all the other authors. **Competing interests:** The authors declare no competing interests. **Data and materials availability:** Our simulation snapshots and simulated subhalo catalogs (both in GADGET file format), along with lens models for the clusters in the reference and CLASH Gold samples (as LENSTOOL parameter files), are available at https://dx.doi.org/10.20371/INAF/DS/2020_00001. The lens models of the clusters in the HFF sample were taken from https://archive.stsci.edu/prepds/frontier/lensmodels/; we used version v4 of the CATS and Sharon maps. The GLAMER software for ray-tracing and the code used to measure the GGSL cross sections are available at Zenodo (*31*, *32*).

SUPPLEMENTARY MATERIALS

science.sciencemag.org/content/369/6509/1347/suppl/DC1
Materials and Methods
Table S1
Figs. S1 to S12
References (*33*–*110*)

9 July 2019; accepted 27 July 2020
10.1126/science.aax5164

TROPHIC CASCADES

Keystone predators govern the pathway and pace of climate impacts in a subarctic marine ecosystem

Douglas B. Rasher[1]*, Robert S. Steneck[2], Jochen Halfar[3], Kristy J. Kroeker[4], Justin B. Ries[5], M. Tim Tinker[4,6], Phoebe T. W. Chan[3,7], Jan Fietzke[8], Nicholas A. Kamenos[9], Brenda H. Konar[10], Jonathan S. Lefcheck[11], Christopher J. D. Norley[12], Benjamin P. Weitzman[10,13], Isaac T. Westfield[5], James A. Estes[4]

Predator loss and climate change are hallmarks of the Anthropocene yet their interactive effects are largely unknown. Here, we show that massive calcareous reefs, built slowly by the alga *Clathromorphum nereostratum* over centuries to millennia, are now declining because of the emerging interplay between these two processes. Such reefs, the structural base of Aleutian kelp forests, are rapidly eroding because of overgrazing by herbivores. Historical reconstructions and experiments reveal that overgrazing was initiated by the loss of sea otters, *Enhydra lutris* (which gave rise to herbivores capable of causing bioerosion), and then accelerated with ocean warming and acidification (which increased per capita lethal grazing by 34 to 60% compared with preindustrial times). Thus, keystone predators can mediate the ways in which climate effects emerge in nature and the pace with which they alter ecosystems.

Predator loss and climate change are defining features of the Anthropocene (*1*–*6*). However, these processes have mostly been explored independently even in well-studied ocean ecosystems where the impacts of predator loss and climate change are both pronounced (*5*, *7*). Because the interplay between these processes and their combined impacts are largely unknown, our ability to predict the mode and pace of ecosystem change in the Anthropocene is limited. Here, we address this limitation by revealing how keystone predator loss and climate change are together reshaping kelp forests of the remote Aleutian archipelago (*8*, *9*) (Fig. 1A).

Aleutian kelp forests are built upon a vast framework of *Clathromorphum nereostratum*, a long-lived red alga that forms massive limestone structures covering 50 to 100% of the shallow seafloor (Fig. 1B). These living reefs, assembled slowly (~0.35 mm of vertical growth/year) over centuries to millennia (*10*), serve as a habitat to many other species (*11*). They dominate the seafloor when kelp forests prevail (*12*) and have persisted through recent centuries when this ecosystem was deforested by herbivores, principally because the alga's calcified morphology makes it especially resistant to grazing (*13*). Like tropical corals (*14*), however, this calcifying reef builder may be especially sensitive to climate-induced changes in seawater temperature and acidity (*15*), and the alga's skeleton indeed appears to have weakened in recent decades (*16*). Moreover, sea otters (*Enhydra lutris*), which maintain Aleutian kelp forests through a trophic cascade (*8*), have rapidly disappeared from southwest Alaska over the past 30 years (table S1) perhaps because of increased predation by killer whales (*9*), which ostensibly shifted their diet in response to industrial whaling (*17*). With this collapse, the sea otter's main prey, the herbivorous sea urchin *Strongylocentrotus polyacanthus*, proliferated and denuded the region of kelp (table S2). We thus hypothesized that *C. nereostratum* reefs may now be susceptible to rapid destruction through overgrazing, given that (i) sea urchins, the system's only major herbivore, are now hyperabundant; (ii) the alga's skeleton weakened rapidly in the early 2000s (*16*), which could have increased the intensity (depth/bite) with which sea urchins can graze (*13*) and thus the lethality of grazing in recent time; and (iii) warming is postulated to elevate herbivore grazing rates in the ocean (*18*). To evaluate this hypothesis, we surveyed multiple islands across >700 km of the archipelago (Fig. 1A), quantifying the impacts of sea urchin grazing on *C. nereostratum* from 2014 to 2017; reconstructed the history of sea urchin grazing frequency on *C. nereostratum* (through grazing scars archived in the alga's skeleton) and modeled the putative drivers of change through time; and used controlled experiments to isolate the manner and degree to which present-day seawater conditions have altered the net impacts of sea urchin grazing relative to the preindustrial era.

Lethal grazing of *C. nereostratum* [i.e., repeated grazing of tissues to a depth of >0.25 mm, far below the regenerative cell layer (*10*, *13*); hereafter referred to as "bioerosion"] was severe and widespread. At each study site in 2014, 40 to 85% of every colony was bioeroded, establishing that much of each colony had lost its living tissue and in turn the capacity to generate new growth (Fig. 1C). Sea urchin grazing scars were up to 2.5 mm deep (Fig. 1D), revealing that up to 7 years of prior algal growth (*10*) can be removed by a single sea urchin bite. Destructive overgrazing was further evidenced by the presence of 40- to 60-mm-deep excavation pits (Fig. 1E) and a relatively reduced algal abundance (Fig. 1F) at Attu and the Semichi Islands, suggesting that decades to centuries of algal growth had already been lost in certain places by 2014. After these observations, we discovered that coralline algal abundance (virtually all *C. nereostratum*) declined across the archipelago during the next 3 years (Fig. 1F) (2014 versus 2017; 25 reefs among $n = 6$ islands, $n = 4$ to 6 sites/island; paired t test: $t = 6.178$, $df = 24$; $P < 0.0001$) such that among all 6 islands, reefs lost on average 24% (± 4 SE; median: 17%) and up to 64% of their total calcified reef framework over the 3-year period. Although marine heat waves occurred across the North Pacific in 2014 and 2015 (*19*), they did not produce local temperatures that would trigger algal mortality (*10*). Overgrazing, but not algal bleaching, was seen during each of our annual surveys, indicating that the most parsimonious driver of the observed reef decline was intense bioerosion.

When sea otters are present at ecologically effective densities (*20*) [six or more individuals per kilometer of coastline (*21*)], they greatly suppress the size and abundance of sea urchins in the ecosystem (*8*). The severe bioerosion of *C. nereostratum* that we are now observing (Fig. 1) is therefore at least partially caused by the functional extinction of this keystone predator (table S1) and the resultant proliferation of large sea urchins (tables S2 and S3), the principal agents of bioerosion (fig. S1). However, unlike in past centuries, when sea otters went functionally extinct because of the maritime fur trade (*22*), their recent population collapse occurred in tandem with rapid ocean warming and acidification due to rising atmospheric P_{CO_2} (*23*). This region has also experienced several ocean heat waves during recent decades (*24*), including in 2014 and 2015 (*19*). The lethal bioerosion that is currently unfolding (Fig. 1) could thus be a function of the interplay among trophic cascades, ocean warming, and ocean acidification. We therefore sought to establish how the process of bioerosion has changed through time and to determine the contributions of each putative driver to that

[1]Bigelow Laboratory for Ocean Sciences, East Boothbay, ME 04544, USA. [2]Darling Marine Center, University of Maine, Walpole, ME 04573, USA. [3]University of Toronto, Mississauga, Ontario L5L 1C6, Canada. [4]University of California Santa Cruz, Santa Cruz, CA 95060, USA. [5]Marine Science Center, Northeastern University, Nahant, MA 01908, USA. [6]Western Ecological Research Center, U.S. Geological Survey, Santa Cruz, CA 95060, USA. [7]Bjerknes Centre for Climate Research, University of Bergen, Bergen 5007, Norway. [8]GEOMAR Helmholtz Centre for Ocean Research, Kiel D-24148, Germany. [9]University of Glasgow, Glasgow, Scotland G12 8QQ, UK. [10]University of Alaska Fairbanks, Fairbanks, AK 99775, USA. [11]Smithsonian Environmental Research Center, Edgewater, MD 21037, USA. [12]University of Western Ontario, London, Ontario N6A 5B7, Canada. [13]Alaska Science Center, U.S. Geological Survey, Anchorage, AK 99508, USA.
*Corresponding author. Email: drasher@bigelow.org

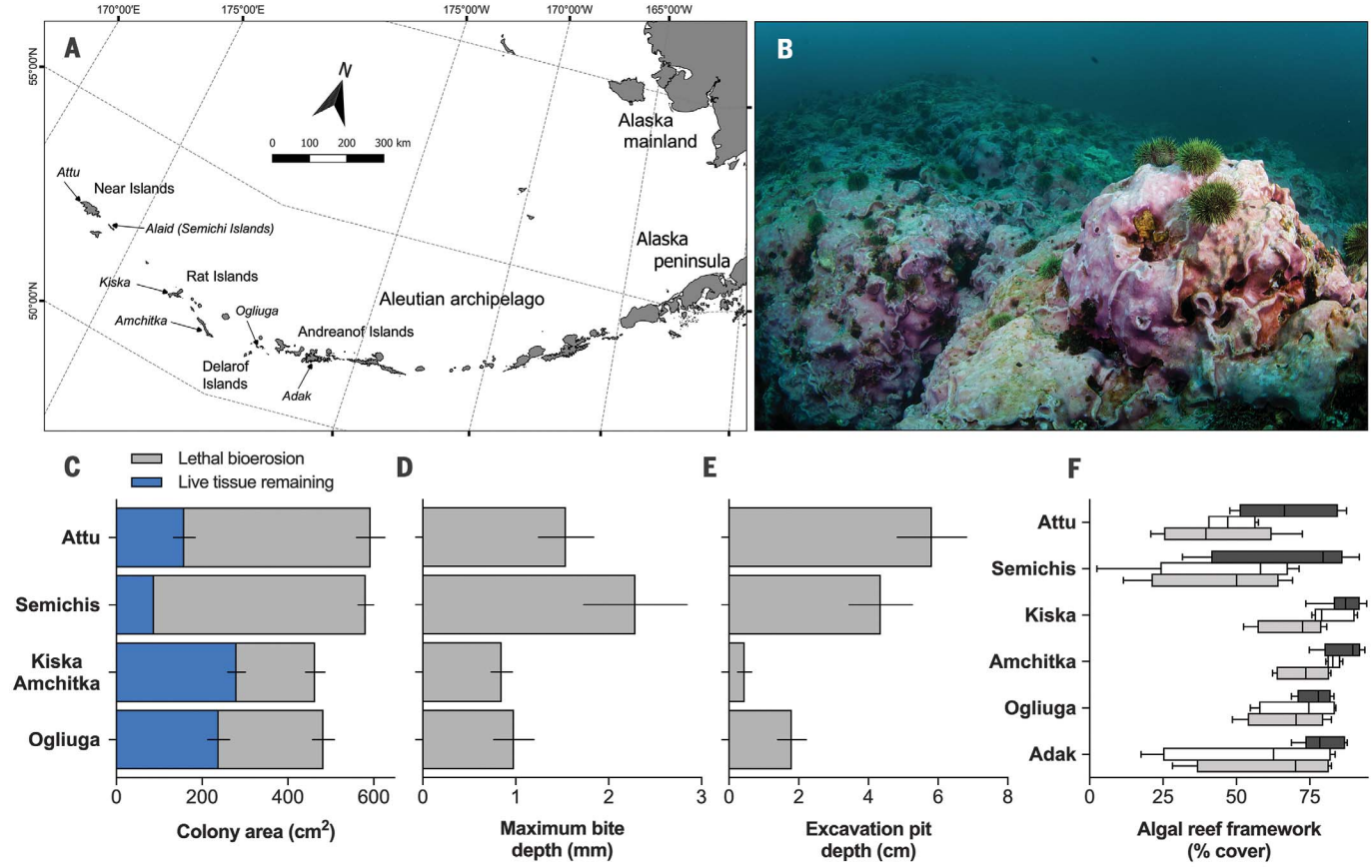

Fig. 1. Erosion of long-lived coralline algal reefs across the Aleutian archipelago. (**A**) Over centuries to millennia, *C. nereostratum* formed massive reefs that structurally underpinned Aleutian kelp forests. (**B**) However, these reefs are now eroding because of overgrazing by sea urchins. (**C**) Area (in square centimeters) of each colony that was grazed to a depth below its regenerative layer (gray bar) versus the area that persisted as living tissue (blue bar). (**D**) Maximum depth (in millimeters) of individual sea urchin bites on each colony. (**E**) Depth (in centimeters) of grazing "excavation pits" on the reef. Bars in (C) to (E) are global means ± SE from each island in 2014 (n = 10 surveys/site; n = 2 sites/island or group; n = 8 sites total). (**F**) Spatial coverage of the coralline algal framework (median and quartiles; whiskers indicate 95% confidence intervals) when assessed at n = 6 islands (n = 20 quadrats/site; n = 4 to 6 sites/island) in 2014 (dark gray bars), 2015 (white bars), and 2017 (light gray bars).

change. To do so, we reconstructed the annual frequency of bioerosion over a 40-year period (1965–2004) through sea urchin grazing scars archived in the skeletons of *C. nereostratum* at Attu, Alaid, Amchitka, and Ogliuga, locations that experienced differing levels of sea otter recovery after cessation of the fur trade but before the recent collapse (*22*). We then modeled the degree to which bioerosion rates were predicted through space and time by the coinciding abundance of sea urchins and by summer sea surface temperatures (SSTs) [note: we focus here on SST because although both seawater temperature and pH are changing because of rising atmospheric P_{CO_2}, only local reconstructions of SST are available (*25*)].

As expected, bioerosion rates through space and time (Fig. 2, A and B, and table S4) were predicted by sea urchin biomass, and thus by sea otter density (*21*). At Amchitka and Ogliuga, islands where sea otters had recovered to near carrying capacity and kelp forests had correspondingly returned by 1965, bioerosion was negligible from 1965 to 1995 (Fig. 2A) but then abruptly increased to high levels thereafter when sea otter populations synchronously collapsed across the region (*22*). At Attu, bioerosion was frequent from 1965 to 1970, when sea otters were absent. Rates then declined over the next 20 years in concert with Attu being repopulated by sea otters (*12*) but returned again to high levels after the aforementioned collapse. Bioerosion at Alaid, an island functionally devoid of sea otters since at least 1912, was frequent throughout the 40-year period. Further, after statistically controlling for the cascading influence of sea otters and sea urchins (Fig. 2B), we discovered that bioerosion covaried positively with SST from 1965 to 2004 (Fig. 2C and table S4). Aleutian SSTs have increased on average 0.5°C since 1965, and this region experienced several warming anomalies during the 20th century (*24*, *25*). Thus, whereas bioerosion was initiated by the loss of sea otters and the resulting trophic cascade, seawater warming appears to have markedly accelerated this process in recent times.

To further establish whether sea urchin grazing has become more lethal to *C. nereostratum* in recent years and to identify the respective roles of seawater temperature versus P_{CO_2} in this process, we cultured *C. nereostratum* and large *S. polyacanthus* for 3 months under an appropriate suite of temperature and P_{CO_2} treatments and then measured the effect of each on the structural integrity of *C. nereostratum* and its susceptibility to sea urchin grazing. Certain treatment combinations mirrored preindustrial, present-day, and predicted near-future mean summer conditions specific to the Aleutians (table S5). Elevating seawater P_{CO_2} reduced the skeletal density of *C. nereostratum*, particularly when temperature was also increased [Fig. 3A and table S6; linear mixed-effects (LME) interaction term: P = 0.007]. Notably, a similar

inverse relationship between skeletal density and seawater temperature has been evident in wild *C. nereostratum* since 1914 (*16*). Elevating temperature increased per capita rates of lethal grazing (LME: $P < 0.001$) irrespective of P_{CO_2} ($P = 0.467$) (Fig. 3B and table S7). Net rates of bioerosion under present-day seawater conditions (470 µatm P_{CO_2}; 6.5 to 8.5°C) were 34 to 60% higher than those seen under preindustrial conditions (340 µatm P_{CO_2}; 6.5°C), suggesting that per capita rates of sea urchin–induced bioerosion are much higher (and thus more lethal) today than they were in the 18th century, a time when sea otters were hunted to near extinction but societies had yet to fully industrialize. Our experiment also suggests that marine heat waves in 2014 and 2015 likely triggered particularly intense bioerosion during those years (i.e., at rates similar to or above those seen at 470 µatm P_{CO_2}; 8.5°C, a 60% increase from preindustrial). Finally, our experiment predicts that without rapid adaptive evolution in *C. nereostratum*, an unlikely event given that it is long-lived and rarely reproduces sexually (*10*), per capita bioerosion will increase another 17 to 39% by the year 2100 with the additional seawater warming (+2°C) and acidification (+360 to 400 µatm P_{CO_2}) projected for this region (*26*, *27*).

Our study reveals that long-lived *C. nereostratum* reefs, which underpin the diversity and stability of Aleutian kelp forests, are in rapid decline. This decline, initiated by a trophic cascade and accelerated by ocean warming and acidification, would have gone undiscovered had we focused solely on the direct effects of climate change on *C. nereostratum* (*15*). Our study reveals that the pathways and pace with which climate change is affecting *C. nereostratum* have been, and will continue to be, contingent upon the outcomes of species interactions, a general dependency that heretofore has neither been widely recognized nor well documented in nature. In the near term, the recovery of Aleutian sea otter populations would effectively buffer this system against a climate-induced decline of its structural foundation. Without sea otter recovery, subtle temperature- and pH-induced changes in *C. nereostratum* and *S. polyacanthus* will continue to amplify "interaction strengths" within the cascade, likely causing *C. nereostratum* reefs to collapse sooner than expected from the direct effects of climate change alone. Studying climate change through an ecological lens is therefore necessary (*28*, *29*) to properly identify its emergent effects and to predict its future impacts.

Our study also highlights the power of trophic cascades in nature (*7*) and the potential for large predators to ameliorate some of the effects of climate change in the near term. Keystone predators are generally thought to act as "biotic multipliers" of climate change (*30*). Our study expands on this view, indicating that in some cases, keystone predators may instead serve as "biotic attenuators" of change and that these predators will amplify or attenuate change only in the places on Earth where they remain at ecologically effective densities (*1*–*3*).

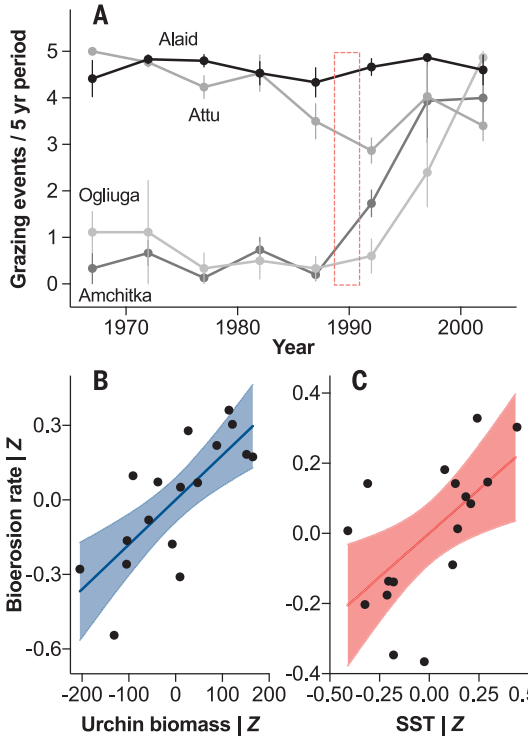

Fig. 2. Historical patterns and causes of bioerosion. (**A**) Annual frequency of sea urchin grazing scars on *C. nereostratum* (mean/5-year period ± SE) from 1965 to 2004 at Attu, Alaid, Amchitka, and Ogliuga (n = 5/island). Rectangle depicts the onset of the recent sea otter decline hindcasted from surveys (*22*). Partial effects plots of (**B**) sea urchin biomass and (**C**) SST reveal their independent effect on bioerosion rate (given the other covariates Z) in the associated model.

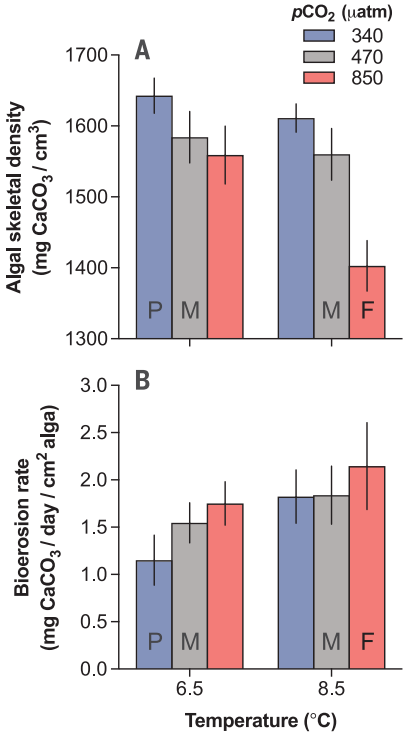

Fig. 3. Effects of seawater temperature and P_{CO_2} on algal integrity and bioerosion rate. (**A**) Skeletal density (in milligrams of $CaCO_3$ per cubic centimeter) of *C. nereostratum* when cultured for 4 months under various temperatures and P_{CO_2} levels, including pairs that represent preindustrial (P), modern (M), and predicted near-future (F) conditions specific to the Aleutian Islands (n = 3/treatment). (**B**) Rate at which large *S. polyacanthus* consumed *C. nereostratum* (in milligrams of $CaCO_3$ per day per square centimeter of alga) during a 20-day grazing assay plotted as a function of the treatments that both experienced for 3 months before and during the assay (n = 9 to 13/treatment). Bars in (A) and (B) are means ± SE.

REFERENCES AND NOTES

1. W. J. Ripple *et al.*, *Science* **343**, 1241484 (2014).
2. R. Dirzo *et al.*, *Science* **345**, 401–406 (2014).
3. D. J. McCauley *et al.*, *Science* **347**, 1255641 (2015).
4. G. T. Pecl *et al.*, *Science* **355**, eaai9214 (2017).
5. T. P. Hughes *et al.*, *Science* **359**, 80–83 (2018).
6. C. M. Free *et al.*, *Science* **363**, 979–983 (2019).
7. J. A. Estes *et al.*, *Science* **333**, 301–306 (2011).

8. J. A. Estes, J. F. Palmisano, *Science* **185**, 1058–1060 (1974).
9. J. A. Estes, M. T. Tinker, T. M. Williams, D. F. Doak, *Science* **282**, 473–476 (1998).
10. W. Adey, J. Halfar, B. Williams, *Smithson. Contrib. Mar. Sci.* **40**, 1–41 (2013).
11. H. Chenelot, S. C. Jewett, M. K. Hoberg, *Mar. Biodivers.* **41**, 413–424 (2011).
12. J. A. Estes, D. O. Duggins, *Ecol. Monogr.* **65**, 75–100 (1995).
13. R. S. Steneck, *Annu. Rev. Ecol. Syst.* **17**, 273–303 (1986).
14. R. Albright *et al*., *Nature* **531**, 362–365 (2016).
15. K. J. Kroeker *et al*., *Glob. Change Biol.* **19**, 1884–1896 (2013).
16. P. T. W. Chan *et al*., *Geology* **48**, 226–230 (2020).
17. A. M. Springer *et al*., *Proc. Natl. Acad. Sci. U.S.A.* **100**, 12223–12228 (2003).
18. I. Nagelkerken, S. D. Connell, *Proc. Natl. Acad. Sci. U.S.A.* **112**, 13272–13277 (2015).
19. E. Di Lorenzo, N. Mantua, *Nat. Clim. Chang.* **6**, 1042–1047 (2016).
20. M. E. Soulé, J. A. Estes, J. Berger, C. M. Del Rio, *Conserv. Biol.* **17**, 1238–1250 (2003).
21. J. A. Estes, M. T. Tinker, J. L. Bodkin, *Conserv. Biol.* **24**, 852–860 (2010).
22. A. M. Doroff, J. A. Estes, M. T. Tinker, D. M. Burn, T. J. Evans, *J. Mammal.* **84**, 55–64 (2003).
23. J. Fietzke *et al*., *Proc. Natl. Acad. Sci. U.S.A.* **112**, 2960–2965 (2015).
24. E. C. J. Oliver *et al*., *Nat. Commun.* **9**, 1324 (2018).
25. B. Huang *et al*., Extended Reconstructed Sea Surface Temperature (ERSST), version 4 (2015); https://10.7289/V5KD1VVF.
26. R. K. Pachauri, L. A. Meyer, "Climate change 2014: Synthesis report" (Geneva, 2014).
27. B. I. McNeil, T. P. Sasse, *Nature* **529**, 383–386 (2016).
28. C. D. G. Harley, *Science* **334**, 1124–1127 (2011).
29. J. L. Blois, P. L. Zarnetske, M. C. Fitzpatrick, S. Finnegan, *Science* **341**, 499–504 (2013).
30. P. L. Zarnetske, D. K. Skelly, M. C. Urban, *Science* **336**, 1516–1518 (2012).

ACKNOWLEDGMENTS

We thank the Alaska Department of Fish and Game for collection permits; the U.S. Fish & Wildlife Service (National Maritime Wildlife Refuge and Marine Mammals Management), the crews of the *R/V Point Sur* and *R/V Tiglax*, the U.S. Geological Survey, and D. Holdsworth for logistical support; M. Kenner, D. Monson, K. Schuster, A. Ravelo, and J. Tomoleoni for collecting field data; the NOAA Kasitsna Bay Laboratory, S. Traiger, and T. Goepfert for laboratory assistance; and R. Pringle for comments that improved the manuscript. Any use of trade, firm, or product names is for descriptive purposes only and does not represent endorsement by the U.S. Government. **Funding:** This work was supported by the U.S. National Science Foundation (grant no. PLR-1316141 to D.B.R., R.S.S., and J.A.E. and grant no. MGG-1459706 to J.B.R.) and the National Sciences and Engineering Council of Canada (discovery grants to J.H. and D.H.). **Author contributions:** D.B.R. conceived the study. D.B.R. designed the study with input from R.S.S., J.B.R., and J.A.E. All authors collected the data. D.B.R., M.T.T., and J.S.L. analyzed the data. D.B.R. wrote the manuscript with contributions from J.A.E. All authors edited the final manuscript. **Competing interests:** The authors declare no competing interests. **Data and materials availability:** The datasets generated for the current study are available in the BCO-DMO public repository (https://www.bco-dmo.org/project/526660).

SUPPLEMENTARY MATERIALS

science.sciencemag.org/content/369/6509/1351/suppl/DC1
Materials and Methods
Fig. S1
Tables S1 to S8
References (*31*–*45*)

24 October 2018; accepted 20 July 2020
10.1126/science.aav7515

STRUCTURAL BIOLOGY

Structural basis of transcription-translation coupling and collision in bacteria

Michael William Webster[1,2,3,4]*, Maria Takacs[1,2,3,4]*, Chengjin Zhu[1,2,3,4], Vita Vidmar[1,2,3,4], Ayesha Eduljee[1,2,3,4], Mo'men Abdelkareem[1,2,3,4], Albert Weixlbaumer[1,2,3,4]†

Prokaryotic messenger RNAs (mRNAs) are translated as they are transcribed. The lead ribosome potentially contacts RNA polymerase (RNAP) and forms a supramolecular complex known as the expressome. The basis of expressome assembly and its consequences for transcription and translation are poorly understood. Here, we present a series of structures representing uncoupled, coupled, and collided expressome states determined by cryo–electron microscopy. A bridge between the ribosome and RNAP can be formed by the transcription factor NusG, which stabilizes an otherwise-variable interaction interface. Shortening of the intervening mRNA causes a substantial rearrangement that aligns the ribosome entrance channel to the RNAP exit channel. In this collided complex, NusG linkage is no longer possible. These structures reveal mechanisms of coordination between transcription and translation and provide a framework for future study.

All organisms express genetic information in two steps. mRNAs are transcribed from DNA by RNA polymerase (RNAP) and then translated by ribosomes to proteins. In prokaryotes, translation begins as the mRNA is synthesized, and the lead ribosome on an mRNA is spatially close to RNAP (*1*, *2*). Coordination of transcription with translation regulates gene expression and prevents premature transcription termination (*3*, *4*). The trailing ribosome inhibits RNAP backtracking, which contributes to the synchronization of transcription and translation rates in vivo and in vitro (*5*–*7*).

Coordination may also involve physical contacts between RNAP and the ribosome. The conserved transcription factor NusG binds RNAP through its N-terminal domain (NusG-NTD) and binds ribosomal protein uS10 through its C-terminal domain (NusG-CTD) both in vitro and in vivo (*8*, *9*). Formation of a NusG-mediated bridge by simultaneous binding has not yet been observed, and the consequences of physical coupling are unknown. RNAP and the ribosome also interact directly (*10*–*12*), and this complex has recently been visualized in situ (*13*). A transcribing-translating expressome complex formed by the collision of ribosomes with stalled RNAP in an in vitro translation reaction was reconstructed at 7.6-Å resolution (*10*). This architecture would not permit a NusG-mediated bridge.

We sought to structurally characterize mechanisms of physical transcription-translation coupling and resolve the relationship between NusG and the collided expressome. Expressomes were assembled by the sequential addition of purified *Escherichia coli* components (70*S* ribosomes, tRNAs, RNAP, and NusG) to a synthetic DNA-mRNA scaffold (fig. S1, A to C). An mRNA with 38 nucleotides separating the RNAP active site from the ribosomal P-site was chosen to imitate a state expected to precede collision (*14*).

A reconstruction of the expressome was obtained at 3.0-Å nominal resolution by cryo–electron microscopy (cryo-EM) (Fig. 1A; fig. S1, D and E; and table S1). RNAP and the ribosome do not adopt a single relative orientation within the expressome, and focused refinement was required to attain a reconstruction of RNAP at 3.8-Å nominal resolution (Fig. 1A and fig. S2; see materials and methods). Refined atomic models collectively present the key steps of prokaryotic gene expression in a single molecular assembly (Fig. 1B).

Direct contacts between RNAP and the ribosome, if they occur, are not stable in this complex, and the mRNA is the only consistent connection. We characterized the dynamics of the complex by plotting the range of RNAP positions relative to the ribosome using the angular assignments of particles from focused reconstructions (Fig. 1C and fig. S3A). RNAP is loosely restrained to a plane perpendicular to an axis connecting the RNAP mRNA exit channel to the ribosomal mRNA entrance channel (movie S1). Within this plane, RNAP rotates freely. Seven clusters represent a series of preferred relative orientations (Fig. 1C and fig. S3A).

RNAP and ribosome models were placed in reconstructions generated from particles in clusters 1 to 6, but a large fraction of cluster 7 was predicted to be incompatible with longer upstream DNA (fig. S3, B to F, and table S2; see materials and methods). Expressome models represent characteristic relative orientations for each cluster, and they collectively suggest a continuous movement of RNAP relative to the ribosome surface involving substantial changes in both rotation (~280°) and translation (~50 Å) (Fig. 1D and movie S1). The closest domain of RNAP to the ribosome is the zinc finger of the β′ subunit (β′-ZF) in all models. In clusters 1 to 3, the β′-ZF sits within a funnel-shaped depression between the head, body, and shoulder domains of the 30*S* subunit, bounded by ribosomal proteins uS3, uS4, and uS5. We predict that RNAP transits from cluster 1 through clusters 2 to 5 to reach positions exemplified by model 6, where the RNAP β′-ZF is between uS3 and uS10 on the 30*S* head domain.

NusG-NTD is bound to RNAP in expressome cluster 6 but not in clusters 1 and 2 (Fig. 1E). We determined that a substantial fraction of the imaged particles lacked NusG because of dissociation during gradient purification (fig. S3G). Notably, the predicted position of the NusG-CTD bound to uS10 (*8*, *9*) is closest to the NusG-NTD bound to RNAP in cluster 6.

An improved reconstruction of the NusG-coupled expressome was obtained from a sample prepared with increased NusG occupancy (Fig. 2A and fig. S4, A and B; see materials and methods). Conformational heterogeneity of the ribosome and RNAP was substantially reduced, but focused refinement was required to obtain well-resolved ribosome and RNAP reconstructions (3.4 and 7.6 Å, respectively) (fig. S4, C to E, and table S1). Continuous density in the unfocused reconstruction confirmed that NusG bridges RNAP and the ribosome (Fig. 2A). We constructed an atomic model of the NusG-coupled expressome by fitting and refining a ribosome model and docking a published RNAP-NusG-NTD model consistent with our map (*15*) into their consensus positions in the unfocused reconstruction (Fig. 2B).

Additional density corresponding to the NusG-CTD bound to uS10 was identified on the ribosome, which otherwise closely resembled that of the uncoupled expressome. The NusG-CTD is a KOW (Kyrpides, Ouzounis, and Woese) domain that consists of a five-stranded β barrel. As in the isolated NusG-uS10 complex, as determined by nuclear magnetic resonance (NMR) (*8*), strand β4 of NusG aligns with strand β4 of uS10, thereby forming an extended intermolecular β sheet (Fig. 2C). However, NusG and uS10 are substantially closer in the expressome than they are in the isolated complex because NusG loops L1 (F141 and F144) and L2 (I164, F165, and R167) insert into a hydrophobic pocket of uS10 that is enlarged by movement of helix α2 (Fig. 2D and fig. S5, A to D). F165 of NusG, in particular, is embedded within uS10. This accounts for its key role in binding uS10, which has been identified by mutational studies (*9*). The altered position of NusG not only increases the area contacting uS10 but avoids clashing with neighboring ribosomal protein uS3 (Fig. 2D).

[1]Department of Integrated Structural Biology, Institut de Génétique et de Biologie Moléculaire et Cellulaire (IGBMC), 67404 Illkirch, France. [2]Université de Strasbourg, 67404 Illkirch, France. [3]CNRS UMR7104, 67404 Illkirch, France. [4]INSERM U1258, 67404 Illkirch, France.
*These authors contributed equally to this work.
†Corresponding author. Email: albert.weixlbaumer@igbmc.fr

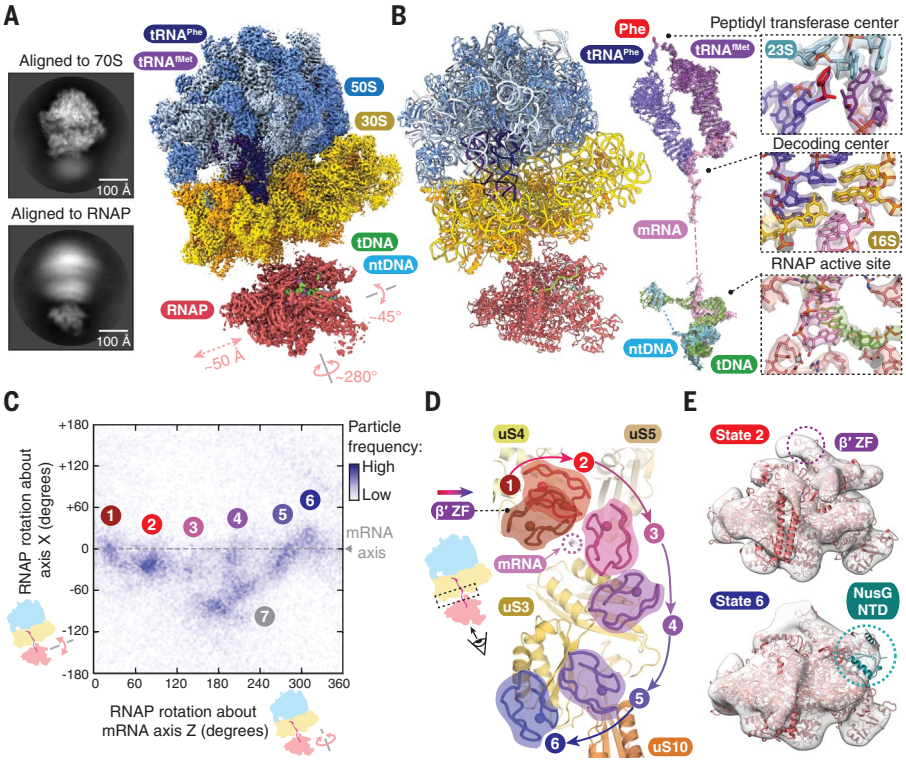

Fig. 1. Structural models of the uncoupled expressome. (**A**) Representative cryo-EM two-dimensional class averages showing conformational variability (left), and cryo-EM maps of the ribosome and RNAP in the uncoupled expressome (right). RNAP is shown in position 2 [see (E)], with measured rotation and translations of RNAP indicated. tDNA, template DNA; ntDNA, nontemplate DNA. (**B**) Atomic model of the uncoupled expressome in ribbon representation (left), and the central steps in gene expression shown by segmented cryo-EM maps with superimposed atomic coordinates (right). (**C**) Plot of RNAP-70S relative orientation with clusters indicating a series of orientations (1 to 6) distinguished by rotation of RNAP. Further characterization of expressome particles resembling cluster 6 (Fig. 2) revealed that these are likely physically coupled through NusG. Cluster 7 primarily includes particles with orientations incompatible with longer upstream DNA, but it also includes states that have been characterized by Wang *et al.* (*26*). (**D**) Representative positions of the RNAP β′-ZF in each expressome model relative to the ribosome surface. (**E**) NusG is present in state 6 (dashed green circle) but not in state 2. The position of β′-ZF is shown (dashed purple circle). The focused cryo-EM maps shown are filtered to 20-Å resolution with fitted coordinates.

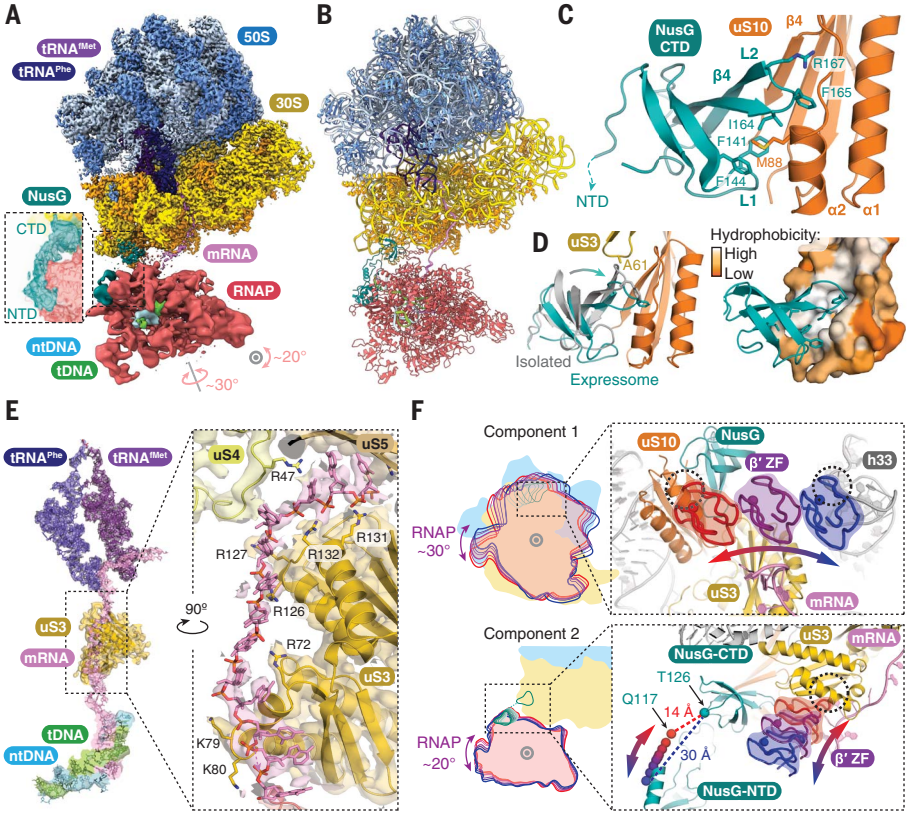

Fig. 2. Structural models of the NusG-coupled expressome. (**A**) Focused cryo-EM maps of the ribosome and RNAP in the NusG-coupled expressome. Inset shows continuous electron density between NusG-NTD and NusG-CTD domains in an unfocused map filtered to 8 Å (slice view). (**B**) Ribbon representations of the NusG-coupled expressome model. (**C**) Interaction of NusG-CTD with ribosomal protein uS10. (**D**) Structural superposition with the isolated NusG-uS10 complex based on alignment to uS10 (gray; PDB code 2KVQ) (left) and hydrophobic pocket created by conformational change of uS10 (right). (**E**) mRNA connecting the ribosome mRNA entrance channel to the RNAP exit channel shown by a cryo-EM map filtered to 4 Å and fitted model. (**F**) The range of RNAP positions relative to the ribosome surface determined by multi-body refinement. Cartoon of two principal components accounting for 44% of variance (left). Component 1 involves rotation in a plane approximately parallel to the surface of the ribosome and is limited by clashes between the β′-ZF of RNAP and either uS10 or h33 (dashed circles). Component 2 is an orthogonal rotation limited by extension of the flexible NusG linker (residues 117 to 126) in one direction (red through purple to blue arrows) and by the clash between β′-ZF and uS3 in the other (dashed circle). Positions of RNAP β′-ZF and NusG residue Q117 indicate trajectories (red through purple to blue arrows). Single-letter abbreviations for the amino acid residues are as follows: A, Ala; C, Cys; D, Asp; E, Glu; F, Phe; G, Gly; H, His; I, Ile; K, Lys; L, Leu; M, Met; N, Asn; P, Pro; Q, Gln; R, Arg; S, Ser; T, Thr; V, Val; W, Trp; and Y, Tyr.

The NusG-CTD recruits Rho to terminate the synthesis of untranslated mRNAs (*16*). In the NusG-coupled expressome, NusG binds uS10 with the same interface it binds Rho, which suggests that the events are mutually exclusive (fig. S5E) (*17*). The structure of the expressome thereby explains how the trailing ribosome is sensed by NusG and how transcription termination is consequently reduced.

The binding of the NusG-NTD to RNAP suppresses backtracking by stabilizing the upstream DNA duplex (*15*, *18*). In the expressome, space for the upstream DNA is further restricted by an extended channel formed by uS10 and NusG (fig. S5F). The interaction of the NusG-CTD with uS10 is predicted to reduce dissociation of NusG-NTD from RNAP through increased avidity (*19*). The RNAP-NusG complex within the coupled expressome is likely stabilized by the trailing ribosome, and transcription elongation is consequently favored.

The mRNA exit channel of RNAP is separated from the entrance channel of the ribosome by ~60 Å. Continuous electron density on the solvent side of uS3 allowed the modeling of the intervening 12 mRNA nucleotides, which completed the mRNA path from synthesis to decoding (Fig. 2E and fig. S6, A to C). The interpretability of the electron density varies considerably, however, and this model is considered one of an ensemble of mRNA conformations.

The RNAP mRNA exit channel is adjacent to uS3 residues R72, K79, and K80, and clear electron density for mRNA in this region suggests a relatively stable contact. The path continues to four arginines immediately outside the ribosomal mRNA entrance channel (R126, R127, R131, and R132) (fig. S6A). R131 and R132 have been previously identified as imparting ribosomal helicase activity (*20*). The mRNA path in this region is close to, but different from, that observed previously in structures of mRNA-bound ribosomes (*21*) (fig. S6, D to F).

Binding of the nascent transcript by uS3 likely modulates secondary structure formation. Structured mRNAs can decrease translation rates (*22*), stabilize transcriptional pauses [e.g., the *E. coli his* pause (*23*)], or induce transcription termination (*24*). Although the ribosome can unwind mRNA secondary structure with basic residues in the mRNA entrance channel (*20*), preventing mRNAs folding downstream likely aids translation efficiency. We propose that by positioning RNAP in line with an extended series of basic residues, NusG helps keep nascent mRNAs single stranded and thereby enhances the efficiency of both transcription and translation.

No stable contacts are observed between the core subunits of RNAP and the ribosome in the NusG-coupled expressome. The relative position of RNAP and the ribosome varies between particles, albeit substantially less than the sample with partial NusG occupancy (fig. S4, A and B). Analysis of movement by multibody refinement (*25*) reveals that RNAP is constrained to avoid clashes between β′-ZF and the cavity formed by uS3, uS10, NusG, and helix 33 of 16*S* rRNA (h33) into which it is inserted (Fig. 2F and movie S2). RNAP is also flexibly tethered to the ribosome by NusG, with the length of the NusG linker (residues 117 to 125) varying in the range of 14 to 30 Å.

To test whether lengthening the intervening mRNA alters the architecture of the expressome, we imaged two samples with four additional mRNA nucleotides (42 in total) separating the RNAP active site from the ribosomal P-site (fig. S7A and table S1). Saturation with NusG increased particle frequencies resembling the NusG-coupled expressome with shorter mRNA, including density linking the complexes (fig. S7, B to E). Compared with shorter mRNA, more particles are observed arranged similarly to cluster 7 of the uncoupled expressome (Fig. 1C). This arrangement is termed transcription-translation complex C (TTC-C) by Wang *et al.* (*26*). However, NusG-CTD is bound to uS10 only in cluster 6 but not cluster 7, which indicates that NusG couples in only one arrangement (fig. S7F).

The mRNA spanning the mRNA exit and entrance channels is in an extended conformation in the NusG-coupled expressome. To test whether coupling by NusG is possible when the spanning mRNA is shorter, we obtained a reconstruction of a NusG-containing expressome with an mRNA shortened to 34 nucleotides between the ribosomal P-site and the RNAP active site (Fig. 3A, fig. S8, and table S1). A model was constructed as described for the coupled expressome (Fig. 3B).

In this model, RNAP is positioned close to the ribosome mRNA entrance channel—more than 50 Å from its location in the NusG-coupled expressome. Consistent with this change, RNAP still binds the NusG-NTD but is no longer tethered through the NusG-CTD to uS10 because the NusG linker (residues 117 to 125; maximum extension of ~30 Å) would need to span an 85- to 145-Å distance. We determined the structure of an equivalent sample lacking NusG and confirmed that the position of RNAP is very similar in this case (fig. S9A and table S1). Therefore, the architecture is not NusG-dependent and is similar to particles from clusters 1 and 2 of the uncoupled expressome (fig. S12). We conclude that RNAP coupling to the ribosome through NusG requires the P-site to be >34 nucleotides from the 3′ end of the mRNA.

The rearrangement of RNAP and the ribosome in our structure with shortened mRNA resembles the expressome formed by the collision of translating ribosomes with stalled RNAP [RNAP backbone root mean square deviation (RMSD) ~3 Å based on 16*S* rRNA superposition] (*10*) (fig. S10, A and B, and fig. S12). We therefore refer to this molecular state as the collided expressome. The previous reconstruction was resolved to 7.6 Å, and

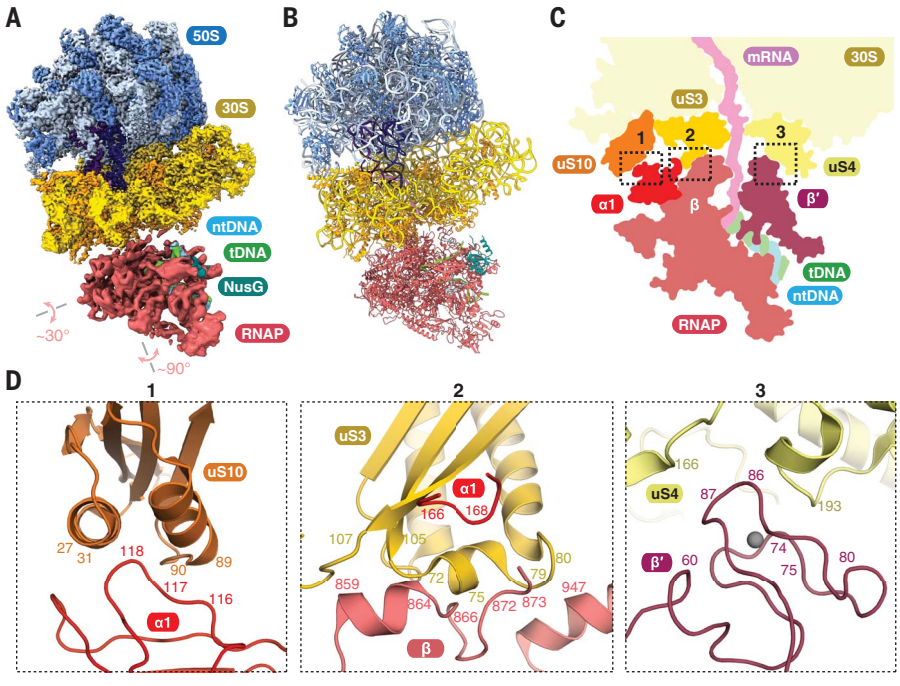

Fig. 3. Structural models of the collided expressome. (**A** and **B**) Cryo-EM map and model of the collided expressome. (**C**) Schematic cross section indicating three regions of close contact between RNAP and ribosome (indicated by dashed rectangles). (**D**) Details of the interaction interfaces of RNAP with the ribosome. Rectangles 1 to 3 correspond to the dashed rectangles in (C).

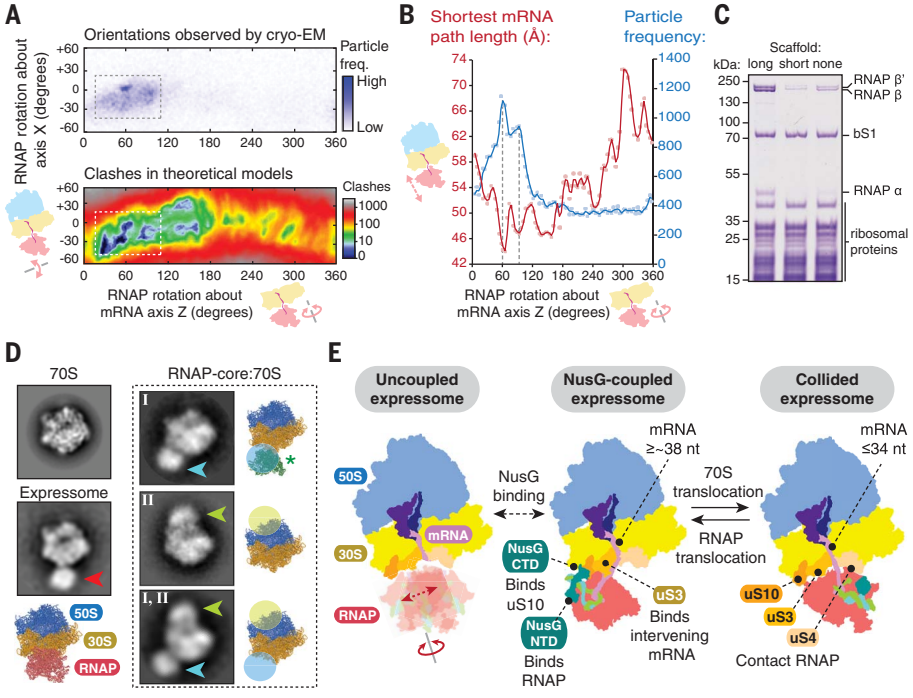

Fig. 4. Formation of RNAP-70S complexes. (**A**) Collided expressome RNAP-70S relative orientations observed by cryo-EM (top) correspond to a restricted space that avoids steric clashes (bottom). freq., frequency. (**B**) The most-common RNAP positions in the collided expressome (blue line) coincide with the minima of the intervening mRNA path length (red line). (**C**) Gradient copurification of RNAP with 70S ribosomes depends on the nucleic acid scaffold. RNAP-70S complexes were formed under low-salt conditions with an mRNA long enough to allow ribosome binding (long), or not long enough to allow ribosome binding (short), or without nucleic acids (none). Coomassie-stained SDS–polyacrylamide gel electrophoresis (SDS-PAGE) of the ribosome-containing sucrose gradient peak is shown. (**D**) Negative stain EM class averages of 70S-RNAP complexes show distinct binding sites for a core RNAP sample (cyan and lime arrowheads) compared with an expressome sample (red arrowhead). The position of RNAP from the 30S-RNAP complex is superimposed (green asterisk). (**E**) Key features and interchange between expressome complexes during transcription-translation coordination. In the uncoupled expressome, RNAP is loosely restrained and adopts various orientations. Coupling by NusG aligns the mRNA with ribosomal protein uS3 and restricts the position of RNAP. Once the ribosome approaches RNAP further, the collided state forms in which the mRNA length is limiting and NusG no longer links the two machineries. nt, nucleotide.

our improved model allowed us to define the interaction surfaces of RNAP and the ribosome in even more detail.

Four regions are in close proximity: uS10 with the NTD of the RNAP α1 subunit, uS3 with RNAP subunits α1 and the β-flap domain, uS4 with β′-ZF, and uS2 with the RNAP ω subunit (Fig. 3, C and D, and fig. S9, B and C). However, density for the ω subunit is very weak, which suggests that partial or complete dissociation occurs upon collision. The contacts bury a total surface area of ~3000 Å^2. However, RNAP moves relative to the ribosome, albeit less than in the samples previously analyzed (fig. S8, B and C). The RNAP-ribosome contacts are likely transient, so the contact area varies. The observed RNAP-ribosome configuration allows notable structural complementarity between the molecular surfaces.

Rotation of RNAP relative to the ribosome beyond the observed position would cause steric clashes (Fig. 4A and fig. S11). We hypothesize that the architecture of the collided expressome is the product of structural complementarity and the energetically favorable minimization of mRNA path length. To test this, we generated ~18,000 hypothetical expressome models representing an exhaustive search of RNAP rotations located about the mRNA axis at a series of distances along it (2° rotational step size, 0.5-Å translational step size). After excluding clashing models, we found that the shortest mRNA path is achieved by the RNAP orientations observed by cryo-EM (Fig. 4B). A simple model is therefore sufficient to explain the observed orientation of RNAP relative to the ribosome: When inserting into the mRNA entrance channel cavity on the ribosome, RNAP adopts an orientation with structural complementarity so that the intervening mRNA spans the shortest distance.

We sought to clarify whether expressome formation is driven by concurrent binding to the same mRNA or whether specific ribosome-RNAP contacts contribute. Copurification of RNAP with ribosomes was substantially reduced when the mRNA did not support concurrent ribosome binding, but RNAP that lacked DNA or mRNA entirely (RNAP-core) bound ribosomes more stably (Fig. 4C and fig. S10, C and D). This observation was previously thought to indicate that expressome formation is not driven by shared mRNA (*10*, *12*).

To examine this, we imaged samples assembled without further purification and lacking nucleic acid scaffolds (RNAP-core-70*S*) by negative stain electron microscopy (EM). No expressomes formed, which suggests that their formation is driven by concurrent mRNA binding and that direct interactions play minor roles. However, we observed at least two alternative RNAP binding sites (Fig. 4D). The sites can be described only approximately from this data, but one (site I) is consistent with an interaction with ribosomal protein uS2 observed in a core RNAP-30*S* complex (*11*). Saturation of ribosomes with ribosomal protein bS1, which has no effect on expressome formation (fig. S13A), abolished the occupancy of site I without affecting the second site (site II). The addition of a nucleic acid scaffold containing just a short mRNA (minimal scaffold) abolished occupancy of site II only, whereas addition of both (short mRNA scaffold and bS1) abolished both (fig. S13). A potential biological role has yet to be shown, but the existence of additional 70*S*-RNAP contact modes highlights the complexity of their interaction.

Thus, the expressome is mRNA-linked and consequently dynamic. A level of structural independence may be required to accommodate internal movements that occur during the reaction cycle of each complex. Coupling by NusG restrains RNAP motions—and happens at variable RNAP ribosome distances (fig. S12)—but not when they collide (Fig. 4E). Relative orientations of the two machineries change in prevalence as a function of their separation (fig. S12). Notably, translation factor binding is compatible with all the observed RNAP orientations. The role of the presented structures in vivo remains to be investigated, and this study provides a basis for elucidating the role of coupling in gene expression, and its regulation by transcription factors and regulatory mRNA structures.

REFERENCES AND NOTES

1. R. Byrne, J. G. Levin, H. A. Bladen, M. W. Nirenberg, *Proc. Natl. Acad. Sci. U.S.A.* **52**, 140–148 (1964).
2. O. L. Miller Jr., B. A. Hamkalo, C. A. Thomas Jr., *Science* **169**, 392–395 (1970).
3. C. Yanofsky, *Nature* **289**, 751–758 (1981).
4. J. P. Richardson, *Cell* **64**, 1047–1049 (1991).
5. S. Proshkin, A. R. Rahmouni, A. Mironov, E. Nudler, *Science* **328**, 504–508 (2010).
6. M. Zhu, M. Mori, T. Hwa, X. Dai, *Nat. Microbiol.* **4**, 2347–2356 (2019).

7. F. Stevenson-Jones, J. Woodgate, D. Castro-Roa, N. Zenkin, *Proc. Natl. Acad. Sci. U.S.A.* **117**, 8462–8467 (2020).
8. B. M. Burmann *et al*., *Science* **328**, 501–504 (2010).
9. S. Saxena *et al*., *Mol. Microbiol.* **108**, 495–504 (2018).
10. R. Kohler, R. A. Mooney, D. J. Mills, R. Landick, P. Cramer, *Science* **356**, 194–197 (2017).
11. G. Demo *et al*., *eLife* **6**, e28560 (2017).
12. H. Fan *et al*., *Nucleic Acids Res.* **45**, 11043–11055 (2017).
13. F. J. O'Reilly *et al*., *Science* **369**, 554–557 (2020).
14. D. Castro-Roa, N. Zenkin, *Nucleic Acids Res.* **40**, e45 (2012).
15. J. Y. Kang *et al*., *Cell* **173**, 1650–1662.e14 (2018).
16. S. L. Sullivan, M. E. Gottesman, *Cell* **68**, 989–994 (1992).
17. M. R. Lawson *et al*., *Mol. Cell* **71**, 911–922.e4 (2018).
18. M. Turtola, G. A. Belogurov, *eLife* **5**, e18096 (2016).
19. G. Vauquelin, S. J. Charlton, *Br. J. Pharmacol.* **168**, 1771–1785 (2013).
20. S. Takyar, R. P. Hickerson, H. F. Noller, *Cell* **120**, 49–58 (2005).
21. H. Amiri, H. F. Noller, *RNA* **25**, 364–375 (2019).
22. X. Qu *et al*., *Nature* **475**, 118–121 (2011).
23. C. L. Chan, R. Landick, *J. Biol. Chem.* **264**, 20796–20804 (1989).
24. I. Gusarov, E. Nudler, *Mol. Cell* **3**, 495–504 (1999).
25. T. Nakane, D. Kimanius, E. Lindahl, S. H. Scheres, *eLife* **7**, e36861 (2018).
26. C. Wang *et al*., *Science* **369**, 1359–1365 (2020).

ACKNOWLEDGMENTS

We thank J. Ortiz, C. Crucifix, X. Guo, and T. C. Cheng for help with data collection at the IGBMC. We thank W. Hagen and F. Weis for help with data collection at the EMBL in Heidelberg, Germany. We thank V. Ramakrishnan and A. C. Kelley for their valuable help in ribosome and tRNA purification. This work has been supported by iNEXT PID 6979, funded by the Horizon 2020 program of the European Union. We acknowledge the European Synchrotron Radiation Facility for the provision of microscope time on CM01, and we thank G. Effantin and M. Hons for their assistance. We thank members of the Weixlbaumer laboratory for critical reading of the manuscript. **Funding:** The authors were supported by the French Infrastructure for Integrated Structural Biology (FRISBI ANR-10-INBS-05, Instruct-ERIC, and grant ANR-10-LABX-0030-INRT, a French State fund managed by the Agence Nationale de la Recherche under the program Investissements d'Avenir ANR-10-IDEX-0002-02). The work was supported by an EMBO long-term fellowship to M.W.W. and the European Research Council starting grant TRANSREG (679734) to A.W. **Author contributions:** M.W.W. and M.T. performed experiments, binding assays, electron microscopy, and data analysis. C.Z. participated in data analysis and purification of NusG. M.W.W., M.T., V.V., A.E., M.A., and A.W. built and refined atomic models. A.W. designed and supervised research. M.W.W., M.T., and A.W. prepared the manuscript with input from all authors. **Competing interests:** The authors declare no competing interests. **Data and materials availability:** Electron density maps for uncoupled, coupled, and collided expressomes (with and without NusG) were deposited in the Electron Microscopy Data Bank (EMD-11418, EMD-11419, EMD-11420, EMD-11421, EMD-11422, EMD-11423, and EMD-11426). Refined coordinates were deposited in the Protein Data Bank database under accession codes 6ZTN (NusG-coupled expressome with RNA-42); 6ZTO, 6ZU1, and 6ZTP (models for uncoupled expressome clusters 1 and 2 and NusG-coupled expressome cluster 6 with RNA-38); 6ZTJ (NusG-coupled expressome with RNA-38); 6ZTL (collided expressome with NusG); and 6ZTM (collided expressome without NusG). Materials are available from the authors on request.

SUPPLEMENTARY MATERIALS

science.sciencemag.org/content/369/6509/1355/suppl/DC1
Materials and Methods
Figs. S1 to S13
Tables S1 and S2
References (*27*–*58*)
MDAR Reproducibility Checklist
Movies S1 to S3

View/request a protocol for this paper from *Bio-protocol*.

28 February 2020; accepted 17 July 2020
Published online 20 August 2020
10.1126/science.abb5036

STRUCTURAL BIOLOGY

Structural basis of transcription-translation coupling

Chengyuan Wang[1]*, Vadim Molodtsov[1]*, Emre Firlar[2], Jason T. Kaelber[2], Gregor Blaha[3], Min Su[4]†, Richard H. Ebright[1]†

In bacteria, transcription and translation are coupled processes in which the movement of RNA polymerase (RNAP)–synthesizing messenger RNA (mRNA) is coordinated with the movement of the first ribosome-translating mRNA. Coupling is modulated by the transcription factors NusG (which is thought to bridge RNAP and the ribosome) and NusA. Here, we report cryo–electron microscopy structures of *Escherichia coli* transcription-translation complexes (TTCs) containing different-length mRNA spacers between RNAP and the ribosome active-center P site. Structures of TTCs containing short spacers show a state incompatible with NusG bridging and NusA binding (TTC-A, previously termed "expressome"). Structures of TTCs containing longer spacers reveal a new state compatible with NusG bridging and NusA binding (TTC-B) and reveal how NusG bridges and NusA binds. We propose that TTC-B mediates NusG- and NusA-dependent transcription-translation coupling.

Bacterial transcription and bacterial translation occur in the same cellular compartment, occur at the same time, and are coordinated processes in which the rate of transcription by the RNA polymerase (RNAP) molecule synthesizing an mRNA is coordinated with the rate of translation by the first ribosome ("lead ribosome") translating the mRNA [(*1*–*9*) but see (*10*)]. Data indicate that the coordination is mediated by transcription elongation factors of the NusG/RfaH family, which contain an N-terminal domain (N) that interacts with RNAP β′ and β subunits and a flexibly tethered C-terminal domain (C) that interacts with ribosomal protein S10. These factors are thought to bridge, and thereby connect, the RNAP molecule and the lead ribosome (*2*, *5*–*9*). Further data indicate that the coordination is modulated by the transcription elongation factor NusA (*11*).

Cramer and colleagues recently reported a 7.6-Å-resolution cryo–electron microscopy (cryo-EM) structure of an *Escherichia coli* transcription-translation complex (TTC) termed the "expressome," obtained by halting a transcription elongation complex (TEC) and allowing a translating ribosome to collide with the halted TEC (*12*). However, the mRNA molecule in the structure was not fully resolved, precluding determination of the number of mRNA nucleotides between the TEC and the ribosome active center in the structure (*12*), and the functional relevance of the structure has been challenged due to its genesis as a collision complex, and due to its incompatibility with simultaneous interaction of NusG-N with RNAP and NusG-C with the ribosome (*6*–*9*). Demo *et al.* recently reported an ~7-Å-resolution cryo-EM structure of a complex of *E. coli* RNAP and a ribosome 30S subunit (*13*). However, the structure did not contain mRNA, did not position RNAP close to the 30S mRNA entrance portal, and was incompatible with the simultaneous interaction of NusG-N with RNAP and NusG-C with the ribosome (*13*).

Here, we report cryo-EM structures of *E. coli* TTCs containing defined-length mRNA spacers between the TEC and the ribosome active-center product site (P site), in both the presence of NusG and absence of NusG (Fig. 1, figs. S1 to S5, and tables S1 and S2). We prepared synthetic nucleic acid scaffolds that contained (i) DNA and mRNA determinants that direct formation of a TEC upon interaction with RNAP, (ii) an mRNA AUG codon that enables formation of a translation complex having the AUG codon positioned in the ribosome active-center P site upon interaction with a ribosome and $tRNA^{fMet}$, and (iii) an mRNA spacer having a length (*n*) of 4, 5, 6, 7, 8, 9, or 10 codons (12, 15, 18, 21, 24, 27, or 30 nt, respectively) between (i) and (ii) (Fig. 1A). We then incubated the nucleic acid scaffolds with RNAP, with ribosome and $tRNA^{fMet}$, and optionally with NusG and/or NusA, and determined structures by single-particle reconstruction cryo-EM (see the materials and methods). With nucleic acid scaffolds having short spacers (n = 4, 5, 6, 7, or 8), we obtained structures matching the expressome of (*12*) (TTC-A; Figs. 1B, left, and 2; figs. S1 to S3; and table S1). However, with nucleic acid scaffolds having longer mRNA spacers (n = 8, 9, or 10), we obtained structures of a new molecular assembly with features strongly suggesting that it functionally mediates NusG-dependent, NusA-dependent transcription-translation coupling in cells (TTC-B; Figs. 1B, center and right, 3, and 4; figs. S3 to S8; table S1; and movies S1 and S2).

TTC-A was obtained with nucleic acid scaffolds having mRNA spacers of 4, 5, 6, 7, or 8 codons, but not with longer mRNA spacers (Figs. 1B, left, and 2; figs. S1 to S3; and table S1). TTC-A was obtained in both the absence and presence of NusG (figs. S1 to S3 and table S1). EM density maps of 3.7 to 6.3 Å resolution were obtained (~7 and ~3.5 Å local resolution for TEC and ribosome, respectively, in the best maps), enabling unambiguous rigid-body docking of atomic structures of TEC, the ribosome 30S subunit, the ribosome 50S subunit with tRNA in the active-center P site and exit site (E site), and, where present, NusG-N, followed by manual fitting of residues in the RNAP-ribosome interface and in DNA and mRNA (Figs. 1B, left, and 2; figs. S1 to S3; and table S1).

Unexpectedly, in TTC-A, the spatial relationship of RNAP relative to the ribosome was identical in structures obtained with nucleic acid scaffolds having mRNA spacer lengths of 4, 5, 6, 7, and 8 codons (fig. S1F). High-resolution data for TTC-A revealed that differences in mRNA spacer length are accommodated through differences in extents of compaction of mRNA in the RNAP RNA-exit channel and RNAP-ribosome interface (Fig. 2B). As mRNA spacer length increases from 4 to 5 to 6 codons, the number of mRNA nucleotides in the RNAP RNA-exit channel and RNAP-ribosome interface increases from 7 nt (5 nt in exit channel; 2 nt in interface) to 10 nt (7 nt in exit channel; 3 nt in interface) to 13 nt (9 nt in exit channel; 4 nt in interface) (Fig. 2B, subpanels 1 to 3), respectively. When the mRNA spacer length increases to 7 or 8 codons, 16 or 19 nt of mRNA, respectively, are accommodated in the RNAP RNA-exit channel and RNAP-ribosome interface, and the 16 or 19 nt of mRNA show disorder, indicating that they adopt an ensemble of different conformations (Fig. 2B, subpanels 4 and 5). The volume of the RNAP RNA-exit channel and RNAP-ribosome interface cannot accommodate more than ~19 nt of mRNA without changing the conformation of the former or disrupting the latter. We suggest that this accounts for our observations that TTC-A is obtained at relatively low particle populations with a nucleic acid scaffold having an mRNA spacer length of 8 codons (18% versus 91% for a nucleic acid scaffold having an mRNA spacer length of 4 codons; figs. S1 and S3) and is not obtained with nucleic acid scaffolds having mRNA spacer lengths >8 codons (figs. S4 and S5). The mRNA spacers analyzed in this work contained only U (Fig. 1A); because U is the RNA nucleotide having the smallest volume, the mRNA spacer length cut-off of 8 codons observed in this work is likely to represent an upper bound.

In TTC-A, the RNAP-ribosome interface is extensive (3742 $Å^2$ buried surface area) and involves contacts of RNAP β′ zinc-binding domain (ZBD), RNAP β flap, and RNAP α^I with

[1]Waksman Institute and Department of Chemistry and Chemical Biology, Rutgers University, Piscataway, NJ 08854, USA. [2]Rutgers New Jersey CryoEM/CryoET Core Facility and Institute for Quantitative Biomedicine, Rutgers University, Piscataway, NJ 08854, USA. [3]Department of Biochemistry, University of California, Riverside, CA 92521, USA. [4]Life Sciences Institute, University of Michigan, Ann Arbor, MI,48109, USA.
*These authors contributed equally to this work.
†Corresponding author. Email: minsu@umich.edu (M.S.); ebright@waksman.rutgers.edu (R.H.E.)

ribosomal proteins S4, S3, and S10, respectively (Fig. 2, C and D).

In EM density maps of TTC-A, density is absent for the RNAP ω subunit, indicating that this subunit is either absent, at a low occupancy level, or disordered (Fig. 2E). Molecular modeling suggests that, if RNAP ω were present and fully folded, then the C-terminal α-helix of ω would clash with the ribosome (Fig. 2E).

In EM density maps of TTC-A obtained in the presence of NusG, EM density is present for NusG-N (residues 1 to 118) at its expected binding location on the RNAP β′ clamp helices and the RNAP β pincer tip [(*14*); Fig. 1B, left, and fig. S1H], but is absent for the NusG linker and NusG-C, consistent with unrestricted motion of the linker and NusG-C relative to NusG-N [(*14*); Fig. 1B, left]. Density maps for TTC-A obtained in the absence of NusG are identical to those obtained in the presence of NusG, except that density for NusG-N is missing (fig. S2). Model building indicates that the shortest sterically allowed distance between NusG-N bound to RNAP and NusG-C modeled as bound to its molecular target on the ribosome, ribosomal protein S10 (*2*, *5*–*9*), is 160 Å in TTC-A; this is 1.9 times the maximum length of the NusG linker, indicating that TTC-A is incompatible with NusG bridging of RNAP and S10 (fig. S9A).

Molecular modeling indicates that TTC-A is also incompatible with other known functional properties of transcription elongation, pausing, and termination in *E. coli*. TTC-A is sterically incompatible with binding of NusA [(*15*); fig. S10A], formation of a 21-Q antitermination complex [(*16*, *17*); fig. S10B], and formation of pause and termination RNA hairpins [(*15*, *18*, *19*); fig. S10, C and D]. TTC-A also appears to be incompatible with ribosome 30S head swiveling, the 21° rotation of the ribosome 30S head relative to the ribosome 30S body that occurs during ribosome translocation [(*20*–*22*); fig. S11A and movie S3]. The RNAP-ribosome interface in TTC-A spans the 30S head and 30S body in the unswiveled state (Fig. 2C and fig. S11A, left) and is expected to be disrupted upon swiveling (loss of 1972 A^2 buried surface area; fig. S11A, right). The finding that TTC-A, the "expressome" of (*12*), lacks the RNAP ω subunit, is incompatible with NusG bridging, and is incompatible with known functional properties of transcription and translation in *E. coli* indicates that TTC-A is unlikely to be functionally relevant to transcription-translation coupling under most conditions in *E. coli*. We propose that TTC-A is either (i) a specialized complex that mediates transcription-translation coupling under specialized circumstances (e.g., transcription-translation coupling by RNAP deficient in ω or by ribosomes inactive in translocation) or (ii) an anomalous complex formed when the mRNA spacer between RNAP and ribosome is anomalously short (e.g., "collisionome" or "crash-ome").

TTC-B was obtained with nucleic acid scaffolds having mRNA spacer lengths of 8, 9, or 10 codons but not with shorter mRNA spacers (Figs. 1B, 3, and 4; figs. S3 to S7; and table S1). TTC-B was obtained only when NusG was present (figs. S3 to S8 and table S1) and was obtained both without and with bound NusA (figs. S3 to S7 and table S1). TTC-B differs from TTC-A by translation of RNAP relative to the

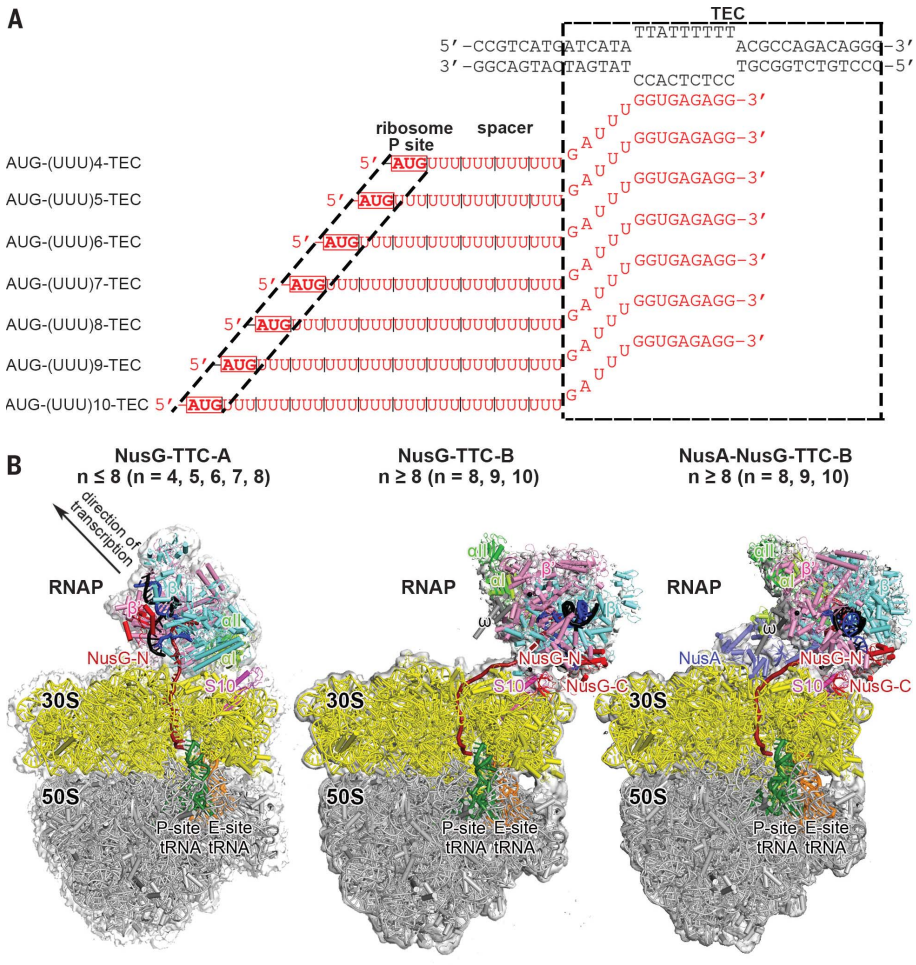

Fig. 1. Structure determination of TTCs. (**A**) Nucleic acid scaffolds. Each scaffold comprises nontemplate- and template-strand oligodeoxyribonucleotides (black) and one of seven oligoribonucleotides having a spacer length *n* of 4, 5, 6, 7, 8, 9, or 10 codons (red), corresponding to mRNA. Dashed black box labeled "TEC" denotes the portion of nucleic acid scaffold that forms the TEC upon addition of RNAP (28 nt nontemplate- and template-strand DNA segments comprising an upstream duplex, a "transcription bubble," and a downstrean duplex; 9 nt of mRNA engaged with template-strand DNA as an RNA-DNA "hybrid"; and 5 nt of mRNA, on the diagonal, in the RNAP RNA-exit channel); dashed black lines labeled "ribosome P-site" denote the mRNA AUG codon intended to occupy ribosome active-center P site upon addition of the ribosome and $tRNA^{fMet}$; "spacer" denotes the mRNA spacer between the TEC and the AUG codon in the ribosome active-center P site. (**B**) Cryo-EM structures of NusG-TTC-A (obtained with spacer lengths of 4 to 8 codons), NusG-TTC-B (obtained with spacer lengths of 8 to 10 codons), and NusA-NusG-TTC-B (obtained with spacer lengths of 8 to 10 codons). Structures shown are NusG-TTC-A (3.7 Å; *n* = 4; table S1), NusG-TTC-B (4.7 Å; *n* = 9; table S1), and NusA-NusG-TTC-B2 (3.5 Å; *n* = 8; table S1). Images show EM density (gray surface) and fit (ribbons) for TEC, NusG, and NusA (at top; direction of transcription, defined by downstream-duplex DNA, indicated by arrow in left panel and directly toward viewer in center and right panels) and for ribosome 30S and 50S subunits and P- and E-site tRNAs (at bottom). RNAP β′, β, α^{I}, α^{II}, and ω subunits are in pink, cyan, light green, and dark green, and gray, respectively; 30S subunit, 50S subunit, P-site tRNA, and E-site tRNA are in yellow, gray, green, and orange, respectively; DNA nontemplate strand, DNA template strand, and mRNA are in black, blue, and brick red (brick-red dashed line where modeled), respectively. NusG, NusA, and ribosomal protein S10 are in red, light blue, and magenta, respectively. The ribosome L7/L12 stalk is omitted for clarity in this and all subsequent images.

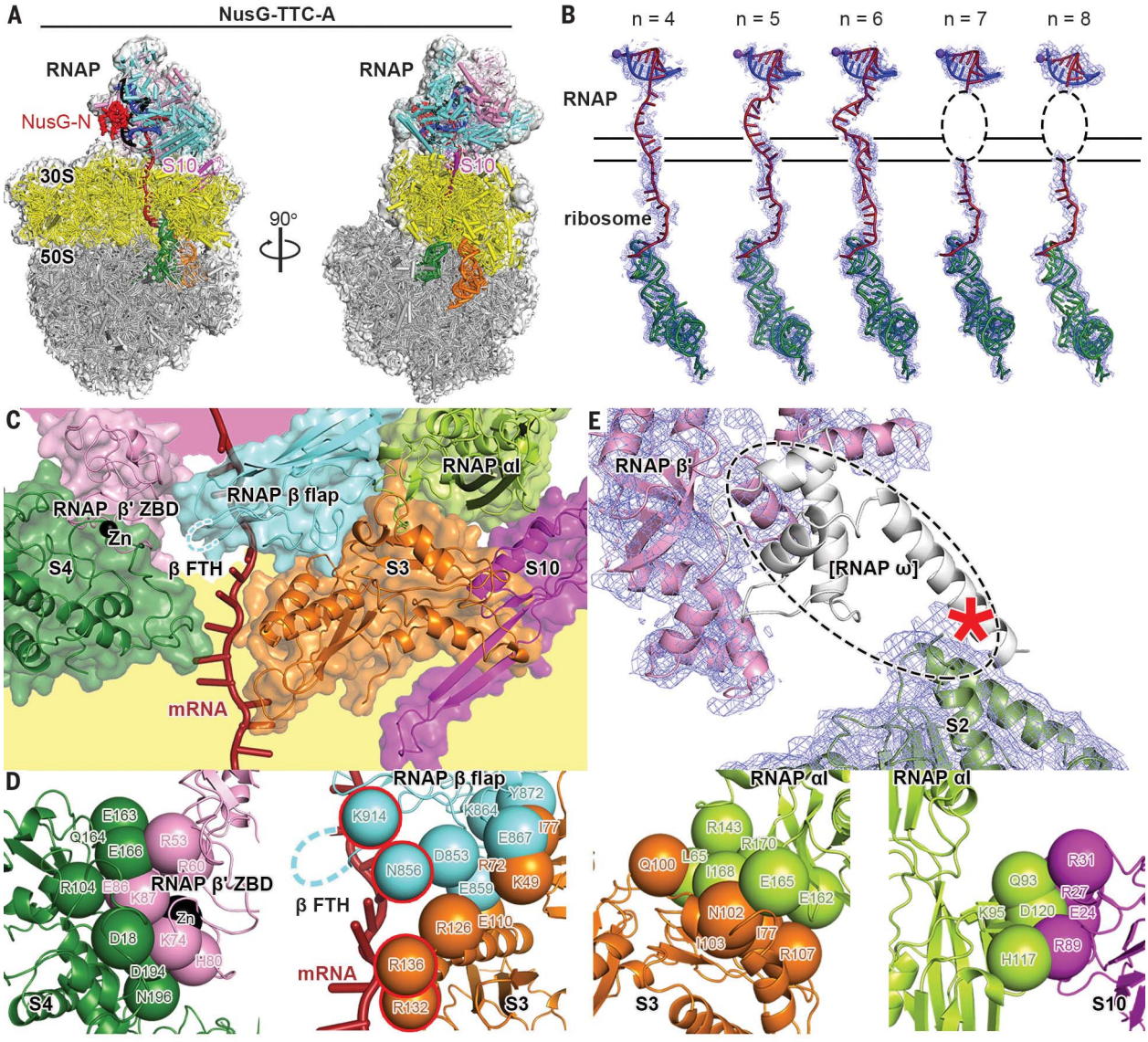

Fig. 2. Cryo-EM structure of NusG-TTC-A. (**A**) Structure of NusG-TTC-A (3.7 Å; n = 4; table S1). Two orthogonal views are shown. Colors are as in Fig. 1B. (**B**) Accommodation of mRNA spacer lengths of 4, 5, 6, 7, and 8 codons in NusG-TTC-A. EM density, blue mesh; mRNA, brick red (disordered mRNA nucleotides indicated by dashed ovals); template-strand DNA in the RNA-DNA hybrid, blue; RNAP active-center catalytic Mg^{2+}, purple sphere; tRNA in ribosome P site, green. Upper and lower black horizontal lines indicate the edges of RNAP and the ribosome. (**C**) RNAP-ribosome interface in NusG-TTC-A (n = 4; identical interface for n = 5, 6, 7, or 8), showing RNAP β′ ZBD (pink; Zn^{2+} ion as black sphere), RNAP β flap (cyan) RNAP β flap tip helix (β FTH; disordered residues indicated by cyan dashed line), and RNAP α^{I} (green) interacting with ribosomal proteins S4 (forest green), S3 (orange), and S10 (magenta) and with mRNA (brick red). Portions of RNAP β′ and ribosome 30S not involved in interactions are shaded pink and yellow, respectively. (**D**) RNAP-ribosome interactions involving RNAP β′ ZBD and S4 (subpanel 1), RNAP β flap and S3 (subpanel 2; β FTH, dashed line; β and S3 residues that interact with mRNA, cyan and orange spheres with red outlines; mRNA, brick red), RNAP α^{I} and S3 (subpanel 3), and RNAP α^{I} and S10 (subpanel 4). Other colors are as in (C). (**E**) Absence of EM density for the RNAP ω subunit. EM density, blue mesh; atomic models for RNAP β′ and S2, pink ribbon and forest-green ribbon, respectively; location of missing EM density for ω, dashed oval; ω in TEC in absence of ribosome [PDB 6P19; (*17*)], white ribbon.

ribosome by ~70 Å and rotation of RNAP relative to the ribosome by ~180° (Fig. 1B and movie S1). EM density maps at 3.1 to 12.6 Å resolution were obtained (~7 and ~3 Å local resolution for TEC and ribosome, respectively, in the best maps), enabling unambiguous rigid-body docking of atomic structures of components, followed by manual fitting (Figs. 3 and 4 and figs. S3 to S7). TTC-B is identical to the NusG-bridged complex reported in a preprint by Weixlbaumer and colleagues (*23*) and is different from the NusA-containing complex reported in a preprint by Mahamid and colleagues (*24*).

Unlike in TTC-A, where the RNAP RNA-exit channel is coupled directly to the ribosome mRNA-entrance portal, in TTC-B, the RNAP RNA-exit channel is separated by ~60 Å from the ribosome mRNA-entrance portal (Fig. 1B). In TTC-B, a ~60-Å, ~11-nt mRNA segment connects the RNAP RNA-exit channel and the ribosome mRNA-entrance portal, running along the surface of the ribosome 30S head, making favorable electrostatic interactions with positively charged residues in ribosomal protein S3 and RNAP β′ ZBD (Figs. 3B and 4B and figs. S3F and S4G). The requirement for this additional ~11-nt mRNA segment accounts for

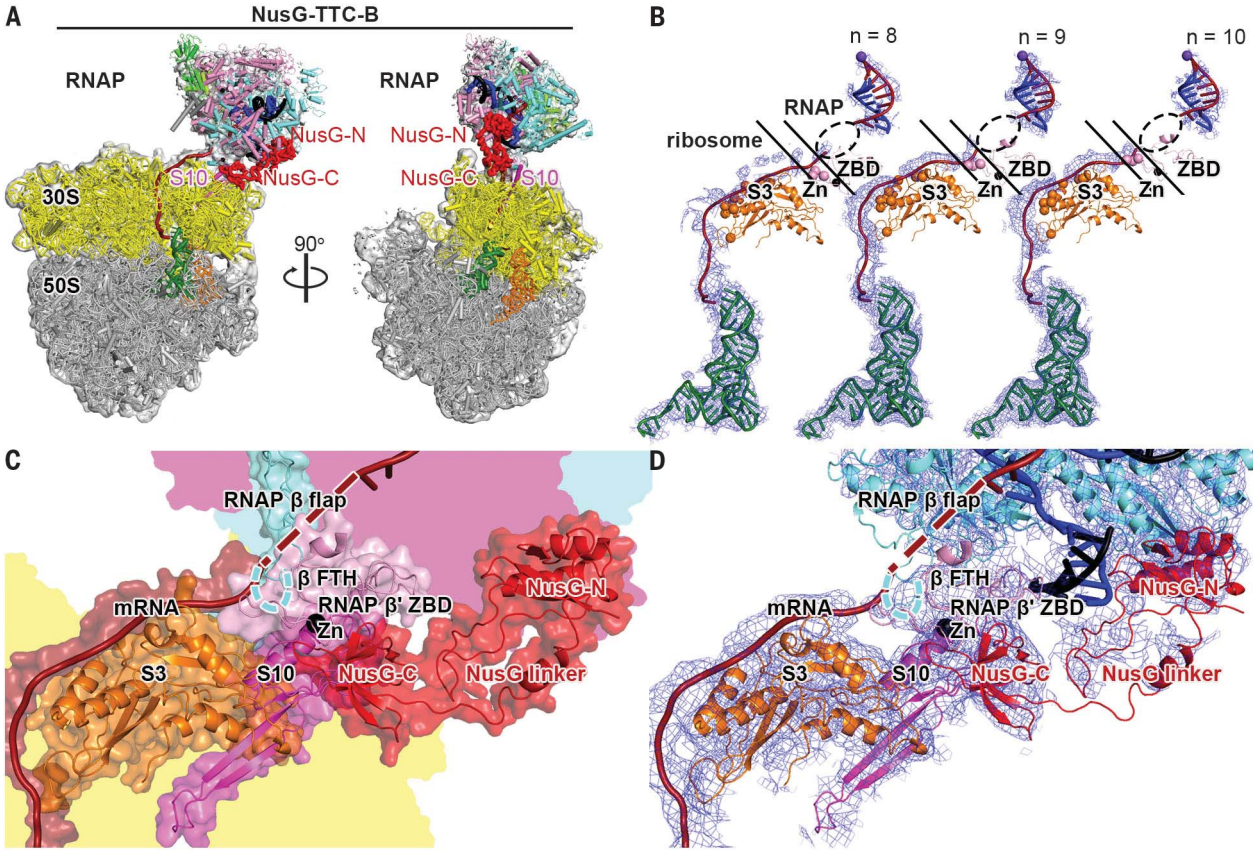

Fig. 3. Cryo-EM structure of NusG-TTC-B. (**A**) Structure of NusG-TTC-B (4.7 Å; *n* = 9; table S1). Views and colors are as in Fig. 2A. (**B**) Accommodation of mRNA spacer lengths of 8, 9, and 10 codons in NusG-TTC-B. EM density, blue mesh; mRNA, brick red (disordered mRNA nucleotides indicated by dashed ovals); template-strand DNA in RNA-DNA hybrid, blue; RNAP active-center catalytic Mg^{2+}, purple sphere; tRNA in ribosome P site, green; ribosomal protein S3, orange (positively charged residues positioned to contact mRNA as orange spheres); RNAP β′ ZBD (pink; Zn^{2+} ion as black sphere; positively charged residues positioned to contact mRNA as pink spheres). Upper and lower black diagonal lines indicate the edges of RNAP and the ribosome. (**C**) RNAP-ribosome interface and NusG bridging in NusG-TTC-B (*n* = 9; identical interface for *n* = 8, 9, or 10). RNAP β′ ZBD (pink; Zn^{2+} ion as black sphere) interacts with ribosomal protein S3 (orange) and mRNA (brick red). NusG (red) bridges RNAP and the ribosome, with NusG-N interacting with RNAP and NusG-C interacting with ribosomal protein S10 (magenta). Portions of RNAP β′, β, and ribosome 30S not involved in interactions are shaded pink, cyan, and yellow, respectively. (**D**) As in (C), showing cryo-EM density as blue mesh.

the fact that TTC-B is obtained only with nucleic acid scaffolds having mRNA spacer lengths ≥8 codons.

In TTC-B, the spatial relationship of RNAP relative to the ribosome is identical in structures obtained with mRNA spacer lengths of 8, 9, and 10 codons (figs. S4F and S5G). Analogously to in TTC-A, in TTC-B, differences in mRNA spacer length are accommodated through differences in extents of compaction of mRNA in the RNAP RNA-exit channel (Figs. 3B and 4B). As mRNA spacer length increases from 8 to 9 to 10 codons, the number of mRNA nucleotides in the RNAP RNA-exit channel increases from ~8 to ~11 to ~14 nt, respectively (disordered in each case; Figs. 3B and 4B). Assuming that the volume of the RNAP RNA-exit channel allows it to accommodate up to ~15 nt of mRNA (see above), it seems likely that mRNA spacer lengths up to ~10 to 11 codons could be accommodated in TTC-B. Noting that the mRNA segments in the RNAP-ribosome interface and near ribosomal protein S3 in TTC-B are solvent accessible, it also seems possible that longer—possibly much longer—mRNA spacer lengths could be accommodated by looping of, or secondary structure formation in, these mRNA segments.

In TTC-B, the interaction between RNAP and the ribosome is small, involving only contact between the RNAP β′ ZBD sequence and ribosomal protein S3 (224-Å^2 buried surface area; Figs. 3, C and D, and 4, C to E).

In TTC-B, the RNAP-ribosome interaction is supplemented by bridging of RNAP and the ribosome by NusG, involving simultaneous binding of NusG-N to RNAP and binding of NusG-C to ribosomal protein S10 (1409-Å^2 buried surface area for NusG-C and S10; Figs. 1B, 3, A, C, and D, and 4, A and C to E; and figs. S3G, S4H, and S9, B and C). NusG-C interacts with S10 in the manner expected from published structures of a complex of NusG and S10 and of a complex of NusG and a ribosome [(*2*, *9*); figs. S3G and S4H). EM density maps show unambiguous density for NusG-N, NusG-C, and most residues of the NusG linker (Figs. 3D and 4D and figs. S3G and S4H), and, at lower contour levels, show density for all residues of the NusG linker (Figs. 3C and 4C). Corresponding EM maps obtained in the absence of NusG do not show TTC-B (fig. S8), indicating that NusG bridging is functionally important for the formation and/or stability of TTC-B. The NusG bridging hypothesized in (*2*) and (*9*) is thus unequivocally verified.

We first obtained structures of TTC-B in the presence of NusG and absence of NusA (NusG-TTC-B; Fig. 3, figs. S3 and S4, and table S1). Molecular modeling indicated that NusG-TTC-B potentially could accommodate binding of NusA (fig. S10A). Therefore, we sought, and obtained,

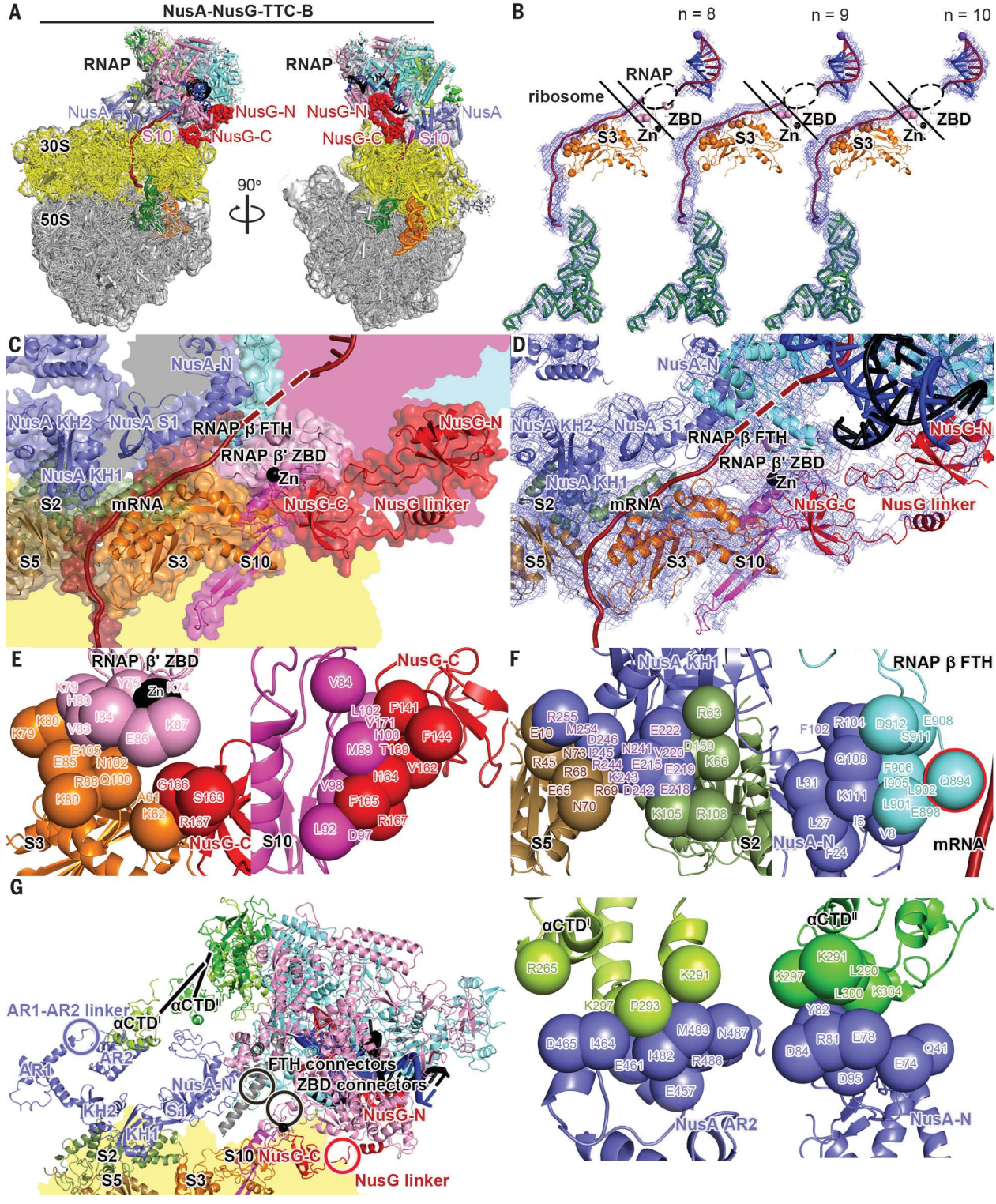

Fig. 4. Cryo-EM structure of NusA-NusG-TTC-B. (**A**) Structure of NusA-NusG-TTC-B (NusA-NusG-TTC-B2; 3.5 Å; *n* = 9; table S1). NusA, light blue. Views and other colors are as in Figs. 2A and 3A. (**B**) Accommodation of mRNA spacer lengths of 8, 9, and 10 codons in NusA-NusG-TTC-B. Views and colors are as in Fig. 3B. (**C**) RNAP-ribosome interface, NusG bridging, and NusA binding in NusA-NusG-TTC-B (*n* = 9; identical interface for *n* = 8, 9, or 10). RNAP β′ ZBD (pink; Zn^{2+} ion as black sphere) interacts with ribosomal protein S3 (orange) and mRNA (brick red). NusG (red) bridges RNAP and ribosome, with NusG-N interacting with RNAP and NusG-C interacting with ribosomal protein S10 (magenta). NusA (light blue) KH1 domain interacts with ribosomal proteins S5 and S2 (brown and forest green, respectively). Portions of RNAP β′, β, ω, and ribosome 30S not involved in interactions are shaded pink, cyan, gray, and yellow, respectively. (**D**) As in (C), showing cryo-EM density as blue mesh. (**E**) RNAP-ribosome interactions involving RNAP β′ ZBD and S3 (subpanel 1) and NusG-ribosome interactions involving NusG-C and S10 (subpanel 2). (**F**) NusA-ribosome interactions involving NusA KH1 and S5 and S2 (subpanel 1) and NusA-RNAP interactions involving NusA-N and

RNAP β FTH (subpanel 2; β FTH residue that interacts with mRNA, cyan sphere with red outline; mRNA, brick red), NusA AR2 and RNAP αCTD^{I} (subpanel 3), and NusA-N and RNAP αCTD^{II} (subpanel 4). (**G**) Points of flexibility in NusA-NusG-TTC-B (NusA coupling pantograph): flexible linkage in NusA structure (AR1-AR2 linker; light blue circle), three flexible linkages between NusA and RNAP (αCTD^{I} linker, αCTD^{II} linker, and β FTH connectors; black lines and black circle), flexible linkage between RNAP and ribosome (β′ ZBD connectors; black circle), and flexible NusG bridging of RNAP and ribosome (NusG linker; red circle).

corresponding structures of TTC-B in the presence of both NusG and NusA (NusA-NusG-TTC-B; Fig. 4, fig. S5, and table S1). Compared to structure determination of TTC-B in the absence of NusA, structure determination in the presence of NusA was associated with substantially higher particle populations (4% versus 45% for n = 8, 18% versus 28% for n = 9, and 17% versus 40% for n = 10) and substantially higher resolutions (12.6 Å versus 3.1 Å for n = 8, 4.7 Å versus 4.2 Å for n = 9, and 5.0 Å versus 3.7 Å for n = 10), indicating that NusA functionally stabilizes TTC-B. Three NusA-NusG-TTC-B subclasses were obtained: TTC-B1, TTC-B2, and TTC-B3, differing by up to 15° rotation of RNAP relative to NusA and ribosome (figs. S5 and S7, A and B, and movie S2).

In all NusA-NusG-TTC-B subclasses, RNAP and NusG interact with the ribosome 30S head, with RNAP β′ ZBD contacting ribosomal protein S3 and NusG contacting ribosomal protein S10 (Fig. 4, C to E, and fig. S6), essentially as in the absence of NusA (Fig. 3, C and D).

In all NusA-NusG-TTC-B subclasses, NusA makes identical—and extensive—interactions with the surface of the ribosome S30 body, involving contacts between NusA KH1 domain and ribosomal proteins S2 and S5 (1755-Å^2 buried surface area; Fig. 4, C to E, and fig. S6). The NusA-ribosome interactions observed here show no similarity to the putative NusA-ribosome interactions reported in (*24*); the orientation of NusA relative to the ribosome differs by ~180°, and the interactions involve a different module of the ribosome 30S subunit (body versus head).

NusA functions in this context as a large, 70 × 50 Å, open rectangular frame that connects RNAP to the ribosome 30S body (Fig. 4G and fig. S7C). One side of the NusA rectangular frame interacts with the ribosome 30S body, and three corners of the NusA rectangular frame interact with RNAP, contacting the RNA α^{I} C-terminal domain (αCTD^{I}), the RNA α^{II} C-terminal domain (αCTD^{II}), and the RNAP β flap-tip helix (FTH) (Fig. 4, F and G, and fig. S7C). The NusA rectangular frame contains an internal flexible linkage, the AR1-AR2 linker (light blue circles in Fig. 4G and fig. S7C), and interacts with RNAP through three flexibly linked modules: αCTD^{I} and αCTD^{II}, which are connected to the rest of RNAP through long, flexible linkers [(*25*); lines in Fig. 4G and fig. S7C], and β FTH, which is connected to the rest of RNAP through flexible connectors [(*15*–*18*); black circle in Fig. 4G and fig. S7C]. The internal flexibility and flexible connections enable the NusA-RNAP subcomplex to maintain constant contact with the ribosome 30S body despite differences in the orientation of RNAP relative to the ribosome 30S body (fig. S7C and movie S2). We refer to the NusA rectangular frame as the "coupling pantograph," analogizing it to an electric-railway coupling pantograph, the open rectangular frame with internal flexibility and flexible connections that enables a locomotive to maintain constant contact with a power cable despite differences in orientation of the locomotive relative to the cable [(*26*); fig. S7C and movie S2].

The separation between the RNAP RNA-exit channel and the ribosome mRNA entry portal in TTC-B, together with the open character of the NusA rectangular frame (coupling pantograph) in TTC-B, provides largely unrestricted access for transcriptional-regulatory factors to bind, and transcriptional-regulatory RNA secondary structures to form, at and adjacent to the mouth of the RNAP RNA-exit channel (fig. S10). Molecular modeling indicates that TTC-B, unlike TTC-A, can accommodate formation of the 21-Q antitermination complex [(*16*, *17*); fig. S10B) and can accommodate formation of pause and termination RNA hairpins [(*15*, *18*, *19*); fig. S10, C and D]. In NusA-NusG-TTC-B, positively charged residues of the NusA N and S1 domains are positioned to make favorable electrostatic interactions with the hairpin loop of a pause or termination RNA hairpin, and thereby potentially to nucleate formation of a pause or termination RNA hairpin [(*15*); fig. S7D]. The different orientations of NusA N and S1 domains in NusA-NusG-TTC-B subclasses B1, B2, and B3 possibly enable interactions with different-length pause and termination RNA hairpins, with B1 accommodating shorter hairpins and B2 and B3 accommodating longer hairpins (fig. S7D).

Molecular modeling also indicates that TTC-B, unlike TTC-A, is compatible with ribosome 30S head swiveling, the rotation of the 30S head relative to the 30S body that occurs during ribosome translocation [(*20*–*22*); fig. S11, B and C, and movies S4 and S5]. In NusG-TTC-B, all RNAP-ribosome and NusG-ribosome interactions involve the ribosome 30S head; accordingly, 30S head swiveling can be accommodated by rotation of RNAP and NusG with the 30S head (fig. S11B, center, and movie S5) and/or by separate rotation of flexibly connected RNAP β′ ZBD and flexibly connected NusG-C with the 30S head (fig. S11B, right, and movie S4). In NusA-NusG-TTC-B, NusA-ribosome interactions involve the ribosome 30S body, and RNAP-ribosome and NusG-ribosome interactions involve the ribosome 30S head; nevertheless, exploiting the internal flexibility and flexible connections of the NusA-RNAP coupling pantograph, 30S head swiveling can be accommodated by rotation of RNAP and NusG with the 30S head (fig. S11B, center, and movie S5) and/or by separate rotation of flexibly connected RNAP β′ ZBD and flexibly connected NusG-C with the 30S head (fig. S11B, right, and movie S5).

Based on the observation that TTC-B is compatible with NusG bridging, NusA binding, known functional aspects of transcription, and known functional aspects of translation, we propose that TTC-B modulates NusG-dependent, NusA-dependent transcription-translation coupling in *E. coli*.

The structures presented were determined in the presence of CHAPSO, a nonionic detergent that has been used extensively in cryo-EM structural analysis of RNAP and RNAP complexes to improve structural homogeneity by disrupting nonspecific complexes and weak complexes, and by improving rotational orientation distributions of particles by reducing interactions with the air-water interface (*14*–*18*). Analogous structure determination in the absence of CHAPSO yielded low-resolution maps of TTC-A for nucleic acid scaffolds with mRNA spacer lengths of 4, 5, 6, and 7 codons (figs. S12 and S13, table S2, and movie S6) and of two additional complexes, TTC-C and TTC-D, for nucleic acid scaffolds with mRNA spacer lengths of 7, 8, and 9 codons (figs. S13 to S16, table S2, and movies S7 to S11). The fact that TTC-C and TTC-D are observed only in the absence of CHAPSO suggests that TTC-C and TTC-D may involve relatively weak interactions. In TTC-C and TTC-D, interactions between RNAP and ribosome are mediated by RNAP β sequence insert 2 [βSI2; also known as βi9 (*27*, *28*)], a 60-Å-long α-helical antiparallel coiled coil flexibly tethered to the rest of RNAP, and the main interaction is an electrostatic interaction between the tip of βSI2 and the ribosome 30S subunit (figs. S15 and S16). In TTC-C, the orientation of RNAP relative to the ribosome is compatible with NusG bridging (fig. S15), and in TTC-D, the orientation of RNAP relative to the ribosome is incompatible with NusG bridging (fig. S16). The structures suggest that TTC-C and TTC-D could play roles in NusG-dependent and NusG-independent transcription-translation coupling, respectively. The structural module that mediates the RNAP-ribosome

interaction in TTC-C and TTC-D, βSI2, is not essential for growth in rich media (*26*), but is essential for growth in minimal media (*26*), implying that TTC-C and TTC-D are unlikely to be important for transcription-translation coupling in general, but may be important for transcription-translation coupling in specific transcription units in specific regulatory contexts (*6*). Further analysis will be needed to determine whether, and, if so, in which contexts, TTC-C and TTC-D function in transcription-translation coupling in *E. coli*.

The results presented here define four structural classes of TTCs: TTC-A [the previously reported expressome; (*12*)], TTC-B, TTC-C, and TTC-D, and show that TTC-B has structural properties indicating that it mediates NusG-dependent, NusA-dependent transcription-translation coupling in *E. coli*.

The results presented reframe our understanding of the structural and mechanistic basis of transcription-translation coupling. The results provide high-resolution structures of the previously described expressome [(*12*); TTC-A] that demonstrate its incompatibility with general transcription-translation coupling. In addition, the results provide high-resolution structures of a new structural state, TTC-B, with properties assignable to general, NusG-dependent, NusA-dependent transcription-translation coupling. Our results also show that NusG stabilizes TTC-B by bridging RNAP and the ribosome 30S head, that NusA stabilizes TTC-B by bridging RNAP and the ribosome 30S body, and that NusA serves as a coupling pantograph that bridges RNAP and the ribosome 30S body in a flexible manner that allows rotation of RNAP relative to the ribosome 30S body. Finally, the results provide testable new hypotheses regarding the identities of the RNAP and NusA structural modules crucial for transcription-translation coupling (RNAP β′ ZBD and NusA KH1) and the interactions made by those structural modules (interactions with ribosomal protein S3 in the S30 head and interactions wit1h ribosomal proteins S2 and S5 in the S30 body).

REFERENCES AND NOTES

1. O. L. Miller Jr., B. A. Hamkalo, C. A. Thomas Jr., *Science* **169**, 392–395 (1970).
2. B. M. Burmann *et al*., *Science* **328**, 501–504 (2010).
3. S. Proshkin, A. R. Rahmouni, A. Mironov, E. Nudler, *Science* **328**, 504–508 (2010).
4. D. Castro-Roa, N. Zenkin, *Nucleic Acids Res.* **40**, e45 (2012).
5. K. McGary, E. Nudler, *Curr. Opin. Microbiol.* **16**, 112–117 (2013).
6. I. Artsimovitch, *Mol. Microbiol.* **108**, 467–472 (2018).
7. S. Saxena *et al*., *Mol. Microbiol.* **108**, 495–504 (2018).
8. F. Stevenson-Jones, J. Woodgate, D. Castro-Roa, N. Zenkin, *Proc. Natl. Acad. Sci. U.S.A.* **117**, 8462–8467 (2020).
9. R. Washburn *et al*., *iScience* **23**, 101352 (2020).
10. M. Chen, K. Fredrick, *Proc. Natl. Acad. Sci. U.S.A.* **115**, 10774–10779 (2018).
11. M. Strauß *et al*., *Nucleic Acids Res.* **44**, 5971–5982 (2016).
12. R. Kohler, R. A. Mooney, D. J. Mills, R. Landick, P. Cramer, *Science* **356**, 194–197 (2017).
13. G. Demo *et al*., *eLife* **6**, e28560 (2017).
14. J. Y. Kang *et al*., *Cell* **173**, 1650–1662 (2018).
15. X. Guo *et al*., *Mol. Cell* **69**, 816–827 (2018).
16. J. Shi *et al*., *Nat. Commun.* **10**, 2925 (2019).
17. Z. Yin, J. T. Kaelber, R. H. Ebright, *Proc. Natl. Acad. Sci. U.S.A.* **116**, 18384–18390 (2019).
18. J. Y. Kang *et al*., *Mol. Cell* **69**, 802–815.e5 (2018).
19. J. W. Roberts, *J. Mol. Biol.* **431**, 4030–4039 (2019).
20. B. S. Schuwirth *et al*., *Science* **310**, 827–834 (2005).
21. A. Ratje *et al*., *Nature* **486**, 714–716 (2010).
22. Z. Guo, H. F. Noller, *Proc. Natl. Acad. Sci. U.S.A.* **109**, 20391–20394 (2012).
23. M. Webster *et al*., bioRxiv 971028 [Preprint]. 2 March 2020; https://doi.org/10.1101/2020.03.01.971028.
24. F. O'Reilly *et al*., *Science* **369**, 554 (2020).
25. E. E. Blatter, W. Ross, H. Tang, R. L. Gourse, R. H. Ebright, *Cell* **78**, 889–896 (1994).
26. Wikipedia, "Pantograph (transport)"; https://en.wikipedia.org/wiki/Pantograph_(transport).
27. I. Artsimovitch, V. Svetlov, K. S. Murakami, R. Landick, *J. Biol. Chem.* **278**, 12344–12355 (2003).
28. W. J. Lane, S. A. Darst, *J. Mol. Biol.* **395**, 671–685 (2010).

ACKNOWLEDGMENTS

We thank the Rutgers University Cryo-EM Core facility, the University of Michigan Life Sciences Institute Cryo-EM Facility, the National Center for Cryo-EM Access and Training (supported by NIH grant no. GM129539, Simons Foundation grant SF349247, and New York state grants), and the Pacific Northwest Center for Cryo-EM (supported by NIH grant no. GM129547 and Department of Energy Environmental Molecular Sciences Laboratory) for microscope access; K. Kuznedelov and K. Severinov for plasmids; L. Minakhin, B. Nickels, and J. Winkelman for discussion; and E. Eng and H. Wei for assistance. **Funding:** This work was supported by University of California discretionary funds to G.B., University of Michigan discretionary funds to M.S., and NIH grant no. GM041376 to R.H.E. **Author contributions:** V.M. and G.B. prepared biomolecules. C.W., V.M., E.F., J.K., and M.S. collected data. C.W., V.M., J.K., M.S., and R.H.E. analyzed data. C.W., V.M., and R.H.E. prepared figures. R.H.E. designed experiments and wrote the manuscript. **Data and materials availability:** Cryo-EM micrographs have been deposited in the Electron Microscopy Public Image Archive Resource (EMPIAR accession codes 10467 and 10468). Cryo-EM maps and atomic models have been deposited in the Electron Microscopy Database (EMDB accession codes 21386, 21468, 21469, 21470, 21471, 21472, 21474, 21475, 21476, 21477, 21482, 21483, 21485, 21486, 21494, 22082, 22084, 22087, 22107, 22141, 22142, 22181, 22192, and 22193) and the Protein Data Bank (PDB accession codes 6VU3, 6VYQ, 6VYR, 6VYS, 6VYT, 6VYU, 6VYW, 6VYX, 6VYY, 6VYZ, 6VZJ, 6VZ2, 6VZ3, 6VZ5, 6VZ7, 6XDQ, 6XDR, 6XGF, 6XII, 6XIJ, 6X6T, 6X7F, 6X7K, and 6X9Q). Materials are available from the authors on request.

SUPPLEMENTARY MATERIALS

science.sciencemag.org/content/369/6509/1359/suppl/DC1
Materials and Methods
Figs. S1 to S16
Tables S1 and S2
References (*29*–*51*)
Movies S1 to S11
MDAR Reproducibility Checklist

View/request a protocol for this paper from *Bio-protocol*.

2 March 2020; accepted 17 July 2020
Published online 20 August 2020
10.1126/science.abb5317

ULTRACOLD PHYSICS

Direct laser cooling of a symmetric top molecule

Debayan Mitra*†, Nathaniel B. Vilas†, Christian Hallas, Loïc Anderegg, Benjamin L. Augenbraun, Louis Baum, Calder Miller, Shivam Raval, John M. Doyle

Ultracold polyatomic molecules have potentially wide-ranging applications in quantum simulation and computation, particle physics, and quantum chemistry. For atoms and small molecules, direct laser cooling has proven to be a powerful tool for quantum science in the ultracold regime. However, the feasibility of laser-cooling larger, nonlinear polyatomic molecules has remained unknown because of their complex structure. We laser-cooled the symmetric top molecule calcium monomethoxide ($CaOCH_3$), reducing the temperature of ~10^4 molecules from 22 ± 1 millikelvin to 1.8 ± 0.7 millikelvin in one dimension and state-selectively cooling two nuclear spin isomers. These results demonstrate that the use of proper ro-vibronic transitions enables laser cooling of nonlinear molecules, thereby opening a path to efficient cooling of chiral molecules and, eventually, optical tweezer arrays of complex polyatomic species.

Laser cooling of atomic systems has enabled substantial advances in quantum simulation, precision clocks, and quantum many-body physics (*1*–*4*). Extension to a diversity of complex polyatomic molecules would provide qualitatively new and improved platforms for these fields. For example, the parity doublets that result from rotations of a molecule around its principal axis, a general feature of symmetric top molecules, give rise to highly polarized states with structural features that are greatly desirable for both quantum science and precision measurement (*5*–*7*). However, the same complexity that provides these advantages makes laser cooling of nonlinear polyatomic molecules, including symmetric tops, challenging. Recent theoretical proposals have nonetheless suggested that laser cooling of some nonlinear molecules is a practical possibility (*8*–*10*).

Laser cooling relies on repeatedly scattering photons from an atom or molecule via rapid optical cycling, removing energy and entropy with directed momentum kicks and spontaneous emission events. Although other direct (*11*–*14*) and indirect (*15*, *16*) methods of slowing, cooling, and trapping molecules have been used, direct laser cooling has successfully brought a number of diatomic (*17*–*20*) and linear triatomic (*21*–*23*) molecules into the submillikelvin regime, with phase-space density increases of many orders of magnitude. The ability to rapidly cycle photons, which is essential to laser cooling, naturally also allows for efficient quantum state preparation and readout (*24*, *25*), which are necessities for proposed quantum computation and simulation platforms using ultracold molecules, including those proposed for symmetric top molecules (*5*, *6*).

The established recipe for achieving optical cycling and laser cooling of molecules requires three key ingredients: strong electronic transitions between two fully bound molecular states; diagonal Franck-Condon factors (FCFs), which limit branching to excited vibrational levels; and rotationally closed transitions. Here, we satisfied these conditions for the symmetric top molecule $CaOCH_3$ using two distinct optical cycling schemes to enable rapid scattering of photons. We efficiently reduced the transverse temperature of a $CaOCH_3$ molecular beam from 22 ± 1 mK to 1.8 ± 0.7 mK and scattered more than 100 photons while using only a few lasers, despite the presence of 12 vibrational modes. The state selectivity of the cooling is intimately connected to the nuclear spin statistics of the molecule as well as to its rigid-body angular momentum along the symmetry axis, denoted by the quantum number K'' in the ground state (Fig. 1, A and D). These distinctive features of symmetric top molecules were not accessible to previously laser-cooled diatomic and triatomic molecules.

We studied laser cooling of both nuclear-spin isomers (NSIs) of $CaOCH_3$, each of which corresponds to a specific set of K states. To cool the symmetric (ortho) NSI, we laser-excited molecules in ground states with $K'' = 0$ (Fig. 1, A to C). To high order, $K'' = 0$ states effectively "freeze out" the particular additional complexity of symmetric top molecules relative to their linear counterparts, and this cooling approach looks similar to that used for diatomic and linear triatomic molecules.

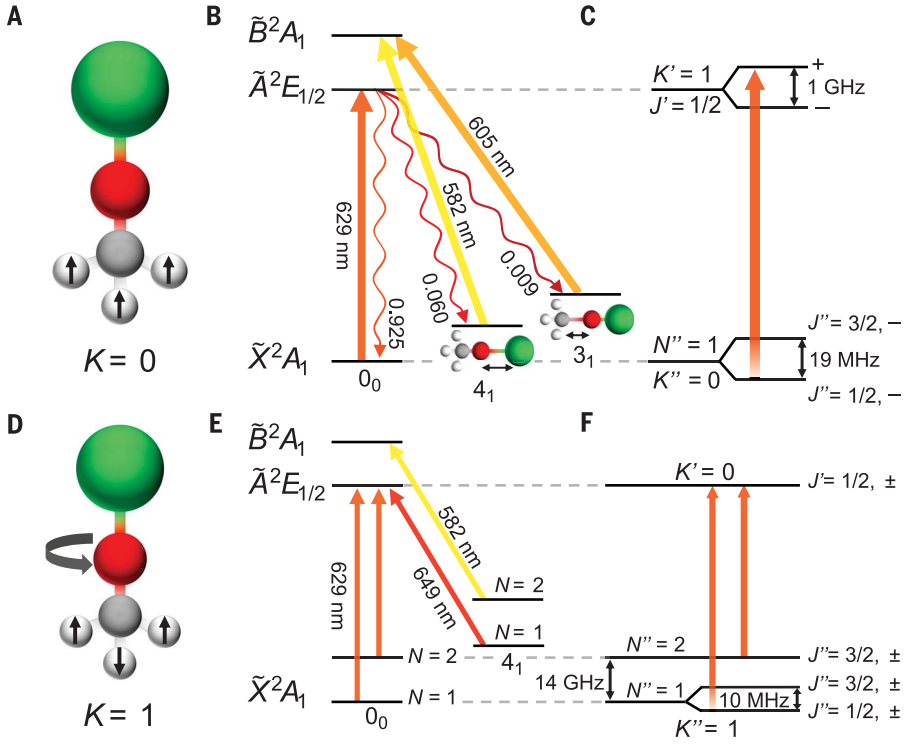

Fig. 1. $CaOCH_3$ laser cooling schemes. (**A** and **D**) We use two optical cycling schemes, which target molecules differing in their angular momentum quantum number K and their nuclear spin statistics (represented by arrows on the hydrogen nuclei). (**B** and **C**) For ortho-$CaOCH_3$, we address the 0_0, 4_1, and 3_1 vibrational levels of the $\tilde{X}^2A_1(K'' = 0)$ ground state. Vibrational branching ratios are illustrated by downward arrows. Rotational closure is achieved by addressing $N'' = 1$, $J'' = 1/2$, 3/2 ground-state manifolds. The total parity of each state is indicated by + and – signs. (**E** and **F**) For para-$CaOCH_3$, we address the 0_0 and 4_1 vibrational levels of the $\tilde{X}^2A_1(K'' = 1)$ electronic ground state, driving transitions from $N'' = 1$ and $N'' = 2$ to achieve rotational closure. Each J state contains an unresolved parity doublet denoted by ±. See (*28*) for further details of the optical cycling scheme.

Department of Physics, Harvard University, Cambridge, MA 02138, USA, and Harvard-MIT Center for Ultracold Atoms, Cambridge, MA 02138, USA.
*Corresponding author. Email: dmitra@g.harvard.edu
†These authors contributed equally to this work.

Because of the favorable FCFs of $CaOCH_3$, we used only three lasers to address the 0_0 (no excitation), 4_1 (Ca–O stretch), and 3_1 (O–C stretch) vibrational manifolds of the $\tilde{X}^2A_1$ electronic ground state, enabling each molecule to scatter an average of 120 photons before being lost to other vibrational levels (*26*, *27*). To laser-cool the asymmetric (para) isomer, we instead excited ground states that have $K'' = 1$ (Fig. 1, D to F). In this case, the existence of unresolved (opposite) parity doublets means that full optical closure required addressing additional rotational components of the $\tilde{X}^2A_1$ ground state. Using three cooling and repumping lasers enabled scattering an average of 30 photons before molecules were optically pumped into a fourth ro-vibronic state. Including three additional lasers would allow scattering 120 photons on average, just as in the ortho-$CaOCH_3$ scheme. Because both cooling schemes are limited only by vibrational decay pathways, scattering >1000 photons could be achieved by adding approximately four additional repumping lasers (*26*, *28*).

Laser cooling of $CaOCH_3$ was accomplished using the magnetically assisted Sisyphus effect, a highly efficient and robust cooling method first demonstrated with atoms (*17*, *21*, *22*, *29*–*31*). In this method, molecules pass through a standing wave of near-resonant, linearly polarized light containing all of the optical frequencies necessary to establish optical cycling. For blue-detuned light ($\Delta > 0$), as a molecule approaches a peak in the periodic, ac Stark-shifted potential landscape formed by the standing wave, it returns nonadiabatically to a potential minimum by a combination of optical pumping and magnetic state remixing (by an external magnetic field $|\mathbf{B}| \approx 1$ G aligned at an angle $\theta \sim 45°$ to the laser polarization axis). Repeated iterations of this process lead to cooling. Red-detuned light ($\Delta < 0$) results in heating via a similar but inverted mechanism (*28*).

The experimental apparatus was similar to one described previously (*23*). A schematic is shown in Fig. 2A. Briefly, $CaOCH_3$ molecules were produced in a cryogenic buffer gas environment by ablation of a calcium metal target in the presence of methanol vapor. The resulting beam had a mean forward velocity of 150 ± 30 m/s and was collimated to a transverse temperature of ~22 mK by a 3 mm × 3 mm square aperture immediately preceding the cooling region, after which ~10^4 molecules (in a single pulse) remained with a density of ~10^3 cm^{-3}. After laser cooling, the molecules propagated ~50 cm and underwent time-of-flight expansion in the direction transverse to propagation, mapping the momentum distribution onto the spatial profile of the beam. Finally, in the detection region, the molecules were addressed with resonant laser light and the resulting fluorescence was imaged onto an electron-multiplying charge-coupled device (EMCCD) camera to extract spatial information, and thus their transverse temperature. Figure 2, B to D, shows representative beam images of the ortho NSI ($K'' = 0$) for unperturbed, Sisyphus-heated ($\Delta < 0$), and Sisyphus-cooled ($\Delta > 0$) configurations; these images clearly indicate strong optical forces manipulating the molecular velocity distribution.

By integrating along the direction of molecular beam propagation, we obtained one-dimensional (1D) beam profiles, shown in Fig. 3 for both the ortho and para NSI cooling schemes. The cooled and heated profiles fit well to a sum of Gaussian distributions with two distinct widths, corresponding to two classes of molecules, those that were Sisyphus-cooled and those that were not (*28*). The cooled molecules were those with transverse velocities less than the capture velocity, $v < v_c$. Molecules with $v > v_c$ were instead subject predominantly to Doppler cooling and heating, depending on laser detuning. For blue detuning ($\Delta > 0$), a large fraction of molecules fell within v_c and were cooled into a central, narrow peak on top of a broad Doppler-heated background. For red detuning ($\Delta < 0$), molecules slower than v_c were heated while faster ones were Doppler-cooled. This competition led to a concentration of molecules at velocities where the Doppler and Sisyphus forces balanced, corresponding to approximately v_c. From the positions of these two peaks, we estimated a capture velocity $v_c \approx 1.5$ m/s for $K'' = 0$ cooling of the ortho NSI, in good agreement with the model described below. Unperturbed and resonantly depleted profiles fit well to single Gaussian distributions.

The integrated area of each of the three ortho-$CaOCH_3$ profiles with 1.1 W/cm^2 of cooling light applied was ~50% that of the unperturbed profile (Fig. 3A). This effect is understood to be due to losses to vibrational states that were not repumped, most notably $\tilde{X}^2A_14_2$ and $\tilde{X}^2A_13_14_18_1$. Combining the observed depletion with branching ratios previously measured for $CaOCH_3$ (*26*), we determined that 80 (+100, –30) photons were scattered in the cooling process and 110 (+150, –40) photons were scattered in resonant depletion (*28*). From this observation we inferred an average scattering rate of ~2 × 10^6 s^{-1} across the cooling region, which is similar to scattering rates observed for laser cooling of diatomic and linear triatomic molecules (*18*–*22*, *32*). We determined the temperature of the molecules by fitting a Monte Carlo simulation of the molecular beam propagation to our data (*28*). This calculation gave an initial transverse temperature $T_\perp = 22 \pm 1$ mK, which was reduced by Sisyphus cooling to $T_\perp = 1.8 \pm 0.7$ mK. Combined with the enhancement in on-axis molecule density seen in Fig. 3A, this substantial temperature reduction corresponded to a factor of 4 increase in the on-axis phase-space density of the molecular cloud (*33*). Finally, we varied the laser detuning, intensity, and magnetic field for ortho-$CaOCH_3$ Sisyphus cooling and compared the results to those of a

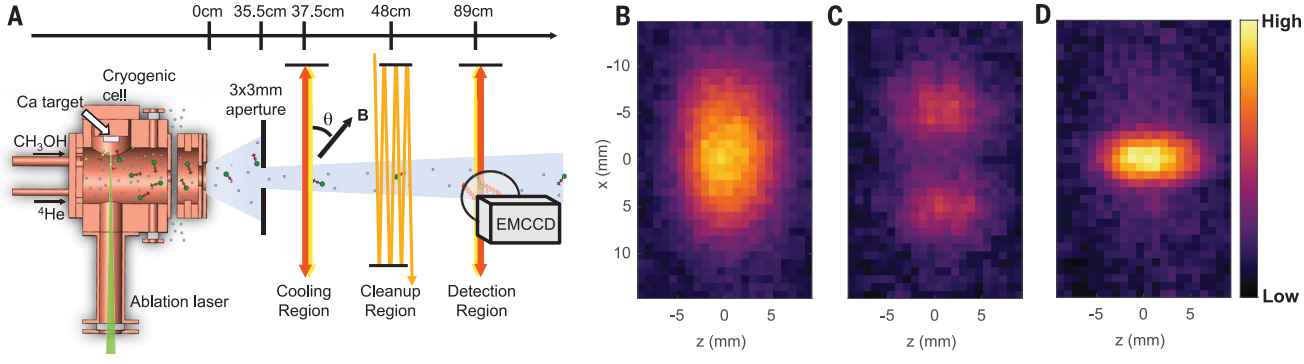

Fig. 2. Apparatus and beam images. (**A**) Schematic of the experimental apparatus, illustrating the beam source, laser cooling, cleanup, and detection regions (not to scale). The cooling region contains a near-resonant standing wave generated by retroreflecting a single, linearly polarized Gaussian laser beam with a 6-mm $1/e^2$ diameter. In the cleanup region, molecules are repumped out of the $\tilde{X}^2A_13_1$ (ortho-$CaOCH_3$) and $\tilde{X}^2A_1(N'' = 2)4_1$ (para-$CaOCH_3$) states before being imaged onto an EMCCD camera via laser-induced fluorescence (LIF) detection. (**B** to **D**) Beam images for ortho-$CaOCH_3$ ($K'' = 0$) are shown for unperturbed (B), Sisyphus-heated ($\Delta = -15$ MHz) (C), and Sisyphus-cooled ($\Delta = +25$ MHz) (D) configurations.

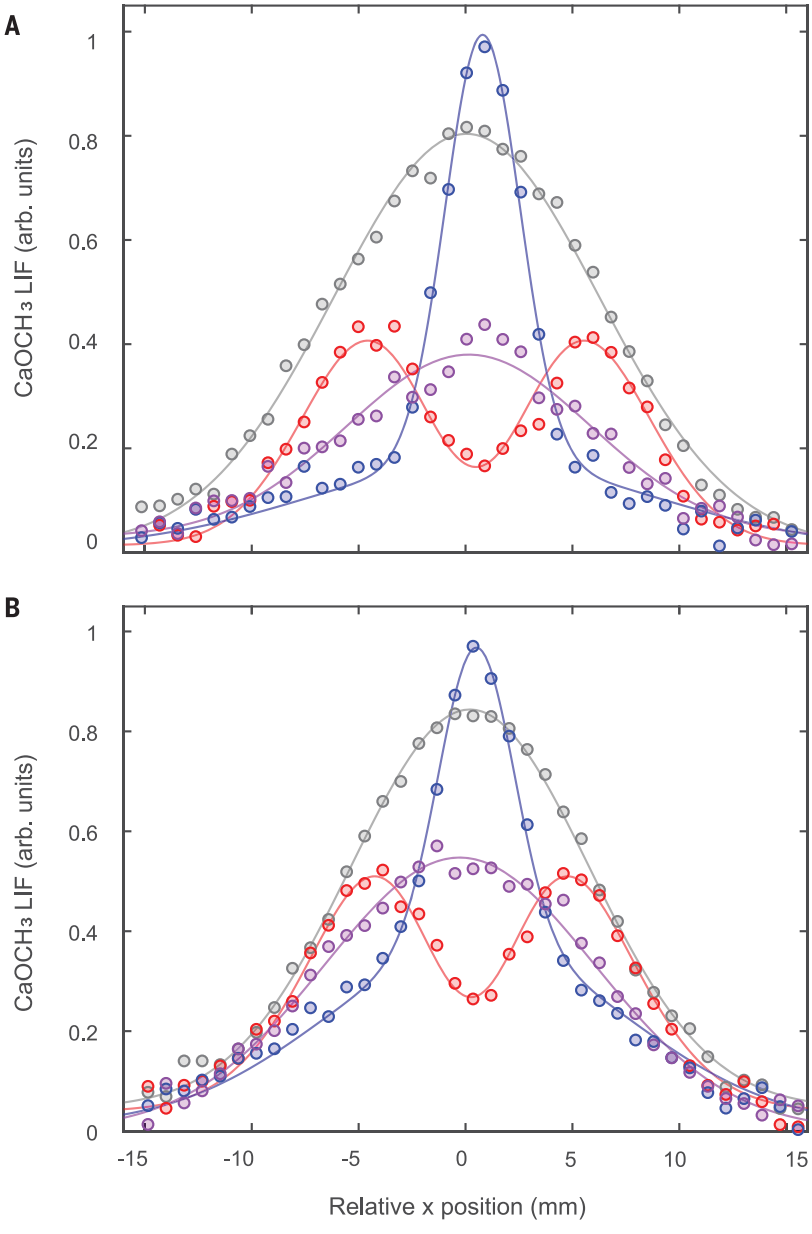

Fig. 3. Sisyphus-cooled and Sisyphus-heated beam profiles. (**A** and **B**) Integrated laser-induced fluorescence (LIF) versus position for ortho-$CaOCH_3$ (K'' = 0) (A) and para-$CaOCH_3$ (K'' = 1) (B) cooling schemes. Sisyphus cooling, at a positive detuning Δ = +25 MHz for the ortho isomer and Δ = +20 MHz for the para isomer, manifests itself as a narrowing of the detected distribution (blue), whereas Sisyphus heating appears as a bimodal distribution (Δ = −15 MHz for both; red). Unperturbed (cooling lasers off; gray) and resonantly depleted (Δ = 0; purple) profiles have the same width but different integrated area due to optical pumping into dark vibrational states. Solid curves are Gaussian fits as described in (*28*).

model obtained by solving optical Bloch equations for molecules subject to the cooling light. We found good agreement between experimental results and the model, further strengthening our understanding of the cooling mechanism involved (*28*).

Figure 3B shows beam profiles for para-$CaOCH_3$ (K'' = 1) laser cooling, taken at a laser intensity of 250 mW/cm^2. We observed notable Sisyphus cooling and heating, although the effect was weaker than for ortho-$CaOCH_3$ (K'' = 0), as expected, because there were more ground states coupled to the same excited electronic state, leading to a lower scattering rate by a factor of ~2 (*28*). Additionally, the reduced laser intensity used, set by technical limitations, resulted in a smaller capture velocity and cooled fraction. Using the same analysis as above, we found that the cooled molecules scattered an average of 25 ± 10 photons, corresponding to an estimated scattering rate of ~0.75 × 10^6 s^{-1}. Cooling of the para NSI would be improved with higher laser intensity and/or interaction length.

Our results demonstrate the feasibility of direct laser cooling of complex, nonlinear polyatomic molecules into the millikelvin temperature regime (*34*, *35*). This work opens the door to a number of future experiments that span a range of modern physical and chemical research frontiers. Because Sisyphus cooling is effective down to the recoil limit (*36*) (corresponding to ~500 nK for molecules with similar mass to $CaOCH_3$), these techniques could be used to achieve bright, highly collimated, few-microkelvin molecular beams useful for precision measurements and studies of ultracold chemistry (*37*). Efficient and state-selective laser cooling of both nuclear spin isomers also offers a method to separate them using radiation-pressure beam deflection of specific spin species, a topic of interest in physical chemistry (*38*–*41*). By adding a small number of other laser frequencies to the laser cooling of $CaOCH_3$ (*26*), optical tweezer arrays of symmetric top molecules should be possible, as recently accomplished with diatomic species (*25*). These arrays would offer an ideal starting point for realizing new polyatomic quantum simulation and computation platforms (*5*, *6*). Laser cooling could also be extended to asymmetric tops, including biochemically relevant chiral molecules (*9*, *10*, *42*, *43*). Finally, laser cooling and trapping of the heavier symmetric top molecule $YbOCH_3$ would allow precise searches for time reversal–violating interactions at a previously inaccessible energy scale, and ultracold chiral molecules such as YbOCHDT could enable precision probes of fundamental parity violation (*7*, *22*).

REFERENCES AND NOTES

1. W. D. Phillips, *Rev. Mod. Phys.* **70**, 721–741 (1998).
2. I. Bloch, J. Dalibard, W. Zwerger, *Rev. Mod. Phys.* **80**, 885–964 (2008).
3. J. L. Bohn, A. M. Rey, J. Ye, *Science* **357**, 1002–1010 (2017).
4. M. S. Safronova *et al.*, *Rev. Mod. Phys.* **90**, 025008 (2018).
5. M. Wall, K. Maeda, L. D. Carr, *New J. Phys.* **17**, 025001 (2015).
6. P. Yu, L. W. Cheuk, I. Kozyryev, J. M. Doyle, *New J. Phys.* **21**, 093049 (2019).
7. I. Kozyryev, N. R. Hutzler, *Phys. Rev. Lett.* **119**, 133002 (2017).
8. T. A. Isaev, R. Berger, *Phys. Rev. Lett.* **116**, 063006 (2016).
9. I. Kozyryev, L. Baum, K. Matsuda, J. M. Doyle, *ChemPhysChem* **17**, 3641–3648 (2016).
10. B. L. Augenbraun, J. M. Doyle, T. Zelevinsky, I. Kozyryev, *Phys. Rev. X* **10**, 031022 (2020).
11. M. Lemeshko, R. V. Krems, J. M. Doyle, S. Kais, *Mol. Phys.* **111**, 1648–1682 (2013).
12. A. Prehn, M. Ibrügger, R. Glöckner, G. Rempe, M. Zeppenfeld, *Phys. Rev. Lett.* **116**, 063005 (2016).
13. X. Wu *et al.*, *Science* **358**, 645–648 (2017).
14. Y. Liu *et al.*, *Phys. Rev. Lett.* **118**, 093201 (2017).
15. K.-K. Ni *et al.*, *Science* **322**, 231–235 (2008).
16. L. De Marco *et al.*, *Science* **363**, 853–856 (2019).
17. E. S. Shuman, J. F. Barry, D. Demille, *Nature* **467**, 820–823 (2010).
18. S. Truppe *et al.*, *Nat. Phys.* **13**, 1173–1176 (2017).
19. L. Anderegg *et al.*, *Phys. Rev. Lett.* **119**, 103201 (2017).
20. A. L. Collopy *et al.*, *Phys. Rev. Lett.* **121**, 213201 (2018).
21. I. Kozyryev *et al.*, *Phys. Rev. Lett.* **118**, 173201 (2017).

22. B. L. Augenbraun *et al*., *New J. Phys.* **22**, 022003 (2020).
23. L. Baum *et al*., *Phys. Rev. Lett.* **124**, 133201 (2020).
24. L. W. Cheuk *et al*., *Phys. Rev. Lett.* **121**, 083201 (2018).
25. L. Anderegg *et al*., *Science* **365**, 1156–1158 (2019).
26. I. Kozyryev, T. C. Steimle, P. Yu, D.-T. Nguyen, J. M. Doyle, *New J. Phys.* **21**, 052002 (2019).
27. The vibrational notation used is $n_{v''}$, where n labels the normal mode of vibration and v'' specifies the number of excited quanta. Here n = 3 is the antisymmetric (O–C) stretching mode, n = 4 is the symmetric (Ca–O) stretching mode, and n = 8 is the doubly degenerate Ca–O–C bending mode. The remaining eight modes play no role in this work. The state with no excited vibrations is labeled 0_0.
28. See supplementary materials.
29. O. Emile *et al*., *J. Phys. II France* **3**, 1709–1733 (1993).
30. B. Sheehy, S.-Q. Shang, P. van der Straten, S. Hatamian, H. Metcalf, *Phys. Rev. Lett.* **64**, 858–861 (1990).
31. J. Lim *et al*., *Phys. Rev. Lett.* **120**, 123201 (2018).
32. J. F. Barry, D. J. McCarron, E. B. Norrgard, M. H. Steinecker, D. DeMille, *Nature* **512**, 286–289 (2014).
33. We defined the phase-space density as $\rho = n\lambda^{dB}{}_x\lambda^{dB}{}_y\lambda^{dB}{}_z$, where n is the number density and $\lambda^{dB}{}_i \sim 1/\sqrt{T_i}$ is the de Broglie wavelength defined in terms of the temperature along the ith spatial direction. Because we cooled in 1D only, ρ scales as $1/\sqrt{T}$.
34. M. V. Ivanov, S. Gulania, A. I. Krylov, *J. Phys. Chem. Lett.* **11**, 1297–1304 (2020).
35. J. Kłos, S. Kotochigova, *Phys. Rev. Res.* **2**, 013384 (2020).
36. M. D. Hoogerland, H. C. W. Beijerinck, K. A. H. van Leeuwen, P. van der Straten, H. J. Metcalf, *Europhys. Lett.* **19**, 669–674 (1992).
37. E. Lavert-Ofir *et al*., *Nat. Chem.* **6**, 332–335 (2014).
38. J. Küpper, F. Filsinger, G. Meijer, *Faraday Discuss.* **142**, 155–173 (2009).
39. Z.-D. Sun, K. Takagi, F. Matsushima, *Science* **310**, 1938–1941 (2005).
40. T. Kravchuk *et al*., *Science* **331**, 319–321 (2011).
41. Z.-D. Sun, M. Ge, Y. Zheng, *Nat. Commun.* **6**, 6877 (2015).
42. M. Quack, *Angew. Chem.* **41**, 4618–4630 (2002).
43. D. G. Blackmond, *Philos. Trans. R. Soc. B* **366**, 2878–2884 (2011).
44. D. Mitra *et al.*, Data for "Direct Laser Cooling of a Symmetric Top Molecule", Open Science Framework; doi:10.17605/osf.io/s4ma3 (2020).
45. OBE and MC simulation, Zenodo; doi:10.5281/zenodo.3937747 (2020).

ACKNOWLEDGMENTS

We thank I. Kozyryev for insightful discussions and comments on the manuscript, and Z. Lasner and P. Yu for useful discussions at various stages of this work. **Funding:** Supported by the AFOSR, with additional support from the ARO and NSF. Also supported by a NDSEG fellowship (N.B.V.), the HQI (L.A.), and the NSF GRFP (B.L.A.). J.M.D. has a visiting professor appointment at Okayama University. **Author contributions:** D.M., N.B.V., C.H., L.A., B.L.A., L.B., and S.R. designed and assembled the apparatus, discussed experimental protocols, and performed the experiment; D.M. and N.B.V. analyzed the data; C.H. and C.M. implemented the laser cooling simulations; J.M.D. supervised all work and contributed to setting the direction of the experiment, as well as the design and development of the experimental apparatus, methods, and analysis of data. All authors discussed the results and contributed to the manuscript. **Competing interests:** None declared. **Data and materials availability:** All data and code needed to reproduce the data analysis are archived in Open Science Framework (*44*). Code associated with the OBE and MC simulations is available from Zenodo (*45*).

SUPPLEMENTARY MATERIALS

science.sciencemag.org/content/369/6509/1366/suppl/DC1
Materials and Methods
Supplementary Text
Figs. S1 to S6
Table S1
References (*46*–*59*)

29 April 2020; accepted 10 July 2020
10.1126/science.abc5357

COLLOIDS

Self-limiting directional nanoparticle bonding governed by reaction stoichiometry

Chenglin Yi[1], Hong Liu[2]*, Shaoyi Zhang[3], Yiqun Yang[1], Yan Zhang[1], Zhongyuan Lu[2], Eugenia Kumacheva[4]†, Zhihong Nie[1,3]†

Nanoparticle clusters with molecular-like configurations are an emerging class of colloidal materials. Particles decorated with attractive surface patches acting as analogs of functional groups are used to assemble colloidal molecules (CMs); however, high-yield generation of patchy nanoparticles remains a challenge. We show that for nanoparticles capped with complementary reactive polymers, a stoichiometric reaction leads to reorganization of the uniform ligand shell and self-limiting nanoparticle bonding, whereas electrostatic repulsion between colloidal bonds governs CM symmetry. This mechanism enables high-yield CM generation and their programmable organization in hierarchical nanostructures. Our work bridges the gap between covalent bonding taking place at an atomic level and colloidal bonding occurring at the length scale two orders of magnitude larger and broadens the methods for nanomaterial fabrication.

Clusters of inorganic nanoparticles (NPs) exhibit synergistic properties, owing to interactions between surface plasmons, excitons, or magnetic moments of the constituent NPs (*1*, *2*). Emerging applications of NP clusters in plasmonics (*3*), photonics (*4*, *5*), and catalysis (*6*) necessitate precise control over their architecture and structural complexity; however, as of now, such control remains a challenge (*1*). Assembly of NPs into small clusters recapitulating the structure and symmetry of molecules—that is, colloidal molecules (CMs)—has emerged as a promising strategy for generating nanostructures with programmable architectures (*7*, *8*).

Assembly of CMs is governed by the delicate balance of attractive forces (e.g., hydrogen bonding, Coulombic attraction, or solvophobic interactions) and repulsive interactions of electrostatic or steric origin (*9*). To achieve directionality in interparticle interactions for CM assembly, colloidal building blocks are functionalized with a discrete number of attractive surface regions (patches) (*10*–*14*) or packed in droplets with subsequent solvent evaporation (*15*). The shortcomings of these approaches, especially for nanometer-sized particles, are low yield and a limited precision of CM fabrication (*14*, *16*, *17*). For nanoscale particles, notable progress has been achieved for DNA-mediated assembly of CMs from NPs functionalized with complementary single-stranded DNA (*13*, *18*–*20*). However, for shape-isotropic NPs, the surface attachment of DNA is not regiospecific and NP bonding is not localized to a specific surface region, thus the self-assembly yields a mixture of CMs with different structures (*21*, *22*). Enhanced control over CM architecture requires extra steps of regiospecific patterning NPs with attractive DNA patches (*23*), or encapsulating NPs within predesigned DNA frames with programmed bonding sites (*24*, *25*).

We show that high-yield directional and self-limiting assembly of spherical NPs uniformly coated with polymer ligands can be achieved without engineering site-specific NP interactions. The concept of directional NP bonding is built on the mechanism of σ-bond formation by hybridization of atomic orbitals in molecules. When the valence shell is completely filled, atoms in a molecule do not form new bonds, and the repulsion between the pairs of valence electrons determines the structure of the molecule (*26*). As an example, Fig. 1A shows a trigonal planar molecule of boron trifluoride (BF_3), in which sp^2 hybridization of atomic orbitals of boron yields three symmetric singly occupied orbitals that bond with orbitals of fluorine atoms.

We used an acid-base neutralization reaction between the ligands capping two types of NPs. Figure 1B shows schematically the formation of a CM with a BF_3 molecular configuration. Two populations of inorganic NPs (designated as NP-A and NP-B), each tethered with distinct block copolymer ligands, mimic atoms of two elements. Each copolymer contains a NP-adjacent reactive block with complementary acid or base groups and an outer block acting as a steric stabilizer of the NPs. A typical combination of copolymer ligands used in the present work was poly(ethelyene oxide)-*b*-(acrylic acid-*r*-styrene) [PEO-*b*-P(AA-*r*-St)] for NP-As and poly(ethelyene oxide)-*b*-poly(*N*,*N*-dimethylaminoethyl methacrylate-*r*-styrene) [PEO-*b*-P(DMAEMA-*r*-St)] for NP-Bs (figs. S1 to S6, tables S1 to S5, and supplementary text section I). Partial deprotonation of acid groups of the ligands on the NP-A makes the particle negatively charged (table S6). After mixing of NP-As and NP-Bs, a neutralization reaction between the acid and base groups in the copolymer ligands leads to directional colloidal bonding. Unlike a reaction between two hard spheres that is limited to their contact zone, the acid and base groups on the NP-A and NP-B pair can access each other, owing to the flexibility of the copolymer molecules. The stoichiometry and reversibility of the reaction between the ligands would regulate the number of bonds between the NP-As and NP-Bs by means of a self-limiting mechanism, that is, when the reactive groups in the ligand shell are completely consumed, no further bonding will take place. Furthermore, the Coulombic repulsion between the colloidal bonds containing charged groups would govern the CM symmetry.

Spherical gold NPs with mean diameter, D, in the range from 10 to 40 nm were end-grafted with brush-like copolymer ligands and dispersed in tetrahydrofuran, a good solvent for the copolymers (figs. S7 and S8) (*27*). The NP-As and NP-Bs had electrokinetic potentials of -65.18 ± 6.56 and 5.30 ± 9.54 mV, respectively (table S6). After mixing of the solutions of NP-As and NP-Bs, the neutralization reaction between the ligands took place (figs. S9 and S10). Within 3 to 5 min, the NP-As and NP-Bs assembled into clusters with AB_2 (40%), AB_3 (30%), and AB (12%) structures (Fig. 1, C and D). In the AB_2 clusters, two NP-Bs preferentially attached at two opposite poles of a NP-A (Fig. 1C, top). The average bonding angle, $\angle B_iAB_j$, formed by NP-A, NP-B_i and NP-B_j ($i \neq j$) was 151.2° ± 19.6°. As time evolved, the fraction of AB_3 structures gradually increased at the expense of the reduced fractions of AB and AB_2 clusters and free NPs (Fig. 1D). After 150 min, ~80% of the clusters had an AB_3 structure (Fig. 1C, bottom), and the average $\angle B_iAB_j$ became 135.4° ± 13.2°. The AB_2 to AB_3 transition was caused by the formation of the new third bond between the NP-A and NP-B and the rearrangement of the two preexisting bonds between NP-A and NP-Bs, reflected by the pronounced increase in the fraction of ~120° bonding angles and the decrease in the population of free NP-Bs (Fig. 1E and fig. S11). In the 6 hours after the beginning of assembly, the AB_3 clusters further optimized their structure to achieve a stable bond length and a symmetric trigonal planar geometry with an average $\angle B_iAB_j$ of 119.8° ± 12.8° (figs. S12 and S13). The importance of electrostatic repulsion between the colloidal bonds was signified by the decrease in AB_3 symmetry in

[1]State Key Laboratory of Molecular Engineering of Polymers, Department of Macromolecular Science, Fudan University, Shanghai 200438, China. [2]State Key Laboratory of Supramolecular Structure and Materials, Institute of Theoretical Chemistry, Jilin University, Changchun 130023, China. [3]Department of Chemistry and Biochemistry, University of Maryland, College Park, MD 20742, USA. [4]Department of Chemistry, University of Toronto, Toronto, Ontario M5S 3H6, Canada.
*Present address: Key Laboratory of Theoretical Chemistry of Environment Ministry of Education, School of Chemistry, South China Normal University, Guangzhou 510006, China.
†Corresponding author. Email: znie@fudan.edu.cn (Z.N.); ekumache@chem.utoronto.ca (E.K.)

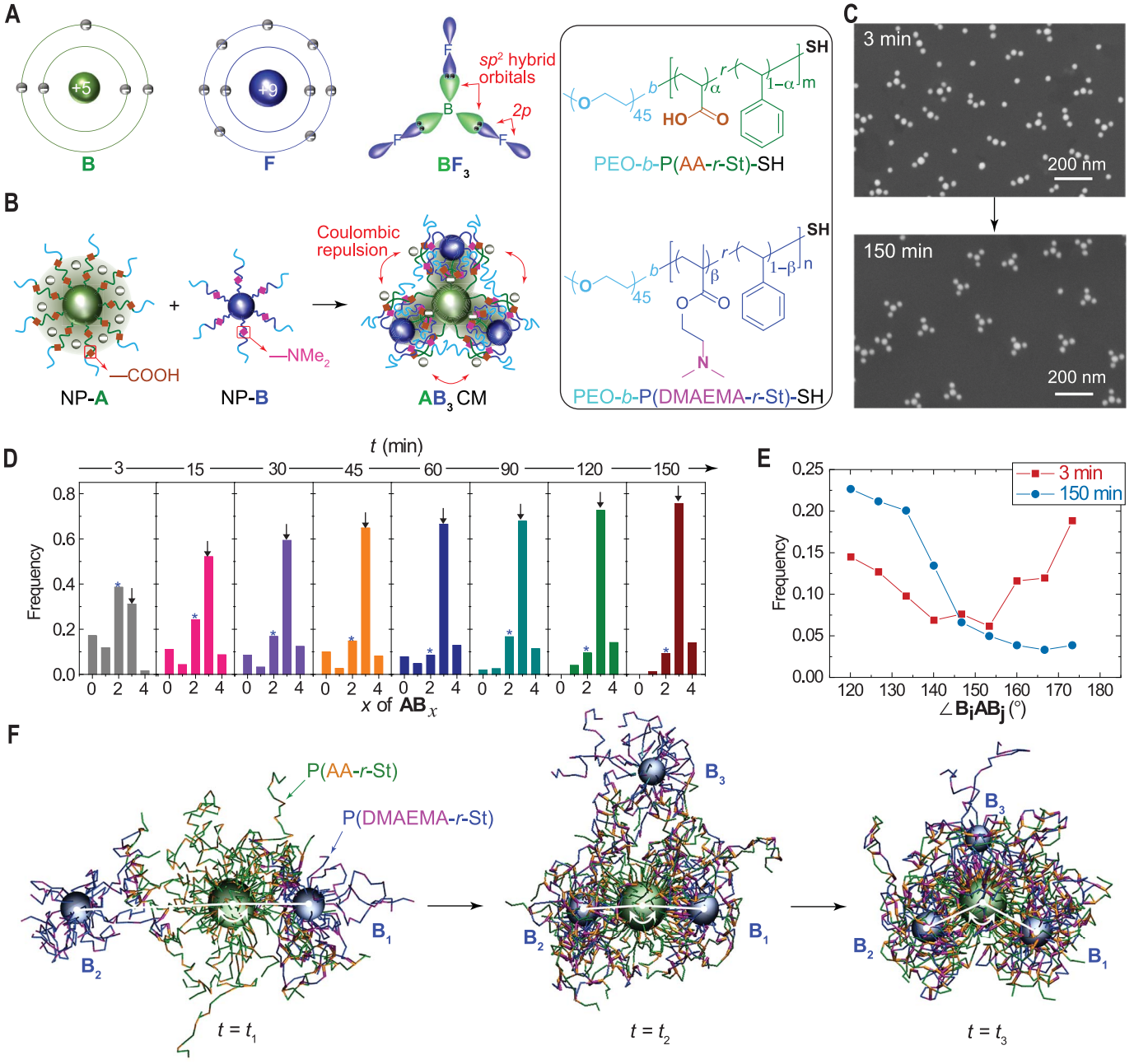

Fig. 1. Directional bonding of distinct NPs. (**A**) Schematic illustration of boron (B) and fluoride (F) atoms and the structure of a sp^2-hybridized BF_3 molecule. (**B**) Illustration of directional bonding of NP-A and NP-B, each coated with distinct block copolymer ligands, to form an AB_3 structure by the stoichiometric reaction between the complementary reactive groups in the ligands. In the polymer formula, *m* and *n* correspond to the number of repeat units, whereas α and β represent content (%) of each comonomer in the randomly copolymerized block. Me, methyl. (**C**) Representative scanning electron microscopy (SEM) images of NP assemblies formed 3 min (top) and 150 min (bottom) after mixing the NP-As and NP-Bs. (**D**) Evolution of CMs with AB_x structure (*x* is the number of NP-Bs) during the course of assembly. The star and arrow symbols are provided to guide the eye. (**E**) Distribution of the bond angles, $\angle B_iAB_j$, in the CMs shown in (C). (**F**) Simulation snapshots illustrating the kinetics of the formation of AB_3 CMs at three different time points, t_1, t_2, and t_3. The PEO blocks in the ligands are not shown for ease of visualization. In (D) and (E), 2000 NPs are analyzed.

the presence of LiBr salt (fig. S14). The NP bonding process to form AB_3 CMs followed a pseudo first-order reaction mechanism (fig. S15).

The evolution of $\angle B_iAB_j$ and the distance d_{A-B_i} between the NP-A and NP-B_i in the AB_3 structures was assessed with coarse-grained Brownian dynamics simulations coupled with the stochastic reaction model (movie S1, table S7, and supplementary text section II) (*28*). Although neutralization of weak acids and bases is reversible (*29*), multiple reaction sites prevented bonded NP-As and NP-Bs from detachment, as indicated by an approximately monotonic decrease in d_{A-B_i} during the bonding process (figs. S16 and S17). When the reaction reached a dynamic equilibrium at a consumption of ~60 to 80% of acid-base moieties, a stable bond formed (table S8). Figure 1F illustrates representative simulation snapshots of the evolution of AB_3 structures. After bonding the first NP-B to the central NP-A to form

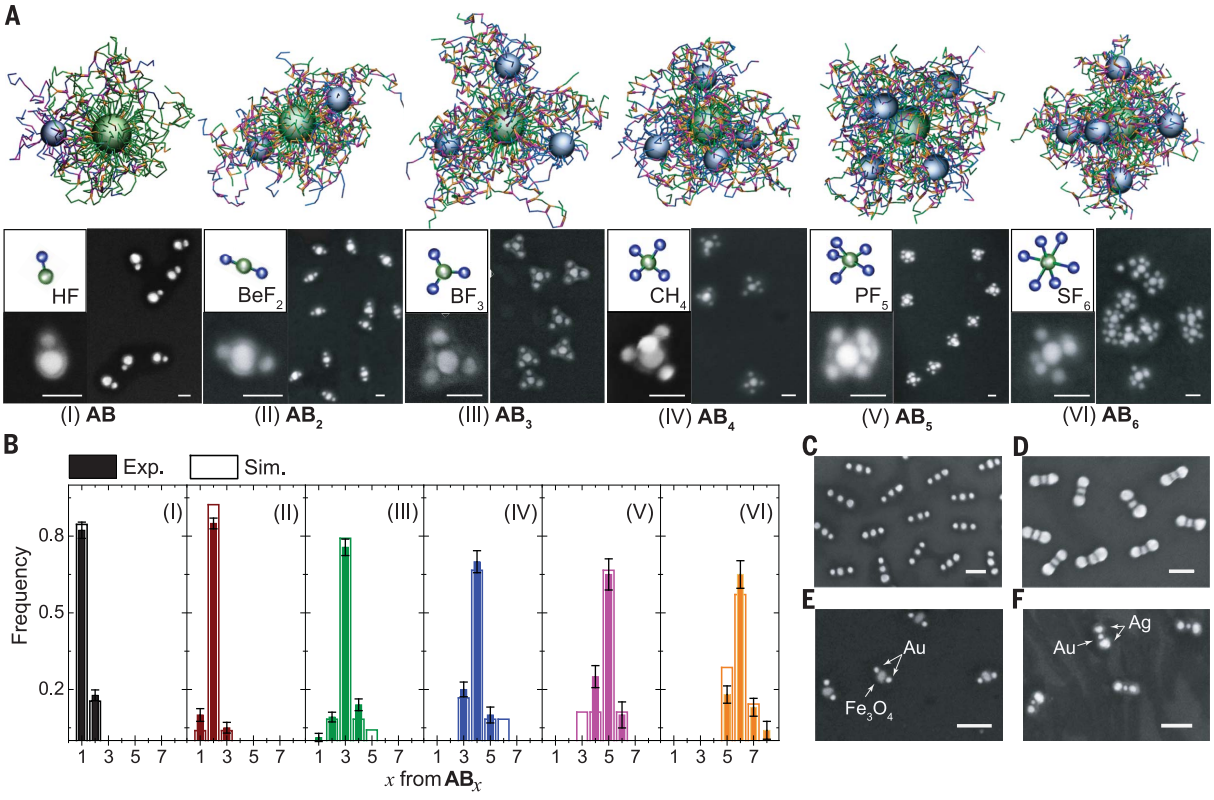

Fig. 2. Experimental and simulation study of the CM formation. (**A**) Simulation snapshots and SEM images of AB_x structures (x = 1 to 6) assembled from 36-nm Au NP-As and 20-nm Au NP-Bs. The M_n of the P(AA-*r*-St) and P(DMAEMA-*r*-St) blocks are, from left to right, 41.9 and 58.3 kg/mol (I), 31.1 and 58.3 kg/mol (II), 40.4 and 35.1 kg/mol (III), 40.4 and 29.3 kg/mol (IV), 40.4 and 20.1 kg/mol (V), and 40.4 and 8.9 kg/mol (VI). (**B**) Distribution of CMs with different structures in simulation (Sim.) and experiments (Exp.), corresponding to I to VI in (A). The error bars indicate standard deviation. (**C** and **D**) SEM images of AB_2 clusters formed from 36-nm Au NP-As and 26-nm Au NP-Bs (C), and 36-nm Au NP-As and 42-nm Au NP-Bs (D). (**E** and **F**) SEM images of CMs formed from 22-nm Fe_3O_4 NP-As and 15-nm Au NP-Bs (E), and 15-nm Au NP-As and 25-nm Ag NP-Bs (F). The M_n of P(AA-*r*-St) and P(DMAEMA-*r*-St) blocks are 43.2 and 58.3 kg/mol (C), 31.1 and 20.1 kg/mol (D), 22.1 and 39.4 kg/mol (E), and 51.6 and 20.1 kg/mol (F). Scale bars are 50 nm in (A), and 100 nm in (C) to (F).

an AB cluster, the second NP-B preferentially attacks the NP-A at a more reaction-active site, that is, opposite to the first bonded NP-B. These two NP-Bs align at a $\angle B_iAB_j$ close to 180° to minimize the Coulombic repulsion between the charged groups within the bonds. After bonding the third NP-B to the NP-A, attachment of other NP-Bs or NP-As to the AB_3 structure is limited, owing to the reaction stoichiometry, Coulombic repulsion between the CM and free NP-As, and steric constraints imposed by the PEO blocks and reacted fragments of the copolymers (fig. S18). Three bonds further rearrange to reach a $\angle B_iAB_j$ of 120°, corresponding to a trigonal planar shape of the CM. Once assembled, the CM retains its structure, although bond angles and lengths fluctuate with time. Furthermore, the simulation shows that the assembly of NP-Bs with NP-As without ionization of the acid groups in ligands yields AB_3 clusters with reduced symmetry (fig. S19).

We generated a library of CMs with different structures by varying the number average molecular weight (M_n) of the P(DMAEMA-*r*-St) block on NP-Bs from 8.9 to 58.3 kg/mol (corresponding to the root-mean-square end-to-end distance of the unperturbed copolymer chain from 8.14 to 25.13 nm). Figure 2A and figs. S20 to S26 show CM structures obtained in experiments and simulations (tables S7 to S9). The CMs had a general formula AB_x, in which x number of NP-Bs were bonded to the central NP-A (where x is a positive integer of $1 \le x \le 6$). To achieve a high yield of CMs with a targeted architecture, the feeding number ratio of NP-Bs to NP-As was equal to x in the AB_x structure. With a decrease in the length and hence the number of base groups of the P(DMAEMA-*r*-St) block on NP-B, x increased from 1 to 6, because a larger number of NP-Bs were required to react with acid groups on NP-A (table S9). The CMs had the structure of binary molecular compounds—namely, a linear HF and BeF_2, trigonal planar BF_3, tetrahedral CH_4, trigonal bipyramidal PF_5, and octahedral SF_6—with the corresponding atomic hybrid orbitals of s (or p), sp, sp^2, sp^3, dsp^3, and d^2sp^3. For instance, the average $\angle B_iAB_j$ for AB_2 and AB_3 clusters was 173.2° ± 6.4° and 119.8° ± 12.8°, respectively (figs. S27 and S28). The simulation results for AB_x structures were in agreement with experimental CM configurations. The AB, AB_2, and AB_3 structures were obtained with 82.3, 86.4, and 75.6% yield, respectively, close to the corresponding values predicted by simulations (Fig. 2B).

The generality of the approach to CMs was demonstrated by assembling NPs with various dimensions and compositions. Figure 2, C and D, shows AB_2 structures formed by bonding 36-nm-diameter Au NP-As with 26- or 42-nm-diameter Au NP-Bs. The increase in NP-B diameter was balanced by reducing the M_n of the P(DMAEMA-*r*-St) block to maintain a stoichiometric number of base groups on NP-Bs (figs. S29 to S31 and tables S10 and S11). We also formed compositionally heterogeneous AB_2 CMs from Fe_3O_4 NP acting as a central NP-A, which were bonded with two Au NP-Bs (Fig. 2E and table S2), and from Au NP-A positioned between two Ag NP-Bs (Fig. 2F).

To validate that the reaction stoichiometry governs the directional NP bonding, we examined the variation of the CM structure with $Z_{A/B} = N_A/N_B$, the ratio of the total number (N_A) of acid groups on a single NP-A to the total number (N_B) of base groups on a single

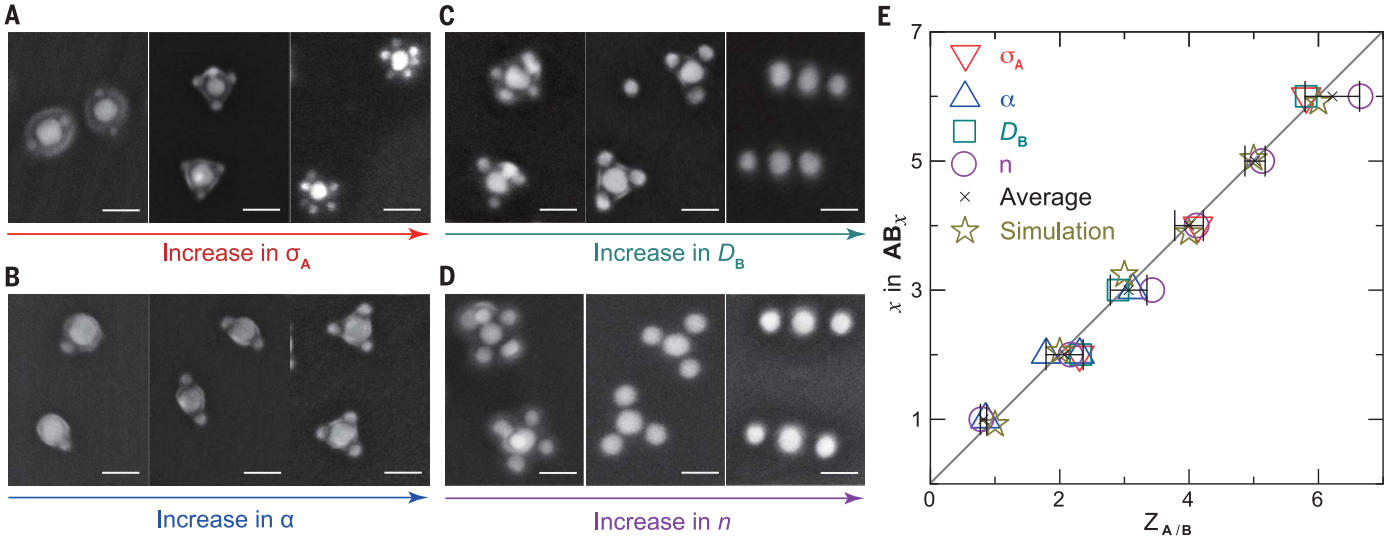

Fig. 3. General principles of directional NP bonding. (**A** to **D**) SEM images of CMs showing the effect of σ_A (A), α (B), D_B (C), and n (D). (**E**) Variation in x in AB_x structures with increasing $Z_{A/B}$, controlled by (∇) σ_A of the ligands on NP-A, (Δ) α in the $P(AA_\alpha\text{-}r\text{-}St_{1-\alpha})_m$ block of ligands on NP-A, (□) D_B of NP-Bs, and (○) n of $P(DMAEMA_\beta\text{-}r\text{-}St_{1-\beta})_n$ on NP-B. For each x, the average values of $Z_{A/B}$ (×) were calculated with standard deviations. The solid line is provided to guide the eye. The results of simulation (☆) correspond to structures in Fig. 2A.

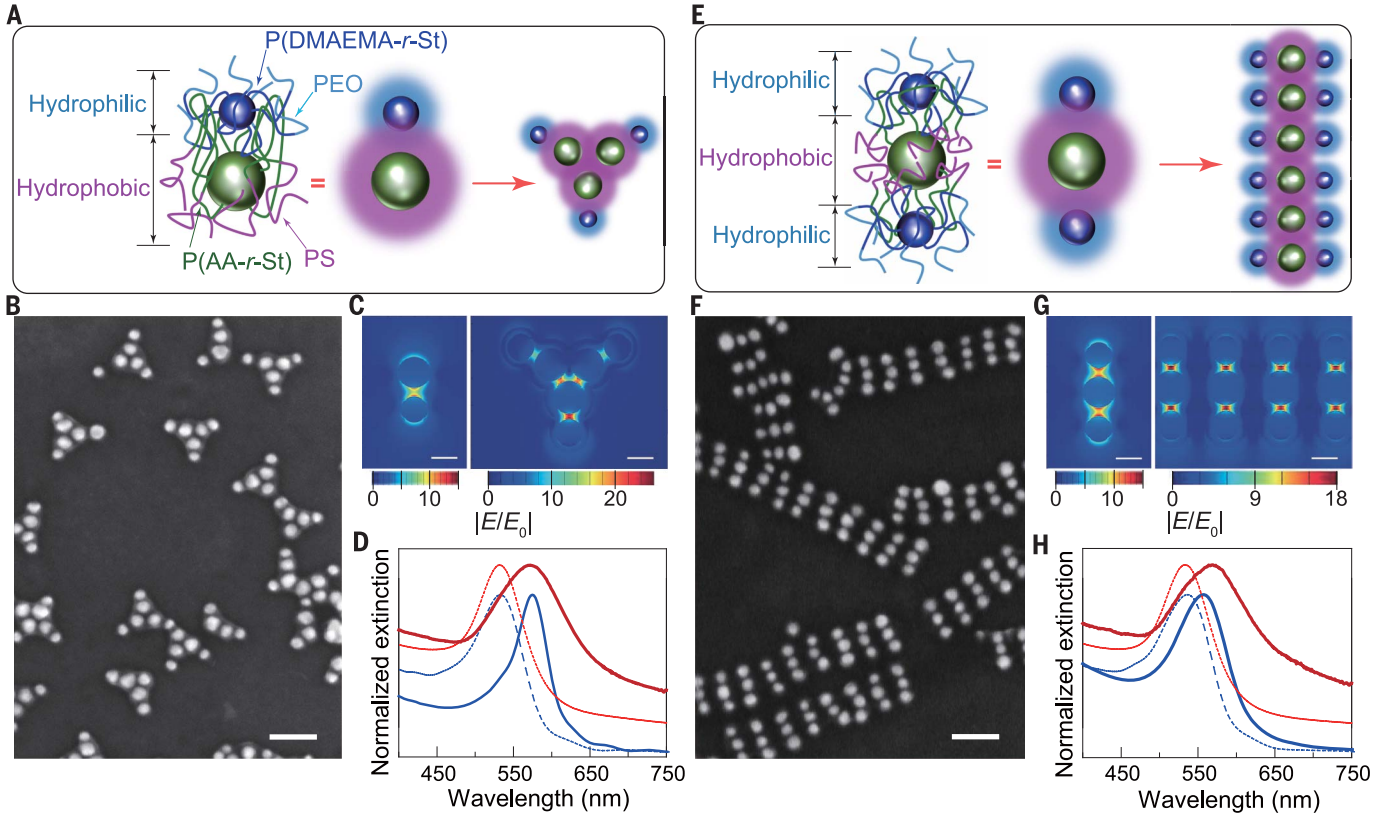

Fig. 4. Hierarchical self-assembly of amphiphilic CMs. (**A** and **E**) Schematics of self-assembly of amphiphilic AB CMs (A) and AB_2 (E) CMs. (**B** and **F**) SEM images of petal-like assemblies from amphiphilic AB CMs (B) and ribbons from amphiphilic AB_2 CMs (F). The copolymers used for NP-A and NP-B are PSt_{267}-*b*-$P(AA_{0.32}\text{-}r\text{-}St_{0.68})_{318}$ and PEO_{45}-*b*-$P(DMAEMA_{0.41}\text{-}r\text{-}St_{0.59})_{463}$ (B), and PSt_{267}-*b*-$P(AA_{0.32}\text{-}r\text{-}St_{0.68})_{318}$ and PEO_{45}-*b*-$P(DMAEMA_{0.36}\text{-}r\text{-}St_{0.64})_{156}$ (F), respectively. (**C** and **G**) Simulated electric field intensity enhancement contours of an AB CM (left) and the corresponding petal-like assemblies (right) (C), and an AB_2 CM (left) and the corresponding ribbon-like assemblies (right) (G) on glass substrates. The electric field is polarized along the vertical direction. $|E/E_0|$, electric field intensity enhancement. (**D** and **H**) Normalized extinction of AB (D) and AB_2 (H) CMs in tetrahydrofuran (dashed lines) and their petal-like (D) and ribbon-like (H) assemblies on glass substrates (solid lines) in experiment (red lines) and simulation (blue lines). Scale bars are 100 nm in (B) and (F) and 50 nm in (C) and (G).

NP-B. The value of $Z_{A/B}$ was changed by varying the D of NP-As or NP-Bs, copolymer structure, or the grafting density σ of copolymers as

$$Z_{A/B} = \frac{\alpha \cdot m}{\beta \cdot n} \cdot \frac{\sigma_A}{\sigma_B} \cdot \left(\frac{D_A}{D_B}\right)^2$$

where subscripts A and B correspond to the characteristics of NP-A and NP-B respectively, and $\alpha{\cdot}m$ and $\beta{\cdot}n$ are the number of acid groups in the $P(AA_\alpha\text{-}r\text{-}St_{1-\alpha})_m$ block and base groups in the $P(DMAEMA_\beta\text{-}r\text{-}St_{1-\beta})_n$ block, respectively, in the copolymer ligands. The value of $Z_{A/B}$ is controlled by varying α, m, σ_A, and D_A for NP-As or β, n, σ_B, and D_B for NP-Bs.

Based on the evaluation of the effect of α, n, σ_A, and D_B by changing one of these parameters at a time, we propose the following stoichiometry-driven NP bonding principles:

1) The grafting density σ determines the total number of reactive groups per NP and hence the value of x in the AB_x structure (fig. S32A). When NP-B characteristics are constant, the increase of σ_A results in a transition from AB_2 to AB_4, and to AB_6 structures (Fig. 3A, fig. S33, and table S12). However, at $\sigma_A \geq 0.30$ chain/nm^2, colloidal bonding is suppressed, owing to the limited interpenetration of the ligands on reacting NPs.

2) The value of x increases with increasing α of the $P(AA_\alpha\text{-}r\text{-}St_{1-\alpha})_m$ block or decreasing β of the $P(DMAEMA_\beta\text{-}r\text{-}St_{1-\beta})_n$ block (fig. S32B). An increase in α results in a transition from AB to AB_2 and to AB_3 structure, because more NP-Bs are required to react with a larger number of acid groups on the NP-A (Fig. 3B, fig. S34, and table S13). In our work, CMs form only in a specific range of α and β values, that is, $0.10 \leq \alpha \leq 0.36$ and $0.29 \leq \beta \leq 0.41$. When α or β is smaller than the minimum values, the CMs form at low yield, owing to the insufficient NP reactivity (fig. S35), whereas when α or β exceeds the maximum values, the NPs are colloidally unstable (fig. S36).

3) The variation in D and n (or m) cooperatively influences NP bonding by controlling both $Z_{A/B}$ and the accessibility of reactive moieties on interacting NP pairs (fig. S32, C and D). The increase in D_B and n for NP-B leads to AB_x structures with a reduced x, because more base groups are available on NP-Bs for reaction (Fig. 3, C and D; figs. S37 and S38; and tables S14 and S15).

Figure 3E shows the experimental and computational results on the dependence of AB_x structures on the ratio $Z_{A/B}$. The variation in the discrete values of x in AB_x structures followed a linear trend of $x \approx Z_{A/B} = N_A/N_B$ (or $N_A \approx xN_B$), which determined the ratio between NP-B and NP-A "reactants" in the reaction.

We engineered copolymer ligands to achieve programmable assembly of CMs in hierarchical structures with tunable optical properties (Fig. 4). In a proof-of-concept experiment, hydrophobic NP-As [generated by replacing the PEO block in the ligands with a polystyrene (PSt) block] were bonded with hydrophilic NP-Bs tethered with PEO-*b*-P(DMAEMA-*r*-St) copolymers to form amphiphilic AB CMs (Fig. 4A and fig. S39A). The CM solution in tetrahydrofuran was placed on top of the saturated aqueous solution of NaCl. (The latter is immiscible with tetrahydrofuran.) After tetrahydrofuran evaporation, hydrophobic interactions between NP-A subunits governed CM assembly into petal-like structures (Fig. 4B). The self-assembly resulted in a polarization-dependent enhancement of electric near-field and red shift of the plasmonic bands of the assemblies, owing to plasmonic coupling between the NP-As in the petal-like structures (Fig. 4, C and D, and fig. S40, A and B). Furthermore, we achieved hierarchical assembly of amphiphilic AB_2 structures with a hydrophobic center and two hydrophilic ends into linear ribbons, owing to the side-by-side association of the hydrophobic NP-As (Fig. 4E and fig. S39B). Compared with AB_2 CMs, additional near-field enhancement and red shift of plasmonic bands were caused by coupling between NPs along the longitudinal axis of ribbons (Fig. 4, F and G, and fig. S40, C and D).

We have developed a stoichiometry mediated colloidal bonding strategy for high-yield fabrication of nanoscale CMs with well-defined structures. The experimental and computational results reveal that the mechanism of colloidal bonding and the CM "formulas" are governed by the reaction between flexible polymer ligands on the NP surface, whereas the CM symmetry (bond angles) is controlled by electrostatic repulsion between the NPs. The design principles for CM generation show that the approach is applicable to NPs with different sizes and compositions. By tailoring the features of the polymer ligands, the interactions between CMs are engineered to guide their assembly at a higher hierarchical level.

REFERENCES AND NOTES

1. M. A. Boles, M. Engel, D. V. Talapin, *Chem. Rev.* **116**, 11220–11289 (2016).
2. Z. Nie, A. Petukhova, E. Kumacheva, *Nat. Nanotechnol.* **5**, 15–25 (2010).
3. J. A. Fan *et al.*, *Science* **328**, 1135–1138 (2010).
4. Y. Zhao, L. Shang, Y. Cheng, Z. Gu, *Acc. Chem. Res.* **47**, 3632–3642 (2014).
5. É. Ducrot, M. He, G. R. Yi, D. J. Pine, *Nat. Mater.* **16**, 652–657 (2017).
6. Y. Yamada *et al.*, *Nat. Chem.* **3**, 372–376 (2011).
7. Av. Blaaderen, *Science* **301**, 470–471 (2003).
8. K. Liu *et al.*, *Science* **329**, 197–200 (2010).
9. Y. Min, M. Akbulut, K. Kristiansen, Y. Golan, J. Israelachvili, *Nat. Mater.* **7**, 527–538 (2008).
10. Y. Wang *et al.*, *Nature* **491**, 51–55 (2012).
11. A. H. Gröschel *et al.*, *Nature* **503**, 247–251 (2013).
12. S. C. Glotzer, M. J. Solomon, *Nat. Mater.* **6**, 557–562 (2007).
13. W. Liu, J. Halverson, Y. Tian, A. V. Tkachenko, O. Gang, *Nat. Chem.* **8**, 867–873 (2016).
14. G. Chen *et al.*, *Nat. Mater.* **18**, 169–174 (2019).
15. V. N. Manoharan, M. T. Elsesser, D. J. Pine, *Science* **301**, 483–487 (2003).
16. R. M. Choueiri *et al.*, *Nature* **538**, 79–83 (2016).
17. H. Qiu *et al.*, *Science* **352**, 697–701 (2016).
18. A. P. Alivisatos *et al.*, *Nature* **382**, 609–611 (1996).
19. T. G. Edwardson, K. L. Lau, D. Bousmail, C. J. Serpell, H. F. Sleiman, *Nat. Chem.* **8**, 162–170 (2016).
20. W. Liu *et al.*, *Science* **351**, 582–586 (2016).
21. X. Xu, N. L. Rosi, Y. Wang, F. Huo, C. A. Mirkin, *J. Am. Chem. Soc.* **128**, 9286–9287 (2006).
22. G. Yao *et al.*, *Nat. Mater.* **19**, 781–788 (2020).
23. M. M. Maye, D. Nykypanchuk, M. Cuisinier, D. van der Lelie, O. Gang, *Nat. Mater.* **8**, 388–391 (2009).
24. Y. Tian *et al.*, *Nat. Nanotechnol.* **10**, 637–644 (2015).
25. Z. Lin, Y. Xiong, S. Xiang, O. Gang, *J. Am. Chem. Soc.* **141**, 6797–6801 (2019).
26. J. N. Murrell, S. F. A. Kettle, J. M. Tedder, *The Chemical Bond* (Wiley, ed. 2, 1985).
27. M. Rubinstein, R. H. Colby, *Polymer Physics* (Oxford Univ. Press, 2003).
28. Hongliu83, hongliu83/Stochastic-reaction-model: Stochastic reaction model. Zenodo (2020); https://doi.org/10.5281/zenodo.3781761.
29. E. Paenurk *et al.*, *Chem. Sci.* **8**, 6964–6973 (2017).

ACKNOWLEDGMENTS

Funding: This work was supported by the National Natural Science Foundation of China (grants 51973038, 91963107, and 21534004), the Startup Fund from Fudan University, the National Science Foundation (grant CHE-1505839), and the Discovery and Canada Research Chair (Tier 1) programs (NSERC Canada). **Author contributions:** Z.N. directed all aspects of the project. Z.N., C.Y., and E.K. conceived the project. C.Y., S.Z., and Y.Z. performed the self-assembly. C.Y., S.Z., Y.Z., and Y.Y. performed the characterization of the assembled structures. H.L. and Z.L. performed the computer simulation. Z.N., E.K., C.Y., and Z.L. wrote the manuscript with input from all co-authors. The authors thank M. Rubinstein for fruitful discussions. **Competing interests:** The authors declare no competing interests. **Data and materials availability:** All data are available in the main text or the supplementary materials.

SUPPLEMENTARY MATERIALS

science.sciencemag.org/content/369/6509/1369/suppl/DC1
Materials and Methods
Supplementary Text
Figs. S1 to S40
Tables S1 to S15
References (*30*–*49*)
Movie S1

12 January 2020; accepted 22 July 2020
10.1126/science.aba8653

ATMOSPHERIC AEROSOLS

Multiphase buffer theory explains contrasts in atmospheric aerosol acidity

Guangjie Zheng[1], Hang Su[2]*, Siwen Wang[2], Meinrat O. Andreae[2,3,4], Ulrich Pöschl[2], Yafang Cheng[1]*

Aerosol acidity largely regulates the chemistry of atmospheric particles, and resolving the drivers of aerosol pH is key to understanding their environmental effects. We find that an individual buffering agent can adopt different buffer pH values in aerosols and that aerosol pH levels in populated continental regions are widely buffered by the conjugate acid-base pair NH_4^+/NH_3 (ammonium/ammonia). We propose a multiphase buffer theory to explain these large shifts of buffer pH, and we show that aerosol water content and mass concentration play a more important role in determining aerosol pH in ammonia-buffered regions than variations in particle chemical composition. Our results imply that aerosol pH and atmospheric multiphase chemistry are strongly affected by the pervasive human influence on ammonia emissions and the nitrogen cycle in the Anthropocene.

Aerosol acidity has attracted increasing interest in atmospheric research because it influences the thermodynamics of gas-particle partitioning and the chemical kinetics of the formation and transformation of air particulate matter (*1*–*8*). Understanding the temporal and spatial variations of aerosol pH in the atmosphere is crucial for accurate predictions of the properties of atmospheric aerosols and their effects on health, ecosystems, and climate (*9*–*12*). In marine environments, the uptake of acidic gases like SO_2, H_2SO_4, and HNO_3 may rapidly consume the alkalinity and reduce the pH of sea salt aerosols (*13*, *14*). For continental air masses in the southeastern United States, Weber *et al.* (*15*) have suggested that aerosol pH is buffered in the range of ~0 to 2 because of the interaction of aqueous $(NH_4)_2SO_4$-NH_4HSO_4 with gaseous NH_3. However, their later studies have attributed the elevated pH levels in northern China (~3 to 6) (*8*, *16*–*19*) mainly to changes in particle chemical compositions—i.e., a shift from sulfate- to nitrate-dominated aerosols (*12*, *19*)—whereas Cheng *et al.* (*8*) have highlighted the role of ammonia and alkaline aerosol components from natural and anthropogenic emissions in understanding aerosol pH in this region.

Despite these advances, it is still unclear how aerosol pH is buffered in other continental regions, such as northern China, compared with the southeastern United States. To answer this question, we first performed numerical model calculations with the state-of-the-art thermodynamic model ISORROPIA (*20*) to examine the response of pH in aerosols upon the addition of sulfuric acid under different conditions that are characteristic of the southeastern United States (*15*, *21*), the North China Plain (*8*, *22*), northern India (*23*), and western Europe (*24*) [table S1 and (*25*)]. For reference, we also calculated the response of an aqueous solution of Na_2SO_4. As shown in fig. S1, the Na_2SO_4 solution exhibits the expected steep decrease of pH upon acid addition. For aerosol systems, however, the pH does not show a substantial decrease until the added amount of acid (H^+ equivalent) reaches ~20% of the initial amount of anions in the aqueous particles (molar ratio), which indicates an additional buffering effect. To further investigate this phenomenon, we focus on the scenarios for the southeastern United States (SE-US) and for the North China Plain (NCP), which have been intensively investigated and discussed in earlier studies. As indicated in table S1, the SE-US scenario is characterized by relatively low aerosol concentration, low aerosol water content (AWC), and high temperature, as observed under clean-air summer conditions in the southeastern United States. By contrast, the NCP scenario is characterized by the high aerosol concentration, high AWC, and low temperature observed during extreme winter haze events in the Beijing region.

In aqueous solutions, the pH of different buffer systems is usually determined by the pK_a (where K_a is the acid dissociation constant) of the buffering agents (*26*). Accordingly, the different pH buffer levels in fig. S1 would suggest different buffering agents corresponding to different particle chemical compositions. To identify the most relevant buffering agents, key controlling parameters, we introduce the concept of a multiphase buffering capacity that describes the resistance to pH changes upon input of acids or bases in an aerosol multiphase system in analogy to the traditional buffering capacity of bulk aqueous solutions. The buffering capacity β is defined as the ratio between the amount of acid or base added to the system (n_{acid} or n_{base}, in moles per kilogram) and the corresponding pH change in the aqueous phase of the system, or $\beta = -dn_{acid}/d\mathrm{pH} = dn_{base}/d\mathrm{pH}$. The larger the buffering capacity β, the less the pH will change upon the addition of acids or bases.

Figure 1A shows the buffering capacities for the SE-US and NCP aerosol scenarios and for bulk aqueous solutions of the individual buffering agents (i.e., conjugate acid-base pairs NH_4^+/NH_3, HSO_4^-/SO_4^{2-}, and HNO_3/NO_3^-) as derived from numerical simulations of the gas-liquid and acid-base equilibria [see materials and methods, section M1; results of the northern India and western Europe scenarios are in fig. S2; and results of organic buffers are in the supplementary text, section S7 (*25*)]. In both aerosol scenarios, the largest buffering capacity is obtained for the acid-base pair NH_4^+/NH_3 followed by HSO_4^-/SO_4^{2-} and HNO_3/NO_3^-. The peak buffer pH value (defined as the pH corresponding to the highest local maximum of β) for the SE-US scenario is ~0.7, and the peak buffer pH value for the NCP scenario is ~4.5. Thus, the buffer pH ranges (i.e., peak buffer pH ± 1) (*26*, *27*) closely match the aerosol pH ranges previously reported for the southeastern United States and for Beijing, respectively. This indicates that the conjugate acid-base pair NH_4^+/NH_3 is the main buffering agent in both the SE-US and NCP aerosol scenarios.

This finding raises the question of how the same buffering agent can stabilize the aerosol pH at very different levels. As shown in Fig. 1A, in bulk aqueous solution, the peak buffer pH of NH_4^+/NH_3 is ~9.2, but in the NCP and SE-US aerosol scenarios, it shifts to much lower values of ~4.5 and ~0.7, respectively. By contrast, the peak buffer pH of the conjugate acid-base pair HNO_3/NO_3^- shifts in the opposite direction from ~−1.5 in the bulk aqueous solution to higher values of ~0.2 and ~3.8 in the NCP and SE-US scenarios, respectively. The conjugate acid-base pair HSO_4^-/SO_4^{2-}, on the other hand, exhibits similar peak buffer pH values of ~2 in all three scenarios (Fig. 1A). These differences and shifts of peak buffer pH reflect special features of the aerosol multiphase buffer system that go beyond the traditional buffer theory for bulk aqueous solutions, and they highlight the need for a mechanistic understanding of the multiphase buffering mechanism in atmospheric aerosols.

To elucidate the underlying mechanisms and key parameters, we have developed a multiphase buffer theory and derived an analytical expression for the buffering capacity of a buffering agent X (conjugate acid-base pair) in an aerosol multiphase buffer system as detailed in section S1 (*25*)

$$\beta = \frac{dn_{base}}{d\mathrm{pH}} = 2.303\left\{\frac{K_w}{[H^+]} + [H^+] + \sum_i \frac{K_{a,i}^*[H^+]}{(K_{a,i}^* + [H^+])^2}[X_i]_{tot}^*\right\} \quad (1)$$

[1]Minerva Research Group, Max Planck Institute for Chemistry, Mainz 55128, Germany. [2]Multiphase Chemistry Department, Max Planck Institute for Chemistry, Mainz 55128, Germany. [3]Scripps Institution of Oceanography, University of California, San Diego, La Jolla, CA 92093, USA. [4]Department of Geology and Geophysics, King Saud University, 11451 Riyadh, Saudi Arabia.
*Corresponding author. Email: yafang.cheng@mpic.de (Y.C.); h.su@mpic.de (H.S.)

Here, K_w is the water dissociation constant, $[X_i]_{tot}^*$ represents the total equivalent molality of the buffering agent X_i, including the gas phase and aqueous phase of both conjugate acid-base species—e.g., the sum of $NH_3(g)$, $NH_3(aq)$, and $NH_4^+(aq)$ for the buffering agent NH_4^+/NH_3. $K_{a,i}^*$ is an effective acid dissociation constant of the buffering agent X_i and can be expressed by

$$K_{a,BOH}^* = \frac{[H^+(aq)]\left([BOH(aq)] + [BOH(g)]\right)}{[B^+(aq)]} = K_{a,BOH}\left(1 + \frac{\rho_w}{H_i\, R\, T\, AWC}\right) \quad (2A)$$

$$K_{a,HA}^* = \frac{[H^+(aq)][A^-(aq)]}{[HA(aq)]+[HA(g)]} = K_{a,HA}/\left(1 + \frac{\rho_w}{H_i\, R\, T\, AWC}\right) \quad (2B)$$

for volatile base BOH and volatile acid HA that dissociate in the form

$$B^+(aq) + H_2O \rightleftharpoons H^+(aq) + BOH(aq) \quad (2C)$$

$$HA(aq) \rightleftharpoons H^+(aq) + A^-(aq) \quad (2D)$$

As shown in Eq. 2, the effective dissociation constant $K_{a,i}^*$ depends on the classical dissociation constant $K_{a,i}$ as well as on the Henry's law coefficient H_i (gas-particle partitioning constant) (in moles per liter per atmosphere) and on the AWC (in micrograms per cubic meter)—i.e., the amount of liquid water in the aerosol multiphase system. Here, ρ_w is the liquid water density (~10^{12} μg m^{-3}), R is the gas constant (8.205 ×10^{-2} atm L mol^{-1} K^{-1}), and T is the absolute temperature (in kelvin). Note that gas concentrations in square brackets are expressed in units of equivalent molality (in moles per kilogram of water) [see section M1 (*25*)]. The expression of Eqs. 1 and 2 in the other unit system can be found in section S2.

By solving Eq. 1, we can find a local maximum of β at pH = $pK_{a,i}^*$; i.e., the peak buffer pH of the agent X_i is determined by $K_{a,i}^*$. Therefore, a single buffering agent can have its peak buffering capacity at very different pH values in an aerosol multiphase buffer system. According to Eq. 2A, for the buffering agent NH_4^+/NH_3 (volatile base), increasing AWC results in a reduced K_a^* and increased pK_a^*. Thus, the traditional alkaline buffering agent NH_4^+/NH_3 effectively becomes an acidic buffering agent ($pK_a^* < 7$) in multiphase systems (Fig. 1A). For volatile acid buffering agents (HNO_3/NO_3^-), the AWC has the opposite effect on pK_a^* (Fig. 1A). Moreover, the shift of pK_a^* upon changes to the AWC is inversely proportional to the partitioning coefficient H_i. Thus, the volatile buffering agents HNO_3/NO_3^- and NH_4^+/NH_3 (low H_i) exhibit large shifts, whereas the peak buffer pH of HSO_4^-/SO_4^{2-} hardly changes (high H_i) (table S2). As shown in Fig. 1B, the effective dissociation constant K_a^* converges with the standard acid-base dissociation constant of the buffering agent for high values of AWC (Eq. 2), and the multiphase buffer theory converges with the conventional buffer theory in solution chemistry [see sections S1 to S4 (*25*)]. Note that activity coefficients must be considered in the calculation of nonideal systems [see section S3 (*25*)].

Figure 2 further explains the thermodynamics that causes the shift of buffer pH in a multiphase system. The conventional bulk buffer solutions (e.g., NH_4^+/NH_3), assuming no exchange with a gas phase, achieve their largest resistance to pH change when the molality of $NH_4^+(aq)$ is equal to that of $NH_3(aq)$ (Eq. 3A) (*26*)

$$pH = pK_{a,NH_3} + \log_{10}\frac{[NH_3(aq)]}{[NH_4^+(aq)]} \quad (3A)$$

where

$$K_{a,NH_3} = \frac{K_w}{K_{b,NH_3}} = \frac{[H^+(aq)][NH_3(aq)]}{[NH_4^+(aq)]} \quad (3B)$$

and K_{b,NH_3} is the base dissociation constant of NH_3 (table S2).

For gas-liquid multiphase systems, this equilibrium is extended to the gas phase, and pH becomes a function of K_a^* and the ratio of total NH_3 in both gas and aqueous phase to NH_4^+ in the aqueous phase [Eq. 4A; section S1 (*25*)]. Accordingly, the largest resistance to pH change under given $[NH_3]_{tot}^*$ ($[NH_3]_{tot}^* = [NH_3(aq)] + [NH_3(g)] + [NH_4^+(aq)]$) is achieved when the molality of $NH_4^+(aq)$ is equal to the sum of $NH_3(aq)$ and $NH_3(g)$. Note that Eq. 3 still holds for the aqueous phase in the multiphase system

$$pH = pK_{a,NH_3}^* + \log_{10}\frac{[NH_3(aq)]+[NH_3(g)]}{[NH_4^+(aq)]} \quad (4A)$$

where

$$K_{a,NH_3}^* = \frac{[H^+(aq)]\left([NH_3(aq)]+[NH_3(g)]\right)}{[NH_4^+(aq)]} = K_{a,NH_3}\left(1 + \frac{\rho_w}{H_{NH_3} RT AWC}\right) \quad (4B)$$

Figure 2 shows the conditions where the peak buffer pH values are achieved in different systems—i.e., the same height of NH_4^+ and NH_3 in each panel represents their same molar numbers in each system. Compared with bulk

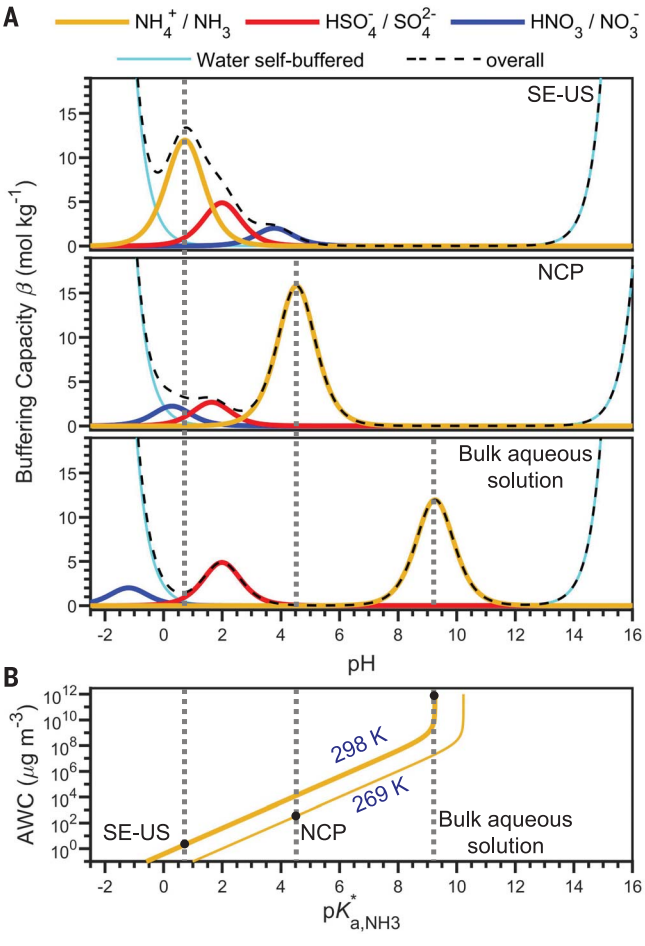

Fig. 1. Buffering capacity for aerosol multiphase systems compared with bulk aqueous solution. (**A**) Buffer capacities (β) for the SE-US and NCP aerosol scenarios and for bulk aqueous solution of individual buffering agents (solid lines). The overall buffering capacity (black dashed lines) is obtained by adding the individual buffer agent contributions to the solvent background of water [fig. S3 and section S5 (*25*)]. The composition of the bulk solution is assumed to have the same aqueous phase molality as in the SE-US scenario. (**B**) Dependence of the peak buffer capacity (pK_a^*) of NH_4^+/NH_3 on aerosol water content (AWC) and temperature.

solution, a fraction of NH_3 partitions to the gas phase in the NCP scenario, which results in less NH_3(aq) and a reduced [NH_3(aq)]/[NH_4^+(aq)] ratio, which leads to a lower pH in the aqueous phase according to Eq. 3. Further reduction of AWC in the SE-US scenario will push more NH_3 to the gas phase and further reduce the aerosol pH.

Figure 3 compares the contribution of individual factors in explaining the difference in aerosol pH between the NCP (~5.4) and SE-US (~0.7) scenarios in fig. S1 [sections M2, S3, S5, and S6 (*25*)]. The AWC appears to be the most important factor, contributing 2.2 units of pH change (ΔpH), followed by *T*, which contributes another 1.6 units of ΔpH. Although earlier studies have hypothesized that the marked observed pH difference is caused by a transition in particle chemical composition from a sulfate- to a nitrate-dominated regime (*12*, *19*), our results show that the change of chemical composition only plays a minor role. Different AWCs [mainly caused by different aerosol concentrations at a given relative humidity (RH)] and *T* values can already explain a shift of ~4 units of aerosol pH. The difference in chemical composition contributes ~0.7 pH units in total, with ~0.5 from the difference in total NH_3 fraction and ~0.1 and ~0.1 from the difference in the fraction of NO_3^- and nonvolatile cations (NVCs), respectively. Overall, different AWCs and *T* values are the main drivers of the pH difference between the NCP and SE-US scenarios, whereas the higher fraction of total NH_3, NVCs, and NO_3^- in the NCP further enlarges the difference.

In Fig. 4, we performed global model simulations to identify the buffered regions and used both simulation and observational data to further compare the roles of AWC and chemical compositions in determining the variabilities of aerosol pH [sections M3, S3, and S6 and table S3 (*25*)]. As shown in Fig. 4A, ~40% of continental surface areas (not including Antarctica) and 71% of urban populated areas were buffered by the NH_4^+/NH_3 agent with aerosol pH values mostly within the buffer range [$pK_{a,NH3}^*$ ± 1 (*26*, *27*)]. In these regions, without knowing the temporal and spatial variability of particle chemical composition, variations in AWC alone explain almost 70% (R^2 = 0.66, simulation; where R^2 is the coefficient of determination) and 80% (R^2 = 0.77, observation) of the variation of aerosol pH, assuming an NH_4^+/NH_3–buffered system (Fig. 4B). On the other hand, when a constant AWC is assumed, distinct variations of aerosol acidity with particle chemical composition were observed, but they only played a secondary role (R^2 = 0.22 and 0.26 for simulation and observation, respectively; Fig. 4C). We also found a reverse role for AWC and composition in regions that are not buffered by NH_4^+/NH_3, where chemical composition differences alone explain >90% of the variations of aerosol pH (fig. S5). Overall,

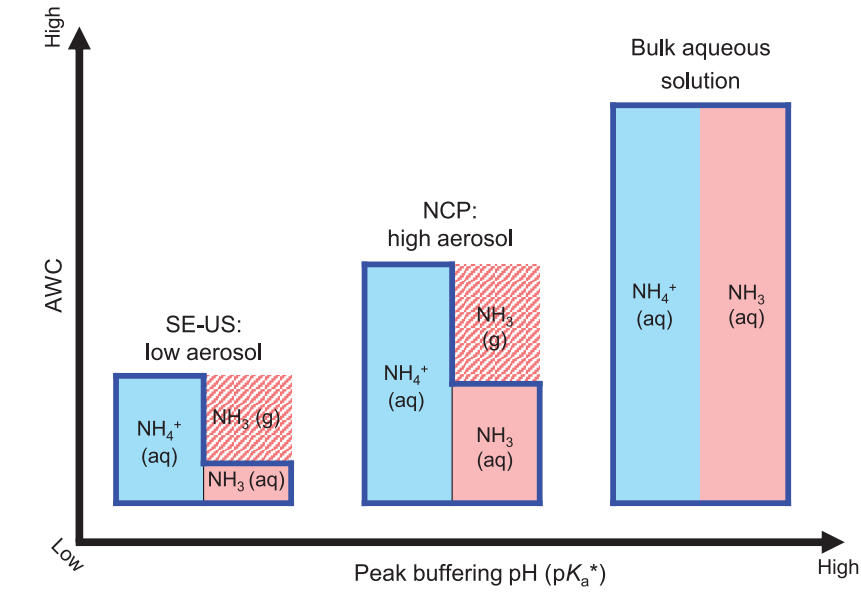

Fig. 2. Schematic diagram of buffer pH transition from aerosol multiphase systems to bulk aqueous solution for NH_4^+/NH_3. AWC concentrations are not drawn to scale, for illustration purposes. Diagrams for a generic volatile acid and base are shown in fig. S4.

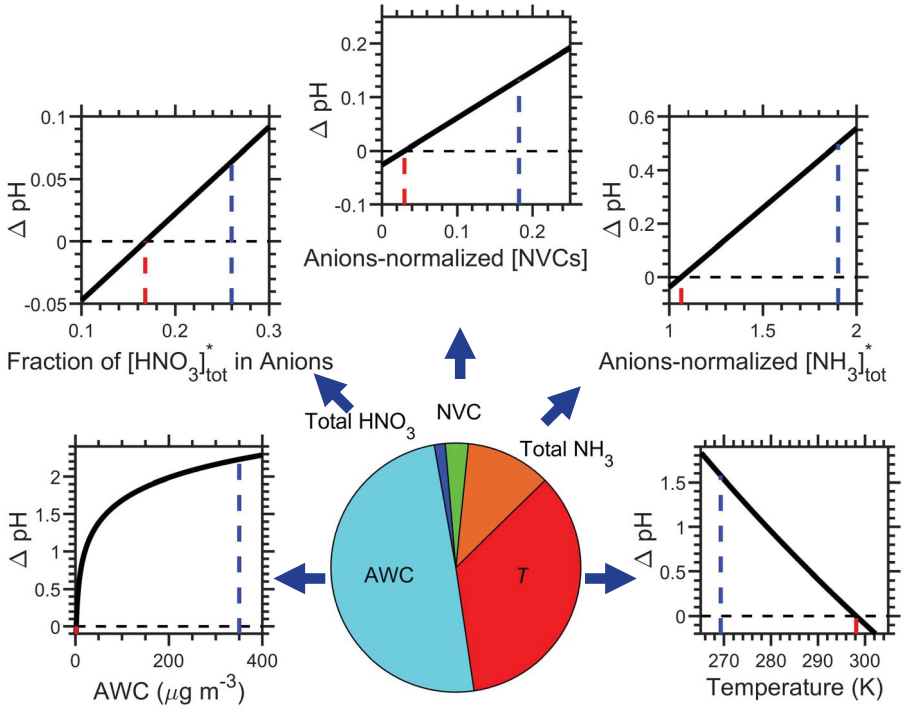

Fig. 3. Fractional contribution of individual drivers to the aerosol pH difference between SE-US and NCP scenarios. Red and blue lines mark the corresponding values in the SE-US and NCP scenarios, respectively [see table S1 for detailed scenario information (*25*)].

the buffering effect of ammonia suppresses the influence of compositional differences, making aerosol water content the primary determinant of aerosol pH.

The multiphase buffering of aerosols and the key role of AWC in determining the peak buffer pH (pK_a^*) have implications for atmospheric research and air pollution control. Drivers of historical trends in aerosol pH can now be better understood and quantified [section S8 (*25*)]. In populated continental regions with high anthropogenic emissions and atmospheric concentrations of ammonia (*28*), aerosol pH is likely controlled by the buffering pair NH_4^+/NH_3 and can thus be approximated on the basis of aerosol mass concentration and

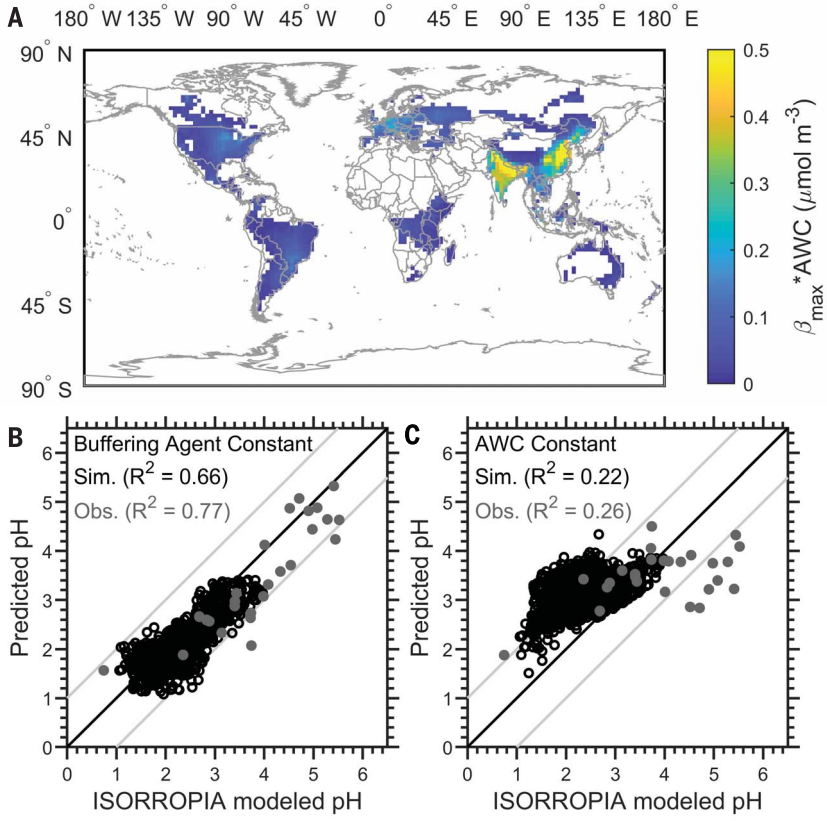

Fig. 4. Drivers of aerosol pH diversity in ammonia-buffered regions. (**A**) Global distribution of continental surface regions buffered by NH_4^+/NH_3. The color coding shows the maximum buffer capacity by NH_4^+/NH_3 (in moles per cubic meter of air). (**B**) Correlation of aerosol pH modeled by ISORROPIA with the predicted pH derived using constant buffering agent and multiphase buffer theory. Sim., simulation; Obs., observation. (**C**) Correlation of aerosol pH modeled by ISORROPIA with the predicted pH by ISORROPIA using constant AWC but variable compositions. Black circles and gray dots represent analysis based on model simulations and observations, respectively (see section M3 and table S3). Note that the observations are based on individual case studies and thus show a wider range of aerosol pH than the annual average simulation results.

water content (Eq. 4). This opens up possibilities to reconstruct long-term trends and large-scale spatial distributions of aerosol pH. Other buffering agents, such as HSO_4^-/SO_4^{2-}, HCl/Cl^-, or HCO_3^-/CO_3^{2-}, are likely to control aerosol pH over the oceans (*13*, *14*, *29*, *30*), but the buffering effects of NH_4^+/NH_3 may extend over ammonia-rich coastal and downwind regions. Thus, the notable human influence on ammonia emissions and the global nitrogen cycle in the Anthropocene substantially affects aerosol pH and atmospheric multiphase chemistry on a global scale.

REFERENCES AND NOTES

1. J. H. Seinfeld, S. N. Pandis, *Atmospheric Chemistry and Physics: From Air Pollution to Climate Change* (Wiley, 2016).
2. D. J. Jacob, J. W. Munger, J. M. Waldman, M. R. Hoffmann, *J. Geophys. Res. Atmos.* **91**, 1073–1088 (1986).
3. D. J. Jacob, J. M. Waldman, J. W. Munger, M. R. Hoffmann, *J. Geophys. Res. Atmos.* **91**, 1089–1096 (1986).
4. A. R. Ravishankara, *Science* **276**, 1058–1065 (1997).
5. M. Jang, N. M. Czoschke, S. Lee, R. M. Kamens, *Science* **298**, 814–817 (2002).
6. S. Gao *et al.*, *Environ. Sci. Technol.* **38**, 6582–6589 (2004).
7. J. D. Surratt *et al.*, *Environ. Sci. Technol.* **41**, 5363–5369 (2007).
8. Y. Cheng *et al.*, *Sci. Adv.* **2**, e1601530 (2016).
9. D. W. Dockery *et al.*, *Environ. Health Perspect.* **104**, 500–505 (1996).
10. W. Li *et al.*, *Sci. Adv.* **3**, e1601749 (2017).
11. E. Harris *et al.*, *Science* **340**, 727–730 (2013).
12. H. O. T. Pye *et al.*, *Atmos. Chem. Phys.* **20**, 4809–4888 (2020).
13. W. C. Keene, A. A. P. Pszenny, J. R. Maben, R. Sander, *Geophys. Res. Lett.* **29**, 1101 (2002).
14. B. Alexander *et al.*, *J. Geophys. Res. Atmos.* **110**, D10307 (2005).
15. R. J. Weber, H. Guo, A. G. Russell, A. Nenes, *Nat. Geosci.* **9**, 282–285 (2016).
16. M. Liu *et al.*, *Geophys. Res. Lett.* **44**, 5213–5221 (2017).
17. G. Shi *et al.*, *Environ. Sci. Technol.* **51**, 4289–4296 (2017).
18. S. Song *et al.*, *Atmos. Chem. Phys.* **18**, 7423–7438 (2018).
19. H. Guo, R. J. Weber, A. Nenes, *Sci. Rep.* **7**, 12109 (2017).
20. C. Fountoukis, A. Nenes, *Atmos. Chem. Phys.* **7**, 4639–4659 (2007).
21. H. Guo *et al.*, *Atmos. Chem. Phys.* **15**, 5211–5228 (2015).
22. G. J. Zheng *et al.*, *Atmos. Chem. Phys.* **15**, 2969–2983 (2015).
23. S. N. Behera, M. Sharma, *Sci. Total Environ.* **408**, 3569–3575 (2010).
24. L. Bencs *et al.*, *J. Environ. Monit.* **10**, 1148–1157 (2008).
25. See supplementary materials.
26. P. Atkins, L. Jones, *Chemical Principles: The Quest for Insight* (Macmillan, 2007).
27. H. N. Po, N. Senozan, *J. Chem. Educ.* **78**, 1499 (2001).
28. M. Van Damme *et al.*, *Nature* **564**, 99–103 (2018).
29. W. C. Keene, D. L. Savoie, *Geophys. Res. Lett.* **25**, 2181–2184 (1998).
30. D. J. Gaspar, A. Laskin, W. Wang, S. W. Hunt, B. J. Finlayson-Pitts, *Appl. Surf. Sci.* **231-232**, 520–523 (2004).

ACKNOWLEDGMENTS

Funding: This study is support by the Max Planck Society (MPG). Y.C. thanks the Minerva Program of MPG. **Author contributions:** Y.C. and H.S. conceived the theory and led the study. G.Z., Y.C., and H.S. performed the research. S.W. performed the GEOS-Chem simulation. M.O.A. commented on the manuscript. H.S., Y.C., G.Z., and U.P. wrote the manuscript with inputs from all coauthors. **Competing interests:** The authors declare no competing interests. **Data and materials availability:** All data used in the analysis are provided in the supplementary materials.

SUPPLEMENTARY MATERIALS

science.sciencemag.org/content/369/6509/1374/suppl/DC1
Materials and Methods
Supplementary Text
Figs. S1 to S15
Table S1 to S4
References (*31*–*97*)
Data S1

29 November 2019; accepted 21 July 2020
10.1126/science.aba3719

TROPICAL FOREST

Long-term forest degradation surpasses deforestation in the Brazilian Amazon

Eraldo Aparecido Trondoli Matricardi[1]*, David Lewis Skole[2]*, Olívia Bueno Costa[1], Marcos Antonio Pedlowski[3], Jay Howard Samek[2], Eder Pereira Miguel[1]

Although deforestation rates in the Brazilian Amazon are well known, the extent of the area affected by forest degradation is a notable data gap, with implications for conservation biology, carbon cycle science, and international policy. We generated a long-term spatially quantified assessment of forest degradation for the entire Brazilian Amazon from 1992 to 2014. We measured and mapped the full range of activities that degrade forests and evaluated the relationship with deforestation. From 1992 to 2014, the total area of degraded forest was 337,427 square kilometers (km^2), compared with 308,311 km^2 that were deforested. Forest degradation is a separate and increasing form of forest disturbance, and the area affected is now greater than that due to deforestation.

Several international initiatives—such as the Aichi Biodiversity Targets in the Convention on Biological Diversity, REDD+ (Reducing Emissions from Deforestation and Forest Degradation) in the United Nations Convention on Climate Change, and the Bonn Challenge, which focuses on restoration of degraded forests—require information on the rate and extent of forest degradation (*1*, *2*). Yet, degradation of forest ecosystems is perhaps one of the more challenging types of disturbances to measure and monitor. The rate and extent of forest degradation in the Brazilian Amazon (BA) is a key component of a national strategy for climate change mitigation and adaptation (*3*). One challenge with monitoring degradation is that it occurs within forests, leaving a standing stock of biomass and canopy cover that can make detection difficult. Forest degradation in the BA and elsewhere is caused by an array of agents or drivers, with greater or lesser degrees of poorly quantified interaction between drivers or with deforestation activities. Unlike deforestation, degradation events may reoccur with varying frequencies at the same location, sometimes several years later, and different types can spatially overlap.

Fundamentally, forest degradation has been widely recognized as an important form of disturbance (*4*–*6*). However, previous efforts to measure and map degradation in the BA have focused on individual agents, such as logging (*7*), burned areas or active fires (*8*, *9*), or fragmentation (*10*). Others have assessed degradation only indirectly; for instance, Baccini *et al*. (*4*) estimated carbon emissions from degradation as the difference between overall canopy damage and that attributed directly to deforestation (*11*). Other analyses have focused on specific sites or subregions (*5*) or on sampling in forest strata spatially associated with concentrated deforestation (*12*). In this analysis, our aim was to map the current BA-wide extent of forest ecosystems that have been degraded since 1992 and compare it with the area deforested. The analysis presented is a long-term (~23 years) BA-wide high-resolution spatial analysis, intended to reveal how degradation has changed in magnitude and geographic distribution and to measure its permanence in the landscape.

Forest disturbance by human activities in the BA occurs across a gradient of severity, from complete forest conversion to various intensities of degradation within forests. Deforestation is the complete conversion of forests to another land use type, usually pasture in the BA. Forest degradation occurs within forests and is characterized by a loss of biomass within an intact canopy (*6*). Forest degradation is also a secondary result of deforestation, which produces edge effects and isolated forest patches in fragmented forests (*13*). These disturbances have important large-scale environmental consequences, including the release of greenhouse gases (*14*–*16*), alteration of water and energy balances (*17*, *18*), loss of biodiversity (*19*, *20*), and increasing incidence of infectious disease (*21*). In the BA, deforestation reached a peak rate in 2003 to 2004 at ~29,000 km^2 year^{-1}, bringing international attention and then national policies that reduced these rates significantly (*22*). By 2014, deforestation rates declined below ~6000 km^2 year^{-1} based on satellite data analysis by the Amazon Deforestation Monitoring Project (PRODES) operated by the Brazilian Space Agency, Instituto Nacional de Pesquisas Espaciais (INPE) (*23*).

To map and analyze the distribution and extent of degraded forest in the BA forest landscape, we needed to use medium-resolution remote-sensing (30 m) data. An existing model (*24*–*28*) uses a stepwise semiautomated analysis of all Landsat images for the forest area of the Legal Amazon of Brazil (*29*). We mapped six types of forest disturbance: (i) deforestation, (ii) selective logging, (iii) understory fires in intact forests, (iv) fires on logged sites, (v) forest edge effects adjacent to deforested areas, and (vi) isolated forest fragments created by deforestation. The method (*29*) uses a visual digital object analysis framework, digital spectral analysis (canopy texture from spectral radiance variation and canopy density from spectral mixture analysis), and then iterative calibration using field data (*26*–*28*). A dataset was constructed from more than 1200 Landsat satellite digital images covering the entire BA forest area, which were then digitally analyzed for seven observation years (OYs): 1992, 1996, 1999, 2003, 2006, 2010, and 2014. The six digital map layers were stacked at each OY to delineate pixel overlay unions of new occurrences, persistent occurrences, overlapping occurrences, and sequential occurrences (figs. S1 to S3).

Digital spatial data layers for deforestation were obtained from INPE's long-term PRODES dataset (*23*) for overlay with degradation layers in OYs after 2000 through 2018. For deforestation mapping before 2000, we processed data as reported in (*24*) and (*26*). The INPE deforestation dataset is the official national reporting source and provides a logical benchmark for comparing our estimates and maps of degradation. We developed and field-validated a periodic measurement model that produces accurate estimates of logging and burned area every 3 to 4 years for moderate- and high-intensity logging of removals of >10 m^3 ha^{-1} (*24*, *27*, *29*, *30*). Forest edges are mapped only in undisturbed forest adjacent to deforested areas to 120 m. Edge areas adjacent to logging or burned scars are not counted in the edge counts. Isolated forests created by deforestation are mapped for all undisturbed forest patches between 1 and 100 km^2 in size. To report degradation of undisturbed forest, each pixel was assigned a single identifier according to a hierarchical rule (table S1). This excluded double counting of degradation occurring multiple times on a single pixel of land, but the combinations and recurrences are retained in the database.

Average annual rates of new degradation are presented in Fig. 1A, compared with the rate of deforestation. These were derived from mapping the remote sensing–detected degradation at each OY and new degradation between each OY (tables S2 and S3). As expected, overall degradation declined with deforestation rates and a concomitant decline in production of edge and isolated forest fragments, which make up a large fraction of all degradation during the early period. Declining deforestation resulting from new policy measures

[1]Department of Forestry, University of Brasilia, Campus Darcy Ribeiro, Brasília 70.900-910, Brazil. [2]Global Observatory for Ecosystem Services, Department of Forestry, Michigan State University, East Lansing, MI 48823, USA. [3]Laboratório de Estudos do Espaço Antrópico (LEEA), Universidade Estadual do Norte Fluminense Darcy Ribeiro, Campos dos Goytacazes, RJ 28013, Brazil.
*Corresponding author. Email: ematricardi@gmail.com (E.A.T.M.); skole@msu.edu (D.L.S.)

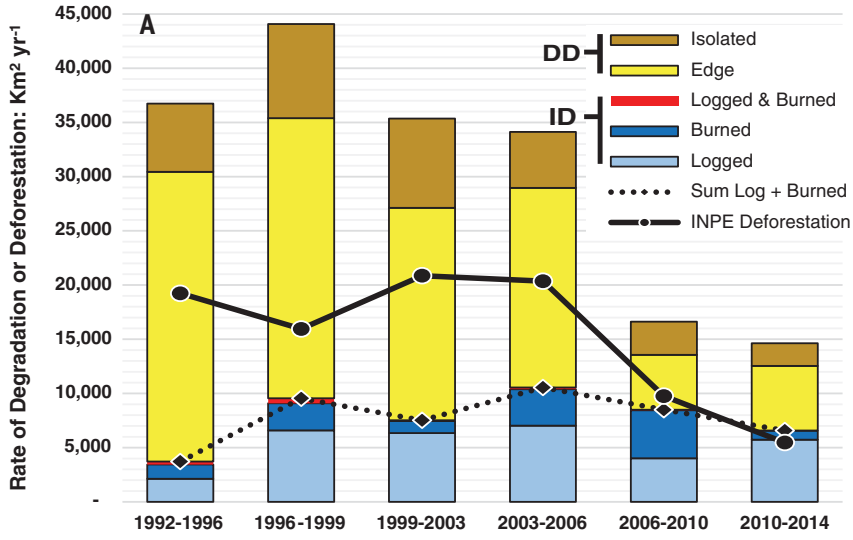

B

Forest disturbance	Area (km)²
Logged forest	98,542
Burned forest	33,476
L + B forest	1,672
Edges not L or B	129,163
Isolated not L or B or E	74,574
Degraded, 1992-2014	337,427
Deforested, 1992-2014	308,311

Fig. 1. Quantitative results of forest degradation in the BA, 1992 to 2014. (**A**) Annual average rates of forest degradation; total and contributions from each type are shown as segmented bars, with the rates of logging and understory burned areas shown by the dashed line and rates of deforestation from INPE by the solid line. DD, dependent degradation types; ID, independent degradation types. (**B**) The cumulative area impact of forest degradation on the forest biome landscape in the BA by each type of degradation and comparison with the total area deforested during the analysis period, 1992 to 2014.

reduced new edges and isolated forest after 2006 to 2010, but edges began to decline earlier while deforestation remained high, most likely as a result of consolidation and fill-in of spatially dense and continuous deforested areas. Overall, the annual rate of all types of degradation declined over the time series, from a peak of 44,075 to 14,625 km^2 $year^{-1}$. Nonetheless, forest degradation rates exceeded deforestation by almost threefold in 2014.

Whereas rates of fragmentation decreased, rates of selective logging and understory burning, two types of heavy-impact forest degradation, slightly increased or remained stable over time. The amount of new selective logging created between 1992 and 1996 increased from 8,498 to 22,952 km^2 between 2010 and 2014, an increase of 270% (table S3). When combined with new burned forest, the area increases from 14,866 km^2 in 1992 to 1996 to 26,327 km^2 in 2010 to 2014, an increase of 177%. By 2006 to 2010, the average annual rates of forest degradation by logging and burning were approximately equal to deforestation rates, and by 2014 degradation exceeded deforestation (Fig. 1A).

To compare the amount of degraded forest in the BA today with the deforested area, all newly created degradation pixels were tracked and accumulated through time. There was no double counting of more than one type of degradation occurring at the same place, and pixels that were deforested by 2014 were removed (Fig. 1B). The total degraded forest created during the period of our analysis and that remain present in the current landscape is 337,427 km^2, compared with 308,311 km^2 of deforested land. This estimate does not include degradation that occurred before 1992. Much of the degradation was from edges and isolated forest fragments, but the total area degraded by logging and burning alone over this period was equivalent to almost half (43%) of the area deforested over this period. In most locations across the BA, there is more degraded forest than deforested land when considering only what occurred during the time frame of analysis (fig. S4). During this long-term period of observation, 40% of all degraded forest can be attributed to intensive logging and understory fires and 60% is due to edges and isolated fragments of forest, which represents a notable increase in the logged and burned fraction later in the record.

BA-wide estimates from the analysis were constructed at the original 30-m resolution and then aggregated in 200-km^2 grid cells for mapping and graphical display (Fig. 2). These maps show the cumulative impact of all degradation types. The map shows the status of forest ecosystems in the BA, including the density and extent of degradation. The mapping is presented for the entire period of analysis and separately for the period before the downturn in deforestation rates and the period after. Generally, degradation is more spatially dispersed across the landscape than deforestation, which is concentrated in the often-cited "arc of deforestation" along the eastern and southern forest interface with the Cerrado Biome in Brazil, which comprises a region with vegetation types similar to African savannah. There are concentrated zones of high degradation close to older areas of deforestation, but degradation is also emerging in the western BA, particularly by new logging (Fig. 3). The spatial organization of logging suggests that it is increasingly decoupled from understory burning (figs. S5 and S6), where logging is relocating more distantly from the so-called arc of deforestation, whereas burned areas remain more restricted closer to the older areas of deforestation (figs. S7 and S8). Furthermore, we found very little overlap of burned areas on logged areas, especially in the short term (4 to 8 years).

The dominant local driver of degradation was mapped for each 200-km^2 grid cell (Fig. 4). Degradation related to deforestation, such as edges and isolated fragments, is important in the BA-wide landscape, not only in the older areas but also along the new frontiers. Logged areas are dominant in some specific areas where degradation is uniformly very high, and they are expanding to the west along a new frontier (Fig. 4 and figs. S7 to S9), whereas nodes of burned dominance are very spatially localized. Edge and isolated forest fragments are spatially and geographically extensive. Edges tend to be the prevalent and extensive type in the earliest years and then in the new frontier of western BA (Fig. 4, B and C), whereas isolated forest dominates some old areas of deforestation and degradation during the later years (Fig. 4C). In most places, all types of degradation are occurring in the landscape, although we found little evidence of significant spatial overlap and co-occurrence, even when considering degradation co-occurrences widely separated in time.

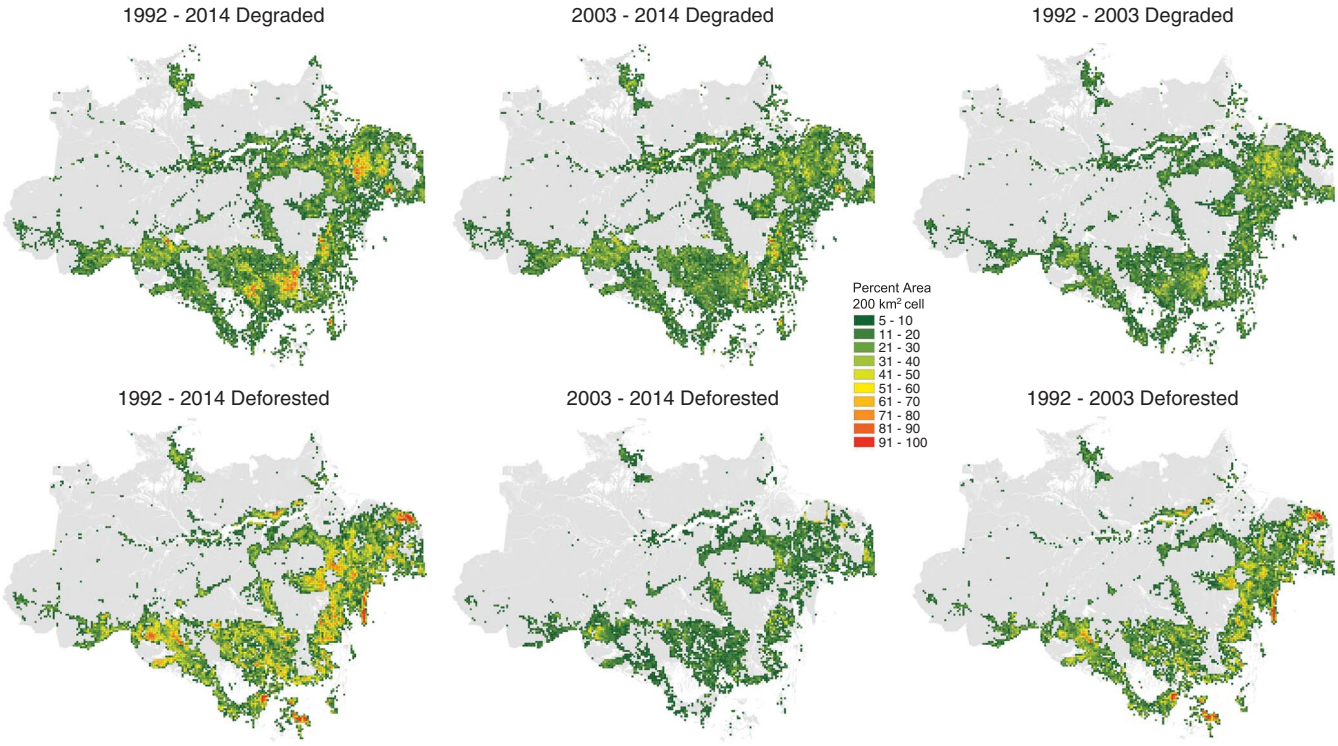

Fig. 2. Spatial mapping of forest degradation in BA forest ecosystems. The maps present separately the inventory of all forest areas degraded by all degradation (top) not deforested, compared with the total deforested land (bottom), between 1992 and 2014. Maps on the left show all degradation or deforestation during the study period. Center maps show degraded forest or deforested areas after the downturn in deforestation rates. Maps on the right show areas degraded or deforested before the downturn in deforestation. The amount of degraded forest is aggregated into 200-km^2 grid cells and represented as the fraction (percentage) of the cell.

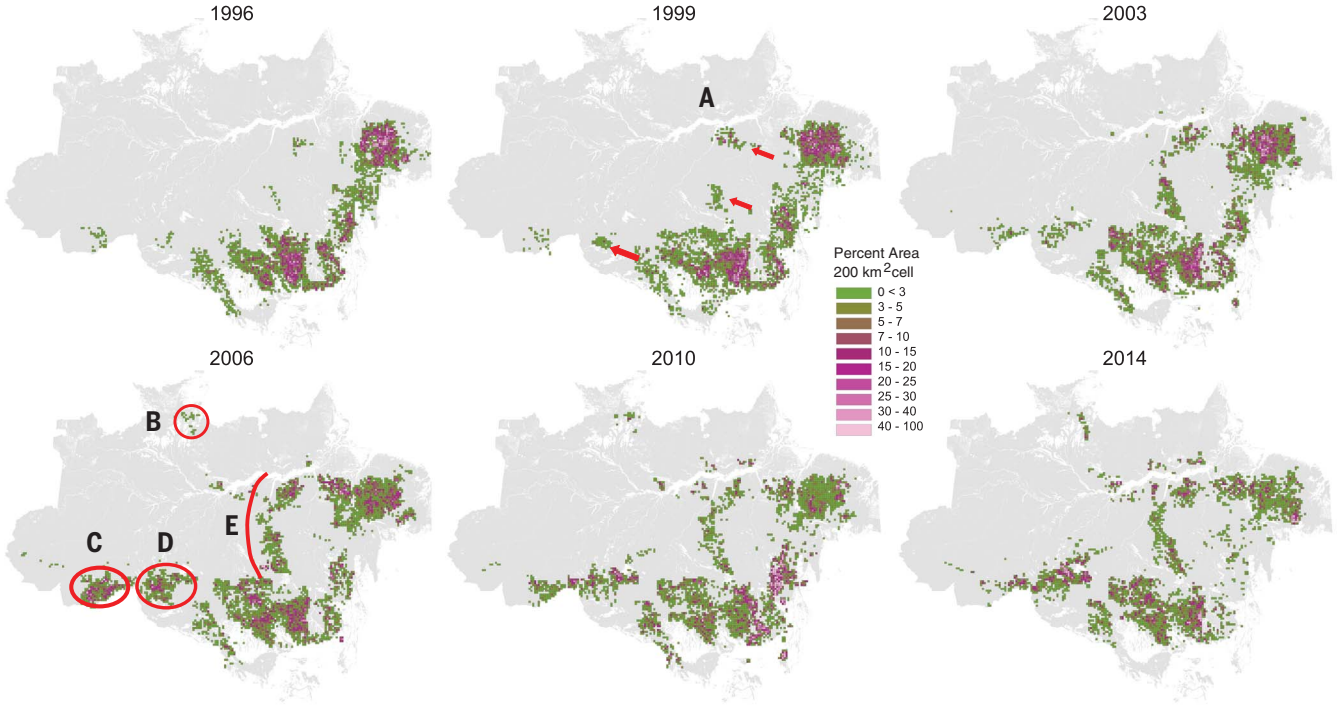

Fig. 3. Detected areas of forest degradation by logging and understory burning at each OY. Areas are mapped as a fraction of a 200-km^2 grid cell for the entire BA. The geography of logging is shown to have expanded from the older deforestation zone, often cited as the arc of deforestation, particularly after 2003. (**A**) Arrows show the general direction of the expanding logging frontier. (**B**) New distant forest degradation in Roraima. (**C** and **D**) New forest degradation from logging in the western Amazon. (**E**) The prominent forest degradation front in western Pará.

Results from an analysis of regional trends were surprising (figs. S7 to S9). New logging areas are demonstrably expanding beyond the older arc of deforestation into a new western frontier (Fig. 3 and fig. S7), but spatiotemporal trends for other types are less clear. Understory burned areas remain predominant in the specific areas of concentrated deforestation, with temporal trends somewhat intermediary or stable, having increased in the early period of record and now declining with deforestation rates. Interestingly, creation of new edges and new isolated forest fragments has generally declined over the entire record, particularly as deforestation rates have declined, although their coverage area remains high in overall magnitude. In fact, areas with highest overall coverage and density are also experiencing declining rates, regardless of type. The new frontiers with high and increasing rates are still quantitatively low in magnitude. The highest densities of degradation are along the long-standing deforestation frontier but present declining trajectories, whereas the emerging frontiers with lower densities have increasing trajectories; these new and expanding regions will likely be dominant in the future.

For degradation to be an important form of forest disturbance in the BA, it must persist in the landscape and not be immediately converted by deforestation. We spatially tracked at the 30-m pixel scale the survivorship of each cohort of new degraded forest through the time series (table S7 and fig. S10). Survivorship is measured as the area and percentage of a cohort of degraded forests that persists without being deforested for a given length of time. Logged areas persisted the longest, as more than half (57%) of the area survived at least 18 years, from 1996 to 2014 (46% from 1996 survived to 2018). Fully one-third of logged areas in 1992 were still present in the 2018 landscape, some of which had been relogged. The other types of degradation had much lower 18-year survivorship by 2014, ranging from 28 to 31%. Interestingly, as much as one-third of logged areas from 1992 were still present in 2018, and one-fifth to one-fourth of the other types of degradation in 1992 were still present in 2018. Through the time series, survivorship was generally consistent but slightly increased after 2003, when deforestation rates declined. Some researchers have reported very low survivorship of logged areas for short periods of up to 4 years (*31*), but we found high short-term survivorship for all types of degradation in general but especially for logged areas, and these ranged from 82 to 93%. Burned areas have considerably lower short-term survivorship, ranging from 50% in the earlier period to 86% later in the time series, as deforestation rates declined. Edge and isolated forest short-term survivorship ranged from ~50% in the early period to ~80% later, but also increased as deforestation rates declined. Although deforestation policy did not influence logging or lead to a decline in burned area degradation, it did relieve conversion pressures so that these logged and burned areas now persist longer. Reduced conversion pressure has extended the persistence of edges and isolated forest, which exacerbates tree mortality and other ecological effects (fig. S10).

A large spatial overlay analysis to understand the co-occurrence of the different types of degradation follows naturally from the persistence analysis. We examined overlays of all degraded forest that were not deforested through 2014. The results were somewhat unexpected, in that spatial co-occurrence of different degradation factors is very low. Throughout the BA, it is common to have all four types of degradation occur, but there is no evidence that they overlap in any significant way, a finding that has implications for degradation intensity and our understanding of the interaction between drivers. Of all degraded forest in the current landscape, 90% has been degraded by only one factor (table S9).

This analysis considered the density, dominance, direction, and duration of five types

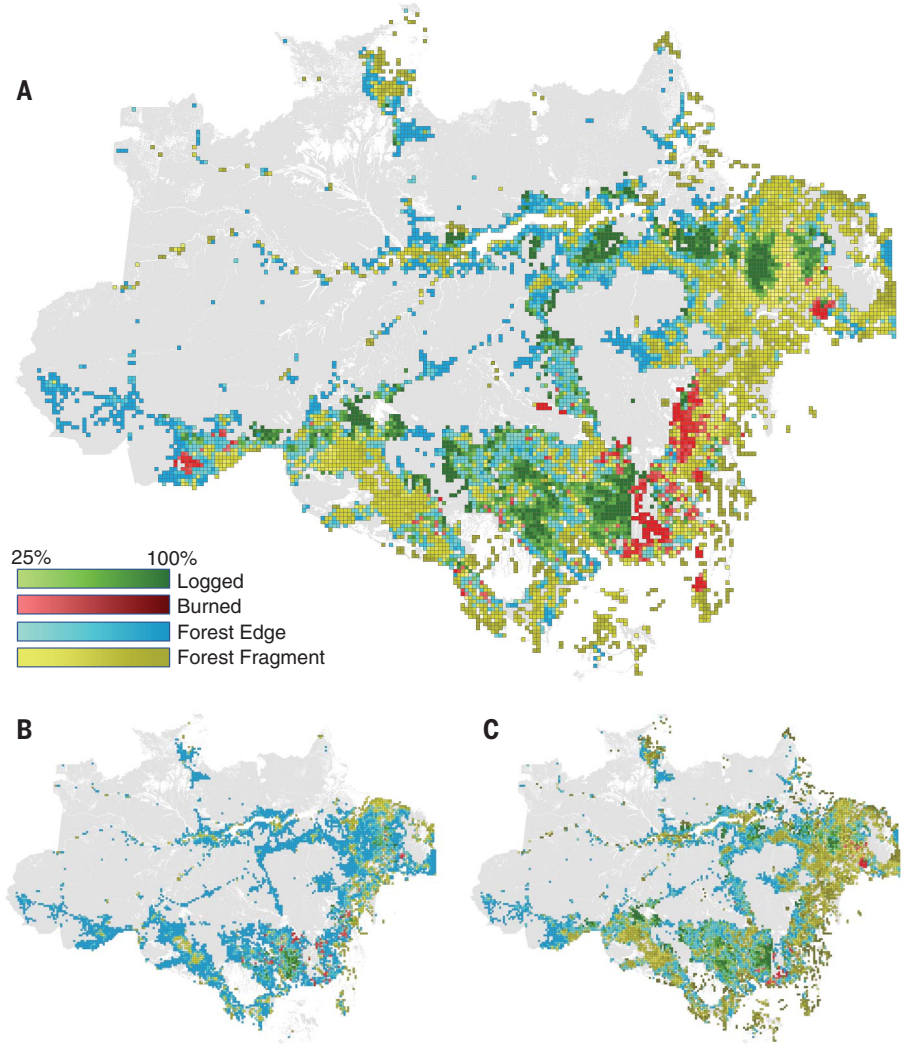

Fig. 4. Maps of dominant drivers of degradation. Four types of degraded forest are shown: logged, understory burning, edges, and isolated forest fragments. The quantitatively most abundant type in each 200-km^2 grid cell is the dominant driver at that local level. The color represents the most dominant type, whereas the tonal gradient indicates how dominant it is compared with other types, as a percentage of all types present. If all four types existed in approximately equal magnitude, the tone would be close to 25%, whereas the color tone would be darker and closer to 100% if there was only one type present. (**A**) The overall status of dominant types cumulatively through the entire time period, 1992 to 2014. (**B**) The dominant type at the start of the period of analysis, observed in 1992. (**C**) The dominant type at the end of the period of analysis, observed in 2014.

of forest degradation over almost three decades. Edge effects and isolated forest fragments have been substantial contributors to the current degraded state of forest over the record, but the fragmentation contribution is declining while overt degradation from logging, and to a lesser degree fire, is becoming more prominent. We observed that there has been a transition from a deforestation-mediated fragmentation regime to one with an elevated importance of new logging and fire, which is geographically shifting to a new western "degradation frontier." We can articulate a simple framework for understanding these dynamics by considering two broad categories of forest degradation types: (i) those that are dependent on, or coupled to, deforestation, such as the fragmentation effects of edges and isolated fragments (DD); and (ii) those that are more independent of, or decoupled from, deforestation, such as logging and to a lesser degree understory fire (ID).

National policies in Brazil have been established in a command-and-control fashion to reduce the rate of deforestation, and they have been effective. In turn, such deforestation policies have influenced rates of DD forest degradation. However, these policies have had minimal effect on curbing ID degradation and have led to more persistent and long-lasting ID degradation in the landscape. Furthermore, annual rates of ID degradation now exceed deforestation rates, while being geographically dispersed to new frontiers not associated with the historical deforestation frontier along the so-called arc of deforestation. With either the current policy situation or a return to laissez faire policies that ignore degradation generally and ID degradation specifically, the rate and extent of forest degradation will likely increase in the future in response to market forces and the establishment of a separate logging sector infrastructure for extraction, processing, and transport. Selective logging has always been one of the first entryways into undisturbed forests, as it occurs within close proximity of existing settlement and clearing. Now, logging is demonstrating the potential to leap further distances into remote areas.

Several of our analytical assumptions and methodological features suggest that our estimates are conservative. Our buffer distance for edges is 120 m, and we did not estimate edges around logged and burned areas. Our logging detection does not include very-low-intensity logging below 10 m^3 ha^{-1}, so it may omit some cases of reduced-impact logging. We also did not include highly selective individual tree logging, which occurs in the process of deforestation or tree removals by individual farmers on their homesteads, or indigenous logging. The periodic use of OYs may miss some low-intensity logging or small burning events. Inclusion of these factors would only increase the estimate of how much degradation exists in the landscape today.

The overall conclusion from this work is that forest degradation is a significant form of landscape and ecosystem disturbance. Degradation in the BA is a persistent form of disturbance, not simply one that is eventually replaced by deforestation. Focusing attention on deforestation alone ignores an additional area of forest degraded by selective logging, understory fire, edge effects, and isolation of fragments that is equal in areal extent to cleared forest.

Improved long-term spatial data on forest degradation are sought by most multilateral environmental agreements. Our analysis provides a cogent example of monitoring data needed to estimate species loss from forest fragmentation and degradation, which is a key element of Target 5 of the United Nations Convention on Biological Diversity. Our results align with long-term ground-based studies of forest fragmentation in conservation biology (*32*, *33*) and contribute to a better understanding of species biodiversity loss (*34*, *35*). Our measurements reemphasize the importance of technical consideration of forest degradation in the international dialog on REDD+, for which most monitoring has been focused on deforestation.

REFERENCES AND NOTES

1. J. E. M. Watson *et al*., *Nat. Ecol. Evol.* **2**, 599–610 (2018).
2. B. Mackey *et al*., *Conserv. Lett.* **8**, 139–147 (2015).
3. Ministry of the Environment, Government of Brazil, "ENREDD+: National Strategy for Reducing Emissions from Deforestation and Forest Degradation, and the Role of Conservation of Forest Carbon stocks, sustainable management of forests and Enhancement of Forest Carbon Stocks" (Ministério do Meio Ambiente, Brasilia, 2016); http://redd.mma.gov.br/.
4. A. Baccini *et al*., *Science* **358**, 230–234 (2017).
5. D. I. Rappaport *et al*., *Environ. Res. Lett.* **13**, 065013 (2018).
6. M. Longo *et al*., *Global Biogeochem. Cycles* **30**, 1639–1660 (2016).
7. C. M. Souza Jr. *et al*., *Remote Sens.* **5**, 5493–5513 (2013).
8. D. C. Morton, Y. Le Page, R. DeFries, G. J. Collatz, G. C. Hurtt, *Philos. Trans. R. Soc. B* **368**, 20120163 (2013).
9. D. P. Roy, S. S. Kumar, *Int. J. Digit. Earth* **10**, 54–84 (2017).
10. E. N. Broadbent *et al*., *Biol. Conserv.* **141**, 1745–1757 (2008).
11. M. C. Hansen *et al*., *Science* **342**, 850–853 (2013).
12. A. Tyukavina *et al*., *Sci. Adv.* **3**, e1601047 (2017).
13. K. Brinck *et al*., *Nat. Commun.* **8**, 14855 (2017).
14. R. A. Houghton *et al*., *Nature* **403**, 301–304 (2000).
15. A. P. D. Aguiar *et al*., *Global Change Biol.* **22**, 1821–1840 (2016).
16. X.-P. Song, C. Huang, S. S. Saatchi, M. C. Hansen, J. R. Townshend, *PLOS ONE* **10**, e0126754 (2015).
17. C. A. Nobre, P. J. Sellers, J. Shukla, *J. Clim.* **4**, 957–988 (1991).
18. C. A. Nobre *et al*., *Proc. Natl. Acad. Sci. U.S.A.* **113**, 10759–10768 (2016).
19. W. F. Laurance *et al*., *Nature* **489**, 290–294 (2012).
20. M. Pfeifer *et al*., *Nature* **551**, 187–191 (2017).
21. M. C. Castro *et al*., *PLOS Biol.* **17**, e3000526 (2019).
22. D. Nepstad *et al*., *Science* **326**, 1350–1351 (2009).
23. Instituto Nacional de Pesquisas Espaciais (INPE), Programa de Monitoramento da Amazônia e demais biomas. Desmatamento: Amazônia Legal (INPE, Coordenação Geral de Observação da Terra, 2019); http://terrabrasilis.dpi.inpe.br/downloads/.
24. E. Matricardi, D. L. Skole, M. A. Pedlowski, W. Chomentowski, *Int. J. Remote Sens.* **34**, 1057–1086 (2013).
25. E. A. T. Matricardi, D. L. Skole, M. A. Cochrane, J. Qi, W. Chomentowski, *Earth Interact.* **9**, 1–24 (2005).
26. E. A. T. Matricardi, D. L. Skole, M. Cochrane, M. A. Pedlowski, W. Chomentowski, *Int. J. Remote Sens.* **28**, 63–82 (2007).
27. E. A. T. Matricardi, D. L. Skole, M. A. Pedlowski, W. Chomentowski, L. C. Fernandes, *Remote Sens. Environ.* **114**, 1117–1129 (2010).
28. O. B. Costa, E. A. T. Matricardi, M. A. Pedlowski, E. P. Miguel, R. O. Gaspar, *Floresta Ambient.* **26**, e20170634 (2019).
29. See supplementary materials.
30. D. L. Skole *et al*., in *Land Change Science: Observing, Monitoring, and Understanding Trajectories of Change on the Earth's Surface*, G. Gutman *et al*., Eds. (Kluwer Academic, 2004), pp. 77–95.
31. G. P. Asner *et al*., *Proc. Natl. Acad. Sci. U.S.A.* **103**, 12947–12950 (2006).
32. W. F. Laurance *et al*., *Biol. Conserv.* **144**, 56–67 (2011).
33. S. L. Pimm, T. Brooks, *Curr. Biol.* **23**, R1098–R1101 (2013).
34. S. L. Pimm *et al*., *Science* **344**, 1246752 (2014).
35. G. Ferraz *et al*., *Proc. Natl. Acad. Sci. U.S.A.* **100**, 14069–14073 (2003).

ACKNOWLEDGMENTS

We thank W. Chomentowski for contributions to the TRFIC deforestation dataset. **Funding:** This study was financed in part by the Coordenação de Aperfeiçoamento de Pessoal de Nível Superior, Brasil (CAPES), Finance Code 001, and the National Council for Scientific and Technological Development (CNPq). Funding was also provided by U.S. National Aeronautics and Space Administration grant NNX14AD93G to Michigan State University, "Monitoring and Mapping the Area, Extent and Shifting Geographies of Industrial Forests in the Tropics," and National Aeronautics and Space Administration grant NNX04AN73G to Michigan State University, "Enhancing Global Scale Observations and Information on Tropical Forest Change." **Author contributions:** D.L.S. and E.A.T.M. designed the study and contributed to the manuscript; D.L.S., E.A.T.M., and M.A.P. led the writing and editing of the manuscript; O.B.C. and E.A.T.M. conducted the remote sensing analysis on selective logging and fire; D.L.S., E.A.T.M., J.H.S., M.A.P., and E.P.M. conducted the data analysis; J.H.S. produced maps and the fragmentation analysis; and all authors contributed data and provided comments on the manuscript. **Competing interests:** The authors declare no competing interests. **Data and materials availability:** All results from data analysis needed to evaluate this report are available in the main text or the supplementary materials in tables and figures. Primary public domain satellite remote sensing data are available from the national satellite data archives in Brazil's Instituto Nacional de Pesquisas Espaciais (INPE) and the U.S. Geological Survey Eros Data Center (EDC) in the United States. The remote sensing–derived products, spatial data layer products, validation data, and Excel spreadsheets of spatial analysis are available from the Tropical Rain Forest Information Center, a NASA ESIP Data Center, now maintained by the Global Observatory for Ecosystem Services at Michigan State University (https://goeslab.us/amazondata), and from the NASA Land Cover and Land Use Change Program data server (https://lcluc.umd.edu/content/metadata). The deep retrospective deforestation record (1988 to 2000) and spatial datasets are available from the Tropical Rain Forest Information Center at the Global Observatory for Ecosystem Services at Michigan State University (https://goeslab.us/amazondata.html). Deforestation spatial data are available from INPE in Brazil (http://terrabrasilis.dpi.inpe.br) for the years 2000 to 2018.

SUPPLEMENTARY MATERIALS

science.sciencemag.org/content/369/6509/1378/suppl/DC1
Materials and Methods
Supplementary Text
Figs. S1 to S11
Tables S1 to S9
References (*36*–*45*)

14 February 2020; accepted 28 July 2020
10.1126/science.abb3021

GLOBAL CLIMATE

An astronomically dated record of Earth's climate and its predictability over the last 66 million years

Thomas Westerhold[1]*, Norbert Marwan[2,3], Anna Joy Drury[1,4], Diederik Liebrand[1], Claudia Agnini[5], Eleni Anagnostou[6], James S. K. Barnet[7,8], Steven M. Bohaty[9], David De Vleeschouwer[1], Fabio Florindo[10,11], Thomas Frederichs[1,12], David A. Hodell[13], Ann E. Holbourn[14], Dick Kroon[15], Vittoria Lauretano[16], Kate Littler[7], Lucas J. Lourens[17], Mitchell Lyle[18], Heiko Pälike[1], Ursula Röhl[1], Jun Tian[19], Roy H. Wilkens[20], Paul A. Wilson[9], James C. Zachos[21]

Much of our understanding of Earth's past climate comes from the measurement of oxygen and carbon isotope variations in deep-sea benthic foraminifera. Yet, long intervals in existing records lack the temporal resolution and age control needed to thoroughly categorize climate states of the Cenozoic era and to study their dynamics. Here, we present a new, highly resolved, astronomically dated, continuous composite of benthic foraminifer isotope records developed in our laboratories. Four climate states—Hothouse, Warmhouse, Coolhouse, Icehouse—are identified on the basis of their distinctive response to astronomical forcing depending on greenhouse gas concentrations and polar ice sheet volume. Statistical analysis of the nonlinear behavior encoded in our record reveals the key role that polar ice volume plays in the predictability of Cenozoic climate dynamics.

Global changes in Earth's climate during the Cenozoic era, the last 66 million years, have long been inferred from stable-isotope data in carbonate shells of benthic foraminifera, which are single-celled amoeboid organisms that live on the seafloor. Stable carbon and oxygen isotope records from deep-sea benthic foraminifera are a proven, invaluable archive of long-term changes in Earth's carbon cycle, deep-sea temperature, and seawater composition driven by changes in ice volume (*1*, *2*). In 1975, Shackleton and Kennett (*3*) produced one of the first deep-sea benthic foraminifer stable isotope records of the Cenozoic. Despite being of low temporal resolution, it revealed that Earth's climate had transitioned from a warm state 60 to 40 million years ago (Ma) to a cool state 10 to 5 Ma. Over the last 45 years, many deep-sea benthic foraminifer stable-isotope records of variable length and quality have been developed, resulting in a more detailed record of Cenozoic climate change. Compilations of these deep-sea isotope records provide a compelling chronicle of past trends, cyclic variations, and transient events in the climate system from the Late Cretaceous to today (*1*, *4*–*10*). However, even the most recent benthic isotope compilations cannot accurately document the full range and detailed characteristics of Cenozoic climate variability on time scales of 10 thousand to 1 million years. Age models and temporal resolution of Cenozoic benthic isotope compilations are too coarse and/or include gaps, particularly before 34 Ma. These weaknesses hamper progress in determining the dynamics of the Cenozoic climate system (*4*, *9*, *11*), for example, because they prohibit application of advanced techniques of nonlinear time series analysis at the required (astronomical) time scales. The lack of highly resolved, continuous, and accurately dated records constitutes a key limitation in our ability to identify and understand the characteristics of Earth's evolving climate during the Cenozoic.

Here, we present a new astronomically tuned deep-sea benthic foraminifer carbon ($\delta^{13}C$) and oxygen ($\delta^{18}O$) isotope reference record uniformly covering the entire Cenozoic, developed in our laboratories by using sediment archives retrieved by the International Ocean Discovery Program and its predecessor programs (Fig. 1). To produce this composite record, we selected 14 ocean drilling records, checked and revised their composite splices if necessary, and preferentially selected records using the genera *Cibicidoides* and *Nuttallides* to minimize systematic interspecies isotopic offsets (*1*, *4*, *12*, *13*). We additionally generated new benthic stable-isotope data spanning the late Miocene and middle to late Eocene to fill intervals inadequately covered by existing records. We collated existing astrochronologies for all records, recalibrated them to the La2010b orbital solution (*14*) if required, and developed an astrochronology for the middle to late Eocene (*13*). We estimate our chronology to be accurate to ±100 thousand years (kyr) for the Paleocene and Eocene, ±50 kyr for the Oligocene to middle Miocene, and ±10 kyr for the late Miocene to Pleistocene. The composite record is affected by some spatial biases arising from the uneven distribution of deep-sea stable isotope data that mainly derive from low to mid-latitudes (*13*). Nevertheless, the resulting Cenozoic Global Reference benthic foraminifer carbon and oxygen Isotope Dataset (CENOGRID) provides a refined record with higher signal-to-noise ratio than any previous compilations (*13*) (supplementary text S1) and better coverage of the Paleocene, Eocene, and late Miocene intervals (fig. S32). The CENOGRID serves as an astronomically tuned, high-definition stratigraphic reference of global climate evolution for the past 66 million years.

On time scales of 10 thousand to 1 million years, global climate is a complex, dynamical system responding nonlinearly to quasi-periodic astronomical forcing. By combining the latest high-resolution generation of Cenozoic deep-sea isotope records on a highly accurate time scale, CENOGRID enables the definition of Earth's fundamental climates and investigation of the predictability of their dynamics. We used recurrence analysis (RA) of the CENOGRID record (*13*, *15*) to identify fundamental climate states that internally share characteristic and statistically distinctive dynamics. Recurrence is a major property of dynamical systems, and RA provides information about nonlinear dynamics, dynamical transitions, and even nonlinear interrelationships (*15*) and facilitates evaluation of underlying dynamical processes—e.g., whether they are stochastic, regular, or chaotic. We present recurrence plots and their quantification of the benthic foraminifer $\delta^{13}C$ and $\delta^{18}O$ records to recognize different climate states and apply the RA measure of "determinism" (DET) to quantify the predictability of Cenozoic climate dynamics.

Four distinctive climate states emerge as separate blocks from our recurrence plots of the $\delta^{18}O$ CENOGRID record, which we designate as

[1]MARUM–Center for Marine Environmental Sciences, University of Bremen, 28359 Bremen, Germany. [2]Potsdam Institute for Climate Impact Research (PIK), Member of the Leibniz Association, 14412 Potsdam, Germany. [3]University of Potsdam, Institute of Geosciences, 14469 Potsdam, Germany. [4]Department of Earth Sciences, University College London, Gower Street, London WC1E 6BT, UK. [5]Dipartimento di Geoscienze, Università degli Studi di Padova, Via Gradenigo 6, I-35131 Padova, Italy. [6]GEOMAR Helmholtz-Zentrum für Ozeanforschung Kiel, Wischhofstrasse 1-3, 24148 Kiel, Germany. [7]Camborne School of Mines and Environment and Sustainability Institute, University of Exeter, Penryn Campus, Penryn, UK. [8]School of Earth and Environmental Sciences, University of St Andrews, St Andrews, Scotland, UK. [9]Ocean and Earth Science, University of Southampton, National Oceanography Centre, Southampton, UK. [10]Istituto Nazionale di Geofisica e Vulcanologia, INGV, Rome, Italy. [11]Institute for Climate Change Solutions, Pesaro e Urbino, Italy. [12]Faculty of Geosciences, University of Bremen, Bremen, Germany. [13]Godwin Laboratory for Palaeoclimate Research, Department of Earth Sciences, University of Cambridge, Cambridge, UK. [14]Institute of Geosciences, Christian-Albrechts-University, Kiel 24118, Germany. [15]School of GeoSciences, University of Edinburgh, Edinburgh, UK. [16]School of Chemistry, University of Bristol, Bristol BS8 1TS, UK. [17]Department of Earth Sciences, Faculty of Geosciences, Utrecht University, Princetonlaan 8a, 3584 CB Utrecht, Netherlands. [18]College of Earth, Ocean, and Atmospheric Science, Oregon State University, Corvallis, OR 97331, USA. [19]State Key Laboratory of Marine Geology, Tongji University, Siping Road 1239, Shanghai 200092, PR China. [20]School of Ocean and Earth Science and Technology, University of Hawaii, Honolulu, HI 96822, USA. [21]Department of Earth and Planetary Sciences, University of California, Santa Cruz, California, USA.
*Corresponding author. Email: twesterhold@marum.de

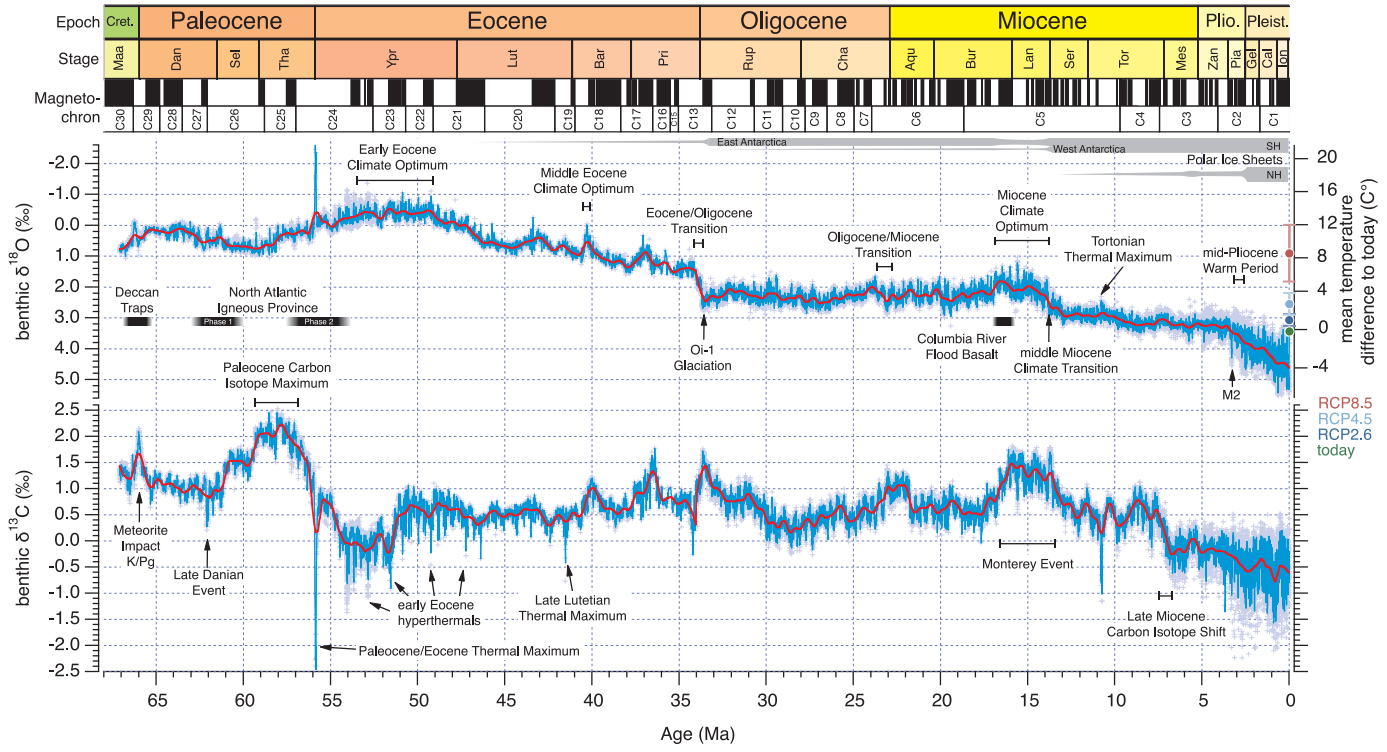

Fig. 1. Cenozoic Global Reference benthic foraminifer carbon and oxygen Isotope Dataset (CENOGRID) from ocean drilling core sites spanning the past 66 million years. Data are mostly generated by using benthic foraminifera tests of the taxa *Cibicidoides* and *Nuttallides* extracted from carbonate-rich deep-sea sediments drilled during Ocean Drilling Program (ODP) and Integrated Ocean Drilling Program (IODP) expeditions. Genus-specific corrections were applied and oxygen isotope data adjusted by +0.64‰ and +0.4‰, respectively (*12*), with the green dot indicating the average oxygen isotope composition of the last 10 kyr. Average resolution for the interval from 0 to 34 Ma is one sample every 2 ky; for the interval from 34 to 67 Ma, it is one sample every 4.4 kyr. After binning, data were resampled and smoothed by a locally weighted function over 20 kyr (blue curve) and 1 Myr (red curve) to accentuate the different rhythms and trends in Earth's carbon cycle and temperature operating on various time scales. Oxygen isotope data have been converted to average temperature differences with respect to today (*13*). Future projections for global temperature (*44*) in the year 2300 are shown by plotting three representative concentration pathways (RCP) scenarios (light blue, dark blue, and red dots). Gray horizontal bars mark rough estimates of ice volume in each hemisphere. Absolute ages for epochs and stages of the Cenozoic (GTS2012) and geomagnetic field reversals (this study) are provided for reference. The oxygen isotope data axis is reversed to reflect warmer temperatures at times of lower $\delta^{18}O$ values. Aqu, Aquitanian; Bur, Burdigalian; Cal, Calabrian; Cha, Chattian; Cret., Cretaceous; Dan, Danian; Gel, Gelasian; Ion, Ionian; K/Pg, Cretaceous/Paleogene boundary; Lan, Langhian; Lut, Lutetian; M2, first major glacial event in the NH; Maa, Maastrichtian; Mes, Messinian; NH, Northern Hemisphere; Oi-1, the first major glacial period in the Oligocene; Pia, Piacenzian; Pleist., Pleistocene; Plio., Pliocene; Pri, Priabonian; Rup, Rupelian; Sel, Selandian; Ser, Serravallian; SH, Southern Hemisphere; Tha, Thanetian; Tor, Tortonian; Ypr, Ypresian; Zan, Zanclean.

the Hothouse, Warmhouse, Coolhouse, and Icehouse states (Fig. 2). Blocklike structures in the recurrence plots identify epochs where the dynamical system is "trapped" in a particular state. This interpretation of Cenozoic climate history is broadly consistent with previous interpretations, but our recurrence plot analysis of the highly resolved CENOGRID data provides a more statistically robust and objective exposition of events.

Characteristic features of the four climate states can be inferred from the isotope profiles (Fig. 1) and scatterplots of the CENOGRID $\delta^{13}C$ and $\delta^{18}O$ data and from atmospheric CO_2 concentration estimates (Fig. 2) (*13*). Warmhouse and Hothouse states prevailed from the Cretaceous/Paleogene boundary (K/Pg, 66 Ma) to the Eocene-Oligocene Transition (EOT, 34 Ma). During the Warmhouse, global temperatures were more than 5°C warmer than they are today (*13*), and benthic $\delta^{13}C$ and $\delta^{18}O$ show a persistent positive correlation with one another. The Hothouse operated between the Paleocene-Eocene Thermal Maximum at 56 Ma and the end of the Early Eocene Climate Optimum (EECO) at 47 Ma (*16*), when temperatures were more than 10°C warmer than they are today and displayed greater amplitude variability. Transient warming events (hyperthermals) are an intrinsic feature of the Hothouse, wherein paired negative excursions in $\delta^{13}C$ and $\delta^{18}O$ reflect warming globally through rapid addition of carbon to the ocean-atmosphere system. The two Warmhouse phases from 66 to 56 Ma (Paleocene) and 47 to 34 Ma (middle-late Eocene) share a similar temperature range but have distinct background $\delta^{13}C$ isotope values and atmospheric CO_2 concentrations (Fig. 2 and fig. S35). At the EOT, the Warmhouse transitioned into the Coolhouse state, marked by a stepwise, massive drop in temperature and a major increase in continental ice volume with large ice sheets appearing on Antarctica (*17*) to establish a unipolar glacial state (*18*). The recurrence plots mark out the EOT as the most prominent transition of the whole Cenozoic, which highlights the important role of ice sheets in modulating Earth's climate state (fig. S33) (*13*).

The Coolhouse state spans ~34 Ma (EOT) to 3.3 Ma (mid-Pliocene M2 glacial) and is divided into two phases by the marked shift in $\delta^{18}O$ increase at 13.9 Ma related to the expansion of Antarctic ice sheets during the middle Miocene Climate Transition (mMCT) (*19*). Warmer conditions culminating in the Miocene Climatic Optimum (MCO; ~17 to 14 Ma) (*20*) characterize the first phase, followed by cooling and increasing $\delta^{18}O$ during the second phase (Fig. 2). RA of carbon isotope data documents an additional major transition in the carbon cycle around 7 Ma related to the

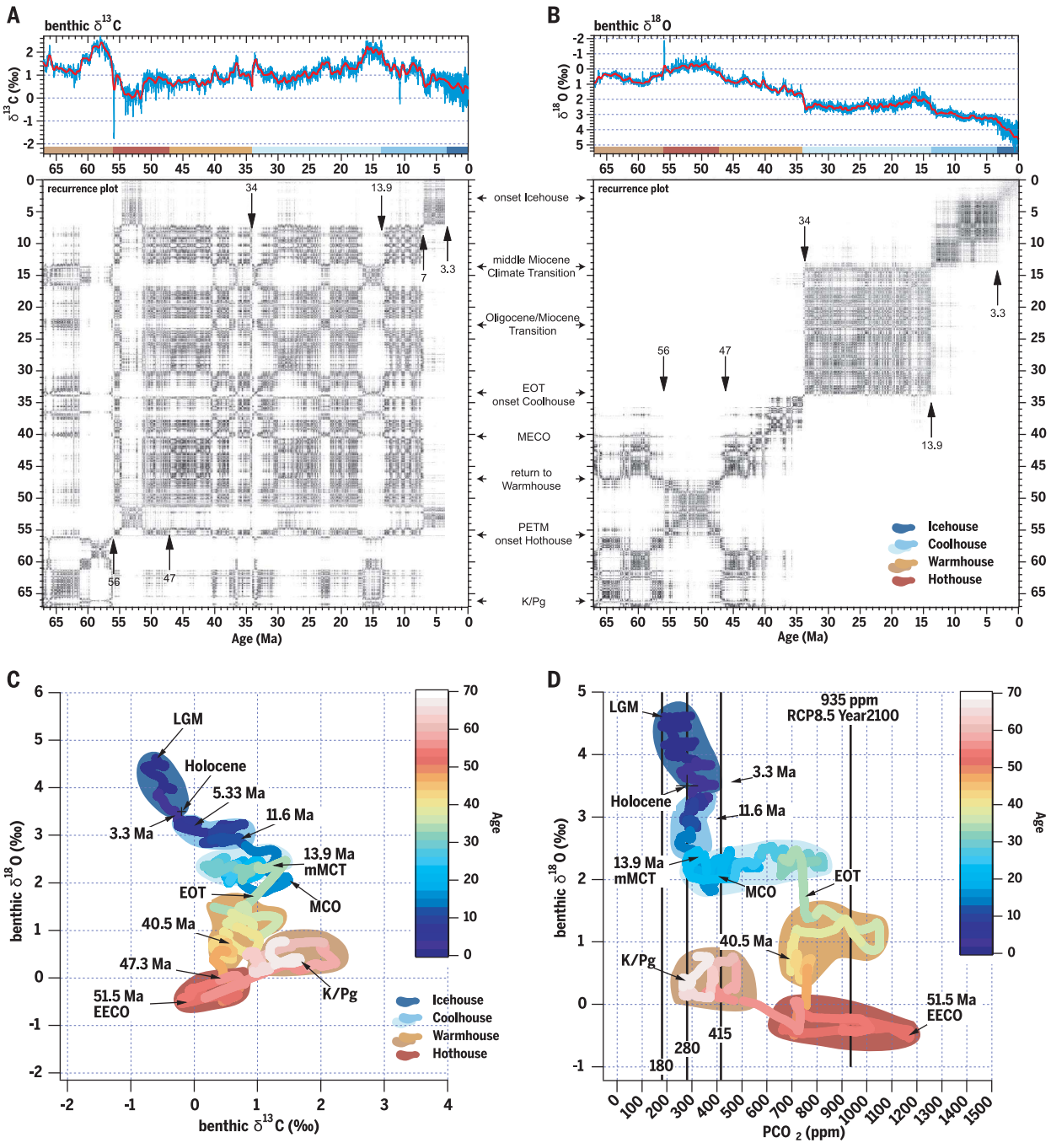

Fig. 2. Climate states of the Cenozoic. Deep-sea benthic foraminifer high-resolution carbon (**A**) and oxygen (**B**) isotope records and the respective recurrence plots as well as scatterplots of long-term benthic foraminifer carbon versus oxygen values (**C**) and oxygen values versus atmospheric CO_2 concentrations (**D**). Recurrence analysis compares climate change patterns occurring in a specific interval to the entire record. If climate dynamics have similar patterns, they will show up as darker areas in the plot; if they have no common dynamics, the plot will remain white. Four distinct climate states can be identified as Hothouse, Warmhouse, Coolhouse, and Icehouse with distinct transitions among them. The relation of oxygen isotopes, representative for average global temperature trends, to atmospheric CO_2 concentrations suggests that the present climate system as of today [415 parts per million (ppm) CO_2] is comparable to the Miocene Coolhouse close to the MCO. If CO_2 emissions continue unmitigated until 2100, as assumed for the RCP8.5 scenario, Earth's climate system will be moved abruptly from the Icehouse into the Warmhouse or even Hothouse climate state. LGM, Last Glacial Maximum; MECO, Middle Eocene Climate Optimum; PETM, Paleocene/Eocene Thermal Maximum.

end of the late Miocene carbon isotope shift (*11*, *21*, *22*). A major change in the correlation between benthic foraminifer $\delta^{13}C$ and $\delta^{18}O$ occurs during the Pliocene epoch (*23*). The Icehouse climate state (Fig. 2), driven by the appearance of waxing and waning ice sheets in the Northern Hemisphere, was fully established by the Pliocene-Pleistocene transition (*24*) (Figs. 1 and 2) with Marine Isotope Stage M2 at 3.3 Ma being a possible harbinger. The recurrence plots are less pronounced and more transparent from 3.3 Ma to today (Fig. 2 and fig. S34), suggesting that Earth's climate cryosphere dynamics entered a state not comparable to anything seen in the preceding 60 or more million years.

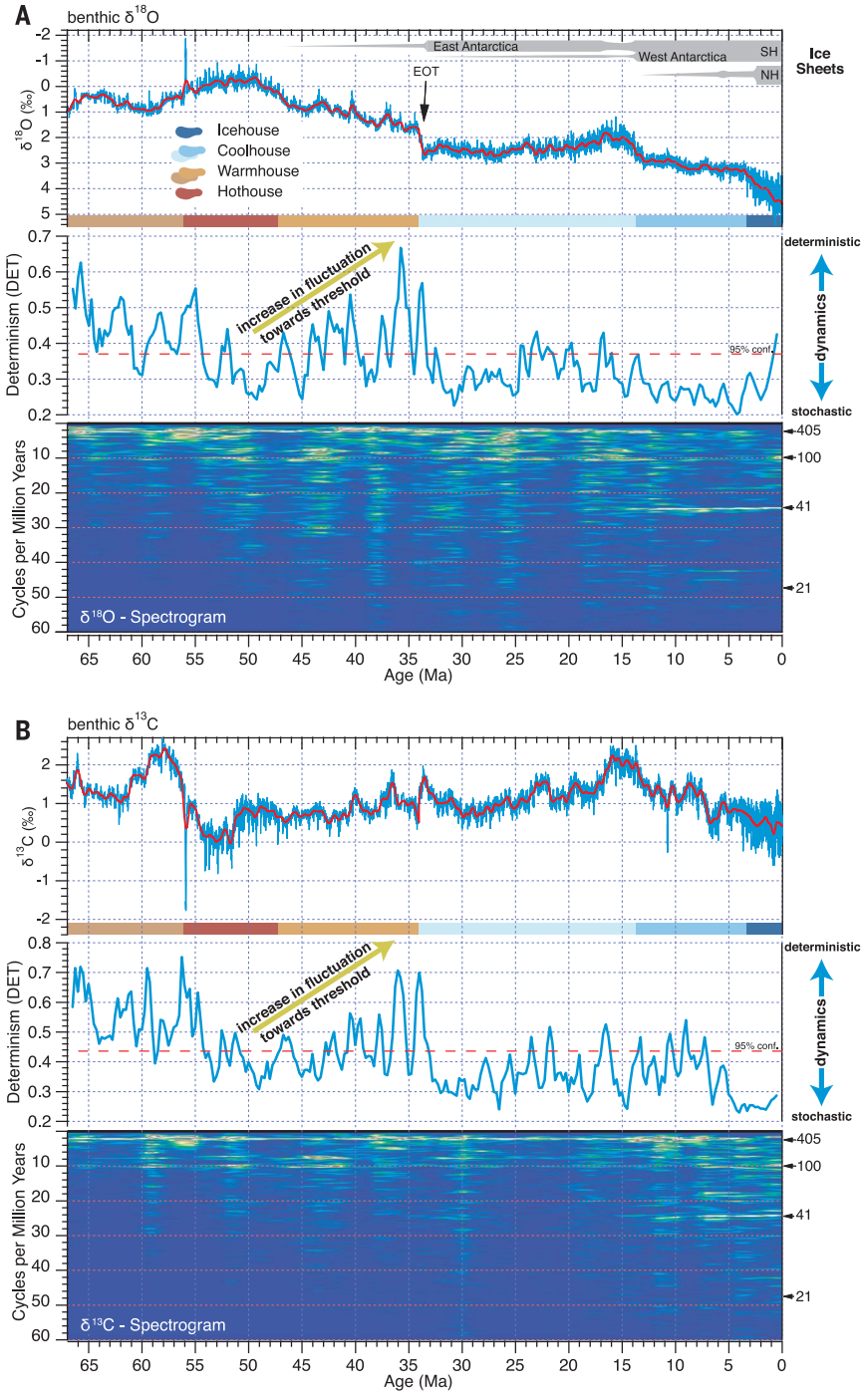

Fig. 3. Quasi-periodic changes and determinism in the global reference carbon cycle and oxygen isotope record. Evolutionary fast Fourier transform (FFT) spectrogram, recurrence determinism analysis, and benthic foraminifer oxygen (**A**) and carbon (**B**) isotope data plotted on age with the four climate states. Frequencies between 2 and 60 cycles per million years are related to changes in Earth's orbital parameters, known as Milankovitch cycles. The FFT spectrograms were computed with a 5-Myr window on the detrended records of benthic carbon and oxygen isotope data. From 67 to 13.9 Ma, cyclic variations in global climate are dominated by the eccentricity cycles of 405 and 100 kyr. Thereafter, in particular in the oxygen isotope record, the influence of obliquity increased, dominating the rhythm of climate in the record younger than ~7.7 Ma. Recurrence analysis of determinism (DET) shows that climate in the Warmhouse state is more deterministic (predictable) than in the Hothouse, Coolhouse, and Icehouse. From 47 Ma toward the EOT at 34 Ma, climate dynamic changes are rising in amplitude, approaching a threshold in the climate system. If DET tends to low values, the dynamics are stochastic, whereas high values represent deterministic dynamics.

The CENOGRID allows us to scrutinize the state dependency of climate system response to CO_2 and astronomical forcing on time scales of 10 thousand to 1 million years (*13*). Astronomical forcing throughout the Cenozoic is consistently uniform, but the RA indicates that the nonlinear response in climate variability to this forcing is strongly influenced by the fundamental state of climate. Evolutionary spectrograms characterize the dominant climatic response to astronomical forcing during the Cenozoic (Fig. 3). We find that the prevailing climate state, as characterized by atmospheric CO_2 concentration and polar ice sheets, orchestrates the response of climate processes to astronomical forcing. Modeled insolation-driven global temperature variability on astronomical time scales suggests that different temperature-response regimes exist: Eccentricity dominates temperature responses in low latitudes, precession in mid-latitudes, and obliquity in high latitudes (*25*). Thus, pronounced astronomical cyclicity in the CENOGRID could reflect climate state–dependent amplifications of latitude-specific climate processes.

In the Hothouse and Warmhouse, as well as the first Coolhouse phase, eccentricity-related cycles dominate the CENOGRID records, indicating a strong influence of low-latitude processes on climate variations. Obliquity-related cycles are sparse in these intervals but have been documented in other geochemical records (*26*, *27*), exhibiting perhaps local lithological responses. Weak response in the obliquity band during the Hothouse and Warmhouse intervals might be related to the absence of a high-latitude ice sheet that could have amplified climate response to obliquity forcing. The driving mechanism for the prevailing eccentricity cyclicity in the benthic $\delta^{13}C$ and $\delta^{18}O$ records is still unknown, but modeling suggests that low- and mid-latitude processes in the climate system respond in a nonlinear way to insolation forcing (*25*, *28*–*30*). In this regard, a key feedback likely involves the hydrological cycle with highly seasonal precipitation patterns during intervals of strong monsoon response to precession-induced insolation change, which could play a major role in the global distribution of moisture and energy (*31*–*34*). The expression of precession is apparently weak in the CENOGRID composite record, despite the dominant eccentricity forcing, likely owing to the long residence time of carbon in the oceans enhancing longer forcing periods (*30*, *35*), as well as our strategy to avoid "overtuning" the record. After the increasing influence of high-latitude cooling and ice growth during the second Coolhouse phase, the obliquity-band response steadily increases after the mMCT before dominating climate dynamics by the late Miocene–early Pliocene (*11*, *22*, *36*). In the Icehouse state, the progressive decrease in

atmospheric CO_2 and major growth of polar ice sheets, which enhanced variability in $\delta^{18}O$, steadily amplified the influence of complex high-latitude feedbacks until they essentially dominated climate dynamics.

To better understand the complexity of climate dynamics recorded in the CENOGRID, we computed the RA measure of DET (*13*). This parameter quantifies the predictability of dynamics in a system's state. Predictability estimates the stochastic (unpredictable) versus the deterministic (predictable) nature of climate dynamics recorded in CENOGRID (*13*). DET values near zero correspond to unpredictable dynamics, whereas large values indicate predictable dynamics, which are especially interesting to examine on the approach to tipping points. Changes in DET can thus reveal transitions between fundamentally different climate regimes.

Our RA suggests that climate dynamics during the Warmhouse and Hothouse Cenozoic states are more predictable or more regular than those of the Coolhouse and Icehouse states (Fig. 3). The growth of polar ice sheets at the EOT enhanced the effect of obliquity pacing of high-latitude climate that interacted with eccentricity-modulated precession forcing at lower latitudes from that point in time. This led to increased nonlinear interactions among astronomically paced climate processes and, thus, more complex, stochastic climate dynamics. The development of a large Antarctic ice volume at the inception of the Coolhouse is associated with a fundamental regime change toward less predictable climate variability (lower DET values calculated from benthic $\delta^{18}O$) (Fig. 3). From 25 to 13.9 Ma DET is elevated again, related to a reduction in ice volume in relatively warmer times of the Coolhouse, culminating in the MCO. Despite the growing influence of ice sheets in the Coolhouse, until ~6 to 7 Ma, carbon-cycle dynamics remain more deterministic than temperature because $\delta^{13}C$ variations are predominantly driven by low-latitude processes and less strongly influenced by the complex interaction with polar ice-sheet fluctuations. After ~6 Ma DET drops, likely because of a stronger cryosphere imprint on the carbon cycle. Upon initiation of the Icehouse at 3.3 Ma, $\delta^{18}O$ recorded climate dynamics become slightly more deterministic (*37*) and carbon-cycle dynamics unpredictable, likely resulting from the complex response to the waxing and waning of polar ice caps (*38*).

The CENOGRID spectrogram displays a broader frequency range during several intervals with low DET values (e.g., Coolhouse), whereas high DET values (e.g., Warmhouse) occur when single frequencies dominate (Fig. 3). This could be signaling a more direct response to astronomical forcing in the Warmhouse compared with that in the Coolhouse. Our RA suggests that the Hothouse is more stochastic (less predictable) than the Warmhouse, presumably induced by the occurrence of extreme hyperthermal events and their strong nonlinear and much-amplified climate response to astronomical forcing (*39*, *40*). The evolving pattern in the DET from the onset of cooling after the EECO to the EOT is pronounced (Fig. 3). The amplitude in fluctuations between stochastic and deterministic dynamics intensifies from 49 Ma to 34 Ma, consistent with how Earth's climate system is suggested to behave (*41*, *42*) as it moves toward a major tipping point. Once that tipping point is reached at the EOT, a rapid shift toward more permanently stochastic dynamics marks the inception of a new climate state (*43*). Thus, not only is polar ice volume critical to defining Earth's fundamental climate state, it also seems to play a crucial role in determining the predictability of its climatological response to astronomical forcing.

REFERENCES AND NOTES

1. J. Zachos, M. Pagani, L. Sloan, E. Thomas, K. Billups, *Science* **292**, 686–693 (2001).
2. K. G. Miller, G. Mountain, J. D. Wright, J. V. Browning, *Oceanography (Wash. D.C.)* **24**, 40–53 (2011).
3. N. J. Shackleton, J. P. Kennett, in *Initial Reports of the Deep Sea Drilling Project* (U.S. Government Printing Office, 1975), vol. 29, pp. 743–755.
4. B. S. Cramer, J. R. Toggweiler, J. D. Wright, M. E. Katz, K. G. Miller, Ocean overturning since the Late Cretaceous: Inferences from a new benthic foraminiferal isotope compilation. *Paleoceanography* **24**, PA4216 (2009).
5. D. De Vleeschouwer, M. Vahlenkamp, M. Crucifix, H. Pälike, *Geology* **45**, 375–378 (2017).
6. O. Friedrich, R. D. Norris, J. Erbacher, *Geology* **40**, 107–110 (2012).
7. K. G. Miller, R. G. Fairbanks, G. S. Mountain, *Paleoceanography* **2**, 1–19 (1987).
8. J. Veizer, A. Prokoph, *Earth Sci. Rev.* **146**, 92–104 (2015).
9. J. C. Zachos, G. R. Dickens, R. E. Zeebe, *Nature* **451**, 279–283 (2008).
10. K. G. Miller, J. V. Browning, W. J. Schmelz, R. E. Kopp, G. S. Mountain, J. D. Wright, Cenozoic sea-level and cryospheric evolution from deep-sea geochemical and continental margin records. *Sci. Adv.* **6**, eaaz1346 (2020).
11. A. J. Drury, T. Westerhold, D. Hodell, U. Röhl, *Clim. Past* **14**, 321–338 (2018).
12. M. E. Katz, D. R. Katz, J. D. Wright, K. G. Miller, D. K. Pak, N. J. Shackleton, E. Thomas, Early Cenozoic benthic foraminiferal isotopes: Species reliability and interspecies correction factors. *Paleoceanography* **18**, 1024 (2003).
13. See supplementary materials.
14. J. Laskar, A. Fienga, M. Gastineau, H. Manche, *Astron. Astrophys.* **532**, A89 (2011).
15. N. Marwan, M. C. Romano, M. Thiel, J. Kurths, *Phys. Rep.* **438**, 237–329 (2007).
16. T. Westerhold, U. Röhl, B. Donner, J. C. Zachos, *Paleoceanogr. Paleoclimatol.* **33**, 626–642 (2018).
17. H. K. Coxall, P. A. Wilson, H. Pälike, C. H. Lear, J. Backman, *Nature* **433**, 53–57 (2005).
18. J. F. Spray *et al.*, *Paleoceanogr. Paleoclimatol.* **34**, 1124–1138 (2019).
19. B. P. Flower, J. P. Kennett, The middle Miocene climatic transition: East Antarctic ice sheet development, deep ocean circulation and global carbon cycling. *Pal. Pal. Pal.* **108**, 537–555 (1994).
20. A. E. Holbourn, W. Kuhnt, K. G. D. Kochhann, N. Andersen, K. J. Sebastian Meier, *Geology* **43**, 123–126 (2015).
21. D. A. Hodell, K. A. Venz-Curtis, Late Neogene history of deepwater ventilation in the Southern Ocean. *Geochem. Geophys. Geosyst.* **7**, Q09001 (2006).
22. A. J. Drury *et al.*, *Earth Planet. Sci. Lett.* **475**, 254–266 (2017).
23. S. K. Turner, *Paleoceanography* **29**, 1256–1266 (2014).
24. I. Bailey *et al.*, *Quat. Sci. Rev.* **75**, 181–194 (2013).
25. T. Laepple, G. Lohmann, Seasonal cycle as template for climate variability on astronomical timescales. *Paleoceanography* **24**, PA4201 (2009).
26. T. Westerhold, U. Röhl, *Clim. Past* **5**, 309–327 (2009).
27. M. Vahlenkamp *et al.*, *Earth Planet. Sci. Lett.* **484**, 329–340 (2018).
28. T. J. Crowley, K.-Y. Kim, J. G. Mengel, D. A. Short, *Science* **255**, 705–707 (1992).
29. D. A. Short, J. G. Mengel, T. J. Crowley, W. T. Hyde, G. R. North, *Quat. Res.* **35**, 157–173 (1991).
30. R. E. Zeebe, T. Westerhold, K. Littler, J. C. Zachos, *Paleoceanography* **32**, 440–465 (2017).
31. K. E. Trenberth, D. P. Stepaniak, J. M. Caron, *J. Clim.* **13**, 3969–3993 (2000).
32. P. X. Wang *et al.*, *Earth Sci. Rev.* **174**, 84–121 (2017).
33. M. Huber, A. Goldner, *J. Asian Earth Sci.* **44**, 3–23 (2012).
34. J. H. C. Bosmans, S. S. Drijfhout, E. Tuenter, F. J. Hilgen, L. J. Lourens, *Clim. Dyn.* **44**, 279–297 (2015).
35. H. Pälike *et al.*, *Science* **314**, 1894–1898 (2006).
36. A. E. Holbourn, W. Kuhnt, S. Clemens, W. Prell, N. Andersen, *Paleoceanography* **28**, 688–699 (2013).
37. S. R. Meyers, L. A. Hinnov, Northern Hemisphere glaciation and the evolution of Plio-Pleistocene climate noise. *Paleoceanography* **25**, PA3207 (2010).
38. D. Liebrand, A. T. M. de Bakker, *Clim. Past* **15**, 1959–1983 (2019).
39. S. Kirtland Turner, P. F. Sexton, C. D. Charles, R. D. Norris, *Nat. Geosci.* **7**, 748–751 (2014).
40. D. J. Lunt *et al.*, *Nat. Geosci.* **4**, 775–778 (2011).
41. V. Dakos *et al.*, *Proc. Natl. Acad. Sci. U.S.A.* **105**, 14308–14312 (2008).
42. M. Scheffer *et al.*, *Nature* **461**, 53–59 (2009).
43. W. Steffen *et al.*, *Proc. Natl. Acad. Sci. U.S.A.* **115**, 8252–8259 (2018).
44. M. D. Palmer, G. R. Harris, J. M. Gregory, *Environ. Res. Lett.* **13**, 084003 (2018).
45. T. Westerhold, Cenozoic global reference benthic carbon and oxygen isotope dataset (CENOGRID). PANGAEA (2020); https://doi.pangaea.de/10.1594/PANGAEA.917503.

ACKNOWLEDGMENTS

We thank H. Kuhnert and his team for stable isotope analyses at MARUM and the teams at the IODP Gulf Coast Core Repository (GCR) and the IODP Bremen Core Repository (BCR) for sampling. **Funding:** This research used samples and/or data provided by the International Ocean Discovery Program (IODP). Funding for this research was provided by the Deutsche Forschungsgemeinschaft (DFG, German Research Foundation) to T.W. (project nos. 320221997, 242225091), U.R. (project nos. 5410858, 28504316, 179386126, 242241969, 320221997), and A.E.H. (project nos. 48739182, 224193684, and 142157224); the Natural Environmental Research Council (NERC) to D.A.H.; the DFG (project nos. 386137731, 405856037) and the European Union's Horizon 2020 research and innovation program under grant agreement no. 820970 to N.M.; the DFG (project no. 408101468) and the European Union's Horizon 2020 research and innovation program under the Marie Sklodowska-Curie grant agreement (no. 796220) to A.J.D.; the National Science Foundation of China (grant no. 41525020, 41776051) to J.T.); the NERC Isotope Geosciences Facility at the British Geological Survey (IP-1581–1115) to J.S.K.B. and K.L.); the NWO-ALW grant (project no. 865.10.001) and Netherlands Earth System Science Centre (gravitation grant no. 024.002.001 to L.J.L.; and the NSF (grant no. EAR-0628719) to J.C.Z. Funded through the Cluster of Excellence "The Ocean Floor – Earth's Uncharted Interface" (research unit Recorder). **Author contributions:** T.W., U.R., A.J.D., and J.C.Z. designed the study; T.W., A.J.D., D.L., and D.D.V. compiled and revised the astrochronology; N.M. applied recurrence analysis; E.A. synthesized the pCO_2 data; C.A. evaluated calcareous nannofossil datums; F.F. and T.F. produced magnetostratigraphic results and interpretation for ODP 1263; D.A.H., A.J.D., T.W., and U.R. provided bulk and benthic isotope data; A.J.D. and R.H.W. wrote the code for data processing and interpretation; and J.S.K.B., S.M.B., A.J.D., N.M., A.E.H., D.K., V.L., D.L., K.L., L.J.L., M.L., H.P., J.T., P.A.W., U.R., and T.W. designed projects and generated data basis for the reference record as well as discussed/modified the manuscript. All authors contributed to writing the final manuscript. **Competing interests:** The authors declare no competing interests. **Data and materials availability:** All data are available in the main text or in the supplementary materials. All data are available open access in electronic form at the PANGAEA data repository (*45*).

SUPPLEMENTARY MATERIALS

science.sciencemag.org/content/369/6509/1383/suppl/DC1
Materials and Methods
Supplementary Text S1 to S4
Figs. S1 to S35
Tables S1 to S34
References (*46*–*184*)

30 December 2019; accepted 28 July 2020
10.1126/science.aba6853

CIRCADIAN RHYTHMS

The hepatocyte clock and feeding control chronophysiology of multiple liver cell types

Dongyin Guan[1,2], Ying Xiong[1,2], Trang Minh Trinh[1,2], Yang Xiao[1,2], Wenxiang Hu[1,2], Chunjie Jiang[1,2], Pieterjan Dierickx[1,2], Cholsoon Jang[3]*, Joshua D. Rabinowitz[3], Mitchell A. Lazar[1,2,4]†

Most cells of the body contain molecular clocks, but the requirement of peripheral clocks for rhythmicity and their effects on physiology are not well understood. We show that deletion of core clock components REV-ERBα and REV-ERBβ in adult mouse hepatocytes disrupts diurnal rhythms of a subset of liver genes and alters the diurnal rhythm of de novo lipogenesis. Liver function is also influenced by nonhepatocytic cells, and the loss of hepatocyte REV-ERBs remodels the rhythmic transcriptomes and metabolomes of multiple cell types within the liver. Finally, alteration of food availability demonstrates the hierarchy of the cell-intrinsic hepatocyte clock mechanism and the feeding environment. Together, these studies reveal previously unsuspected roles of the hepatocyte clock in the physiological coordination of nutritional signals and cell-cell communication controlling rhythmic metabolism.

Biological rhythms are intricately involved in sleeping-waking, feeding-fasting, and activity-rest phenomena, and they are essential to maintaining physiological homeostasis (*1*). The mammalian core clock includes transcriptional activators BMAL1/CLOCK and transcriptional repressors REV-ERBα and REV-ERBβ that function in interlocked transcriptional feedback loops (*2*). Central clocks in the suprachiasmatic nucleus (SCN) are believed to synchronize clocks in peripheral tissues (*3*), and dyssynchrony of this system is associated with metabolic dysfunction (*4*, *5*). Nevertheless, major questions remain as to how the environment and genetic factors control the clocks in peripheral tissues and whether communication exists between clocks in different cell types within an organ.

To dissect the cell-autonomous and nonautonomous regulation of diurnal rhythms in peripheral tissues, we focused on the liver, a metabolic hub (*6*). REV-ERBα and REV-ERBβ were specifically deleted in hepatocytes (HepDKO; DKO, double knockout) by injecting the AAV8-TBG-CRE virus into adult REV-ERBα/β floxed mice. This model excludes developmental effects and potential confounding due to direct manipulation of the clock in other tissues (*7*, *8*). Expression of both REV-ERBα and REV-ERBβ was nearly undetectable after 2 weeks, even at zeitgeber time 10 (ZT10), when REV-ERBs were highly expressed at the mRNA (Fig. 1A) and protein level (fig. S1). REV-ERBs physiologically repress *Bmal1* and *Npas2* in a circadian manner (*9*, *10*), and both of these genes were constitutively derepressed in the REV-ERB HepDKO (Fig. 1B). Other core clock genes also demonstrated reduced rhythmicity (Fig. 1B).

We next examined the effect of REV-ERB HepDKO on the liver rhythmic transcriptome. Two weeks after adeno-associated virus (AAV) treatment, RNA sequencing (RNA-seq) performed on livers harvested every 3 hours revealed the attenuation of the rhythmicity of a large group of transcripts that were highly rhythmic in the controls, including genes involved in diurnal rhythm pathways such as *Bmal1*, *Npas2*, and *Clock* (Fig. 1C, fig. S2A, and table S1A). This observation fits the prevailing hypothesis that REV-ERBs are major controllers of the clock and suggests that the rhythmic expression of these genes depends on the intrinsic core clock feedback loop. Many genes, however, maintained diurnal rhythmicity in the absence of REV-ERBs (Fig. 1D, fig. S2B, and table S1B). Among these were ~170 genes, enriched for lipid metabolism, that showed enhanced rhythmic amplitudes (Fig. 1E, fig. S2C, and table S1C). KEGG (Kyoto Encyclopedia of Genes and Genomes) and gene set enrichment analysis (GSEA) indicated that rhythmic transcripts regulated by REV-ERBs were involved in circadian rhythms, hormone secretion, and lipid metabolism (fig. S2, A to D). These results indicated an unexpected rhythmic transcriptomic reprogramming in the liver upon the depletion of REV-ERBs in adult hepatocytes. Importantly, rhythmic locomotor activity (fig. S3A), feeding (fig. S3B), and plasma insulin levels (fig. S3C) were not much affected in REV-ERB HepDKO mice, indicating that disruption of the hepatocyte clock did not affect diurnal activity and feeding responses and excluding the possibility that the remodeling of the liver rhythmic transcriptome was due to changes in behavior.

Rhythmic expression of REV-ERB directly regulates many target genes by binding to ROR/REV-ERB-response element (RORE), where it represses transcription by recruiting co-repressors, by competing with ROR nuclear receptors, and by tethering to liver factors (*11*). ROR targets represented a high percentage of rhythm disrupted but not enhanced transcripts (fig. S3D), suggesting that REV-ERB's direct binding was more relevant to the rhythmically disrupted transcripts. Rhythmic transcriptome remodeling was confirmed in livers expressing REV-ERBα DNA binding domain deficient mutant and lacking REV-ERBβ (fig. S3E) (*12*).

To explore the transcriptional mechanism underlying rhythmic disruption in hepatocytes upon REV-ERB HepDKO, we used CistromeDB (*13*) to perform transcription factor (TF) binding similarity screening based on all published liver cistromes. REV-ERBs and their co-repressors HDAC3 and NCOR1 were the top TFs bound near genes whose diurnal rhythm was disrupted by REV-ERB HepDKO (Fig. 1F and table S2A). The binding sites of BMAL1, PER2, and CRY1 were enriched in rhythm-retained transcripts, suggesting that systemic signals drive rhythmic gene expression via these core clock genes (*14*) (fig. S3F and table S2B).

Although there is no REV-ERBα binding site near *Srebf1*, SREBF1 was the most enriched TF near genes whose diurnal rhythms were induced by the loss of REV-ERBs (Fig. 1G and table S2C). The rhythmic expression of *Srebf1* was enhanced upon REV-ERB HepDKO, as was that of many of its target genes that are involved in de novo lipogenesis (DNL) (Fig. 1H), which is consistent with a previous REV-ERBα whole-body knockout mouse model (*15*). Enhanced diurnal rhythmic expression of *Srebf1* was also observed in livers from reverse phase feeding (RPF) $Cry1^{-/-}$;$Cry2^{-/-}$ mice (*16*), suggesting a general role of core clock TF repressors in maintaining the homeostasis of hepatic lipid metabolism. The physiological significance of this finding was assessed by directly measuring DNL using deuterated water as a tracer. Consistent with the enhanced rhythm of *Srebf1* and the DNL pathway, the normal rhythm of DNL was markedly amplified in the livers of the REV-ERB HepDKO mice (Fig. 1I). This amplification was accompanied by an increase in the amplitude of plasma triglyceride rhythms, both on normal chow (Fig. 1J) and on high-fat, high-sucrose (HFHS) diet (Fig. 1K). Consistent with the increase in DNL, liver TG concentration was also increased in the livers of the HFHS-fed mice (Fig. 1L). Thus, REV-ERBs in hepatocytes

[1]Institute for Diabetes, Obesity, and Metabolism, Perelman School of Medicine, University of Pennsylvania, Philadelphia, PA 19104, USA. [2]Division of Endocrinology, Diabetes, and Metabolism, Department of Medicine, Perelman School of Medicine, University of Pennsylvania, Philadelphia, PA 19104, USA. [3]Lewis-Sigler Institute for Integrative Genomics and Department of Chemistry, Princeton University, Princeton, NJ 08544, USA. [4]Department of Genetics, Perelman School of Medicine, University of Pennsylvania, Philadelphia, PA 19104, USA.
*Present address: Department of Biological Chemistry, University of California Irvine, Irvine, CA 92697, USA.
†Corresponding author. Email: lazar@pennmedicine.upenn.edu

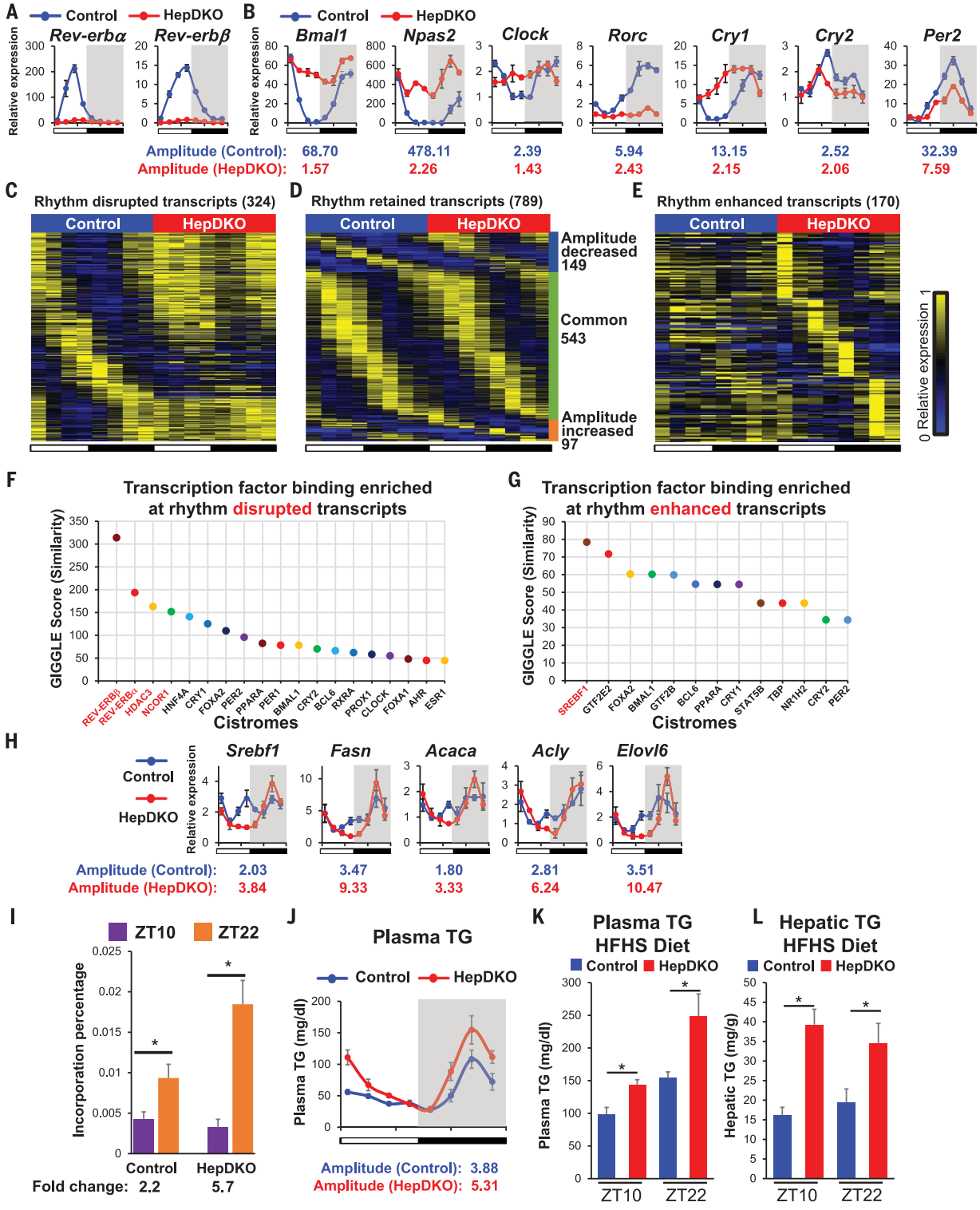

Fig. 1. Disruption of REV-ERBα and REV-ERBβ in hepatocytes remodels the liver diurnal rhythmic transcriptome and lipid metabolism. (**A** and **B**) Relative mRNA expression of *Rev-erbα* and *Rev-erbβ* (A) and REV-ERBs target genes (B) in control and HepDKO livers. (**C** to **E**) Heatmap of the relative expression of rhythm disrupted (C), retained (D), and enhanced (E) transcripts in control and HepDKO livers. The color bar indicates the scale used to show the expression of transcripts across eight time points, with the highest expression normalized to 1. JTK_CYCLE (*48*), adjusted $P < 0.01$, 21 hours ≤ period (t) ≤ 24 hours, peak-to-trough ratio > 2 (n = 3 mice per time point). (**F** and **G**) TF binding similarity screening on rhythm disrupted (F) and enhanced (G) transcripts based on all published liver cistromes from CistromeDB (*13*). (**H**) Relative mRNA expression of *Srebf1* and its target genes in control and HepDKO livers (n = 4 to 6 mice per time point). (**I**) Incorporation of deuterated water into liver fatty acids was measured in mice 6 hours after oral gavage of D_2O at ZT8 or ZT20. Data are presented as mean ± SEM. *$P < 0.05$ in Student's t test (n = 6 mice per group). (**J**) Serum triglyceride (TG) measurements in control and HepDKO mice. (**K** and **L**) Serum TG (K) and hepatic TG (L) measurements in HFHS-fed control and HepDKO mice. Data are presented as mean ± SEM (n = 4 to 6 mice per time point).

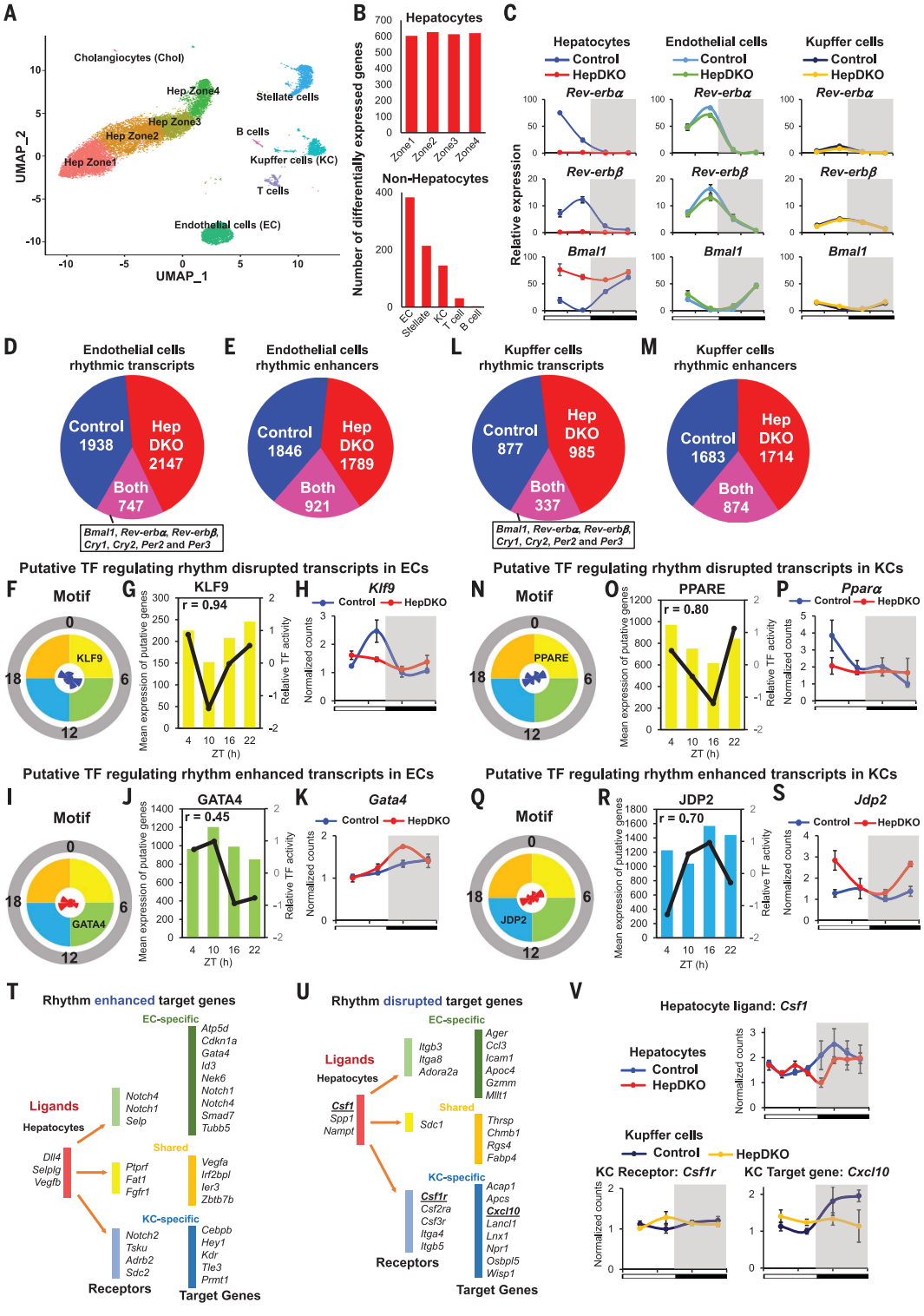

Fig. 2. Hepatocyte REV-ERBs control nonhepatocytic diurnal rhythmic transcriptomes. (**A**) Uniform manifold approximation and projection (UMAP) visualization of liver cell clusters based on 18,239 single-cell transcriptomes. (**B**) The number of differentially expressed transcripts in hepatocytes (top) or nonhepatocytes (bottom) upon REV-ERBs HepDKO. (**C**) Relative mRNA expression of *Rev-erbα*, *Rev-erbβ*, and *Bmal1* in isolated hepatocytes, ECs, and KCs from control and HepDKO livers. (**D** and **E**) Identification of diurnal rhythmic transcripts (D) and enhancers (E) in isolated ECs from control and HepDKO livers. JTK_CYCLE, adjusted $P \leq 0.05$, 21 hours ≤ period (t) ≤ 24 hours, peak-to-trough ratio > 1.5. (**F** and **I**) Rose diagrams showing the prevalence of rhythmic transcripts in each phase group, and motifs enriched at sites of rhythmic enhancers, which were correlated with rhythm disrupted (F) and enhanced (I) transcripts and enhancers from IMAGE in isolated ECs. (**G** and **J**) Correlation of mean expression of putative target genes and relative TF transcription activity in four phase groups in isolated ECs from control (G) and HepDKO (J) livers. In each plot, the bars represent the mean expression of putative TF target genes of each phase, and the black line represents the predicted TF relative transcription activity. Correlation coefficient r shows the strength of the relationship between the mean expression of putative TF target genes and relative transcription activity. (**H** and **K**) Expression level (normalized read counts) of *Klf9* (H) and *Gata4* (K) in isolated ECs from control and HepDKO livers. (**L** and **M**) Identification of diurnal rhythmic transcripts (L) and enhancers (M) in isolated KCs from control and HepDKO livers. (**N** and **Q**) Rose diagrams showing the prevalence of rhythmic transcript in each phase group, and motifs enriched at sites of rhythmic enhancers, which were correlated with rhythm disrupted (N) and enhanced (Q) transcripts and enhancers from IMAGE in isolated KCs. (**O** and **R**) Correlation of mean expression of putative target genes and relative TF transcription activity in four phase groups in isolated KCs from control (O) and HepDKO (R) livers. In each plot, the bars represent the mean expression of putative TF target genes of each phase, and the black line represents the predicted TF relative transcription activity. Correlation coefficient r shows the strength of the relationship between the mean expression of putative TF target genes and relative transcription activity. (**P** and **S**) Expression level (normalized read counts) of *Pparα* (P) and *Jbp2* (S) in isolated KCs from control and HepDKO livers. Data are presented as mean ± SEM (n = 4 mice per time point). (**T** and **U**) Ligand-receptor interaction analysis. Top three putative ligands from hepatocytes affect receptors (in ECs and KCs) for the regulation of rhythm enhanced (T) and disrupted (U) transcripts in ECs and KCs. (**V**) Examples of rhythm disrupted ligand (*Csf1*) from hepatocytes, receptor (*Csf1r*), and rhythm disrupted target gene (*Cxcl10*) in KCs.

are required to maintain lipid metabolism homeostasis.

Although hepatocytes are the most abundant cell type in the liver, the organ is composed of many other cell types that have critical roles in metabolic diseases (*17*–*19*). To better understand the effects of hepatocyte clock disruption, we performed single-nucleus RNA sequencing (sNuc-seq) on livers harvested at ZT8, when REV-ERBs are highly expressed, from control and HepDKO mice. sNuc-seq avoided skewing the results against lipid-laden hepatocytes that may be lost because of lysis or size exclusion during single-cell isolation, and ~3000 genes were detected per nucleus. On the basis of cell-specific markers (fig. S4, A and B), populations of hepatocytes, endothelial cells (ECs), Kupffer cells (KCs), stellate cells, and immune cells were clearly distinguishable, as were the subpopulations of hepatocytes corresponding to the previously defined markers of zonation (*20*) (Fig. 2A). As expected, many changes in gene expression were observed between control and HepDKO hepatocytes (Fig. 2B), with about two-thirds of the changes being common to hepatocytes in different zones (fig. S4C). The percentage of different cell populations in the liver was largely unchanged (fig. S4D), but gene expression in nonhepatocyte cells in the REV-ERB HepDKO livers was markedly altered, with the largest number of changes observed in ECs (Fig. 2B). Considerable changes were also noted in KCs, which are liver-resident macrophages that have critical roles within the organ (*17*). Together, these two cell types were selected for more detailed studies.

To quantify whole-cell transcriptomes with greater depth than is possible using sNuc-Seq, we performed diurnal rhythmic transcriptomics on ECs and KCs isolated every 6 hours, 2 weeks after hepatocyte-specific deletion of REV-ERBs. The deletion of *Rev-erbα* and *Rev-erbβ*, along with their constitutively induced repression target *Bmal1*, was confirmed in isolated hepatocytes. *Rev-erbα*/β gene expression was virtually unchanged in the ECs and KCs from the HepDKO livers, although the amplitude of *Rev-erbα*/β rhythms was muted in KCs (Fig. 2C). The relative expression of lineage-specific markers *Stab2* (ECs) and *Csf1r* (KCs) confirmed the specificity of the cell populations (fig. S4E).

Despite the physiologically rhythmic expression of the core clock genes, the diurnal rhythmic transcriptomes were extensively remodeled in ECs (Fig. 2D, fig. S5A, and table S3). These results indicated that disruption of the hepatocyte clock was communicated to the ECs. In addition, we quantified enhancer RNA expression in isolated ECs by mapping RNA-seq reads to intergenic regions of open chromatin determined by assay for transposase-accessible chromatin using sequencing (ATAC-seq) (*21*), which identified a widespread reprogramming of rhythmic enhancers (Fig. 2E, fig. S5B, and table S3).

We next used integrated analysis of motif activity and gene expression (IMAGE) (*22*) to ascertain sequence motifs enriched at sites of rhythmic enhancers associated with rhythmic genes to identify potential TFs with corresponding binding preferences and diurnal

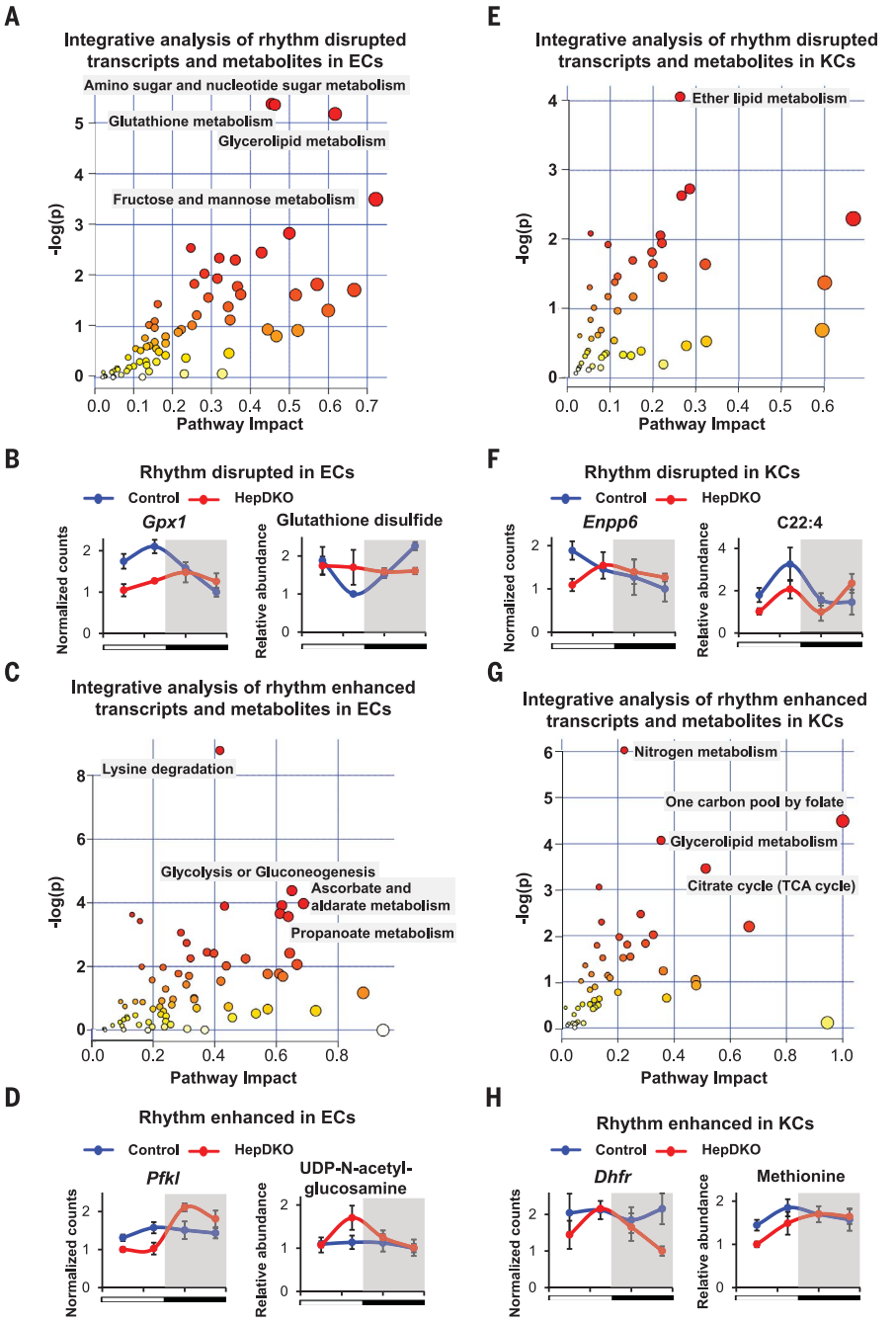

Fig. 3. Hepatocyte REV-ERBs regulate nonhepatocytic diurnal rhythmic metabolic process. (**A** and **C**) Metabolic pathway analysis integrating the enrichment of genes and metabolites in rhythm disrupted (A) and enhanced (C) transcripts and metabolites in isolated ECs. (**B** and **D**) Examples of rhythm disrupted (B) and enhanced (D) metabolites and related transcripts in ECs upon REV-ERBs DKO in hepatocytes. (**E** and **G**) Metabolic pathway analysis integrating the enrichment of genes and metabolites in rhythm disrupted (E) and enhanced (G) transcripts and metabolites in isolated KCs. (**F** and **H**) Examples of rhythm disrupted (F) and enhanced (H) metabolites and related transcripts in KCs upon REV-ERBs DKO in hepatocytes. Pathways were considered significant if $P < 0.01$ using hypergeometric test. Metabolites and transcripts data are presented as mean ± SEM (n = 3 or 4 mice per time point).

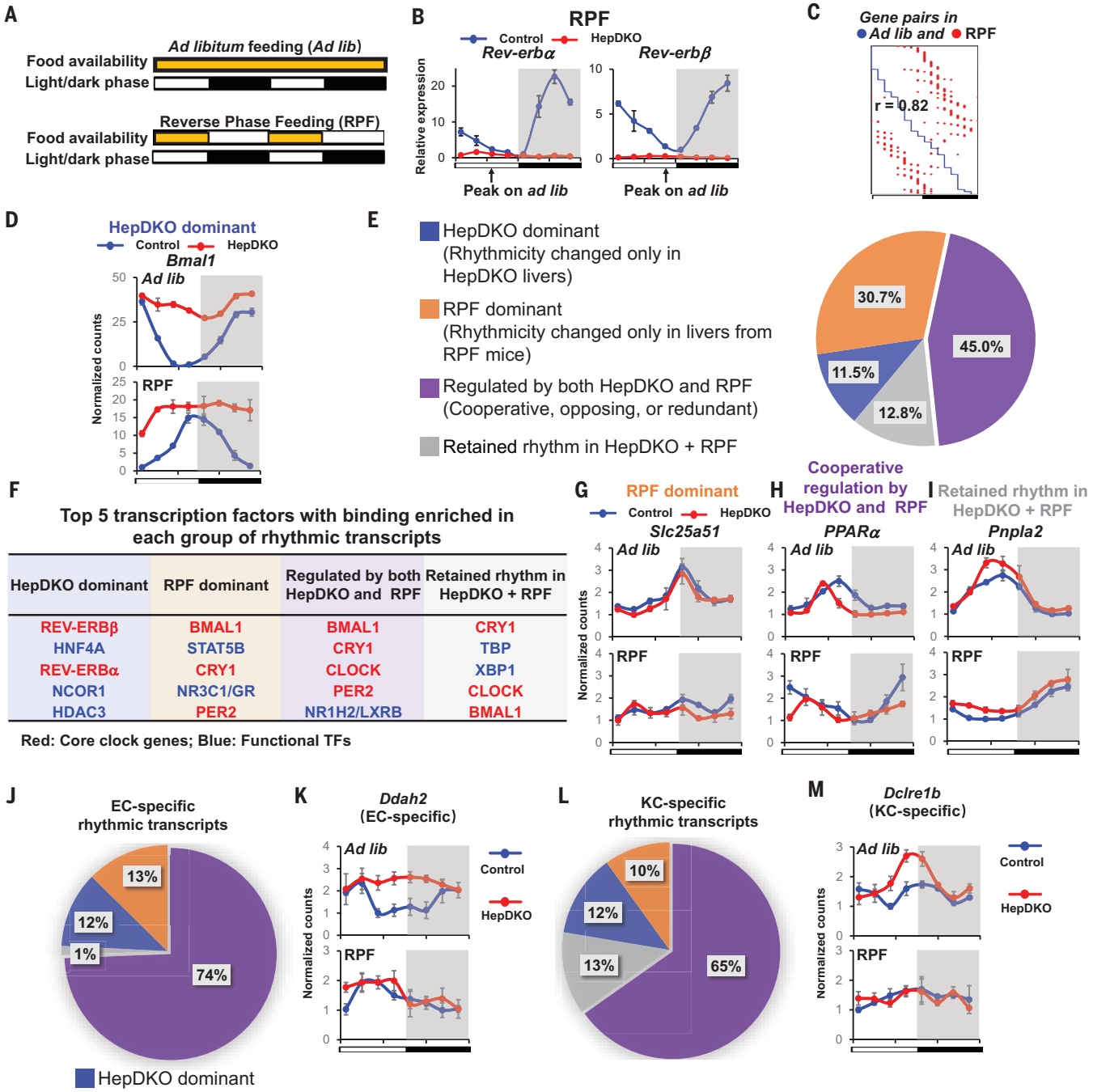

Fig. 4. Control of liver diurnal rhythms by the hepatocyte clock and feeding. (**A**) Diagram of feeding schedule of ad lib feeding and RPF. (**B**) Relative expression of *Rev-erbα* and *Rev-erbβ* in control and HepDKO livers from RPF mice. (**C**) Phase correlation of hepatic rhythmic transcripts between ad lib and RPF mice. Each row has a unique pair of hepatic rhythmic transcripts in ad lib mice (blue dot) and RPF mice (red dot). (**D**) Expression level (normalized read counts) of *Bmal1* in control and HepDKO livers from ad lib and RPF mice. (**E**) Identification of rhythmic transcripts that were dominantly regulated by HepDKO (blue) or RPF (orange), regulated by both HepDKO and RPF (purple), or retained in HepDKO+RPF (gray). (**F**) Top five TFs from four groups in (E) identified from TF binding similarity screening based on all published liver cistromes from CistromeDB (*13*). (**G** to **I**) Expression level (normalized read counts) of *Slc25a51*, *Pparα*, and *Pnpla2* in control and HepDKO livers from ad lib and RPF mice. (**J** and **L**) Identification of EC-specific (J) and KC-specific (L) rhythmic transcripts that were dominantly regulated by HepDKO (blue) or RPF (orange), regulated by both HepDKO and RPF (purple), or retained in HepDKO+RPF (gray). (**K** and **M**) Expression level (normalized read counts) of EC-specific gene *Ddah2* (K) and KC-specific gene *Dclre1b* (M) in control and HepDKO livers from ad lib and RPF mice. Data are presented as mean ± SEM (*n* = 3 mice per time point).

rhythmicity. These putative factors that were potentially responsible for rhythm disrupted and enhanced enhancers and transcripts were identified (table S4). For example, Kruppel-like factor 9 (KLF9), a ubiquitous regulator of oxidative stress (*23*), was identified as one of the putative TFs responsible for the loss of rhythmic enhancers associated with lost rhythmic genes that peaked between ZT0 and ZT6 (fig. S5C and Fig. 2F), and there was a positive correlation between KLF9 transcription activity and its putative target gene expression (Fig. 2G). Indeed, the expression of *Klf9* was rhythmic in control cells but not in ECs from HepDKO livers (Fig. 2H). Conversely, gained rhythmic enhancers peaking between ZT6 and ZT12 (fig. S5D and Fig. 2I) were enriched for the GATA-binding motif (Fig. 2J), corresponding to a gained rhythmic expression of *Gata4*, a known regulator of the hepatic microvasculature (*24*) (Fig. 2K).

Similarly, the KC rhythmic transcriptome was extensively reprogrammed in REV-ERB HepDKO livers (Fig. 2L, fig. S5E, and table S5), and this was associated with both the loss and gain of rhythmic enhancers (Fig. 2M, fig. S5F, and table S5). The factors identified as potentially responsible for rhythmic disrupted and enhanced enhancers and transcripts are listed in table S4. As an example, the PPAR-binding motif was enriched at sites of ZT0 to ZT6 rhythmic enhancers that decreased in KCs of the HepDKO livers (fig. S5G and Fig. 2N) and was associated with the highest transcriptional activity in this phase (Fig. 2O). Consistent with the transcriptional activity, the expression of *Pparα*, a regulator of the macrophage inflammatory response (*25*), was also rhythmic, peaking between ZT0 and ZT6 in control cells but not in KCs isolated from HepDKO livers (Fig. 2P). In contrast, the motif of Jun dimerization protein 2 (JDP2) was enriched in REV-ERB HepDKO-specific enhancers whose activity peaked between ZT12 and ZT18 (fig. S5H and Fig. 2Q) and also had the highest predicted transcriptional activity in this phase (Fig. 2R). The phase of the gained rhythmic expression of JDP2 was antiphase to its transcriptional activity (Fig. 2S), consistent with its transcriptional repression function (*26*). Moreover, comparative analysis of rhythmic remodeled transcripts between hepatocytes, ECs, and KCs revealed little overlap between different cell types, indicating a cell type–specific response to loss of REV-ERB in hepatocytes (fig. S6, A to C).

To uncover potential signals from hepatocytes lacking REV-ERBs to other cell types, we used NicheNet (*27*) to identify ligand-receptor pairs in which the ligand was altered in HepDKO hepatocytes, and the receptor was expressed in ECs, or KCs and the downstream genes exhibited enhanced (Fig. 2T and fig. S6D) or disrupted (Fig. 2U and fig. S6E) rhythms. For example, the colony stimulating factor 1 gene *Csf1* lost rhythmicity in HepDKO hepatocytes (Fig. 2V). The CSF1 receptor was expressed in KCs, and although it was not rhythmically expressed, downstream genes of the CSF1 signaling pathways such as *Cxcl10 (28)* lost rhythmicity (Fig. 2V). These results demonstrate how disruption of the hepatocyte clock could lead to altered diurnal rhythms of gene expression in surrounding nonhepatocytic cells. Note that this analysis does not incorporate posttranscriptional regulation of predicted ligands and receptors that were not regulated at the transcript level (table S6) (*29*).

To understand the impact of HepDKO-induced diurnal rhythm remodeling on nonhepatocytic cells, we performed GSEA on the rhythmic transcriptomes of ECs and KCs. Lipid metabolism–related pathways were found to be enriched in both ECs and KCs (fig. S7, A and B). This rhythm remodeling may be regulated not only via mapped ligand-receptor pairs but also via metabolites from hepatocytes, because we observed rhythmic metabolome reprogramming in isolated hepatocytes in the liver upon depletion of REV-ERBs (fig. S7, C and D, and table S7). Consistently, mouse phenotype enrichment analysis (*30*) indicates that phenotypes most enriched in altered rhythmic transcripts of both ECs and KCs from HepDKO livers were related to homeostasis and metabolism (fig. S7, E and F).

To test this prediction, we performed diurnal rhythmic metabolomic profiling, identifying many metabolites whose diurnal rhythms were disrupted or enhanced in ECs and KCs from HepDKO livers (fig. S7G and table S7). Integrated analysis of rhythm-remodeled transcripts and metabolites by MetaboAnalyst (*31*) revealed a number of significantly affected metabolic pathways. In ECs, multiple rhythmic metabolic pathways were disrupted, including glutathione metabolism (Fig. 3A and fig. S8), as illustrated by expression of the *Gpx1* gene and glutathione disulfide (Fig. 3B). Other pathways exhibited enhanced diurnal rhythmicity, including glucose metabolism and its conversion into hexosamines (Fig. 3C), as illustrated by the gained rhythm of *Pfkl* gene expression and uridine diphosphate-*N*-acetyl-glucosamine levels (Fig. 3D). These changes likely affect the function of ECs, which rely on glycolysis for energy production, with the hexosamine pathway controlling nitric oxide (NO) production and angiogenesis (*32*). In KCs, the correlated rhythmic disrupted transcripts and metabolites were related to lipid metabolism (Fig. 3E), exemplified by *Enpp6* gene expression and docosatetraenoic acid (C22:4) levels (Fig. 3F) (*33*, *34*), whereas rhythm enhanced pathways included one-carbon metabolism (Fig. 3G) regulated by the *Dhfr* gene (Fig. 3H). Together, the cell type–specific rhythm remodeling in nonhepatocytic cells upon the loss of hepatocyte REV-ERBs identifies a previously unknown, coordinated response to hepatocyte clock disturbance.

Although light-dark cycles act as zeitgebers to entrain behavioral rhythms via the central rhythmic oscillator in the SCN of the hypothalamus, feeding-fasting cycles are important synchronizers of peripheral clocks (*35*–*37*), and time-restricted feeding uncouples liver rhythms from behavioral rhythms (*35*). Having demonstrated the role of the hepatocyte clock in controlling cell-autonomous and non-cell-autonomous rhythms in the liver, we next considered its role in the response to nutrition by performing diurnal rhythmic transcriptomic analysis on mice subjected to 3 weeks of RPF, in which food was available only during the light phase (Fig. 4A). As expected, based on previous work (*35*), RPF of control mice led to a 12-hour phase shift in the rhythms of core clock genes such as *Rev-erbα* and *Rev-erbβ* (Fig. 4B). Transcriptomic analysis indicated that nearly all rhythmic transcripts exhibited a 12-hour phase shift in the livers of control mice under RPF (Fig. 4C), suggesting a dominant role of feeding on rhythmic phase regulation.

The rhythm of the core clock gene *Bmal1* was also phase shifted by ~12 hours under RPF in control livers. In contrast, in the livers of REV-ERB HepDKO mice, *Bmal1* expression was constitutive, robust, and nonrhythmic both under RPF and ad libitum (ad lib) feeding (Fig. 4D), indicating cell-autonomous clock regulation of the hepatocyte endogenous clock by REV-ERBs. Because most rhythmic genes were phase shifted ~12 hours by RPF, we assessed changes in rhythmicity using a classification that integrated amplitude (fold change of peak-to-trough ratio > 2), period (between 21 and 24 hours), and adjusted *P* value (<0.01) from the JKT algorithm (*38*). This analysis identified four categories of rhythmic genes: (i) HepDKO dominant (rhythmicity of transcripts is changed only in HepDKO livers); (ii) RPF dominant (rhythmicity of transcripts is changed only in livers from RPF mice); (iii) regulated by both HepDKO and RPF (including cooperative, redundant, or opposing changes); and (iv) retained rhythm in HepDKO and RPF (rhythmicity unchanged in HepDKO+RPF).

Of all rhythmic transcripts, 11.5% were HepDKO dominant (Fig. 4E, fig. S9A, and table S8A), and on the basis of TF binding similarity screening analysis, this group of rhythmic transcripts was likely directly regulated by REV-ERB and its corepressor complexes (Fig. 4F). RPF-dominant transcripts represented 30.7% of rhythmic transcripts (Fig. 4E and table S8B), implying non-cell-autonomous regulation by feeding. For example,

the diurnal rhythmicity of *Slc25a51* was indistinguishable in control and HepDKO livers from ad lib fed mice but disrupted in both control-RPF and HepDKO-RPF livers (Fig. 4G). Binding sites for STAT (signal transducer and activator of transcription) and GR (glucocorticoid receptor) TFs were enriched near these genes (Fig. 4F) (*39*, *40*).

Forty-five percent of rhythmic transcripts were regulated by both HepDKO and RPF, either cooperatively, oppositely, or redundantly (Fig. 4E and fig. S9B). Binding sites enriched near these genes included those of lipid-regulating liver X receptor (Fig. 4F), whose activation was reported to be rhythmically enhanced in livers of REV-ERBα whole-body knockout mice (*15*). Cooperative changes were exemplified by the *Pparα* gene (Fig. 4H and table S8C). Note that these results largely reflect hepatocytes, whose *Pparα* expression pattern was different from that shown for KCs. In contrast, the HepDKO-induced diurnal rhythmic enhancement of *Phf8* was negated by RPF while the rhythmic disrupting effect by RPF on *Ccnd1* was counteracted by HepDKO (fig. S9, B and C). The cooperative and opposing effects on rhythmicity demonstrate interdependence of the hepatocyte clock and feeding. However, for genes classified as redundant, the separate effects of HepDKO and RPF on rhythmicity were similar to each other and to the combination (e.g., *Srebf1*) (fig. S9, B and D).

In the final group of rhythmic transcripts, although the phase was dependent on food entrainment, the rhythmicity per se was retained in both HepDKO and RPF, suggesting that the rhythmic expression of transcripts in this group was controlled by other signals independent of the intrinsic clock and feeding (Fig. 4, E and I, and table S8D). Interestingly, although the rhythmic mRNA expression of core clock genes *Bmal1*, *Cry1*, and *Per2* was attenuated upon REV-ERB depletion, the binding sites were still enriched in these nonintrinsic rhythmic transcripts (Fig. 4F), suggesting that systemic signals drive the rhythmic transcription activity of these TFs (*14*, *41*).

Finally, we sought to determine the extent to which the hepatocyte clock and feeding-fasting cycles control diurnal rhythms in nonhepatocytes. We defined the EC-specific rhythmic genes using RNA-seq data from ECs isolated from the HepDKO livers and then determined their rhythmic expression during RPF, both in control and REV-ERB HepDKO livers. Notably, ~74% of rhythmic genes (Fig. 4J and Table S9A) were regulated by both HepDKO and RPF, with enrichment for genes regulating NO synthesis (fig. S9E), including EC-specific *Ddah2* (*42*) (Fig. 4K). Similarly, in KCs, ~65% of cell-specific rhythmic genes were regulated by both HepDKO and RPF (Fig. 4L and table S9B), with enrichment for genes regulating histone-serine phosphorylation (fig. S9F), including *Dclre1b*, which regulates DNA repair (*43*) and whose rhythmic expression was KC-specific in the liver (Fig. 4M). Thus, nonautonomous signals resulting from feeding and communication from hepatocytes play vital roles in the rhythmic gene expression of nonhepatocytic cells in the liver.

Our studies shed light on the physiological importance and function of peripheral clocks, whose existence was originally established in vitro (*44*–*46*). We demonstrate that some but not all hepatocyte diurnal rhythms are controlled by the core clock in a cell-autonomous manner in vivo. Moreover, the enhanced diurnal rhythms upon REV-ERB deletion (e.g., DNL genes) suggest that the clock not only anticipates daily environment changes but also buffers against certain fluctuations. Previous studies manipulating the liver clock found that it was not essential for weight loss due to food restriction during the normal feeding period (*47*) or behavioral diurnal rhythms for which the light-dark cycle acts as a zeitgeber (*7*). However, when feeding is restricted to the light phase, it becomes the predominant hepatocytic zeitgeber for the liver (*35*), and our studies demonstrate the hierarchy and interdependence of feeding and the cell-autonomous clock for diurnal rhythmic hepatocyte gene expression. Moreover, rhythmic gene expression and metabolism in nonhepatocytic cells in the liver are highly influenced both by the hepatocyte clock and feeding. These findings are likely to apply to peripheral clocks in other cell types.

REFERENCES AND NOTES

1. J. Bass, J. S. Takahashi, *Science* **330**, 1349–1354 (2010).
2. J. S. Takahashi, *Nat. Rev. Genet.* **18**, 164–179 (2017).
3. D. K. Welsh, J. S. Takahashi, S. A. Kay, *Annu. Rev. Physiol.* **72**, 551–577 (2010).
4. C. B. Green, J. S. Takahashi, J. Bass, *Cell* **134**, 728–742 (2008).
5. S. Panda, *Science* **354**, 1008–1015 (2016).
6. E. Trefts, M. Gannon, D. H. Wasserman, *Curr. Biol.* **27**, R1147–R1151 (2017).
7. K. B. Koronowski *et al.*, *Cell* **177**, 1448–1462.e14 (2019).
8. M. K. Bunger *et al.*, *Cell* **103**, 1009–1017 (2000).
9. C. Crumbley, Y. Wang, D. J. Kojetin, T. P. Burris, *J. Biol. Chem.* **285**, 35386–35392 (2010).
10. F. Guillaumond, H. Dardente, V. Giguère, N. Cermakian, *J. Biol. Rhythms* **20**, 391–403 (2005).
11. Y. Zhang *et al.*, *Science* **348**, 1488–1492 (2015).
12. H. Cho *et al.*, *Nature* **485**, 123–127 (2012).
13. R. Zheng *et al.*, *Nucleic Acids Res.* **47**, D729–D735 (2019).
14. B. Kornmann, O. Schaad, H. Bujard, J. S. Takahashi, U. Schibler, *PLOS Biol.* **5**, e34 (2007).
15. G. Le Martelot *et al.*, *PLOS Biol.* **7**, e1000181 (2009).
16. C. Vollmers *et al.*, *Proc. Natl. Acad. Sci. U.S.A.* **106**, 21453–21458 (2009).
17. O. Krenkel, F. Tacke, *Nat. Rev. Immunol.* **17**, 306–321 (2017).
18. M. Xu *et al.*, *Cell* **178**, 1478–1492.e20 (2019).
19. X. Xiong *et al.*, *Mol. Cell* **75**, 644–660.e5 (2019).
20. K. B. Halpern *et al.*, *Nature* **542**, 352–356 (2017).
21. Z. Zhang *et al.*, *Nat. Commun.* **10**, 4562 (2019).
22. J. G. S. Madsen *et al.*, *Genome Res.* **28**, 243–255 (2018).
23. S. N. Zucker *et al.*, *Mol. Cell* **53**, 916–928 (2014).
24. C. Géraud *et al.*, *J. Clin. Invest.* **127**, 1099–1114 (2017).
25. C. N. Brocker *et al.*, *Am. J. Physiol. Gastrointest. Liver Physiol.* **312**, G283–G299 (2017).
26. C. Jin *et al.*, *Mol. Cell. Biol.* **22**, 4815–4826 (2002).
27. J. Bonnardel *et al.*, *Immunity* **51**, 638–654.e9 (2019).
28. T. Barrett *et al.*, *Nucleic Acids Res.* **41**, D991–D995 (2013).
29. F. Atger *et al.*, *Proc. Natl. Acad. Sci. U.S.A.* **112**, E6579–E6588 (2015).
30. M. P. Weng, B. Y. Liao, *Bioinformatics* **33**, 3505–3507 (2017).
31. J. Chong, D. S. Wishart, J. Xia, *Curr. Protoc. Bioinformatics* **68**, e86 (2019).
32. P. Stapor, X. Wang, J. Goveia, S. Moens, P. Carmeliet, *J. Cell Sci.* **127**, 4331–4341 (2014).
33. G. D. Norata *et al.*, *Immunity* **43**, 421–434 (2015).
34. W. Wahli, L. Michalik, *Trends Endocrinol. Metab.* **23**, 351–363 (2012).
35. F. Damiola *et al.*, *Genes Dev.* **14**, 2950–2961 (2000).
36. B. J. Greenwell *et al.*, *Cell Rep.* **27**, 649–657.e5 (2019).
37. F. Mange *et al.*, *Genome Res.* **27**, 973–984 (2017).
38. M. E. Hughes *et al.*, *J. Biol. Rhythms* **32**, 380–393 (2017).
39. A. Kalvisa *et al.*, *PLOS Biol.* **16**, e2006249 (2018).
40. F. Quagliarini *et al.*, *Mol. Cell* **76**, 531–545.e5 (2019).
41. E. L. McDearmon *et al.*, *Science* **314**, 1304–1308 (2006).
42. A. J. Pope, K. Karrupiah, P. N. Kearns, Y. Xia, A. J. Cardounel, *J. Biol. Chem.* **284**, 35338–35347 (2009).
43. J. Ye *et al.*, *Cell* **142**, 230–242 (2010).
44. E. Nagoshi *et al.*, *Cell* **119**, 693–705 (2004).
45. R. Öllinger *et al.*, *J. Cell Sci.* **127**, 4322–4328 (2014).
46. J. C. Dunlap, *Cell* **96**, 271–290 (1999).
47. A. Chaix, T. Lin, H. D. Le, M. W. Chang, S. Panda, *Cell Metab.* **29**, 303–319.e4 (2019).
48. M. E. Hughes, J. B. Hogenesch, K. Kornacker, *J. Biol. Rhythms* **25**, 372–380 (2010).

ACKNOWLEDGMENTS

We thank H. J. Richter, K. Zhu, Y. Zhang, Y. H. Kim, and other members of the Lazar lab for technical support and valuable discussions, particularly during the revision of this manuscript while sheltered in place during the coronavirus pandemic. We thank J. G. S. Madsen and S. Mandrup for advice on using the IMAGE program. **Funding:** We thank the Functional Genomics Core and the Viral Vector Core of the Penn Diabetes Research Center (P30 DK19525) for next-generation sequencing and virus preparation, respectively. We also acknowledge the Penn DRC Metabolomics Core at Princeton (DK19525). This work was supported by the JPB Foundation (M.A.L.) and the Cox Medical Research Institute (M.A.L.), as well as by National Institutes of Health grants R01-DK045586 (M.A.L.) and F32DK116519 (D.G.). C.Ja. and W.H. were supported by American Diabetes Association Training Grants [1-17-PDF-076 (C.Ja.) and 1-18-PDF-132 (W.H.)]. P.D. was supported by a postdoctoral fellowship from the American Heart Association (20POST35210738). **Author contributions:** D.G. and M.A.L. conceptualized the study, interpreted data, and wrote the manuscript, which was revised and approved by all authors. D.G. performed RNA-seq, ATAC-seq, and bioinformatics analysis. Y.Xio. and T.M.T. performed real-time qPCR. D.G. and Y.Xia. performed sNuc-seq. C.Ji. performed IMAGE analysis. C.Ja. and J.D.R. designed and performed metabolomics and FA synthesis rate. Y.Xio., T.M.T., W.H., P.D., and D.G. assisted with animal husbandry. **Competing interests:** J.D.R. is a consultant for Pfizer, scientific adviser to Colorado Research Partners, and cofounder of Toran. M.A.L. is a consultant to Pfizer, Novartis, Madrigal Pharmaceuticals, and Calico. **Data and materials availability:** The GEO accession number for the RNA-seq, ATAC-seq, and sNuc-seq data reported in this paper is GSE143528. M.A.L. obtained REV-ERBβ floxed mice under a material transfer agreement with the Centre Europeen de Recherche en Biologie et Medecine.

SUPPLEMENTARY MATERIALS

science.sciencemag.org/content/369/6509/1388/suppl/DC1
Materials and Methods
Figs. S1 to S10
Tables S1 to S10
References (*49*–*60*)
MDAR Reproducibility Checklist

View/request a protocol for this paper from *Bio-protocol*.

14 January 2020; accepted 16 July 2020
10.1126/science.aba8984

CORONAVIRUS

A molecular pore spans the double membrane of the coronavirus replication organelle

Georg Wolff[1], Ronald W. A. L. Limpens[1], Jessika C. Zevenhoven-Dobbe[2], Ulrike Laugks[3], Shawn Zheng[4], Anja W. M. de Jong[1], Roman I. Koning[1], David A. Agard[5], Kay Grünewald[3,6], Abraham J. Koster[1], Eric J. Snijder[2], Montserrat Bárcena[1]*

Coronavirus genome replication is associated with virus-induced cytosolic double-membrane vesicles, which may provide a tailored microenvironment for viral RNA synthesis in the infected cell. However, it is unclear how newly synthesized genomes and messenger RNAs can travel from these sealed replication compartments to the cytosol to ensure their translation and the assembly of progeny virions. In this study, we used cellular cryo–electron microscopy to visualize a molecular pore complex that spans both membranes of the double-membrane vesicle and would allow export of RNA to the cytosol. A hexameric assembly of a large viral transmembrane protein was found to form the core of the crown-shaped complex. This coronavirus-specific structure likely plays a key role in coronavirus replication and thus constitutes a potential drug target.

Severe acute respiratory syndrome coronavirus 2 (SARS-CoV-2) is the third and most impactful example of a potentially lethal coronavirus infection in humans within the past 20 years (*1*–*3*). Coronaviruses are positive-stranded RNA (+RNA) viruses that replicate their unusually large genomes in the host cell's cytoplasm. This process is supported by an elaborate virus-induced network of transformed endoplasmic reticulum (ER) membranes known as the viral replication organelle (RO) (*4*–*7*). Double-membrane vesicles (DMVs) are the RO's most abundant component and the central hubs for viral RNA synthesis (*5*). The DMV's interior accumulates double-stranded (ds) RNA, presumably intermediates of viral genome replication and subgenomic mRNA synthesis (*4*, *5*). DMVs may offer a favorable microenvironment for viral RNA synthesis and may shield viral RNA from innate immune sensors that are activated by dsRNA. However, coronaviral DMVs have been characterized as compartments that lack openings to the cytosol (*4*–*6*), despite the fact that newly-made viral mRNAs need to be exported for translation. Moreover, the coronavirus genome needs to be packaged by the cytosolic nucleocapsid (N) protein before being targeted to virus assembly sites on secretory pathway membranes (*8*).

In this study, we used cryo–electron microscopy (cryo-EM) to analyze the structure of coronavirus-induced ROs in their native host cellular environment. The murine hepatitis coronavirus (MHV) is a well-studied model for the genus *Betacoronavirus*, which also includes severe acute respiratory syndrome coronavirus (SARS-CoV), Middle East respiratory syndrome coronavirus (MERS-CoV), and SARS-CoV-2. One advantage of MHV over these class 3 agents is the absence of serious biosafety constraints, thus making MHV suitable for in situ cryo-EM studies. We performed electron tomography (ET) on cryo-lamellae prepared by focused ion beam milling of cells in the middle stage of MHV infection. The tomograms revealed abundant perinuclear DMVs with an average diameter of 257 ± 63 nm (±SD), occasionally interconnected or connected to the ER as part of the reticulovesicular network

[1]Section Electron Microscopy, Department of Cell and Chemical Biology, Leiden University Medical Center, Leiden 2333 ZC, Netherlands. [2]Molecular Virology Laboratory, Department of Medical Microbiology, Leiden University Medical Center, Leiden 2333 ZA, Netherlands. [3]Department of Structural Cell Biology of Viruses, Centre for Structural Systems Biology, Heinrich Pette Institute, Leibnitz Institute of Experimental Virology, 22607 Hamburg, Germany. [4]Howard Hughes Medical Institute, Department of Biochemistry and Biophysics, University of California San Francisco, San Francisco, CA 94143, USA. [5]Department of Biochemistry and Biophysics, University of California San Francisco, San Francisco, CA 94143, USA. [6]Department of Chemistry, MIN Faculty, Universität Hamburg, 20146 Hamburg, Germany.
*Corresponding author. Email: m.barcena@lumc.nl

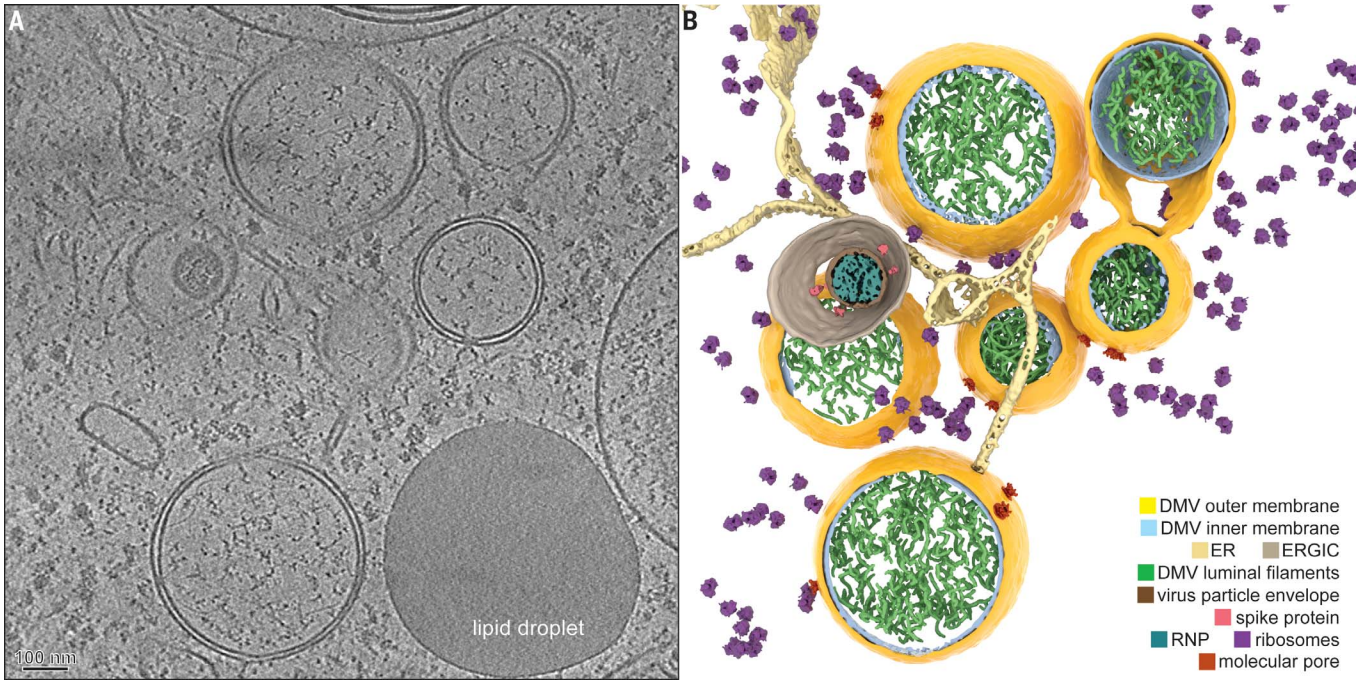

Fig. 1. Coronavirus-induced DMVs revealed by cryo-ET. (**A**) Tomographic slice (7 nm thick) of a cryo-lamella milled through an MHV-infected cell at a middle stage of infection. (**B**) Three-dimensional (3D) model of the tomogram, with the segmented content annotated. See also movie S1. ERGIC, ER-to-Golgi intermediate compartment.

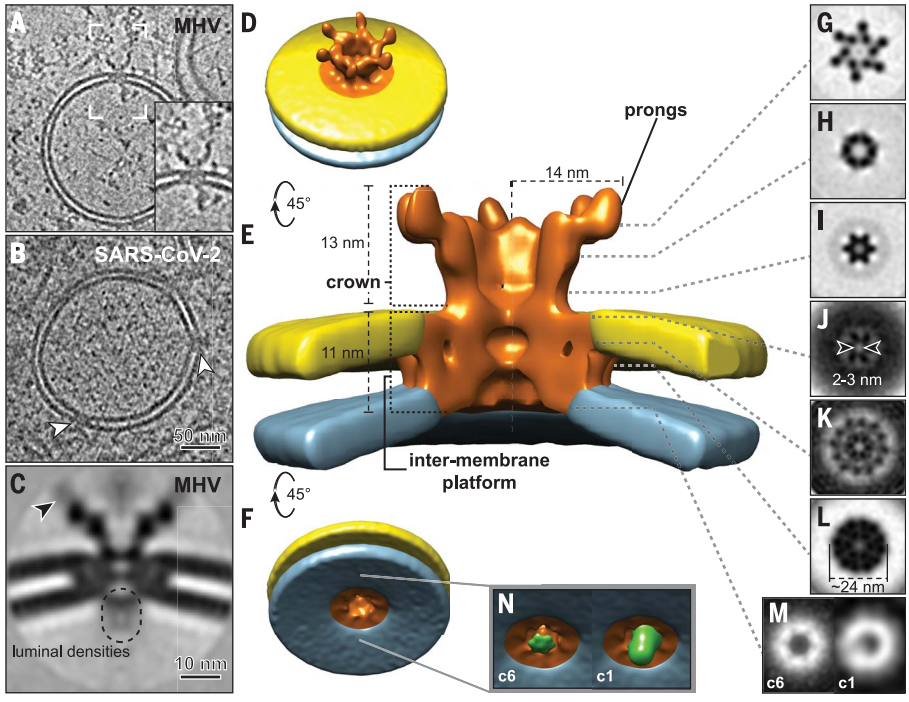

Fig. 2. Architecture of the molecular pores embedded in DMV membranes. Tomographic slices (7 nm thick) revealed that pore complexes were present in both (**A**) MHV-induced DMVs and (**B**) prefixed SARS-CoV-2–induced DMVs (white arrowheads). The inset in (A) is a close-up view of the area delineated by white brackets. (**C** to **L**) Sixfold-symmetrized subtomogram average of the pore complexes in MHV-induced DMVs. (C) Central slice through the average, suggesting the presence of flexible or variable masses near the prongs (black arrowhead) and on the DMV luminal side. (D to F) Different views of the 3D surface-rendered model of the pore complex (copper colored) embedded in the outer (yellow) and inner (blue) DMV membranes. (G to L) 2D cross-section slices along the pore complex at different heights (see also movie S2). (**M** and **N**) An additional density at the bottom of the sixfold-symmetrized volume (c6, green) appeared as an off-center asymmetric density in the unsymmetrized average (c1).

described in previous work (Fig. 1, fig. S1, and movie S1) (*4*–*7*). In addition, macromolecular features that had not been discerned in conventional EM samples became apparent (figs. S2 to S4). The DMV lumen appeared to primarily contain filamentous structures that likely correspond to viral RNA (Fig. 1 and fig. S4). In part, this is expected to be present as dsRNA (*4*, *5*), as supported by the relatively long, straight stretches observed in some of these filaments, consistent with the persistence length of dsRNA (*9*) (fig. S4).

Each DMV contained multiple copies of a molecular complex that spanned both membranes, connecting the DMV interior with the cytosol (Fig. 2A and supplementary text). Such complexes were also found in DMVs in prefixed SARS-CoV-2–infected cells (Fig. 2B and fig. S5). We surmise that this pore represents a generic coronaviral molecular complex that has a pivotal role in the viral replication cycle. Most likely, it allows the export of newly synthesized viral RNA from the DMVs to the cytosol. Functionally analogous viral complexes used for RNA export include those in the capsids of the *Reoviridae* (*10*) and, notably, the molecular pore in the neck of the invaginated replication spherules induced by flock house virus (*11*). None of these complexes, however, are integrated in a double-membrane organelle.

Subtomogram averaging of the double-membrane–spanning complexes in MHV-induced DMVs revealed an overall sixfold symmetry (Fig. 2, fig. S6, and movie S2). A cytosolic crown-like structure extended ~13 nm into the cytosol and was based on a ~24-nm-wide platform embedded in the DMV membranes. The two membranes did not fuse and maintained the typical DMV intermembrane spacing of ~4.5 nm (fig. S2). The complex formed a channel that followed its sixfold axis. On the DMV luminal side, the channel started with a ~6-nm-wide opening, narrowed toward the cytosol, and had two tight transition points (Fig. 2, J and L). The one at the level of the DMV outer membrane (Fig. 2J) was the most constricted, with an opening of ~2 to 3 nm, but would still allow the transition of RNA strands. Toward the cytosolic space, the complex opened into a crown-like structure, exposing six cytosolic "prongs." With an achieved resolution of 3.1 nm, we roughly estimate that the complex has a total molecular mass of 3 MDa, of which the crown represents ~1.2 MDa (fig. S6).

We then considered the possible constituents of this complex. Coronaviruses express two large replicase polyproteins that are proteolytically cleaved into 16 nonstructural proteins (nsps) (*12*). Three of these nsps—nsp3 (222 kDa in MHV), nsp4 (56 kDa), and nsp6 (33 kDa)—are transmembrane proteins and thus are potential components of the pore. These nsps contain two, four, and six transmembrane domains (TMDs), respectively (*13*–*15*) (Fig. 3A), and engage in diverse homotypic and heterotypic interactions (*16*) thought to drive the formation of double-membrane ROs (*17*–*19*). On the basis of its size, the multidomain MHV nsp3 subunit is an attractive putative constituent of the pore. MHV nsp3 consists of a large cytosolic region of ~160 kDa, followed by two TMDs and a C-terminal cytosolic domain of ~41 kDa (*13*). Whereas the TMDs and C-terminal domain are highly conserved, the domain composition and size of the N-terminal part of nsp3 is quite variable among coronaviruses (*16*, *20*). Several nsp3 domains, including the conserved N-terminal ubiquitin-like domain 1 (Ubl1; 12.6 kDa) that binds both single-stranded RNA (*21*) and the N protein (*22*, *23*), may interact with viral RNA (*16*).

To investigate whether nsp3 is a component of the DMV molecular pore, we imaged cells infected with a well-characterized engineered MHV expressing nsp3 with an enhanced green fluorescent protein (EGFP) moiety fused to the Ubl1 domain [MHV-Δ2-GFP3 (*24*)] (fig. S7). This mutant lacks nsp2, which is dispensable for replication in cell culture (*25*). Subtomogram averaging of the pore complexes in these samples (Fig. 3B) revealed the presence of six additional densities on top of the prongs, each representing a mass compatible with that of EGFP (Fig. 3, C to E, and movie S3). These results identified nsp3 as a major constituent of the complex and provided insight into its orientation, with the Ubl1 domain residing in the prongs. Six copies of nsp3 can be envisioned to constitute most of the cytosolic crown-like structure (~1.2 MDa). Other viral and/or host proteins and lipids are probably also part of the ~1.8-MDa intermembrane platform, with nsp4 and nsp6 being prominent candidates. Notably, different studies suggest that nsp3-nsp4 interactions drive membrane pairing and determine DMV biogenesis and morphology (*17*–*19*, *26*).

The molecular pores frequently appeared to interact with other macromolecules on both the cytosolic and DMV luminal sides (fig. S8). In the subtomogram averages, these appeared as largely blurred out densities (Fig. 2C), which suggests that the interactions are dynamic. A small region on the luminal side, however, had a relatively higher density and was resolved in the unsymmetrized average as a closely

associated and slightly off-center mass (Fig. 2, M and N, and fig. S6D). We speculate that this mass may be part of the viral replication machinery. The coronaviral replication-transcription complex (RTC) is thought to consist of a subset of relatively small (~10 to 110 kDa) nsps, with the RNA-dependent RNA polymerase (nsp12) at its core (*27*–*29*). However, some of these subunits may associate with the RTC only transiently, and the nsp stoichiometries of the complex are unknown.

The luminal partners of the pore complex, prominent as masses varying in shape and size, appeared to interact with the putative RNA content of the DMVs (fig. S8).

The interaction partners of the cytosolic nsp3 prong ranged from chain-like masses to larger assemblies (fig. S8, black arrowheads). The subdomains of the long N-terminal nsp3 domain engage in a range of viral and virus-host interactions (*16*, *20*); consequently, the list of possible interactors is substantial. Among them, the viral N protein (55 kDa), which binds to the nsp3 Ubl1 domain (*22*, *23*), is a prominent candidate. The Ubl1-N interaction has been proposed to target viral RNA to replication sites at early stages of infection (*23*), but it may also modulate RNA exit and encapsidation on the cytosolic side of the pore complex. Notably, DMV-rich regions of the cytosol were crowded with protein assemblies that had a diameter of ~15 nm (fig. S9). These proteins strongly resembled the nucleocapsid structure in coronavirus particles, a helical ribonucleoprotein (RNP) complex that consists of the RNA genome and N protein oligomers (*30*) (fig. S9).

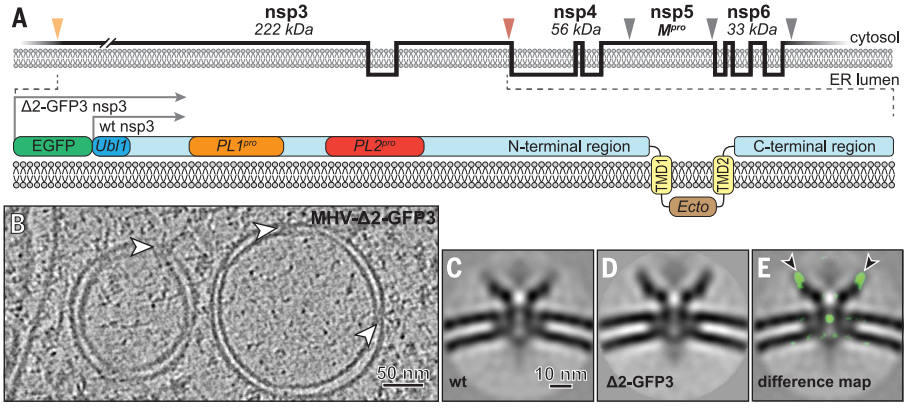

Fig. 3. The coronavirus transmembrane protein nsp3 is a component of the pore complex. (**A**) (Top) Membrane topology of MHV transmembrane nsps, with protease cleavage sites indicated by orange ($PL1^{pro}$), red ($PL2^{pro}$), and gray (M^{pro}) arrowheads. (Bottom) Detailed depiction of nsp3, showing some of its subdomains and the position of the additional EGFP moiety present in MHV-Δ2-GFP3. PL^{pro}, papain-like protease; M^{pro}, main protease. (**B**) Tomographic slice of DMVs induced by MHV-Δ2-GFP3, with embedded pore complexes (white arrowheads). (**C** and **D**) Comparison of the central slices of the sixfold-symmetrized subtomogram averages of the pore complexes in DMVs induced by (C) wild-type (wt) MHV and (D) MHV-Δ2-GFP3. (**E**) Density differences of 3 standard deviations between the mutant and wild-type structures, shown as a green overlay over the latter, revealed the presence of additional (EGFP) masses in the mutant complex (black arrowheads; see also movie S3).

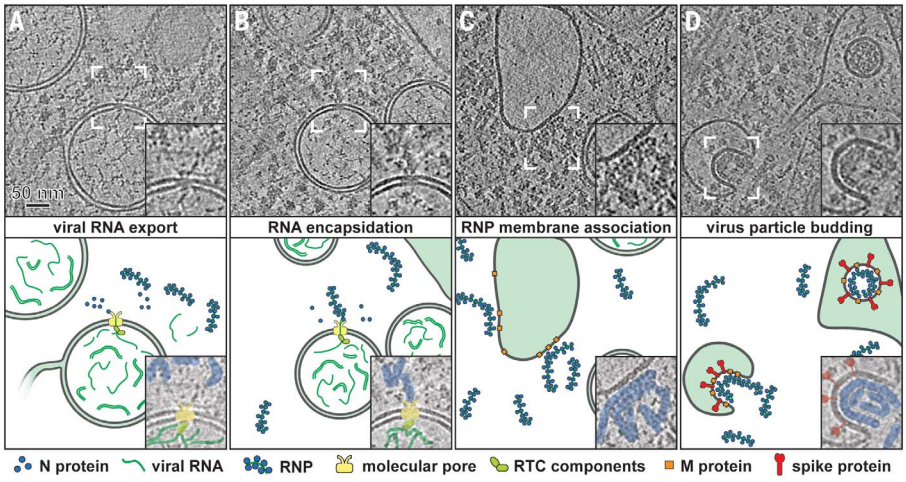

Fig. 4. Model of the coronavirus genomic RNA transit from the DMV lumen to virus budding sites. Tomographic slices from MHV-infected cells (top) highlight the respective steps in the model (bottom). (**A**) The molecular pore exports viral RNA into the cytosol, (**B**) where it can be encapsidated by N protein. (**C**) Cytosolic RNP complexes can then travel to virus assembly sites for membrane association and (**D**) subsequent budding of virions. The insets in the top panels provide close-up views of the areas delineated by white brackets.

Our findings suggest a pathway for newly made viral genomic RNA from the DMV interior, via the channel of the pore, to the cytosolic sites of encapsidation. In our model, specific replicase subunits may associate with the pore complex to guide the newly synthesized RNA toward it (Fig. 4A). As proposed for other +RNA viral ROs (*11*), only +RNAs would need to be exported, whereas negative-stranded templates and/or dsRNA intermediates could remain inside the DMVs. On the cytosolic side, all exported viral mRNAs may associate with the N protein (Fig. 4B). Alternatively, the accumulating N protein could serve to select part of the newly made genomes for packaging. The remainder would then be used for translation, together with the much smaller, though much more abundant, subgenomic mRNAs (*31*). Genome-containing RNP complexes would travel to the membranes where the viral envelope proteins accumulate and engage in the assembly of progeny virions (Fig. 4C) (*32*). These bud into single-membrane compartments (Fig. 4D), typically derived from the ER-to-Golgi intermediate compartment (*8*), and travel along the secretory pathway to be released into extracellular space.

The double-membrane–spanning molecular pore revealed here may constitute the exit pathway for coronaviral RNA products from the DMV's interior toward the cytosol, with the large and multifunctional nsp3 being its central component. Although the exact mode of function of this molecular pore remains to be elucidated, it seems to be a key structure in the viral replication cycle that is likely conserved among coronaviruses and thus may offer a coronavirus-specific drug target.

REFERENCES AND NOTES

1. T. G. Ksiazek *et al.*, *N. Engl. J. Med.* **348**, 1953–1966 (2003).
2. A. M. Zaki, S. van Boheemen, T. M. Bestebroer, A. D. Osterhaus, R. A. Fouchier, *N. Engl. J. Med.* **367**, 1814–1820 (2012).
3. N. Zhu *et al.*, *N. Engl. J. Med.* **382**, 727–733 (2020).
4. K. Knoops *et al.*, *PLOS Biol.* **6**, e226 (2008).
5. E. J. Snijder *et al.*, *PLOS Biol.* **18**, e3000715 (2020).
6. H. J. Maier *et al.*, *mBio* **4**, e00801–e00813 (2013).
7. M. Ulasli, M. H. Verheije, C. A. de Haan, F. Reggiori, *Cell. Microbiol.* **12**, 844–861 (2010).
8. C. A. de Haan, P. J. Rottier, *Adv. Virus Res.* **64**, 165–230 (2005).

9. J. A. Abels, F. Moreno-Herrero, T. van der Heijden, C. Dekker, N. H. Dekker, *Biophys. J.* **88**, 2737–2744 (2005).
10. K. Ding *et al.*, *Nat. Commun.* **10**, 2216 (2019).
11. K. J. Ertel *et al.*, *eLife* **6**, e25940 (2017).
12. E. J. Snijder, E. Decroly, J. Ziebuhr, *Adv. Virus Res.* **96**, 59–126 (2016).
13. M. Oostra *et al.*, *J. Virol.* **82**, 12392–12405 (2008).
14. M. Oostra *et al.*, *J. Virol.* **81**, 12323–12336 (2007).
15. A. Kanjanahaluethai, Z. Chen, D. Jukneliene, S. C. Baker, *Virology* **361**, 391–401 (2007).
16. B. W. Neuman, *Antiviral Res.* **135**, 97–107 (2016).
17. M. M. Angelini, M. Akhlaghpour, B. W. Neuman, M. J. Buchmeier, *mBio* **4**, e00524–e13 (2013).
18. D. Oudshoorn *et al.*, *mBio* **8**, e01658–e17 (2017).
19. M. C. Hagemeijer *et al.*, *Virology* **458–459**, 125–135 (2014).
20. J. Lei, Y. Kusov, R. Hilgenfeld, *Antiviral Res.* **149**, 58–74 (2018).
21. P. Serrano *et al.*, *J. Virol.* **81**, 12049–12060 (2007).
22. K. R. Hurst, C. A. Koetzner, P. S. Masters, *J. Virol.* **87**, 9159–9172 (2013).
23. Y. Cong, M. Ulasli, H. Schepers, M. Mauthe, *J. Virol.* **94**, e01925–e19 (2020).
24. M. C. Freeman, R. L. Graham, X. Lu, C. T. Peek, M. R. Denison, *J. Virol.* **88**, 5319–5327 (2014).
25. R. L. Graham, A. C. Sims, R. S. Baric, M. R. Denison, *Adv. Exp. Med. Biol.* **581**, 67–72 (2006).
26. M. J. Gadlage *et al.*, *J. Virol.* **84**, 280–290 (2010).
27. R. N. Kirchdoerfer, A. B. Ward, *Nat. Commun.* **10**, 2342 (2019).
28. M. Sevajol, L. Subissi, E. Decroly, B. Canard, I. Imbert, *Virus Res.* **194**, 90–99 (2014).
29. L. Subissi *et al.*, *Antiviral Res.* **101**, 122–130 (2014).
30. M. Gui *et al.*, *Protein Cell* **8**, 219–224 (2017).
31. N. S. Ogando *et al.*, *J. Gen. Virol.* 10.1099/jgv.0.001453 (2020).
32. L. Kuo, C. A. Koetzner, P. S. Masters, *Virology* **494**, 100–107 (2016).

ACKNOWLEDGMENTS

We thank M. Denison for sharing MHV-Δ2-GFP3, L. Caly and J. Druce for providing SARS-CoV-2 isolate betaCoV/Australia/VIC01/2020, N. Ogando for BSL3 assistance, F. Faas for technical support, S. Howes and T. Sharp for advice on image processing and helpful discussions, J. Plitzko and M. Schaffer for introducing us to cryo–focused ion beam milling, and J. Wolff, Y. van der Meer, and H. Friedrich for support during the lockdown. EM tomography data of MHV-infected samples were collected at the Netherlands Centre for Electron Nanoscopy (NeCEN) with assistance from C. Diebolder and R. Dillard. **Funding:** Access to NeCEN was made possible through financial support from the Dutch Roadmap Grant NEMI (NWO grant 184.034.014). D.A.A. was supported by NIH grants R35GM118099 and U19 AI135990. S.Z. was supported by the Howard Hughes Medical Institute. K.G. was supported by BMBF grant 05K18BHA and DFG grants EXC 2155, INST 152/772-1, and INST 777-1 FUGG. E.J.S. was supported by the #wakeuptocorona crowdfunding initiative of the Leiden University Fund (LUF) and LUMC Bontius Foundation and by the SCORE project (European Union's Horizon 2020 research and innovation program, grant 101003627). **Author contributions:** Conceptualization: M.B., A.J.K., E.J.S., and G.W. Software: D.A.A. and S.Z. Validation: M.B. and G.W. Formal analysis: M.B. and G.W. Investigation: M.B., A.W.M.d.J., U.L., R.W.A.L.L., G.W., and J.C.Z.-D. Resources: K.G., A.J.K., and E.J.S. Data curation: M.B., R.I.K., and G.W. Writing – original draft: M.B., E.J.S., and G.W. Writing – review & editing: D.A.A., M.B., K.G., A.J.K., U.L., E.J.S., and G.W. Visualization: M.B., R.I.K., R.W.A.L.L., and G.W. Supervision: M.B., A.J.K., and E.J.S. Project administration: M.B. and E.J.S. Funding acquisition: A.J.K. and E.J.S. **Competing interests:** The authors declare no competing interests. **Data and materials availability:** SARS-CoV-2 isolate betaCoV/Australia/VIC01/2020 and MHV-Δ2-GFP can be shared on request upon authorization from their original source (SARS-CoV-2: Leon Caly and Julian Druce, Doherty Institute, Melbourne, Australia; MHV-Δ2-GFP3: Mark Denison, Vanderbilt University Medical Centre, Nashville, TN, USA). Cryo-EM maps have been deposited in the Electron Microscopy Data Bank under accession codes EMD-11514 (wild-type MHV–induced molecular pore) and EMD-11515 (MHV-Δ2-GFP3–induced molecular pore). This work is licensed under a Creative Commons Attribution 4.0 International (CC BY 4.0) license, which permits unrestricted use, distribution, and reproduction in any medium, provided the original work is properly cited. To view a copy of this license, visit https://creativecommons.org/licenses/by/4.0/. This license does not apply to figures/photos/artwork or other content included in the article that is credited to a third party; obtain authorization from the rights holder before using such material.

SUPPLEMENTARY MATERIALS

science.sciencemag.org/content/369/6509/1395/suppl/DC1
Materials and Methods
Supplementary Text
Figs. S1 to S9
References (*33–50*)
MDAR Reproducibility Checklist
Movies S1 to S3

View/request a protocol for this paper from *Bio-protocol*.

22 June 2020; accepted 31 July 2020
Published online 6 August 2020
10.1126/science.abd3629

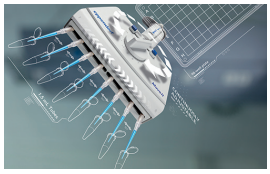

Adjustable Tip Spacing Pipettes

Eppendorf announces Move It Adjustable Tip Spacing Pipettes, an efficient, safe solution for synchronous pipetting of a series of samples between different vessel formats, such as between tubes and plates. Their operating time compared to that of single-channel pipettes is thus significantly reduced. Autoclavability is also enabled, which additionally increases user and sample safety. In practice, single-channel pipettes have been used to transfer individual samples from one vessel format to another—an inefficient, tedious, and error-prone method for routine work. Move It significantly accelerates and simplifies the workflow when frequent format changes are required. Further, manual adjustment of the tip distance with the adjustment knob allows the user to maintain a relaxed, ergonomic hand position even during format change. Move It is available with 4, 6, 8, and 12 channels, and can be mechanical or electronic.

Eppendorf
For info: 800-645-3050
www.eppendorf.com/move-it

SARS-CoV-2 IgG ELISA Kit

Our SARS-CoV-2 IgG ELISA Kit is an enzyme-linked immunosorbent assay (ELISA) designed for qualitative detection of immunoglobulin G (IgG) antibodies specific to SARS-CoV-2 in human serum samples issued under emergency use authorization as an aid in identifying individuals with an adaptive immune response to SARS-CoV-2. Formatted in a 96-well microplate (12 × 8 well strips), the assay is easily adapted for either automated open platforms or manual workflows. Designed for accurate and sensitive detection, the indirect ELISA has a two-step binding process involving a specific SARS-CoV-2 antigen and a horseradish peroxidase–conjugated antihuman IgG secondary antibody.

Enzo Life Sciences
For info: 800-942-0430
www.enzolifesciences.com/enz-kit170/sars-cov-2-igg-elisa-kit

Anti-Certolizumab Pegol Antibodies

Bio-Rad Laboratories has launched a range of anti-certolizumab pegol inhibitory antibodies to support the development of assays for therapeutic drug monitoring for all five marketed tumor necrosis factor alpha (TNFα) inhibitor biologics and their biosimilars. The range comprises three antibodies that are highly specific for the monoclonal antibody antigen-binding fragment certolizumab pegol (Cimzia) and that inhibit the binding of this drug to its target, TNFα. The antibodies are fully human in full-length immunoglobulin G (IgG) format and can be used as a surrogate positive control or calibration standard for an antidrug antibody (ADA) assay to measure levels of patient antidrug antibodies. TNFα inhibitors are used to treat a wide range of inflammatory conditions, such as rheumatoid arthritis, Crohn's disease, and psoriasis. The levels of serum drug and ADA concentrations are monitored in patients receiving TNFα antagonists to help guide clinical decision-making, optimize treatment, improve outcomes, and reduce health care costs.

Bio-Rad
For info: 800-424-6723
www.bio-rad-antibodies.com

Skeletal Muscle Differentiation Kit

AMS Biotechnology offers a Skeletal Muscle Differentiation Kit that enables you to differentiate human pluripotent stem cells to skeletal muscle myotubes with high yields, without cell sorting or genetic manipulation. Myotubes are contractile, express typical muscle markers, and show striated sarcomeres. Until recently, methods of studying muscular disease and potential therapies depended on invasive muscle biopsies to produce limited batches of primary cells. Use of primary cells presents challenges, not only in the collection process but also related to inconsistencies in cell growth, behavior, and life span, making it difficult to generate reliable experimental models. Our revolutionary Skeletal Muscle Differentiation Kit allows researchers to generate muscle from human pluripotent stem cells in three easy steps, via satellite-like or progenitor cells and myoblasts that then fuse to multinucleated myotubes in the third step. The kit protocol generates a highly pure population of approximately 70% skeletal muscle myotubes in a reproducible fashion.

AMS Biotechnology
For info: 617-945-5033
www.amsbio.com/skeletal-muscle-differentiation-kits.aspx

Inflammation Panel Kit

The Human QBeads Inflammation Panel Kit allows the measurement of seven human cytokines and chemokines typically associated with inflammatory responses to disease states, such as autoimmune diseases, chronic inflammation, and infections—including viral infections such as COVID-19. These custom-built, ready-to-run kits provide solution to monitor key biomarkers involved in cytokine release syndrome. Analytes offered in the Human QBeads Inflammation Panel Kit include human interferon gamma, Interleukin-2, Interleukin-6, CCL2 (MCP-1), CCL3 (MIP-1α), CXCL9 (MIG), and CXCL10 (IP-10). Cytokine storm syndrome, also known as cytokine release syndrome, is an inflammatory response commonly caused by viral infections. It is characterized by excessive or uncontrolled release of proinflammatory cytokines. Respiratory virus infections can induce abnormal cytokine production in the host. To better understand host defense mechanisms against viruses, it is important to monitor cytokine production and signaling pathways during viral infection.

Intellicyt
For info: 734-769-1600
intellicyt.com/inflammation-panel-kit

Liquid Nitrogen–Based Automated Storage System

Brooks Life Sciences offers BioStore IIIv, an automated, next-generation alternative to manual –80°C mechanical freezers. BioStore IIIv operates like a vending machine; after a secure login has been entered on the touchscreen, the patented design automatically locates and lifts the storage racks and will eject the targeted material upon the user, indicating they are ready to receive it. This design protects all materials by providing a stable temperature during inventory interactions. For comparison, a mechanical freezer chamber can warm by as much as 40° during a routine door opening, with additional time required for the system to recool when the door is closed. A single BioStore IIIv freezer holds up to 63,000 2.0-mL vials. In the event of a natural or man-made disaster, BioStore IIIv has built-in protection—maintaining safe temperatures for upwards of 4 days—an improvement of 16X over –80°C mechanical freezers.

Brooks Life Sciences
For info: 800-379-7221
www.brooks.com

Electronically submit your new product description or product literature information! Go to www.sciencemag.org/about/new-products-section for more information.

Newly offered instrumentation, apparatus, and laboratory materials of interest to researchers in all disciplines in academic, industrial, and governmental organizations are featured in this space. Emphasis is given to purpose, chief characteristics, and availability of products and materials. Endorsement by *Science* or AAAS of any products or materials mentioned is not implied. Additional information may be obtained from the manufacturer or supplier.

ScienceCareers online @sciencecareers.org

VANDERBILT UNIVERSITY
MEDICAL CENTER

FACULTY POSITION IN COMPUTATIONAL MICROBIOLOGY AND IMMUNOLOGY

VANDERBILT UNIVERSITY MEDICAL CENTER
Department of Pathology, Microbiology, and Immunology
Department of Medicine
Program in Computational Microbiology and Immunology
Vanderbilt Center for Immunobiology
Vanderbilt Institute for Infection, Immunology and Inflammation

Vanderbilt University Medical Center, through an institution-wide initiative, invites applications for faculty positions in Computational Microbiology and Immunology at all levels. Successful candidates will be expected to establish and maintain an independent research program focusing on the development and application of computational methods in the areas of microbiology and/or immunology, and to participate in teaching of graduate and medical students. Areas of particular interest include, but are not limited to, host-pathogen interactions, cancer immunology, microbiome research, evolutionary microbiology, and systems immunology. Candidates should have substantial post-graduate training highlighted by peer-reviewed publications that demonstrate research productivity.

Vanderbilt University Medical Center, located on the Vanderbilt University campus, is home to internationally recognized programs in bioinformatics, drug discovery, global health, inflammation, imaging science, pharmacology, proteomics, and vaccine science. The School of Medicine consistently ranks in the Top 20 US Medical Schools and provides outstanding opportunities for scholarship, collaboration, and teaching.

The Vanderbilt University campus is located in the heart of Nashville, the capital of Tennessee, known internationally as "Music City, USA". Nashville is also the home to professional sports teams, the Nashville Symphony, the Frist Center for the Visual Arts, and numerous activities for outdoor enthusiasts. Nashville is a wonderful place to live, work, and raise a family.

Applicants should send a curriculum vitae, a statement of current and future research interests, and at least 3 letters of reference to: Ivelin Georgiev, Ph.D., Director, Program in Computational Microbiology and Immunology, Vanderbilt University Medical Center at **vi4.cmi@vumc.org**. Review of applications will commence immediately, but all applications received by **October 31, 2020** will receive full consideration.

Vanderbilt University Medical Center is an Affirmative Action/ Equal Opportunity Employer. Women and minority candidates are encouraged to apply.

Yale University
School of Medicine

FACULTY POSITION AT THE ASSISTANT PROFESSOR LEVEL

DEPARTMENT OF CELLULAR AND MOLECULAR PHYSIOLOGY

The Department of Cellular and Molecular Physiology is conducting a search for new faculty members at the assistant professor level.

The search seeks candidates whose research connects the properties of molecules to the properties of physiological systems.

Excellent opportunities are available for collaborative research, as well as for graduate and medical student teaching. Candidates must hold a Ph.D., M.D., or equivalent degree. Applicants should include a cover letter, curriculum vitae, a statement that describes past research accomplishments and future goals, and should arrange to have three letters of reference sent. Applicants should apply at the following website: **http://apply.interfolio.com/78493**

Application Deadline: **November 2, 2020**

Yale University is an Affirmative Action/Equal Opportunity Employer and welcomes applications from women, persons with disabilities, protected veterans, and members of minority groups.

SAINT LOUIS UNIVERSITY

POSTDOCTORAL POSITIONS

DEPARTMENT OF BIOCHEMISTRY
AND MOLECULAR BIOLOGY
SAINT LOUIS UNIVERSITY SCHOOL OF MEDICINE

Saint Louis University, a Catholic Jesuit institution dedicated to education, research, health care, and service, is seeking outstanding applicants for **postdoctoral positions** to study the structure and enzymology of several coagulation factors in the laboratory of Dr. Enrico Di Cera in the Edward A. Doisy Department of Biochemistry and Molecular Biology (**https://biochem.slu.edu/faculty/dicerawp**). Experience in rapid kinetics, smFRET, X-ray crystallography, NMR, or cryoEM is required. Please submit CV to **enrico@slu.edu** and a cover letter, curriculum vitae, application, and addresses of three references to: **https://slu.wd5.myworkdayjobs.com/en-US/Careers/job/SLU-Saint-Louis-MO/Post-Doctoral-Fellow_2020-00705**.

Saint Louis University is an Affirmative Action, Equal Opportunity Employer, and encourages nominations and applications of women and minorities.

The Paris Region Fellowship Program 2020

Two calls for a total of 52 post-doctoral positions in a large panel of disciplines for international researchers of all nationalities,

Professional training programme and career development opportunities for recruited researchers,

Call deadline October, 21st, 2020

Further information :
parisregion.eu/parisregionfp.html

Application Website :
https://parisregionfp.sciencescall.org/

This project has received funding from the European Union's Horizon 2020 research and innovation programme under the Marie Skłodowska-Curie actions Grant Agreement n° 945298-ParisRegionFP.

Région îledeFrance

Fellowships for Postdoctoral Scholars at Woods Hole Oceanographic Institution

New or recent doctoral recipients are encouraged to submit applications prior to October 15, 2020.

Awards related to the following areas are anticipated: Applied Ocean Physics & Engineering; Biology; Geology & Geophysics; Marine Chemistry & Geochemistry; Physical Oceanography; The Center for Marine and Environmental Radioactivity; The National Ocean Sciences Accelerator Mass Spectrometry Facility; The Ocean Bottom Seismic Instrument Center; The Ocean Twilight Zone Project; and a joint USGS/WHOI award. Interdepartmental research is also encouraged.

Awards are competitive, with primary emphasis on research promise. Scholarships are 18-months with an annual stipend of $62,250, a health and welfare allowance and a research budget. Recipients are encouraged to pursue their own research interest in association with resident staff. Communication with potential WHOI advisors prior to submitting an application is encouraged. Recipients of awards can begin any time after January 1 and before December 1, 2021.

WOODS HOLE OCEANOGRAPHIC INSTITUTION

www.whoi.edu/postdoctoral

VIRGINIA TECH™

Faculty Position in Quantitative Neuroscience

We seek a motivated individual to be part of a next generation effort in human neuroscience organized around novel approaches in neuroimaging, neuro-modeling, and human neuroscience. We are particularly interested in applicants with an interest in applying their approaches or developing new ones in the area of Computational Psychiatry. In this area, we seek applications for a tenure-track Assistant Professor. While there are no restrictions on the training trajectory of the successful applicant, it is paramount that they demonstrate through their publication history a capacity for transdisciplinary work. The successful applicant will be expected to interact with the existing group of investigators in the Center for Human Neuroscience Research and the Computational Psychiatry Unit (**http://labs.vtc.vt.edu/cpu/**) at the Fralin Biomedical Research Institute at Virginia Tech Carilion (**https://research.vtc.vt.edu**). The institute has three state-of-the-art 3T MRI machines dedicated to research, a state-of-the-art optically pumped magnetometry suite, laboratory facilities focused on *in vivo* electrochemical measurement of neurotransmitters, a large server farm dedicated to computational neuroscience and a focus on decision-making that underlies health behaviors and psychopathology.

Applications will be reviewed continuously until the position is filled. It is expected that initial interviews will begin in September of 2020. To apply, please submit your application including curriculum vitae, detailed statement of research accomplishments and plans and teaching/mentoring philosophy at **www.jobs.vt.edu**, posting # 01101F. Also, have at least three references post their letters of support to the same site.

Virginia Tech recognizes the critical importance of diverse teams of scholars. It seeks to diversify its faculty along multiple dimensions. Virginia Tech is a public global land-grant university, committed to research, teaching and learning, and outreach to the Commonwealth of Virginia, the nation, and the world. Building on its motto of *Ut Prosim* (that I may serve), Virginia Tech is dedicated to InclusiveVT-**https://www.inclusive.vt.edu/** serving in the spirit of community, diversity, and excellence. We seek candidates who adopt and practice the Principles of Community (**https://www.inclusive.vt.edu/Programs/vtpoc0.html**), which are fundamental to our on-going efforts to increase access and inclusion and to create a community that nurtures learning and growth for all of its members.

Inquiries about the position should be directed to the chair of the search committee, P. Read Montague (**read@vtc.vt.edu**) or the director of the institute, Michael J. Friedlander (**friedlan@vtc.vt.edu**).

Virginia Tech is an Equal Opportunity Employer. For inquiries regarding non-discrimination policies, contact the Office of Equity and Access at 540-231-2010 or Virginia Tech, North End Center, Suite 2300 (0318), 300 Turner St. NW, Blacksburg, VA 24061.

Science Careers online @sciencecareers.org

By **Abigail M. Brown**

Data-driven advice for grad school

"Do you have any advice for future graduate students?" I asked. The student had recently defended his Ph.D., and I was conducting an exit interview—something I do with every graduating biomedical Ph.D. student at my university, where I am in charge of evaluating our medical school's Ph.D. training programs. He sat back in his chair and thought for a minute before responding: He wished he had started to plan for his post-Ph.D. career earlier. My shoulders dropped and I let out a sigh. "Program directors recommend this to incoming students every year, but some don't seem to hear it," I said. "How do you think we can get them to listen?" This time, he didn't hesitate. "They are graduate students in *science*," he exclaimed. "Show them the data!"

That was my aha moment. I immediately began to document the responses to this question in subsequent interviews. It has been 3 years now, and the data I've collected confirm my suspicions—the same answers come up again and again. As a new cohort of Ph.D. students starts grad school this fall, here are the five pieces of advice graduates offer most frequently.

"Even when you're just getting started, you need to look forward."

CHOOSE YOUR MENTOR CAREFULLY

Thirty-two percent of graduating students said this is the most critical decision a Ph.D. student can make. Many students gravitate toward mentors who work in areas they find interesting and exciting, but it is also important to think about what style of mentoring you respond to best. Finding a mentor with the right mentoring approach for you is at least as important as finding one who studies a specific topic.

START PLANNING YOUR FUTURE CAREER EARLY

You need time to (a) decide which career paths you find appealing and (b) start preparing for those careers. Twenty percent of graduating students recommended exploring future careers as early as possible so you can use your time in grad school to build additional skills you will need. To learn about specific professions, you can conduct informational interviews, attend seminars where alumni discuss their careers, do an internship, or engage in a variety of other options.

PAY ATTENTION TO YOUR MENTAL HEALTH

Graduate school is full of ups and downs. Thirteen percent of graduates said that if you feel the need to talk to someone on or off campus, don't hesitate. "If you are not happy, try to do something about it and make a change," one student said. If you feel isolated, another student recommended joining a campus group to connect with others.

MAP OUT YOUR GOALS

Twelve percent of graduates recommended that students consistently and critically evaluate their progress throughout their training. Make an outline of your research and career goals and when you want to achieve them, and hold yourself to that plan. Some students use an individual development plan to prompt discussions with their mentor and thesis committee. But don't wait for these meetings; setting goals and holding yourself accountable should be a continuous habit.

FIND WORK-LIFE BALANCE

This looks different for different people, but don't ignore it. You should expect to work hard in grad school, but the right work-life balance can have an important influence on your mental health and overall quality of life. Nine percent of graduates recommended finding something that helps you unwind, such as pursuing hobbies, getting together with friends, or volunteering in the community.

Observant readers may notice that the numbers above only add up to 86%. Other pieces of advice included be assertive and ask for what you need, learn to trust your experimental results as long as the controls work, and plan your projects around what's needed for a publishable paper. But the most important thing is to take these pointers to heart early on. Even when you're just getting started, you need to look forward. ■

Abigail M. Brown is the director of outcomes research for biomedical Ph.D. programs at Vanderbilt University School of Medicine in Nashville, Tennessee. Send your career story to SciCareerEditor@aaas.org.

ILLUSTRATION: ROBERT NEUBECKER

Published by AAAS